

This item was submitted to Loughborough University as a PhD thesis by the author and is made available in the Institutional Repository (<https://dspace.lboro.ac.uk/>) under the following Creative Commons Licence conditions.



For the full text of this licence, please go to:  
<http://creativecommons.org/licenses/by-nc-nd/2.5/>



**Pilkington Library**

Author/Filing Title ..... GRUNERT .....

Vol. No. .... Class Mark ..... T .....

**Please note that fines are charged on ALL  
overdue items.**

OPEN SHELF COPY

REFERENCE ONLY

0402450795



**ANALYSIS OF CRANKSHAFT-CRANKCASE  
INTERACTION FOR THE PREDICTION OF THE  
DYNAMIC STRUCTURAL RESPONSE AND NOISE  
RADIATION OF IC-ENGINE STRUCTURES**

by


**Thomas Grünert**

A Doctoral Thesis

Submitted in partial fulfilment of the requirements  
for the award of the  
Degree of Doctor of Philosophy  
in the Department of  
Aeronautical and Automotive Engineering and Transport Studies  
Loughborough University

2000

© T.Grünert 2000

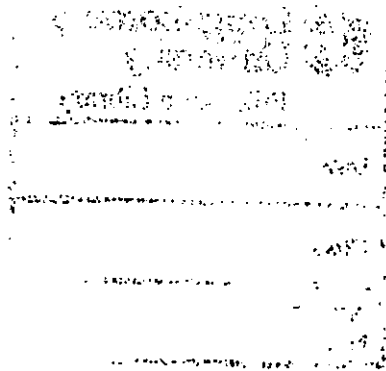
 Loughborough University Physical Library
Date <i>Dec 01</i>
Class
Acc No. <i>040246079</i>

*Dedication*

*To*

*My Family and Friends*

*For their patience, encouragement and faith throughout the work*



## *Acknowledgments*

*I would like to take this opportunity to thank several colleagues for their various contribution to the ground work presented in this thesis. Particularly thanks are due to B.Pfingsthorn, M.Joerres, P.O'Mahony, D.Liebe, S.Kraf, D.Ottersbach, R.Grosse, T.Eutebach, and C.Jubel. Further, I would like to thank all colleagues contributing to the measurements taken throughout this project, especially Ford Vibration and Acoustic Laboratories, FEV Motorentchnik, and Ricardo Engineering.*

*I would also like to thank the management of Engine Engineering at Ford for their support of this project. Special thanks are due to J.Meyer, B.Wallbrück, L.Brouwer and G.Schwertfirm.*

*Last but not least I wish to express my appreciation for the time and effort spent by Dr.R.Ali and Dr.S.Wang. Their guidance and hints, as well as interesting discussions on the subject, were essential to the successful completion of this work.*

*Thomas Grünert*

*August 2000*

## **Abstract**

This thesis presents research work which is concerned with the development of analytical and numerical methods for the dynamic analysis of the crankshaft-crankcase assembly. The effects of interaction of crankshaft and crankcase on the dynamic response of an IC engine block structure are studied. These methods are especially attractive for the simulation of the steady state response of rotating systems with many degrees of freedom which are forced by multiple periodic excitations. A major novelty of the methods is the ability to model the system non-linearities successfully as frequency dependent properties.

An ideal application of the methods is in the analysis of the dynamic response of a modal model of the crankshaft-crankcase assembly in the frequency domain. This includes non-linear main-bearing and rotating properties. The differences, drawbacks and advantages between the applied methodology and other approaches are assessed and discussed.

The dynamic response of engine surfaces are obtained and used for radiated noise analyses. Appropriate noise radiation methodology and software are developed and some existing software are enhanced. Comparisons are made with measurements and other accepted noise radiation codes. Advantages, differences and shortcomings of the applied noise radiation methods are discussed.

The developed methodologies for the description of the dynamic characteristics of a running engine and the noise radiation phenomenon are applied to a comprehensive study of various designs of IC engines. Different engine block bottom-end and flywheel design alternatives are studied for the prediction of noise characteristics. The analytical results are compared with laboratory measurements for the validation of theoretical predictions.

Finally, open issues and further envisaged work in the area of modelling, excitation prediction and accuracy enhancements are discussed and an approach for the next steps is outlined.

## Contents

1 Introduction .....	-1-
2 Engine Bottom-End and Crankshaft Design Basics .....	-12-
2.1 Engine Bottom-End Design Basics .....	-13-
2.2 Crankshaft Design Basics .....	-16-
2.3 Flywheel Design Basics .....	-21-
3 Dynamics of Rotating Systems .....	-26-
3.1 Introduction .....	-27-
3.2 Undamped Rotating Structures with Rigid and Elastic Bearings .....	-29-
3.3 Laval-Rotor with internal and external Damping .....	-40-
3.4 Resonance Phenomenon and Stability Criteria .....	-43-
3.5 Laval-Rotor with Hydrodynamic Bearings .....	-45-
3.6 Gyroscopic Effect .....	-51-
3.7 Non-Uniform Rotating Structures .....	-62-
3.8 Second Order Vibration of Flexible Shafts .....	-68-
4 Hydrodynamic Bearings .....	-71-
4.1 Introduction to Non Stationary Loaded Radial Bearings .....	-72-
4.2 Definition of Spring- and Damping-Coefficients .....	-75-
4.2.1 Comparison of Theoretical Results and Measurements .....	-80-
4.2.2 Simplified Approximation-Model .....	-83-
4.3 Development of Frequency Dependent Bearing Properties .....	-89-
5 Development of Forcing Function .....	-120-
5.1 General Overview .....	-121-
5.2 Applied Approach .....	-129-
6 Frequency Domain Solution for Crankshaft-Crankcase Dynamics .....	-138-
6.1 Fourier Solution for Linear Time-Variant Systems .....	-141-
6.2 Slider Crank and Other General Mechanisms .....	-150-
6.3 Frequency Domain Solution for Non-Linear Coupled Systems .....	-151-
6.3.1 Investigation of Applied Initial Stiffness Properties .....	-151-
6.3.2 Non-Linear Coupled Vibrations of Elastic Systems .....	-156-
6.3.3 Stability of Non-Linear Coupled Systems .....	-158-
6.4 Forced Response Analysis .....	-161-
6.5 Solution Method / FEM-Application .....	-164-
7 Noise Analysis Methodologies .....	-165-
7.1 General Overview and Analysis Methods .....	-167-
7.2 Noise Evaluation Methods .....	-176-
7.2.1 General Overview and Existing Methods .....	-176-
7.2.2 Development of Noise Estimation Model .....	-178-
7.3 Rayleigh-Method .....	-189-
7.3.1 Theory .....	-189-
7.3.2 Application and Verification using Component Models .....	-192-
7.3.3 Enhancements .....	-204-
8 Design Analysis and Verification .....	-205-
8.1 Design Studies .....	-206-
8.1.1 Engine Description and Modelling Approach .....	-207-
8.1.2 Powertrain Modal Analysis .....	-218-
8.2 Crankshaft and Flywheel Whirling .....	-219-
8.2.1 Analytical Approach .....	-220-
8.2.2 Measurements and Verification .....	-236-
8.3 Noise Radiation .....	-242-
8.3.1 Surface Velocity Investigation .....	-242-
8.3.2 Noise Measurements .....	-250-
8.3.3 Noise Analysis and Verification .....	-252-



8.3.4 Auralisation .....	-262-
9 Discussions and Conclusions .....	-265-
References .....	-271-
Appendices .....	-281-
Appendix 1 Frequency Dependent Forcing Function .....	-281-
Appendix 2 Frequency Coupled System Matrices .....	-284-
Appendix 3 Flywheel Whirl Test and Analysis Procedure .....	-286-
Appendix 4 Figures .....	-289-
Appendix 5 Tables .....	-344-
Appendix 6 Description of Ford Zetec-SE Engine .....	-353-
Publications .....	-357-

## Notation

$a_{pr}$	component of acceleration at crank pin in r (radial) direction of crank
$a_{p\Theta_{cr}}$	component of acceleration at crank pin in $\Theta_{cr}$ (tangential) direction of crank
$a_k$	Fourier displacement coefficients (sin-coefficients)
$b_{ik}$	dimensional damping coefficients of bearing
$b_k$	Fourier displacement coefficients (cos-coefficients)
$c_0$	speed of sound in air
$c_{ik}$	dimensional stiffness coefficients of bearing
$c, c_x, c_y, c_h, c_v$	stiffness property, either general or directional
$c_{total\ h,v}$	bearing stiffness properties of simplified approach in principal directions
$d = 2r$	shaft diameter
$e$	absolute eccentricity
$e_r$	unit vector in radial direction of the crank
$e_{\Theta_{cr}}$	unit vector in tangential direction of the crank
$\tilde{f}$	frequency coupled forcing function referring to time domain forcing function $F(t)$
$f_{i,g,o}$	border frequencies of radiation efficiency
$f(t)$	vector of generalised externally applied forces.
$f_w$	force matrix of inertia
$h$	wrist piston offset
$h_{pl}$	height (thickness) of noise radiating plate
$k$	inertia radius
$k_i$	linear viscous damping property
$k_{He}$	frequency relation of Helmholtz
$l_r$	connecting rod centre distance
$m$	mass of body, shaft, inertia
$m_c$	rotating mass of connecting rod
$m_p$	reciprocating mass of piston assembly and rod
$n_T$	number of tips
$n_R$	number of correct tips
$p$	pressure of medium (oil or air)
$p_T$	single tip probability
$p(\Theta_{cr})$	gas pressure acting on the piston
$r_{se}$	radius of eccentricity of centre of eccentricity
$r_{we}$	radius of eccentricity of shaft
$r_s$	radius of centre of shaft
$r_w$	radius of centre of inertia
$t$	independent variable of time
$\tilde{u}$	frequency coupled complex mode shape assembled referring to time domain response vector $u(t)$

$u(t)$	variable system response vector (displacement vector)
$u_{gg}$	assembled displacement vector, g-set
$u_{hh}$	assembled displacement vector, h-set
$v$	sound velocity of the surface structure
$x_w$	displacement matrix of inertia
$y_s$	shaft centre of gravity displacement in y-direction
$y_w$	shaft displacement in y-direction
$z_s$	shaft centre of gravity displacement in z-direction
$z_w$	shaft displacement in z-direction
$A$	surface of structure
$A_{0,i}$	solution coefficients of characteristic equation
$AN$	parameter of polynomial bearing equation
$A_p$	area of piston
$\tilde{A}$	assembled spin vibration and inertia matrix
$B$	bearing width
$B_{gg}$	assembled damping matrix, g-set
$B_{hh}$	assembled damping matrix, h-set
$\tilde{B}(\Omega)$	spin vibration, dynamic stiffness matrix
$B_L$	damping matrix of bearing pin
$BN$	parameter of polynomial bearing equation
$C_L$	stiffness matrix of bearing pin
$CN$	parameter of polynomial bearing equation
$D = 2R$	bearing diameter
$D_a$	external, non-dimensional damping property
$D_i$	internal, non-dimensional damping property
$D_{nom}$	constant damping matrix (sub-matrix)
$D(\omega)$	frequency dependent damping matrix
$D(t)$	variable dissipative and mechanism dependent damping matrix
$F, F_x, F_y$	force, either general or directional
$F_c$	crankpin force
$F_{stat}$	static load
$G$	gyroscopic matrix
$G_r$	function of Green
$G_{gh}$	transformation matrix (g-set to h-set)
$G(t)$	variable gyroscopic and mechanism dependent Coriolis matrix
$\tilde{G}$	assembled gyroscopic matrix
$I_x, I_y$	mass moment of inertia about x,y-axis
$K$	constant, real symmetric stiffness matrix
$K_0$	constant stiffness matrix
$K_{L(\alpha)}$	geometric non-linear stiffness matrix

$K_\delta$	initial stiffness matrix
$K_{\text{constant}}$	constant part of stiffness matrix $\bar{K}$
$\bar{K}$	assembled, non-linear stiffness matrix (no time variant)
$K(\omega)$	frequency dependent stiffness matrix
$K_{gg}$	assembled stiffness matrix, g-set
$K_{hh}$	assembled stiffness matrix, h-set
$K_{\text{nom}}$	constant stiffness matrix (sub-matrix)
$K_{\text{is,ic}}$	Fourier stiffness matrix coefficients
$K(t)$	variable dissipative and mechanism dependent stiffness matrix
$\tilde{K}$	assembled, frequency coupled stiffness matrix, associated with the time variant stiffness matrix $K(t)$
$L$	sound intensity level
$L_{x,y,z}$	angular moement in x,y,z-direction
$M$	constant, the real symmetric mass matrix
$M_{gg}$	assembled mass matrix, g-set
$M_{hh}$	assembled mass matrix, h-set
$M_{w,y,z}$	equilibrium moment for shaft displacement
$M(t)$	variable mass and mechanism geometric inertia matrix
$\tilde{M}$	assembled mass matrix
$P$	sound power
$P_g$	force vector, g-set
$P_h$	force vector, h-set
$P_{\text{stat}}$	bearing load under static condition
$P_D$	bearing oil pressure due to angular movement
$P_R$	resulting bearing oil pressure
$P_V$	bearing oil pressure due to radial movement
$P_T$	total probability of sample
$Q_{hh}$	complex, non-linear frequency dependent damping and stiffness properties matrix
$R$	radius of crank
$\Delta R = R - r$	bearing clearance
$S_o$	Sommerfeld number
$T$	period
$V$	volume
$X_L$	displacement matrix of bearing pin
$\alpha$	solution coefficient for bearing stability
$\beta$	angle between the rod and the crank
$\beta_{ik}$	non-dimensional damping coefficients of bearing
$\delta$	eccentricity of bearing journal
$\delta_w$	elastic deflection of shaft
$\delta(t)$	second order,torsional fluction of rotating shaft

$\varepsilon$	eccentricity of shaft, centre of mass or bearing journal
$\eta = \Omega/\omega$	frequency ratio of shaft angular velocity and shaft eigenfrequency
$\eta_{oil}$	oil viscosity
$\eta_w$	complex coordinates of shaft (imaginary component)
$\gamma$	phase angle
$\gamma_{ik}$	non-dimensional stiffness coefficients of bearing
$\lambda_i$	eigenvalue, solution of characteristic equation
$\mu$	stiffness and frequency ratio of non-uniform rotating shaft
$\mu_{pl}$	poisson ratio of noise radiating plate
$\psi = (D-d)/d$	relative bearing clearance
$\omega$	eigenfrequency
$\omega_{\eta, \zeta}$	eigenfrequency of non-uniform rotating shaft in principal directions
$\omega_v$	eigenfrequency of rotating gyroscopic system
$\omega_y$	eigenfrequency of the shaft in y-direction
$\omega_z$	eigenfrequency of the shaft in z-direction
$\rho$	angle of eccentricity
$\rho_0$	density of air
$\rho_s$	angle of centre of shaft
$\rho_{pl}$	density of noise radiating plate
$\rho_w$	angle of centre of inertia
$\rho_{y,z}$	directional angular displacement of inertia
$\sigma_{rad}$	radiation efficiency or radiation ratio
$\theta$	associated eigenvector
$\zeta_w$	complex coordinates of shaft (real component)
$\Delta_{cr}$	stability condition for contra-rotating system
$\Delta_{sr}$	stability condition for synco-rotating system
$\tilde{\Lambda}$	assembled vibration harmonic order matrix being specified as multiple of the engine spin order referring to the used system degree of harmonics
$\Omega$	$\frac{\partial \theta_{cr}}{\partial t}$ , rotational speed of crank; shaft angular velocity
$\Omega_{cut-off}$	shaft speed of beginning instability with bearing properties
$\Omega_{cr}$	contra-rotating bending critical speed of shaft
$\Omega_{sr}$	synco-rotating bending critical speed of shaft
$\Phi$	angle between connecting rod and cylinder axis
$\Pi$	pressure code for Reynold's equation
$\frac{\partial \Phi}{\partial t}$	oscillating velocity of the connecting rod
$\frac{\partial^2 \Phi}{\partial t^2}$	oscillating acceleration of the connecting rod
$\Theta$	mass moment of inertia
$\Theta_a$	axial mass moment of inertia
$\Theta_p$	polar mass moment of inertia
$\Theta_{cr}$	crank angle

## List of Figures

Figure 1.1	Proportional Weight of Engine Components .....	-4-
Figure 1.2	Drive-By Noise Participation .....	-5-
Figure 1.3	Engine Noise Radiation Participation .....	-5-
Figure 1.4	Zetec-SE 1.4l Noise Radiation Participation (Base Engine) .....	-6-
Figure 2.1.1	Skirt Length Design Principles .....	-14-
Figure 2.1.2	Crankcase Design and Main Bearing Support .....	-15-
Figure 2.2.1	Basic Crankshaft Dimensions .....	-16-
Figure 2.2.2	Structure Borne Noise Influenced by Throw Stiffness .....	-18-
Figure 2.2.3	Flywheel Whirl Excitation .....	-18-
Figure 2.2.4	Effect of Torsional Vibration on Radiated Noise .....	-19-
Figure 2.2.5	Hollow Pin Crankshaft .....	-19-
Figure 2.2.6	Solid Pin Crankshaft .....	-20-
Figure 2.2.7	Weight Reduction by Balancing Optimisation .....	-20-
Figure 2.3.1	Clutch Design Principles .....	-22-
Figure 2.3.2	Noise Radiation of Conventional Flywheel vs. DFC .....	-23-
Figure 2.3.3	Asymmetric Flywheel .....	-24-
Figure 2.3.4	Whirling Frequencies vs. Inertia Ratio .....	-24-
Figure 2.3.5	Flexible Flywheel .....	-25-
Figure 3.1.1	Laval-Rotor Representation .....	-28-
Figure 3.1.2	Rotor Idealisation .....	-28-
Figure 3.1.3	Shaft Deflection of Single-Mass Rotor .....	-28-
Figure 3.1.4	Shaft Deflection of Multi-Mass Rotor .....	-28-
Figure 3.2.1	Deformed Rotor with Rigid Bearings .....	-30-
Figure 3.2.2	Inertia with Fixed Coordinate-System .....	-30-
Figure 3.2.3	Fixed and Rotating Coordinate-System .....	-32-
Figure 3.2.4	Main Bearing Stiffness Study .....	-35-
Figure 3.2.5	Elastic Supported Rotor .....	-35-
Figure 3.2.6	Response of Anisotropic Supported Shaft .....	-37-
Figure 3.2.7	Syncro- and Contra-Rotating Circular Orbits .....	-38-
Figure 3.2.8	Condition of Syncro- and Contra-Rotation .....	-40-
Figure 3.3.1	Viscous Material Model Representation .....	-41-
Figure 3.5.1	Rotor Resonances with Hydrodynamic Bearings .....	-45-
Figure 3.5.2	Hydrodynamic Bearing Spring-Damper Model .....	-47-
Figure 3.5.3	Rigid Rotor with Slide Bearings .....	-48-
Figure 3.5.4	Elastic Rotor with Slide Bearings .....	-49-
Figure 3.6.1	Rotor Principles .....	-51-
Figure 3.6.2	Deformed Rotor and Forces .....	-51-
Figure 3.6.3	Gyroscopic Principle .....	-52-
Figure 3.6.4	Displaced Coordinate System .....	-52-
Figure 3.6.5	Angular Momentum in Fixed Coordinate System .....	-53-
Figure 3.6.6	Eigenfrequencies with respect to angular velocity .....	-55-
Figure 3.6.7	Bending-Critical Speed .....	-58-
Figure 3.6.8	Bending-Critical Speed .....	-58-
Figure 3.6.9	Shaft with Harmonic Excitation of Constant Direction .....	-59-
Figure 3.6.10	Contra-Rotating Critical-Bending Speeds .....	-60-
Figure 3.6.11	Syncro- and Contra-Rotating Critical Speeds .....	-61-
Figure 3.6.12	Eigenfrequencies of Anisotropic Supported Shaft .....	-62-
Figure 3.7.1	Stability Chart .....	-65-
Figure 3.7.2	Stability / Eigenfrequency Chart .....	-66-
Figure 3.7.3	Stability Chart with Damping Properties .....	-67-
Figure 3.8.1	Engine Front-End Fluctuation .....	-70-
Figure 4.1.1	Radial Bearing Parameters .....	-73-
Figure 4.2.1	Force Map of 360° Bearing .....	-76-
Figure 4.2.2	Coordinate System of Spring- and Damping-Coefficients .....	-77-
Figure 4.2.3	Components of Resulting Oilfilm Pressure .....	-77-
Figure 4.2.4	Stiffness Properties of Circular Bearing .....	-79-
Figure 4.2.5	Damping Properties of Circular Bearing .....	-79-
Figure 4.2.6	Bearing Measuring Device .....	-80-
Figure 4.2.7	Comparison of Stiffness Coefficients .....	-81-

Figure 4.2.8	Comparison of Damping Coefficients .....	-81-
Figure 4.2.9	Averaged 1%-Error .....	-82-
Figure 4.2.10	Stiffness- and Damping Coefficients .....	-84-
Figure 4.2.11	Combined Crankshaft and Powertrain Eigenvector .....	-85-
Figure 4.2.12	Shift of First Powertrain Eigenfrequency .....	-85-
Figure 4.2.13	Plain Bearing Representation .....	-88-
Figure 4.3.1	Principle Bearing Configuration .....	-91-
Figure 4.3.2	Pressure Summation (Schaffrath Approach) .....	-92-
Figure 4.3.3	Pressure Summation (Klumpp Approach) .....	-92-
Figure 4.3.4	Main Bearing Analysis Process .....	-95-
Figure 4.3.5	Plain Bearing Modelling Approach .....	-99-
Figure 4.3.6	Comparison of Structure and Oilfilm Stiffness .....	-102-
Figure 4.3.7	Comparison of Oilfilm Damping Properties .....	-103-
Figure 4.3.8	Vertical Main Bearing Acceleration (1000 rpm;Constant) .....	-105-
Figure 4.3.9	Vertical Main Bearing Acceleration (1000 rpm;Dependent) .....	-105-
Figure 4.3.10	Vertical Main Bearing Acceleration (5000 rpm;Constant) .....	-106-
Figure 4.3.11	Vertical Main Bearing Acceleration (5000 rpm;Dependent) .....	-106-
Figure 4.3.12	Horizontal Main Bearing Acceleration (4000 rpm;Constant) .....	-107-
Figure 4.3.13	Horizontal Main Bearing Acceleration (4000 rpm;Dependent) .....	-107-
Figure 4.3.14	Horizontal Main Bearing Acceleration (6000 rpm;Constant) .....	-108-
Figure 4.3.15	Horizontal Main Bearing Acceleration (6000 rpm;Dependent) .....	-108-
Figure 4.3.16	Horizontal Main Bearing Acceleration (3000 rpm;Dependent) .....	-110-
Figure 4.3.17	Horizontal Main Bearing Acceleration (3000 rpm;Dependent) .....	-111-
Figure 4.3.18	Diff. Surface Velocity (4000 rpm;Constant vs. Dependent) .....	-113-
Figure 4.3.19	Diff. Surface Velocity (5000 rpm;Constant vs. Dependent) .....	-113-
Figure 4.3.20	Diff. Surface Velocity (6000 rpm;Constant vs. Dependent) .....	-114-
Figure 4.3.21	Diff. Surface Velocity (4000 rpm;Constant vs. Dependent) .....	-114-
Figure 4.3.22	Diff. Surface Velocity (6000 rpm;Constant vs. Dependent) .....	-115-
Figure 4.3.23	Near Field Intensity Data (Inlet Side) .....	-117-
Figure 4.3.24	Near Field Intensity Data (Bottom Side) .....	-117-
Figure 4.3.25	Integrated Surface Velocity (3000 rpm; 1/1 vs. 1/3 Load) .....	-118-
Figure 4.3.26	Integrated Surface Velocity (3000 rpm; 1/1 vs. 1/3 Load) .....	-119-
Figure 5.1.1	Combustion Excitation Spectra; Full Load (Zetec-E) .....	-121-
Figure 5.1.2	Transfer Function of Acceleration/Force (Zetec-E) .....	-122-
Figure 5.1.3	Averaged Main Bearing Spectra (Zetec-E) .....	-122-
Figure 5.1.4	System Representation for Bearing Force Calculation .....	-124-
Figure 5.1.5	Bearing Forces with Bearing No.1 Changes .....	-124-
Figure 5.1.6	Bearing Forces with Bearing No.2 Changes .....	-124-
Figure 5.1.7	Bearing Forces with Bearing No.3 Changes .....	-125-
Figure 5.1.8	Bearing Forces with Bearing No.4 Changes .....	-125-
Figure 5.1.9	Bearing Forces with Bearing No.5 Changes .....	-125-
Figure 5.1.10	Journal Bearing Representation in Powertrain Model .....	-127-
Figure 5.1.11	Analysis Model of Inertia Forces .....	-127-
Figure 5.1.12	Analysis Model of Combustion Forces .....	-127-
Figure 5.2.1	Schematic Diagram of the Conrod-Crank Mechanism .....	-129-
Figure 5.2.2	Connecting Rod Kinematics .....	-129-
Figure 5.2.3	Applied Loads on Crank Pins .....	-130-
Figure 5.2.4	Connecting Rod Elastic Deformation .....	-132-
Figure 5.2.5	Midspan Rod and Crank Bending Moment (300rpm) .....	-133-
Figure 5.2.6	Midspan Rod and Crank Bending Moment (5000rpm) .....	-133-
Figure 5.2.7	Midspan Rod and Crank Axial Forces (300rpm) .....	-134-
Figure 5.2.8	Midspan Rod and Crank Axial Forces (5000rpm) .....	-134-
Figure 5.2.9	Excitation- and Measurement-Locations of the Cranktrain .....	-135-
Figure 5.2.10	Transfer Function of Piston .....	-135-
Figure 5.2.11	Transfer Function of Piston Pin .....	-135-
Figure 5.2.12	Transfer Function of Connecting Rod .....	-136-
Figure 5.2.13	Transfer Function of Connecting Rod, Piston Pin, and Piston .....	-136-
Figure 6.1	Indeterminate Full Engine Representation .....	-140-
Figure 6.3.1	Beam Representation with Additional Effects .....	-153-
Figure 6.3.2	Forcing Dependent Instability Chart of Mathieu-Equation .....	-157-
Figure 6.3.3	Ljapunov's Stability Criterion .....	-158-

Figure 6.3.4	Stability Chart of Multi-Cylinder Engine (Part I) .....	-161-
Figure 6.3.5	Stability Chart of Multi-Cylinder Engine (Part II) .....	-161-
Figure 7.1	Structure Borne Noise Path .....	-166-
Figure 7.1.1	Analysis Methods for Structure and Air Borne Noise .....	-167-
Figure 7.1.2	Near Field Intensity Measurement (Zetec-SE) .....	-170-
Figure 7.1.3	Sound Power Measurement .....	-171-
Figure 7.1.4	Summation of Sound Participation .....	-171-
Figure 7.1.5	Analysis Process .....	-172-
Figure 7.1.6	Summed Noise Intensity Plot .....	-172-
Figure 7.1.7	Variation of Vibration over Engine Block Surface .....	-174-
Figure 7.1.8	Analysis Points on Engine Surface .....	-175-
Figure 7.1.9	Noise Intensity of Engine Block Surface .....	-175-
Figure 7.2.1	Noise Radiation Phenomena .....	-178-
Figure 7.2.2	Radiation Efficiency of a Plate .....	-179-
Figure 7.2.3	Measured and Calculated Radiation Efficiency .....	-180-
Figure 7.2.4	Measured Radiation Efficiency .....	-181-
Figure 7.2.5	Analysis Process .....	-183-
Figure 7.2.6	Integrated Surface Velocity vs. Engine Speed .....	-185-
Figure 7.2.7	Overall Surface Velocity .....	-186-
Figure 7.2.8	Component Surface Velocity .....	-187-
Figure 7.2.9	Third Octave Band Integrated Surface Velocity .....	-187-
Figure 7.2.10	Third Octave Band Waterfall Diagram .....	-188-
Figure 7.2.11	Differential Third Octave Band Waterfall Diagram .....	-188-
Figure 7.3.1	Model of Catalytic Converter .....	-193-
Figure 7.3.2	Position of Measurement Locations 'A' .....	-193-
Figure 7.3.3	Position of Measurement Locations 'B' .....	-194-
Figure 7.3.4	Envelope Surface 1 .....	-194-
Figure 7.3.5	Envelope Surface 2 .....	-195-
Figure 7.3.6	Spatial Sound Pressure (Mode 1; Location 'A') .....	-196-
Figure 7.3.7	Spatial Sound Pressure (Mode 2; Location 'A') .....	-197-
Figure 7.3.8	Structural Aluminium Oil-Pan .....	-198-
Figure 7.3.9	Oil-Pan Sound Pressure Comparison (Location 'B') .....	-199-
Figure 7.3.10	Oil-Pan Sound Pressure Comparison (Location 'C'; 100 mm) .....	-199-
Figure 7.3.11	Oil-Pan Sound Pressure Comparison (Location 'C'; 500 mm) .....	-200-
Figure 7.3.12	Physical Model of Engine Assembly .....	-201-
Figure 7.3.13	Comparison of Acoustic Results at 0.1 m .....	-202-
Figure 7.3.14	Comparison of Acoustic Results at 0.3 m .....	-203-
Figure 7.3.15	Comparison of Acoustic Results at 1 m .....	-203-
Figure 8.1.1	Zetec-SE Engine Cut-away .....	-208-
Figure 8.1.2	Aluminium Engine Block and Bearing Beam .....	-209-
Figure 8.1.3	Sound Power Level Spreadband .....	-209-
Figure 8.1.4	Sound Intensity Participation (Entire Engine) .....	-209-
Figure 8.1.5	Cylinder Block (RHS) .....	-211-
Figure 8.1.6	Bearing Beam (Single Piece; Cast Aluminium) .....	-211-
Figure 8.1.7	Cylinder Block (LHS;Rear) .....	-212-
Figure 8.1.8	Oil Pan (Cast Aluminium) .....	-212-
Figure 8.1.9	Crankshaft (Cast Iron) .....	-213-
Figure 8.1.10	Flywheel (Cast Iron) .....	-213-
Figure 8.1.11	Cranktrain Assembly .....	-214-
Figure 8.1.12	Flexible Flywheel .....	-215-
Figure 8.1.13	Individual Bearing Caps .....	-215-
Figure 8.1.14	Individual Bearing Caps (Assembly) .....	-216-
Figure 8.1.15	Powertrain FEM Model .....	-217-
Figure 8.1.16	Crankshaft Assembly .....	-218-
Figure 8.2.1	Powertrain Whirling Frequencies .....	-222-
Figure 8.2.2	2nd Longitudinal Vibration .....	-222-
Figure 8.2.3	1st Torsional Vibration .....	-223-
Figure 8.2.4	1st Flywheel Whirling ('CP') .....	-224-
Figure 8.2.5	1st Pulley Whirling ('CP') .....	-225-
Figure 8.2.6	Flywheel Whirl (Conventional Flywheel) .....	-228-
Figure 8.2.7	Whirling Frequencies of Conventional Flywheel System .....	-229-



Figure 8.2.8	Whirling Frequencies of Flexible Flywheel System .....	-229-
Figure 8.2.9	Long.+Tors. Vibration of Conventional vs. Flexible Flywheel .....	-230-
Figure 8.2.10	1st Flywheel Whirling of Conventional vs. Flexible Flywheel .....	-231-
Figure 8.2.11	1st Flywheel Whirling of Conventional vs. Flexible Flywheel .....	-232-
Figure 8.2.12	Pulley Whirling of Conventional vs. Flexible Flywheel .....	-233-
Figure 8.2.13	Flywheel Whirl (Conventional vs. Flexible Flywheel) .....	-233-
Figure 8.2.14	Flywheel Whirl (Conventional vs. Flexible Flywheel) .....	-234-
Figure 8.2.15	Pulley Whirl (Conventional vs. Flexible Flywheel) .....	-234-
Figure 8.2.16	Flywheel Axial Displacement [No Load] .....	-237-
Figure 8.2.17	Flywheel Rotational Displacement [No Load] .....	-237-
Figure 8.2.18	Flywheel Vertical Displacement [No Load] .....	-238-
Figure 8.2.19	Flywheel Horizontal Displacement [No Load] .....	-239-
Figure 8.2.20	Flywheel Whirl Frequency Correlation .....	-241-
Figure 8.2.21	Flywheel Whirl Amplitude Correlation .....	-241-
Figure 8.3.1	Summed Surface Velocity .....	-243-
Figure 8.3.2	Integrated Surface Velocity (Solid Flywheel) .....	-243-
Figure 8.3.3	Integrated Surface Velocity (Flexible Flywheel) .....	-244-
Figure 8.3.4	Integrated Surface Velocity (Solid vs. Flexible Flywheel) .....	-245-
Figure 8.3.5	Integrated Surface Velocity - 2400rpm .....	-246-
Figure 8.3.6	Integrated Surface Velocity - 2700rpm .....	-246-
Figure 8.3.7	Integrated Surface Velocity - 3400rpm .....	-246-
Figure 8.3.8	Integrated Surface Velocity - 3500rpm .....	-246-
Figure 8.3.9	Integrated Surface Velocity - 3600rpm .....	-246-
Figure 8.3.10	Integrated Surface Velocity - 4700rpm .....	-246-
Figure 8.3.11	Integrated Surface Velocity - 5100rpm .....	-246-
Figure 8.3.12	Integrated Surface Velocity - 5200rpm .....	-246-
Figure 8.3.13	Surface Velocity Measurement - Left Engine Side .....	-247-
Figure 8.3.14	Surface Velocity Measurement - Right Engine Side .....	-247-
Figure 8.3.15	Surface Velocity Measurement - Oilpan .....	-248-
Figure 8.3.16	Left Engine Side Surface Velocity (Test @ 4918 rpm) .....	-249-
Figure 8.3.17	Left Engine Side Surface Velocity (Analysis @ 5000 rpm) .....	-249-
Figure 8.3.18	Oilpan Surface Velocity (Test @ 5101 rpm) .....	-249-
Figure 8.3.19	Oilpan Surface Velocity (Analysis @ 5000 rpm) .....	-250-
Figure 8.3.20	Powertrain in Anechoic Cell - Exhaust Side .....	-251-
Figure 8.3.21	Powertrain in Anechoic Cell - Intake Side .....	-251-
Figure 8.3.22	Measured vs. Analytical Octave Band [3000rpm;Left Side] .....	-258-
Figure 8.3.23	Measured vs. Analytical Octave Band [3000rpm;Bottom Side] .....	-259-
Figure 8.3.24	Total Sound Pressure Level Comparison [Left Side] .....	-261-
Figure 8.3.25	Noise Auralisation Comparison [3000 rpm; Left Side] .....	-263-
Figure App.4.1	Stiffness Properties [1st Principal Direction; 1/1 Load] .....	-291-
Figure App.4.2	Stiffness Properties [2nd Principal Direction; 1/1 Load] .....	-293-
Figure App.4.3	Stiffness Properties [1st Principal Direction; 1/3 Load] .....	-295-
Figure App.4.4	Stiffness Properties [2nd Principal Direction; 1/3 Load] .....	-297-
Figure App.4.5	Stiffness Properties [1st Principal Direction; 2/3 Load] .....	-299-
Figure App.4.6	Stiffness Properties [2nd Principal Direction; 2/3 Load] .....	-301-
Figure App.4.7	Damping Properties [1st Principal Direction; 1/1 Load] .....	-303-
Figure App.4.8	Damping Properties [2nd Principal Direction; 1/1 Load] .....	-305-
Figure App.4.9	Damping Properties [1st Principal Direction; 1/3 Load] .....	-307-
Figure App.4.10	Damping Properties [2nd Principal Direction; 1/3 Load] .....	-309-
Figure App.4.11	Spatial Sound Pressure (Mode 1; Location 'A'+ 'B') .....	-310-
Figure App.4.12	Spatial Sound Pressure (Mode 2; Location 'A'+ 'B') .....	-311-
Figure App.4.13	Spatial Sound Pressure (Mode 3; Location 'A'+ 'B') .....	-312-
Figure App.4.14	Spatial Sound Pressure (Mode 4; Location 'A'+ 'B') .....	-313-
Figure App.4.15	Spatial Sound Pressure (Mode 7; Location 'A'+ 'B') .....	-314-
Figure App.4.16	Spatial Sound Pressure (Mode 8; Location 'A'+ 'B') .....	-315-
Figure App.4.17	Powertrain Modal Analysis (1st Flywheel vertical) .....	-316-
Figure App.4.18	Powertrain Modal Analysis (1st Flywheel lateral) .....	-317-
Figure App.4.19	Powertrain Modal Analysis (1st Powertrain lateral) .....	-318-
Figure App.4.20	Powertrain Modal Analysis (1st Powertrain vertical) .....	-319-
Figure App.4.21	Powertrain Modal Analysis (2nd Powertrain lateral) .....	-320-
Figure App.4.22	Powertrain Modal Analysis (Mode Indicator Function) .....	-321-

Figure App.4.23	Flywheel Axial Displacement [Full Load] .....	-322-
Figure App.4.24	Flywheel Rotational Displacement [Full Load] .....	-322-
Figure App.4.25	Flywheel Horizontal Displacement [Full Load] .....	-323-
Figure App.4.26	Flywheel Vertical Displacement [Full Load] .....	-323-
Figure App.4.27	Oilpan Surface Velocity (Test @ 3067 rpm) .....	-324-
Figure App.4.28	Oilpan Surface Velocity (Analysis @ 3000 rpm) .....	-324-
Figure App.4.29	Oilpan Surface Velocity (Test @ 3723 rpm) .....	-325-
Figure App.4.30	Oilpan Surface Velocity (Test @ 4235 rpm) .....	-325-
Figure App.4.31	Oilpan Surface Velocity (Analysis @ 4000 rpm) .....	-325-
Figure App.4.32	Oilpan Surface Velocity (Test @ 5101 rpm) .....	-326-
Figure App.4.33	Oilpan Surface Velocity (Analysis @ 5000 rpm) .....	-326-
Figure App.4.34	Left Engine Side Surface Velocity (Test @ 2985 rpm) .....	-326-
Figure App.4.35	Left Engine Side Surface Velocity (Analysis @ 3000 rpm) .....	-327-
Figure App.4.36	Left Engine Side Surface Velocity (Test @ 3945 rpm) .....	-327-
Figure App.4.37	Left Engine Side Surface Velocity (Test @ 4030 rpm) .....	-327-
Figure App.4.38	Left Engine Side Surface Velocity (Analysis @ 4000 rpm) .....	-328-
Figure App.4.39	Left Engine Side Surface Velocity (Test @ 4918 rpm) .....	-328-
Figure App.4.40	Left Engine Side Surface Velocity (Analysis @ 5000 rpm) .....	-329-
Figure App.4.41	Right Engine Side Surface Velocity (Test @ 3160 rpm) .....	-329-
Figure App.4.42	Right Engine Side Surface Velocity (Analysis @ 3000 rpm) .....	-330-
Figure App.4.43	Right Engine Side Surface Velocity (Test @ 3940 rpm) .....	-330-
Figure App.4.44	Right Engine Side Surface Velocity (Analysis @ 4000 rpm) .....	-331-
Figure App.4.45	Measured Narrow Band Results [3000 rpm; Bottom Side] .....	-332-
Figure App.4.46	Measured Third-Octave Band Results [3000 rpm; Bottom Side] .....	-332-
Figure App.4.47	Measured Octave Band Results [3000 rpm; Bottom Side] .....	-333-
Figure App.4.48	Analysis Narrow Band Results [3000 rpm; Bottom Side] .....	-333-
Figure App.4.49	Analysis Third-Octave Band Results [3000 rpm; Bottom Side] .....	-334-
Figure App.4.50	Analysis Octave Band Results [3000 rpm; Bottom Side] .....	-334-
Figure App.4.51	Measured Narrow Band Results [3000 rpm; Left Side] .....	-335-
Figure App.4.52	Measured Third-Octave Band Results [3000 rpm; Left Side] .....	-335-
Figure App.4.53	Measured Octave Band Results [3000 rpm; Left Side] .....	-336-
Figure App.4.54	Analysis Narrow Band Results [3000 rpm; Left Side] .....	-336-
Figure App.4.55	Analysis Third-Octave Band Results [3000 rpm; Left Side] .....	-337-
Figure App.4.56	Analysis Octave Band Results [3000 rpm; Left Side] .....	-337-
Figure App.4.57	Measured Narrow Band Results [6000 rpm; Bottom Side] .....	-338-
Figure App.4.58	Measured Third-Octave Band Results [6000 rpm; Bottom Side] .....	-338-
Figure App.4.59	Measured Octave Band Results [6000 rpm; Bottom Side] .....	-339-
Figure App.4.60	Analysis Narrow Band Results [6000 rpm; Bottom Side] .....	-339-
Figure App.4.61	Analysis Third-Octave Band Results [6000 rpm; Bottom Side] .....	-340-
Figure App.4.62	Analysis Octave Band Results [6000 rpm; Bottom Side] .....	-340-
Figure App.4.63	Measured Narrow Band Results [6000 rpm; Left Side] .....	-341-
Figure App.4.64	Measured Third-Octave Band Results [6000 rpm; Left Side] .....	-341-
Figure App.4.65	Measured Octave Band Results [6000 rpm; Left Side] .....	-342-
Figure App.4.66	Analysis Narrow Band Results [6000 rpm; Left Side] .....	-342-
Figure App.4.67	Analysis Third-Octave Band Results [6000 rpm; Left Side] .....	-343-
Figure App.4.68	Analysis Octave Band Results [6000 rpm; Left Side] .....	-343-
Figure App.6.1	Zetec-SE Engine Assembly Cut-away .....	-354-
Figure App.6.2	Zetec-SE Side View .....	-354-
Figure App.6.3	Zetec-SE Front View .....	-354-
Figure App.6.4	Zetec-SE 16-Valve Cylinder Head Assembly .....	-355-
Figure App.6.5	Zetec-SE 1.25l Torque and Power Output .....	-355-
Figure App.6.6	Zetec-SE Powertrain Installation .....	-356-

## List of Tables

Table 1	Main Dimensions of Crankshafts .....	-17-
Table 2	Flywheel Design Alternatives .....	-22-
Table 3	Non-Dimensional Second Order Critical Speeds .....	-69-
Table 4	Polynomial Coefficients .....	-84-
Table 5	Definite Limits of Powertrain Eigenfrequencies .....	-86-
Table 6	Main Bearing Peak Resonances .....	-108-
Table 7	Integrated Surface Velocities (Constant vs. Dependent Model) .....	-112-
Table 8	Comparison of Analytical and Measured Radiated Noise .....	-116-
Table 9	Comparison of Main Journal Forces by Different Approaches .....	-126-
Table 10	Influence of External Effects on Eigenfrequency .....	-153-
Table 11	Available Measurement Techniques .....	-168-
Table 12	Tools and Related Output .....	-184-
Table 13	Spatial Measurement Location .....	-193-
Table 14	Envelope Surfaces .....	-194-
Table 15	Total Sound Power (Envelope Surface 1) .....	-195-
Table 16	Total Sound Power (Envelope Surface 2) .....	-195-
Table 17	Comparison of CPU-Requirements .....	-202-
Table 18	Basic Engine Data .....	-210-
Table 19	Powertrain Modal Analysis .....	-219-
Table 20	Percentage Difference in Whirling Frequencies .....	-226-
Table 21	Percentage Difference in Whirling Frequencies .....	-232-
Table 22	Total Sound Pressure (3000 rpm) .....	-253-
Table 23	Total Sound Pressure (6000 rpm) .....	-253-
Table 24	Differential Sound Pressure (3000 rpm) .....	-255-
Table 25	Differential Sound Pressure (6000 rpm) .....	-256-
Table 26	Averaged Octave Band Correlation .....	-256-
Table 27	Octave Band Correlation .....	-256-
Table 28	Third Octave Band Correlation .....	-257-
Table 29	Averaged Third-Octave Band Correlation .....	-258-
Table 30	Octave Band Correlation [-500 Hz] .....	-260-
Table 31	Audible Sound Files .....	-263-
Table 32	Example Input Format .....	-344-
Table 33	Input of Program 'FREQ_DEP_STIFF' .....	-348-
Table 34	MSC/Nastran Frequency Dependent Input .....	-352-
Table 35	Zetec-SE 1.251 Technical Data .....	-353-

## **Chapter 1**

### **Introduction**

This chapter gives an introduction to the subject of the work presented in this thesis. For this purpose a brief overview of the historical background is given and the developed analytical methods and procedures to describe the interaction of the crankshaft and crankcase are presented. Based on this background the goals of this work and the motivation to carry it out are introduced and discussed.

Vehicle requirements have changed in the last few years. This is owing to a variety of factors. Legislation is becoming increasingly restrictive in terms of absolute measurable noise and emissions. The increased consciousness of the customer towards comfort leads to an objective quantity, overall sound level, and a subjective assessment known as 'Sound Quality'. For the development of an engine this means additional challenges to the standard requirements such as performance, durability, and economy, because of the necessity for required optimised vibration and noise behaviour. These requirements are partially conflicting, and development has to aim at the best compromise. To achieve this, much effort is spent on the reduction of the absolute noise level and on the improvement of sound quality, whereas the definition of sound quality is somewhat difficult and dependent upon human perception. Whilst from the customer's point of view only the perceptible noise is relevant, the design engineer has to consider the noise emitted as well as the path transmitting the vibration and obviously, the excitation sources. Knowledge of the theoretical background and practical effects of changing design variables is required to optimise the overall system. Bearing in mind that optimisation is always a decision between conflicting requirements, the best compromises can be found by applying either many tests or analytical investigations of competing design alternatives prior to the existence of hardware.

In the past this compromise was commonly achieved by extensive engine development work. Currently, a number of factors are leading to the demand for a more efficient solution.

- Competition among manufacturers now requires shorter development cycles.
- Development budgets are more stringently controlled and reduced.
- Consumer demands are increasing from year to year in terms of noise, vibration and comfort, performance, fuel efficiency and quality.

Cost-neutral solutions can be obtained faster and more easily if they are made during the concept phase of a design. The requirement is clearly for more predictive engineering at a stage where no hardware is available. Here we need to have sufficient CAE (Computer Aided Engineering) predictive tools in-hand, to analyse different concepts with respect to their system behaviour at both comparative and absolute levels. Such

tools are available for a wide range of applications in the engine design. For example, engine performance is analysed using gas exchange simulation tools, which can be based on 1 to 3 dimensional approaches. Engine losses are studied by applying friction models. All kinds of dynamic processes are investigated, utilising multi-body simulation tools. Flow predictions are made for coolant and oil flows. A wide range of applications are found for structural predictions, to check either the structural integrity or dynamic response of either components or assemblies. This list of examples is endless and develops as methods and computer hardware improve.

From the past it is well known that engine blocks and particular crankshafts failed due to extreme load histories. But both components may fail also as a consequence of vibrations, a fact which has been known since the beginning of the century. The commonly applied approach is that the crankshaft fatigue failures generally occur as a result of severe torsional vibrations. This led to the known effort of establishing various torsional vibration models to predict the crankshaft dynamic response early in the design phase. But the description of pure torsional, axial or bending crankshaft vibration is not accurate enough. In the mid thirties Lürenbaum [1]<sup>1</sup> wrote '...in view of the interdependence of the three degrees of freedom it is not wholly sound to speak of the vibration frequencies of the individual degrees of freedom; more accurately, there are only vibration frequencies and forms characteristic of the interrelated system as a whole'. He was saying, that, firstly, the crankshaft vibrations may not be studied independently and, secondly, the assembled system of the crankshaft and crankcase must be incorporated within detailed investigations, as the system responses vary significantly from the component responses.

There has been a continuous upgrading of power by the use of higher compression ratios and engine speeds during the development of the internal combustion engine. A significant step in power increase was achieved in the late thirties and early forties for fighter aeroplane application. At that time this progress was accompanied by a significant increase in crankshaft failures and, hence, fighter losses. Unusual failures occurred that could not be assigned to torsional vibrations. The aeroplane shows an uncommon installation of the engine. The flywheel, or in this specific case, the propeller, is relatively free to tilt without the constraint of a clutch or gearbox. A further effect occurred as the first propellers are designed with two blades only showing a dramatic uneven distribution of the inertia about the main axes. The step towards a three blade propeller reduced this effect. Failures of the crankshaft had been observed within 20-30 hours in service.

---

*1: Numbers in parentheses designate references at the end of the paper*

It was considered (Kimmel[2] 1941 *et al*) that the vibration which causes failures could be a significant bending or axial vibration of the shaft, as torsional failures were left out of consideration through torsional investigations. If a rotating shaft is subjected to a bending vibration, the rotating shaft will have a motion that exhibits a whirling path.

Some twenty-five years ago this subject occurred again in relation to petrol and diesel engines in combination with power increases. Benz[3] 1971 and Hodgetts[4] 1971 *et al* disclosed the known theories and developed first computational tools for predicting the whirling speeds of cranked systems carrying an inertia.

It was in the early nineties that the emphasis changed towards noise and vibration[5]. Severe engine noise could be associated with vibrations of the crankshaft in a bending mode and these vibrations could be excited by fast combustion. It was suggested that the engine main bearings and, per definition, the crankshaft, is the prime path for the noise transmission to the structure of the engine. The published assumption that the crankshaft is a rigid component and can be disregarded for noise and vibration phenomena may be misleading when considering the forces transmitted to the bearings and the noise radiation from the engine bottom-half.

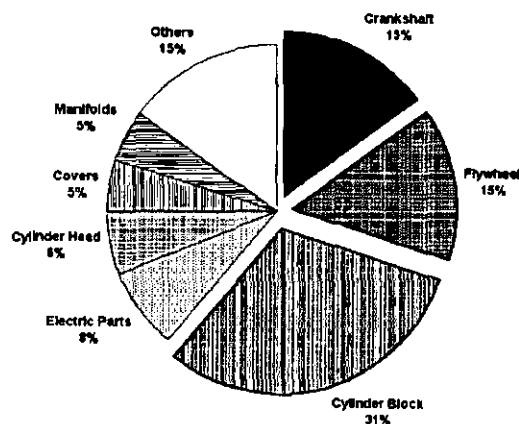


Figure 1.1 Proportional Weight of Engine Components

Within the preceding years more than 70% of the analysis work done was investigating the structural response regarding NVH aspects. Some important enhancements were achieved by performing normal mode analyses. The standard method of solution was to stiffen the corresponding components or component to shift the resonance frequencies above critical values. This often leads to increased weight. Against this, weight reduction is realised by reducing engine block wall thickness or crankshaft pin diameters and cheek thickness with the resulting effect of debasing the NVH performance. The weight proportions of a typical four-cylinder engine, assembled with a cast iron engine

block, crankshaft, flywheel, and aluminium cylinder head, are shown in Figure 1.1. The engine block and the cranktrain components take up over 50% of the overall engine weight and are, therefore, the subject of most weight reduction efforts.

With the recent demand for resource and energy conservation the objectives tend towards weight reduction together with optimisation of the NVH behaviour.

In analysing the emitted noise of either a passenger or commercial vehicle, one can show that the engine is the major contributor for drive-by noise as displayed in Figure 1.2.

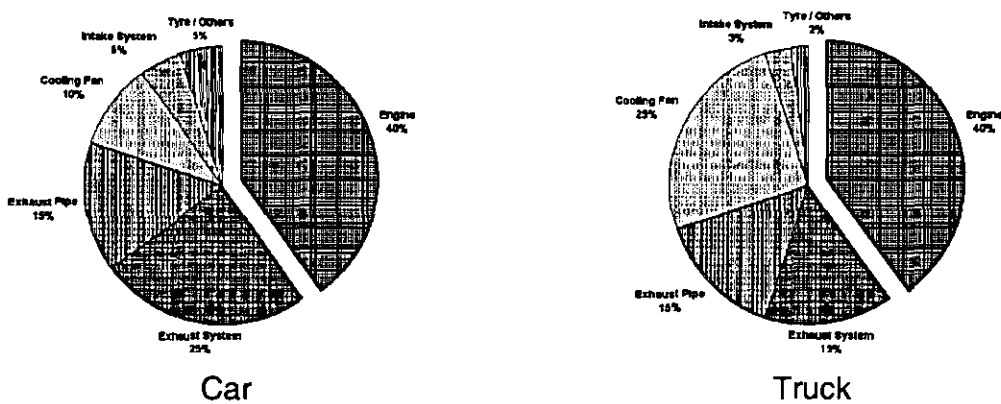


Figure 1.2 Drive-By Noise Participation

For a typical 4 cylinder inline spark ignition engine, running at 4000rpm wide open throttle (WOT), the sound energy that the individual components typically contribute to the total is shown in Figure 1.3. Obviously an outstandingly high contribution is originated by the lower part of the crank case [6], in which the oilpan and cylinder block approximately have an equal share and together emit more than 50% of the total sound energy. The reason for this is the vibrational excitation the cylinder block and oilpan receive from the bearing forces and gas pressure variations.

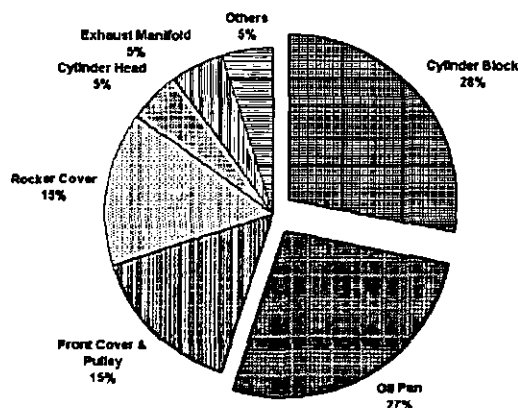


Figure 1.3 Engine Noise Radiation Participation



The data shown reflect noise participation data of engines designed 15 years ago. Equivalent results [7] are shown in Figure 1.4 for a recent engine design. This engine is the state of the art in radiated noise performance and one of the best in its class.

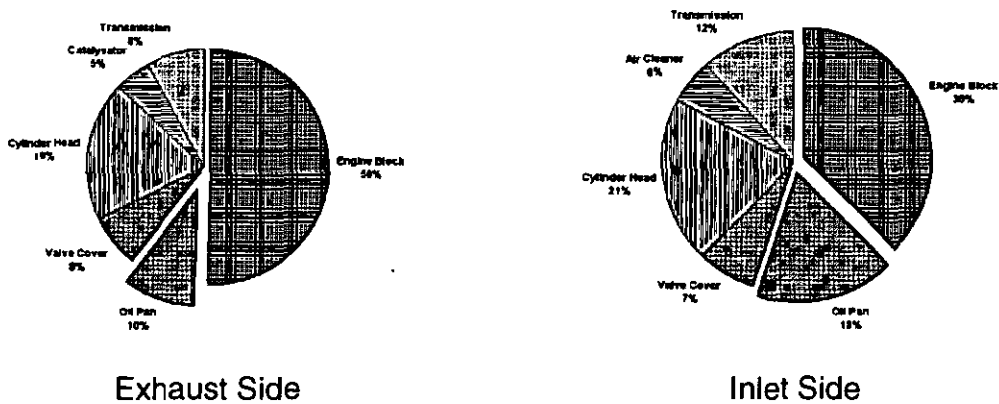


Figure 1.4 Zetec-SE 1.4l Noise Radiation Participation (Base Engine)

As shown before, the cylinder block has a very significant effect on the total radiated engine noise, showing an even increasing contribution with recent engine designs. This effect is mainly driven by optimised component noise radiation accentuating the engine block and oil pan participation. The task is to find an optimum design in which sufficient consideration is given to the relationship between cylinder block weight, structure and vibration excited by the main bearing forces as well as noise radiation phenomena. Thus, both light weight and low noise characteristics must be achieved in the same engine block design.

If the NVH behaviour is to be analysed during the concept phase, one must have data of the excitation forces and, obviously, a description of the transferring systems and their functionalism available.

In terms of internal combustion piston engines, which are kinematically ordinary crank slider mechanisms, the translational movement of the piston is converted into a rotational movement by the crankshaft. This results in a non-continuous movement of the moving parts which are permanently accelerated and decelerated. Hence, the resulting inertia forces and the non-continuous gas forces are the main excitation sources at the engine bottom half.

The participating transferring components are identified as a system assembled to the cranktrain. The individual components are from top to bottom the piston, connecting rod, crankshaft and the engine block assembled with the oil pan. Therefore, the analysis of the structural response and the predictions of the radiated noise behaviour demand the analysis of the dynamic interaction of the participating components. The approach

considered in this thesis tries to make the interaction between the engine block and crankshaft transparent in its coupled behaviour. This enables both excitation optimisation and assessment of the influence of structural changes on the engine bottom-end NVH.

All levels of modelling considered in the literature are discussed, and all can be seen as state of the art for their specific application. However it will be shown that for the purpose of this work they all lack specific properties.

*The aim of this study is the analysis of coupled crankshaft-crankcase systems with the main emphasis on the radiated noise behaviour throughout the engine speed range.*

The choice with the availability of today's computing capacity to fulfil this aim is a formal analysis approach to calculate the crankshaft-crankcase interaction throughout the entire speed range. Such methods have recently been used for the analysis and optimisation of the response of the coupled cranktrain. This was carried out by optimising the main bearing excitation by reducing the main bearing forces at each bearing individually (Pfungsthor *et al* 1998 [8]) taking into account the engine load and speed domain. However it turns out that although this method allows the main bearing forces throughout the entire engine speed range to improve, their potential to predict and optimise the coupled dynamic response of the crankshaft and the crankcase components and the engine radiated noise behaviour is very limited. This is essentially because the contributing components are statically reduced and the contributing higher frequency content is disregarded. But any reduction tends to conflict strongly with the main objective of this study, which is to provide an efficient tool set for noise prediction.

In current practice noise prediction is attempted to be realised by traditional engineering methods. Typically a single engine speed is selected and the corresponding linear frequency response and noise radiation analyses are performed. This corresponds with the engineering practice to select one specific load/speed condition as a target for NVH performance and develop the engine to meet this specific target. Typically for a new engine design more than a dozen alternatives may be studied before a satisfactory solution is obtained. However, this process is time consuming, expensive and not necessarily successful, as the system response is optimised for a single operating condition. Applying this approach within an analytical loop accounting for multiple engine speeds is not practicable due to timing and computation time constraints. Clearly an efficient tool would help to improve on these early decisions.

Two controversial aspects have to be considered in making a decision as to this tool.

It is mandatory that the model is solved many times, especially if the number of considered engine speeds is large or multiple load conditions are investigated. Clearly this suggests a very efficient model such as the simple modal or linear frequency response approach.

The second aspect is the capability of the model to represent the real system response accurately enough. Here we find the material non-linearities, mainly the oilfilm properties at the crankshaft bearings and some pre-stressing effects. Further non-linear effects are introduced by the rotating components through geometrical changes, gyroscopic effects and variational excitation forces. This can clearly be represented through discrete models. However the required computation times for discrete models strongly conflict with the first aspect.

These considerations suggest that a new model or tool is demanded that sufficiently balances both requirements.

Therefore, in performing this investigation the following objectives have to be addressed for the analysis of the engine bottom end with respect to the radiated noise phenomena:

- 1) A suitable model has to be developed and verified; this must consider efficiency and accuracy aspects to cope with the entire engine speed range.
- 2) Physical plain bearing properties have to be established for the analysis domain and to be transformed into suitable idealised parameters. The bearing design and the resulting dynamic properties are necessarily linked to this set of parameters.
- 3) The dynamic behaviour of rotating structures is described by the application of gyroscopic and differential stiffness effects.
- 4) Tools have to be established for noise radiation, tracking and audibility prediction.
- 5) With respect to the necessary assumptions and idealisations, the results from the noise investigation should be validated with experimental data and subjective listening studies.

With regard to objective 1, the most important property is the frequency range covered by the applied model. Theoretically, noise radiation analysis should consider frequencies of up to 6000 Hz being representative for comparisons between various design alternatives. Experience shows that restricting the upper frequency range to i.e. 3000 Hz or even lower values may result in misleading interpretation of design alternatives. As a consequence of this, the coupled crankshaft-crankcase system must represent the

dynamic behaviour of at least 4500-5000 Hz for the 3000 Hz border frequency, or frequencies up to 7500-8000 Hz for 6000 Hz as the upper border frequency. To solve such a system, one may choose to integrate the crankcase-crankshaft model in the time domain, starting with some initial conditions and monitor the results until a stage where the results of subsequent cycles show a sufficient small difference. This indicates that a steady state solution has been achieved. This may be applicable for heavily damped systems and for systems with a relative small number of degrees of freedom. Unfortunately, the crankshaft-crankcase system is very lightly damped, in the order of 3-6% modal damping, so numerical integration would be required over a significant number of crankshaft cycles of 720° before theoretically steady state response could be achieved. Accounting for the requested upper frequency values, a significant number of degrees of freedom must be considered in the reduced analysis set. Accordingly the mathematical effort of solving this approach in the time domain seems to be unrealistic given today's hardware and software. The more promising approach appears to be a solution of this problem within the frequency domain. This is especially valid for those linear systems with constant coefficients. Since the principle of superposition can be applied for such systems and the contributing sub-systems, the requested result can be achieved by separating the solution into the response of individual modes excited with the appropriate harmonic forcing function. The results obtained are finally summed. The major drawback of this approach is that the solution is not entirely valid in the main sense of the theory for non-linear systems or linear systems with changing coefficients. But this problem may be overcome by applying the previously discussed assumption of decoupled vibration. This may be used to transform the non-linear problem into a linear modal model with periodically time variant coefficients. One major task of this thesis is to describe a frequency domain solution for time dependent coefficient modal models by the application of Fourier representation.

In line with objective 2 the way the non-linear plain bearing properties are described within the model has to be considered. What has to be discussed is whether the plain bearing properties are calculated internally within the dynamic response analysis of the coupled system or whether the required properties are derived externally and independently from the vibration analysis. The advantage of a combined or linked approach is that the solution of the bearing description would deliver the properties for the specific operational condition calculated at a time and only for the one requested. But the major disadvantage of this type of solution would be that the dynamic system must solve the bearing description again and again while looping through the frequency domain. The solution to that issue comes also from the previously described approach of utilising a modal model with variant coefficients. The plain bearing properties can be described

utilising a cartesian coordinate system and two pairs of coupled stiffness and damping properties. These properties are established externally applying an independent tool and are stored in so called 'look-up' or impedance tables. The tables are transformed into the modal or frequency domain and can then be applied as one part of the variant coefficients. The drawback of this solution is that the bearing properties must be established in advance for all theoretically possible conditions to describe the entire operational domain. This may cause an enormous amount of computation time for solutions, which may not be necessarily used later in the dynamic response analysis. But this effort is required once only and the data obtained can be applied in many analyses, whereas the direct solution would cause the bearing analysis to be performed again and again. The approach of look-up tables seems on balance to be the most efficient solution for the description of the non-linear bearing properties.

Having considered that the coupled crankshaft-crankcase system is significantly influenced by the dynamic response of the crankshaft assembly, one has to account for the dynamic effects of a rotating component to address objective 3. The dynamic behaviour of the crankshaft assembly is described by means of the basic differential equation of motion as known from non-rotating structures. This system is then overlaid with those matrices describing the rotational behaviour of the crankshaft assembly, namely the gyroscopic effect and the pre-stress or pre-load effect resulting from external loads. It is assumed that the crankshaft assembly can be described applying invariable matrices under the constraint that all the matrices are described within a synchro-rotating coordinate system. IC-engines face changes in angular velocity originating from fluctuations in excitation forces. But it will be shown that the corresponding matrices can be treated as constant with respect to variations in angular velocity at a fixed operating condition.

In line with objective 4, tools are discussed and established which may be used to formally analyse the noise radiation, track the noise sources and make first steps to establish audible noise comparison of investigated design alternatives. For this purpose the entire engine speed range is scanned, applying a simplified noise radiation approach based on a surface velocity analysis. Once critical operation conditions are established, more detailed tools are considered to track the noise and vibrational sources for that demeanour. Finally, a noise radiation analysis is performed at that condition establishing the sound pressure at defined points in space. These data are then applied within a post-processing procedure to make the calculated noise results audible.

Finally, to validate the analytical work, objective 5 is addressed by defining various design proposals and performing the entire procedure on the basis of those examples. The work was then finalised by an extensive engine test study carried out for the studied design proposals. These tests clearly validate the findings from the analytical work, and also reveal further challenges for future research work from both the modelling and accuracy points of view.

All analytical and measurement work considered the FORD ZETEC-SE engine, if not mentioned otherwise. The engine details are given in Appendix 6. For complete powertrain application the IB5 transmission is utilised.

The content of the work outlined above has been structured in 9 chapters. Chapter 2 establishes a basic understanding of engine crankcase bottom-end, crankshaft and flywheel design and functionality. In Chapter 3 the dynamics of rotating structures are addressed and the required depth of modelling is discussed. Chapter 4 covers the description of the plain bearing properties and the transformation to the frequency domain. The look-up tables are generated and presented in graphical form in the appendix. Chapter 5 concentrates on the description of the forcing function and the considered approach of model boundaries. The model boundaries are discussed and verified through analyses. Chapter 6 concentrates on developing a frequency domain solution method for crankshaft-crankcase dynamics. Chapter 7 provides a brief review of noise analysis methodologies to establish the requirements for a practical approach within this thesis. The required tools are then discussed in detail and derived. The numerical analysis, comparison and verification with test results are carried out in Chapter 8. Finally Chapter 9 gives a brief discussion of the achievements and conclusion of the work.

## **Chapter 2**

### **Engine Bottom-End and Crankshaft Design Basics**

The objective of this chapter is to summarise the available engine bottom-end design alternatives together with implications for the coupled crankshaft-crankcase behaviour. The most important components, namely crankcase, crankshaft and flywheel, are described in detail and the contributing effects on structural vibration are discussed.

During the history of engine design a number of techniques has been tried to convert the combustion pressure into a rotational movement which can be deployed to drive a system or to generate power. Such designs are for example the 'Wankel-', the 'Stern-', 'W-', 'H-' engine and others. But for modern high speed, large volume production engines, only standard crank-slider mechanisms are being used. The contributing components of the crank-slider mechanism are the piston assembly, the connecting rod, the crankshaft with attached inertias or dampers and the crankcase carrying the cranktrain assembly. As highlighted in Chapter 1 the basis of an acoustically optimised engine is significantly influenced by the engine bottom-end noise radiation. Therefore particular attention must be paid to the subject: optimisation of components. Attention is given to the three influencing parameters: excitation, transfer and radiation of vibration. While the excitation is mainly influenced by the combustion pressure (neglecting the inertia forces for the time being), this will not be discussed here, as this is a totally different subject and is related to e.g., emissions, performance and fuel economy. The excitation forces are mutually transferred through the crankshaft to the crankcase and the outer surfaces. The main bearings act as the coupling device. The crankcase must be considered as relatively weak compared to the crankshaft stiffness [9]. Influenced by the relatively large design freedom in bottom-end design, significant improvements are achieved by optimising the engine block bottom-half and by structural integration of the main bearing caps ([10],[11],[12]). The commonly considered approach was to increase the stiffness following the axiom "the stiffer the better". But the influence of structural design changes has not been completely considered, as the crankshaft assembly and the crankcase perform as a coupled system influencing each other. It is therefore essential to study the effect of structural changes within a coupled system releasing the approach of optimisation of individual components.

In this chapter, known design features are presented and discussed in the order of crankcase bottom-end, crankshaft and flywheel design alternatives. Some of this will be applied in Chapter 8 and studied for potential noise reduction proficiency.

## **2.1 Engine Bottom-End Design Basics**

The engine bottom-end is principally characterised through the engine block skirt length and the approach as to how the main bearing caps are attached or stiffened. The most important design principles for alternate skirt lengths are shown in Figure 2.1.1.



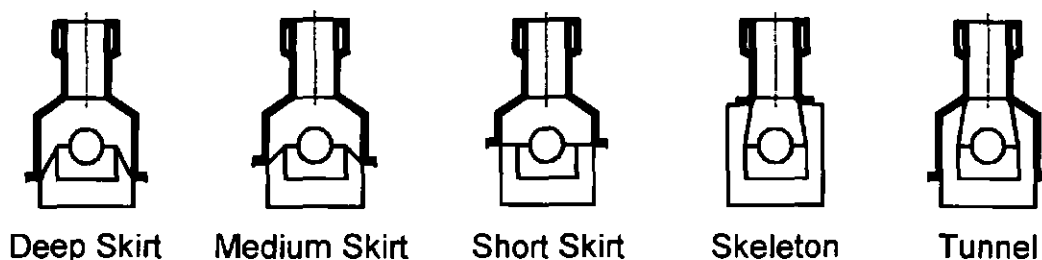


Figure 2.1.1 Skirt Length Design Principles

The different alternatives are characterised as 'Short Skirt', 'Medium Skirt' and 'Deep Skirt' engine blocks. The medium skirt block is commonly not accounted for and this design is usually rated as short or deep skirt depending on the length of the skirts. Newer engine designs showed that there is no significant advantage or disadvantage in a specific skirt length. Potential drawbacks as detailed by Vorwerk [13] can be overcome with specific compensation actions. Today's short skirt engines commonly have stiffeners attached, improving both the radiated noise of the engine and the powertrain resonance frequencies ([14],[15],[16]).

An alternative engine design can be found with the skeleton engine. This engine type is commonly applied within research projects, showing a significant reduction in mass and noise radiation. The engine outer surfaces are completely decoupled from the main bearings and mainly designed using composite material. Variations of the skeleton design are available showing either short or deep skirt characteristics combined with a decoupled main bearing aisle. A typical example is the AVL 'Tunnel' concept.

The main bearing aisle is normally designed without consideration of the skirt length. The upper half of the main bearing is integrated in the crankcase walls, whereas the lower half is designed independently and bolted to the engine block. Various design alternatives are known to improve the vibrational and hence the acoustical behaviour of the engine bottom-half. The powertrain rigidity increases also as the main bearing stiffeners are usually designed to connect to the transmission bell housing. Typical examples are displayed in Figure 2.1.2

'Individual Bearing Caps' (IBC) are applied widely. The most important arguments are cost and weight issues.

The 'Bearing Beam' connects individual bearing caps with each other. The detailed design varies between a bridge design connecting all bearing caps or as a split or paired bearing beam attaching two neighbored bearing caps only. The bearing beam is bolted to the block via the main bearing bolts and is not connected to the block rail and skirts

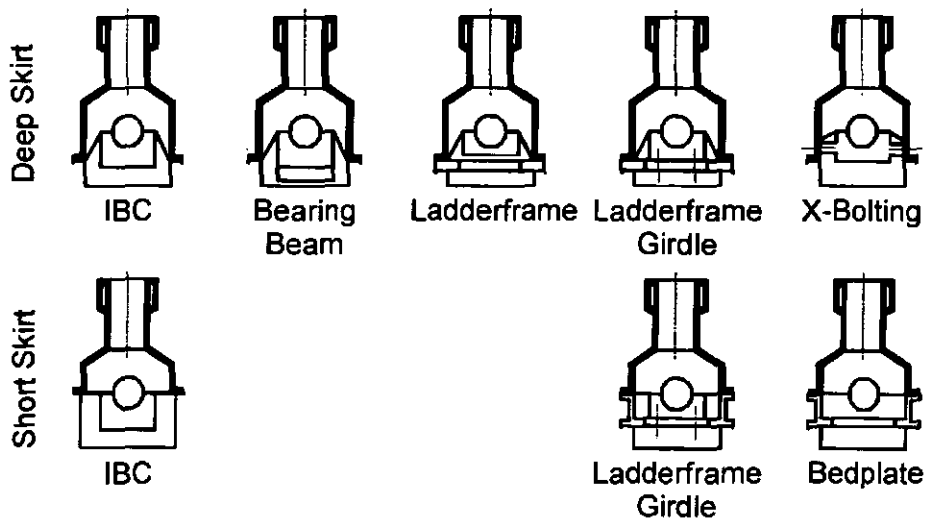


Figure 2.1.2 Crankcase Design and Main Bearing Support

or even the oilpan. Short and deep skirt blocks may be equipped with the bearing beam. Two design alternatives are known. The integrated bearing beam is a one piece design integrating the beam and the bearings. The bolted bearing beam, which is not widely used, is bolted to the individual bearing caps. The improvements are gained from the axial rigidity of the main bearings also reducing the engine block panel vibration.

The 'Ladderframe Girdle' connects the main bearing caps with the engine block rail and skirts. Axial main bearing vibration are reduced as well as panel vibration of the engine block.

A 'Ladderframe' is a simplified ladderframe girdle. The engine skirts are connected via the ladderframe without being bolted to the main bearing caps. The advantage is that main bearing cap vibration is not introduced into the ladderframe and hence can not excite the engine panels.

A 'Bedplate' design shows significant equivalence to the ladderframe girdle. The advantage is comparable to the ladderframe girdle, but the bearings caps are an integral part of the bedplate design. This design can be applied for short and deep skirts, but is typically applied to short skirt blocks only.

'Cross-Bolting' or 'X-Bolting' is applied at engines with either deep skirts or structural aluminium oil-pans. However this alternative is rarely used within in-line engines. V-engines hardly apply this feature due to cost and sealing issues.

Reviewing the described principal engine bottom-end design alternatives, a common trend is shown exhibiting a stiffened bottom-end design as the most effective solution for improved dynamic behaviour. Multiple investigations showed that bedplate [17], ladderframe girdle [18], cross-bolting [19] and bearing beam [20] exhibit improvements compared to the individual bearing caps. But a decisive design leader can not be established in terms of noise radiation.

Considering the main bearing aisle design, one has to account for the number of main bearings also. There are in-line engines on the market designed with a pair of bearings for two cylinders. A typical example is a four cylinder in-line engine with three main bearings only. This approach is considered for low friction and low cost engines. Modern or noise radiation optimised engines do not show this design feature any more.

## 2.2 Crankshaft Design Basics

Since the design of the crankshaft is often constrained by other factors, such as the length or width of the engine or the need to satisfy a specific bore to stroke ratio, the changes of the structure of a crankshaft may be limited practically to a marginal amount. Apart from these geometrical constraints further limitations are defined through actions reducing the engine friction and hence the bearing diameters or reducing the oscillating and rotating masses of the connecting rod by decreasing the connecting rod big-end diameter.

Geometrical relations have been obtained in the past describing the design of a crankshaft in relation to the bore diameter of the engine. These relations are no hard constraints but can be considered as rough guide-lines for first design iterations as shown in Table 1. These values do not reflect the limits of a design achievable today, but a summary of designs showing no general faults.

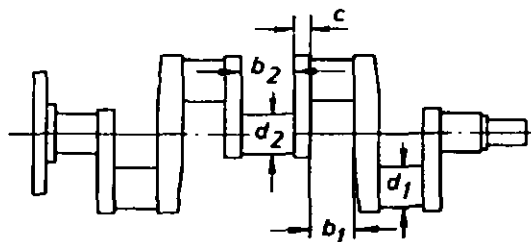


Figure 2.2.1 Basic Crankshaft Dimensions

Accounting for these principals, various design alternatives are available suiting different applications. Neglecting stationary and commercial vehicle applications as well as motorcycle and 2-stroke engines, one can easily characterise the design alternatives.

	Main Pin Diameter		Small Pin Diameter		Cheek Width	Cheek Thickness	Piston to Piston
	$d_2$ [mm]	$b_2$ [mm]	$d_1$ [mm]	$b_1$ [mm]	[mm]	$c$ [mm]	[mm]
I-Gasoline	0.7	0.6	0.55	0.6	0.9	0.5	1.1
	-	-	-	-	-	-	-
V-Gasoline	0.8	0.3	0.7	0.45	1.2	0.2	1.5
	0.75	0.6	0.6	0.55	0.9	0.45	1.2
I-Diesel	-	-	-	-	-	-	-
	0.85	0.3	0.75	0.4	1.2	0.2	1.6
V-Diesel	0.7	0.65	0.65	0.6	1.0	0.4	1.25
	-	-	-	-	-	-	-
V-Diesel	0.8	0.55	0.7	0.45	1.3	0.25	1.6
	0.7	0.6	0.7	0.6	1.0	0.35	1.4
V-Diesel	-	-	-	-	-	-	-
	0.85	0.5	0.75	0.4	1.35	0.2	2.0

Table 1 Main Dimensions of Crankshafts [21]  
(as factors of cylinder bore diameter)

The crankshaft is produced as a single piece out of cast iron or forged steel depending on the engine load and design parameters. Here Japanese manufacturers commonly select forged steel while the European based manufacturers prefer cast iron crankshafts for standard application. This may be affiliated to the machining process or other secondary reasons not being directly dependent on the design requirements. Because of this only few general design principles can be shown, as crankshaft design is commonly related to the manufacturer's philosophy.

Generally care is taken to avoid high stresses at the crankshaft fillets influenced through the crankshaft cheek thickness, the main and connecting rod bearing diameters and pin overlap. Additionally the engine noise radiation is influenced through the bending stiffness of the throws. Typical results are derived by Atsumi [22] and are shown in Figure 2.2.2.

The increase in bending stiffness will also affect the low frequency whirl of the flywheel. Whirl frequencies of vibration are influenced by low masses and inertias at the crankshaft and the stiffening effects of large journals (pins), overlaps of the pins and the cheek width and thickness as drawn in Figure 2.2.3. However, some of these factors are more significant than others. The low frequency flywheel whirl, which causes additional noise radiation due to increased bearing loads (by a factor of 5 to 10), is influenced most effectively by increasing the pin diameter, the web thickness and width of the cheek

crankshaft durability but also affects the radiated noise of the engine. This is mainly influenced by torsional modes being always coupled with bending oscillation. The crankcase is thereby excited and a significant noise radiation participation can be obtained at the torsional eigenfrequency and multiples as shown in Figure 2.2.4. This effect may be overcome by introducing a torsional damper and hence reducing the coupled bending displacements significantly.

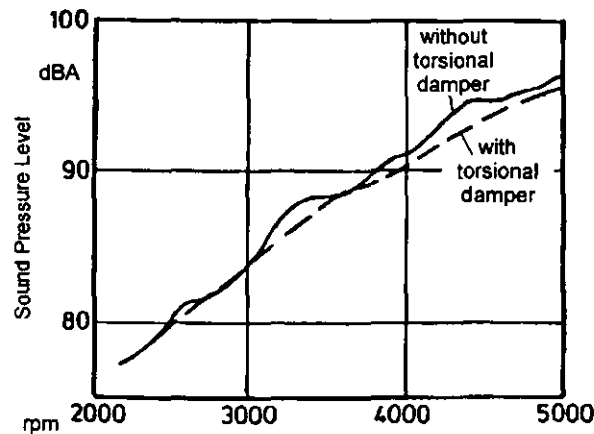


Figure 2.2.4 Effect of Torsional Vibration on Radiated Noise

As the crankshaft is one of the main contributors to engine weight, many weight reduction efforts are assigned to the cranktrain components. A typical approach of reducing the crankshaft weight is to introduce hollow-pins as detailed in Figure 2.2.5. But this design feature is ordinarily linked to cast crankshafts only (Figure 2.2.6). The advantage is a reduction in weight of 5%. The major disadvantage can be found in the reduced bending stiffness and thus reduced whirling frequency, which may have a significant effect on the engine noise radiation [23].

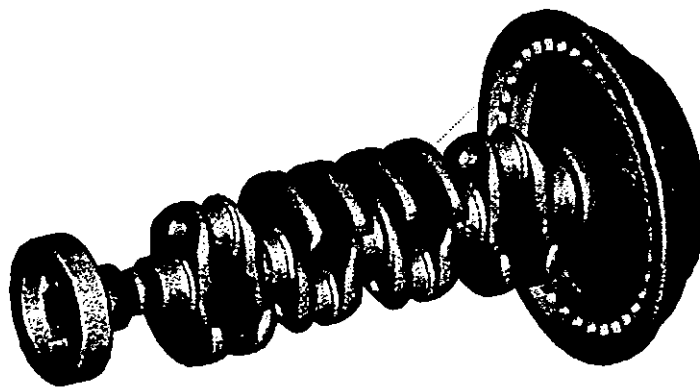


Figure 2.2.5 Hollow Pin Crankshaft

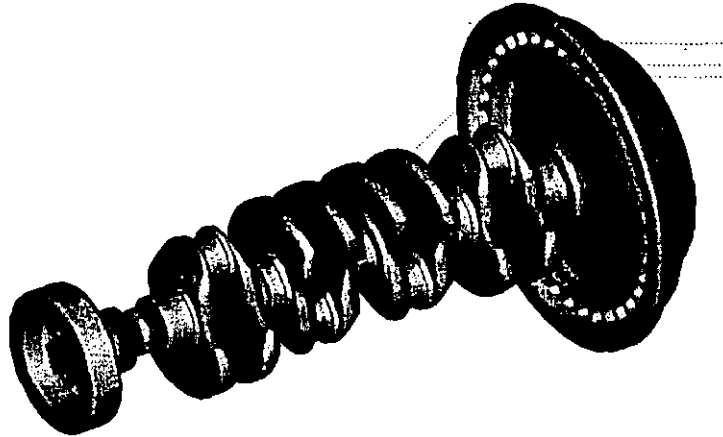


Figure 2.2.6 Solid Pin Crankshaft

Another opportunity to reduce the crankshaft weight is to reduce the mass of the counterweights. This can be achieved by either reducing the balancing of the system or by changing the balance weights without restricting the balancing approach. A typical example is shown in Figure 2.2.7 for a crankshaft with identical balancing and reduced weight of 1kg [24].

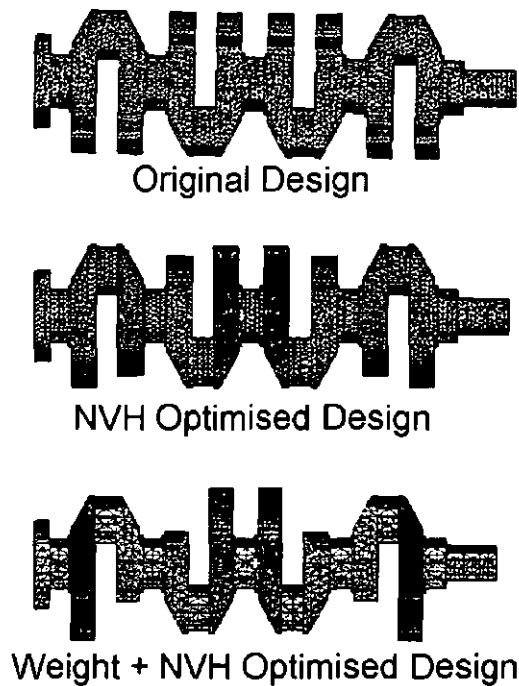


Figure 2.2.7 Weight Reduction by Balancing Optimisation

## 2.3 Flywheel Design Basics

The design of a flywheel assembly is not characterised by the definition of the mass moment of inertia only. Consideration must be given to the clutch or coupling device specific requirements. This is an extremely wide ranging field and cannot be covered in full detail within this section. The discussion of flywheel and coupling devices will therefore be limited to subjects of significant importance to the crankshaft-crankcase dynamics. Further stipulations are defined by considering manual systems only. Automatic systems such as torque converters and hydrostatic clutches are not considered within this section as the subsequently utilised and tested engine is assembled with a manual transmission. But some specific issues will be covered when discussing the flexible flywheel, as torque converters and hydrostatic clutches are also assembled with a flexible diaphragm. Hence the system resonance is to some extent identical to the flexible flywheel perception.

In studying the published flywheel assemblies in more detail one has to distinguish between design alternatives influencing the torsional and the bending behaviour of the system. A further design characteristic may be introduced by classifying the options as 'passive' or 'active' designs. Passive components, as the words indicate, act on behalf of their design and material properties. Active designs introduce mechanisms or devices with properties reducing specific response phenomena. A first characterisation of known flywheel and clutch designs is given in Table 2.

The active designs of dual mass flywheel and damped flywheel clutch are customarily introduced to reduce the torsional vibration transmitted to the transmission, without considering an effect on the crankshaft and crankcase. The idea is to increase the mass moment of inertia of the rotating components of the transmission without increasing the mass moment of inertia of all rotating components. This results in lowered transmission torsional resonance frequencies below idle. As this domain will not be excited during engine operation, this resonance frequency cannot be noticed by the driver. The design idea is to split the traditional flywheel mass into two parts. The primary mass increases the engine mass moment of inertia while the secondary mass increases the transmission mass moment of inertia. A spring and damping device links both inertias. Principle sketches of both systems are shown in Figure 2.3.1 compared to a conventional flywheel.

The dual mass flywheel and the damped flywheel clutch are physically based on the same principle: to reduce the torsional vibration of the drivetrain by introducing frictional losses. The dual mass flywheel aims for the luxury vehicle segment and the damped flywheel clutch targets for the medium vehicle segment. A typical effect on radiated

Passive Systems	Active Systems
conventional flywheel asymmetric flywheel flexible flywheel	dual mass flywheel damped flywheel clutch

Table 2 Flywheel Design Alternatives

noise gained from the damped flywheel clutch is shown in Figure 2.3.2. This improvement is based on the reduction of torsional vibration and hence reduced crankshaft displacements and bearing excitation.

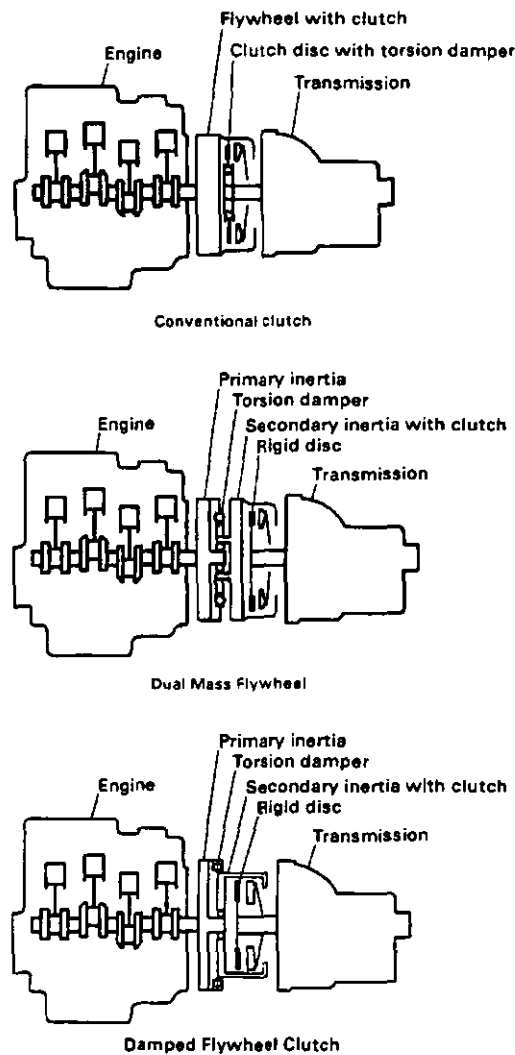


Figure 2.3.1 Clutch Design Principles [25]



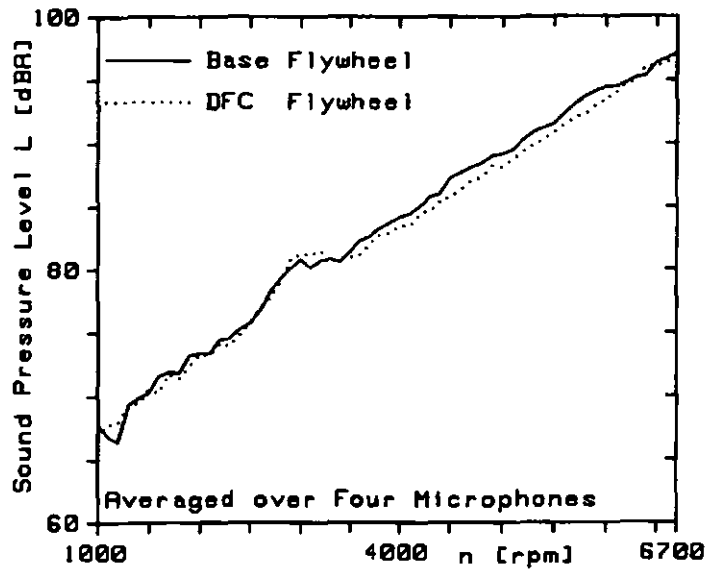


Figure 2.3.2 Noise Radiation of Conventional Flywheel vs. Damped Flywheel Clutch

Returning to the design principles of a passive flywheel, one has to account that the flywheel is the largest mass and mass moment of inertia of the cranktrain assembly. It vibrates at the lowest frequencies of whirl almost as a rotor on the crankshaft extension from the last bearing. It has therefore a significant effect on the lower frequencies of crankshaft whirl.

As a consequence of this, approaches are considered to modify these resonance frequencies by changing the flywheel inertia and mass. This action is commonly restricted, as lower inertias increase the whirling frequencies but at the same time dramatically exaggerate the torsional resonance characteristic of the entire drivetrain. Increasing the inertia diminishes the torsional fluctuation but reduces the whirling frequency and the vehicle acceleration performance. The inertia is mainly pre-defined by other requirements and may not be changed to avoid or shift whirling frequencies unless they cause major engine failures or problems. So, it is necessary to introduce design alternatives keeping the mass moment of inertia constant and modifying the lower whirling frequencies of the cranktrain assembly. Two design proposals are commonplace, namely the asymmetric flywheel and the flexible flywheel.

The asymmetric flywheel is characterised through a mass moment of inertia being identical to a conventional flywheel and two different moments of inertia about the vertical and horizontal axis as shown in Figure 2.3.3. This is achieved by an uneven mass distribution about the axis of rotation.

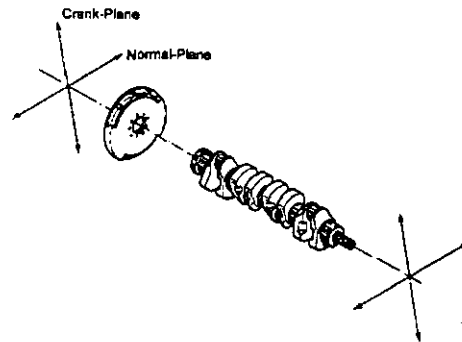


Figure 2.3.3 Asymmetric Flywheel

The crankshaft has two primary planes in which the first two bending eigenfrequencies occur. The inertia of the flywheel is modified in a way such that the larger inertia value coincides with the crankshaft plane exhibiting a higher resonance frequency, which will consistently be lowered. The reduced inertia value coincides with the plane showing the lower bending frequency. This whirling frequency will increase compared to the fully symmetrical flywheel. The final intention is that the two bending frequencies are shifted to a single value. This single frequency can then be effectively damped, if necessary, by a combined torsional and bending damper. Significant work has been done in this field and improvements of up to 4 dB(A) in structure borne noise were achieved on an in-line four cylinder engine [26]. Internal studies [27] confirmed the general findings and showed a significant influence of the ratio of the principal inertias as shown in Figure 2.3.4.

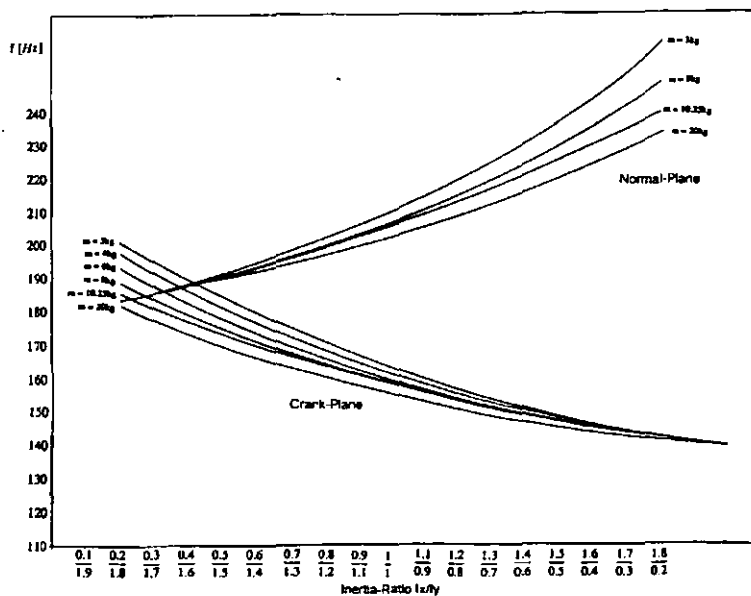


Figure 2.3.4 Whirling Frequencies vs. Inertia Ratio

As it is known that the bolted joint of the flywheel and the crankshaft introduces some flexibility and damping into the system, one must consider a rigid link, as more detailed information about this joint is not available. A specific flywheel design introduces a significant amount of flexibility into the system. The design relies on a flexible membrane bolted to the crankshaft and to the inertia ring (Figure 2.3.5). This detunes the bending or whirling frequencies of the crankshaft assembly and keeps the torsional rigidity. The drive plate separates the flywheel mass and the crankshaft dynamically because of its flexible connection. It eliminates the resonance of the crankshaft-flywheel system from the problem range of sound quality during acceleration, as described by Unisia [28].

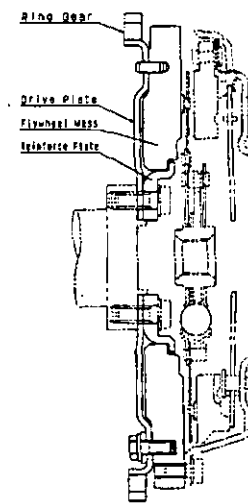


Figure 2.3.5 Flexible Flywheel

As mentioned earlier, torque converters and hydrostatic clutches are configured in the same way. The inertia ring of the manual clutch is replaced by either the converter or the clutch, hence the dynamic behaviour is identical to that exhibited by the flexible flywheel and can be covered by approaching a corresponding analytical model. For flywheels of automotive engines, the diaphragm is usually about 2.5mm thick to give an axial stiffness high enough to carry the axial thrust when the clutch is disengaged. Yamanouchi et al [29] published achieved advantages of up to 3-4dB(A) applying a flexible versus a conventional flywheel for in-line four cylinder application. Nissan [30] stated an improvement of about 2-3dB(A) in structure borne noise. Applying the flexible flywheel to the engine studied within this thesis, only 0.5 (max. 1.5)dB(A) could be gained from that design. Although the practical advantage of the flexible flywheel is known and sufficient to justify their use by at least some Japanese manufacturers, little is known about the fundamental background, the effect on the vibration characteristics of the crankshaft and the noise of the engine. Consequently, the design of the device is somewhat arbitrary and cannot be tuned for a specific engine application.

## **Chapter 3**

### **Dynamics of Rotating Systems**

This chapter will deploy the theoretical prerequisites for the later development of the characteristic engine rotating system. The shaft vibration and related theoretical aspects are covered, which are essential for predicting crankshaft vibration.

### 3.1 Introduction

The dynamics of rotating structures has been studied extensively in the past and the mind was commonly focused on centrifuge, turbine, or power-station technology [31]. The mechanical prerequisites from a definition point of view are: rotor, casing, bearings, bearing-structures, seals, clutch and transmission. Transferring this to the engine design, an identical set of components can be listed: crankshaft, engine-block, bearings, bearing-caps, seals, clutch and transmission. No significant differences exist when comparing these components. At first glance, one may suppose that a rotor design is significantly different to a crankshaft design in terms of geometry and utilisation, but this is not so. Rotors, and especially those in practice, can be described utilising the subsequent technical features: hydrodynamic bearing (section 3.5), gyroscopic and coriolis effects (section 3.6), and non-uniform rotating structures (section 3.7). If a rotor is treated in depth as listed, all the related rotor theory can be applied to the crankshaft and therefore the engine application, hence, all of the crankshaft specific differences are covered. They will be explained in detail in the referenced sections.

Later, a brief introduction is given for the 'Laval-Rotor' showing the principles of the dynamic response. This system is then developed to include all the necessary theory to cover the dynamic behaviour of a crankshaft system.

A 'Laval-Rotor' is defined as a flexible shaft carrying concentrated masses [32]. This is a significant simplification compared with reality, but all necessary and essential phenomenon can be developed applying this system. Typical system descriptions are shown in Figure 3.1.1 for the one-mass system and in Figure 3.1.2 for a multi-mass system. As the theoretical principles will not change with increasing numbers of masses and corresponding stiffnesses, a continuous shaft can be represented in principle as a 'Laval-Rotor'. The accuracy of the system description will increase with increasing numbers of masses and stiffnesses (Degree of Freedom's; DOF's).

The elastic deflection  $\delta_w$  of the shaft at an arbitrary location on the shaft is calculated using  $F$  as the centrifugal force:

$$\delta_w = \epsilon \frac{(\Omega/\omega)^2}{1 - (\Omega/\omega)^2} \quad 3.1.1$$

$$F = (\epsilon + \delta_w)m\Omega^2 \quad 3.1.2$$

where  $\Omega$ ,  $\omega$ ,  $\epsilon$ ,  $m$  and  $\delta_w$  are the shaft angular velocity, shaft eigenfrequency, shaft mass eccentricity, shaft mass and shaft elastic displacement respectively.

The shaft eigenfrequency  $\omega$  is defined for the one-mass system with  $\sqrt{c/m}$ . The shaft deflection increases proportionally to  $\epsilon m \Omega^2$  for rotational speeds  $\Omega < 0.5\omega$ . The deflection magnitude is equal to the mass eccentricity  $\epsilon$  at  $\Omega = \sqrt{1/2}\omega$ . The critical shaft speed is defined at  $\Omega = \omega$ , where the theoretical deflection becomes unlimited. For shaft speeds that are significantly higher compared to the critical speed, the shaft deflection is derived as an asymptote towards the magnitude of the mass eccentricity. A typical result for a one-mass system is shown schematically in Figure 3.1.3. Laval rotors carrying multiple masses can be treated similarly and the system response is equivalent. The only difference is that multiple critical shaft speeds occur at multiple corresponding shaft eigenfrequencies (Figure 3.1.4).



Figure 3.1.1 Laval-Rotor Representation

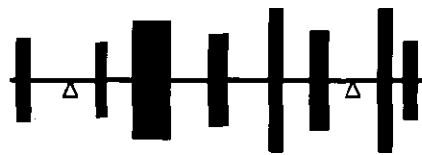


Figure 3.1.2 Rotor Idealisation

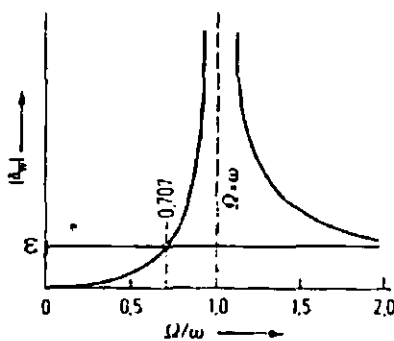


Figure 3.1.3 Shaft Deflection of Single-Mass Rotor

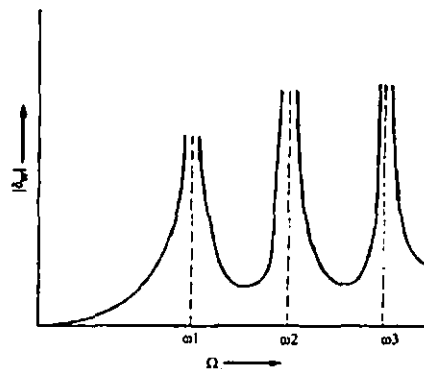


Figure 3.1.4 Shaft Deflection of Multiple Mass Rotor

The rotor dynamic systems described later can be represented with a linear differential equation or a system of linear differential equations. A solution of the differential equation consists of a homogeneous part and a particular part. The solution of the homogeneous

part gives the eigenfrequencies of the rotating system, from which one can derive the system critical speeds. Additionally, a stability assessment can be performed using the homogeneous solution. The particular solution is derived from either constant or periodic external excitation.

### 3.2 Undamped Rotating Structures with Rigid and Elastic Bearings

The first part of this section is dedicated to the elastic rotor supported by rigid bearings. It is also assumed that the inertia is perpendicular to the axis of rotation throughout the entire operation range. This assumption will be dropped later. The differential equation of motion will be derived for the system using two different formulations, firstly accounting for a global, fixed coordinate system and secondly accounting for a coordinate system rotating with the shaft speed  $\Omega$ .

*Fixed Coordinate System:* A fixed rectangular coordinate system  $(x,y,z)$  is introduced. The  $x$ -axis is defined as the axis of rotation and the origin is defined at the centre of the inertia on the axis between the constraints. The centre of the inertia  $W$  is defined by the coordinates  $z_w$  and  $y_w$ . The centre of gravity of the inertia  $S$  is defined accordingly ( $z_s$  and  $y_s$ ). A schematic picture is shown in Figure 3.2.1. The number of degrees of freedom of the inertia is given with two lateral displacements in the coordinate directions  $y,z$  and the rotational angle about the centre of the deflected axis  $W$  (Figure 3.2.2). Applying Newton's law, the mass forces must be equalised through the elastic reaction forces of the deformed shaft.

$$\begin{aligned} m\ddot{z}_s &= -cz_w \\ m\ddot{y}_s &= -cy_w \end{aligned} \quad 3.2.1$$

where  $m$ ,  $c$ ,  $y$  and  $z$  are the inertia mass, shaft stiffness, displacement in  $y$  and displacement in  $z$  direction.

The relation of the coordinates between  $W$  and  $s$  are given with:

$$\begin{aligned} z_s &= z_w + \varepsilon \cos \rho \\ y_s &= y_w + \varepsilon \sin \rho \end{aligned} \quad 3.2.2$$

Because the eccentricity  $\varepsilon$  is difficult to measure, it is much more convenient to replace  $y_s$  and  $z_s$  with the definition of the shaft deflection ( $y_w$  and  $z_w$ ) [33]. Applying two differentiations to  $z_s$  and  $y_s$  and using the definition for  $\omega = \sqrt{c/m}$ , two heterogeneous differential equations can be derived:

$$\ddot{z}_w + \omega^2 z_w = \epsilon \dot{\rho}^2 \cos \rho + \epsilon \ddot{\rho} \sin \rho$$

$$\ddot{y}_w + \omega^2 y_w = \epsilon \dot{\rho}^2 \sin \rho - \epsilon \ddot{\rho} \cos \rho$$

3.2.3

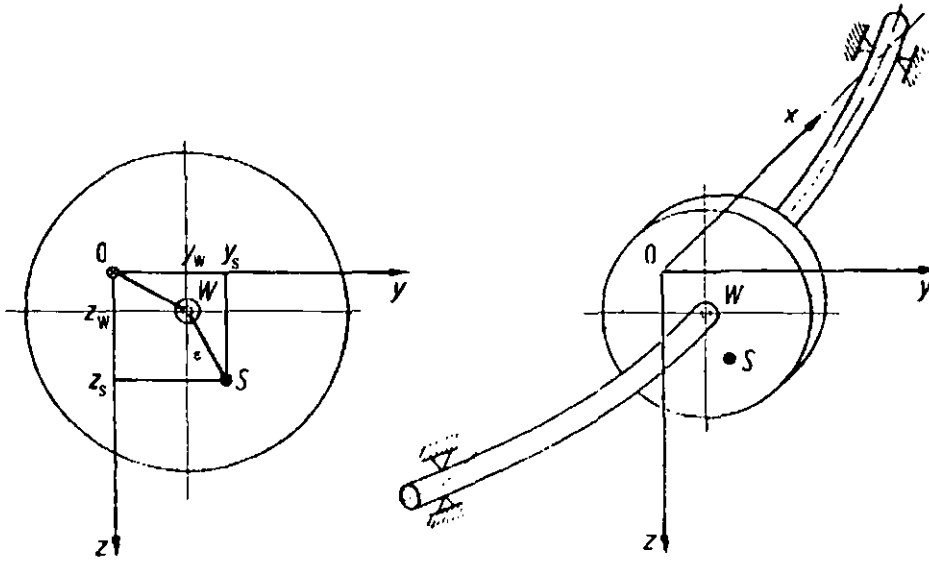


Figure 3.2.1 Deformed Rotor with Rigid Bearings

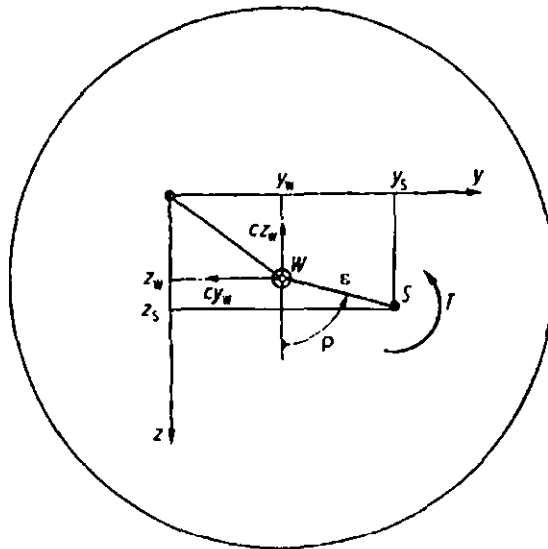


Figure 3.2.2 Inertia with Fixed Coordinate-System

By using the angular momentum relative to an axis perpendicular to the inertia and centred about S the equilibrium of moments results in :

$$\Theta \ddot{\rho} = T + c \epsilon (y_w \cos \rho - z_w \sin \rho)$$

3.2.4



The moment of inertia is defined as  $\Theta$  and  $T$  is the external torsional moment driving the system. Assuming a stationary system,  $T$  is equal to zero. Replacing  $\Theta$  with  $\Theta = mk^2$ , where  $k$  is the inertia radius, the angular acceleration may be written as:

$$\ddot{\rho} = \frac{\varepsilon}{k^2}(y_w \cos \rho - z_w \sin \rho)\omega^2 \quad 3.2.5$$

From this we are able to deduce that in a system running in a stationary condition the following conditions apply:

$$\dot{\rho} = \text{const} = \Omega \quad 3.2.6$$

$$\rho = \Omega t + \beta$$

The shaft eccentricity  $\varepsilon$  and the shaft deflection  $z_w$  and  $y_w$  are much smaller compared to the inertia-radius  $k$ , and from a practical point of view,  $\ddot{\rho}$  equals zero. The integration constant  $\beta$  is negligible, as  $\beta$  can be dropped by selecting an appropriate starting condition. The equilibrium of moments can therefore be dropped and the differential equation of motion of the two remaining degrees of freedom are written as:

$$\ddot{z}_w + \omega^2 z_w = \varepsilon \Omega^2 \cos(\Omega t + \beta) \quad 3.2.7$$

$$\ddot{y}_w + \omega^2 y_w = \varepsilon \Omega^2 \sin(\Omega t + \beta)$$

This set of heterogeneous linear differential equation is uncoupled. The generic solution for  $z_w$  and  $y_w$  is described as the combination of the homogeneous solution  $z_{w0}$  and  $y_{w0}$ , and the heterogeneous solution  $z_{w\varepsilon}$  and  $y_{w\varepsilon}$ . The subscript  $\varepsilon$  indicates that the heterogeneous part is driven by the system eccentricity  $\varepsilon$ . Neglecting the extreme condition that  $\Omega = \omega$ , one possible solution for the heterogeneous part is given with

$$z_{w\varepsilon} = \hat{z}_{w\varepsilon} \cos(\Omega t + \beta) \quad 3.2.8$$

$$y_{w\varepsilon} = \hat{y}_{w\varepsilon} \sin(\Omega t + \beta)$$

and the amplitudes of the enforced deflection are calculated as

$$\hat{z}_{w\varepsilon} = \hat{y}_{w\varepsilon} = \varepsilon \frac{\Omega^2}{\omega^2 - \Omega^2} \quad 3.2.9$$

Introducing a relation  $\eta = \frac{\Omega}{\omega}$  [34] for the frequency ratio of  $\omega$  and  $\Omega$ , the heterogeneous solution is given by:

$$z_{W\epsilon} = \epsilon \frac{\eta^2}{1 - \eta^2} \cos(\Omega t + \beta)$$

$$y_{W\epsilon} = \epsilon \frac{\eta^2}{1 - \eta^2} \sin(\Omega t + \beta)$$
3.2.10

Studying these equation in more detail it is evident that the oscillation of the centre of the shaft W is of common frequency and amplitude in the z- and y-direction. The phase shift is derived with 90°. The frequency of oscillation is identical to the angular velocity of the shaft  $\Omega$ . The amplitudes are proportional to the eccentricity and are dependent on the frequency ratio  $\eta$ . For  $\eta \rightarrow 1$  [ $\Omega = \omega$ ] one perceives unlimited amplitudes of the rotor and this is called a 'bending critical speed of the shaft'.

Last two equations describe a circular movement with a radius of:

$$r_{W\epsilon} = \sqrt{z_{W\epsilon}^2 + y_{W\epsilon}^2} = \epsilon \left| \frac{\eta^2}{1 - \eta^2} \right|$$
3.2.11

That is, the centre of the shaft W rotates with  $\Omega$  on a circular path with a radius of  $r_{W\epsilon}$ . The centre of gravity of the inertia S rotates with  $\Omega$  on a circular path with a radius of  $r_{S\epsilon}$ , which is:

$$r_{S\epsilon} = \sqrt{z_{S\epsilon}^2 + y_{S\epsilon}^2} = \epsilon \left| \frac{1}{1 - \eta^2} \right|$$
3.2.12

It is thus obvious that O, W, and S are lying on a straight line and that the shaft revolves with a constant amplitude in a deformed state.

*Rotating Coordinate System:* For some instances it is more convenient to derive the differential equation of motion within a coordinate system, which is syncro-rotating with the shaft. A typical example is given with a non-uniform rotating structure (see section 3.7). The results derived within the rotating coordinate system will lead to the same results as derived within the fixed coordinate system.

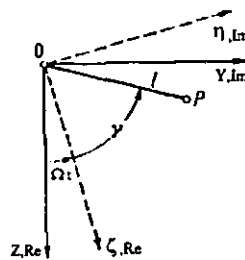


Figure 3.2.3 Fixed and Rotating Coordinate-System

This coordinate system rotates with the shaft angular speed  $\Omega$ . Applying a complex formulation for the system equation, it is a straightforward task to develop the new equations from the already derived equation of motion. As shown in Figure 3.2.3 an arbitrary point P is defined through the distance  $l$  from the origin of the coordinate system  $O$  and the angle  $\gamma$  defined between the real axis of the rotating coordinate system and the straight line between the origin  $O$  and the point  $P$ . The location of  $P$  within the fixed and rotating coordinate system is defined with

$$\begin{aligned} r &= z + jy = le^{j(\Omega t + \gamma)} \\ \delta &= \zeta + j\eta = le^{j\gamma} \end{aligned} \quad 3.2.13$$

The equation of transformation are therefore derived and can be written as:

$$r = \delta e^{j\Omega t} \quad 3.2.14$$

and backwards

$$\delta = r e^{-j\Omega t} \quad 3.2.15$$

The differential equations of motion of this system from eqn. 3.2.7 are rewritten in complex form [35]:

$$\ddot{r}_w + \omega^2 r_w = \varepsilon \Omega^2 e^{j(\Omega t + \beta)} \quad 3.2.16$$

Differentiating equation 3.2.14 with respect to time gives

$$\dot{r}_w = (\dot{\delta}_w + j\Omega \delta_w) e^{j\Omega t} \quad 3.2.17$$

$$\ddot{r}_w = (\ddot{\delta}_w + 2j\Omega \dot{\delta}_w - \Omega^2 \delta_w) e^{j\Omega t} \quad 3.2.18$$

The terms within the bracket in eqn. 3.2.18 represent in the order of occurrence: relative acceleration, Coriolis acceleration and guiding acceleration.

The differential equation of motion within the rotating coordinate system is then derived using eqns. 3.2.14, 16 and 18:

$$\ddot{\delta}_w + 2j\Omega \dot{\delta}_w + (\omega^2 - \Omega^2) \delta_w = \varepsilon \Omega^2 e^{j\beta} \quad 3.2.19$$

or

$$\begin{aligned} \ddot{\zeta}_w - 2\Omega \dot{\eta}_w + (\omega^2 - \Omega^2) \zeta_w &= \varepsilon \Omega^2 \cos \beta \\ \ddot{\eta}_w + 2\Omega \dot{\zeta}_w + (\omega^2 - \Omega^2) \eta_w &= \varepsilon \Omega^2 \sin \beta \end{aligned} \quad 3.2.20$$

which will be used in section 3.7 for non-uniform rotating structures.

*Laval Rotor with Elastic Bearings:* The assumption made so far covers rigid bearings. Traupel et Al [36] stated that this assumption is valid for those rotor applications representing a ratio of shaft stiffness versus casing stiffness of 1:10. The effect can easily be studied for IC-engine application by performing an eigenvalue analysis of a crankshaft. The shaft is supported through linear and isotropic springs at the main bearing. The spring stiffness for all the bearings are altered simultaneously for each analysis. The resulting eigenfrequencies are displayed in Figure 3.2.4. The changes in engine-block stiffnesses, which can practically be achieved, are highlighted. An averaged engine block bearing stiffness can be defined for a standard grey-cast-iron block with approximately  $1.0E5$  N/mm. Practical variation in engine block stiffness are in the order of approximately  $\pm 20\%$ . It can be seen that the influence on the eigenfrequencies of the bearing stiffness is considerable in the region of practical interest. Therefore, it is obvious that the rotor system must be studied utilising elastic bearing properties.

Practical bearing structures are not quite symmetric about the major coordinate directions. It is apparent that an anisotropic system representation must be introduced to cover the different stiffness properties. A possible simplification can be made by introducing two stiffness properties for the vertical and horizontal direction. It must be considered that the critical speeds of the rotor will be influenced by the different stiffness values.

- First, elastic bearing properties will reduce the critical speed significantly.
- Secondly, isotropic bearing properties will affect the number of critical speeds. A critical speed will occur for each major coordinate direction (i.e.: 2 critical speeds versus 1 for isotropic bearing properties)
- Thirdly, the shaft centre  $W$  will oscillate on an elliptical orbit for anisotropic bearings. This ellipse will be passed in a synchro-rotating or contra-rotating manner depending on the angular velocity  $\Omega$  of the shaft. For isotropic bearing properties, the shaft centre  $W$  will pass a circular orbit in a synchro-rotating manner as described before.

The casing or bearing stiffness of the rotor can be treated as a sequential spring to the rotor elasticity  $c$  as schematically sketched in Figure 3.2.5. Assuming paired identical springs for the casing structure within the vertical and horizontal direction, the resulting spring stiffnesses are derived as:

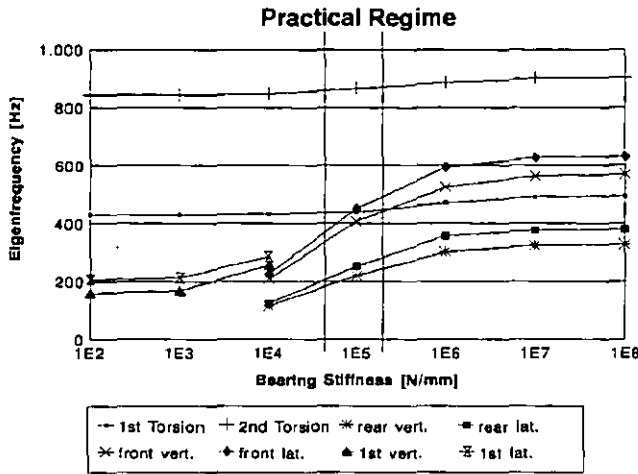


Figure 3.2.4 Main Bearing Stiffness Study

$$c_z = \frac{2c_v c}{2c_v + c}$$

3.2.21

and

$$c_y = \frac{2c_h c}{2c_h + c}$$

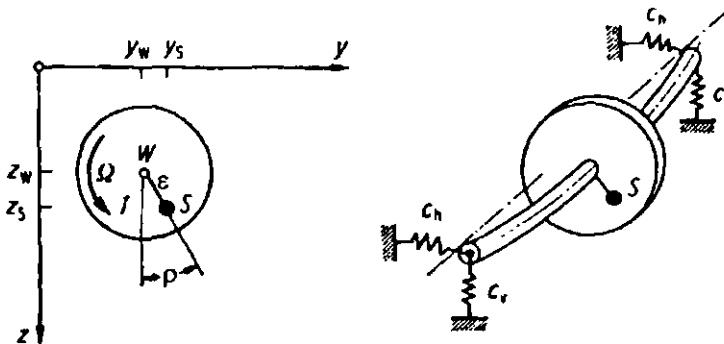


Figure 3.2.5 Elastic Supported Rotor

The equilibrium condition of the deflected rotor is shown in eqn. 3.2.22. Assuming a stationary mode of operation, eqn. 3.2.23 shows the conditions derived from this. The integration constant  $\beta$  can be dropped, as described previously. The coordinates of the centre of gravity S and the shaft centre W are again described, as shown in eqn. 3.2.2. Differentiating eqn. 3.2.24 twice and applying eqn. 3.2.22 and 3.2.23, the anisotropically supported shaft can be described as shown in eqn. 3.2.25.

$$m\ddot{z}_S = -c_z z_W \quad 3.2.22$$

$$m\ddot{y}_S = -c_y y_W$$

$$\Theta\ddot{\rho} = \varepsilon(y_W c_y \cos \rho - z_W c_z \sin \rho) + T$$

$$\ddot{\rho} = 0 \quad , \quad \dot{\rho} = \Omega \quad , \quad \rho = \Omega t + \beta \quad 3.2.23$$

$$z_S = z_W + \varepsilon \cos \rho \quad 3.2.24$$

and

$$y_S = y_W + \varepsilon \sin \rho$$

$$m\ddot{z}_W + c_z z = \varepsilon \Omega^2 m \cos \Omega t \quad 3.2.25$$

$$m\ddot{y}_W + c_y y = \varepsilon \Omega^2 m \sin \Omega t$$

The solution of the uncoupled differential equation is then given with:

$$z_W = \hat{z}_{w0} \cos(\omega_z t + \gamma_z) + \varepsilon \frac{\Omega^2}{\omega_z^2 - \Omega^2} \cos \Omega t \quad 3.2.26$$

$$y_W = \hat{y}_{w0} \cos(\omega_y t + \gamma_y) + \varepsilon \frac{\Omega^2}{\omega_y^2 - \Omega^2} \sin \Omega t$$

The displacement and velocity integration constants  $\hat{z}_{w0}, \hat{y}_{w0}, \gamma_z, \gamma_y$  are defined at the initial condition for  $t=0$  in the main coordinate directions. The eigenfrequencies  $\omega_z$  and  $\omega_y$  are defined as

$$\omega_z = \sqrt{\frac{c_z}{m}} \quad \text{and} \quad \omega_y = \sqrt{\frac{c_y}{m}} \quad 3.2.27$$

The values of these eigenfrequencies are no longer identical, as the supporting stiffnesses are different for the vertical and horizontal directions. It is important to emphasize that these two eigenfrequencies will drive two critical speeds. The exceptional case of identical stiffnesses for the vertical and horizontal direction ( $c_v=c_h$ ) will result in only one critical speed. A principal response of such a system is described in Figure 3.2.6.

With the assumption that all disturbances, due to initial conditions, no longer pertain, the stationary enforced displacements of the shaft centre are described as

$$z_{w\varepsilon} = \hat{z}_{w\varepsilon} \cos(\Omega t) = \varepsilon \frac{\Omega^2}{\omega_z^2 - \Omega^2} \cos \Omega t$$

$$y_{w\varepsilon} = \hat{y}_{w\varepsilon} \sin(\Omega t) = \varepsilon \frac{\Omega^2}{\omega_y^2 - \Omega^2} \sin \Omega t$$
3.2.28

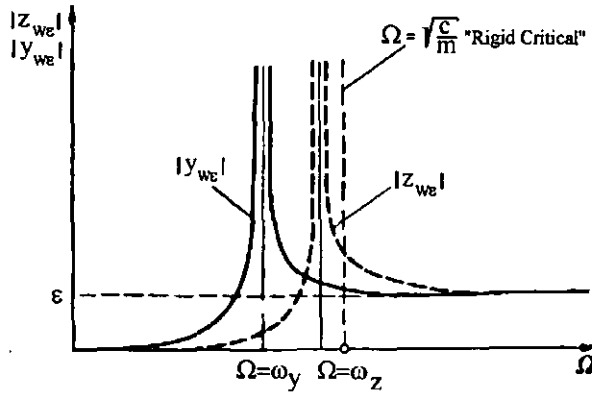


Figure 3.2.6 Response of Anisotropic Supported Shaft

The absolute amplitudes are shown in the previous Figure with respect to  $\Omega$ . The centre of the shaft rotates on an elliptical orbit. This can easily be shown by squaring the previous set of equations and summing the results. This gives us the mathematical description of an ellipse.

$$\left( \frac{z_{w\varepsilon}}{\hat{z}_{w\varepsilon}} \right)^2 + \left( \frac{y_{w\varepsilon}}{\hat{y}_{w\varepsilon}} \right)^2 = 1$$
3.2.29

The main axis of this ellipse are derived with:

$$\hat{z}_{w\varepsilon} = \varepsilon \frac{\Omega^2}{\omega_z^2 - \Omega^2} = \varepsilon \frac{\left( \frac{\Omega}{\omega_z} \right)^2}{1 - \left( \frac{\Omega}{\omega_z} \right)^2} = \varepsilon \frac{\eta_z^2}{1 - \eta_z^2}$$

$$\hat{y}_{w\varepsilon} = \varepsilon \frac{\Omega^2}{\omega_y^2 - \Omega^2} = \varepsilon \frac{\left( \frac{\Omega}{\omega_y} \right)^2}{1 - \left( \frac{\Omega}{\omega_y} \right)^2} = \varepsilon \frac{\eta_y^2}{1 - \eta_y^2}$$
3.2.30

with  $\eta_y = \frac{\Omega}{\omega_y}$  ,  $\omega_y = \sqrt{\frac{c_y}{m}}$

and  $\eta_z$  and  $\omega_z$  are similarly defined.

*Synco- and Contra-Rotating:* Studying this elliptical orbit in more detail, one may introduce a complex formulation in such a way that the y-axis is defined as the imaginary- and the z-axis as the real-axis. Applying the Euler equations

$$\cos x = \frac{1}{2}(e^{jx} + e^{-jx}) \tag{3.2.31}$$

$$\sin x = \frac{1}{2j}(e^{jx} - e^{-jx})$$

$z_{w\epsilon}$  and  $y_{w\epsilon}$  can be written as:

$$\begin{aligned} r_{w\epsilon} &= z_{w\epsilon} + jy_{w\epsilon} \\ &= \hat{z}_{w\epsilon} \cos \Omega t + j \hat{y}_{w\epsilon} \sin \Omega t \end{aligned} \tag{3.2.32}$$

and the complex formulation of the time dependent radius  $r_{w\epsilon}(t)$  is established. Using eqn. 3.2.31, this expression can be rewritten as

$$\begin{aligned} r_{w\epsilon}(t) &= \frac{1}{2}(\hat{z}_{w\epsilon} + \hat{y}_{w\epsilon})e^{j\Omega t} + \frac{1}{2}(\hat{z}_{w\epsilon} - \hat{y}_{w\epsilon})e^{-j\Omega t} \\ &= \hat{r}_+ e^{j\Omega t} + \hat{r}_- e^{-j\Omega t} \end{aligned} \tag{3.2.33}$$

The first part of the equation describes a circle with a radius of  $|\hat{r}_+|$  within the complex plane, which is a synco-rotating with the rotating shaft. The second part of the equation describes a circle with a radius of  $|\hat{r}_-|$ , which is a contra-rotating. A schematic description is shown in Figure 3.2.7.

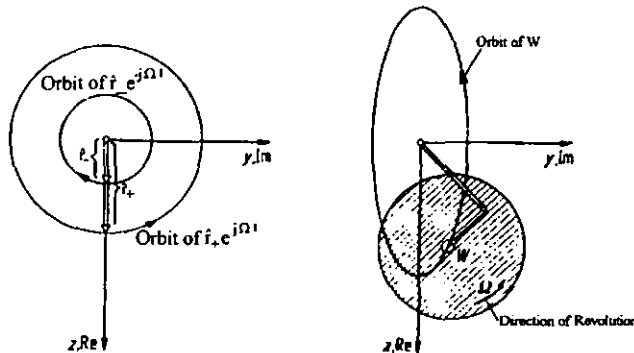


Figure 3.2.7 Synco- and Contra-Rotating Circular Orbits



The superposition of both circular paths results in an elliptical orbit of the centre of the shaft  $W$ . The direction of rotation is dependent on the magnitude of the individual radii  $|\hat{r}_+|$  and  $|\hat{r}_-|$ :

$ \hat{r}_+ $	$>$	$ \hat{r}_- $	Elliptical Orbit; Syncro-Rotation
$ \hat{r}_+ $	$<$	$ \hat{r}_- $	Elliptical Orbit; Contra-Rotation
$ \hat{r}_+ $	$=$	$ \hat{r}_- $	Oscillating Straight Orbit; Degenerated Ellipse

By combining eqns. 3.2.30 and 3.2.33 the magnitude of the radius  $|\hat{r}_+|$  and  $|\hat{r}_-|$  are derived as:

$$\hat{r}_+ = \frac{\varepsilon \Omega^2 (\omega_z^2 + \omega_y^2 - 2\Omega^2)}{2(\omega_z^2 - \Omega^2)(\omega_y^2 - \Omega^2)} \quad 3.2.34$$

and

$$\hat{r}_- = \frac{\varepsilon \Omega^2 (\omega_y^2 - \omega_z^2)}{2(\omega_z^2 - \Omega^2)(\omega_y^2 - \Omega^2)}$$

A typical example is shown in Figure 3.2.8. It is assumed that the relation of  $\omega_y$  and  $\omega_z$  is defined with  $\omega_y = 0.9\omega_z$ , and the horizontal supporting stiffness  $c_y$  is smaller than the vertical stiffness  $c_z$  with  $\eta = \frac{\Omega}{\omega} = \frac{0.85\Omega}{\omega_y} = \frac{0.944\Omega}{\omega_z}$

The system response obtained changes twice.

Within  $0 < \Omega < \omega_y$ , in other words below the first critical speed, a syncro-rotation is perceived. The rotation of the shaft and the orbital path are heading in the same direction. Within  $\omega_y < \Omega < \omega_z$ , in other words between the lower and the upper critical speeds, a contra-rotation occurs. The rotation of the shaft and the orbital path are heading towards different directions.

Within  $\Omega > \omega_z$ , in other words above the second critical speed, a syncro-rotation is perceived again.

The two critical conditions of  $\Omega = \omega_y$  and  $\Omega = \omega_z$  present 'unlimited' amplitudes of the orbits and a sudden change from contra- to syncro-rotation and vice versa [37]. A circular orbit can be obtained under two conditions: for values of  $\Omega = \sqrt{(\omega_y^2 + \omega_z^2)/2}$  and  $\Omega \gg \omega_z$ . At the latter condition a self-stabilising effect occurs. The centre of inertia stabilises at the centre of rotation with the radius  $|\hat{r}_+| \cong |\hat{r}_-| \cong \varepsilon$ .

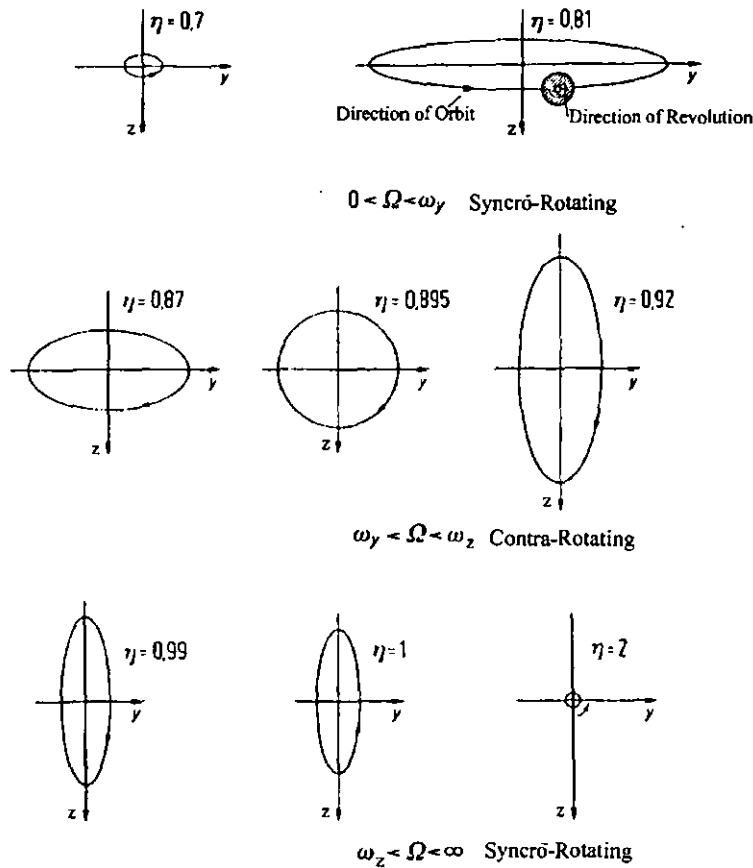


Figure 3.2.8 Condition of Syncro- and Contra-Rotation

### 3.3 Laval-Rotor with internal and external Damping

All damping effects have been neglected up to this point. This assumption is valid for most technical problems. Hence, measured critical eigenfrequencies or speeds are commonly marginally different from the theoretical solutions neglecting damping effects [38]. A case study will show in Chapter 8 that the material damping properties do not have a significant influence on the crankshaft whirling eigenfrequencies. Nevertheless it is known that resonances or critical speeds still have a significant effect on the system response amplitudes. The amplitudes are limited partially through the damping properties. To discuss damping properties in more details, it is important to distinguish the different damping categories and their corresponding effects on the dynamic behaviour of a vibrating system.

Two types of damping can be defined for describing all practical damping effects [39], i.e. external and internal damping.

External damping is generated through a system moving with a velocity  $v$  within a medium. The shear forces of the viscous fluid act reversely to the direction of movement. It is important to highlight that these forces are defined within the global stationary coordinate system. Transferring this to the engine application, it is a straightforward matter to identify the air as the fluid. As the design intend is that no component splashes through the oil in the sump, this must not be considered. Experience shows that external damping effects can be neglected for air damped rotor systems when no extensive turbine blades are attached to the rotor. The external damping properties are therefore not included in the theoretical discussion and the modelling approach of this research work.

Internal damping is induced by elastic deformations of the rotor during operation. A simple representation of the damping mechanism is shown in Figure 3.3.1. If the shaft is not rotating, the effects of internal damping are identical to those generated through external damping mechanism. The damping forces act contrarily to the shaft deformation. It is straightforward to develop the differential equation of motion for  $\Omega=0$ . They are expressed as:

$$\begin{aligned} m\ddot{z}_w + k_i\dot{z}_w + cz_w &= 0 \\ m\ddot{y}_w + k_i\dot{y}_w + cy_w &= 0 \end{aligned} \quad 3.3.1$$

where  $k_i$  represents a linear viscous damping property.

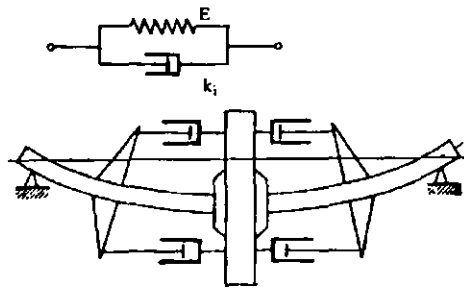


Figure 3.3.1 Viscous Material Model Representation

For rotating shafts the internal damping changes the rotor's behaviour dramatically. The damping properties are not proportional to the absolute velocities  $\dot{z}_w$  and  $\dot{y}_w$ , because the internal damping does not act against a fixed location within a fixed coordinate system. But the internal damping is proportional to those velocities  $\dot{\zeta}_w$  and  $\dot{\eta}_w$  defined within a rotating coordinate system. This coordinate system rotates with the same angular velocity  $\Omega$  as the shaft. It is identical to the coordinate system used in section 3.2 for the definition of the differential equation of motion, i.e. eqn. 3.2.20 . This equation

must be extended by those components representing the internal damping properties which are described with  $k_i \dot{\zeta}_w$  and  $k_i \dot{\eta}_w$ . Normalising these values with  $m$ , the differential equation is written as:

$$\ddot{\zeta}_w - 2\Omega \dot{\eta}_w + \left(\frac{k_i}{m}\right) \dot{\zeta}_w + (\omega^2 - \Omega^2) \zeta_w = \varepsilon \Omega^2 \cos \beta \quad 3.3.2$$

$$\ddot{\eta}_w + 2\Omega \dot{\zeta}_w + \left(\frac{k_i}{m}\right) \dot{\eta}_w + (\omega^2 - \Omega^2) \eta_w = \varepsilon \Omega^2 \sin \beta$$

Multiplying the second equation with  $j$  and introducing a new variable  $\delta_w = \zeta_w + j\eta_w$  the differential equation becomes:

$$\ddot{\delta}_w + (2j\Omega + (k_i/m)) \dot{\delta}_w + (\omega^2 - \Omega^2) \delta_w = \varepsilon \Omega^2 e^{j\beta} \quad 3.3.3$$

Assuming the homogeneous solution as

$$\delta_{w0} = \delta_{w0} e^{\lambda^* t} \quad 3.3.4$$

we can obtain the characteristic equation for the system,

$$\lambda^{*2} + (2j\Omega + k_i/m) \lambda^* + (\omega^2 - \Omega^2) = 0 \quad 3.3.5$$

which leads to

$$\lambda_{1,2}^* = -(j\Omega + k_i/2m) \pm \sqrt{(j\Omega + k_i/2m)^2 - (\omega^2 - \Omega^2)}$$

This equation is simplified by dropping the terms consisting of  $k_i^2$ , since  $k_i$  is of very small value. Another approximation is made using  $\sqrt{1-x} \approx 1 - 1/2x$ , when  $x \ll 1$ . Thus, we have

$$\begin{aligned} \lambda_1^* &= j(\omega - \Omega) - \frac{k_i}{2m} + \frac{k_i \Omega}{2m\omega} = -(\omega - \Omega)(D_i - j) \\ \lambda_2^* &= j(-\omega - \Omega) - \frac{k_i}{2m} - \frac{k_i \Omega}{2m\omega} = -(\omega + \Omega)(D_i - j) \end{aligned} \quad 3.3.6$$

with 
$$D_i = \frac{k_i}{2m\omega}$$

$D_i$  is defined as a measure for the internal non-dimensional damping property compared to the external damping property  $D_a$ .

When the shaft speed ( $\Omega$ ) is larger than the natural frequency ( $\omega$ ), i.e.  $\Omega > \omega$ , the internal damping increases the response amplitude. That is, the system is unstable for operational conditions above the critical speed in case no external damping is applied. This can be explained by examining the real part of  $\lambda_1^*$ , the positive nature leads to

unbounded rotation if  $\Omega > \omega$ . Consequently, operating an internally damped system above its critical speed requires the introduction of an external damping mechanism [40]. The critical rotor speed is derived as  $\Omega_{cr} = (1 + (D_a/D_i))\omega$  and is dependent on the ratio of internal and external damping rather than their absolute magnitude.

### 3.4 Resonance Phenomenon and Stability Criteria

As noted in section 3.3, it is important to determine whether a system is stable. When it is stable, it is important to determine the degree of stability. The stability analyses of systems are a totally independent area of research. Only a brief introduction is presented here. Some basic literature is given in the list of references, and a more detailed and theoretical approach is given in section 6.3.3 for non-linear coupled systems.

How can stability be defined ?

If the output of a system grows, even at a reasonable rate, when there is no input or when the input is not demanding an increase in the output, the system is defined as unstable and is, therefore, of no practical use. It is a characteristic of enforced dynamic systems that for certain values of the operational parameters the response is 'unlimited' and the system becomes unstable. It is, therefore, very important that a dynamic system is designed not only for principal functions but also for stability within the specified range of operation conditions.

A system shows a trend towards instability, if the response is greater than the requested output level. However, if the oscillations die out and become zero within infinite time, the system is defined as absolutely stable. If the oscillations do not die out but remain at a constant level or amplitude, the system is considered to be of limited stability. Should the response continue to increase in amplitude, then the system is absolutely unstable.

The differential equation of motion can be treated as a description of a dynamic system, as this equation describes the relationship between the input signal, in this case the forcing function, and the response function, in this case the physical displacement and the corresponding derivatives [41]. From the analytical system description one can determine the transient response to specific inputs and the resulting steady-state value of the output, which would exhibit the stability of the system. However, the stability of a linear or linearised system can be determined directly from the differential equation of motion with no knowledge of the input signal being required.

Two questions must be answered for any system [42]:

- 1.) Is the system absolutely stable?

After this has been determined and if the answer is yes, the second question must be asked:

- 2.) How stable is the system ( regarding parameter changes) ?

The answers to these questions are not easy to find, as an analysis of the system is required in order to establish whether it is stable or not.

Now, let's consider a homogeneous differential equation, i.e. eqn. 3.4.1 .

$$a_n x^{(n)} + \dots + a_k x^{(k)} + \dots + a_2 \ddot{x} + a_1 \dot{x} + a_0 x = 0 \quad 3.4.1$$

The coefficients  $a_k$  may be real or complex. Assuming an exponential function for  $x$ , i.e.

$$x = \hat{x} e^{\lambda t} \quad 3.4.2$$

eqn. 3.4.1 gives

$$H(\lambda) = a_n \lambda^n + \dots + a_2 \lambda^2 + a_1 \lambda + a_0 = 0 \quad 3.4.3$$

which is called characteristic equation of eqn. 3.4.1 . The  $n$ -roots of  $\lambda$ , also called eigenvalues of the system, describe the system response. The solution is commonly complex:

$$\lambda_v = \delta_v + j\omega_v \quad (v = 1, 2, \dots, n) \quad 3.4.4$$

If all of the coefficients  $a_k$  are real, all  $\lambda_v$  become paired conjugate complex. If all roots  $\lambda_v$  contain negative real parts  $\delta_v$ , then the system is absolutely stable [43]. The response of the system, excited by an external forcing function, will fade out within infinite time, because the negative real part results in a multiplied exponential slope of decreasing amplitude. Positive real parts  $\delta_v$  of one or more  $\lambda_v$  result in an unstable system with increasing response.

$$x_v(t) = \hat{x}_v e^{\lambda_v t} = \hat{x}_v e^{\delta_v t} e^{j\omega_v t} \quad 3.4.5$$

Generally, there must be no eigenvalues with positive real parts and the negative parts must be sufficiently large so that every mode is satisfactorily damped and sufficiently stable [44].

The system equation, i.e. 3.4.1, is a single differential equation. But in reality, coupled differential equations are the common description of dynamic systems. The stability analysis of those systems can be accomplished in a similar manner by calculating the root of a characteristic equation and investigating the negative or positive real components of the solution. The known approaches are basically specific for the individual description and formulation of the differential equation of motion. It is not necessary to discuss all available theories and techniques to evaluate the system stability. Stability methods are explained and described in more detail at the time that method is applied (section 6.3.3).

Some publications are given in the references, which may be used as a guide for detailed information ([45],[46],[47]).

### 3.5 Laval-Rotor with Hydrodynamic Bearings

Rotors with hydrodynamic bearings show a specific dynamic response. A generic investigation was done by Tondl [48] from which the obtained results are shown in Figure 3.5.1. The measured absolute displacements in vertical direction of the disk are shown in the upper left graph. The frequencies are shown in the lower left graph. The corresponding time dependent amplitudes of the disk in the vertical direction are displayed on the right hand side for six different rotation speeds marked in the upper left graph. The upper curves describe the vibration of the shaft centre within the hydrodynamic bearing. The lower graph displays the vibration of the inertia. The two vibration amplitudes are not scaled to the same gauge.

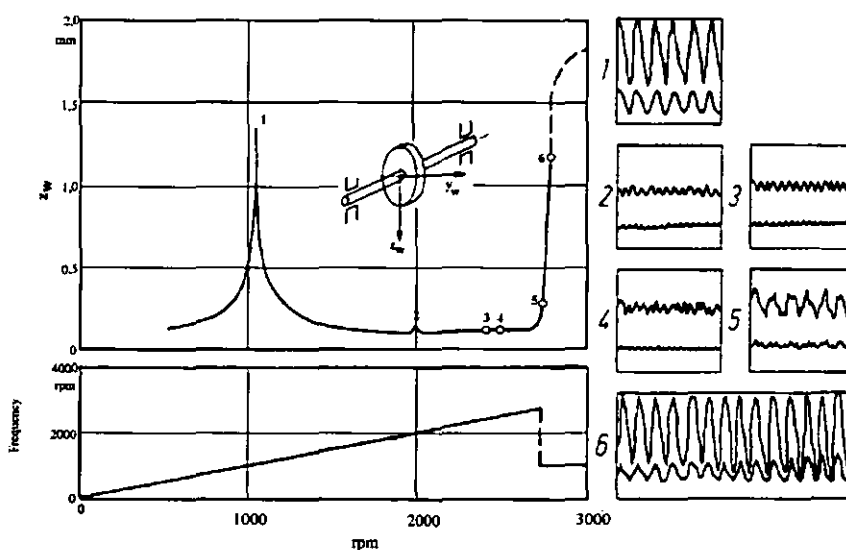


Figure 3.5.1 Rotor Resonances with Hydrodynamic Bearings [by Tondl]

The results from the upper left graph show the expected response of a rotor carrying one inertia. One critical speed or resonance condition is detected at approximately 1000 rpm. The amplitude of this resonance is limited, as the hydrodynamic bearings are operating as external damping properties as being described in section 3.3. The response of the rotor decreases monotonically above 1000 rpm. An insignificant peak is measured at 2000 rpm, but no explanation is given and this effect is still unknown. At approximately 2700 rpm the measured amplitudes of the rotor and the shaft centres increase dramatically. Looking at condition 6 at the lower right graph it is clear that the operation condition is not stable and the amplitudes still increases. The displacement magnitudes at the critical condition 1 are smaller than those at condition 6. The resonance frequency drops to approximately the same level as that at the critical speed as shown in the frequency graph. This frequency is then no longer dependent on the angular velocity of the system  $\Omega$ , as it should be according to the previously described theory. This is therefore a strong indication that this effect is invoked by introducing hydrodynamic bearings. Apart from the enforced rotational vibration at condition 1 another critical speed is detected at condition 6. The dynamic behaviour at or above this condition can be described as a self-excited vibration of monotonically increasing amplitude oscillating with the system eigenfrequency  $\omega$ . There are unquestionably limits for these resonance amplitudes. The limiting factors are material contact within the hydrodynamic bearing and non-linear oil-film properties. But the main interest is to calculate this critical cut-off speed, the effect on the system stability and the corresponding resonance amplitude at this speed.

The subsequent theoretical discussion is organised in two steps. The first step concentrates on the effect of hydrodynamic bearings supporting a rigid shaft. The resulting distinct effects are derived from the hydrodynamic bearing properties. Secondly, hydrodynamic bearings and elastic shafts are combined and the consequences are discussed. While the theory and application of hydrodynamic slide bearings are reported in Chapter 4, it is essential to introduce some basic definitions and equations which are relevant for the understanding of the subsequent theoretical deployment.

The bearing properties presented in an earlier case as a combination of shaft and casing stiffnesses are detached from the shaft description. This is a prerequisite to the introduction of different descriptions for the shaft, casing and bearing. The properties include stiffness and damping description for all components.

One common model for the description of hydrodynamic slide bearings is shown in Figure 3.5.2. The bearing is described through a parallel application of spring and damping devices. The springs and dampers are approximated as linear elements around



the specific operation conditions. The theory is based on a piece by piece linear approximation for the whole range of operation conditions. The matrix relation for the stiffness properties are shown in eqn. 3.5.1 . Eqn. 3.5.2 depicts the damping model. Both properties are measured ([49];[50];[51];[52];[53]) or can be predicted analytically [Chapter 4]. The Sommerfeld number is shown in eqn. 3.5.3, which describes the bearing characteristics.

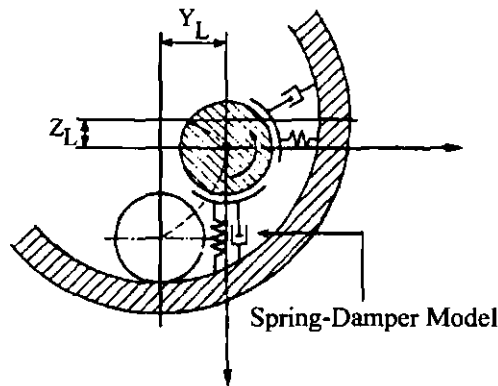


Figure 3.5.2 Hydrodynamic Bearing Spring-Damper Model

$$\begin{bmatrix} F_z \\ F_y \end{bmatrix}_c = \begin{bmatrix} c_{zz} & c_{zy} \\ c_{yz} & c_{yy} \end{bmatrix} \begin{bmatrix} z_L \\ y_L \end{bmatrix} \quad 3.5.1$$

$$\mathbf{f}_c = \mathbf{C}_L \mathbf{x}_L$$

$$\begin{bmatrix} F_z \\ F_y \end{bmatrix}_b = \begin{bmatrix} b_{zz} & b_{zy} \\ b_{yz} & b_{yy} \end{bmatrix} \begin{bmatrix} \dot{z}_L \\ \dot{y}_L \end{bmatrix} \quad 3.5.2$$

$$\mathbf{f}_b = \mathbf{B}_L \dot{\mathbf{x}}_L$$

$$So = \frac{F_{stat} \psi^2}{BD \eta_{oil} \Omega} \quad 3.5.3$$

where  $F_{stat}$ ,  $\psi = (D - d)/d$ ,  $B$ ,  $D$ ,  $\eta_{oil}$ ,  $\Omega$  are the static bearing load, relative bearing clearance, bearing length and diameter, viscosity of oil and shaft angular velocity respectively. The absolute radial clearance is defined as the difference between the casing and shaft radii, i.e.  $\Delta R = R - r$ .

The differential equation of motion and margins of stability for rigid rotors will be developed first to show the significance of individual variables of the slide bearings. Referring to Figure 3.5.3 the differential equations of motion for  $z_w = z_L$  and  $y_w = y_L$  are written as:

$$\frac{m}{2} \begin{bmatrix} \ddot{z}_w \\ \ddot{y}_w \end{bmatrix} + \begin{bmatrix} b_{zz} & b_{zy} \\ b_{yz} & b_{yy} \end{bmatrix} \begin{bmatrix} \dot{z}_w \\ \dot{y}_w \end{bmatrix} + \begin{bmatrix} c_{zz} & c_{zy} \\ c_{yz} & c_{yy} \end{bmatrix} \begin{bmatrix} z_w \\ y_w \end{bmatrix} = \frac{\epsilon \Omega^2 m}{2} \begin{bmatrix} \cos & \Omega & t \\ \sin & \Omega & t \end{bmatrix} \quad 3.5.4$$

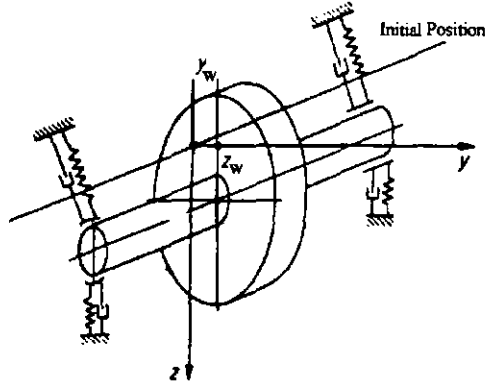


Figure 3.5.3 Rigid Rotor with Slide Bearings

Multiplying with  $So\Delta R/F_{stat}$  and using  $F_{stat}=mg/2$  the equations of motion become [52]:

$$\frac{So\Delta R}{g} \begin{bmatrix} \ddot{z}_w \\ \ddot{y}_w \end{bmatrix} + \frac{1}{\Omega} \begin{bmatrix} \beta_{zz} & \beta_{zy} \\ \beta_{yz} & \beta_{yy} \end{bmatrix} \begin{bmatrix} \dot{z}_w \\ \dot{y}_w \end{bmatrix} + \begin{bmatrix} \gamma_{zz} & \gamma_{zy} \\ \gamma_{yz} & \gamma_{yy} \end{bmatrix} \begin{bmatrix} z_w \\ y_w \end{bmatrix} = \frac{\epsilon \Omega^2 So\Delta R}{g} \begin{bmatrix} \cos & \Omega & t \\ \sin & \Omega & t \end{bmatrix} \quad 3.5.5$$

In eqn. 3.5.5 the damping and stiffness coefficients are replaced by non-dimensional coefficients as a function of the Sommerfeld number.

$$\gamma_{ik} = c_{ik} \frac{So\Delta R}{F_{stat}} \quad \beta_{ik} = b_{ik} \frac{So\Delta R\Omega}{F_{stat}} \quad 3.5.6$$

Assuming the homogeneous solution  $\begin{bmatrix} z_{wo} \\ y_{wo} \end{bmatrix} = \begin{bmatrix} \hat{z}_{wo} \\ \hat{y}_{wo} \end{bmatrix} e^{\lambda t}$  yields the characteristic equation

$$\alpha^2 \left( \frac{\lambda}{\Omega} \right)^4 + \alpha A_3 \left( \frac{\lambda}{\Omega} \right)^3 + (\alpha A_4 + A_2) \left( \frac{\lambda}{\Omega} \right)^2 + A_1 \left( \frac{\lambda}{\Omega} \right) + A_0 = 0$$

with:

$$A_0 = \gamma_{zz}\gamma_{yy} - \gamma_{yz}\gamma_{zy}$$

$$A_1 = \beta_{zz}\gamma_{yy} + \beta_{zz}\gamma_{zz} - (\beta_{zy}\gamma_{yz} + \beta_{yz}\gamma_{zy})$$

$$A_2 = \beta_{zz}\beta_{yy} - \beta_{yz}\beta_{zy}$$

$$A_3 = \beta_{zz} + \beta_{yy}$$

$$A_4 = \gamma_{zz} + \gamma_{yy}$$

$$\alpha = \frac{So\Delta R\Omega^2}{g}$$

3.5.7

The real parts of all the four parts are negative, if the following condition is fulfilled [54], with  $r_i$  being the polynomial coefficients.

$$r_1 r_2 r_3 - r_0 r_3^2 - r_4 r_1^2 \geq 0 \quad 3.5.8$$

which develops to:

$$\alpha^2 A_1^2 - A_1(\alpha A_4 + A_2)\alpha A_3 + \alpha^2 A_3^2 A_0 \leq 0 \quad 3.5.9$$

That is, under this condition the system is stable, and the margin of stability is reached, if eqn. 3.5.9 equals to zero. Using the expression for  $\alpha$  in eqn. 3.5.7, the cut-off speed for the beginning of instability is obtained as:

$$\Omega_{Cut-off} = \sqrt{\frac{g}{\Delta R S o} \frac{A_1 A_2 A_3}{(A_1^2 - A_1 A_3 A_4 + A_0 A_3^2)}} \quad 3.5.10$$

It is seen that the critical or cut-off speed is a function of the Sommerfeld number, as all  $A_i$  are functions of the Sommerfeld number. A change in cut-off speed can only be achieved by modifying the bearing geometry. There is no effect by changing the rotor or reducing the eccentricity.

*Differential Equation of Motion and Stability Margins for Elastic Rotors:* According to Figure 3.5.4 the equations of equilibrium are:

$$\begin{aligned} m \ddot{z}_s &= -c(z_w - z_L) \\ m \ddot{y}_s &= -c(y_w - y_L) \end{aligned} \quad 3.5.11$$

where

$$\begin{aligned} z_s &= z_w + \varepsilon \cos \Omega t \\ y_s &= y_w + \varepsilon \sin \Omega t \end{aligned} \quad 3.5.12$$

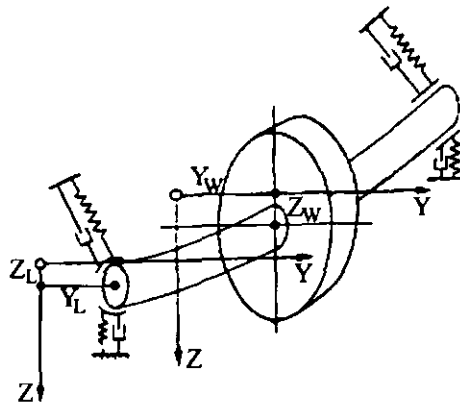


Figure 3.5.4 Elastic Rotor with Slide Bearings

The equation of equilibrium at the slide bearings develops to:

$$c_{zz}z_L + c_{zy}y_L + b_{zz}\dot{z}_L + b_{zy}\dot{y}_L - \frac{c}{2}(z_w - z_L) = 0 \quad 3.5.13$$

$$c_{yz}z_L + c_{yy}y_L + b_{yz}\dot{z}_L + b_{yy}\dot{y}_L - \frac{c}{2}(y_w - y_L) = 0$$

The differential equation of motion can then be obtained as:

$$\begin{bmatrix} m & & & \\ & m & & \\ & & 0 & \\ & & & 0 \end{bmatrix} \begin{bmatrix} \ddot{z}_w \\ \ddot{y}_w \\ \ddot{z}_L \\ \ddot{y}_L \end{bmatrix} + \begin{bmatrix} 0 & & & \\ & 0 & & \\ & & b_{zz} & b_{zy} \\ & & b_{yz} & b_{yy} \end{bmatrix} \begin{bmatrix} \dot{z}_w \\ \dot{y}_w \\ \dot{z}_L \\ \dot{y}_L \end{bmatrix} + \begin{bmatrix} c & 0 & -c & 0 \\ 0 & c & 0 & -c \\ -\frac{1}{2}c & 0 & c_{zz} + \frac{1}{2}c & c_{zy} \\ 0 & -\frac{1}{2}c & c_{yz} & c_{yy} + \frac{1}{2}c \end{bmatrix} \begin{bmatrix} z_w \\ y_w \\ z_L \\ y_L \end{bmatrix} = \begin{bmatrix} \epsilon m \Omega^2 \\ 0 \\ 0 \\ 0 \end{bmatrix} \cos \Omega t + \begin{bmatrix} 0 \\ \epsilon m \Omega^2 \\ 0 \\ 0 \end{bmatrix} \sin \Omega t \quad 3.5.14$$

or in matrix form

$$\mathbf{M} \cdot \ddot{\mathbf{x}} + \mathbf{B} \cdot \dot{\mathbf{x}} + \mathbf{C} \cdot \mathbf{x} = \hat{\mathbf{a}} \cos(\Omega t) + \hat{\mathbf{b}} \sin(\Omega t)$$

Solution of these four differential equations is difficult to achieve without numerical methods. An eigenvalue extraction is one possible method for deriving the stability criteria. For stable motion there must be no eigenvalues with positive real parts. The negative parts must be sufficiently large that every mode is satisfactorily damped and sufficiently stable. The method described in section 3.4 is not able to give any information about the critical speed, but will indicate whether stability or instability occurs. If knowledge about the cut-off speed is essential, one has to perform multiple numerical analyses with different operation conditions. Each analysis will answer the question of stability or instability. Therefrom, one can draw a multidimensional stability chart for this system. The potentially explored parameters are  $S_o$ ,  $m$ ,  $c$ ,  $\Omega$ , and  $\epsilon$ .

### 3.6 Gyroscopic Effect

The results and conclusions derived thus far are restricted to rotors and inertias defined as concentrated or point masses; or that the rotor disk is not deflected with an angular displacement (Figure 3.6.1 left). This simplification can be used for those systems with very stiff shafts and concentrated masses or rotor disks with low inertias. This assumption is not applicable in most rotor systems with large inertias. Engine application especially faces a significant effect originated from the flywheel and pulley inertias. The angular degree of freedom must be considered. This significantly affects the dynamic response of the rotating system and the corresponding bearing and excitation forces of the casing structure (Figure 3.6.1 right).

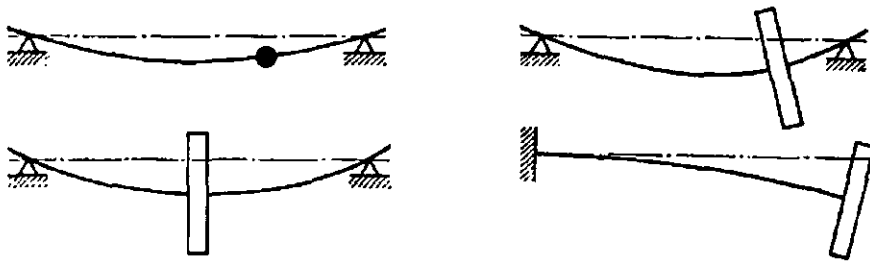


Figure 3.6.1 Rotor Principles

The transverse and angular motion are described in a fixed coordinate system as shown in Figure 3.6.2 where the transverse and angular displacements and the corresponding moments are shown. The gyroscopic effect occurs if the rotating disk is deflected to a direction perpendicular to the rotation axis. This effect increases with increasing angular velocity, angular moment of inertia, and speed of deflection. A principle experiment is shown in Figure 3.6.3 and the equation of motion can be written as:

$$M_{wy} = -\Theta_p \Omega \dot{\rho}_z + \Theta_a \ddot{\rho}_y \tag{3.6.1}$$

where the first term is the gyroscopic couple or moment.  $\Theta_p$  is the polar moment of inertia and  $\Theta_a$  is the moment of inertia about a diameter.

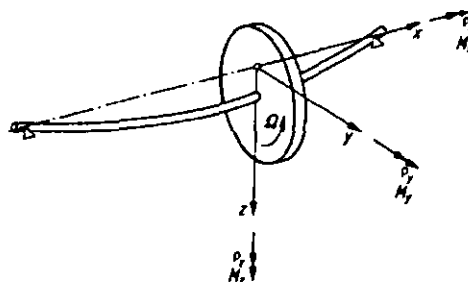


Figure 3.6.2 Deformed Rotor and Forces

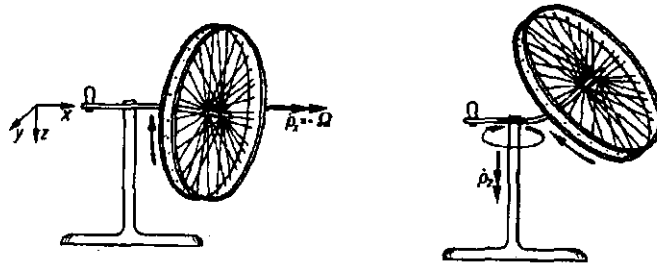


Figure 3.6.3 Gyroscopic Principle

The rotor eigenfrequencies become a functional of the angular velocity  $\Omega$  embarked by the gyroscopic moment. The critical speed of a rotor carrying a thin disk increases compared to the critical speed obtained from a concentrated mass system. The critical speed is reduced for those inertias with  $\Theta_a > \Theta_p$  compared to the concentrated mass system.

An additional eigenfrequency is obtained for the added degree of freedom describing the angular displacement. This eigenfrequency describes an additional critical speed of the system.

The differential equation of motion of this system is derived below. Utilising the equilibrium of forces and moments at the centre of the disk the stiffness matrix is written as:

$$\begin{bmatrix} F_z \\ M_y \\ F_y \\ M_z \end{bmatrix}_w = \begin{bmatrix} c_{11} & c_{12} \\ c_{21} & c_{22} \\ & c_{11} & -c_{12} \\ & -c_{21} & c_{22} \end{bmatrix} \begin{bmatrix} z_w \\ \rho_{wy} \\ y_w \\ \rho_{wz} \end{bmatrix} \quad \begin{matrix} z, x - plane \\ y, x - plane \end{matrix} \quad 3.6.2$$

or

$$\mathbf{f}_w = \mathbf{C} \cdot \mathbf{x}_w$$

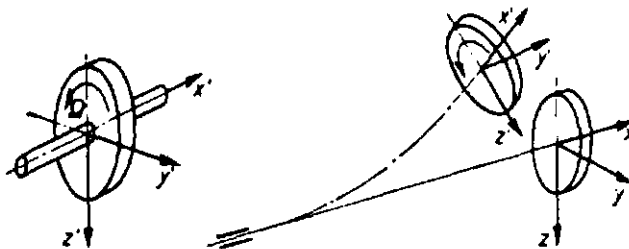


Figure 3.6.4 Displaced Coordinate System

The mass and the gyroscopic matrices are derived by considering the transverse and the angular motion of the disk. Applying a coordinate system with transverse and angular displacement  $(x', y', z')$  (Figure 3.6.4) being congruent with those of the centre of the inertia, the components of the angular momentum are:

$$\begin{aligned}
 L_{x'} &= \Theta_p \dot{\rho}_{Sx} \\
 L_{y'} &= \Theta_a \dot{\rho}_{Sy} \\
 L_{z'} &= \Theta_a \dot{\rho}_{Sz}
 \end{aligned}
 \tag{3.6.3}$$

These can be transformed into the fixed coordinate system (x,y,z) as shown in Figure 3.6.5 assuming small angular displacements. The results are:

$$\begin{aligned}
 L_x &= L_{x'} = -\Omega \Theta_p \\
 L_y &= L_{y'} + L_{x'} \rho_{Sz} \\
 L_z &= L_{z'} - L_{x'} \rho_{Sy}
 \end{aligned}
 \tag{3.6.4}$$

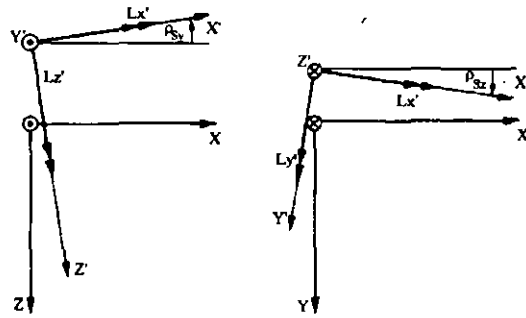


Figure 3.6.5 Angular Momentum in Fixed Coordinate System

Therefore, the equations of angular motion are:

$$\begin{aligned}
 M_y = \dot{L}_y &= \Theta_a \ddot{\rho}_{Sy} - \Omega \Theta_p \dot{\rho}_{Sz} \\
 M_z = \dot{L}_z &= \Theta_a \ddot{\rho}_{Sz} + \Omega \Theta_p \dot{\rho}_{Sy}
 \end{aligned}
 \tag{3.6.5}$$

In eqn. 3.6.5,  $\Theta_a \ddot{\rho}_{Sy}$  and  $\Theta_a \ddot{\rho}_{Sz}$  represent the rotational inertia. Both components are independent of  $\Omega$ . The terms  $-\Omega \Theta_p \dot{\rho}_{Sz}$  and  $\Omega \Theta_p \dot{\rho}_{Sy}$  represent the gyroscopic effect which diminishes with decreasing rotational speed and vanishes at  $\Omega=0$ .

The whole set of equations of motion are then expressed as:

$$\begin{bmatrix} F_z \\ M_y \\ F_y \\ M_z \end{bmatrix} = \begin{bmatrix} m & 0 \\ 0 & \Theta_a \\ & m & 0 \\ & 0 & \Theta_a \end{bmatrix} \begin{bmatrix} \ddot{z}_S \\ \ddot{\rho}_{Sy} \\ \ddot{y}_S \\ \ddot{\rho}_{Sz} \end{bmatrix} + \begin{bmatrix} 0 & 0 \\ 0 & -\Omega \Theta_p \\ 0 & 0 \\ 0 & +\Omega \Theta_p \end{bmatrix} \begin{bmatrix} \dot{z}_S \\ \dot{\rho}_{Sy} \\ \dot{y}_S \\ \dot{\rho}_{Sz} \end{bmatrix}
 \tag{3.6.6}$$

or

$$\mathbf{f}_S = \mathbf{M} \cdot \ddot{\mathbf{x}}_S + \mathbf{G} \cdot \dot{\mathbf{x}}_S$$

Since  $f_s + f_w = 0$ , eqn. 3.6.2 and 3.6.6 give

$$\begin{bmatrix} m & 0 \\ 0 & \Theta_a \end{bmatrix} \begin{bmatrix} \ddot{z}_s \\ \ddot{\rho}_{sy} \end{bmatrix} + \begin{bmatrix} 0 & 0 \\ 0 & +\Omega\Theta_p \end{bmatrix} \begin{bmatrix} \dot{z}_s \\ \dot{\rho}_{sy} \end{bmatrix} + \begin{bmatrix} c_{11} & c_{12} \\ c_{21} & c_{22} \end{bmatrix} \begin{bmatrix} z_w \\ \rho_{wy} \end{bmatrix} = 0 \quad 3.6.7$$

Using the following complex representations

$$\begin{aligned} r_s &= z_s + jy_s & r_w &= z_w + jy_w \\ \rho_s &= \rho_{sz} + j\rho_{sy} & \rho_w &= \rho_{wz} + j\rho_{wy} \end{aligned} \quad 3.6.8$$

eqn. 3.6.7 becomes

$$\begin{bmatrix} m & 0 \\ 0 & \Theta_a \end{bmatrix} \begin{bmatrix} \ddot{r}_s \\ \ddot{\rho}_s \end{bmatrix} + \begin{bmatrix} 0 & 0 \\ 0 & -j\Theta_p\Omega \end{bmatrix} \begin{bmatrix} \dot{r}_s \\ \dot{\rho}_s \end{bmatrix} + \begin{bmatrix} c_{11} & -jc_{12} \\ jc_{12} & c_{22} \end{bmatrix} \begin{bmatrix} r_w \\ \rho_w \end{bmatrix} = 0 \quad 3.6.9$$

Since the centres of the shaft and inertia are not identical, for uniformly rotating shafts  $r_s$  is rewritten in terms of  $r_w$  as:

$$r_s = r_w + \epsilon e^{j(\Omega t + \beta)} \quad 3.6.10$$

If the shaft is not perpendicular to the inertia disk, for some tolerance reasons, an angle  $\alpha$  describes the angular mismatch between both components.

$$\rho_s = \rho_w + \alpha e^{j(\Omega t + \gamma)} \quad 3.6.11$$

Using the last two relations and eqn. 3.6.9 the differential equation of motion for a shaft with an inertia disk is written as:

$$\begin{bmatrix} m & 0 \\ 0 & \Theta_a \end{bmatrix} \begin{bmatrix} \ddot{r}_w \\ \ddot{\rho}_w \end{bmatrix} + \begin{bmatrix} 0 & 0 \\ 0 & -j\Theta_p\Omega \end{bmatrix} \begin{bmatrix} \dot{r}_w \\ \dot{\rho}_w \end{bmatrix} + \begin{bmatrix} c_{11} & -jc_{12} \\ jc_{12} & c_{22} \end{bmatrix} \begin{bmatrix} r_w \\ \rho_w \end{bmatrix} = \Omega^2 \begin{bmatrix} m\epsilon e^{j\beta} \\ (\Theta_a - \Theta_p)\alpha e^{j\gamma} \end{bmatrix} e^{j\Omega t} \quad 3.6.12$$

It is a straightforward task to solve this differential equation numerically for different values of  $\Omega$ . But it is necessary to discuss the solutions of this equation to aid understanding of the numerical results.

The homogeneous solution of this differential equation of motion can be obtained by assuming exponential form, i.e. eqn. 3.6.13, and applying the symmetric condition of matrix C.

$$\begin{bmatrix} r_{w0} \\ \rho_{w0} \end{bmatrix} = \begin{bmatrix} \hat{r}_{w0} \\ \hat{\rho}_{w0} \end{bmatrix} e^{\lambda_v t} \quad 3.6.13$$

It was shown by Stodola [55] that the solution has only imaginary eigenvalues  $\lambda_v$ . This yields a further simplification:



$$\lambda_v = j\omega_v \tag{3.6.14}$$

Thus, substituting eqn. 3.6.13 into the homogeneous part of eqn. 3.6.12 yields the following characteristic equation for a non-trivial solution.

$$\begin{vmatrix} (m\omega_v^2 + c_{11}) & -jc_{12} \\ jc_{12} & (-\Theta_a\omega_v^2 + \Theta_p\Omega\omega_v + c_{22}) \end{vmatrix} = 0 \tag{3.6.15}$$

or in the expanded form

$$m\Theta_a\omega_v^4 - m\Theta_p\Omega\omega_v^3 - (c_{22}m + c_{11}\Theta_a)\omega_v^2 + c_{11}\Theta_p\Omega\omega_v + (c_{11}c_{22} - c_{12}^2) = 0 \tag{3.6.16}$$

The solution of this characteristic equation yields four real roots  $\omega_v$ . The eigenfrequencies or natural frequencies of the rotating system are dependent on the system properties ( $m, \Theta_a, \Theta_p, c_{ik}$ ) and the rotational speed  $\Omega$ . As already stated above, it is a tedious task to calculate the individual eigenfrequencies of the system analytically. A qualitative discussion of the expected results is of more interest and can be compared later with numerical results. A qualitative description of the results is obtained by describing the eigenfrequencies  $\omega_v$  versus  $\Omega$  for the condition of  $\Theta_a < \Theta_p$ . A comparison is given for various relations between  $\Theta_a$  and  $\Theta_p$  later within this section. The graphs in Figure 3.6.6 exhibit two positive values of  $\omega_v$  and two negative ones. The graphs are point-symmetric. This is shown in eqn. 3.6.16 by replacing  $\omega_v$  with  $-\omega_v$  and  $\Omega$  with  $-\Omega$ . The gyroscopic effect equals to zero for resting shafts ( $\Omega=0$ ), but four eigenfrequencies are still perceived, because of the effect of the rotational inertia  $\Theta_a$ .

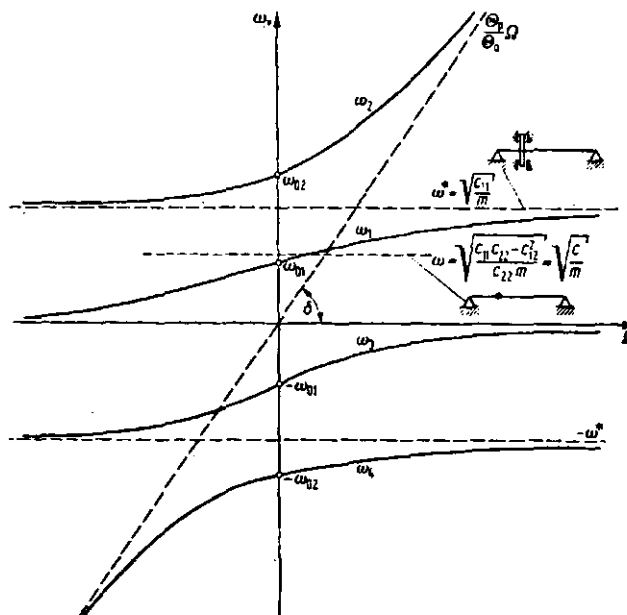


Figure 3.6.6 Eigenfrequencies with respect to angular velocity  $[\omega_v (v=1,2,3,4) \text{ and } \Theta_p > \Theta_a]$

Applying concentrated masses ( $\Theta_a = \Theta_p = 0$ ) to eqn. 3.6.16  $\omega_{01}$  is perceived as a smaller value compared to  $\omega$ . This formulates to:

$$\omega_{01} < \omega = \sqrt{\frac{c}{m}} = \sqrt{\frac{c_{11}c_{22} - c_{12}^2}{c_{22}m}} \quad 3.6.17$$

The eigenfrequency  $\omega_{02}$  is greater compared to  $\omega^*$ , derived from a guided system. This formulates to:

$$\omega_{02} > \omega^* = \sqrt{\frac{c_{11}}{m}} \quad 3.6.18$$

The limiting values of eqn. 3.6.16 for various values of  $\Omega$  are derived as:

$$\begin{array}{ll} \Omega \rightarrow -\infty & \Omega \rightarrow +\infty \\ \omega_1 \rightarrow 0 & \omega_1 \rightarrow \omega^* \\ \omega_2 \rightarrow \omega^* & \omega_2 \rightarrow \frac{\Theta_p}{\Theta_a} \Omega \\ \omega_3 \rightarrow -\omega^* & \omega_3 \rightarrow 0 \\ \omega_4 \rightarrow \frac{\Theta_p}{\Theta_a} \Omega & \omega_4 \rightarrow -\omega^* \end{array} \quad 3.6.19$$

The asymptote is defined through the ratio of  $\Theta_p/\Theta_a$  and the angle  $\delta$  varies from a maximum value of  $63.5^\circ$  for  $\Theta_p = 2\Theta_a$  to  $45^\circ$  for  $\Theta_p = \Theta_a$  [56]. The slope of this asymptote becomes much smaller for values of  $\Theta_a \gg \Theta_p$ .

Applying the system description thus derived it is important to investigate the resonance criteria for internal and external excitation. The internal excitation is imposed by unbalance forces syncro-rotating with the shaft's angular velocity. External excitation is originated by external forces. Within the engine application, these forces are the cranktrain dynamic forces including the gas and mass forces. The resonance criteria will be described independently as both effects are not linked to each other.

Focussing on the internal excitation first, eqn. 3.6.12 must be solved for the heterogeneous condition. Since the inertia eccentricity  $\varepsilon$  and the inertia angular mismatch  $\alpha$  are independent, one can derive the heterogeneous solution apart from each other and may superimpose the derived results later. A practicable solution is given by:

$$\begin{bmatrix} r_{w\varepsilon} \\ \rho_{w\varepsilon} \end{bmatrix} = \begin{bmatrix} \hat{r}_{w\varepsilon} \\ \hat{\rho}_{w\varepsilon} \end{bmatrix} e^{j(\Omega t + \beta)} \quad 3.6.20$$

Benz [57] showed that the solution for this heterogeneous system can be developed with:

$$\begin{bmatrix} \hat{f}_{w\epsilon} \\ \hat{p}_{w\epsilon} \end{bmatrix} = \frac{\epsilon m \Omega^2}{\Delta_{sr}} \begin{bmatrix} (\Theta_p - \Theta_a)\Omega^2 + c_{22} \\ -j c_{12} \end{bmatrix} \quad 3.6.21$$

with

$$\Delta_{sr} = \begin{vmatrix} -m\Omega^2 + c_{11} & -j c_{12} \\ j c_{12} & (\Theta_p - \Theta_a)\Omega^2 + c_{22} \end{vmatrix}$$

The shaft amplitudes will become unlimited under the condition that  $\Delta_{sr}$  equals to zero. The condition for those values of  $\Omega$  is called bending critical speed of the shaft. It is sometimes usual to call this resonance condition syncro-rotating bending-critical speed  $\Omega_{sr}$  of the shaft. This expression is used to emphasise the syncro-rotating effect of this resonance and to distinguish it from the later described contra-rotating critical bending speed. The determinant solves in terms of  $\Omega$  for the condition  $\Delta_{sr}=0$  with:

$$\Omega_{sr} = \pm \sqrt{\frac{1}{2} \left\{ \frac{c_{11}}{m} - \frac{c_{22}}{\Theta_p - \Theta_a} \pm \sqrt{\left( \frac{c_{11}}{m} - \frac{c_{22}}{\Theta_p - \Theta_a} \right)^2 + \frac{4(c_{11}c_{22} - c_{12}^2)}{m(\Theta_p - \Theta_a)}} \right\}} \quad 3.6.22$$

The solution for  $\Omega_{sr}$  denotes positive and negative values. The negative sign represents a system rotating in the reverse direction. But the values of the critical speed are independent of the direction of rotation. Eqn. 3.6.22 results in complex solution for inertia values with  $\Theta_p > \Theta_a$ , because the second or internal root is larger compared to the first part of the external root. A complex solution for a shaft speed is not meaningful in any physical sense and can be neglected. Therefore, only positive signs before the roots are applicable. From the physical point of view, this means that only a single syncro-rotating critical bending speed can exist for systems with polar inertias larger than diameter inertias. The physical principle is explained as a kind of moment trying to straight up the deflected inertia. This formulates as a type of reinforcement for the shaft and the resulting bending critical speed must be higher compared with a system critical speed  $\omega$  without gyroscopic effect. This is also shown in Figure 3.6.6. Resonances can be obtained if the excitation frequency is identical to the shaft eigenfrequency  $\omega_v$ . While the excitation is based on the eccentricity of the inertia, both frequency values, excitation and shaft rotation are identical ( $\Omega = \Omega_o$ ). Syncro-rotating bending-critical speeds are then obtained from the graph, if the straight line representing the excitation frequency  $\Omega_o$  crosses the graphs of the eigenfrequencies of the rotating shaft  $\omega_v$ . This is shown in Figure 3.6.7 for inertia values of  $\Theta_p > \Theta_a$ . A second syncro-rotating bending-critical speed cannot be obtained, because the slope of  $\Omega_o$  is less than that of the asymptote of the second resonance. An intersection of the excitation frequency with the second eigenfrequency is, therefore, not possible.

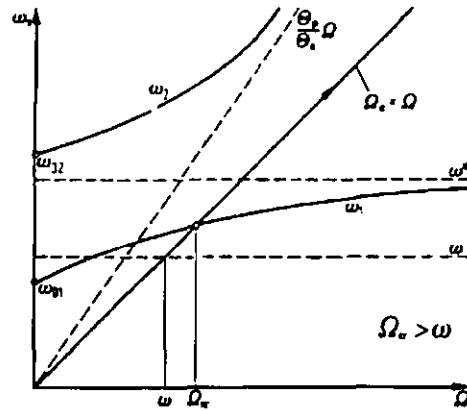


Figure 3.6.7 Bending-Critical Speed ( $\Theta_p > \Theta_a$ )

A similar picture can be drawn for inertia values of  $\Theta_p < \Theta_a$  (Figure 3.6.8). The slope of the excitation frequency is unchanged at  $45^\circ$ , but the gradient of the asymptote of the second eigenfrequency alters to values below  $45^\circ$ . A second intersection provides the second bending-critical speed of such a system. While the bending-critical frequency of the system  $\Theta_p > \Theta_a$  is increased, the bending-critical speeds for systems with  $\Theta_p < \Theta_a$  are reduced compared with a system description without gyroscopic effect.

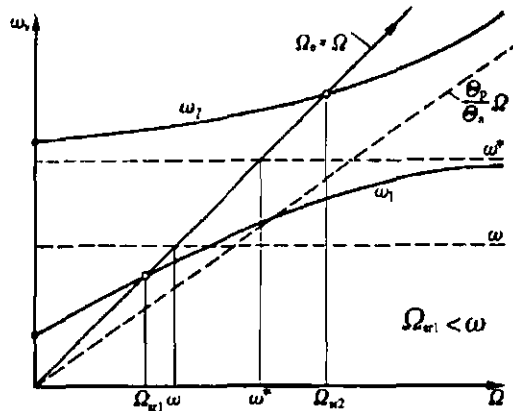


Figure 3.6.8 Bending-Critical Speed ( $\Theta_p < \Theta_a$ )

As shown before, syncro-rotational vibration can be obtained from syncro-rotational excitation only. Forced contra-rotating vibration of cylindrical shafts and inertias can be distinguished only in those systems excited by contra-rotational forces; i.e. spurious terms with  $e^{-j\Omega t}$ . Practical examples are given by those systems excited by sinusoidal external forces of constant direction. A typical example is shown in Figure 3.6.9 and one can imagine that this example is also applicable to the crankshaft system. The external force acting on the crankshaft is originated by the conrod mass force and combustion pressure.

Now, we assume that the direction of the excitation force is in the z-direction and has the form:

$$F = \hat{F} \cos \Omega t = \frac{\hat{F}}{2} (e^{j\Omega t} + e^{-j\Omega t}) \quad 3.6.23$$

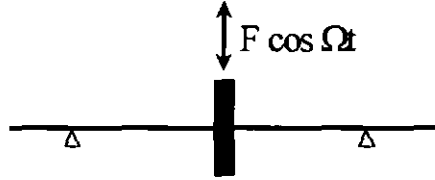


Figure 3.6.9 Shaft with Harmonic Excitation of Constant Direction

The differential equation of motion under this excitation force can be derived from eqn. 3.6.12 by assuming  $\epsilon=\alpha=0$ . It has the form,

$$\begin{bmatrix} m & 0 \\ 0 & \Theta_a \end{bmatrix} \begin{bmatrix} \dot{r}_w \\ \dot{\rho}_w \end{bmatrix} + \begin{bmatrix} 0 & 0 \\ 0 & -j\Theta_p\Omega \end{bmatrix} \begin{bmatrix} \dot{r}_w \\ \dot{\rho}_w \end{bmatrix} + \begin{bmatrix} c_{11} & -jc_{12} \\ jc_{12} & c_{22} \end{bmatrix} \begin{bmatrix} r_w \\ \rho_w \end{bmatrix} = \begin{bmatrix} \frac{1}{2}\hat{F} \\ 0 \end{bmatrix} (e^{j\Omega t} + e^{-j\Omega t}) \quad 3.6.24$$

The solution of this forced vibration can be achieved by the superposition of a synco-rotating response and a contra-rotating response. The synco-rotating response is obtained by applying the approach as shown previously. It is, therefore, only necessary to investigate the contra-rotating response of the system. A possible solution is assumed as:

$$\begin{bmatrix} r_w \\ \rho_w \end{bmatrix}_{cr} = \begin{bmatrix} \hat{r}_w \\ \hat{\rho}_w \end{bmatrix}_{cr} e^{-j\Omega t} \quad 3.6.25$$

This creates a response, which is rotating with the angular speed  $\Omega$  of the shaft, but the rotation is defined in the opposite direction. Substituting eqn. 3.6.25 into eqn. 3.6.24, Benz and Kowalewski [58] obtained:

$$\begin{bmatrix} \hat{r}_w \\ \hat{\rho}_w \end{bmatrix}_{cr} = \frac{\hat{F}}{2\Delta_{cr}} \begin{bmatrix} -(\Theta_p + \Theta_a)\Omega^2 + c_{22} \\ -jc_{12} \end{bmatrix} \quad 3.6.26$$

with 
$$\Delta_{cr} = \begin{vmatrix} -m\Omega^2 + c_{11} & -jc_{12} \\ jc_{12} & -(\Theta_p + \Theta_a)\Omega^2 + c_{22} \end{vmatrix}$$

Solving the characteristic equation  $\Delta_{cr}=0$  yields:

$$\Omega_{cr} = \pm \sqrt{\frac{1}{2} \left\{ \frac{c_{11}}{m} + \frac{c_{22}}{\Theta_p + \Theta_a} \pm \sqrt{\left( \frac{c_{11}}{m} + \frac{c_{22}}{\Theta_p + \Theta_a} \right)^2 - \frac{4(c_{11}c_{22} - c_{12}^2)}{m(\Theta_p + \Theta_a)}} \right\}} \quad 3.6.27$$

A comparison between eqn. 3.6.27 and 3.6.22 reveals that the only difference is the sign of  $\Theta_p$ . This difference, however, causes significant changes in the dynamic behaviour of the crankshaft. At least two critical speeds are obtained independent of the ratio of  $\Theta_a$  and  $\Theta_p$ . A pictorial description is shown in Figure 3.6.10. The contra-rotating excitation frequencies are defined through the line with a negative slope of  $45^\circ$ . This is applicable to a system with a positive angular speed of the shaft. This line will intersect the graphs of  $\omega_3$  and  $\omega_4$ . The intersection points represent the contra-rotating critical-bending speeds  $\Omega_{cr1/2}$  of the system.

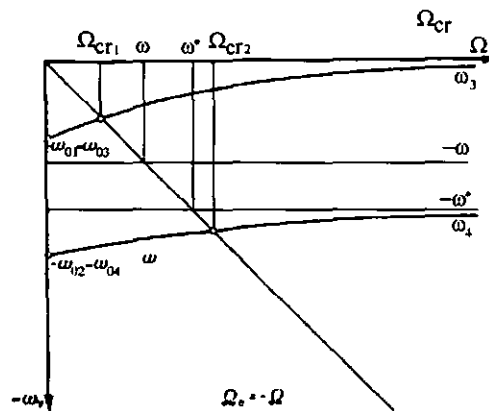


Figure 3.6.10 Contra-Rotating Critical-Bending Speeds

Usually, the conrod forces are not purely harmonic forces. It is, therefore, necessary to use multiple orders of the basic harmonic excitation to approximate these forces. The summed multiple signal contains various harmonics of higher order. Enforcing the summed harmonics to a rotating crankshaft will result in synco- and contra-rotating critical speeds of the appropriate order. A typical example is shown for the first and second harmonics in Figure 3.6.11. The critical speeds are derived for synco- and contra-rotating conditions.

The system descriptions and solutions discussed thus far are based on rigid bearings. The isotropic bearing properties are contained within the elastic properties of the shaft stiffness  $c_{ik}$  as described in section 3.2. There, the anisotropic supported shafts show a different response. Now, the anisotropic effect is considered. The principal directions of the supporting bearing stiffnesses are assumed to be in parallel with the axes of the fixed coordinate system. This assumption does not change the solution, but reduces the necessary effort by saving two coordinate transformations. The differential equations of motion are shown to be:

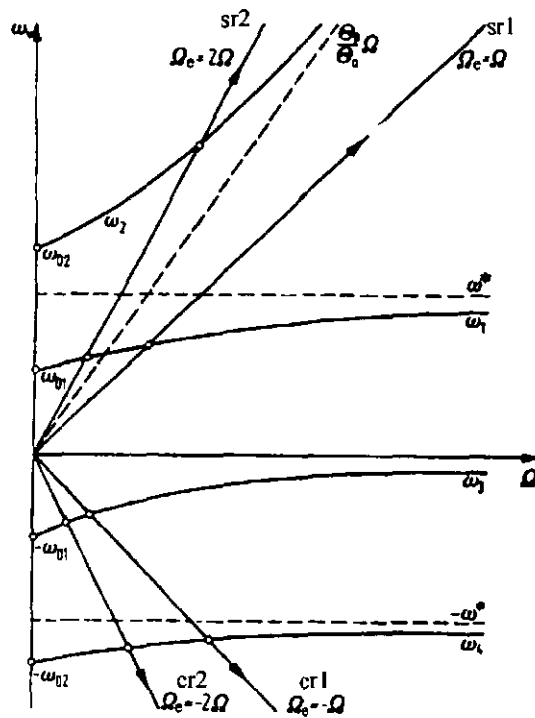


Figure 3.6.11 Syncro- and Contra-Rotating Critical Speeds (First and Second Order Excitation)

$$\begin{bmatrix} m & 0 \\ 0 & \Theta_a \end{bmatrix} \begin{bmatrix} \ddot{z}_w \\ \ddot{\rho}_{wy} \\ \ddot{y}_w \\ \ddot{\rho}_{wz} \end{bmatrix} + \begin{bmatrix} 0 & 0 \\ 0 & -\Omega\Theta_p \\ 0 & 0 \\ 0 & +\Omega\Theta_p \end{bmatrix} \begin{bmatrix} \dot{z}_w \\ \dot{\rho}_{wy} \\ \dot{y}_w \\ \dot{\rho}_{wz} \end{bmatrix} + \begin{bmatrix} c_{11}^z & c_{12}^z \\ c_{21}^z & c_{22}^z \\ & c_{11}^y & c_{12}^y \\ & c_{21}^y & c_{22}^y \end{bmatrix} \begin{bmatrix} z_w \\ \rho_{wy} \\ y_w \\ \rho_{wz} \end{bmatrix} = \Omega^2 \begin{bmatrix} m\epsilon \cos(\Omega t + \beta) \\ (\Theta_a - \Theta_p)\alpha \sin(\Omega t + \gamma) \\ m\epsilon \sin(\Omega t + \beta) \\ (\Theta_a - \Theta_p)\alpha \cos(\Omega t + \gamma) \end{bmatrix} \tag{3.6.28}$$

The eigenfrequencies  $\omega_n$  are derived using the same approach as before. Since eqn. 3.6.28 consists of four second order equations, eight eigenfrequencies are derived for each value of  $\Omega$ . A typical example of this solution is shown in Figure 3.6.12. The asymptotes are defined by:

$$\omega_v = 0$$

$$\omega_v = \pm \omega_y^* = \pm \sqrt{\frac{c_{11}^y}{m}}$$

$$\omega_v = \pm \omega_z^* = \pm \sqrt{\frac{c_{11}^z}{m}}$$

3.6.29

$$\omega_v = \pm \frac{\Theta_p}{\Theta_a} \cdot \Omega$$

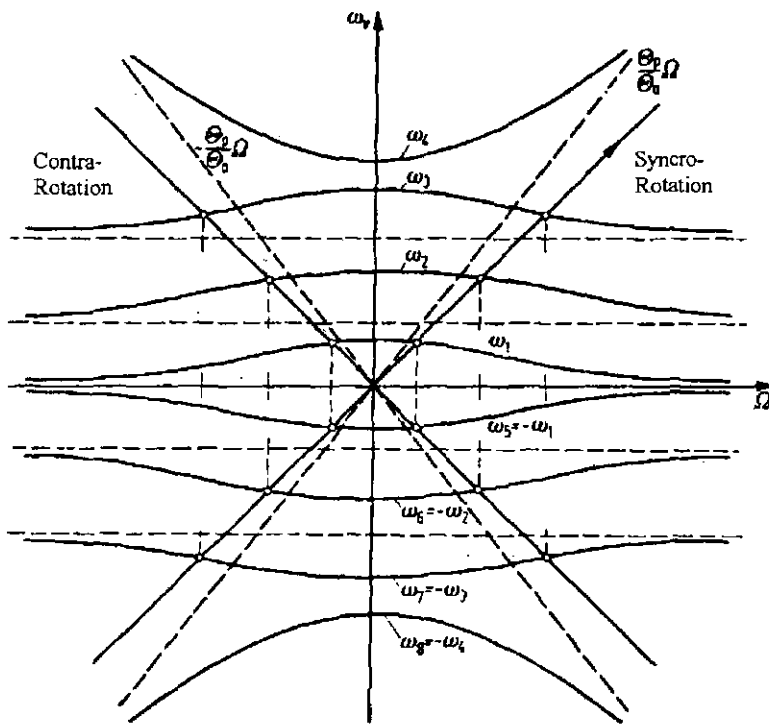


Figure 3.6.12 Eigenfrequencies of Anisotropic Supported Shaft

The critical bending speeds are defined through the intersection of the individual curve of the eigenfrequency with the line representing the excitation frequency. The syncro- and contra-rotating critical bending speeds are identical. The number of critical speeds depends on the ratio of  $\Theta_a$  and  $\Theta_p$ . Three critical speeds are encountered for ratios of  $\Theta_a < \Theta_p$ , while four for  $\Theta_a > \Theta_p$ .

### 3.7 Non-Uniform Rotating Structures

The theory described so far deals with circular components only. But a crankshaft is a non-circular system and even the flywheel may be of non-circular shape (e.g. 'asymmetrical flywheel'). Theoretically, the number of changes in properties is unlimited.



For practical applications (crankshaft, flywheel, turbine-shaft, generator-shafts etc.), however, stiffness and inertia properties are usually unequal in two major directions. The crankshaft or flywheel is better described by applying two different properties for the vertical and horizontal directions. It is therefore assumed in the following formulation of the system equation that the system properties can be described using two major directions. Before developing the differential equation of motion one has to account for two different categories of excitation. The first kind of excitation comes from the eccentricity of the inertia and oscillates with  $\Omega$ . This results in two critical eigenfrequencies controlled by the two major stiffness properties of the shaft. The second category arises from the mass of the shaft. The excitation frequency is of second order, because two different stiffness values are applied to this type of loading twice per crankshaft revolution. This critical eigenfrequency occurs almost at half the value of the resonance frequency due to eccentricity excitation. If we study the deflection of a crankshaft due to the gravity force in more detail, it becomes clear that this type of loading is negligible. The elastic deflections are less than a micron assuming the worst case in which the crankshaft is supported at the first and last bearing. If all bearings are used to support the crankshaft, this deflection is even smaller. From this it follows that gravity force generated deflections are only important for long shafts with few supporting bearings [59]. For crankshaft type application one can omit this loading. Therefore, the development of the differential equation of motion of non-uniform rotating structures is limited to the eccentricity loading alone.

The differential equation of motion can be derived in both fixed and rotating coordinate systems. In the fixed coordinate system it can be derived from eqn. 3.6.28 . Differences between the non-uniform and uniform system supported by anisotropic bearings are limited to the stiffness matrix.  $\hat{c}_{\zeta ij}^z$  and  $\hat{c}_{\eta ij}^y$  are the stiffness properties of the rotating, non-uniform shaft transformed to the fixed coordinate system. The final form is shown as:

$$\begin{bmatrix} m & 0 \\ 0 & \Theta_a \end{bmatrix} \begin{bmatrix} \ddot{z}_w \\ \ddot{\rho}_{wy} \\ \ddot{y}_w \\ \ddot{\rho}_{wz} \end{bmatrix} + \begin{bmatrix} 0 & 0 \\ 0 & -\Omega\Theta_p \end{bmatrix} \begin{bmatrix} \dot{z}_w \\ \dot{\rho}_{wy} \\ \dot{y}_w \\ \dot{\rho}_{wz} \end{bmatrix} + \begin{bmatrix} m & 0 \\ 0 & \Theta_a \end{bmatrix} \begin{bmatrix} \ddot{z}_w \\ \ddot{\rho}_{wy} \\ \ddot{y}_w \\ \ddot{\rho}_{wz} \end{bmatrix} + \begin{bmatrix} 0 & 0 \\ 0 & +\Omega\Theta_p \end{bmatrix} \begin{bmatrix} \dot{z}_w \\ \dot{\rho}_{wy} \\ \dot{y}_w \\ \dot{\rho}_{wz} \end{bmatrix} = \Omega^2 \begin{bmatrix} z_w \\ \rho_{wy} \\ y_w \\ \rho_{wz} \end{bmatrix} = \Omega^2 \begin{bmatrix} m \epsilon \cos(\Omega t + \beta) \\ (\Theta_a - \Theta_p) \alpha \sin(\Omega t + \gamma) \\ m \epsilon \sin(\Omega t + \beta) \\ (\Theta_a - \Theta_p) \alpha \cos(\Omega t + \gamma) \end{bmatrix} \tag{3.7.1}$$

It is seen that the differential equations are still linear but the stiffness properties vary. A self-excitation may occur due to this oscillating change of stiffness. This type of differential equation is called ‘Mathieu Differential Equations’, which are much more complicated to investigate and solve. A numerical solution is usually required. A more detailed interpretation can be made in a rotating coordinate system as proposed by Maske[60]. This coordinate system is defined as a synchro-rotating system with the axes being parallel to the principal axes  $\eta, \zeta$  of the shaft. The stiffness  $c_\eta$  and  $c_\zeta$  are defined accordingly. Analogous to the circular shaft theory, two eigenfrequencies of the non-uniform shaft are defined for the principal directions, i.e.:

$$\omega_\zeta = \sqrt{\frac{c_\zeta}{m}} \tag{3.7.2}$$

and 
$$\omega_\eta = \sqrt{\frac{c_\eta}{m}}$$

respectively. By introducing the following definition [61]:

$$\omega^2 = \frac{c_\zeta + c_\eta}{2m} = \frac{\omega_\zeta^2 + \omega_\eta^2}{2} \tag{3.7.3}$$

and

$$\mu = \frac{c_\eta - c_\zeta}{c_\eta + c_\zeta} = \frac{\omega_\eta^2 - \omega_\zeta^2}{\omega_\eta^2 + \omega_\zeta^2} = \frac{\omega_\eta^2 - \omega_\zeta^2}{2\omega^2} \tag{3.7.4}$$

eqn. 3.7.2 becomes:

$$\begin{aligned} \omega_\zeta &= \omega\sqrt{1 - \mu} \\ \omega_\eta &= \omega\sqrt{1 + \mu} \end{aligned} \tag{3.7.5}$$

The parameter  $\omega$  represents a shaft of averaged stiffness, while  $\mu$  ( $0 \leq \mu \leq 1$ ) represents the ratio or level of imbalance between the principle stiffness properties of the shaft, which can cause self-excitation called parametric resonance.

The differential equation of motion has been derived in section 3.2 for rotating coordinate systems. The anisotropic properties are covered by applying eqn. 3.2.20 and substituting  $\omega_\zeta$  for  $\omega$  in the first equation and  $\omega_\eta$  for  $\omega$  in the second. This operation leads to:

$$\begin{aligned} \ddot{\zeta}_w - 2\Omega\dot{\eta}_w + [(1 - \mu)\omega^2 - \Omega^2]\zeta_w &= \epsilon\Omega^2 \cos \beta \\ \ddot{\eta}_w + 2\Omega\dot{\zeta}_w + [(1 + \mu)\omega^2 - \Omega^2]\eta_w &= \epsilon\Omega^2 \sin \beta \end{aligned} \tag{3.7.6}$$

A stability analysis of the unforced system is obtained by equating the coefficient determinate to zero as shown by Maske [60]:

$$\lambda^{*4} + 2(\omega^2 + \Omega^2)\lambda^{*2} + (\omega^2 - \Omega^2)^2 - \mu^2\omega^4 = 0 \tag{3.7.7}$$

Solving this equation yields:

$$\lambda_1^* = \sqrt{-(\omega^2 + \Omega^2) + \sqrt{4\omega^2\Omega^2 + \mu^2\omega^4}}$$

$$\lambda_2^* = \sqrt{-(\omega^2 + \Omega^2) - \sqrt{4\omega^2\Omega^2 + \mu^2\omega^4}} \tag{3.7.8}$$

$$\lambda_3^* = -\lambda_1^*$$

$$\lambda_4^* = -\lambda_2^*$$

It is seen that the eigenvalues  $\lambda_{2/4}^*$  are always imaginary while  $\lambda_{1/3}^*$  are real when

$$\sqrt{4\omega^2\Omega^2 + \mu^2\omega^4} > \omega^2 + \Omega^2 \tag{3.7.9}$$

Real eigenvalues are a prerequisite for unstable system response. Eqn. 3.7.9 is rewritten as 3.7.10 to calculate the speed range of the shaft  $\Omega$  for which unstable response is expected.

$$\omega\sqrt{1-\mu} < \Omega < \omega\sqrt{1+\mu} \tag{3.7.10}$$

or

$$\omega_\zeta < \Omega < \omega_\eta$$

The last equation shows that the instability domain of a shaft rotating with  $\Omega$  occurs between  $\omega_\zeta < \Omega < \omega_\eta$ . The values of  $\omega_\zeta$  and  $\omega_\eta$  are calculated from eqn. 3.7.2 . This can be shown in a stability chart as displayed in Figure 3.7.1 for all values of  $\mu$  ( $0 \leq \mu \leq 1$ ) derived from eqn. 3.7.4 . The border lines are defined through two parts of parabolic curves. The unstable domain is a function of  $\mu$  showing only a small region of instability for small values of  $\mu$ . Small values of  $\mu$  represent shafts with increased circular properties.

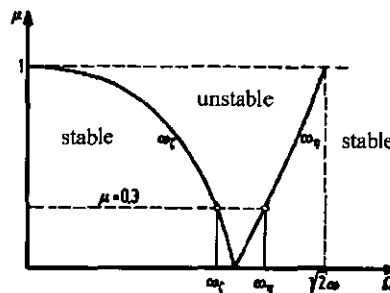


Figure 3.7.1 Stability Chart (for values of  $\mu$  and  $\Omega$ )

The eigenfrequencies  $\omega'$  of the shaft can be found as:

$$\omega_{1,2}^* = -j\lambda_{1,2} = \sqrt{(\omega^2 + \Omega^2) \pm \sqrt{4\omega^2\Omega^2 + \mu^2\omega^4}} \tag{3.7.11}$$

with  $\sqrt{4\omega^2\Omega^2 + \mu^2\omega^4} < \omega^2 + \Omega^2$

which are, of course, dependent on the shaft angular velocity  $\Omega$ . For an arbitrary but fixed value of i.e.  $\mu=0.5$  the eigenfrequencies  $\omega_{1,2}^*$  are shown in Figure 3.7.2. The eigenvalues  $\lambda_1^*$  are positive for the speed range between  $\omega_\zeta$  and  $\omega_\eta$  and the system response is, therefore, unstable. Further, a stable solution is perceived due to  $\lambda_3^* = -\lambda_1^*$ .

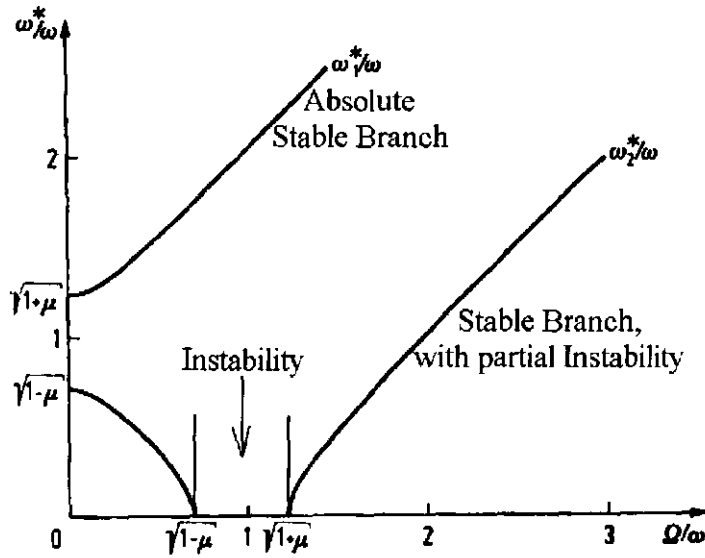


Figure 3.7.2 Stability / Eigenfrequency Chart ( $\mu=0.5$ )

Utilising the method of analysis derived earlier, it is a straightforward task to solve the unbalanced excited system. The unbalance forces due to eccentricity are given by the right hand side of eqn. 3.7.6 . This term is constant, because of the rotating coordinate system. The particular solution is:

$$\zeta_{w\varepsilon} = \frac{\Omega^2}{(1 - \mu)\omega^2 - \Omega^2} \varepsilon \cos \beta = \frac{\left(\frac{\Omega}{\omega_\zeta}\right)^2}{1 - \left(\frac{\Omega}{\omega_\zeta}\right)^2} \varepsilon \cos \beta \tag{3.7.12}$$

$$\eta_{w\varepsilon} = \frac{\Omega^2}{(1 + \mu)\omega^2 - \Omega^2} \varepsilon \sin \beta = \frac{\left(\frac{\Omega}{\omega_\eta}\right)^2}{1 - \left(\frac{\Omega}{\omega_\eta}\right)^2} \varepsilon \sin \beta$$

The  $\zeta$ -displacement is unbounded for values of  $\Omega=\omega_\zeta$  and the  $\eta$ -displacement is unbounded for values of  $\Omega=\omega_\eta$ . Both values of  $\Omega$  are the bending-critical speeds of the system. Thus, a non-symmetric shaft exhibits two critical speeds with:

$$\begin{aligned} \Omega_1 &= \omega_\zeta = \omega\sqrt{1-\mu} \\ \Omega_2 &= \omega_\eta = \omega\sqrt{1+\mu} \end{aligned} \tag{3.7.13}$$

External damping properties may alter the resonance and stability response of a rotating system as shown in sections 3.3 and 3.4. It is therefore necessary to investigate the stability criterion of a non-symmetric shaft with external damping properties. The external damping force  $-k_a \dot{r}_w$  needs to be transformed to the rotating coordinate system. By introducing the damping property  $D_a = k_a/2m\omega$  into eqn. 3.7.6 we have

$$\begin{aligned} \begin{bmatrix} \ddot{\zeta}_w \\ \ddot{\eta}_w \end{bmatrix} + \begin{bmatrix} 2D_a\omega & -2\Omega \\ 2\Omega & 2D_a\omega \end{bmatrix} \begin{bmatrix} \dot{\zeta}_w \\ \dot{\eta}_w \end{bmatrix} + \begin{bmatrix} (1-\mu)\omega^2 - \Omega^2 & -2D_a\omega\Omega \\ 2D_a\omega\Omega & (1+\mu)\omega^2 - \Omega^2 \end{bmatrix} \begin{bmatrix} \zeta_w \\ \eta_w \end{bmatrix} \\ = \varepsilon\Omega^2 \begin{bmatrix} \cos\beta \\ \sin\beta \end{bmatrix} \end{aligned} \tag{3.7.14}$$

The stability criterion can be derived from the homogeneous solution of eqn. 3.7.14. Michatz [62] showed that the stability criterion can be achieved by applying the Hurwitz approach. It has the form

$$\left(1 - \frac{\Omega^2}{\omega^2}\right)^2 - \mu^2 + 4D_a^2 \frac{\Omega^2}{\omega^2} \geq 0 \tag{3.7.15}$$

From eqn. 3.7.15 borders of stability are shown in Figure 3.7.3 for various damping properties  $D_a$ . The results for  $D_a=0$  are identical to those shown in Figure 3.7.1. The domain of instability diminishes with increasing damping properties and the system response is finally stable throughout the entire range of  $\Omega$ . Two critical eigenfrequencies  $\Omega_{1,2}$  of the externally excited system are identical to those of the undamped system and match the margins of stability.

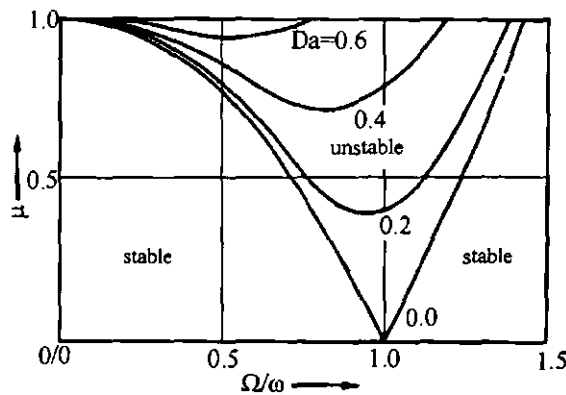


Figure 3.7.3 Stability Chart with Damping Properties

### 3.8 Second Order Vibration of Flexible Shafts

Second order bending vibration of shafts are induced through changes of the shaft torque. All the previous analyses are based on the assumption of constant shaft velocity  $\dot{\rho} = \Omega$ . Systems driven by combustion engines or combustion engines themselves encounter significant changes in torque and hence velocity. The shaft angular rotation  $\rho$  is the sum of a constant angular velocity i.e.  $\Omega t + \beta$ , and a fluctuating component  $\delta(t)$ . Namely,

$$\rho(t) = \beta + \Omega t + \delta(t) \quad 3.8.1$$

The fluctuating component is relatively small of only a few degrees for practical vehicle engine application ( $\delta(t) \ll 1$  [63]). The periodic oscillation is embarked by periodic mass and combustion forces. Rotary inertias may be used to minimise velocity fluctuation. Velocity fluctuation can not be neutralised by any technique but can be minimised and decoupled between two technical systems.

The differential equation of motion as derived earlier must be modified to include the second order vibration. The displacement written in a complex manner is of the form:

$$e^{j\rho} = e^{j(\Omega t + \beta)} \cdot e^{j\delta} \quad 3.8.2$$

The component  $e^{j\delta}$  is replaced by the first two components of a series expansion for  $\delta \ll 1$ :

$$e^{j\delta} = 1 + \frac{j\delta}{1!} + \left( -\frac{\delta^2}{2!} + \dots \right) \quad 3.8.3$$

Substituting eqn. 3.8.3 into 3.8.2 gives:

$$e^{j\rho} = (1 + j\delta)e^{j(\Omega t + \beta)} \quad 3.8.4$$

Assuming that the changes of  $\delta$  are of periodic nature,  $\delta(t)$  can be represented by a Fourier series.

$$\delta(t) = \sum_{n=1}^{\infty} \delta_n \sin(n\nu\Omega t + \alpha_n)$$

$$\text{or} \quad \delta(t) = \frac{1}{2j} \sum_{n=1}^{\infty} \delta_n [e^{j(n\nu\Omega t + \alpha_n)} - e^{-j(n\nu\Omega t + \alpha_n)}] \quad 3.8.5$$

$$\text{with} \quad \sin x = \frac{1}{2j}(e^{jx} - e^{-jx})$$

The base period of the overlaying oscillation depends on the drive configuration and is generally written as  $\nu\Omega$  which may become a fraction or multiple of the base drive angular velocity  $\Omega$ . Four stroke engines show  $\nu\Omega$  as  $\Omega/2$  and two stroke engines as  $\Omega$ . The expression of the displacements is finally obtained as:

$$e^{j\rho} = e^{j(\Omega t + \beta)} + \frac{1}{2} \sum_{n=1}^{\infty} \delta_n e^{j\beta} \{ e^{+j[(n\nu + 1)\Omega t + \alpha_n]} - e^{-j[(n\nu - 1)\Omega t + \alpha_n]} \} \tag{3.8.6}$$

From section 3.2 the first component of the right hand side relates to the displacement at constant speed  $\Omega$  due to unbalance (see eqn. 3.2.7). This part controls the first or 'main' critical speed  $\Omega_{cr}$  of the system. The second term relates to the second order bending displacement induced by the torque fluctuation. This part controls the second order critical speed  $\Omega_{cr2}$  of the system. Resonance frequencies are dependent on the shaft eigenfrequency  $\omega$  and obtained as [64]:

$$\Omega_{cr2} = \frac{\omega}{|n\nu \pm 1|} \tag{3.8.7}$$

The non-dimensional second order critical speeds  $\frac{\Omega_{cr2}}{\omega}$  are summarised in Table 3 [64]

for various values of  $\nu$  and orders  $n=1,2,3$ .

$\frac{\Omega_{cr2}}{\omega}$	n=1		n=2		n=3	
	$\nu = \frac{1}{2}$	$\nu = 1$	$\nu = \frac{3}{2}$	$\nu = 2$	$\nu = \frac{5}{2}$	$\nu = 3$
$\nu = \frac{1}{2}$	$\frac{2}{3}$	2	$\frac{1}{2}$	$\infty$	$\frac{2}{5}$	2
$\nu = 1$	$\frac{1}{2}$	$\infty$	$\frac{1}{3}$	1	$\frac{1}{4}$	$\frac{1}{2}$
$\nu = \frac{3}{2}$	$\frac{2}{5}$	2	$\frac{1}{4}$	$\frac{1}{2}$	$\frac{2}{11}$	$\frac{2}{7}$
$\nu = 2$	$\frac{1}{3}$	1	$\frac{1}{5}$	$\frac{1}{3}$	$\frac{1}{7}$	$\frac{1}{5}$
$\nu = 3$	$\frac{1}{4}$	$\frac{1}{2}$	$\frac{1}{7}$	$\frac{1}{5}$	$\frac{1}{10}$	$\frac{1}{8}$

Table 3 Non-Dimensional Second Order Critical Speeds

Referring to eqn. 3.8.6 and eqn. 3.2.3 second order critical vibrations are proportional to  $\epsilon\omega\delta/2$  which is the approximate amplitude of the excitation source due to the rotation fluctuation. Through transient torsional vibration studies Pfingsthorn [63] pointed out that the worst case angular fluctuation is less than  $2^\circ$  for standard gasoline engine application. Representative front-end fluctuations are shown in Figure 3.8.1 versus crankangle. The modelled configuration is a four cylinder in-line engine with 1.3l capacity. Results are obtained with respect to engine speeds between 1000 rpm and 6000 rpm. The corresponding maximum increase at  $\Omega=1000\text{rpm}$  is  $\delta_r/2=0.017$ . The magnitude of the second order excitation is only 1.7% of that of the eccentricity excitation. In order to minimise the mathematical and computational effort to solve the cranktrain dynamics it may be assumed that this effect within this approach may be neglected. Nevertheless, it should be noted that an additional critical speed is obtained below the first or 'main' critical speed. If, for eccentricity reasons, a system exhibits a resonance below the first critical speed, second order critical vibrations are commonly the cause and can be avoided by increasing the balancing of the crankshaft, thus increasing the inertia.

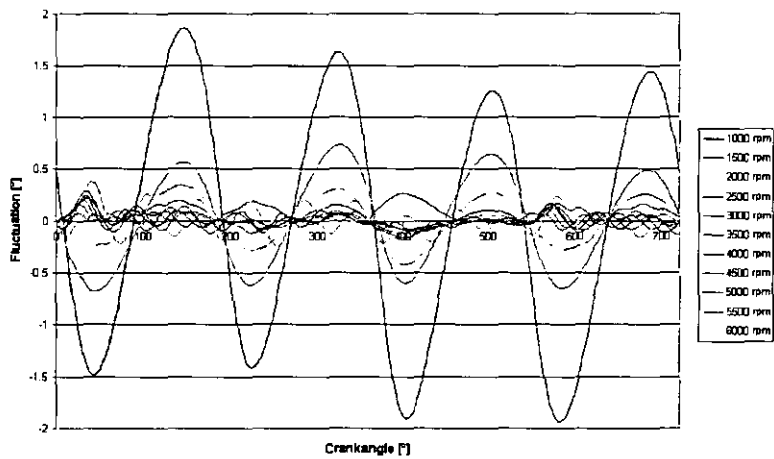


Figure 3.8.1 Engine Front Pulley Fluctuation



## **Chapter 4**

### **Hydrodynamic Bearings**

This chapter presents an overview of the theoretical description of non-stationary operating radial plain bearings applied as crankshaft main bearings. A common approach is to characterize bearing properties as independent stiffness and damping quantities. This method is then applied to quantify the main bearing properties of the studied engine.

A detailed description or theoretical survey of radial plain bearings is far beyond the scope of this work. It is, therefore, assumed that the reader is familiar with the basic principles of plain bearings. For details, the reader may refer to the textbook "Plain Bearings" [70]. It seems that the works of Someya ([65],[66]) were the first studies on the stiffness and damping properties of plain bearings. In these studies, measured resonances were used to determine the corresponding stiffness and damping properties in the way of inversion. Another study was done by Glienicke [67] in 1967. The bearing capacity was studied experimentally for turbine bearings with non-cylindrical shape. Again, resonance phenomena were studied for simple rotors and the measured resonance frequencies of the system were then used to determine the stiffness and damping properties.

The first theoretical approach was conducted by Schaffrath [68] in 1969. His method was then applied by Klumpp [69] to establish a computer program for predicting the spring and damping coefficients. The method and program are capable of dealing with all kinds of plain bearing geometry which can be described by partially approximated sectors of a circle. Additionally, the bearing shape must be unique throughout the bearing width and radial grooves must be in the middle of the bearing.

The theory of Glienicke and the program of Klumpp will be basically applied to predict the spring and damping coefficients of the plain bearings in this work. A brief description of the theory is given in section 4.2. The application of the coefficients is detailed in section 4.3.

#### **4.1 Introduction to Non-Stationary Loaded Radial Bearings**

The analysis of non-stationary operating plain bearings is possible with regard to the time dependent orbit of the shaft centre, the time dependent minimum gap clearance within the bearing, oil pressures and durability aspects. The restriction is that the external load history is of cyclic characteristic. The time dependent orbit of a non-stationary loaded plain bearing results from the non-stationary movement of the shaft centre within the bearing clearance. This phenomenon is described by Reynold's differential equation [70]:

$$\frac{\partial}{\partial \rho} \left[ (1 + \varepsilon \cos \rho)^3 \frac{\partial \Pi}{\partial \rho} \right] + \left( \frac{D}{B} \right)^2 \frac{\partial}{\partial z} \left[ (1 + \varepsilon \cos \rho)^3 \frac{\partial \Pi}{\partial z} \right]$$

$$= 6 \frac{\partial}{\partial \rho} (1 + \varepsilon \cos \rho) + \frac{12}{\omega} \frac{\partial}{\partial t} (1 + \varepsilon \cos \rho)$$

with  $\frac{B}{D} \hat{=} \text{width-diameter relation}$

4.1.1

$\psi = \frac{R-r}{R} \hat{=} \text{relative bearing clearance}$

$\varepsilon = \frac{e}{R-r} = \frac{e}{R\psi} \hat{=} \text{relative eccentricity}$

$\Pi = \frac{p\psi^2}{\eta\omega} \hat{=} \text{pressure code}$

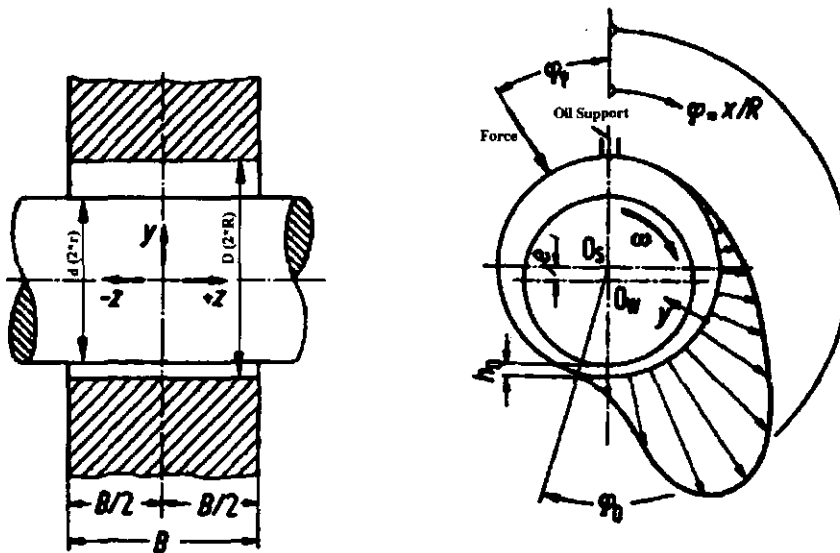


Figure 4.1.1 Radial Bearing Parameters

Plain bearings with non-stationary characteristics have either non-stationary load histories or non-stationary geometrical orbits. Eqn. 4.1.1 describes the oilfilm pressure and hence the integrated load history within the plain bearing as a function of the pin's orbit. This formulation is a reverse prediction of the standard procedure of analysis. In reality, the external load history is known and the resulting oilfilm pressures and the orbit of the shaft are the unknowns.

The right hand side of eqn. 4.1.1 describes the perturbation from which the changes of the shaft's orbit are derived. The hydrodynamic effective angular velocity is given by

$$\bar{\omega} = \omega_s + \omega_c - 2\dot{\delta} \quad 4.1.2$$

which consists of the non-stationary rotation of the shaft  $\omega_s$  and the casing  $\omega_c$  and the angular rotation of the appearing gap ( $-2\dot{\delta}$ ). This displacement can be represented by linearised displacements in radial and tangential direction for time intervals that are small enough. The tangential displacement is represented by the change of the gap angle  $\delta$ , so  $\dot{\delta}$  is the angular velocity. The radial component of the displacement is described by the radial velocity  $\dot{\epsilon}$ . Hence, all relevant components which are required to describe the orbit of the shaft are available.

It should be noted that this equation results in different solutions for different initial conditions. A single solution can be obtained only in the case in which the initial condition is known. Initial conditions are known for stationary operating conditions and for conditions changing from one stationary condition to another stationary condition. In reality, most of the applications can be assumed to be of a periodic nature with respect to the external load history. Therefore, it is practical to replace the stationary initial condition with a known periodic condition and to apply another convergence criterion. The convergence criterion assumes that the orbit of the shaft is of periodic and closed nature with a periodic external load history.

The direct solution of the Reynold's differential equation requires a known periodic orbit of the shaft. But this orbit is unknown and the external load history is known. The work presented by Fränkel [71] and Ott [72] developed an inversion method which calculated the integrated oilfilm pressures first to balance the known external load history for each specified time interval. With that knowledge, the orbit of the shaft was determined under that load condition. In this method it was assumed that the orbit was discretised by linearised orbits with constant velocities. This approach is valid for those condition that the linearised displacement vector is small enough.

Booker [73] developed the so called 'Mobility Method'. The basic principle of this approach is that pre-calculated look-up tables for linearised, small displacements are applied. These tables are used to establish the corresponding pressure and load distribution for a large but limited number of conditions with known states of  $\epsilon$  and  $\delta$  and assumed changes in tangential and radial direction.

At the same time, Hahn [74] developed the method of 'Overlaid Pressures' and Holland [75] derived the method of 'Contributing Portative Forces'. The major difference between the two methods is the definition of the boundary pressure distribution at the plain bearing under rotation and displacement. The most recent comparisons between the two methods indicate that the latter is more accurate and will be applied herein to predict the spring and damping coefficients.

A detailed description of the theory of Holland will not be given here, as this is common technology. The interested reader may refer to the above mentioned textbook or the referenced literature.

### 4.2 Definition of Spring and Damping Coefficients

Reynold's differential equation for non-stationary conditions describes the influences of the plain bearing in terms of oilfilm pressures. Changes in oilfilm pressure are imposed by either the eccentric journal location  $\epsilon, \delta$  and the journal angular velocity  $\dot{\epsilon}, \dot{\delta}$ . This is shown in eqn. 4.2.1, which is a slightly modified form of the original Reynold's differential eqn. 4.1.1 .

$$\begin{aligned} \frac{\partial}{\partial \rho} \left[ (1 + \epsilon \cos \rho)^3 \frac{\partial \Pi}{\partial \rho} \right] + \left( \frac{D}{B} \right)^2 \frac{\partial}{\partial z} \left[ (1 + \epsilon \cos \rho)^3 \frac{\partial \Pi}{\partial z} \right] & \quad 4.2.1 \\ = -6 \left[ \epsilon \sin(\rho - \delta) - 2 \frac{\epsilon \dot{\delta}}{\omega} \sin(\rho - \delta) - 2 \frac{\dot{\epsilon}}{\omega} \cos(\rho - \delta) \right] & \end{aligned}$$

The changes occur on the right hand side of the equation and are discussed in more detail. The first term, i.e.  $\epsilon \sin(\rho - \delta)$ , represents the stationary pressure introduced through the pure rotation of the journal within a declining crevice. This describes the progressive increasing stiffness properties of the plain bearing as a function of  $\epsilon$ .

The second and third terms, i.e.  $-2(\epsilon \dot{\delta} / \omega) \sin(\rho - \delta)$ ,  $-2(\dot{\epsilon} / \omega) \cos(\rho - \delta)$ , represent a pressure increase impeding the journal's motion. Therefore, they are characterised as impedance components or are commonly called damping forces. The damping forces are proportional to the radial( $\dot{\epsilon}$ ) and tangential ( $\dot{\omega}$ ) velocities of the journal.

As discussed by Schaffrath [68], the common approach used for studying the stiffness and damping characteristics of plain bearings is that the stiffness and damping properties are linearised around the condition of static operation. Additionally, it is assumed that the changes in deflection are small. The accuracy and applicability of this approach is verified in section 4.2.1 by comparing measured and analytically derived plain bearing properties.

The subsequent formulation is derived for a cylindrical 360° plain bearing. Non-cylindrical plain bearings or bearings with less than 360° are approximated by multiple segments of a circle. The approach is then applicable to the individual sectors and the overall behaviour can be superimposed from the single sector analysis. This approach was introduced by Klumpp [69].

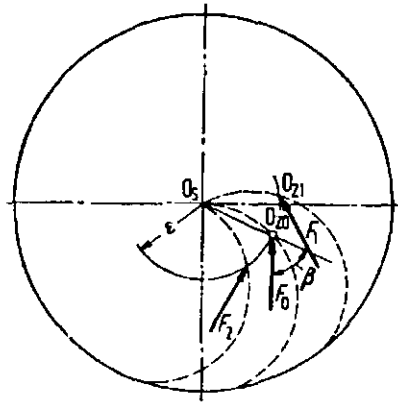


Figure 4.2.1 Force Map of 360° Bearing

The stiffness properties can be derived from the stationary characteristic map of the plain bearing. A bearing force specified in direction and amplitude is defined for each location of the journal within the bearing. This map is shown in Figure 4.2.1. The displacement curve for a vertical load  $F_0$  is defined by the curve of 'Gümbel' showing an eccentricity  $\epsilon$  for the equilibrium condition  $O_{z0}$ . All equilibrium conditions of the same eccentricity  $\epsilon$  are defined through the same magnitude of external load, but with modified load direction. The load direction is altered by  $\beta$  which is constant for the change in load vector and a minimum gap clearance of the plain bearing. It is therefore a straightforward task to establish the load in the geometrical neighbourhood of the equilibrium condition  $O_{z0}$ , if the Sommerfeld function  $So_0(\epsilon, B/D)$  and the function of  $\beta(\epsilon, B/D)$  are known. This can be drawn for small displacements  $x_1, x_2$  applying a Cartesian coordinate system as shown in Figure 4.2.2. The forces related to these small displacements are defined with:

$$\begin{aligned} \Delta F_1 &= c_{11}x_1 + c_{12}x_2 \\ \Delta F_2 &= c_{21}x_1 + c_{22}x_2 \end{aligned} \tag{4.2.2}$$

The stiffness coefficients in this equation are represented by  $c_{ij}$ . The solution of the Reynold's differential equation gives the resulting force  $F$  and the corresponding orientation  $\beta$ . It is therefore appropriate to replace the fixed coordinate system with one rotating with  $\omega$  so that the radial direction is oriented to the minimum gap clearance of the bearing. This is shown in Figure 4.2.3.

The force components  $F_r$  and  $F_\beta$  are also termed  $f$  and  $g$ .

$$F_r \equiv f = F \cos \beta \quad , \quad F_\beta \equiv g = -F \sin \beta \tag{4.2.3}$$

The forces within the x-y-system are defined as:

$$F_x \equiv F_1 = f \cos \delta - g \sin \delta$$

$$F_y \equiv F_2 = f \sin \delta + g \cos \delta$$

4.2.4

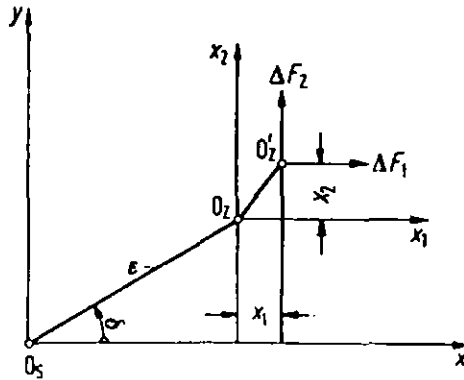


Figure 4.2.2 Coordinate System for Spring and Damping Coefficients

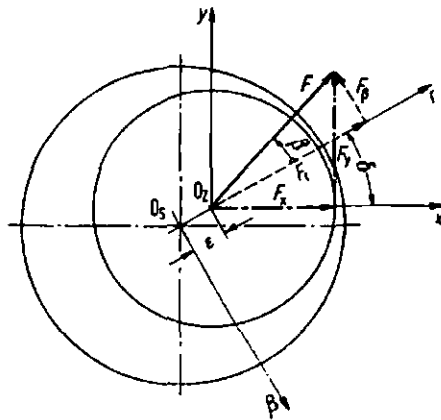


Figure 4.2.3 Components of Resulting Oilfilm Pressure

The gradients of  $f$  and  $g$  with respect to  $\epsilon$  and  $\epsilon\delta$  are:

$$f_\epsilon = \frac{\partial f}{\partial \epsilon} \quad , \quad f_\delta = \frac{\partial f}{\epsilon \partial \delta} \tag{4.2.5}$$

$$g_\epsilon = \frac{\partial g}{\partial \epsilon} \quad , \quad g_\delta = \frac{\partial g}{\epsilon \partial \delta} \tag{4.2.6}$$

which are the stiffness coefficients in the  $\gamma\beta$  coordinate system. In the  $x$ - $y$  coordinate system by considering the following four assumed equilibrium conditions at the geometrical neighbourhood of  $(\epsilon, \delta)$  or  $(x, y)$

$$(x + \Delta x, y); \quad (x - \Delta x, y); \quad (x, y + \Delta y); \quad (x, y - \Delta y) \tag{4.2.7}$$

the stiffness coefficients are determined as:

$$\gamma_{11} = \frac{F_x(x + \Delta x, y) - F_x(x - \Delta x, y)}{2\Delta x} \quad 4.2.8$$

$$\gamma_{12} = \frac{F_x(x, y + \Delta y) - F_x(x, y - \Delta y)}{2\Delta y} \quad 4.2.9$$

$$\gamma_{21} = \frac{F_y(x + \Delta x, y) - F_y(x - \Delta x, y)}{2\Delta x} \quad 4.2.10$$

$$\gamma_{22} = \frac{F_y(x, y + \Delta y) - F_y(x, y - \Delta y)}{2\Delta y} \quad 4.2.11$$

The damping coefficients are derived by applying a similar approach. As shown in eqn. 4.2.1 the second and third components of the right hand side represent the damping coefficients. The bearing forces are calculated with respect to pure rotation ( $\omega - 2\dot{\delta}$ ) and tangential and radial displacements. They are

$$F_r \equiv \frac{F_r \psi^2}{BD\eta\omega} = \frac{\omega - 2\dot{\delta}}{\omega} f_D + \frac{\dot{\epsilon}}{\omega} f_v \quad 4.2.12$$

$$F_\beta \equiv \frac{F_\beta \psi^2}{BD\eta\omega} = \frac{\omega - 2\dot{\delta}}{\omega} g_D + \frac{\dot{\epsilon}}{\omega} g_v \quad 4.2.13$$

The partial derivatives with respect to  $\epsilon'$  and  $\epsilon\delta'$  are:

$$\frac{\partial F_r}{\partial \epsilon'} = \frac{\partial}{\partial \epsilon'} \left( \frac{\dot{\epsilon}}{\omega} f_v \right) = f_v \quad 4.2.14$$

$$\frac{\partial F_r}{\partial \epsilon\delta'} = \frac{\partial}{\partial \epsilon\delta'} \left( -2 \frac{\dot{\delta}}{\omega} f_D \right) = -\frac{2}{\epsilon} f_D \quad 4.2.15$$

$$\frac{\partial F_\beta}{\partial \epsilon'} = \frac{\partial}{\partial \epsilon'} \left( \frac{\dot{\epsilon}}{\omega} g_v \right) = g_v \quad 4.2.16$$

$$\frac{\partial F_\beta}{\partial \epsilon\delta'} = \frac{\partial}{\partial \epsilon\delta'} \left( -2 \frac{\dot{\delta}}{\omega} g_v \right) = -\frac{2}{\epsilon} g_v \quad 4.2.17$$

The transformation into the x-y-system is similar to that for the stiffness properties and is not detailed here.

The non-dimensional stiffness and damping properties can be transformed to absolute values by applying the subsequent relations:

$$c_{ij} = \gamma_{ij} \frac{F}{\Delta R} \quad ; \quad b_{ij} = \beta_{ij} \frac{F}{\omega \Delta R} \quad 4.2.18$$



Some typical results are shown for the stiffness properties in Figure 4.2.4 and for the damping properties in Figure 4.2.5. The displayed properties are derived for a fully circular 360° bearing without grooves and oil-support features.

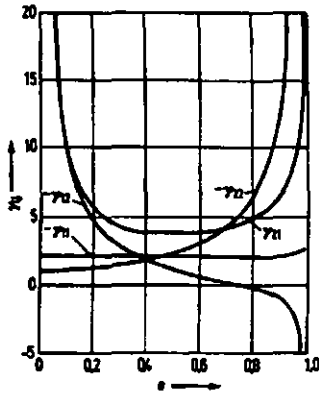


Figure 4.2.4 Stiffness Properties of Circular Bearing

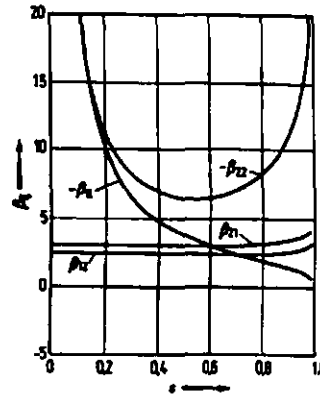


Figure 4.2.5 Damping Properties of Circular Bearing

The stiffness and damping properties can also be derived for other bearing shapes as long as the geometry can be described by partially approximated sectors of a circle. Some results are given in the work of Someya ([65],[66]), Schaffrath [68] and Glienicke [67].

At this point it should be noted that Glienicke [67] applied the same theoretical approach but the definition of the stiffness and damping properties are not identical to those used by Someya ([65],[66]) and Schaffrath [68]. Someya and Schaffrath relate the stiffness and damping properties to the Sommerfeld number  $S_o$  for the static equilibrium condition, whilst Glienicke's definition is given as:

$$\gamma_{ij}^* = \gamma_{ij} S_o \quad ; \quad \beta_{ij}^* = \beta_{ij} S_o \tag{4.2.19}$$

The bearing forces are derived for small deflections  $(x_1, x_2)$  and related changes in velocities  $(\dot{x}_1, \dot{x}_2)$  as:

$$F_1 = (\gamma_{11}x_1 + \gamma_{12}x_2) \frac{F}{\Delta R} + (\beta_{11}\dot{x}_1 + \beta_{12}\dot{x}_2) \frac{F}{\omega \Delta R} \tag{4.2.20}$$

$$F_2 = (\gamma_{21}x_1 + \gamma_{22}x_2) \frac{F}{\Delta R} + (\beta_{21}\dot{x}_1 + \beta_{22}\dot{x}_2) \frac{F}{\omega \Delta R} \tag{4.2.21}$$

The dissimilar definitions of the stiffness and damping properties do not affect the analysis or the results obtained if the properties are applied in a correct manner, but

the reader may find graphs in various textbooks which show an unmatched behaviour. This is due to the applied incongruous definition and the different properties  $S_0$  and  $\epsilon$  shown on the x-axis.

The analytical approach applied in this study is based on the publications of Someya ([65],[66]) and Schaffrath [68] and the stiffness and damping properties are defined accordingly. The application of the properties thus derived is described in section 4.3. A Fourier series approach is applied to study the frequency dependent properties of the plain bearings.

#### 4.2.1 Comparison of Theoretical Results and Measurements

Comparisons of theoretical and measured stiffness and damping coefficients are mainly based on the work presented by Glienicke [67] in the late sixties. The procedure applied to determine the stiffness and damping coefficients from measured data is an indirect method. The bearing properties are derived from the response of a known system. The external loads applied to the shaft and the corresponding static and dynamic shaft displacements within the bearing housing are measured and then used in an analysis procedure to evaluate the bearing stiffness and damping coefficients. A measurement configuration used by Glienicke is shown in Figure 4.2.6.



Figure 4.2.6 Bearing Measuring Device [by Glienicke]

Once the geometric configuration of the system, the applied external forces and the corresponding displacements of the journal within the bearing are known, one can calculate the bearing stiffness and damping coefficients in the way of inversion analyses.

Based on the analytical approach [69] computer programs were developed to carry out the predictions which are compared with the measurement results from Glienicke [67]. The comparisons are shown in Figure 4.2.7 and in Figure 4.2.8, for stiffness and damping coefficients, respectively.

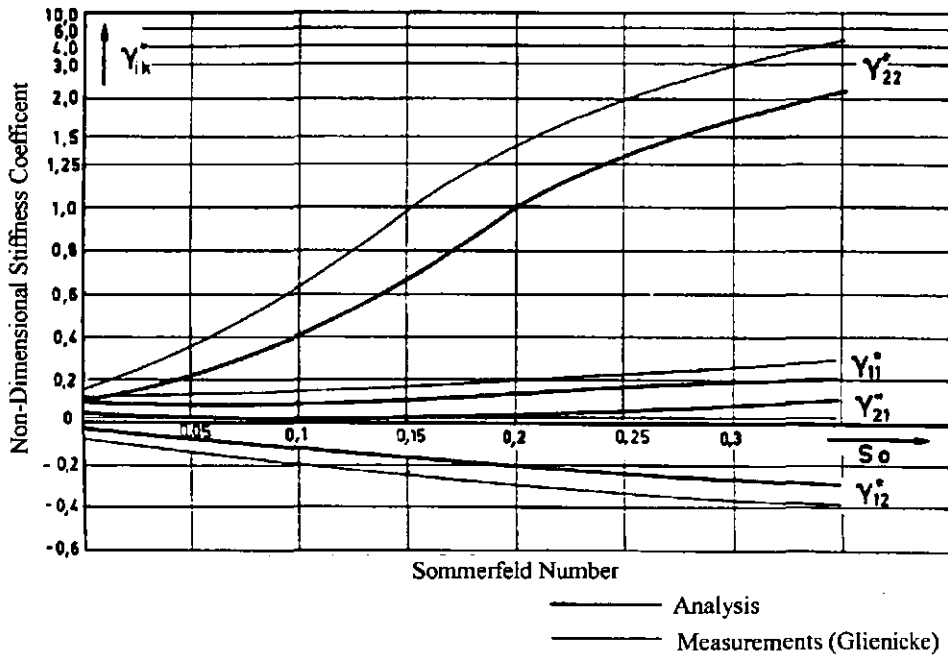


Figure 4.2.7 Comparison of Stiffness Coefficients

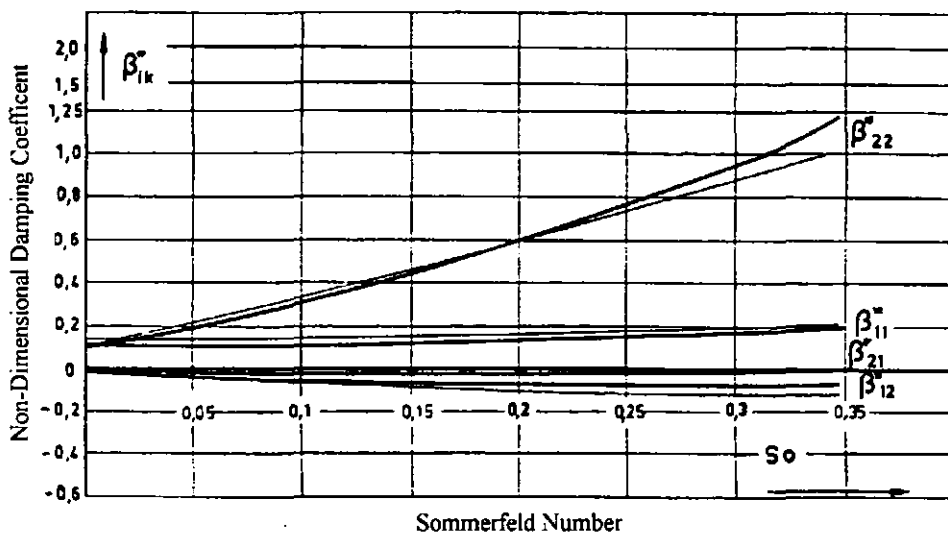


Figure 4.2.8 Comparison of Damping Coefficients

Based on the theory of linearised perturbation of bearing load and oilfilm pressure, close correlation is shown between the measured data and analytical predictions for the bearing with  $B/D=0.5$  and  $\Psi=3.9$ . The differences are mainly due to the assumption of constant oil viscosity, the differences between the assumed and real bearing geometry, the exclusion of elastic bearing deformation in the theory, and oil backflow near the oil support drilling and grooves.

It must be considered that the measurement results involve errors. Glienicke showed in his research work that measurement errors of less than 1% may influence the derived system properties significantly. A comparison of derived results with those registering a 1%-error is shown in Figure 4.2.9. A significant influence is seen for  $\beta_{22}$  while the influence on the other properties is of lower magnitude. A detailed discussion of the achievable accuracy is given by Glienicke and the interested reader may refer to the publication [67].

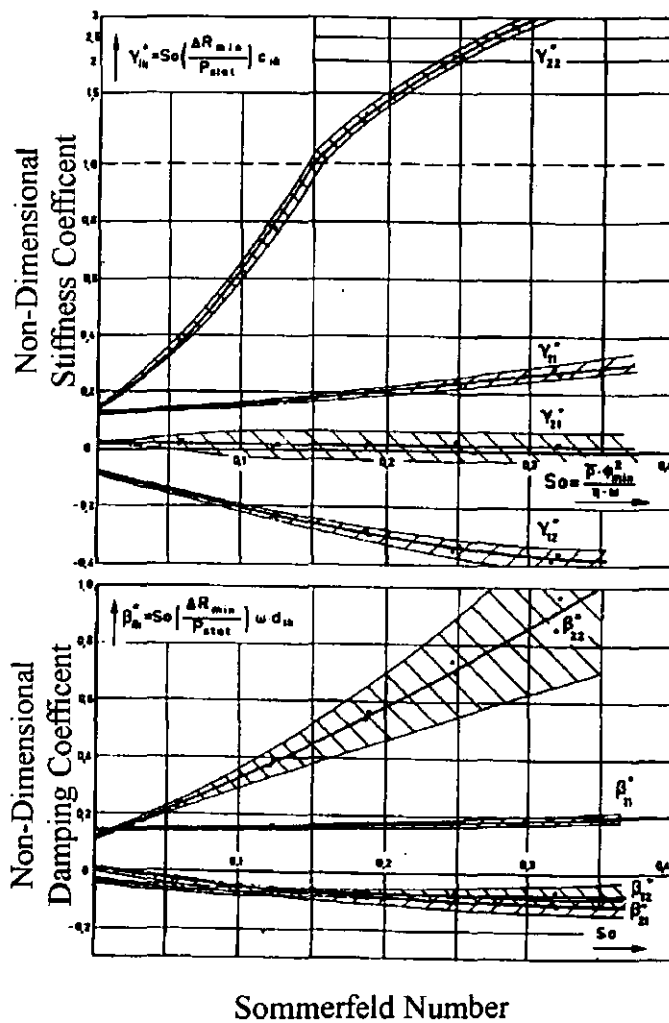


Figure 4.2.9 Averaged 1%-Error [by Glienicke]

### 4.2.2 Simplified Approximation-Model

According to the theory described in section 4.2 the non-dimensional spring and damping coefficients are similarity measures. Either the analytically derived or measured properties, i.e. the dimensional and absolute measures of the damping values ( $\omega_{d,ik}$ ) and stiffness values ( $c_{ik}$ ), can be transformed to a non-dimensional state by multiplying by the Sommerfeld number  $S_o$  and the bearing clearance ( $\Delta R$ ) and by dividing by the static load ( $P_{stat}$ ). The Sommerfeld number is changed according to the changed static load with a constant angular velocity of the shaft. This results in non-dimensional representations of the stiffness and damping properties. The external load  $P$  can also be replaced by the shaft eccentricity ( $\epsilon$ ) as a simple measure or as a system variable for the external load. The obtained stiffness and damping properties show that their most critical measures increase progressively with increasing in load and eccentricity. This formulation has a significant advantage, as the values of  $\dot{\gamma}_{ik}^*$  and  $\dot{\beta}_{ik}^*$  can be easily described using the following polynomial function:

$$\dot{\gamma}_{i,k}^* = AN * S_o^{BN} + CN \quad 4.2.22$$

$$\dot{\beta}_{i,k}^* = AN * S_o^{BN} + CN \quad 4.2.23$$

The values for AN, BN, and CN are different for each graph representing the values of  $\dot{\gamma}_{ik}^*$  and  $\dot{\beta}_{ik}^*$ . The polynomial coefficients are derived from the measured or analytically obtained graphs of  $\dot{\gamma}_{ik}^*$  and  $\dot{\beta}_{ik}^*$  applying the method of averaged values. This approach was developed by Bronstein-Semendjajew [76]. When applying this method to the above problem attention must be given to the related errors introduced for representing the bearing properties. Bronstein-Semendjajew also discussed the accuracy of the approach and the interested reader may refer to the literature [76]. The errors are significantly below the 1%-error shown in Figure 4.2.9 . The accuracy of the approach is therefore good enough to be applied in the analytical procedure to describe the stiffness and damping properties of plain bearings.

This approach gains mainly two advantages. First, the results for  $\dot{\gamma}_{ik}^*$  and  $\dot{\beta}_{ik}^*$  are easily described in mathematical acronyms without obtaining values for a pictorial description. Secondly, this description can be applied within an analysis tool to predict the vibration of an elastic supported rotating shaft. Moreover, the polynomial function can be applied as a description for the bearing properties rather than deriving values from impedance charts or tables. Additionally, interpolating routines are avoided.

A description is given in Table 4 for a bearing with a geometric relation of  $B/D=0.5$  . The derived stiffness and damping coefficients are shown in Figure 4.2.10 .

	$\gamma_{11}$	$\gamma_{12}$	$\gamma_{21}$	$\gamma_{22}$	$\beta_{11}$	$\beta_{12}$	$\beta_{21}$	$\beta_{22}$
AN	2.5000	0.6000	3.2000	6.2400	0.7490	2.2700	1.1900	3.6200
BN	1.1300	3.0700	1.8900	1.7200	0.9980	0.9810	0.8540	1.6500
CN	0.2500	-0.9500	0.9000	-0.1000	2.2500	0.2000	0.4000	2.0000

Table 4 Polynomial Coefficients

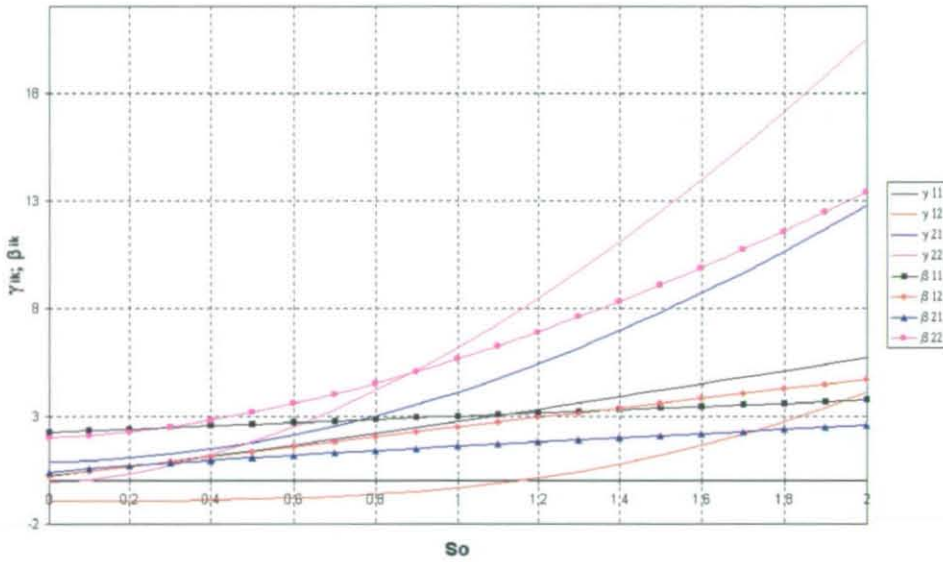


Figure 4.2.10 Stiffness and Damping Coefficients

A further simplification is considered when either a model check-out run is needed in the pre-phase of the final analysis or the detailed bearing description is not required for a specific type of analysis.

First, a model check-out analysis is done, in which finite-element models are checked for their suitability for later complex dynamic analysis and their numerical 'conditioning' of the model matrices. Ill conditioned matrices and poor models may result in abnormal failures of the matrix manipulation process. It is therefore recommended that the condition of the assembled models and hence the generated matrices is investigated. For simplification reasons however, the effect of the bearing model is not required at that time.

Secondly, an application of a more detailed bearing model is not desired. The purpose of the analysis should therefore focus on detailed modelling of the crankshaft and the crankcase. Typical examples are powertrain bending investigation and noise radiation studies of various engine component designs.

Recent studies [77] show that powertrain eigenfrequencies and eigenvectors are significantly influenced by crankshaft modes as shown in Figure 4.2.11. This picture exposes a coupled global powertrain and local crankshaft mode.

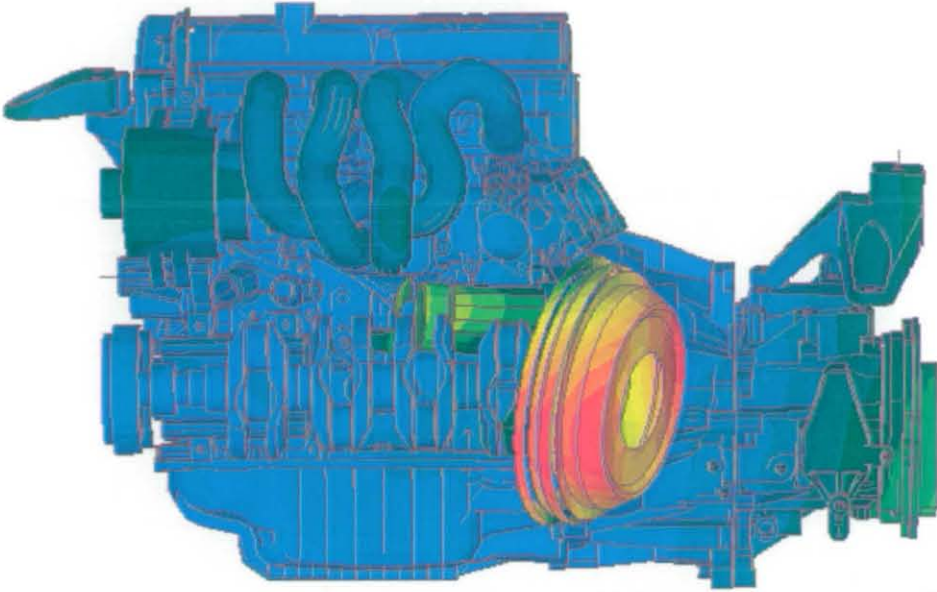


Figure 4.2.11 Combined Crankshaft and Powertrain Eigenvector

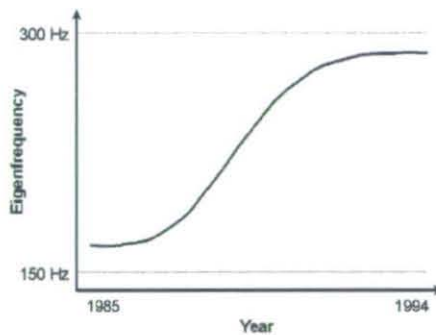


Figure 4.2.12 Shift of First Powertrain Eigenfrequency over Model Years

As with upcoming powertrain designs, the first powertrain eigenfrequencies (first vertical and lateral eigenvector) are shifted towards higher values as displayed in Figure 4.2.12. The frequencies are within a similar frequency band as the crankshaft eigenfrequencies. Such powertrains anticipate combined global powertrain and local crankshaft modes at the same frequency as shown in analyses and tests. In this case powertrain design changes are of no or minor significant effect, as the crankshaft is the limiting factor. An

identical characteristic is obtained for crankshaft design changes observing the powertrain as the constraining factor for design improvements. Additionally, a further theoretical investigation was performed to study the definite limit of the achievable first vertical and lateral powertrain bending eigenfrequency. This is modelled by increasing the stiffness properties of either the crankshaft or the powertrain casing to infinity. The results are given in Table 5.

	Elastic Powertrain	Rigid Casing	Rigid Crankshaft
1. vertical mode	273 Hz	312 Hz	317 Hz
1. lateral mode	282 Hz	317 Hz	317 Hz

Table 5 Definite Limits of Powertrain Eigenfrequencies

Consequently, one must be capable of establishing a coupled model of the crankshaft and engine assembly for powertrain bending analysis. As powertrain bending analyses are accomplished by applying standard normal modes analysis techniques, a stiffness representation of the slide bearing is all that is required.

On the other hand, coupled crankshaft and engine assembly models may be put into use within component noise radiation investigations. A typical noise radiation study is the analysis of various oilpan design proposals. It is known from experience that there is some influence of the crankshaft vibration on the oilpan radiated noise. In this case, the crankshaft acts as a significant contributor to the lower engine block excitation and must be covered within the analysis process. Nevertheless, a reversed influence of the oilpan to the crankshaft is of minor importance for noise radiation studies. Hence, a detailed coupling investigation and the related computational effort may be far beyond the scope of that kind of analysis. A simplified bearing model will handle the coupling of the crankshaft and the crankcase but at a reduced level of accuracy. Therefore, it is debatable whether a detailed bearing model is required for a specific analysis or whether a simplified approach will cover the analysis purpose. Discussing the above characteristic example, one may argue that a detailed model is required as there are vibrational effects of the oilpan influencing the crankshaft dynamic demeanour. This is obvious and test results are available showing this effect. Crankshaft vibration amplitudes were measured and compared with each other applying different oilpan designs at the same engine. The differences obtained in crankshaft vibration are significant at specific frequencies and gain different magnitudes of up to approximately 10% at these frequencies. This has been measured at the engine bottom-end design studied within



this project. Other engine bottom-end designs were not studied for this effect and hence no proven information is available. Regardless of this lack of information, it seems reasonable to assume that similar effects should be measurable at other engines, despite which assumption, the above findings should be treated with caution prior to their general application. On the other hand, no well founded or detailed information is available that crankshaft vibrations impact on the dynamic response of various oilpan designs. It must be assumed that there is an effect, as the above mentioned altered crankshaft vibration will again influence the forcing and therefore the excitation spectra at the main bearings. Hence different vibration results should be obtained from the oilpan or engine block lower-half due to the different excitation spectrum. But when obtaining the different vibrational results for various oilpan designs at these locations from either measurement or analysis, it is not possible to separate the effect of the different oilpan designs from the influence of the coupled crankshaft and crankcase system. Neither in the literature nor internal papers could detailed discussion of this phenomenon be discovered. The common approach to this problem is that the calculated or measured differences are imputed to the oilpan design changes only. The effects of the coupled crankshaft and crankcase dynamics are ignored within that assumption. Hence, no detailed model is required to describe the plain bearing properties.

The only requisite features are the force transmitting properties of the plain bearings. Out of this, the crankshaft is treated as an elastic system stiffening the lower half of the engine block.

Considering the simplification, a reduced approach of coupled crankshaft and engine block dynamics can be applied within that kind of engine bottom-half component noise analysis. Accordingly, only a stiffness formulation is required. This represents the plain bearing property as the coupling effect between the crankshaft and the engine block. Analyses thus performed must be treated as competitive studies. One has to consider that the results obtained do not reflect a repercussion of the oilpan to the crankshaft dynamics. Significant changes in oilpan or bottom-end design and, hence, major changes in stiffness allocation within the bottom-end will effect the accuracy of the results. The accuracy will diminish with increasing difference in stiffness properties between the investigated design alternatives.

The above described polynomial formulation of plain bearing properties is combined with the previously defined transformation procedure (section 4.2) to gain the dimensional and absolute values of the stiffness and damping values. These values can then

be utilised within the above discussed simplified powertrain bending and component noise radiation studies. A pictorial description of the required modelling approach is shown in Figure 4.2.13.

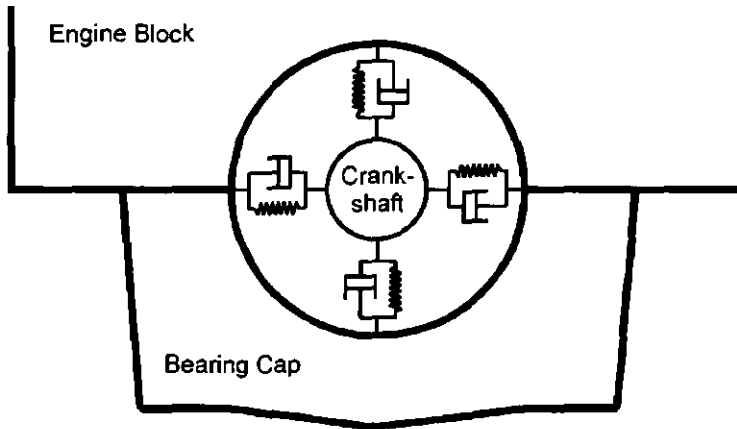


Figure 4.2.13 Plain Bearing Representation

The linearised formulation gained from this approach is shown in the subsequent equations. The main directions  $c_{11}$  and  $c_{22}$  are covered by the description of the vertical and horizontal direction. The diagonal terms  $c_{12}$  and  $c_{21}$  are also covered by this formulation. Nevertheless, this effect is of minor significance and the resulting error by neglecting the diagonal terms would be of minor importance.

Damping properties of the plain bearings are not covered within this simplified approach. Since eigenvalue analyses do not account for damping properties, and competitive noise investigations commonly apply global damping properties through modal or percentage structural damping, it is not necessary to introduce a simplified approach for the viscous damping commodities of the plain bearings. The horizontal and vertical stiffness properties calculate as:

$$c_{total,vertical} = \frac{9 * F_{Bearing}}{\Delta R} = \frac{9 * F_{Bearing}}{R - r} \quad 4.2.24$$

$$c_{total,horizontal} = \frac{2.75 * F_{Bearing}}{\Delta R} = \frac{2.75 * F_{Bearing}}{R - r} \quad 4.2.25$$

The factors '9.0' and '2.75' in the equations are derived from the engine studied in this project under the consideration of wide open throttle (WOT), standard oil viscosities at 3000 rpm and an oil temperature of approximately 120°C. Competitive investigations show that this simplified approach and the above given factors can also be applied for other engine speeds and load conditions. The variations are within the accuracy of the simplified approach and can therefore be neglected. A limitation is defined by the engine

or lubricant temperature. The given factors are valid for warm engines only. Significant changes in lubricant temperature requires a further analysis of the factors, as the oil viscosity changes significantly with engine temperature.

First investigations indicate that this simplified approach can also be applied on other engine families, if the basic variables, such as loads, operating conditions and geometries, do not differ too much from the above discussed engine type.

Nevertheless, one should utilise these values carefully and with respect to the discussed limitations.

### **4.3 Development of Frequency Dependent Bearing Properties**

There are several different approaches available for predicting the journal orbit of an externally loaded shaft. Knowing the shaft orbit within the bearing clearance, one can calculate the minimum oilfilm thickness and the absolute and relative eccentricity. The stiffness and damping properties of the bearing can thereby be derived as described theoretically in section 4.2.

The standard approaches used are concerned with cylindrical 360° bearing configurations. The first convenient tools were developed by Hahn [78] and Ott [79]. Ott's approach is limited to endless bearings and simple bearing designs. Hahn developed a more generally applicable approach for limited bearing widths. But his method is a mixed graphical and analytical approach. Based on the method of Hahn, Someya [66] developed an analytical approach to predict the journal orbit and the stiffness and damping properties. Throughout several investigations Hahn showed that coupled shaft and bearing vibration analyses can be performed applying linearised bearing properties. The results are acceptable for vibrational and stability investigations. Nevertheless, this technique is limited to cylindrical 360° bearing geometries.

In reality, bearing geometries are commonly not of cylindrical shape, owing to design restrictions or thermal and external loads. Vogelpohl [80], Someya [81] and Gnanadoss-Osborne [82] described theories for predicting the oilfilm pressures within radial bearings of an arbitrary geometry. The described method of Vogelpohl has been utilised by Frössel [83] for the prediction of oilfilm pressures of planar and curved oil wedges. A first rudimentary approach was developed by Warner [84] describing the stiffness and damping properties of radial bearings with a single circular segment. There are also some other approaches available such as Sassenfeld-Walther [52], but all these techniques are restricted to a single circular segment.

Schaffrath [85] developed a theory for dynamically loaded bearings with arbitrary geometries. The geometry is described by utilising multiple segments of circular shape. Any practical radial bearing geometry can be described mathematically by a set of circular segments being coupled to represent the full 360° circle. A limitation in geometry complexity is given through the program memory requirements and computational effort only. The individual segments are linked to the neighbouring elements through axial grooves or oil support holes. A geometrical restriction is given with a defined constant bearing width and the limitation of only one potential single circumferential groove in the centre of the bearing width. Some typical examples are shown in Figure 4.3.1. This approach is utilised to predict the common bearing results such as the shaft journal, minimum oilfilm thickness, absolute or relative eccentricity and the oilfilm pressure.

The analysis of the shaft journal orbit presupposes knowledge of the transient and local pressure distribution within the plain bearing. Schaffrath [85] developed an approach by calculating the pressure distribution via a series development. This series is one potential solution of the Reynolds' equation. The x- and y-components of the portative force, equivalent to the external load, are the integrals of the vertical and horizontal components of the positive local pressures throughout the bearing width and circumferential dimension. The integral of the local pressures, also called the 'averaged pressure distribution', is described through two ordinary second order differential equations. Schaffrath compared his method with tests performed by Glienecke and theoretical solutions solving the Reynolds equation for a single circular segment. The results gained from Schaffrath's approach for the portative force as an equivalent for the averaged pressure distribution are comparable to the portative forces derived from the solution of the Reynolds' equation. The advantage gained from his method is the enormous reduction in computational processing time and the application for arbitrary bearing geometries.

Utilising this technique one has to consider the method for establishing the averaged pressure distribution for an individual segment and the pressure added together for all bearing segments. For that it is necessary to introduce the theory of pressure generation within an non-stationary loaded bearing.

An arbitrary movement of a bearing pin is assumed within the bearing sleeve. This movement can be split into a radial and rotational component. It is a general approach to employ these two components and derive the radial and circumferential velocities of the pin. These are then used to calculate the according pressure distribution for the radial ( $P_V$ ) and angular ( $P_D$ ) movement of the pin by applying Reynolds' equation. The resulting pressure distribution ( $P_R$ ) is derived from the summation of  $P_V$  and  $P_D$ . The

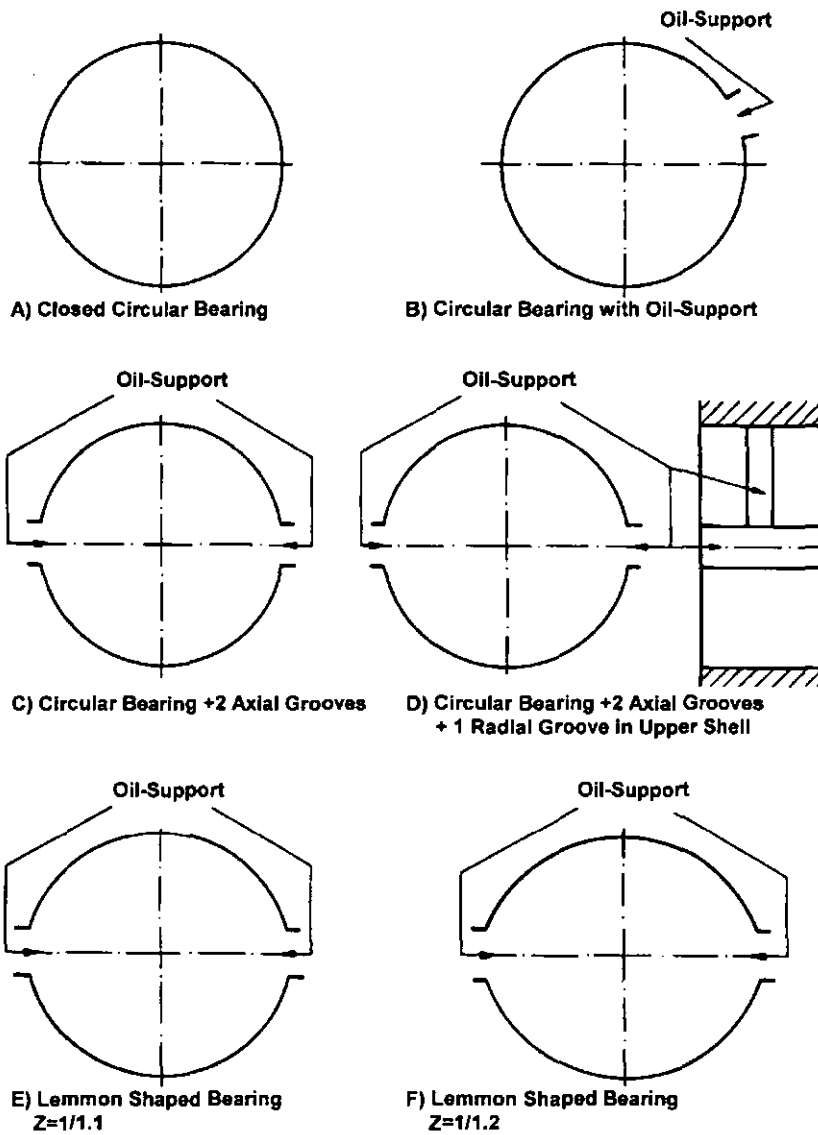


Figure 4.3.1 Principle Bearing Configuration

mathematical solution delivers positive and negative pressures ( $P_0$ ) for the rotation of the pin. Attention must be given to that effect, because negative pressures are physically not permissible. If negative pressures are calculated for some instances, one has to restrict this and correct these values manually through a subroutine. The so corrected pressures must be set to zero.

The solution applied by Schaffrath accounts for negative pressures. His correction takes only account of negative pressures at the pressures added together. Negative component pressures are accounted for those instances that the summed pressure is still positive. A typical example is shown graphically in Figure 4.3.2.

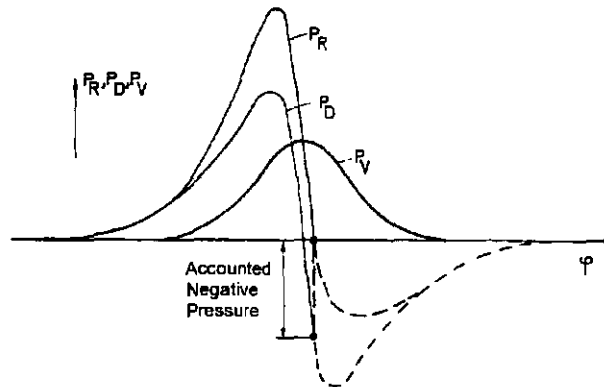


Figure 4.3.2 Pressure Summation (Schaffrath Approach)

Harbott and Klumpp [86] applied the theory of Schaffrath and derived a modified procedure of summing the component pressures. The component pressures are checked against negative pressure values and corrected to zero. A typical example is shown graphically in Figure 4.3.3. While the theoretical solution for  $P_V$  and  $P_D$  are identical, the accounted component pressure is skipped for those values of  $\rho$  showing a negative pressure value. The calculated summed pressure shows a significant increase for specific values of  $\rho$ . The increase in pressure is cross-hatched. This delivers a higher resulting portative force whence are derived higher stiffness properties.

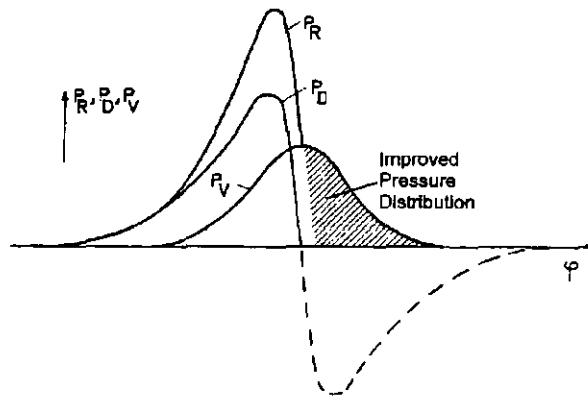


Figure 4.3.3 Pressure Summation (Klumpp Approach)

Experiments performed by Radermacher [87] and comparisons with analysis results showed a significant influence of the different adding routines. The dissimilarity depends on the state of the external load applied to the bearing. Major differences between the two methods could be perceived for load conditions showing significant and fast changes in load amplitudes and directions (oscillating loads). The component pressure  $P_V$  is principally influenced by that condition and is increased. Load conditions representing

either constant loads or unbalance loads do not affect an increase in  $P_v$  and the obtained differences between both adding techniques are of minor significance. Applying this to a reciprocating engine it is clear that the method of Klumpp and Harbodt will yield more accurate results than the method of Schaffrath.

Nevertheless, some further limitations and ensued effects on the derived results must be considered applying the above described method. The drawbacks are mainly based on the applied oil properties and the used formulation of the pressure derivation.

The oilfilm restrictions are mainly based on the assumption that the lubricant can be treated as an incompressible fluid and the viscosity can be set as a constant. No variation is recorded regarding time and location. The oil properties are treated as constants with respect to local pressure and temperature distribution. Oilfilm viscosities are defined as an averaged, externally derived dynamic viscosity. These properties should to a certain extent reflect oil temperature and viscosity changes. A more detailed description would lead to an enormous computational effort and would by no means be applicable for this study.

Further restrictions apply partly to the geometry and operating condition. Inertia effects of the fluid flow within the bearing are disregarded. While the operating conditions do not exceed standard ranges of bearing application, it is known from literature that this effect can be neglected. The shear forces generated by the lubricant are much more significant. The applied method is restricted to shaft speeds up to approximately 8000 rpm. As a consequence one cannot apply this technique for high speed racing engines or applications within turbo machinery. Beside this, one can neglect the relative velocity of the fluid in radial direction (in direction of the minimum clearance) compared to the fluid's angular velocity.

Finally, restrictions are based on geometric assumptions. The oilfilm thickness is defined as being of much smaller size compared to the dimensional extension in radial and axial direction. Hence, this approach cannot be applied for relative small bearing widths or bearings with large clearances. The assumption for the pressure distribution within the bearing would be false. A curvature effect on the fluid flow is neglected. This restricts the bearing diameter to a minimum value in order that the changes in tangential flow are minimal. No recommendation could be found in literature that standard reciprocating engine diameters would exceed this restriction. Another constraint is that matching slide planes are treated as ideal smooth surfaces. The ultimately derived minimum clearance and shear losses are dependent on the oil properties and the geometry only. Shear losses due to metal to metal or mixed friction states and corresponding effects on the pressure distribution are not taken into account.

Additionally the shaft and casing centre lines are defined as parallel lines. An inclination is not considered. A further constraint is introduced by modelling the slide planes as rigid surfaces.

Judging the previous constraints with respect to their application within IC-engines, one may find the most significant negligence within the rigid surfaces, parallel centre lines and missing mixed friction state. The first two will significantly modify the calculated pressure distribution and the stiffness and damping properties deduced therefrom. Rigid bearings face much higher peak pressure values combined with smaller areas of high pressures, whilst elastic structures will face lower peak pressures but larger areas of high pressures. The portative forces as an integral measure are mainly identical, but the bearing itself is not treated correctly. Additionally, radius contacts are not covered, neither through elastic structures nor through an inclination between the centre lines. Peak pressures cannot be predicted and the derived stiffness properties will lack some accuracy. This effect competes against the reduction in radius contact peak pressures derived from elastic structures. A detailed judgment on absolute accuracy cannot be given herein.

The computer programs utilised to predict the damping and stiffness properties of the plain bearings are based on the revised approach published by Harbodt and Klumpp [86]. This software has been developed for the German Research Council for Combustion Engines (FVV). The program was also changed to support externally calculated bearing forces from a Ford developed tool [88] and to interface with a developed software accounting for the conversion into the frequency domain. The analysis flowchart is shown in Figure 4.3.4. The bearing forces are calculated in the time domain for each main bearing. The obtained forces are converted into the corresponding X- and Y-components. Applying the Fourier transformation, we have the Fourier coefficients of the bearing forces for the two main directions. Assessing the magnitudes of the derived Fourier coefficients a significant contribution of high order coefficients is not contained. Coefficients of the eleventh or higher orders do not show a significant contribution. The Fourier transformation is therefore limited to the tenth order.

A short abstract is given subsequently for the standard solution sequence of a frequency response analysis. This strategy will then be applied to introduce the frequency dependent stiffness and damping properties and the corresponding modified solution sequence. The solution strategies are related to the FEM software MSC/Nastran. This is especially important, as the solution sequence for non-linear and frequency dependent properties needs software related matrix manipulation routines.



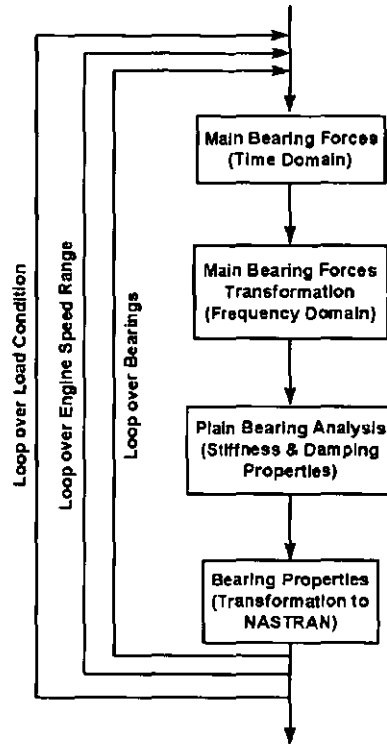


Figure 4.3.4 Main Bearing Analysis Process

The standard differential equation of excited systems can be written as:

$$\mathbf{M}\ddot{\mathbf{x}} + \mathbf{D}\dot{\mathbf{x}} + \mathbf{K}\mathbf{x} = \hat{\mathbf{F}} \sin \omega t \quad 4.3.1$$

The MSC/Nastran formulation of this differential equation is given utilising  $\mathbf{M}$  as mass,  $\mathbf{B}$  as damping and  $\mathbf{K}$  as stiffness matrices, respectively.

$$[M_{gg}] \{\ddot{u}_{gg}\} + [B_{gg}] \{\dot{u}_{gg}\} + [K_{gg}] \{u_g\} = \{P_g\} \sin(\omega t) \quad 4.3.2$$

The subscript 'gg' indicates that the assembled matrices are of the so called G-set without any applied reduction actions. The G-set matrices are then applied to a reduction effort, eliminating all pre-defined degrees of freedom. The matrices thus reduced are then diagonalised. The reduction to the so called H-set is established applying the following matrix transformations.

$$[M_{hh}] = [G_{gh}]^T [M_{gg}] [G_{gh}] \quad 4.3.3$$

$$[B_{hh}] = [G_{gh}]^T [B_{gg}] [G_{gh}] \quad 4.3.4$$

$$[K_{hh}] = [G_{gh}]^T [K_{gg}] [G_{gh}] \quad 4.3.5$$

$$[P_h] = [G_{gh}]^T [P_g] \quad 4.3.6$$

The equation of motion is re-written as:

$$[M_{hh}] \{\ddot{u}_h\} + [B_{hh}] \{\dot{u}_h\} + [K_{hh}] \{u_h\} = \{P_h\} \quad 4.3.7$$

The properties of the applied matrices are of diagonal structure. The matrices are constant and do not represent any frequency dependent properties. They can be solved much faster compared to the formulation applying the G-set.

The solution of this differential equation is given in the H-set and the corresponding solution vector  $\{u_h\}$  must be transformed to the G-set vector  $\{u_g\}$  applying the transformation matrix  $[G_{gh}]^T$ .

By introducing frequency dependent stiffness and damping properties, eqn. 4.3.1 is rewritten as:

$$\mathbf{M}\ddot{\mathbf{x}} + \mathbf{D}(\omega)\dot{\mathbf{x}} + \mathbf{K}(\omega)\mathbf{x} = \hat{\mathbf{F}} \sin \omega t \quad 4.3.8$$

This equation includes all relevant frequency dependent properties in the non-constant damping and stiffness matrices. The equation can be solved by applying standard FEM methodology. The  $\{u_g\}$  vectors are calculated for every frequency. The described solution strategy is applied as many times as analysis frequencies are defined.

This approach theoretically solves the problem.

Investigating the required computational effort in more detail it must be considered that for each value of  $\omega$  one has to assemble  $[B_{gg}]$  and  $[K_{gg}]$ , reduce the complete differential equation and re-transform the solution vector  $\{u_h\}$ .

The required cpu-time multiplies with the number of calculated solution frequencies  $\omega$ . A single solution for the applied powertrain model requires approximately 5000-6000 CPU seconds on a CRAY C916. The final cpu-time amounts to a total of more than 1.000.000 seconds applying only 200 frequency increments. This is not a practically or financially feasible solution. A different solution strategy must therefore be developed, which significantly reduces the computational effort.

The equation with variable coefficients can be rewritten so that the variable matrices are described through a constant matrix and a variable matrix as:

$$\mathbf{M}\ddot{\mathbf{x}} + [\mathbf{D}_{nom} + \Delta\mathbf{D}(\omega)]\dot{\mathbf{x}} + [\mathbf{K}_{nom} + \Delta\mathbf{K}(\omega)]\mathbf{x} = \hat{\mathbf{F}} \sin \omega t \quad 4.3.9$$

This is written in MSC/Nastran formulation as:

$$[B_{gg}(\Omega)] = [B_{gg}^{nom}] + [\Delta B_{gg}(\Omega)] \quad 4.3.10$$

$$[K_{gg}(\Omega)] = [K_{gg}^{nom}] + \Delta K_{gg}(\Omega) \quad 4.3.11$$

The matrices indexed with 'nom' ( $\Leftrightarrow$ nominal) represent the constant component and the incremental matrices represent the frequency dependent components. The transformation to the H-set is formulated as:

$$[B_{hh}(\Omega)] = [G_{gh}]^T \{ [B_{gg}] + [\Delta B_{gg}(\Omega)] \} [G_{gh}] \quad 4.3.12$$

$$[K_{hh}(\Omega)] = [G_{gh}]^T \{ [K_{gh}] + [\Delta K_{gg}(\Omega)] \} [G_{gh}] \quad 4.3.13$$

This transformation technique does not reduce the required computational effort. But with matrix algebra it is possible to independently transform the matrices  $X_{gg}$  and  $\Delta X_{gg}$  to the H-set. The computational effort to transform  $B_{gg}$  and  $K_{gg}$  is identical to that required for the transformation of the constant property system. Additional resources are required for the transformation of the difference matrices  $\Delta B_{gg}(\Omega)$  and  $\Delta K_{gg}(\Omega)$ . This transformation must be done for each increment of  $\omega$ . But the coupling matrices  $\Delta B_{gg}(\Omega)$  and  $\Delta K_{gg}(\Omega)$  are small and contain only 30 coupling elements for the applied powertrain model. The required computational resources are therefore acceptable.

The derived differential equation is written in MSC/Nastran terminology as:

$$[-\omega^2 [M_{hh}] + i\omega [[B_{hh}] - Im[Q_{hh}^e]] + [[K_{hh}] - Re[Q_{hh}^e]]] [u_h] = [P_h] \quad 4.3.14$$

The difference matrices  $\Delta B_{hh}(\Omega)$  and  $\Delta K_{hh}(\Omega)$  are stored in a single complex matrix  $Q_{hh}(\Omega)$  for internal reasons which have to do with the program. The solution strategy applies the real components of  $Q_{hh}(\Omega)$  to establish the nominal stiffness matrix. The imaginary components of  $Q_{hh}(\Omega)$  are applied to calculate the nominal damping matrix. The so evolved assembled differential equation is solved for the  $\{u_h\}$  vector. This vector is then transformed back to the G-set applying an identical computational effort compared with the linear solution for each value of  $\omega$ .

Applying the above solution it is possible to apply frequency dependent non-linear damping and stiffness properties to the forced response analysis within MSC/Nastran. Nevertheless, this approach is also limited with respect to the added resource requirements and therefore number of investigated excitation frequencies  $\omega$ . Theoretically one may apply non-linear properties to every element within the stiffness and damping matrices. The described approach of difference matrices converts to the first approach developed, resulting in an enormous computational effort. Various studies applying the difference matrix technique showed that the computational effort doubles overall for approximately 30 non-linear elements within a base model of about 5000 elements. This includes matrix generation, assembly, solution and data-recovery. The required CPU time increases from about 5000-6000 seconds to an average of 11000 CPU seconds. But this increase in computer resources is acceptable given the acquired modelling methodology of non-linear frequency dependent properties. This tool is used to model the previously explained non-linear plain bearing properties to couple the crankshaft and the crankcase.

Applying the above described technology to MSC/Nastran, a specific user interface is required to model the damping and stiffness properties and to input the frequency dependent coefficients. The applied approach is described below.

The stiffness and damping of vibration isolation devices can be modelled as uncoupled springs and dampers between two coincident grid points using standard CELAS2 elements of the MSC/Nastran element library. The global coordinate system of these points must align with the principal axes of the CELAS2 elements. The definition of the stiffness and damping properties is in line within those principal coordinate directions. Nominal spring properties are used to compute the modes of the system. These springs are defined by CELAS2 elements or DMIG matrices selected by the K2GG case control command. Experience shows that this nominal spring stiffness should be placed at the average stiffness of the tabulated spring stiffness, or at the spring stiffness at the most important excitation frequency. The method used introduces approximations to the frequency response calculation and minimizes at the nominal spring stiffness. The frequency-dependent stiffness and damping values are defined as data tables vs. frequency on DMI and DTI bulk data entries. This capability is limited to properties being represented in the residual structure only. The non-linear properties cannot be modelled with superelements. Other structural elements may appear in superelements. Experience shows that a modelling approach having the non-linear coupling elements in the residual structure and the other structural elements in the upstream superelements is the most efficient in terms of computer resources. The tabulated stiffness, damping and frequency terms are defined using DMI bulk data entries. The name KFZ is used for stiffness values, BFZ for damping, and OMEGAZ for frequency values. While it is recommended that the frequency range on the DMI entries should correlate to those frequencies listed on the FREQi entries, matching each frequency on the FREQi entries with each OMEGAZ entry is not required. A beam spline interpolation and extrapolation routine is provided to calculate the values at each excitation frequency not tabulated. The frequency dependent values are mapped onto grid point and component numbers with bulk data entries called 'DMIG, UGX.'

Templates for these entries and a sample input record of the applied bulk data deck are shown in the appendix. Typical examples are listed for the modelling approach of three CELAS2 elements over the bearing width and two major coordinate directions. The corresponding schematic picture is shown in Figure 4.3.5. The tabulated input for the software generating the Nastran bulk data deck and the resulting output for MSC/Nastran are attached.

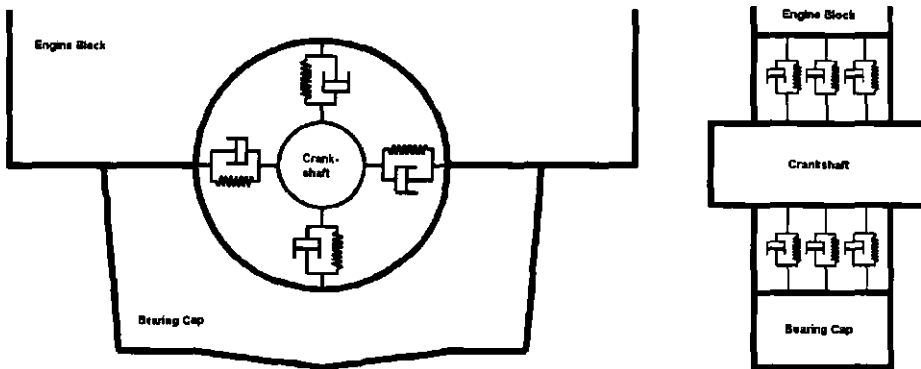


Figure 4.3.5 Plain Bearing Modelling Approach

Competitive studies were accomplished for different modelling strategies of the plain bearing properties. Various numbers of layers representing the stiffness and damping properties have been investigated. The graphically described approach of applying three independent planar representations of the bearing properties was found to be the most comprehensive version. The accuracy achieved balances the required computational effort. Introducing less than three independent planes does not properly represent the bearing stiffness for angular distortion. Additionally, mesh distortion effects are observed due to excessive load patterns yielded through the plain bearing elements. Introducing more than three planes representing the bearing properties through the bearing width does not deliver a significant increase in accuracy but increases the required computational effort dramatically. A further drawback can be found with the required mesh density over the bearing width. Applying  $X$ -layers of spring-damper elements requires  $(X-1)$ -elements over the bearing width. A considerable increase in the engine block mesh density is pre-defined by increasing the number of layers representing the bearing. The increase in computational resources from 5000-6000 seconds to an average of 11000 seconds must be considered, applying 30 non-linear and 5000 linear elements only. It is clear that more linear and non-linear elements will dramatically effect the CPU time. The introduction of an additional layer of non-linear spring and damper elements will raise the CPU requirements by around 2000 seconds. This does not account for the required computational expenditures of an increased mesh density.

Summarising the relationship between achieved accuracy and analysis effort the previously described approach of applying three independent planes was found to be the most comprehensive version. The stiffness and damping properties are represented by making use of the horizontal and vertical direction as the two principle bearing property directions  $c_1$ ,  $c_2$ ,  $\beta_1$  and  $\beta_2$ .

Because the main effort of this work has been concentrated on the dynamic resonances of the coupled crankshaft-crankcase system and the corresponding effect upon the radiated noise, a thorough investigation of the effect of the engine operating conditions on the properties of the coupling elements must be carried out. This allows to judge about the expected changes in system resonance introduced by altered coupling properties. Therefore, it is useful to have some knowledge of how the engine load, speed and ignition timing affect the plain bearing stiffness and damping properties. While the knowledge of a look-up table should be as close as possible, one has to consider the computational effort required. The major advantage of this kind of look-up table is that the work must be undertaken only once. The calculated stiffness and damping properties can be utilised for this engine application as many times as required compared to other solutions, solving the coupling properties for each application independently.

The operation conditions for the initial analyses were selected to cover the entire load and speed range. Having studied these initial operating conditions, an initial judgment can be made on the density required to generate the complete look-up table for this application. Covering the operational domain of this I4-engine, four different loadcases are applied for full, 2/3, 1/2 and 1/3 load condition. The considered engine speed range covers 1000 to 6000 rpm with 1000 rpm increments for each load condition. One further loadcase is considered, applying a 15° spark advance for part (1/2) load. This loadcase will be used to study the effect of spark advance with respect to variations in oilfilm properties. As the spark advance alters the burn rate, the load history and the frequency content may be influenced significantly. The effect is studied in compliance with the perceived changes in load characteristic and frequency domain properties of the main bearings. While the analysis procedure covers these changes in forcing function, it should be possible to do similar studies for fast burn rates or other combustion process specific changes.

Applying the described analysis procedure the plain bearing stiffness and damping properties are calculated for the above defined operation conditions. Results for each main bearing are given as stiffness and damping properties versus frequency. The derived stiffness commodities are shown for full, 2/3 and 1/3 load in the appendix in Figure Appendix 4.1a to Figure Appendix 4.6f . The corresponding damping values are displayed in Figure Appendix 4.7a to Figure Appendix 4.10f for full and 1/3 load condition. The damping properties for the other load conditions have been omitted, because the obtained values do not diverge significantly from the full load condition. As the damping properties are mainly influenced by the change in radial velocity and viscosity, one can draw a simplified picture to explain this phenomenon.

Recalling the approach whereby the hydrodynamic effects can be represented in the easiest form as a parallel combination of a non-linear spring and a damper, one can describe the main bearing by a simple model.

The crankshaft pin is accelerated into the reverse direction each time the bearing force travels through zero. In the lubricant cleavage a hydro-dynamic oil pressure is generated which develops a reaction force, the so called portative force. This force increases exponentially with decreasing cleavage. Emphasising the damping coefficients, significant damping can be generated only under operation conditions showing a significant oil displacement. This occurs only under those circumstances if the pin is travelling through the bearing clearance. A pictorial description may be given with a pin travelling on a mostly diagonal path through the bearing clearance rather than 'rolling' along the bearing shells. Considering the absolute values and the direction of main bearing forces this may occur mainly under conditions with high peak pressures and little mass forces, i.e. full load and low engine speeds.

The most extreme conditions studied in the first instance are those of full and 1/3 load state from 1000 rpm to 6000 rpm. Comparing the damping properties obtained in the vertical and horizontal directions, one finds the largest difference at 1000 rpm engine speed. The damping properties differ by approximately 10-15% for the vertical direction showing higher values for the full load condition. The differences level off with increasing engine speed due to the increased bearing loads. Notable differences cannot be detected at engine speeds above 4000 rpm. This is mainly influenced by the mass forces of either the crankshaft or the oscillating components.

Further correlation is done by comparing the derived stiffness and damping properties in the frequency domain with studies applying a time domain solution. The frequency domain properties are therefore transformed to the time domain, so that the properties can be drawn within a single picture. Comparisons of the stiffness properties are shown in Figure 4.3.6.

The displayed structural stiffnesses of the engine block assembly are obtained from a non-linear finite element analysis. No significant non-linearity is observed for the structural stiffness. The oilfilm stiffness properties are predicted under the assumptions of an infinite stiff bearing structure. This exhibits that the oilfilm stiffness is significantly larger than the bearing structural stiffness as shown in the shaded area. The resulting stiffness  $C_{sum}$  shown to the crankshaft is calculated from a serial combination of the structure and oilfilm stiffness respectively. Competitive calculations performed by AVL [89] utilising the theory of elasto-hydro-dynamics (EHD) and accounting for the elasticity of the bearing structure show a change in the effective stiffness  $C_{sumEHD}$  of

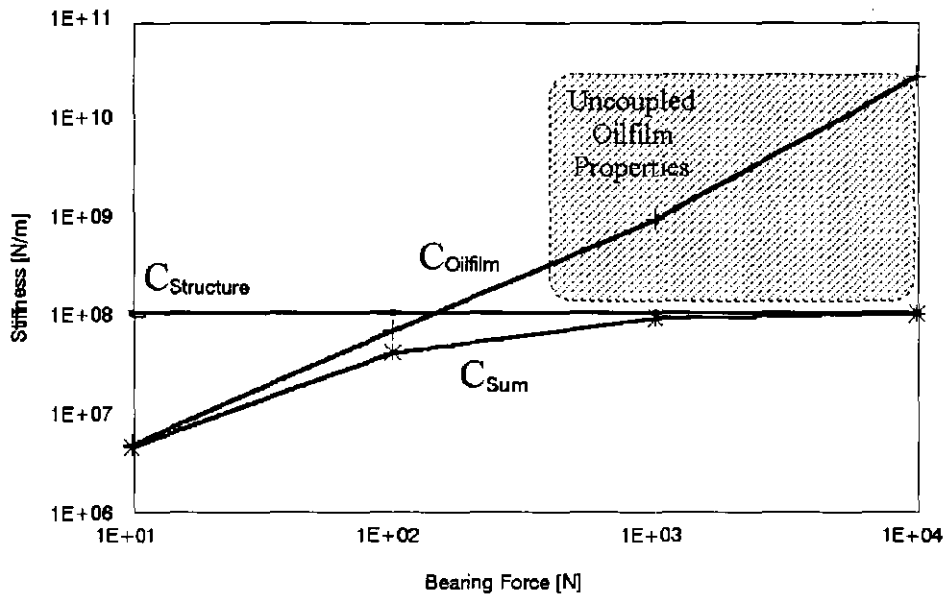


Figure 4.3.6 Comparison of Structure and Oilfilm Stiffness

$\pm 5\text{-}10\%$  at low bearing loads in relation to  $C_{\text{sum}}$ . Comparisons for higher bearing loads indicate that the differences diminish between the stiffness properties derived from a coupled elasto-hydro-dynamic analysis and an uncoupled analysis. The stiffness properties from the uncoupled external analysis are shown as the shaded area in the previous figure. A comparison between both results indicates a good correlation as both analyses show similar results for practical bearing forces above 800 N. Considering the actual main bearing forces, the main bearing stiffness can be approximated with good results by non-linear springs, because the plain bearing is operating mainly under conditions dominated by the stiffness of the bearing structure.

The damping coefficient of the plain bearing decreases with the increase in load. This supports the theory of increasing transmissibility of the bearing under pre-loaded condition. Studies of AVL [90] confirmed this by measurements as shown in Figure 4.3.7. The analytically derived damping coefficients are shown as shaded area. An overall good correlation can be assessed for higher bearing loads, whereas the analytically derived damping coefficients are smaller for lower bearing loads. Comparing measured and calculated properties, the maximum percentage difference is calculated with  $-15\%$  for lower bearing loads from the previously shown results. It should be noted that the measured damping coefficients are not given for the two principle directions but as an integrated value for all directions. The damping values of the primarily (highly) loaded direction are well correlated. When studying the analytical results shown in the appendix



in more detail, it can be found that the damping properties do oscillate, whereas the damping properties of the primary direction show a distinct behaviour. This effect may relate to the relatively low bearing loads in the secondary direction.

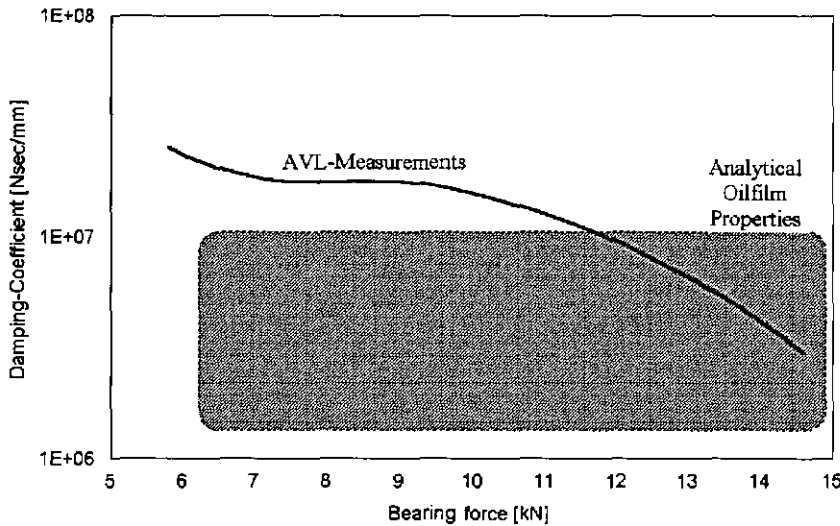


Figure 4.3.7 Comparison of Oilfilm Damping Properties

A detailed investigation [91] evaluated the differences between the 'original' powertrain model and the 'modified' (frequency dependent property) powertrain model. The main bearing properties used in the original powertrain are represented by constant stiffness and damping properties. Thus are mean averaged values derived from an external oilfilm analysis and do reflect the oilfilm behaviour under full load running condition. As already discussed in previous sections, one may apply this modelling approach for those studies only investigating relative differences and design investigations without influences on the coupling properties of the crankshaft and crankcase. The most significant disadvantage is that this simplified approach cannot be applied for studies modifying the coupling conditions requiring a new external analysis of the bearing properties. These are mainly load and speed dependent studies and analyses changing either the crankshaft or the crankcase lower bottom half design.

The objective of this study was to evaluate the appropriateness of the theoretical approach to apply the frequency dependent coupling modelling for main bearings in noise radiation studies. The results are compared to the approach using constant bearing properties. Utilised changes cover variations in load from full load to 1/3-load and spark advance. The analysis concentrates on main bearing acceleration studies and radiated noise investigation by applying surface velocity plots of absolute and differential data. The analysis concentrates on the differential plots of the integrated surface velocities,

as the study is of competitive character between various design alternatives only. One may also refer to Chapter 7 for the nature of the integrated surface velocity data and the appropriateness of the results for comparisons of designs. Firstly, the analysis concentrates on the comparison of the constant property model with the frequency dependent model with the engine speed range from 1000-6000 rpm under full load condition. The model's attributes are investigated with respect to main bearing acceleration and integrated surface velocity data from which the differential values are obtained. Secondly, the analysis covers a comparison of frequency dependent models applying different load conditions. The studies include load sweep analyses of 1/1, 2/3, 1/2, and 1/3 load condition. The explored measures are again main bearing acceleration and differential surface velocity data.

Comparing the constant property model with the frequency dependent property model, significant characteristics are examined for the main bearing excitation data in all major directions. The significant difference between both models is investigated with a more balanced course of the main bearing accelerations regardless of the absolute values and the general trend. The differences in acceleration amplitudes between each main bearing cap are reduced for the frequency dependent model. This phenomenon accentuates especially for the Y-direction (vertical), namely the highest loaded direction of the crankshaft and the main bearings. Investigating this in more detail, a significant effect can be obtained from the main bearing forces. The loads between all main bearings are more evenly distributed for the frequency dependent model than those of the constant property model. The acceleration results in the vertical direction show a similar behaviour to the characteristic excitation spectra applied to the combustion chamber. The acceleration levels decrease with exponential slope. Again this correlates to the state of equilibrium as discussed in Chapter 5. The obtained differences between the original and the modified model are relatively small in vertical direction. This mainly applies to low engine speeds between 1000 and 2000 rpm. The calculated vertical main bearing accelerations are shown in Figure 4.3.8 and Figure 4.3.9 for the constant coefficient and dependent coefficient model respectively. The displayed accelerations are shown for five main bearings being labelled as MB1 through MB5. Main bearing 1 is defined as the first main bearing looking from the engine front pulley towards the transmission. The analysis direction is identified as subscript of the main bearing label. The vertical direction is defined as Y, the horizontal direction is labelled as X respectively.

A significant increase in response amplitude can be detected in the original model at constant 1600 Hz with increasing engine speed. The frequency dependent model shows a similar behaviour. The amplification is of significance and the peaks occur at frequency

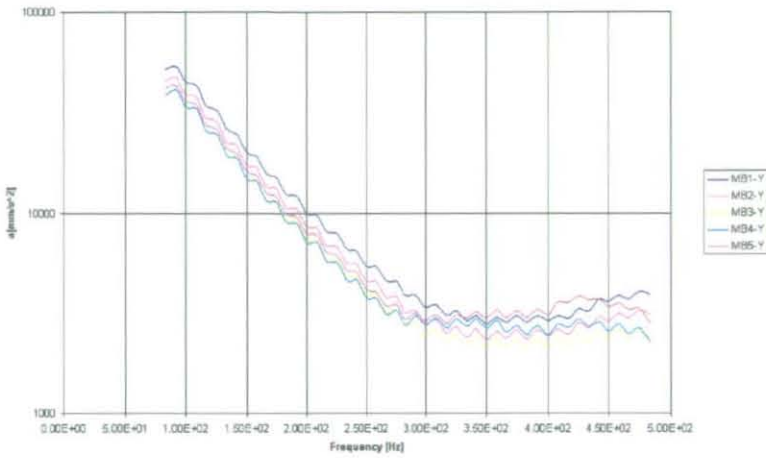


Figure 4.3.8 Vertical Main Bearing Acceleration (1000 rpm; Constant Model)

values 150-200 Hz higher compared to the original one. The absolute change in acceleration response varies between approximately 40% and 100% for a frequency range from 1000 Hz to 2000 Hz. This is presented in Figure 4.3.10 and Figure 4.3.11. The main reason for the shift of the resonance peaks is due to the coupling effects. The low frequency domain is mainly influenced by the main bearing forces and no significant change is found between the linear and non-linear approach. The vertical directions especially show this behaviour. With increasing frequency, the dynamic responses of individual components are becoming more important. Knowing that bearing beam eigenfrequencies are in the range between 1400 Hz and 1600 Hz, a significant influence of this component is shown in the non-linear frequency dependent analysis.

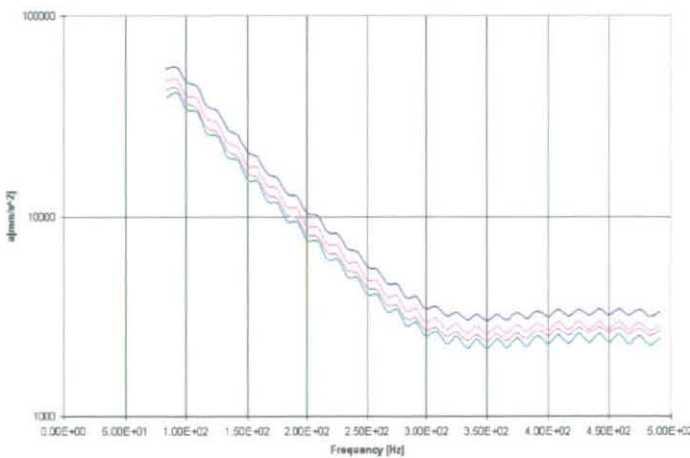


Figure 4.3.9 Vertical Main Bearing Acceleration (1000 rpm; Dependent Model)

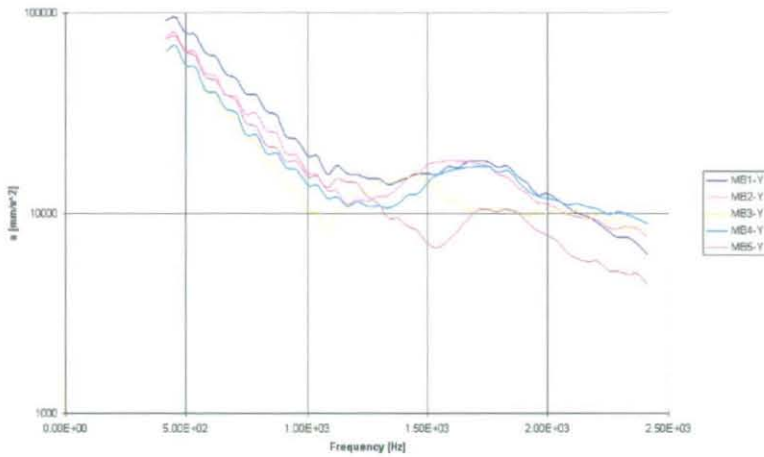


Figure 4.3.10 Vertical Main Bearing Acceleration (5000 rpm; Constant Model)

A similar result can be observed for the horizontal main bearing acceleration results. The original model has two substantial peaks at approximately 700 and 1200 Hz at 4000 rpm (Figure 4.3.12). The non-linear approach shows up with peak levels at 850 Hz through 1100 Hz and at 1450 Hz (Figure 4.3.13). Further, main bearing accelerations are shown for 6000 rpm in Figure 4.3.14 and 4.3.15 respectively. The peak between 850 Hz through 1100 Hz is unchanged, while the peak at 1450 Hz of the non-linear model is more balanced than at 4000 rpm due to increased bearing stiffness and damping properties at higher engine speeds. It is important to point to the acceleration peak values which are unchanged for both approaches, whereas the linear method develops generally more balanced resonances compared to the non-linear one. The non-linear modelling technique shows up with significantly reduced main bearing acceleration values at higher frequencies with increasing engine speeds.

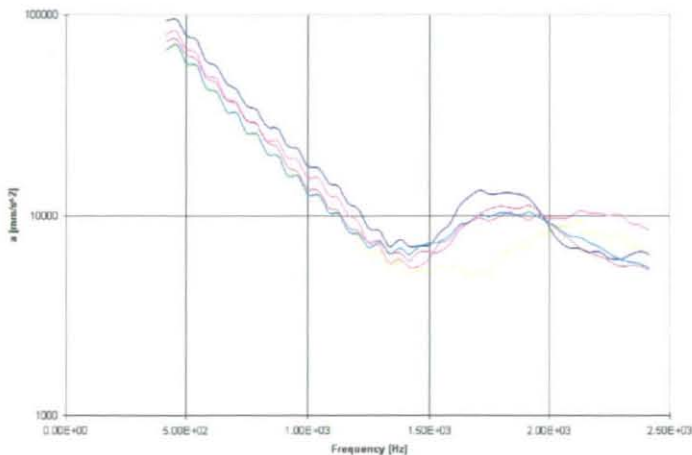


Figure 4.3.11 Vertical Main Bearing Acceleration (5000 rpm; Dependent Model)

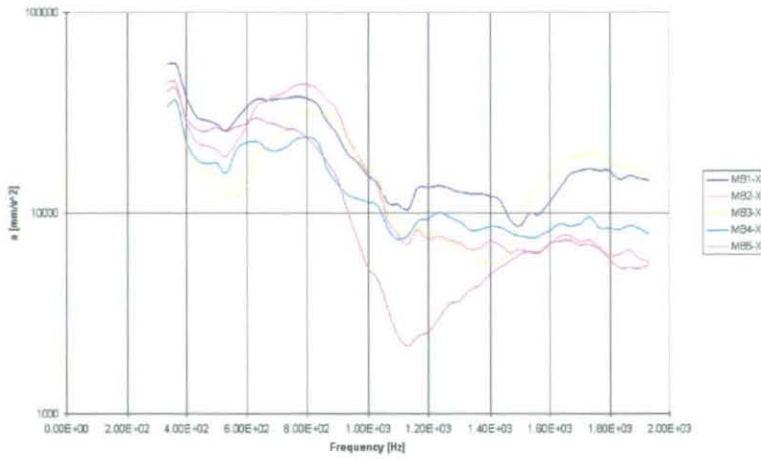


Figure 4.3.12 Horizontal Main Bearing Acceleration (4000 rpm; Constant Model)

The detailed examination of both modelling technologies shows that the main bearing acceleration from the non-linear approach are in general more balanced. Main bearing one, three and five are less conspicuous. The response of these bearings are over-estimated significantly by the linear approach. Table 6 presents the frequencies at which accelerations peaks are observed. The accomplished significances are that both modelling approaches generally show an identical behaviour regarding absolute peak amplitudes but the frequency values at which peak resonances occur increase with increasing engine speed for the frequency dependent model only. The constant model is characterised with constant frequencies at which extremes occur.

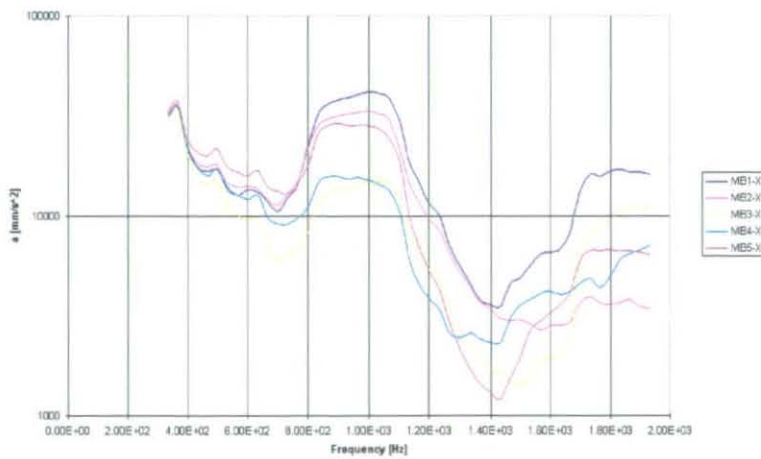


Figure 4.3.13 Horizontal Main Bearing Acceleration (4000 rpm; Dependent Model)

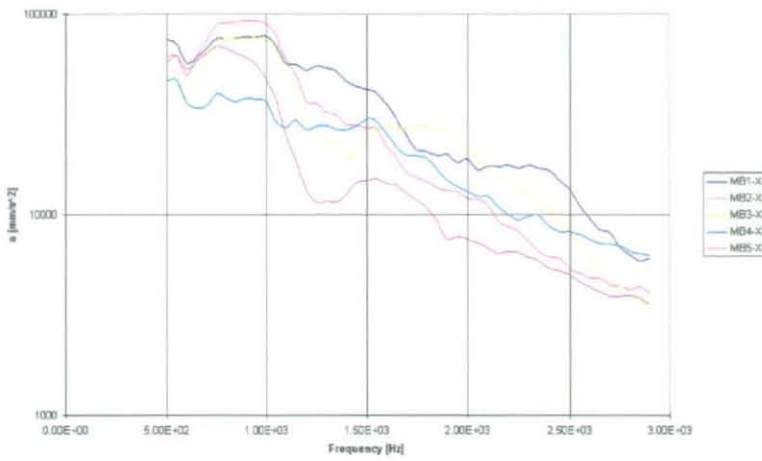


Figure 4.3.14 Horizontal Main Bearing Acceleration (6000 rpm; Constant Model)

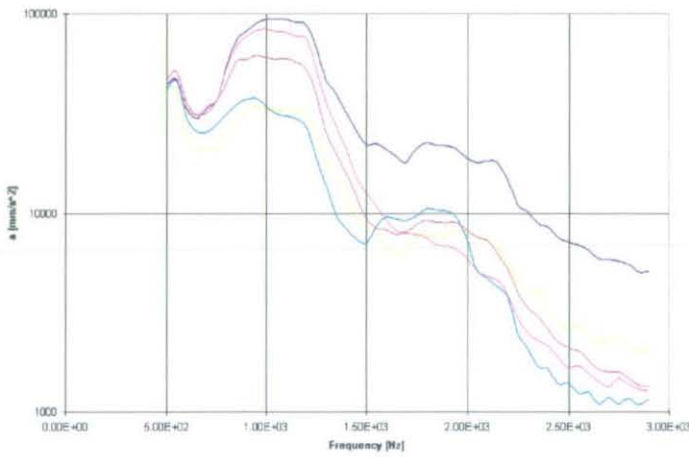


Figure 4.3.15 Horizontal Main Bearing Acceleration (6000 rpm; Dependent Model)

Linear Model	Non-Linear Model
1600 Hz (X,Y-direction)	1750-1800 Hz (X,Y-direction)
700 Hz (X-direction)	850-1000 Hz (X-direction)
1400 Hz (X-direction)	1500-1800 Hz (X-direction)

Table 6 Main Bearing Peak Resonances

The differences can be explained by the non-linear behaviour of the coupling properties. These properties are adjusted with respect to load and speed conditions according to the externally calculated data tables. The increasing frequencies of the peak values are related to the non-linear behaviour of the plain bearings. The stiffness properties

increase with increase in speed, while the damping characteristics diminish. Hence, the non-linear coupled system registers increasing resonance frequencies with increasing engine speeds.

The load dependent effect upon the main bearing acceleration will be discussed later. By analysing the acceleration data one significant effect can be obtained. The perceived levels of main bearing acceleration do vary for all bearings and all directions between the full- and 1/3-load condition. This behaviour is expected and is proven by experience and experimental data not shown here. It therefore suffices to discuss the system response for the full and 1/3-load condition. Load conditions showing the expected results between both extremes are omitted.

The results for low engine speeds (1000-2000 rpm) do not show a significant difference between full- and 1/3-load condition. This is caused by relatively small differences in the gas pressure function at those engine speeds. Substantial deviations are generated between 2000 and 3000 rpm with increasing differences in the combustion pressure. The perceived response spectrum at full-load is more uniform than those under part load condition as shown in Figures 4.3.16 and 4.3.17 . The responses in the horizontal direction at main bearings 3 and 4 reveal an increased level of approximately 20-25% . This occurs at frequencies between 1000-1400 Hz at 1/3-load condition and an engine speed of 3000 rpm. Especially main bearing 5 has an extreme increase in acceleration amplitudes of about 50% at frequencies above 1000 Hz compared to other main bearings. Similar responses can be obtained for 4000 and 5000 rpm engine speed. The 1/3-load condition exhibit a 20% lower level at main bearings 4 and 5 . Additionally one perceives an increase in acceleration level for main bearing 1 with increasing engine speed. This is mainly due to the corresponding whirling effect of the pulley inertia and is comparable to the engine rear end response.

Both effects have also been reported by other researchers. It is well known that torsional vibrations are excited mainly by gas pressure forces and therefore that any factor increasing the gas forces will directly increase the torsional amplitudes of the crankshaft. But torsional vibration cannot be detected clearly by main bearing acceleration data as these are significantly decoupled from main bearing accelerations. The situation with respect to the whirling modes of vibration appears to be more complex. Two overlaying effects occur. On one hand we find that the whirling amplitudes of the crankshaft and the corresponding complex eigenvectors from the vibrational analysis are dependent on the structural design and the engine speed. On the other hand we find that the excitation forces influence the deformation characteristic of the crankshaft. At lower engine speeds the stabilizing gyroscopic effects are negligible compared to the gas

pressure forces. This effect vanishes with increasing engine speed. At high engine speeds we find high levels of stabilizing gyroscopic effects and the main bearing forces and hence accelerations do not show that significant response to load changes compared to lower engine speeds, at which the excitement of this vibration is mainly due to the gas pressure forces.

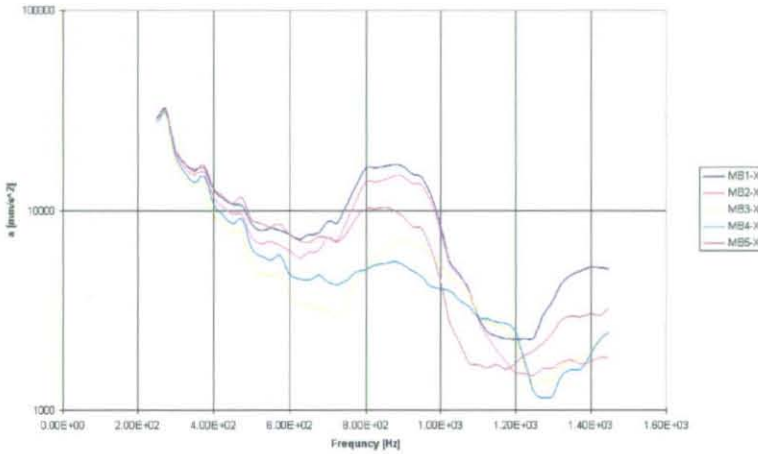


Figure 4.3.16 Horizontal Main Bearing Acceleration  
(1/3-Load; 3000 rpm; Dependent Model)

Summarising the results obtained the most significant changes could be perceived in the horizontal (X-direction) direction between the main bearing acceleration. Gyroscopic effects disguise the results mainly at the rear end main bearings No. 4 and 5. Identical effects are obtained at lower amplitudes for the front end bearing No. 1. The vertical (Y-direction) acceleration levels show a more homogeneous characteristic, although the peak amplitudes are mainly driven by the peak gas pressures. The gyroscopic effect could be assessed but at significant lower amplitudes. Peak acceleration levels are obtained at constant frequencies of about 700 and 1000 Hz indicating that system eigenfrequencies are detected. A modal analysis of the crankcase and bearing beam assembly substantiate this interpretation. The assembled bearing beam exhibits eigenfrequencies at these values.

Analyses of the model holding the spark advance feature do not show a difference in main bearing acceleration data. The obtained differences are marginal. Studying the applied forcing function in more detail, one must consider the loss of data by applying the frequency domain solution. The time dependent forcing function of the spark advance model reflects the change in pressure increase with respect to crank angle. Transferring the forcing function into the frequency domain, one will lose the relation to the crank angle and finally will also skip the timing signal of the signal. The frequency domain



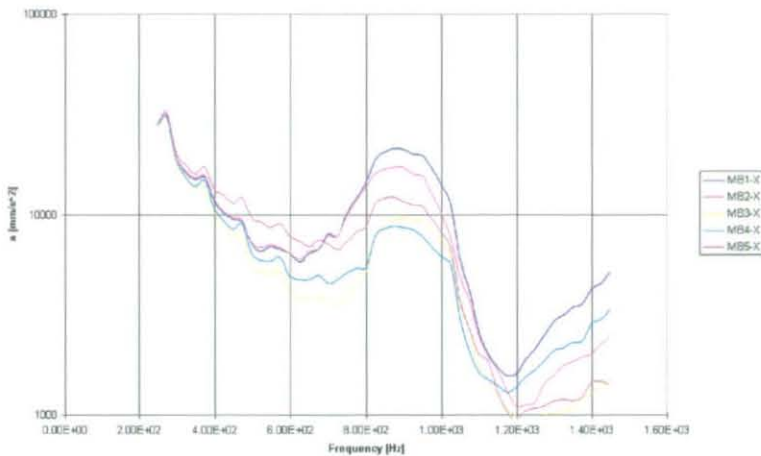


Figure 4.3.17 Horizontal Main Bearing Acceleration  
(Full-Load; 3000 rpm; Dependent Model)

representation of the full-load forcing function with and without spark-advance are identical from an engineering point of view. The obtained differences are caused through mathematical inaccuracies. This effect is introduced through the definition of the spark advance. The currently applied spark advance model does not reflect the changes in burn-rate or burn-angle. The introduced changes are only related to the timing signal of the pressure function. The signal to crankangle relation is omitted by transferring the forcing function into the frequency domain. Consequently, this approach is not capable of representing a correct relation of temporally changed forcing functions. Hence, this approach may not be applied for temporally changed forcing functions. A further discussion of the spark advance model is, therefore, not appropriate and will be skipped.

It should be recalled at this point that the main emphasis of the project is to predict the radiated noise influenced by crankshaft dynamics. Hence, one has to evaluate the effects of the introduced non-linear main bearing properties on the radiated noise. The approach of evaluating the radiated noise characteristics of an engine structure is, therefore, required. The physical and mathematical backgrounds and the correlation will be shown and discussed in Chapter 7 in more detail. But it is essential, for understanding, to apply the later derived approach at this point.

Comparison between the calculated data for the integrated surface velocities from the original model and that from the frequency dependent model reveal a data range between 140 and 150 dB. Main noise sources for both models are examined at the oilpan either in horizontal or vertical direction. The linear approach additionally shows a highlighted area of high levels in the region of main bearing No. 3. A direct visual comparison of these absolute values is difficult, as the deviations are small compared

to the absolute values. A quantitative investigation is done by calculating the numerical differences of the integrated surface velocities of both models. A competitive investigation is done by defining one model as the reference model. The differential results indicate for positive values that the reference model shows higher integrated surface velocities and therefore radiate more noise. Negative values indicate that the reference model emits less noise than the compared model. The obtained results are available for each node. Hence, this data can be displayed as nodal results on the finite element model.

A first comparison is made between the linear and the non-linear approach similar to that performed for the main bearing acceleration. We shall then compare speed and load dependent characteristics of the non-linear model.

Studying the integrated surface velocities of the vertical direction in detail, a significant characteristic is observed in the region of the third and fourth main bearing. The levels are commonly higher for the linear model under full load condition compared to the non-linear approach. The area at the first main bearing exhibits a contradictory response. Here, we perceive the non-linear model with higher values. Significant differences occur for the engine speed range between 3000 and 6000 rpm. The corresponding results are shown for 4000, 5000 and 6000 rpm in Figure 4.3.18, 4.3.19, and 4.3.20 respectively. Table 7 summarises the differences obtained from the comparison of the linear and non-linear models.

rpm	Horizontal Direction		Vertical Direction	
	MIN	MAX	MIN	MAX
1000	0,4	5,7	-0,6	0,2
2000	0,2	5,3	-0,7	0,3
3000	0,2	5,7	-0,5	0,4
4000	-0,3	5,5	-1,0	0,3
5000	-0,8	5,2	-1,2	-0,2
6000	-0,9	5,7	-0,7	0,7

Table 7 Integrated Surface Velocities (Constant vs. Dependent Model) [dB rel  $v_0$ ]

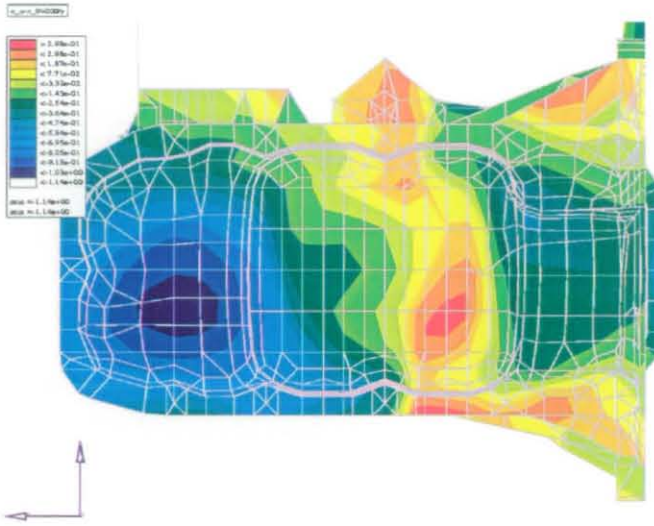


Figure 4.3.18 Differential Surface Velocity (4000 rpm; Constant vs. Dependent Model; [mm/s])

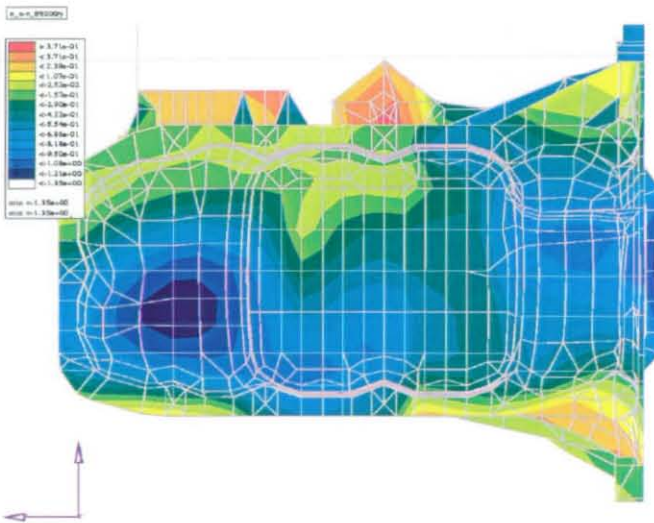


Figure 4.3.19 Differential Surface Velocity (5000 rpm; Constant vs. Dependent Model; [mm/s])

A significantly unique figure can be drawn for the differences of integrated surface velocities in horizontal direction. The maximum deviation occurs in the upper front area of the engine block. This pattern does not change over the entire engine speed range. The slightest difference is perceived in the area of the fourth main bearing. According

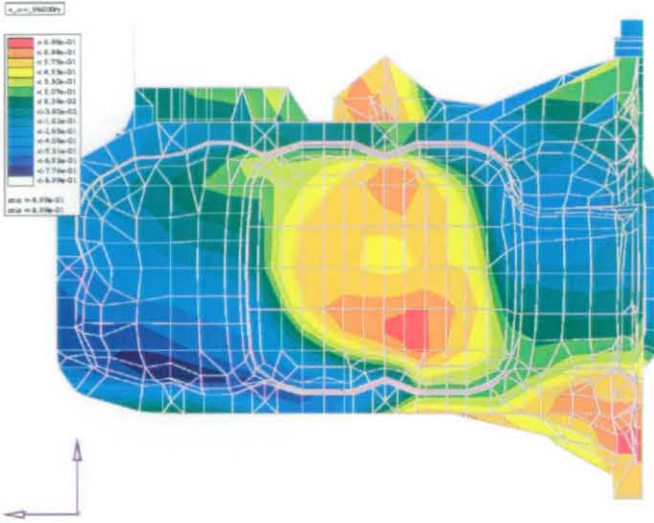


Figure 4.3.20 Differential Surface Velocity (6000 rpm; Constant vs. Dependent Model; [mm/s])

to the previously discussed whirling effect one observes increasing surface velocities with increasing engine speed. A typical picture of the differential results obtained is shown for 4000 and 6000 rpm in Figures 4.3.21 and 4.3.22.

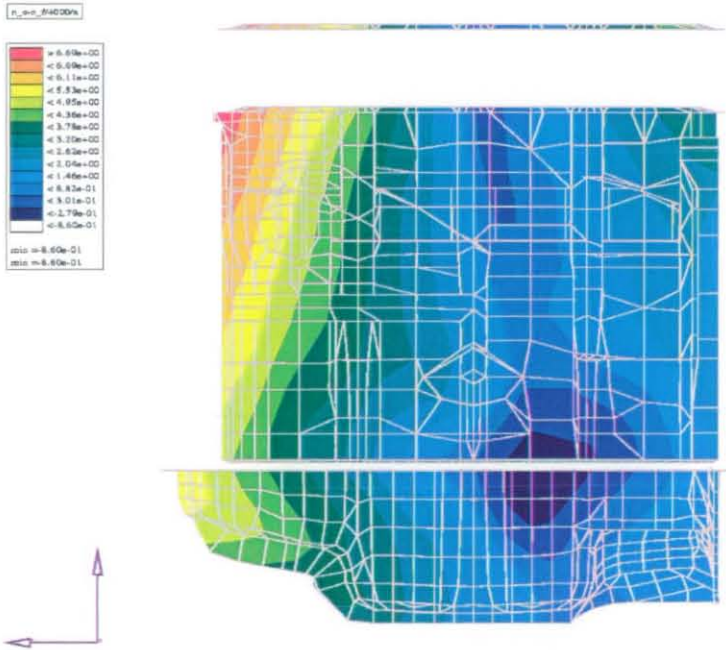


Figure 4.3.21 Differential Surface Velocity (4000 rpm; Constant vs. Dependent Model; [mm/s])

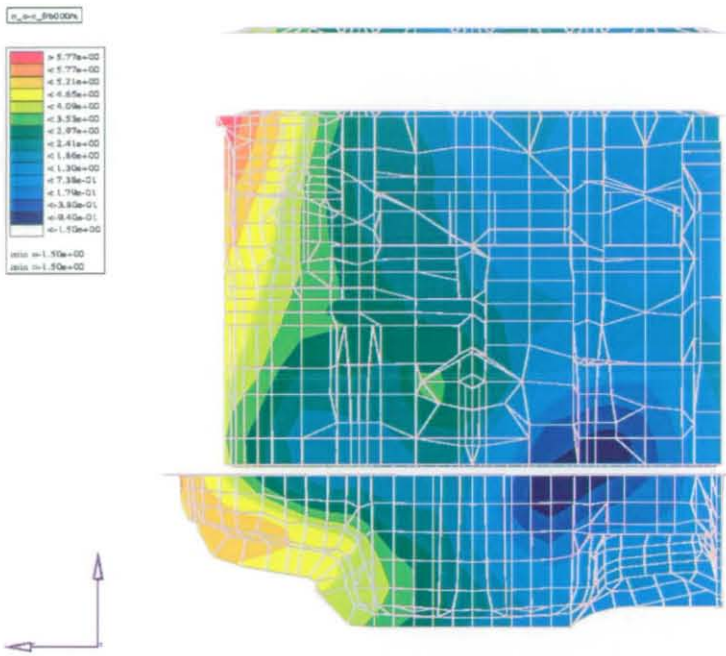


Figure 4.3.22 Differential Surface Velocity  
(6000 rpm; Constant vs. Dependent Model; [mm/s])

The integrated surface velocity data are compared likewise to the main bearing acceleration. Measurements were done to establish the radiated noise of the engine with respect to speed and load. These data are measured for the inlet and bottom side only. The inlet side was chosen, because the exhaust side is covered by the catalyst and the attached heat-shielding. The top side is not applied within this comparison as these phenomena are not covered by this research work.

The calculated differences between full- and 1/3-load condition are listed in Table 8 with respect to the engine speed range. The measured data are given correspondingly. It must be considered that the measurements are done for full- and no-load condition. Hence, the measurements will generally show a more significant difference compared to the analytical solution. The analytical solution does not consider the no-load condition, because the characteristic gas pressure function and the required engine losses cannot be predicted accurately enough for that condition. Competitive investigations showed that a 1/3-load condition is at least required to achieve an acceptable level of accuracy in gas pressure prediction.

rpm	Horizontal Direction (Inlet Side) [dB rel $v_0$ ]		Vertical Direction (Bottom Side) [dB rel $v_0$ ]	
	Analytical	Measured	Analytical	Measured
1000	0	-	0	-
2000	0	3	0	1.5
3000	0.9	1.5	1.2	2.4
4000	0.8	2.5	0.6	1
5000	0.6	2	1.0	2
6000	0.2	1	0	3

Table 8 Comparison of Analytical and Measured Radiated Noise

Some discrepancies are perceived when comparing the listed values. The analytical and measured results do not match. At this point it is necessary to emphasise that the integrated surface velocities may not be directly compared with radiated noise data. Measured data are obtained at 1 m distance from the object as an integral value of the total engine surface. But integrated surface velocities can be applied to predict areas of high noise radiation and to judge the general trend of a structure for varying load and speed conditions. For interpreting the results in more detail it is evident that the studied configurations must be discussed. The measurements are obtained with a fully dressed engine including transmission. The measurements showed that the transmission and the accessories, especially the alternator at the inlet side, make a significant contribution to the overall noise level. The analytical solution does not cover these components. It follows that it is questionable whether one may compare the radiated sound pressure with the calculated integrated surface velocities. Considering these issues one may look at the results in compliance with a tendency investigation. In that context we find an acceptable analogy between measurements and predicted results.

Additional measurements were performed to establish near field intensity data of the running engine. The measurements were done manually. A test engineer points the microphone to significant locations at the engine surface. The data are measured at 10-15 cm distance, while the engine is operating. These measurements are tedious and to some extent dangerous to the engineer. Hence, data are available for only a single engine speed and two load conditions. The obtained differences are shown for the inlet- and bottom-side in Figures 4.3.23 and 4.3.24. The point of operation considered is 3000 rpm engine speed for full- versus no-load condition.

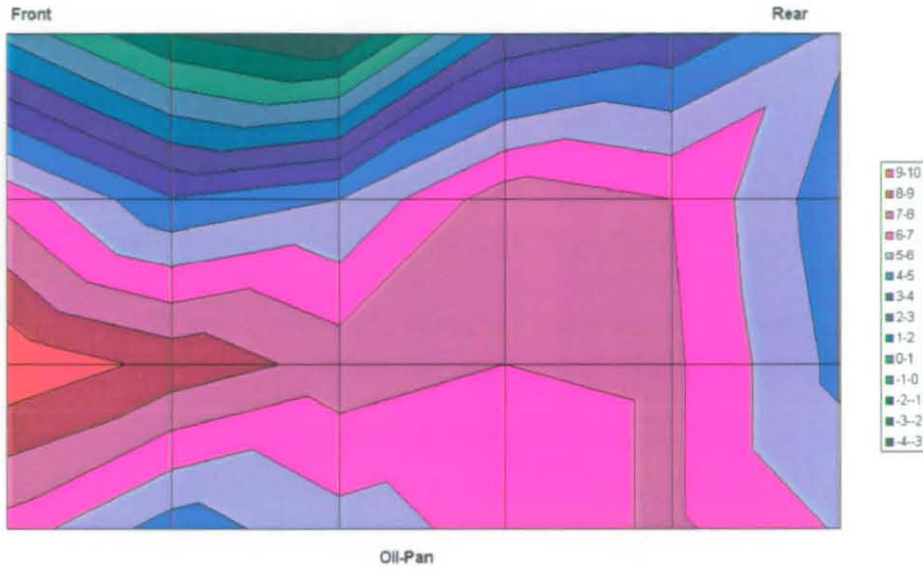


Figure 4.3.23 Near Field Intensity Data (Inlet Side)

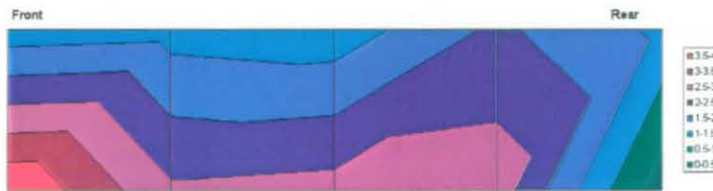


Figure 4.3.24 Near Field Intensity Data (Bottom Side)

Significant areas of high noise levels are perceived at the front side of the engine. This is caused by the belt drive. A similar effect is shown at the bottom side. One further significance is observed at the top of the engine block. This may be related to the so called 'piston slap' or secondary piston movement. Piston originated excitation is covered only as piston side forces introduced from the angular displacement of the connecting rod. The secondary piston movement is not considered in the applied excitation function. The analytical description will therefore give lower difference levels than the measurement configuration. Studying the more general distribution of low and high level areas, one must consider a similar distribution for the analytical and measurement results. This is especially true for the lower engine block which is significantly influenced by the crankshaft dynamics as displayed in Figure 4.3.25.

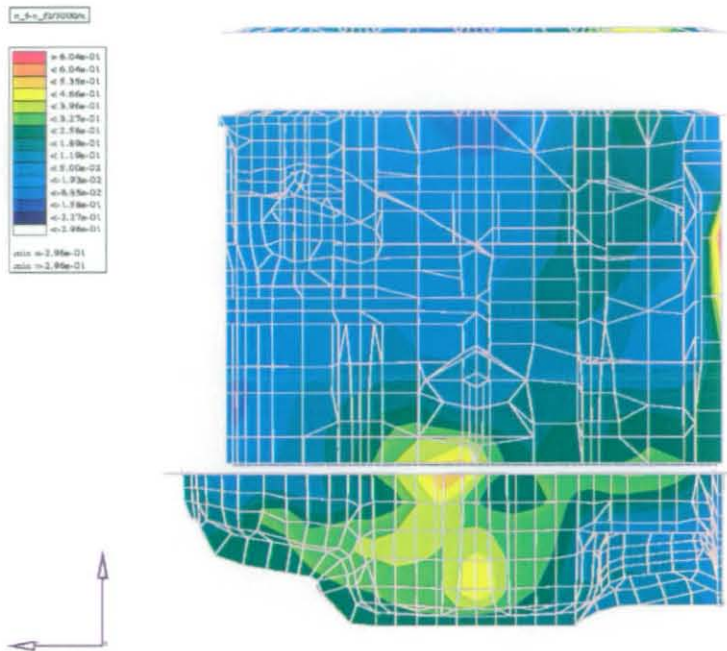


Figure 4.3.25 Integrated Surface Velocity (3000 rpm; Full- vs. 1/3-Load; [mm/s])

A comparison at the bottom-side of the engine does not show a significant peak value as derived from the analytical description. This is shown in Figure 4.3.26. However, one has to account for the reduced number of measurement locations. The near field intensity data are derived for 8 locations only. Two lines of four measurement locations are each defined over the engine length. But the centre of the oilpan has not been considered in the measurements. It is, therefore, conceivable that the analytically derived peak value at the oilpan centre is disregarded.

The analytical results for 1/2- and 3/4-load conditions are calculated but not discussed herein. The perceived results of integrated surface velocity show a similar behaviour to that of main bearing acceleration. The results are adapted to those retrieved under 1/3- and full-load conditions and match between the established lower and upper limits.

Summarising the explored results one may draw the following conclusions. The predictions of integrated surface velocities exhibit the general trend of the system under load and speed variation. Absolute values are not established correctly, as the modelling approach does not cover all excitation phenomena. Missing excitations are mainly secondary piston movement, accessory noise, and Front-End-Accessory-Drive (FEAD) effects. One has to consider that the studied design proposals do not alter or affect the previously mentioned limitations. Block changes can be studied, if the design work concentrates on the lower half of the engine block. Studies at the upper-half may be of



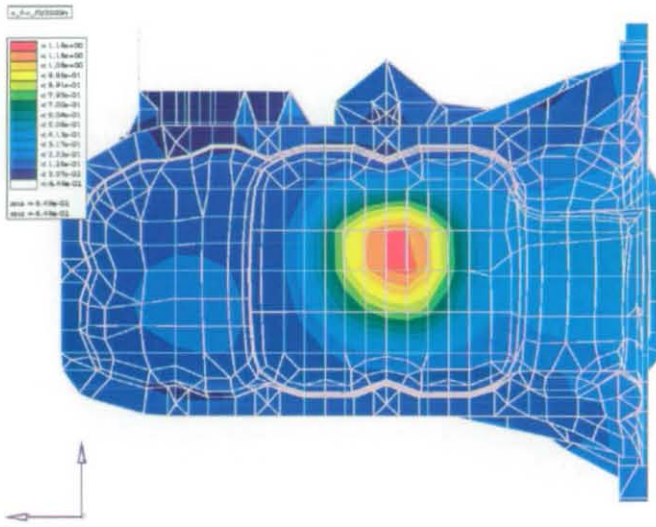


Figure 4.3.26 Integrated Surface Velocity (3000 rpm; Full- vs. 1/3-Load; [mm/s])

limited accuracy with respect to the missing secondary piston movement excitation. But relative and trend studies are practicable and allow for competitive investigations of alternative design proposals.

## **Chapter 5**

### **Development of Forcing Function**

A literature survey is performed to evaluate the available methodologies of measuring and calculating cranktrain forces. An overview of published treatments of forcing strategies is given and discussed regarding their advantages and disadvantages. The development of the frequency dependent forcing function is described. If not mentioned otherwise, all data refers to the studied ZETEC-SE engine.

## 5.1 General Overview

An intensive literature survey has been carried out to review recent methodologies in crankshaft forcing applications. There are many papers available concerned with either the time dependent or the frequency dependent forcing formulation. The basis of all these reports and publications is that the crankshaft and the cranktrain sub-systems are not included in the modelling approach. The forcing functions are either calculated or measured for the different main bearings and the time dependent forcing function is then transferred to the frequency domain by Fourier series. An exemplary work is done by the FVV research consortium of German engine manufacturers [92].

Two different methods are known to measure the forcing function. In the first process the combustion pressure is measured and then transformed into the frequency domain. With the measured transfer function from the piston surface to the main bearings, the gas pressure excitation spectrum can then be transferred to the main bearing excitation spectrum. An exemplary measured gas force spectrum is shown in Figure 5.1.1 for engine speeds between 1500 rpm and 5000 rpm at wide open throttle (WOT) load condition; the corresponding transfer function is given in Figure 5.1.2, and the resulting main bearing excitation spectrum is shown in Figure 5.1.3.

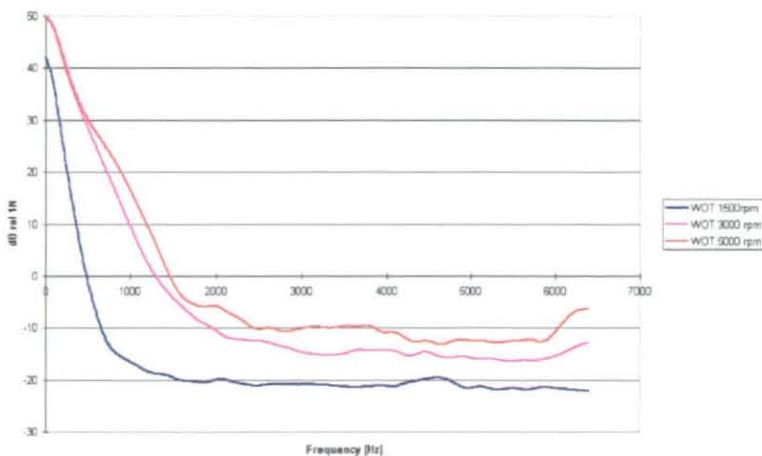


Figure 5.1.1 Combustion Excitation Spectra; Full Load (Zetec-E)

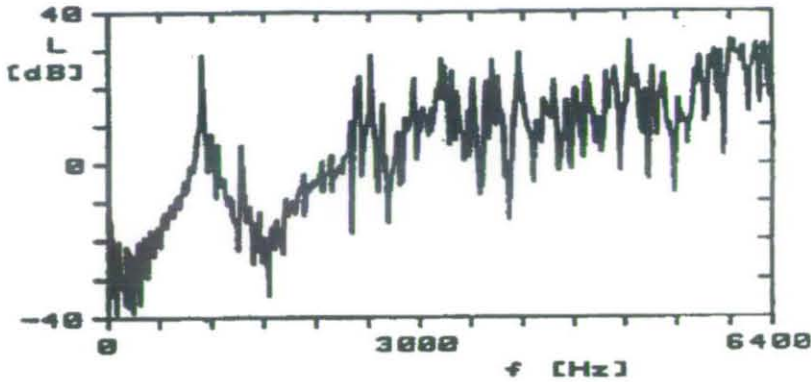


Figure 5.1.2 Transfer Function of Acceleration/Force (Zetec-E)

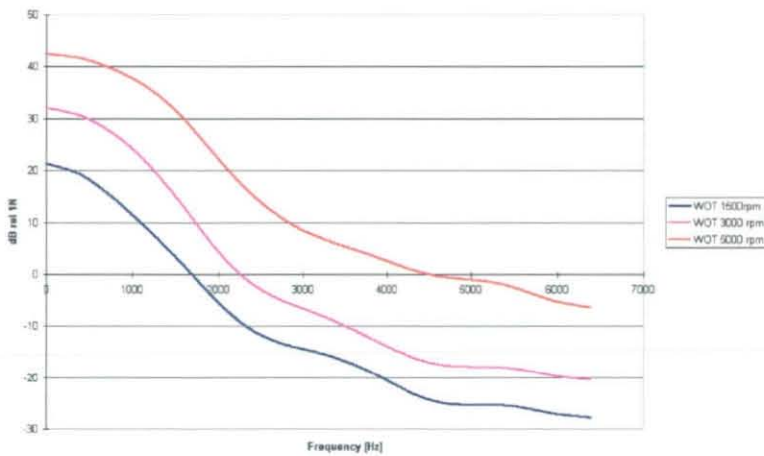


Figure 5.1.3 Averaged Main Bearing Excitation Spectra (Zetec-E)

Another method of measuring the forcing functions is an indirect method. The accelerations of the excited components (i.e. piston sides, combustion chamber, and main bearings) are measured by fitting accelerometers next to the excited regions. With the obtained transfer function between the excitation source and the measurement location, the data obtained at the accelerometer can then be re-transferred to the excitation forcing function. The major deficiency of this method is that the obtained signal carries total or absolute dynamic signals which are not related to the forcing function. These overlaid signals are generated by for example the overall engine acceleration as a rigid body about the principal axes of inertia and all other participating vibration sources. It is almost impossible to filter or subtract these data from the total signal to observe the required signal describing the elastic and dynamic behaviour of the structure.

Hence, the first methodology will be applied in the planned measurement process to validate the analytical model.

On the analytical side of calculating the forcing functions of a cranktrain, one has to consider different approaches. On one hand we find the simple kinematic approach from standard engineering textbooks treating the cranktrain components as rigid parts, and on the other hand there is the total dynamic approach, accounting for sub-system elasticities. The accuracy of the second methodology is much superior to that of the kinematic approach. But, this method is currently in a research status and cannot be applied on a daily basis to calculate the dynamic time dependent forces of the cranktrain because these methods are too complicated and difficult to handle. From my own experience, these methods can be said to require an extensive amount of computational effort of approximately 12-20 hours for an in-line four cylinder engine and two revolutions. Using analytical methods, the simple kinematic approach is commonly used to calculate the cranktrain internal forces. These common tools cover the kinematic loads acting on a crankshaft and the corresponding bearings. Effects included are gas pressure, inertia forces, centrifugal forces of rotating masses, and the main journal reactions. The calculation of the dynamic loads consists of two parts. The first part calculates the combustion forces and the inertia forces of the reciprocating masses transmitted to the crankshaft through the piston, piston pin and the connecting rod. The second part covers the reactions at the main journals. The methods most often used for the prediction of the main journal loads are the Statically Determinate Sharing (SDS) approach and the Statically Indeterminate Uniform Beam (SIUB) approach. In the SDS approach each individual throw of the crankshaft is considered as a simply supported beam and hence statically determined. The loads are distributed to the two adjacent bearings. In the SIUB approach the crankshaft is modelled as a beam with uniform cross-section. The resulting main bearing loads are derived using an elastic beam theory to share the loads not only between the adjacent but also between all main bearings.

The effect of the crankshaft on the crankcase and *vice versa* must be studied to get a reasonable understanding of the required engine block representation in terms of which effects must be included in the modelling approach. While the effect on the main bearing forces is obvious, the connecting rod forces are altered as well. Elastically coupled systems (e.g. crankshaft-crankcase-system) exhibit a retrospective force to the introducing system (e.g. connecting rod). The engine block can be represented from the crankshaft point of view as springs. The springs are connected to the crankshaft via the main bearing coordinates and grounded at the opposite end. For the purpose of this investigation, a simplistic system representation (Figure 5.1.4) has been developed to evaluate the effect of different crankcase stiffnesses on the distribution of the main bearing forces.

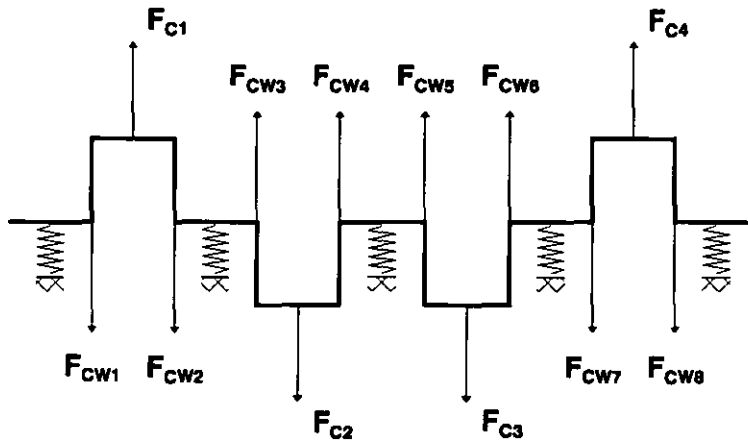


Figure 5.1.4 System Representation for Bearing Force Calculation

The crankshaft is modelled using a straight line beam model with equivalent and constant bending stiffness properties throughout the shaft length. The applied loads reflect the centrifugal load case only. Applying connecting rod inertia and combustion forces in addition to the centrifugal loads the magnitude of the resulting loads will be changed, but the general system response will be identical. For demonstration purposes and to limit the modelling work for this principle study, centrifugal loads only are applied. The crankcase stiffnesses are varied over a wide range without any respect to practical limitations. Theoretically, additional investigations are possible by changing more than one parameter at a time or using non-uniform stiffnesses for the crankshaft model and changing these values as well. To keep the effort reasonable, concentration is centred on the main bearing stiffnesses only and hence one parameter is changed at a time. The effects of changing each of the five main bearing stiffness coefficients have been investigated separately, i.e. bearing No.1 from 5E2 N/m to 5E14 N/m. Graphical representations of the results obtained are given in Figures 5.1.5;6;7;8 and 9.

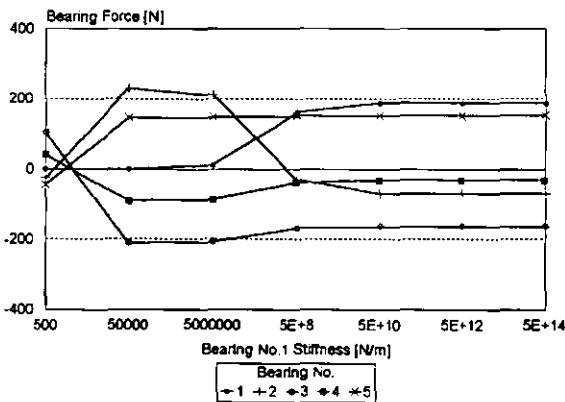


Figure 5.1.5 Bearing Forces with Bearing No. 1 Changes

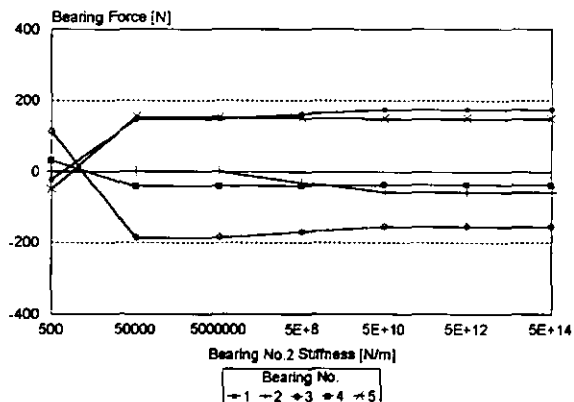


Figure 5.1.6 Bearing Forces with Bearing No. 2 Changes

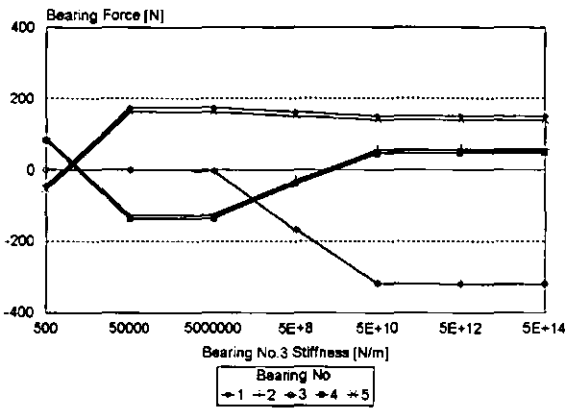


Figure 5.1.7 Bearing Forces with Bearing No. 3 Changes

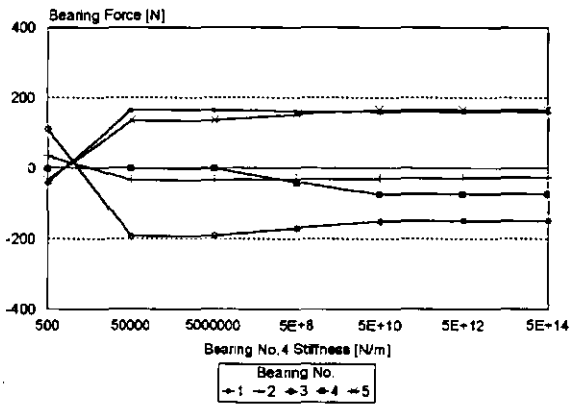


Figure 5.1.8 Bearing Forces with Bearing No. 4 Changes

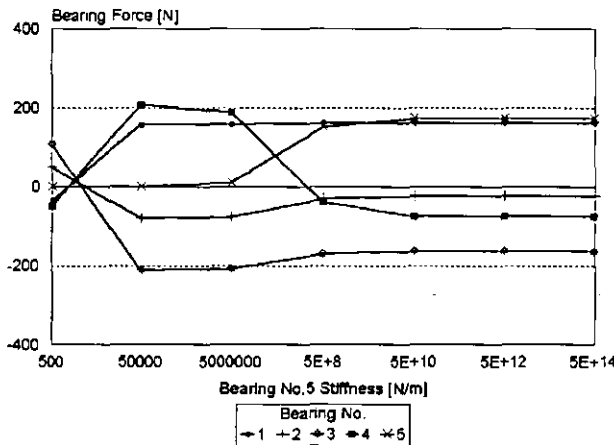


Figure 5.1.9 Bearing Forces with Bearing No. 5 Changes

Additional analyses of the main bearing forces and the matching load distribution show that the force on bearings with low stiffness compared to the standard value of  $5E8$  N/m are lower than the average. The bearings next to the weak one are loaded with higher forces. The developed influence on bearing forces is not limited to neighbouring bearings, even forces on the bearings at the opposite end are affected. The important consequence of this investigation is that it is possible to produce all kinds of bearing forces, load distributions, and therefore system responses by changing the significant structural stiffness parameters of the crankcase. Similar results can be achieved by changing the crankshaft stiffnesses within different sections. If we consider an elastic crankcase deformation behaviour and apply the above developed results, it is obvious that the representation and modelling of the crankcase need to be an exact image of the bearing stiffnesses, yet requires the detailed linkage between the crankcase walls and engine block bottom-half. The transferred bearing forces are not limited to the radial direction. Other directions will be loaded as well because of bending and axial defor-

mation of the crankshaft.

Because of this result, a full three dimensional representation of the engine cylinder block is required if all the above findings are to be incorporated.

Comparing the main bearing loads for an in-line four cylinder engine applying the above described methodologies, the following set of results can be calculated [93] as shown in Table 9:

Method	Bearing 1	Bearing 2	Bearing 3	Bearing 4	Bearing 5
SDS	-15751	-8620	25783	2427	-16226
SIUB	-12902	-20321	41504	-5512	-15155
Elastic Sub-System	-6118	-19160	21048	-3060	-7700

Table 9 Comparison of Main Journal Forces (in N) by Different Approaches

The displayed results are for one time interval only and show the significance of the most accurate crankshaft modelling. Due to the elastic crankshaft in SIUB and the elastic crankshaft and block treatment in the third approach, the main bearing forces are reduced significantly. This can be explained with the elastic deformation of the crankshaft and the engine block leading to a more uniform share of the main bearing forces.

Recalling the original problem of establishing the frequency domain forcing function, the time dependent loads of the above described approaches can be applied to formulate the main bearing forcing functions by applying Fourier series. The so derived spectrum can then be compared with those obtained from measurements as described before.

Both methods, the analytical and the measurements, have one drawback. The crankshaft is not treated as a dynamic sub-system and no dynamic interaction of crankshaft and crankcase is considered. Therefore, neither procedure can be applied to study the crankshaft-crankcase interaction with respect to dynamic phenomena.

Two papers ([94],[95]) were recently published and describe the Nissan approach of forcing crankshafts for vibration analysis. Their analysis is mainly concerned with acceleration noise in the frequency range of 250-800 Hz. This method will be described and comments given on expected accuracy and modelling approaches.

A finite element model of the powerplant is presented, consisting of an in-line four-cylinder engine and a front-wheel-drive transaxle. The model includes not only the structural elements of the powerplant, but also the crankshaft system, accessories, and the intake and exhaust manifolds. Within this model the oilfilm between the crankshaft



and the engine block is considered as a series of linear elastic springs. The spring stiffness is given as  $K=1.0 \cdot 10^{12}$  N/m in vertical and lateral direction. The modelling approach of the elastic coupling of crankshaft and block is described in Figure 5.1.10.

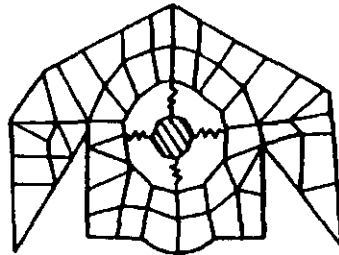


Figure 5.1.10 Journal Bearing Representation in Powertrain Model

The applied method for developing the engine forcing functions is described as an analytical kinematic approach as described earlier. The reciprocating inertia and combustion forces are treated separately. The inertia forces split into three individual forces, namely the cylinder liner force, the vertical and the horizontal crankpin force. A schematic description is given in Figure 5.1.11. The forces are calculated externally and transformed from time domain to frequency domain by Fourier series.

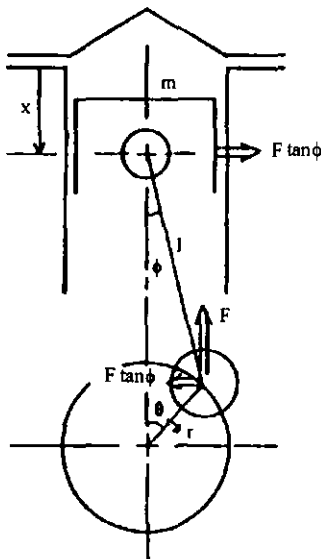


Figure 5.1.11 Analysis Model of Inertia Forces

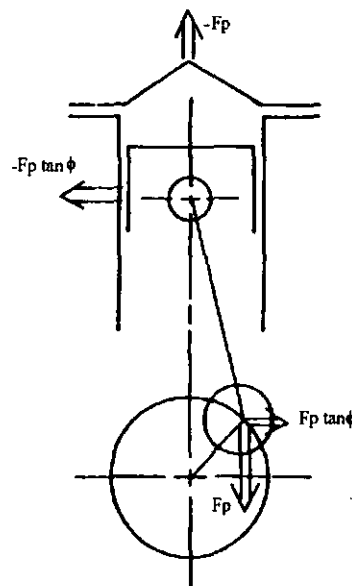


Figure 5.1.12 Analysis Model of Combustion Forces

The force generated through the combustion process is applied to the cylinder head, and results in cylinder liner forces, crank-pin vertical forces and crank-pin horizontal forces as shown in Figure 5.1.12. These forces are transformed to the frequency domain and applied to the model accounting for the phase due to the cylinder firing scheme.

Analysing the described method in more detail, some major drawbacks can be examined in both the modelling and forcing evaluation.

The applied modelling scheme for the main bearings is described with four springs. These linear stiffness properties are arranged in groups of two in vertical and horizontal directions. This grouping will result in dynamic crankshaft pin vibration levels being much higher than in reality. The engine-block stiffness properties, or more precisely the main bearing cap stiffness, are underestimated by this approach as the transferred forces will displace these four nodes much more than a distributed load sharing approach. This effect is comparable with forces applied in static analysis to individual nodes. Furthermore, it is well known from practice and theory that this kind of approach will lead to wrong results in the area of applied forces. A crank-journal displacement in a specific direction, e.g. horizontal displacement, will result in both compressive and tensional forces of the horizontal springs. Bearing in mind that the coupling of the main bearing is through hydrodynamic radial bearings, no tension within the oilfilm is viable. This modelling approach will violate this assessment. Studying the utilised spring stiffness property of  $K=1.0 \cdot 10^{12}$  N/m this stiffness relates to main bearing loads of approximately 40-50 kN. Hence, this coupling cannot be assessed to represent the elastic hydrodynamic bearing. As the maximum main bearing forces are in the order of 20-30 kN and the averaged forces are well below 20 kN. This interaction is modelled with elasticities, but represents in reality a rigid link between the crankshaft and the engine-block.

Analysing the applied forcing strategy, some major errors can be derived from the described theory and the displayed inertia and combustion forcing scheme.

As shown in the inertia forcing scheme picture, i.e. Figure 5.1.11, cylinder liner forces and the horizontal crankpin force are set to be equal with opposite directions. This approach is not correct, as these forces are not equal due to the inertia effects of the piston-connecting-rod assembly. Investigating the combustion forcing scheme, an equivalent error can be assessed. Both, cylinder liner forces and the horizontal crankpin forces, as well as the combustion pressure forces and the vertical crankpin forces are set to be equal in pairs. This is not correct, as the kinematic piston-connecting-rod assembly is not treated in the approach. The kinematic inertia effects are ignored, which will lead to incorrect forcing functions of the cylinder liner, the tangential, and radial crankpin forces.

In view of the above shortcomings this approach cannot be applied to model the crankshaft frequency dependent forcing function.

### 5.2 Applied Approach

If a schematic picture of the connecting rod crank mechanism is drawn, a picture similar to Figure 5.2.1 can be derived. There are four types of loads acting on a crankshaft: gas pressure, inertia forces, main journal reaction forces and the centrifugal forces of rotating masses. The gas pressure generated from combustion acts on the piston. The inertia forces of the piston assembly are originated by the reciprocating movement of the assembly. Both gas pressure and inertia loads are transmitted to the crank pin through piston, piston pin and connecting rod. As already discussed above, the crankshaft loading calculation can be divided into two parts. The first is the inertia and combustion loads transmitted to the crankshaft. The second is the main journal loads calculated by using an appropriate crankshaft engine-block representation model.

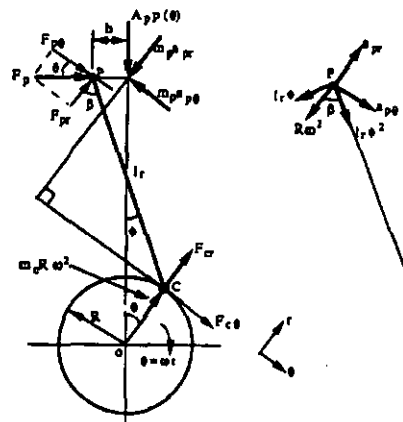
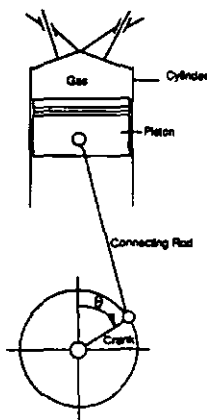


Figure 5.2.1 Schematic Diagram of the Connecting-Rod Crank Mechanism      Figure 5.2.2 Connecting Rod Kinematics

Analysing the cranktrain kinematics and the corresponding forces at the individual joints of the piston pin and the crankpin, Figure 5.2.2 can be drawn. The inertia forces of the rod can be determined by applying d'Alembert's principle to the rod, when the complete kinematics of the motion are obtained. With the inertia loads and the gas pressure force, the resultant forces on the rod at the wrist pin and the crank pin are calculated by use of a free-body diagram. The resultant connecting rod big-end forces are then applied to the crank pin.

With the applied loads on the crank pins and the additional centrifugal forces due to the rotation of the crankshaft, the reaction forces at the main bearings can be calculated by applying the corresponding analysis methods to the beam representation of the crankshaft as described earlier. As the utilised finite-element model already covers the load distribution between the crankshaft and the engine block structure, this approach can be used to identify the crankshaft pin forces and the centrifugal forces of the rotating

crankshaft. Applying these forces the frequency dependent forcing function can easily be derived for the crankshaft pins by fourier transformations. A schematic picture of the applied forces are shown in Figure 5.2.3. The engine structure is, for display reasons only, replaced by main bearings described as springs.

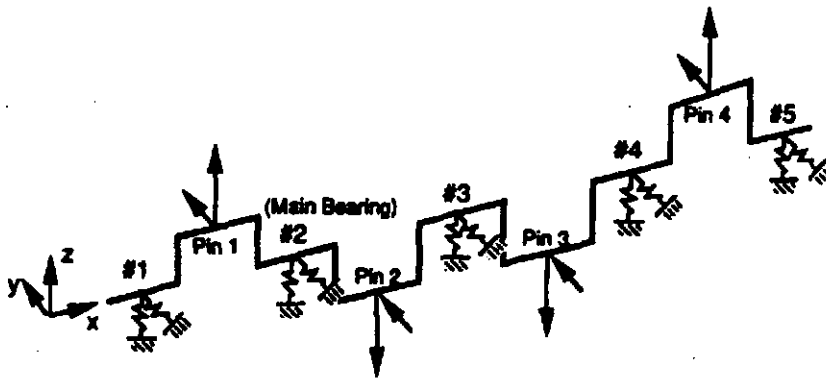


Figure 5.2.3 Applied Loads on Crank Pins

To compute the loads transmitted by the connecting rod, the kinematics of the connecting rod are analysed first. Then the inertia forces are obtained by applying d'Alembert's principle to the connecting rod. As this is a straightforward task to do, and has already been done many times, only a brief description of the applied formulae are given. For details, several textbooks are available concerned with cranktrain kinematics [96].

The connecting rod is treated to be dynamically equivalent to two masses concentrated at the small and big ends of the rod and having the same total mass and inertia as the actual rod. The kinematics of the connecting rod is derived as follows. All notations are given in the previous figures.

The accelerations at the piston pin end are found to be:

$$a_p = - \left( R\Omega^2 + l_r \left( \frac{\partial \Phi}{\partial t} \right)^2 \cos \beta + l_r \frac{\partial^2 \Phi}{\partial t^2} \sin \beta \right) e_r + \left( l_r \left( \frac{\partial \Phi}{\partial t} \right)^2 \sin \beta - l_r \frac{\partial^2 \Phi}{\partial t^2} \cos \beta \right) e_{\Theta_{cr}} \tag{5.2.1}$$

$$a_p = a_{pr} e_r + a_{p\Theta_{cr}} e_{\Theta_{cr}}$$

with  $\Theta_{cr} = \text{crank angle}(\omega t)$

The geometric relations are defined with:

$$\Phi = \sin^{-1} \left( \frac{R \sin \Theta_{cr} + h}{l_r} \right) \tag{5.2.2}$$

$$\beta = \Theta_{cr} + \Phi \tag{5.2.3}$$

The oscillating velocity and acceleration of the rod are given with:

$$\frac{\partial \Phi}{\partial t} = \frac{R \cos \Theta_{CR}}{l_r \cos \Phi} \Omega \quad 5.2.4$$

$$\frac{\partial^2 \Phi}{\partial t^2} = \left( \frac{\partial \Phi}{\partial t} \right)^2 \tan \Phi - \left( \frac{\partial \Theta_{cr}}{\partial t} \right)^2 \frac{R \sin \Theta_{cr}}{l_r \cos \Phi} \quad 5.2.5$$

With the sum of the moments about the crank end C being equal to zero,

$$\sum M_c = 0 \quad 5.2.6$$

one can get the reaction force at the piston pin end,  $F_p$  with:

$$\begin{aligned} F_p &= A_p p(\Theta_{cr}) \left( \tan \Phi - \frac{h}{l_r \cos \Phi} \right) + m_p a_{pr} \left( \frac{\sin \beta}{\cos \Phi} - \frac{h \cos \Theta_{cr}}{l_r \cos \Phi} \right) \\ &+ m_p a_{p\Theta_{cr}} \left( \frac{\cos \beta}{\cos \Phi} - \frac{h \sin \Theta_{cr}}{l_r \cos \Phi} \right) \end{aligned} \quad 5.2.7$$

The forces at the crank pin end are found as:

$$F_{cr} = -m_c R \Omega^2 - F_p \sin \Theta_{cr} + m_p a_{pr} + A_p p(\Theta_{cr}) \cos \Theta_{cr} \quad 5.2.8$$

$$F_{c\Theta_{cr}} = -F_p \cos \Theta_{cr} + m_p a_{p\Theta_{cr}} - A_p p(\Theta_{cr}) \sin \Theta_{cr} \quad 5.2.9$$

These are the forces acting on the connecting rod. The reaction forces acting on the crank pin are given as follows:

$$R_{cr} = -F_{cr} = m_c R \Omega^2 + F_p \sin \Theta_{cr} - m_p a_{pr} - A_p p(\Theta_{cr}) \cos \Theta_{cr} \quad 5.2.10$$

$$R_{c\Theta_{cr}} = -F_{c\Theta_{cr}} = F_p \cos \Theta_{cr} - m_p a_{p\Theta_{cr}} + A_p p(\Theta_{cr}) \sin \Theta_{cr} \quad 5.2.11$$

All cylinder pressures are defined to be equal, but with the corresponding phase regarding the engine firing order. After the crank pin forces are calculated, the frequency dependent forcing function can be obtained through Fourier series expansion.

Up to this level all participant systems of the cranktrain are treated as rigid components. As discussed earlier this is not necessarily the case. While the engine block and the crankshaft are modelled with the appropriate stiffness properties, it is necessary to study whether the participating components, i.e. connecting rod and piston assembly, can be treated as rigid parts or must be modelled as elastic bodies. This would affect the above equations, which then cannot be applied for the development of the forcing function. This would lead to the incorporation of the mass elastic systems of the connecting rod and the piston assembly to the overall calculation process as described in Chapter 6. Studying the elastic deformation behaviour of the piston and connecting rod assembly

under gas loads, a schematic picture can be drawn as shown in Figure 5.2.4. For studying reasons, two different approaches are applied. The first one is concerned with an analytical description of the problem, while the second is a procedure with applied measurement techniques.



Figure 5.2.4 Connecting Rod Elastic Deformation

As a part of study for Ford, the University of Missouri-Rolla supported MacNeal-Schwendler in the development of a Nastran-based flexible mechanism capability [97]. The specific purpose of this capability is to allow the formulation of finite element models containing operating flexible connecting rods and pistons. External forces at the joints are calculated internally and applied to the structures. This capability allows for more detailed investigations of the connecting-rod piston assembly.

In this study, a rigid connecting rod and piston assembly is compared with the elastic representation of the investigated engine. The perceived results are analysed regarding vibrational effects of the individual components. On the basis of the results a final judgment is given, as to whether the sub-system connecting rod or piston assembly must be idealised using elastic bodies or a rigid representation is accurate enough for the development of crankpin forces.

Comparing the obtained Nastran results of either an elastic or rigid connecting rod, it is necessary to establish an absolute measure for the effect to be studied. Looking at the deformation shape described in the previous figure, the elastic deformation of the flexible connecting rod overlays to the overall body motion within the cranktrain. Hence displacements cannot be easily applied to study the bending effect. While the bending stress in the connecting rod is proportional to the out of plane deformation, this measure is an absolute criterion for the dynamic behaviour of the component. The results shown in Figure 5.2.5 and Figure 5.2.6 display the bending moment in the rod and the crank for two engine speeds. The results marked as 'VECTOR ANALYSIS' are derived from a program treating the components as rigid bodies with the appropriate mass and inertia

properties. No significant difference in bending moments can be observed from these figures for the two approaches. Figure 5.2.7 and Figure 5.2.8 show the axial forces in the rod and crank for two engine speeds. Again, no significant differences are seen for the two approaches.

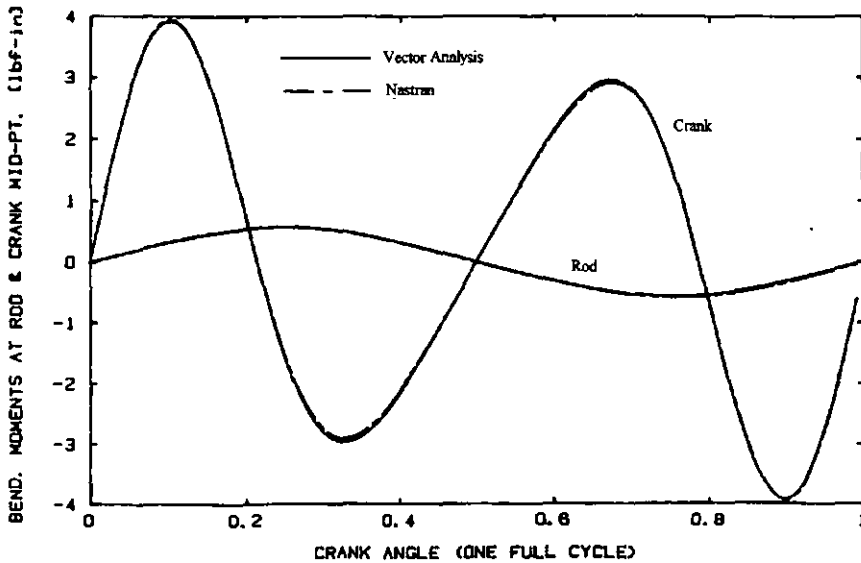


Figure 5.2.5 Midspan Rod and Crank Bending Moment (300rpm)

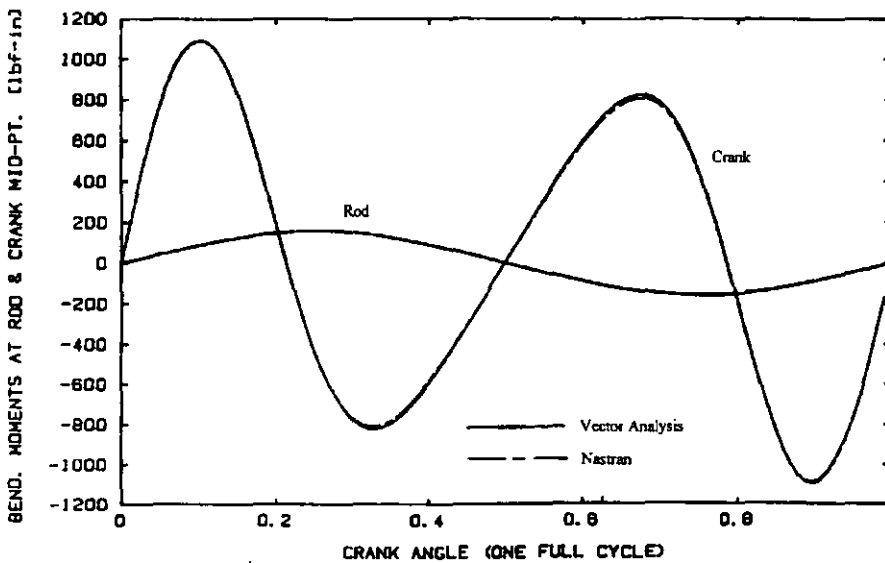


Figure 5.2.6 Midspan Rod and Crank Bending Moment (5000rpm)

The analytical results derived in this study yield an excellent correlation between the elastic and rigid treatment of the cranktrain components connecting rod and piston

assembly. A rigid modelling approach for the connecting rod and the piston assembly may therefore be deemed as appropriate for the derivation of the crankshaft forcing function.

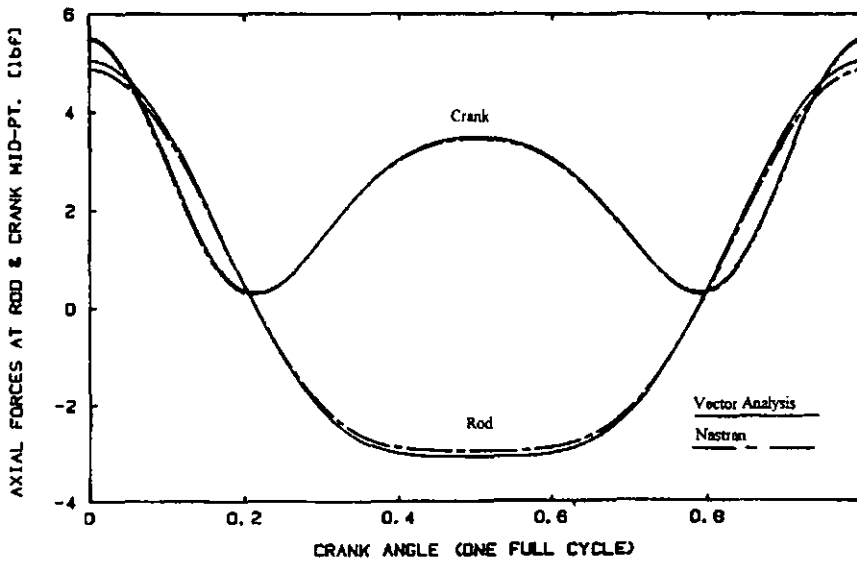


Figure 5.2.7 Midspan Rod and Crank Axial Forces (300rpm)

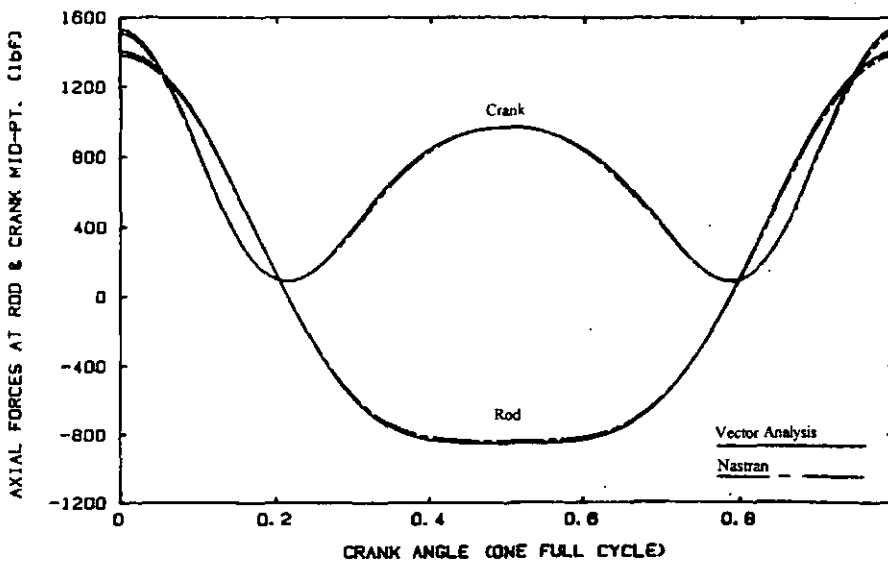


Figure 5.2.8 Midspan Rod and Crank Axial Forces (5000rpm)

This is correlated with test results. The measurements are obtained by assessing the transmissibility of individual components or assemblies [98] and are performed by applying the impact hammer methodology within a frequency range from 0 to 6.4 kHz. The analysed components are shown in Figure 5.2.9 with the appropriate points of interest.



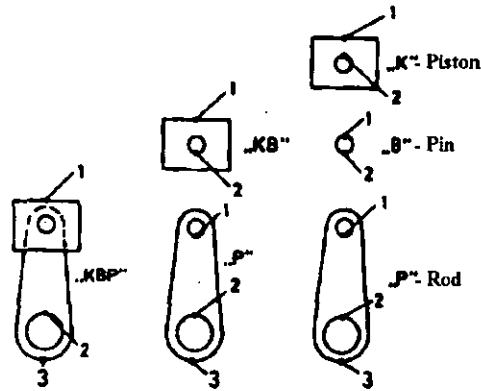


Figure 5.2.9 Excitation- and Measurement-Locations of the Cranktrain

The obtained transfer functions are shown in Figure 5.2.10, 11 and 12 for individual components and in Figure 5.2.13 for the piston, piston pin and rod assembly.

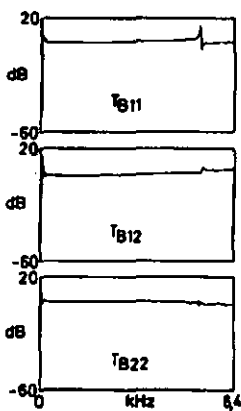


Figure 5.2.10 Transfer Function of Piston

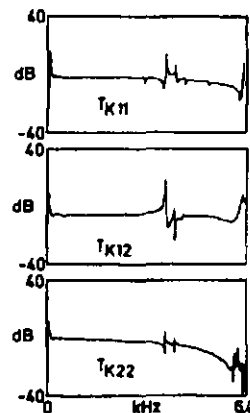


Figure 5.2.11 Transfer Function of Piston Pin

Piston and piston pin results show that both components behave as concentrated masses over a wide frequency range. In the piston transfer function no amplitude-modulation can be observed. The amplitude-modulation of the piston pin shows a little peak at approximately 4 kHz. Comparing the modulation with those for the connecting rod transfer function, the former can be neglected. Observing the transfer function of the connecting rod, significant amplitude variation can be seen from a frequency range of 3 kHz and above. Two individual modes can be derived from the function  $T_{C13}$  at about 3kHz and 6.2kHz. Accounting for the upper engine speed limit of roughly 7000 rpm, a 3 kHz or higher eigenfrequency is excited with the 25th and higher

engine orders. The excitation level of these orders is low compared with those of lower orders as shown in Figure 5.1.1. Hence, the connecting rod eigenfrequencies do not alter the obtained crankshaft pin forces at lower engine orders.

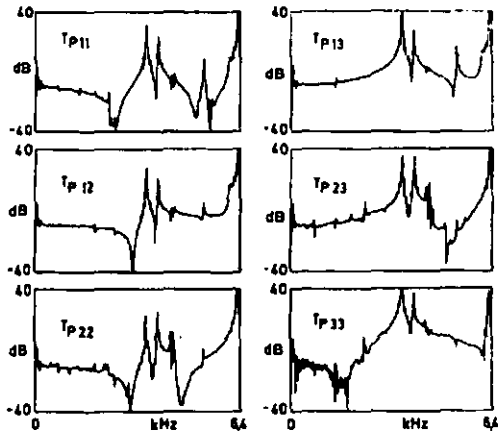


Figure 5.2.12 Transfer Function of Connecting Rod

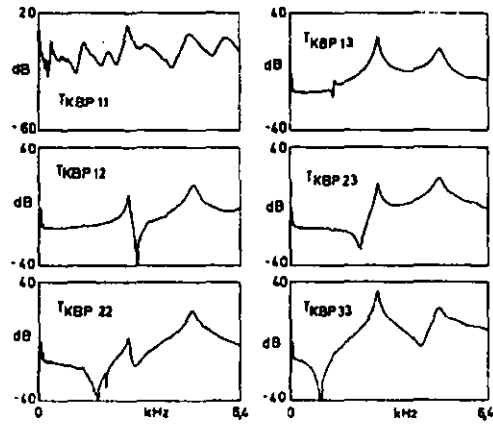


Figure 5.2.13 Transfer Function of Connecting Rod, Piston Pin, and Piston

Summarising the above findings, it is clear that the connecting rod and the piston assembly can be treated as rigid components with an acceptable accuracy in the frequency range up to 3 kHz. If combustion irregularities are included in the analysis, this assumption can no longer be accepted as accurate enough. The combustion irregularities occur at frequencies of 8-10 kHz. Hence, the elastic, dynamic behaviour of the piston assembly and connecting rod must then be considered.

Consequently, assuming that suitable information are available for the stiffness of the oil films at the connecting rod small end and big end, it is a simple task to connect the elastic connecting rod sub-system to the crankshaft for a fixed position of the crankshaft. In the case of a rotating crankshaft the problem is complicated by the variation of the receptances with the movement of the crank and the slider-crank mechanism. Also the connecting rod vibrations are now in a moving system that translates and rotates. This coordinate system must then be transformed for each increment to be compatible with the rotating coordinate system of the rotating crankshaft. This is a tremendous computational task, which is vital only for those cases showing a significant effect of the connecting rod vibrations on the overall system behaviour [see section 6.2]. Having demonstrated that the connecting rod dynamics occur at frequencies at 3 kHz and above, one has to consider the resultant oilfilm properties of the connecting rod bearings to allow for a final discussion of the modelling approach of the crank slider mechanism.

It is extremely difficult to evaluate the stiffness of the oil films of the slider crank mechanism, but experience suggests that they are likely to be of the order of  $1.75 \cdot 10^5$  to  $1.75 \cdot 10^7$  N/cm [99]. At stiffnesses below  $1.75 \cdot 10^4$  to  $1.75 \cdot 10^5$  N/cm the oil films become significant. Ignoring the possibility of very low oilfilm stiffnesses, which is unlikely over the important range of frequencies, Hodgetts' study [99] suggests that the dynamic elasticity of the oilfilm stiffnesses can be ignored. Accounting for the above described findings that the connecting rod itself describes a constant receptance independent of the applied load for frequencies below 3 kHz, it is suggested that the complete crank slider mechanism can be treated as a constant receptance at the time or frequency averaged value, since the perturbation is small.

The foregoing remarks and discussion apply primarily to vibrations in the longitudinal direction of the connecting rod and hence in the plane of the throws. For most modes of crankshaft vibration the axial displacements of the crank-pins are small and it is unlikely that the axial constraints of the connecting rod are significant. Considering the difficulty of the assessment of the oilfilm stiffness properties and the transformation of the translating and rotating coordinate system it was judged to be unnecessary to consider the elastic dynamic slider crank mechanism further. Nevertheless, it should be noted that in general it is possible to account for the elastic crank slider mechanism and that the described and developed theories do not limit the introduction of the elastic crank slider mechanism.

Recalling the foregoing description of the crankshaft forcing function, the derivation of the Nastran input deck for the frequency response analysis is tedious. A Fortran program was developed to read the calculated engine cranktrain loads from an external file, perform the Fourier series expansion, and derive the necessary MSC/Nastran input decks for both, the CASE control and BULK DATA deck. The corresponding program output is given in Appendix 1 for display purposes for a single speed only. This method can be applied to evaluate the whole engine speed range from idle to cut-off speed. The only limitation is the computational effort to calculate all frequency steps with the corresponding frequency range of interest. When applying this program, one should consider the model accuracy and the amount of response data to achieve. These effects will be discussed later.

## **Chapter 6**

### **Frequency Domain Solution for Crankshaft-Crankcase Dynamics**

This chapter gives an overview of complex modal and forced frequency response analysis of linear, Gyroscopic conservative, crankshaft-crankcase systems with non-autonomous, stiffness modulation, which includes the analysis of characteristic crankshaft-flywheel whirl.

When analysing an internal combustion engine, one would break down the whole into several sub-systems with their corresponding properties and effects on the whole system. The standard design of a four cylinder in-line IC-engine is represented in Figure 6.1. The sub-systems are namely: cylinder block and head, connecting-rod and piston assembly, crankshaft, flywheel, and pulley. The coupling of these is by hydrodynamic bearings.

The difference between traditional FEM-analyses, such as static or eigenvalue investigations, and this investigation is the existence of a crank slider mechanism and the rotation of the crankshaft assembly. Considering the individual components, it is easy to develop the stiffness and mass matrices from FEM analyses. But, if we assemble the components and set-up the stiffness and mass matrices by just combining the individual matrices, we get a system description only for a specific time. All dynamic effects resulting from moving parts are then neglected. Therefore, we have to link the single components into a global system using time dependent matrices. Additionally, bearing non-linear stiffness and stabilising and de-stabilising inertia effects must be introduced.

Hence, equations will be developed for a system as described. In the first section concentration will be emphasized on a linear, gyroscopic conservative vibration system with non-autonomous time domain stiffness modulation. Further, an extension will be made to non-linear coupled vibration systems with time and load susceptible parameters. The consequences of structural preloads on dynamic systems is then studied in detail.

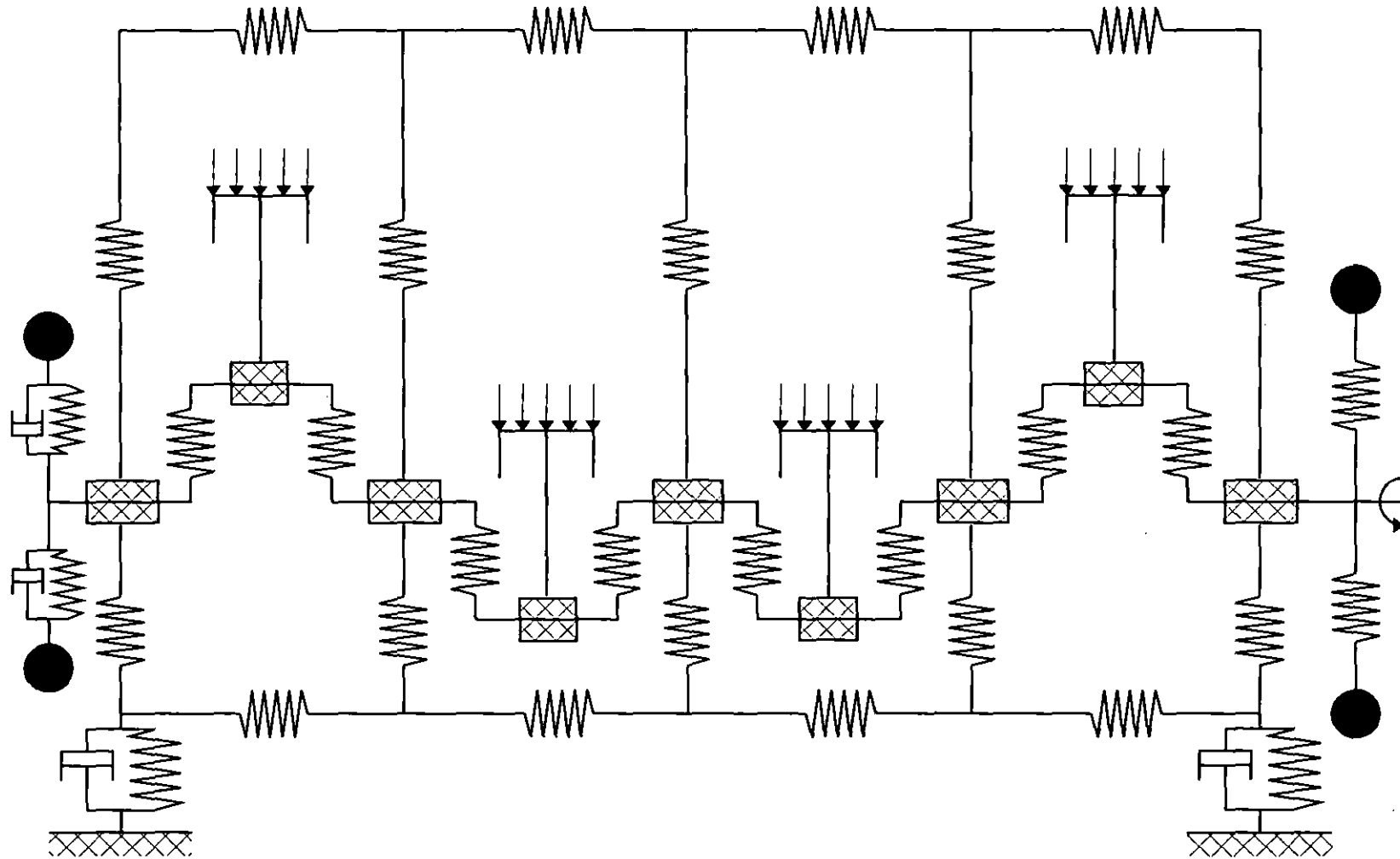


Figure 6.1 Indeterminate Full Engine Representation

## 6.1 Fourier Solution for Linear Time-Variant Systems

The most widely understood vibration analyses are those dealing with real modal analysis and forced frequency response analyses of linear, conservative and autonomous systems. These systems are commonly formulated with a second order differential equation of motion as follows:

$$\mathbf{M}\ddot{\mathbf{u}}(t) + \mathbf{K}\mathbf{u}(t) = \mathbf{f}(t) \quad 6.1.1$$

The most fundamental results of eqn. 6.1.1 is that the unforced system can vibrate characteristically at specific independent frequencies. The motion for any characteristic frequency proceeds according to a single phased harmonic motion, i.e. all degrees of freedom move in phase with respect to each other and with fixed relative amplitudes.

An actual operating engine, with a rotating mass-elastic crankshaft-flywheel subsystem, may dramatically violate the conditions of the system represented by eqn. 6.1.1. This is due to the rotating subsystem which changes the overall engine system in two ways. Firstly, a rotating flywheel introduces gyroscopic coupling because of its high angular momentum which increases with engine speed. Secondly, a rotating elastic crankshaft introduces time dependent, or non-autonomous, stiffness variations, because the rotation changes the stiffness matrix relative to the engine structure through coordinate transformation. From this, it is evident that eqn. 6.1.1 is no longer valid for a rotating mass-elastic crankshaft-flywheel system. Moreover, structural non-linearities usually arises from load dependent variables, i.e. oilfilm stiffness and damping properties or rubber components applied in dampers. Therefore, for a general dynamic system, the equation of motion is of the form:

$$\mathbf{M}(t)\ddot{\mathbf{u}}(t) + \mathbf{D}(t)\dot{\mathbf{u}}(t) + \mathbf{K}(t)\mathbf{u}(t) = \mathbf{f}(t) \quad 6.1.2$$

Initially, neglecting the damping effect, but adding the gyroscopic effect, eqn. 6.1.2 changes to be:

$$\mathbf{M}(t)\ddot{\mathbf{u}}(t) + \Omega\mathbf{G}\dot{\mathbf{u}}(t) + \mathbf{K}(t)\mathbf{u}(t) = \mathbf{f}(t) \quad 6.1.3$$

This equation can be used to represent a realistic engine model containing the mass-elastic system of the crankshaft and flywheel assembly to introduce the theory of frequency dependent analysis. In eqn. 6.1.2  $\mathbf{G}$  is assumed to be a constant matrix representing the gyroscopic inertia effects with  $\Omega$  as the angular velocity of the engine. The damping will be taken into account in subsequent theoretical treatments.

The excitation term is modulated by the response  $\mathbf{u}(t)$ , because the participating elastic components influence each other. Hence, the solution of this equation differs from that of a constant-parameter system. Because of the introduction of the gyroscopic coupling

effect, the concept that the free or unforced vibration proceeds at a single common phase must be altered, i.e. components of the system do not vibrate in a common fixed displaced relationship. These motions can be classified as complex modes. Also, because of the introduction of the non-constant elasticity matrix, the motion of the system cannot be represented by a sinusoidal vibration of single frequency. Because the modulation of the time domain forcing function and stiffness matrix generates frequency domain shifts, no frequency participating in the motion can be considered to be independent of all other frequencies. This can be stated as a frequency coupling effect caused by stiffness modulation. Therefore, the free response and obviously the forced response must be considered in terms of superposition of dependent modes acting simultaneously at many frequencies. It must be pointed out that even if the variation of the stiffness matrix  $K(t)$  or the forcing function  $f(t)$  are harmonic and periodic, the system response may be aperiodic in general ([100],[101]).

The intention, here, is to investigate the vibration problem analyses related to eqn. 6.1.3. Free vibration will be considered first. The forcing function will be derived and applied later, and the solution of the forced response analysis will be dealt with afterwards. The system is assumed to be gyroscopically conservative, which means the inertia effects are axis symmetric resulting in a constant matrix  $G$ . The mass and stiffness matrices are symmetric, while the gyroscopic matrix is skew-symmetric. That is,

$$\begin{aligned} \mathbf{M} &= \mathbf{M}^T \\ \mathbf{G} &= -\mathbf{G}^T \\ \mathbf{K}(t) &= \mathbf{K}^T(t) \end{aligned} \tag{6.1.4}$$

If we accept that the orientation of the crankshaft and flywheel assembly is defined by the crank angle  $\Theta$  relative to the engine block and deviates negligibly from the angle of the rigid model representation rotating with a constant angular velocity  $\Omega$  about a fixed axis, the stiffness matrix can be transformed to a Fourier series [102]. With  $\mathbf{K}_{0c}$ ,  $\mathbf{K}_{1c}$ ,  $\mathbf{K}_{1s}$ ,  $\mathbf{K}_{2c}$  and  $\mathbf{K}_{2s}$  as the Fourier stiffness matrix coefficients, one can develop a time dependent, orthogonal similarity transformation limited to the second order:

$$\mathbf{K}(t) = \frac{\mathbf{K}_{0c}}{2} + \mathbf{K}_{1c} \cos \Theta + \mathbf{K}_{1s} \sin \Theta + \mathbf{K}_{2c} \cos 2\Theta + \mathbf{K}_{2s} \sin 2\Theta \tag{6.1.5}$$

or

$$\mathbf{K}(t) = \frac{\mathbf{K}_{0c}}{2} + \mathbf{K}_{1c} \cos \Omega t + \mathbf{K}_{1s} \sin \Omega t + \mathbf{K}_{2c} \cos 2\Omega t + \mathbf{K}_{2s} \sin 2\Omega t \tag{6.1.6}$$



Substituting eqn. 6.1.6 in eqn. 6.1.3 we get the following matrix differential equation of motion, which is linear, but has a periodically varying stiffness matrix which is synchronised to the first and second engine orders.

$$\mathbf{M}\ddot{\mathbf{u}}(t) + \Omega\mathbf{G}\dot{\mathbf{u}}(t) + \left[ \frac{\mathbf{K}_{Oc}}{2} + \mathbf{K}_{1c} \cos \Omega t + \mathbf{K}_{1s} \sin \Omega t + \mathbf{K}_{2c} \cos 2\Omega t + \mathbf{K}_{2s} \sin 2\Omega t \right] \mathbf{u}(t) = 0 \quad 6.1.7$$

Although the solution  $\mathbf{u}(t)$  of eqn. 6.1.7 will not necessarily be a periodic function for any given arbitrary angular velocity  $\Omega$ , it is important to recognize that specific angular velocities might result in a periodic solution which is not necessarily harmonic. For development purposes, we will concentrate on solutions which have a period of either one-half or one engine order. This is justified, because the major engine forces can be expected to be of either half or whole orders or their multiples. Therefore, the solution  $\mathbf{u}(t)$  can be expressed in the following Fourier series:

$$\mathbf{u}(t) = \frac{\mathbf{a}_0}{2} + \sum_{k=\frac{1}{2}, 1, \frac{3}{2}, \dots}^{\infty} (\mathbf{a}_k \cos k\Omega t + \mathbf{b}_k \sin k\Omega t) \quad 6.1.8$$

which gives the generalised velocity and acceleration vectors as follows, respectively:

$$\dot{\mathbf{u}}(t) = \Omega \sum_{k=\frac{1}{2}, 1, \frac{3}{2}, \dots}^{\infty} k(-\mathbf{a}_k \sin k\Omega t + \mathbf{b}_k \cos k\Omega t) \quad 6.1.9$$

$$\ddot{\mathbf{u}}(t) = -\Omega^2 \sum_{k=\frac{1}{2}, 1, \frac{3}{2}, \dots}^{\infty} k^2(\mathbf{a}_k \cos k\Omega t + \mathbf{b}_k \sin k\Omega t) \quad 6.1.10$$

Thus, we have

$$\begin{aligned} \mathbf{M}(t)\ddot{\mathbf{u}}(t) + \Omega\mathbf{G}\dot{\mathbf{u}}(t) &= -\Omega^2\mathbf{M} \sum_{k=\frac{1}{2}, 1, \frac{3}{2}, \dots}^{\infty} k^2(\mathbf{a}_k \cos k\Omega t + \mathbf{b}_k \sin k\Omega t) \\ &+ \Omega^2\mathbf{G} \sum_{k=\frac{1}{2}, 1, \frac{3}{2}, \dots}^{\infty} k(-\mathbf{a}_k \sin k\Omega t + \mathbf{b}_k \cos k\Omega t) \quad 6.1.11 \\ &= -\Omega^2 \sum_{k=\frac{1}{2}, 1, \frac{3}{2}, \dots}^{\infty} [(k^2\mathbf{M}\mathbf{a}_k - k\mathbf{G}\mathbf{b}_k) \cos k\Omega t + (k\mathbf{G}\mathbf{a}_k + k^2\mathbf{M}\mathbf{b}_k) \sin k\Omega t] \end{aligned}$$

Similarly, the stiffness term of eqn. 6.1.7 becomes,

$$\begin{aligned}
\mathbf{K}(t)\mathbf{u}(t) &= \left[ \frac{\mathbf{K}_{Oc}}{2} + \mathbf{K}_{1c} \cos \Omega t + \mathbf{K}_{1s} \sin \Omega t + \mathbf{K}_{2c} \cos 2\Omega t + \mathbf{K}_{2s} \sin 2\Omega t \right] \\
&\quad * \left[ \frac{\mathbf{a}_0}{2} + \sum_{k=\frac{1}{2}, 1, \frac{3}{2}, \dots}^{\infty} (\mathbf{a}_k \cos k\Omega t + \mathbf{b}_k \sin k\Omega t) \right] \\
&= \frac{\mathbf{K}_{Oc}\mathbf{a}_0}{4} + (\mathbf{K}_{1c} \cos \Omega t + \mathbf{K}_{1s} \sin \Omega t) \frac{\mathbf{a}_0}{2} + (\mathbf{K}_{2c} \cos 2\Omega t + \mathbf{K}_{2s} \sin 2\Omega t) \frac{\mathbf{a}_0}{2} \\
&\quad + \frac{\mathbf{K}_{Oc}}{2} \sum_{k=\frac{1}{2}, 1, \frac{3}{2}, \dots}^{\infty} (\mathbf{a}_k \cos k\Omega t + \mathbf{b}_k \sin k\Omega t) \\
&\quad + \sum_{k=\frac{1}{2}, 1, \frac{3}{2}, \dots}^{\infty} (\mathbf{K}_{1c}\mathbf{a}_k \cos k\Omega t \cos \Omega t + \mathbf{K}_{1s}\mathbf{b}_k \sin k\Omega t \sin \Omega t \\
&\quad \quad + \mathbf{K}_{1s}\mathbf{a}_k \cos k\Omega t \sin \Omega t + \mathbf{K}_{1c}\mathbf{b}_k \sin k\Omega t \cos \Omega t) \\
&\quad + \sum_{k=\frac{1}{2}, 1, \frac{3}{2}, \dots}^{\infty} (\mathbf{K}_{2c}\mathbf{a}_k \cos k\Omega t \cos 2\Omega t + \mathbf{K}_{2s}\mathbf{b}_k \sin k\Omega t \sin 2\Omega t \\
&\quad \quad + \mathbf{K}_{2s}\mathbf{a}_k \cos k\Omega t \sin 2\Omega t + \mathbf{K}_{2c}\mathbf{b}_k \sin k\Omega t \cos 2\Omega t)
\end{aligned} \tag{6.1.12}$$

By applying trigonometrical identities eqn. 6.1.12 changes to be

$$\begin{aligned}
\mathbf{K}(t)\mathbf{u}(t) &= \frac{\mathbf{K}_{Oc}\mathbf{a}_0}{4} + (\mathbf{K}_{1c} \cos \Omega t + \mathbf{K}_{1s} \sin \Omega t) \frac{\mathbf{a}_0}{2} + (\mathbf{K}_{2c} \cos 2\Omega t + \mathbf{K}_{2s} \sin 2\Omega t) \frac{\mathbf{a}_0}{2} \\
&\quad + \frac{\mathbf{K}_{Oc}}{2} \sum_{k=\frac{1}{2}, 1, \frac{3}{2}, \dots}^{\infty} (\mathbf{a}_k \cos k\Omega t + \mathbf{b}_k \sin k\Omega t) \\
&\quad + \sum_{k=\frac{1}{2}, 1, \frac{3}{2}, \dots}^{\infty} \left[ \frac{\mathbf{K}_{1c}\mathbf{a}_k}{2} [\cos(k-1)\Omega t + \cos(k+1)\Omega t] \right. \\
&\quad \quad \left. + \frac{\mathbf{K}_{1s}\mathbf{b}_k}{2} [\cos(k-1)\Omega t - \cos(k+1)\Omega t] \right. \\
&\quad \quad \left. + \frac{\mathbf{K}_{1s}\mathbf{a}_k}{2} [-\sin(k-1)\Omega t + \sin(k+1)\Omega t] \right. \\
&\quad \quad \left. + \frac{\mathbf{K}_{1c}\mathbf{b}_k}{2} [\sin(k-1)\Omega t + \sin(k+1)\Omega t] \right] \\
&\quad + \sum_{k=\frac{1}{2}, 1, \frac{3}{2}, \dots}^{\infty} \left[ \frac{\mathbf{K}_{2c}\mathbf{a}_k}{2} [\cos(k-2)\Omega t + \cos(k+2)\Omega t] \right. \\
&\quad \quad \left. + \frac{\mathbf{K}_{2s}\mathbf{b}_k}{2} [\cos(k-2)\Omega t - \cos(k+2)\Omega t] \right. \\
&\quad \quad \left. + \frac{\mathbf{K}_{2s}\mathbf{a}_k}{2} [-\sin(k-2)\Omega t + \sin(k+2)\Omega t] \right. \\
&\quad \quad \left. + \frac{\mathbf{K}_{2c}\mathbf{b}_k}{2} [\sin(k-2)\Omega t + \sin(k+2)\Omega t] \right]
\end{aligned} \tag{6.1.13}$$

By collecting terms with same trigonometric arguments eqn. 6.1.13 becomes,

$$\begin{aligned}
 \mathbf{K}(t)\mathbf{u}(t) &= \frac{\mathbf{K}_{0c}\mathbf{a}_0}{4} + (\mathbf{K}_{1c}\cos\Omega t + \mathbf{K}_{1s}\sin\Omega t)\frac{\mathbf{a}_0}{2} + (\mathbf{K}_{2c}\cos 2\Omega t + \mathbf{K}_{2s}\sin 2\Omega t)\frac{\mathbf{a}_0}{2} \\
 &+ \frac{\mathbf{K}_{0c}}{2} \sum_{k=\frac{1}{2}, 1, \frac{3}{2}, \dots}^{\infty} (\mathbf{a}_k \cos k\Omega t + \mathbf{b}_k \sin k\Omega t) \\
 &+ \frac{1}{2} \sum_{k=\frac{1}{2}, 1, \frac{3}{2}, \dots}^{\infty} [(\mathbf{K}_{1c}\mathbf{a}_k + \mathbf{K}_{1s}\mathbf{b}_k) \cos(k-1)\Omega t + (-\mathbf{K}_{1s}\mathbf{a}_k + \mathbf{K}_{1c}\mathbf{b}_k) \sin(k-1)\Omega t \\
 &\quad + (\mathbf{K}_{1c}\mathbf{a}_k - \mathbf{K}_{1s}\mathbf{b}_k) \cos(k+1)\Omega t + (\mathbf{K}_{1s}\mathbf{a}_k + \mathbf{K}_{1c}\mathbf{b}_k) \sin(k+1)\Omega t] \\
 &+ \frac{1}{2} \sum_{k=\frac{1}{2}, 1, \frac{3}{2}, \dots}^{\infty} [(\mathbf{K}_{2c}\mathbf{a}_k + \mathbf{K}_{2s}\mathbf{b}_k) \cos(k-2)\Omega t + (-\mathbf{K}_{2s}\mathbf{a}_k + \mathbf{K}_{2c}\mathbf{b}_k) \sin(k-2)\Omega t \\
 &\quad + (\mathbf{K}_{2c}\mathbf{a}_k - \mathbf{K}_{2s}\mathbf{b}_k) \cos(k+2)\Omega t + (\mathbf{K}_{2s}\mathbf{a}_k + \mathbf{K}_{2c}\mathbf{b}_k) \sin(k+2)\Omega t]
 \end{aligned} \tag{6.1.14}$$

Further expanding the summation terms yields:

$$\begin{aligned}
 \mathbf{K}(t)\mathbf{u}(t) &= \frac{1}{2} \left[ \frac{\mathbf{K}_{0c}}{2} \mathbf{a}_0 + (\mathbf{K}_{1c}\mathbf{a}_1 + \mathbf{K}_{1s}\mathbf{b}_1) + (\mathbf{K}_{2c}\mathbf{a}_2 + \mathbf{K}_{2s}\mathbf{b}_2) \right] \\
 &+ \frac{1}{2} \left[ (\mathbf{K}_{0c} + \mathbf{K}_{1c})\mathbf{a}_{\frac{1}{2}} + \mathbf{K}_{1s}\mathbf{b}_{\frac{1}{2}} + (\mathbf{K}_{1c} + \mathbf{K}_{2c})\mathbf{a}_{1\frac{1}{2}} + (\mathbf{K}_{1s} + \mathbf{K}_{2s})\mathbf{b}_{1\frac{1}{2}} + (\mathbf{K}_{2c}\mathbf{a}_{2\frac{1}{2}} + \mathbf{K}_{2s}\mathbf{b}_{2\frac{1}{2}}) \right] \cos \frac{\Omega t}{2} \\
 &+ \frac{1}{2} \left[ \mathbf{K}_{1s}\mathbf{a}_{\frac{1}{2}} + (\mathbf{K}_{0c} - \mathbf{K}_{1c})\mathbf{b}_{\frac{1}{2}} + (-\mathbf{K}_{1s} + \mathbf{K}_{2s})\mathbf{a}_{1\frac{1}{2}} + (\mathbf{K}_{1c} - \mathbf{K}_{2c})\mathbf{b}_{1\frac{1}{2}} + (-\mathbf{K}_{2s}\mathbf{a}_{2\frac{1}{2}} + \mathbf{K}_{2c}\mathbf{b}_{2\frac{1}{2}}) \right] \sin \frac{\Omega t}{2} \\
 &+ \frac{1}{2} [\mathbf{K}_{1c}\mathbf{a}_0 + (\mathbf{K}_{0c} + \mathbf{K}_{2c})\mathbf{a}_1 + \mathbf{K}_{2s}\mathbf{b}_1 + (\mathbf{K}_{1c}\mathbf{a}_2 + \mathbf{K}_{1s}\mathbf{b}_2) + (\mathbf{K}_{2c}\mathbf{a}_3 + \mathbf{K}_{2s}\mathbf{b}_3)] \cos \Omega t \\
 &+ \frac{1}{2} [\mathbf{K}_{1s}\mathbf{a}_0 + \mathbf{K}_{2s}\mathbf{a}_1 + (\mathbf{K}_{0c} - \mathbf{K}_{2c})\mathbf{b}_1 + (-\mathbf{K}_{1s}\mathbf{a}_2 + \mathbf{K}_{1c}\mathbf{b}_2) + (-\mathbf{K}_{2s}\mathbf{a}_3 + \mathbf{K}_{2c}\mathbf{b}_3)] \sin \Omega t \\
 &+ \frac{1}{2} \left[ (\mathbf{K}_{1c} + \mathbf{K}_{2c})\mathbf{a}_{\frac{1}{2}} + (-\mathbf{K}_{1s} + \mathbf{K}_{2s})\mathbf{b}_{\frac{1}{2}} + \mathbf{K}_{0c}\mathbf{a}_{1\frac{1}{2}} + \mathbf{K}_{1c}\mathbf{a}_{2\frac{1}{2}} + \mathbf{K}_{1s}\mathbf{b}_{2\frac{1}{2}} + (\mathbf{K}_{2c}\mathbf{a}_{3\frac{1}{2}} + \mathbf{K}_{2s}\mathbf{b}_{3\frac{1}{2}}) \right] \cos \frac{3\Omega t}{2} \\
 &+ \frac{1}{2} \left[ (\mathbf{K}_{1s} + \mathbf{K}_{2s})\mathbf{a}_{\frac{1}{2}} + (\mathbf{K}_{1c} - \mathbf{K}_{2c})\mathbf{b}_{\frac{1}{2}} + \mathbf{K}_{0c}\mathbf{b}_{1\frac{1}{2}} - \mathbf{K}_{1s}\mathbf{a}_{2\frac{1}{2}} + \mathbf{K}_{1c}\mathbf{b}_{2\frac{1}{2}} + (-\mathbf{K}_{2s}\mathbf{a}_{3\frac{1}{2}} + \mathbf{K}_{2c}\mathbf{b}_{3\frac{1}{2}}) \right] \sin \frac{3\Omega t}{2} \\
 &+ \frac{1}{2} [\mathbf{K}_{2c}\mathbf{a}_0 + \mathbf{K}_{1c}\mathbf{a}_1 - \mathbf{K}_{1s}\mathbf{b}_1 + \mathbf{K}_{0c}\mathbf{a}_2 + (\mathbf{K}_{1c}\mathbf{a}_3 + \mathbf{K}_{1s}\mathbf{b}_3) + (\mathbf{K}_{2c}\mathbf{a}_4 + \mathbf{K}_{2s}\mathbf{b}_4)] \cos 2\Omega t \\
 &+ \frac{1}{2} [\mathbf{K}_{2s}\mathbf{a}_0 + \mathbf{K}_{1s}\mathbf{a}_1 + \mathbf{K}_{1c}\mathbf{b}_1 + \mathbf{K}_{0c}\mathbf{b}_2 + (-\mathbf{K}_{1s}\mathbf{a}_3 + \mathbf{K}_{1c}\mathbf{b}_3) + (-\mathbf{K}_{2s}\mathbf{a}_4 + \mathbf{K}_{2c}\mathbf{b}_4)] \sin 2\Omega t \\
 &+ \frac{1}{2} \sum_{k=2\frac{1}{2}, 3, 3\frac{1}{2}, 4, 4\frac{1}{2}, \dots}^{\infty} [(\mathbf{K}_{2c}\mathbf{a}_{(k-2)} - \mathbf{K}_{2s}\mathbf{b}_{(k-2)}) + (\mathbf{K}_{1c}\mathbf{a}_{(k-1)} - \mathbf{K}_{1s}\mathbf{b}_{(k-1)}) \\
 &\quad + \mathbf{K}_{0c}\mathbf{a}_k + (\mathbf{K}_{1c}\mathbf{a}_{(k+1)} + \mathbf{K}_{1s}\mathbf{b}_{(k+1)}) + (\mathbf{K}_{2c}\mathbf{a}_{(k+2)} + \mathbf{K}_{2s}\mathbf{b}_{(k+2)})] \cos k\Omega t \\
 &+ \frac{1}{2} \sum_{k=2\frac{1}{2}, 3, 3\frac{1}{2}, 4, 4\frac{1}{2}, \dots}^{\infty} [(\mathbf{K}_{2s}\mathbf{a}_{(k-2)} + \mathbf{K}_{2c}\mathbf{b}_{(k-2)}) + (\mathbf{K}_{1s}\mathbf{a}_{(k-1)} + \mathbf{K}_{1c}\mathbf{b}_{(k-1)}) \\
 &\quad + \mathbf{K}_{0c}\mathbf{b}_k + (-\mathbf{K}_{1s}\mathbf{a}_{(k+1)} + \mathbf{K}_{1c}\mathbf{b}_{(k+1)}) + (-\mathbf{K}_{2s}\mathbf{a}_{(k+2)} + \mathbf{K}_{2c}\mathbf{b}_{(k+2)})] \sin k\Omega t
 \end{aligned} \tag{6.1.15}$$

From eqn. 6.1.11 and 6.1.15, the equation of motion for full engine orders can be shown as:

$$\begin{aligned}
 & \mathbf{M}(t)\ddot{\mathbf{u}}(t) + \Omega\mathbf{G}\dot{\mathbf{u}}(t) + \mathbf{K}(t)\mathbf{u}(t) = \mathbf{0} = \\
 & -\frac{1}{2}\Omega^2 \sum_{k=1,2,3,\dots}^{\infty} [(k^2\mathbf{M}_{0c}\mathbf{a}_k - k\mathbf{G}_{0c}\mathbf{b}_k) \cos k\Omega t + (k\mathbf{G}_{0c}\mathbf{a}_k + k^2\mathbf{M}_{0c}\mathbf{b}_k) \sin k\Omega t] \\
 & + \frac{1}{2} \left[ \frac{\mathbf{K}_{0c}}{2} \mathbf{a}_0 + (\mathbf{K}_{1c}\mathbf{a}_1 + \mathbf{K}_{1s}\mathbf{b}_1) + (\mathbf{K}_{2c}\mathbf{a}_2 + \mathbf{K}_{2s}\mathbf{b}_2) \right] \\
 & + \frac{1}{2} [\mathbf{K}_{1c}\mathbf{a}_0 + (\mathbf{K}_{0c} + \mathbf{K}_{2c})\mathbf{a}_1 + \mathbf{K}_{2s}\mathbf{b}_1 + (\mathbf{K}_{1c}\mathbf{a}_2 + \mathbf{K}_{1s}\mathbf{b}_2) + (\mathbf{K}_{2c}\mathbf{a}_3 + \mathbf{K}_{2s}\mathbf{b}_3)] \cos \Omega t \\
 & + \frac{1}{2} [\mathbf{K}_{1s}\mathbf{a}_0 + \mathbf{K}_{2s}\mathbf{a}_1 + (\mathbf{K}_{0c} - \mathbf{K}_{2c})\mathbf{b}_1 + (-\mathbf{K}_{1s}\mathbf{a}_2 + \mathbf{K}_{1c}\mathbf{b}_2) + (-\mathbf{K}_{2s}\mathbf{a}_3 + \mathbf{K}_{2c}\mathbf{b}_3)] \sin \Omega t \\
 & + \frac{1}{2} [\mathbf{K}_{2c}\mathbf{a}_0 + (\mathbf{K}_{1c}\mathbf{a}_1 - \mathbf{K}_{1s}\mathbf{b}_1) + \mathbf{K}_{0c}\mathbf{a}_2 + (\mathbf{K}_{1c}\mathbf{a}_3 + \mathbf{K}_{1s}\mathbf{b}_3) + (\mathbf{K}_{2c}\mathbf{a}_4 + \mathbf{K}_{2s}\mathbf{b}_4)] \cos 2\Omega t \\
 & + \frac{1}{2} [\mathbf{K}_{2s}\mathbf{a}_0 + (\mathbf{K}_{1s}\mathbf{a}_1 + \mathbf{K}_{1c}\mathbf{b}_1) + \mathbf{K}_{0c}\mathbf{b}_2 + (-\mathbf{K}_{1s}\mathbf{a}_3 + \mathbf{K}_{1c}\mathbf{b}_3) + (-\mathbf{K}_{2s}\mathbf{a}_4 + \mathbf{K}_{2c}\mathbf{b}_4)] \sin 2\Omega t \\
 & + \frac{1}{2} \sum_{k=3,4,5,6,\dots}^{\infty} [(\mathbf{K}_{2c}\mathbf{a}_{(k-2)} - \mathbf{K}_{2s}\mathbf{b}_{(k-2)}) + (\mathbf{K}_{1c}\mathbf{a}_{(k-1)} - \mathbf{K}_{1s}\mathbf{b}_{(k-1)}) + \mathbf{K}_{0c}\mathbf{a}_k \\
 & \quad + (\mathbf{K}_{1c}\mathbf{a}_{(k+1)} + \mathbf{K}_{1s}\mathbf{b}_{(k+1)}) + (\mathbf{K}_{2c}\mathbf{a}_{(k+2)} + \mathbf{K}_{2s}\mathbf{b}_{(k+2)})] \cos k\Omega t \\
 & + \frac{1}{2} \sum_{k=3,4,5,6,\dots}^{\infty} [(\mathbf{K}_{2s}\mathbf{a}_{(k-2)} + \mathbf{K}_{2c}\mathbf{b}_{(k-2)}) + (\mathbf{K}_{1s}\mathbf{a}_{(k-1)} + \mathbf{K}_{1c}\mathbf{b}_{(k-1)}) + \mathbf{K}_{0c}\mathbf{b}_k \\
 & \quad + (-\mathbf{K}_{1s}\mathbf{a}_{(k+1)} + \mathbf{K}_{1c}\mathbf{b}_{(k+1)}) + (-\mathbf{K}_{2s}\mathbf{a}_{(k+2)} + \mathbf{K}_{2c}\mathbf{b}_{(k+2)})] \sin k\Omega t
 \end{aligned}
 \tag{6.1.16}$$

Similarly, the equation of motion for half engine orders is shown to be

$$\begin{aligned}
 & \mathbf{M}(t)\ddot{\mathbf{u}}(t) + \Omega\mathbf{G}\dot{\mathbf{u}}(t) + \mathbf{K}(t)\mathbf{u}(t) = \mathbf{0} = \\
 & -\frac{1}{2}\Omega^2 \sum_{k=\frac{1}{2},\frac{3}{2},\frac{5}{2},\dots}^{\infty} [(k^2\mathbf{M}_{0c}\mathbf{a}_k - k\mathbf{G}_{0c}\mathbf{b}_k) \cos k\Omega t + (k\mathbf{G}_{0c}\mathbf{a}_k + k^2\mathbf{M}_{0c}\mathbf{b}_k) \sin k\Omega t] \\
 & + \frac{1}{2} [(\mathbf{K}_{0c} + \mathbf{K}_{1c})\mathbf{a}_{\frac{1}{2}} + \mathbf{K}_{1s}\mathbf{b}_{\frac{1}{2}} + (\mathbf{K}_{1c} + \mathbf{K}_{2c})\mathbf{a}_{\frac{1}{2}} + (\mathbf{K}_{1s} + \mathbf{K}_{2s})\mathbf{b}_{\frac{1}{2}} + (\mathbf{K}_{2c}\mathbf{a}_{\frac{3}{2}} + \mathbf{K}_{2s}\mathbf{b}_{\frac{3}{2}})] \cos \frac{\Omega t}{2} \\
 & + \frac{1}{2} [\mathbf{K}_{1s}\mathbf{a}_{\frac{1}{2}} + (\mathbf{K}_{0c} - \mathbf{K}_{1c})\mathbf{b}_{\frac{1}{2}} + (-\mathbf{K}_{1s} + \mathbf{K}_{2s})\mathbf{a}_{\frac{1}{2}} + (\mathbf{K}_{1c} - \mathbf{K}_{2c})\mathbf{b}_{\frac{1}{2}} + (-\mathbf{K}_{2s}\mathbf{a}_{\frac{3}{2}} + \mathbf{K}_{2c}\mathbf{b}_{\frac{3}{2}})] \sin \frac{\Omega t}{2} \\
 & + \frac{1}{2} [(\mathbf{K}_{1c} + \mathbf{K}_{2c})\mathbf{a}_{\frac{1}{2}} + (-\mathbf{K}_{1s} + \mathbf{K}_{2s})\mathbf{b}_{\frac{1}{2}} + \mathbf{K}_{0c}\mathbf{a}_{\frac{1}{2}} + \mathbf{K}_{1c}\mathbf{a}_{\frac{3}{2}} + \mathbf{K}_{1s}\mathbf{b}_{\frac{3}{2}} + (\mathbf{K}_{2c}\mathbf{a}_{\frac{5}{2}} + \mathbf{K}_{2s}\mathbf{b}_{\frac{5}{2}})] \cos \frac{3\Omega t}{2} \\
 & + \frac{1}{2} [(\mathbf{K}_{1s} + \mathbf{K}_{2s})\mathbf{a}_{\frac{1}{2}} + (\mathbf{K}_{1c} + \mathbf{K}_{2c})\mathbf{b}_{\frac{1}{2}} + \mathbf{K}_{0c}\mathbf{b}_{\frac{1}{2}} - \mathbf{K}_{1s}\mathbf{a}_{\frac{3}{2}} + \mathbf{K}_{1c}\mathbf{b}_{\frac{3}{2}} + (-\mathbf{K}_{2s}\mathbf{a}_{\frac{5}{2}} + \mathbf{K}_{2c}\mathbf{b}_{\frac{5}{2}})] \sin \frac{3\Omega t}{2} \\
 & + \frac{1}{2} \sum_{k=2\frac{1}{2},3\frac{1}{2},4\frac{1}{2},\dots}^{\infty} [(\mathbf{K}_{2c}\mathbf{a}_{(k-2)} - \mathbf{K}_{2s}\mathbf{b}_{(k-2)}) + (\mathbf{K}_{1c}\mathbf{a}_{(k-1)} - \mathbf{K}_{1s}\mathbf{b}_{(k-1)}) + \mathbf{K}_{0c}\mathbf{a}_k \\
 & \quad + (\mathbf{K}_{1c}\mathbf{a}_{(k+1)} + \mathbf{K}_{1s}\mathbf{b}_{(k+1)}) + (\mathbf{K}_{2c}\mathbf{a}_{(k+2)} + \mathbf{K}_{2s}\mathbf{b}_{(k+2)})] \cos k\Omega t \\
 & + \frac{1}{2} \sum_{k=2\frac{1}{2},3\frac{1}{2},4\frac{1}{2},\dots}^{\infty} [(\mathbf{K}_{2s}\mathbf{a}_{(k-2)} + \mathbf{K}_{2c}\mathbf{b}_{(k-2)}) + (\mathbf{K}_{1s}\mathbf{a}_{(k-1)} + \mathbf{K}_{1c}\mathbf{b}_{(k-1)}) + \mathbf{K}_{0c}\mathbf{b}_k \\
 & \quad + (-\mathbf{K}_{1s}\mathbf{a}_{(k+1)} + \mathbf{K}_{1c}\mathbf{b}_{(k+1)}) + (-\mathbf{K}_{2s}\mathbf{a}_{(k+2)} + \mathbf{K}_{2c}\mathbf{b}_{(k+2)})] \sin k\Omega t
 \end{aligned}
 \tag{6.1.17}$$

In eqns. 6.1.16 and 6.1.17,  $\mathbf{M}_{0c} = 2\mathbf{M}$  and  $\mathbf{G}_{0c} = 2\mathbf{G}$ . For all values of  $t$  the solution of eqns. 6.1.16 and 6.1.17 requires that the coefficients of every single component of each harmonic must be separately zero. Therefore, for full engine orders we have,

$$\frac{\mathbf{K}_{0c}}{2} \mathbf{a}_0 + (\mathbf{K}_{1c} \mathbf{a}_1 + \mathbf{K}_{1s} \mathbf{b}_1) + (\mathbf{K}_{2c} \mathbf{a}_2 + \mathbf{K}_{2s} \mathbf{b}_2) = 0$$

$$\mathbf{K}_{1c} \mathbf{a}_0 + (-\Omega^2 \mathbf{M}_{0c} + \mathbf{K}_{0c} + \mathbf{K}_{2c}) \mathbf{a}_1 + (\Omega^2 \mathbf{G}_{0c} + \mathbf{K}_{2s}) \mathbf{b}_1 \\ + (\mathbf{K}_{1c} \mathbf{a}_2 + \mathbf{K}_{1s} \mathbf{b}_2) + (\mathbf{K}_{2c} \mathbf{a}_3 + \mathbf{K}_{2s} \mathbf{b}_3) = 0$$

$$\mathbf{K}_{1s} \mathbf{a}_0 + (-\Omega^2 \mathbf{G}_{0c} + \mathbf{K}_{2s}) \mathbf{a}_1 + (-\Omega^2 \mathbf{M}_{0c} + \mathbf{K}_{0c} - \mathbf{K}_{2c}) \mathbf{b}_1 \\ + (-\mathbf{K}_{1s} \mathbf{a}_2 + \mathbf{K}_{1c} \mathbf{b}_2) + (-\mathbf{K}_{2s} \mathbf{a}_3 + \mathbf{K}_{2c} \mathbf{b}_3) = 0$$

$$\mathbf{K}_{2c} \mathbf{a}_0 + (\mathbf{K}_{1c} \mathbf{a}_1 - \mathbf{K}_{1s}) \mathbf{b}_1 + (-2\Omega^2 \mathbf{M}_{0c} + \mathbf{K}_{0c}) \mathbf{a}_2 + 2\Omega^2 \mathbf{G}_{0c} \mathbf{b}_2 \\ + (\mathbf{K}_{1c} \mathbf{a}_3 + \mathbf{K}_{1s} \mathbf{b}_3) + (\mathbf{K}_{2c} \mathbf{a}_4 + \mathbf{K}_{2s} \mathbf{b}_4) = 0$$

6.1.18

$$\mathbf{K}_{2s} \mathbf{a}_0 + (\mathbf{K}_{1s} \mathbf{a}_1 + \mathbf{K}_{1c} \mathbf{b}_1) - 2\Omega^2 \mathbf{G}_{0c} \mathbf{a}_2 \\ + (-2\Omega^2 \mathbf{M}_{0c} + \mathbf{K}_{0c}) \mathbf{b}_2 + (-\mathbf{K}_{1s} \mathbf{a}_3 + \mathbf{K}_{1c} \mathbf{b}_3) + (-\mathbf{K}_{2s} \mathbf{a}_4 + \mathbf{K}_{2c} \mathbf{b}_4) = 0$$

$$(\mathbf{K}_{2c} \mathbf{a}_{(k-2)} - \mathbf{K}_{2s} \mathbf{b}_{(k-2)}) + (\mathbf{K}_{1c} \mathbf{a}_{(k-1)} - \mathbf{K}_{1s} \mathbf{b}_{(k-1)}) \\ + (-k^2 \Omega^2 \mathbf{M}_{0c} + \mathbf{K}_{0c}) \mathbf{a}_k + k \Omega^2 \mathbf{G}_{0c} \mathbf{b}_k \\ + (\mathbf{K}_{1c} \mathbf{a}_{(k+1)} + \mathbf{K}_{1s} \mathbf{b}_{(k+1)}) + (\mathbf{K}_{2c} \mathbf{a}_{(k+2)} + \mathbf{K}_{2s} \mathbf{b}_{(k+2)}) = 0$$

$$(\mathbf{K}_{2s} \mathbf{a}_{(k-2)} + \mathbf{K}_{2c} \mathbf{b}_{(k-2)}) + (\mathbf{K}_{1s} \mathbf{a}_{(k-1)} + \mathbf{K}_{1c} \mathbf{b}_{(k-1)}) \\ + (-k^2 \Omega^2 \mathbf{M}_{0c} + \mathbf{K}_{0c}) \mathbf{b}_k - k \Omega^2 \mathbf{G}_{0c} \mathbf{a}_k \\ + (-\mathbf{K}_{1s} \mathbf{a}_{(k+1)} + \mathbf{K}_{1c} \mathbf{b}_{(k+1)}) + (-\mathbf{K}_{2s} \mathbf{a}_{(k+2)} + \mathbf{K}_{2c} \mathbf{b}_{(k+2)}) = 0$$

$k = 3, 4, 5, 6, \dots$

Similarly, for half engine orders the corresponding set of equations can be derived as:

$$\begin{aligned} & \left( -\frac{1}{2^2} \Omega^2 \mathbf{M}_{0c} + \mathbf{K}_{0c} + \mathbf{K}_{1c} \right) \mathbf{a}_{\frac{1}{2}} + \left( \frac{1}{2} \Omega^2 \mathbf{G}_{0c} + \mathbf{K}_{1s} \right) \mathbf{b}_{\frac{1}{2}} \\ & + (\mathbf{K}_{1c} + \mathbf{K}_{2c}) \mathbf{a}_{\frac{1}{2}} + (\mathbf{K}_{1s} + \mathbf{K}_{2s}) \mathbf{b}_{\frac{1}{2}} + \left( \mathbf{K}_{2c} \mathbf{a}_{\frac{3}{2}} + \mathbf{K}_{2s} \mathbf{b}_{\frac{3}{2}} \right) = 0 \end{aligned}$$

$$\begin{aligned} & \left( -\frac{1}{2} \Omega^2 \mathbf{G}_{0c} + \mathbf{K}_{1s} \right) \mathbf{a}_{\frac{1}{2}} + \left( -\frac{1}{2^2} \Omega^2 \mathbf{M}_{0c} + \mathbf{K}_{0c} - \mathbf{K}_{1c} \right) \mathbf{b}_{\frac{1}{2}} \\ & + (-\mathbf{K}_{1s} + \mathbf{K}_{2s}) \mathbf{a}_{\frac{1}{2}} + (\mathbf{K}_{1c} - \mathbf{K}_{2c}) \mathbf{b}_{\frac{1}{2}} + \left( -\mathbf{K}_{2s} \mathbf{a}_{\frac{3}{2}} + \mathbf{K}_{2c} \mathbf{b}_{\frac{3}{2}} \right) = 0 \end{aligned}$$

$$\begin{aligned} & (\mathbf{K}_{1c} + \mathbf{K}_{2c}) \mathbf{a}_{\frac{1}{2}} + (-\mathbf{K}_{1s} + \mathbf{K}_{2s}) \mathbf{b}_{\frac{1}{2}} + \left( -\frac{3^2}{2^2} \Omega^2 \mathbf{M}_{0c} + \mathbf{K}_{0c} \right) \mathbf{a}_{\frac{1}{2}} + \frac{3}{2} \Omega^2 \mathbf{G}_{0c} \mathbf{b}_{\frac{1}{2}} \\ & + \mathbf{K}_{1c} \mathbf{a}_{\frac{3}{2}} + \mathbf{K}_{1s} \mathbf{b}_{\frac{3}{2}} + \mathbf{K}_{2c} \mathbf{a}_{\frac{3}{2}} + \mathbf{K}_{2s} \mathbf{b}_{\frac{3}{2}} = 0 \end{aligned}$$

6.1.19

$$\begin{aligned} & (\mathbf{K}_{1s} + \mathbf{K}_{2s}) \mathbf{a}_{\frac{1}{2}} + (\mathbf{K}_{1c} - \mathbf{K}_{2c}) \mathbf{b}_{\frac{1}{2}} + \left( -\frac{3}{2} \Omega^2 \mathbf{G}_{0c} \right) \mathbf{a}_{\frac{1}{2}} \\ & + \left( -\frac{3^2}{2^2} \Omega^2 \mathbf{M}_{0c} + \mathbf{K}_{0c} \right) \mathbf{b}_{\frac{1}{2}} + \left( -\mathbf{K}_{1s} \mathbf{a}_{\frac{3}{2}} + \mathbf{K}_{1c} \mathbf{b}_{\frac{3}{2}} \right) - \mathbf{K}_{2s} \mathbf{a}_{\frac{3}{2}} + \mathbf{K}_{2c} \mathbf{b}_{\frac{3}{2}} = 0 \end{aligned}$$

$$\begin{aligned} & (\mathbf{K}_{2c} \mathbf{a}_{(k-2)} - \mathbf{K}_{2s} \mathbf{b}_{(k-2)}) + (\mathbf{K}_{1c} \mathbf{a}_{(k-1)} - \mathbf{K}_{1s} \mathbf{b}_{(k-1)}) + (-k^2 \Omega^2 \mathbf{M}_{0c} + \mathbf{K}_{0c}) \mathbf{a}_k + k \Omega^2 \mathbf{G}_{0c} \mathbf{b}_k \\ & + (\mathbf{K}_{1c} \mathbf{a}_{(k+1)} + \mathbf{K}_{1s} \mathbf{b}_{(k+1)}) + (\mathbf{K}_{2c} \mathbf{a}_{(k+2)} + \mathbf{K}_{2s} \mathbf{b}_{(k+2)}) = 0 \end{aligned}$$

$$\begin{aligned} & (\mathbf{K}_{2s} \mathbf{a}_{(k-2)} + \mathbf{K}_{2c} \mathbf{b}_{(k-2)}) + (\mathbf{K}_{1s} \mathbf{a}_{(k-1)} + \mathbf{K}_{1c} \mathbf{b}_{(k-1)}) + (-k \Omega^2 \mathbf{G}_{0c}) \mathbf{a}_k + (-k^2 \Omega^2 \mathbf{M}_{0c} + \mathbf{K}_{0c}) \mathbf{b}_k \\ & + (-\mathbf{K}_{1s} \mathbf{a}_{(k+1)} + \mathbf{K}_{1c} \mathbf{b}_{(k+1)}) + (-\mathbf{K}_{2s} \mathbf{a}_{(k+2)} + \mathbf{K}_{2c} \mathbf{b}_{(k+2)}) = 0 \end{aligned}$$

$$k = 2\frac{1}{2}, 3\frac{1}{2}, 4\frac{1}{2}, \dots$$

Equations 6.1.18 and 6.1.19 are two sets of linear homogeneous equations in terms of Fourier coefficients. Also, it is worth mentioning that these two set of equations are uncoupled, that is, the whole-order and half-order equations can be dealt with separately. In matrix form, they can be expressed in assembled form as:

$$[-\Omega^2(\tilde{\mathbf{M}}\tilde{\Lambda}^2 + \tilde{\mathbf{G}}\tilde{\Lambda}) + \tilde{\mathbf{K}}]\tilde{\mathbf{u}} = 0 \quad 6.1.20$$

Where the details of the corresponding matrices are recorded in Appendix 2. Equation 6.1.20 is in the frequency domain, and it can be seen that different constituent components of frequency response are coupled. It can be shown that there is not necessarily a solution available for every chosen value of angular velocity  $\Omega$ , except the trivial one of:

$$\tilde{\mathbf{u}} = 0 \quad 6.1.21$$

Nevertheless, it is quite usual that some values of  $\Omega$  exist with non-trivial solutions:

$$\tilde{\mathbf{u}} \neq 0 \quad 6.1.22$$

Therefore, eqn. 6.1.20 represents a standard eigenvalue problem whose solution gives the angular velocity  $\Omega$  at which non-trivial solutions, i.e. eqn. 6.1.22 exist. For simplicity eqn. 6.1.20 is rewritten as:

$$(-\Omega^2\tilde{\mathbf{A}} + \tilde{\mathbf{K}})\tilde{\mathbf{u}} = 0 \quad 6.1.23$$

with

$$\tilde{\mathbf{A}} = \tilde{\mathbf{M}}\tilde{\Lambda}^2 + \tilde{\mathbf{G}}\tilde{\Lambda}$$

Referencing to the recorded matrices in Appendix 2 it can be seen that the stiffness matrix consists of all symmetric sub-matrices which occur symmetrically about the main diagonal of the assembled stiffness matrices for both the half- and whole-order cases. Therefore, the stiffness matrices are symmetric. The mass and gyroscopic matrices are symmetric and skew-symmetric, respectively. From the construction of the assembled mass matrix, it can be observed that all of the non-zero terms occur on the main diagonal blocks. Therefore, the assembled mass matrix is of banded form. The assembled harmonic order matrices are all diagonal matrices. The order of eqn. 6.1.23 is related to the chosen number of Fourier series used to approximate the time dependent variables. However, for many physical and engineering problems the magnitudes of the Fourier coefficients in the characteristic displacement vector reduce continuously with increase in frequencies. Therefore, for practical reasons, such as balance between accuracy and computational efficiency or machine limitations, it is justifiable to truncate the series and utilise only a few significant terms as an approximation to the infinite Fourier series expansion. However, the required accuracy and therefore the number of mandatory coefficients can only be judged from experience with the assumption of the time dependent system behaviour. Several test cases should be performed to investigate the effect of increased numbers of Fourier coefficients on the analytical system responses. These results must be compared with the obtained measured data.

Several algorithms for solving eigenvalue problems may be applicable to this specific analysis, but additional consideration must be paid to the large size of the matrices, which are not necessarily coupled by the physical degrees of freedom but by the Fourier coefficients. Some other factors influencing the solution of this matrix equation may be worth mentioning. These are singularities and definiteness of the matrices, because the number of real non-negative roots for specific  $\Omega^2$  might be less than the order of the matrices  $\tilde{A}$  and  $\tilde{K}$ . The spin stabilisation by gyroscopic effects is a reason for the numeral reduction of natural or characteristic solutions. A lot of experimental work was done on this subject in the thirties and forties in foundation to the asymmetric crankshaft-propeller system used in military aircraft [103].

## 6.2 Slider Crank and Other General Mechanisms

Each slider crank mechanism of a multi-cylinder engine, as well as other general mechanisms which may be introduced into the system, generally affect the coefficients of the matrix equation of motion, and usually in a time dependent way, such as through geometric, as well as mass and elastic effects on the system kinetic and potential energies. However, for an engine operating in a steady state condition these effects can be represented as periodic changes in the coefficients. For example, if it is assumed that the stiffness matrix contains not only elastic effects, but also geometric effects which requires to have a period of one engine revolution, then this stiffness could be represented in terms of the following matrix Fourier series:

$$\mathbf{K}(t) = \frac{\mathbf{K}_{0c}}{2} + \sum_{k=N,2N,3N,\dots}^{\infty} (\mathbf{K}_{kc} \cos(k\Omega t) + \mathbf{K}_{ks} \sin(k\Omega t)) \quad 6.2.1$$

Utilising eqn. 6.2.1 as a general periodic stiffness matrix, instead of eqn. 6.1.5, with the matrix differential equation of motion in the time domain, i.e. eqn. 6.1.3, we could again develop the assembled matrix equation of motion in the frequency domain. However, the assembled stiffness matrices  $\tilde{K}$ , which are specified in the appendix, would now need to be replaced by more general ones.

As already established in section 5.2, it is not necessary to introduce the vibration elastic representation of the crank slider mechanism for the purpose of this investigation. It is suggested to by-pass the theoretical derivation of the combination of the system equations described in section 6.1 and the above given crank slider mechanism. Nevertheless, it is clear that this approach is capable of treating this problem in an appropriate manner.



### 6.3 Frequency Domain Solution for Non-Linear Coupled Systems

Up to this point linear systems are analysed only, because eqns. 6.1.1 and 6.1.2 do only include linear terms. If one or more of this terms is now replaced by a non-linear one, at least one of the terms on the left hand side will have either a power different or a product between them. The power different occurs from either the dependent function or the derivation of the non-linear term. The product will appear if the individual factorials are linked together by the non-linear effect. If the harmonic motion from eqn. 6.1.13 is now applied, we finally receive a auto-modulated system. This type of modulation will cause frequency coupling effects. This phenomenon is known in the vibration theory as sub-harmonic and super-harmonic resonances of the non-linear systems, with either hardening or softening springs.

The applied models are therefore to be investigated regarding their non-linear behaviour in terms of coupled vibrations and requirement for a non-linear description of their stiffness matrices. The initial stiffness properties are discussed in section 6.3.1, whereas the coupled vibration phenomenon is considered in section 6.3.2 applying linear sub-system properties.

#### 6.3.1 Investigation of Applied Initial Stiffness Properties

As already described in section 6.1, a time variant stiffness matrix  $K(t)$  is used to describe relative movements between elastic sub-systems. The resulting changes in stiffness are only related to the rotation of the crankshaft with respect to the engine block grounded within the basic coordinate system. Considering the fact that the crankshaft and cylinder block are loaded with time varying forces and coupled via the main bearings, we have to validate whether the assumption of a linear stress-strain relation within a single element, the sub-system and the assembly is satisfactory. The corresponding theory assuming non-linear system properties will be developed subsequently, followed by an analytical investigation to study the conditions of significant non-linear stiffness properties of the individual sub-system.

There are different non-linear stiffness effects. One is that of the non-linear relationships between stress and strain, often called material non-linearity. This might either be plasticity, creeping, hardening, softening or any other material dependent property. Another non-linear stiffness property is of geometric nature, where the deflection will increase much faster than the corresponding force, or large displacements with small stress and strain in applications such as torsional springs.

For all systems, the equilibrium conditions between internal work and applied external work can be developed. This is valid without consideration of linear or non-linear relationship between stresses and strains. Furthermore, the recognition of large displacements does not affect the equilibrium conditions. Therefore, for a finite number of degrees of freedom  $\alpha$  and applying the theorem of virtual work we get [104]:

$$\Psi(\alpha) = \int_V \bar{\mathbf{K}}^T \boldsymbol{\sigma} dV - f = 0 \quad 6.3.1$$

where  $\Psi$  represents the summation of the internal and external forces.  $\bar{\mathbf{K}}$  is given with the definition derived from the strain relation:

$$d\boldsymbol{\varepsilon} = \bar{\mathbf{K}} d\alpha \quad 6.3.2$$

Within this equation  $\bar{\mathbf{K}}$  represents a matrix with strains being, in the case of large displacements, non-linearly related to the deformation, i.e. the matrix  $\bar{\mathbf{K}}$  is a functional of  $\alpha$ . This matrix splits into three partitions with respect to linear and non-linear properties such as:

$$\bar{\mathbf{K}} = \mathbf{K}_0 + \mathbf{K}_L(\alpha) + \mathbf{K}_\sigma \quad 6.3.3$$

with  $\mathbf{K}_0$  being the equivalent matrix similar to the linear treatment of the problem.  $\mathbf{K}_L$  is a functional in  $\alpha$ , the displacement vector representing the geometric non-linear action.  $\mathbf{K}_\sigma$  is the stiffness matrix due to initial stress. These problems are solved applying iterative techniques. Few mathematical algorithms are available for the computational solution such as direct iteration, Newton-Raphson-Iteration and others. The reader may refer to publications given in the references explaining the pros and cons of the different methodologies and their fields of application, e.g.: [105], [106], [107].

A simple beam representation is used for studying the different effects of  $\mathbf{K}_L$  and  $\mathbf{K}_\sigma$  solving the differential equation by hand. The effect of different loadcases and support conditions on this beam system supported with two bearings as shown in Figure 6.3.1 is studied by calculating the system vibration parameters and the corresponding dynamic response. The results obtained will give some reasonable insight in the effects occurring with static pre-loads and varying support conditions and an arrangement, which can be to some extent compared with a crankshaft image (cranked beam).

A significant property, which is affected by the stiffness and mass matrices only, is the eigenfrequency. Now, if it is assumed that the system mass matrix is constant, we can use the calculated eigenfrequencies of the specific systems for comparative analysis on effectiveness of the initial stiffness matrix  $\mathbf{K}_\sigma$ . For the specific beam representation

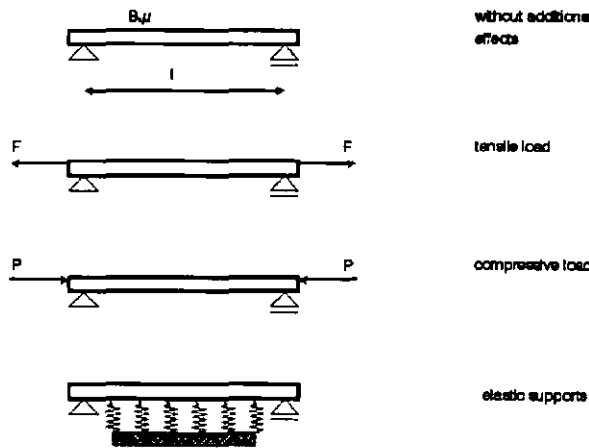


Figure 6.3.1 Beam Representation with Additional Effects

without any kinematic effects, the mass matrix is constant. Applying this technique to the assembled engine system, unquestionably we have to ensure that no kinematics, i.e. no rotational effects and no relative movements but the elastic ones, are included in the analysis. So, with kinematics included, the initial stiffness matrix must be developed at every time step or position with the loads calculated within the previous iteration loop. Returning again to the given example and obtaining the differential equations from standard engineering textbooks, we summarise the results in Table 10.

System	Parameters	Eigenfrequency
without additional effects	$\omega_B^2 = \frac{B\pi^4}{\mu l^4}$	$\omega_n^2 = n^4 \omega_B^2$
axial tensile load	$\omega_N^2 = \frac{N\pi^2}{\mu l^2}$	$\omega_n^2 = n^4 \omega_B^2 + n^2 \omega_N^2$
axial compressive load	$v = \frac{P}{P_{Kr}}$  buckling load $P_{Kr} = \frac{\pi^2 B}{l^2}$	$\omega_n = n^2 \omega_B \sqrt{1 - \frac{v}{n^2}}$
including elastic support	$\omega_c^2 = \frac{c}{\mu}$	$\omega_n^2 = n^4 \omega_B^2 + \omega_c^2$

Table 10 Influence of External Effects on Eigenfrequency

In the above given cases two fundamental categories of behaviour can be obtained for the straight beam. In the cases of axial tensile preload and additional support, the load or the grounded springs perform as parallel spring stiffnesses 'increasing' the overall stiffness matrix. In the case of a compressive preload we realise a decrease of the natural eigenfrequencies. For the lowest eigenfrequency ( $n=1$ ) this effect is dominant and with an axial preload balanced with the critical buckling load the first eigenfrequency will become zero. For all the above mentioned cases the influence of the pre-loading or boundary effect declines with higher orders. These findings are not commonly certain and depend on the analysed system or applied loads. Therefore, the actual effect on the engine can not be assessed directly from this theory but requires a system analysis including the actual mass and stiffness representations.

Returning to the original problem of the rotating crankshaft assembled in the engine block an investigation was performed to study the eventual effects of non-linear stiffness properties. These non-linear properties may only be introduced from the combustion and other external forces applied to the sub-system crankshaft or engine block. This investigation is essential for the further progress of this project, as the obtained results will allow either the discretion as a constant stiffness matrix of the sub-systems or the requirement of the non-linear stiffness matrix treatment. The later finding would result in a dramatic increase of computational effort, as the individual sub-system stiffness matrix  $\bar{\mathbf{K}}_{\text{sub-system}}$  would require an update within the solution strategy. Hence, the assembled system stiffness matrix  $\bar{\mathbf{K}}_{\text{total-system}}$  must be also updated.

Applying the above described theory of varying system behaviour to the crankshaft and engine-block individually, the system eigenfrequencies will alter with increasing loads. The varying loads on the crankshaft are the centrifugal or gyroscopic and the connecting-rod forces. The varying loads on the engine-block are the main-bearing forces and the combustion pressure. Non-linear modal and geometric non-linear analyses were performed to study the dynamic and static behaviour and the corresponding change due to non-linearities. Hence, emphasis is given to the crankshaft assembly, first including the crankshaft, fly-wheel and the pulley assembly. Applying the centrifugal load feature within Abaqus, the crankshaft assemble is analysed using linear stiffness coefficients as representation of the crankcase stiffness properties. The results are derived for engine speed varying from 1000-8000 rpm. For completeness crankpin forces, derived from an external examination of the dynamic crankshaft bearing loads, are applied. The influence on eigenfrequencies and static response due to modification of the initial stiffness matrix  $\mathbf{K}_\alpha$  is investigated. Examining the obtained modal results, no significant change in eigenfrequencies could be obtained, but in the

first mode. This mode, showing a quite significant increase of eigenfrequency from about 0 Hz to roughly 18 Hz, is a rotational rigid body mode of the crankshaft due to unbounded rotational degrees of freedom. This increase in eigenfrequency can be explained by the gyroscopic stabilising effect of rotating masses. Without a gyroscopic effect no change could be assessed in the dynamic crankshaft behaviour. The results perceived from the static analysis simulating a load at an arbitrary moment showed no non-linear effect. From this it can be deduced that a spinning crankshaft can be treated as a linear system, if the gyroscopic effects are covered separately. The previously explained theoretical approach covers the gyroscopic effects independent of the stiffness properties of the crankshaft. Therefore the crankshaft can be assessed as a linear sub-system within the assembled non-linear cranktrain. The changes obtained are insignificant compared with the resultant behaviour considerably influenced by the structural properties stiffness  $\mathbf{K}_0$  and mass matrix.

From recent research work [108] differences in eigenfrequencies can be achieved in the order of 3-10% within an engine speed range of 1000-6000 rpm, particular for the first lateral and vertical bending modes. These results have been obtained by analysing a crankshaft of similar engine size, but with four counterweights being significant larger than the utilised counterweights with an additional effect on the gyroscopic term. No data are available for either flywheel, pulley, crankshaft balancing or other properties. A comparison of the differences is therefore doubtful. Comparing the eigenfrequencies of this configuration under free-free condition with the calculated crankshaft frequencies, one discovers that the used I4-crankshaft assembly is stiffer in lateral and vertical directions. The influence of the incremental  $\mathbf{K}_\alpha$  matrix will therefore be of less significance compared with the  $\mathbf{K}_0$  matrix.

Utilising the equivalent analysis strategies to the engine-block, no non-linear property could be assessed in terms of  $\mathbf{K}_\alpha$ . The applied loads are the engine-block forces and pressures as described above. An examination of related literature showed that no material could be found describing a non-linear characteristic of engine-blocks in terms of structural stiffness properties.

As an essential outcome from the performed analyses and literature survey, the system response can be treated as a functional of mainly crankshaft and flywheel inertia, crankshaft mass and stiffness and obviously engine-block stiffness and mass properties. Therefore, all applied stiffness properties of the crankshaft and crankcase will be treated as constant matrices. This view may not be mixed with the time varying stiffness property  $\mathbf{K}(t)$  of the crankshaft due to the rotation.

### 6.3.2 Non-Linear Coupled Vibrations of Elastic Systems

Up to now we have analysed stand-alone systems. If we consider a system with two or even more modes of vibration coupled by nonlinear stiffnesses, vibrations of one externally excited mode leads to a parametric excitation in the other mode. These systems are said to be *autoparametric*. In the present case the crankshaft assembly is coupled via non-linear main bearings to the engine block and this unit itself is coupled via non-linear engine mounts to the body members. The vibration in the autoparametrically excited modes will often, but not always, be different from the frequency of vibration in the externally excited mode. Recalling eqn. 6.1.1 we write:

$$\mathbf{M}\ddot{\mathbf{u}}(t) + [\mathbf{K}_{constant} + \varepsilon\mathbf{K}(t)]\mathbf{u}(t) = \mathbf{f}(t) \quad 6.3.4$$

where  $\mathbf{K}_{constant}$  is the constant stiffness matrix and  $\mathbf{K}(t)$  is the periodic participant which can be written in Fourier series as given in eqn. 6.1.6. The coefficient  $\varepsilon$  indicate that the parameter excitation is of small amplitude, i.e. ( $|\varepsilon\mathbf{K}(t)| \ll \mathbf{K}_{constant}$ ). Rewriting eqn. 6.1.6 as a Fourier series, with  $c_n$  as the Fourier coefficients of the periodic stiffness, we get:

$$\mathbf{K}(t) = \sum_{-\infty}^{+\infty} c_n e^{in\Omega t} \quad 6.3.5$$

Using a series expansion for the solution of the differential eqn. 6.3.4 such as

$$\mathbf{u}(t) = \mathbf{u}_0 + \varepsilon\mathbf{u}_1 + \varepsilon^2\mathbf{u}_2 + \dots \quad 6.3.6$$

we finally get the following solution for  $\mathbf{u}_0$ , if all factorials with order one or higher are neglected:

$$\mathbf{u}_0 = A e^{i\omega t} + B e^{-i\omega t} \quad 6.3.7$$

$$\omega = \sqrt{\frac{s_0}{m}}$$

This is the standard solution for a non-excited system. Neglecting orders of  $\varepsilon^2$  and higher [109], the first order term  $\mathbf{u}_1$  can be developed as:

$$\mathbf{M}\ddot{\mathbf{u}}_1 + \mathbf{K}_{constant}\mathbf{u}_1 = -(A e^{i\omega t} + B e^{-i\omega t}) \sum_n c_n e^{in\Omega t} + \mathbf{f}(t) \quad 6.3.8$$

Applying the generic equation of periodic excitation in complex form for 'f(t)'

$$\mathbf{f}(t) = -A \sum_n c_n e^{i(n\Omega + \omega)t} - B \sum_n c_n e^{i(n\Omega - \omega)t} \quad 6.3.9$$

we easily acknowledge why the complex form is much easier to understand. The solution for  $\mathbf{u}_1$  will be unlimited if the exciting frequency of the right hand side is equal to the eigenfrequency of the homogeneous eqn. 6.3.8. This results in

$$\omega = (n\Omega \pm \omega) \tag{6.3.10}$$

or

$$\frac{\Omega}{\omega} = \frac{2}{n} \quad \text{with } n = 1, 2, 3, \dots \tag{6.3.11}$$

With this relation between the parametric exciting frequency  $\Omega$  and the eigenfrequency  $\omega$ , unlimited amplitudes could occur but not necessarily because of the system damping. If we consider higher orders of  $\epsilon$ , an equivalent relation for instability can be derived, but the regions of instability are rather small and, from the technical point of view, not critical. A characteristic graph is shown in Figure 6.3.2. The response amplitude  $\mu$  increases with increasing excitation amplitude  $\gamma$ . From experience ([114],[115]) it is known that instability regions will disappear, if there is only little damping in the system.

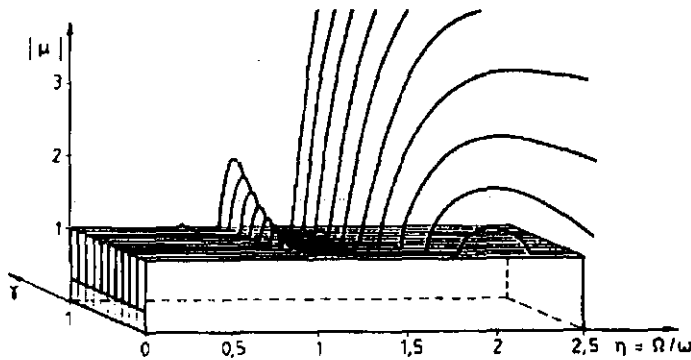


Figure 6.3.2 Forcing Dependent Instability Chart of Mathieu-Equation

The given stability chart will be analysed in more detail. For low values of parametric excitation amplitude  $\gamma$  and zero damping ( $D=0$ ), if the exciting frequency  $\Omega$  is increased from zero to higher than twice the system's eigenfrequency  $\omega$ , the following behaviour of the system can be obtained. The parametric resonance areas of the order  $\epsilon_2$ ,  $\epsilon_3$  or even higher are negligibly small, hence a system crossing this areas will remain stable. Only the order of  $\epsilon_1$  with the range of  $1.8 < \frac{\Omega}{\omega} < 2.2$  will cause unstable behaviour. For values of  $\gamma < 0.1$  instability will not appear at higher frequency ratios. But with increasing excitation amplitude, instability regions will develop at every frequency ratio greater than 1.8 and also at 1.0, which is originated by the second order  $\epsilon_2$ . Another significant feature of the system is that damping will reduce or at higher orders eliminate the area of instability.

### 6.3.3 Stability of Non-Linear Coupled Systems

As already briefly described in section 3.4 a system differential equation of motion describes the system response with respect to a perturbation on the right hand side of the equation. The differential equation therefore describes also the stability of a system with respect to this perturbation. The solution of the differential equation of motion will answer the question of stability of the investigated system.

A common approach is to use 'Ljapunov's first direct stability criterion'.

The system described by eqn. 6.3.14 is studied with respect to the response to an external perturbation.

$$\dot{x} = f(x, t) \tag{6.3.12}$$

Ljapunov ([110],[111],[112]) defines stability of a system as follows:

If for every positive value  $\epsilon > 0$  a positive value  $\delta(\epsilon, t_0)$  exists, so that for all perturbation  $x_0$  a solution  $x(t)$  exists with limited response in respect to  $\epsilon$ .

$$\|x_0\| < \delta \tag{6.3.13}$$

This is written as:

$$\|x_t\| < \epsilon, \quad t \geq t_0 \tag{6.3.14}$$

The asymptotic stability is defined as:

$$\lim_{t \rightarrow \infty} x(t) = 0 \tag{6.3.15}$$

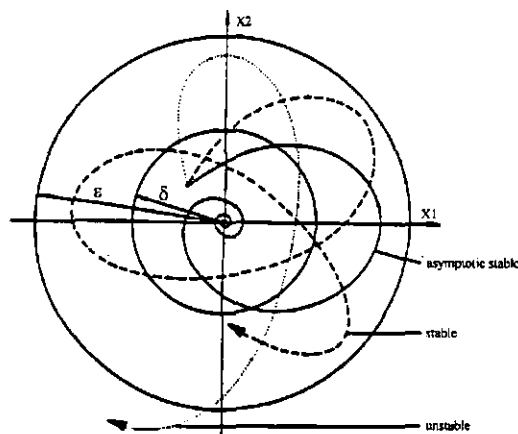


Figure 6.3.3 Ljapunov's Stability Criterion

The system has marginal stability if it is stable, but not asymptotically stable. Stability is defined as homogeneous if it is not related or dependent upon the initial time  $t_0$ . The system has global stability if the complete range of operation may be initial conditions.



The system is consequently defined as unstable if none of the above descriptions can be applied. A principle graphical description of Ljapunov's stability criterion is shown in Figure 6.3.3

Applying this definition, stability criteria are relatively easy to establish for those systems characterised by time-invariant properties. The system with time-invariant coefficients is described with:

$$\dot{x} = A_0x \tag{6.3.16}$$

The system stability criterion are derived such as [113]:

- asymptotic stable       $\text{Re} (\lambda_i (A_0)) < 0 , i=1, \dots, n$
- marginal stable         $\text{Re} (\lambda_i (A_0)) \leq 0 , i=1, \dots, n$   
and  
at least one  $\text{Re} (\lambda_i (A_0)) = 0$
- unstable                 $\text{Re} (\lambda_i (A_0)) > 0$

A similar approach can be developed for periodical systems by applying the theory of Floquet [114]. It is assumed that the properties of periodic time-variant systems are similar to those of time-invariant systems, so that the Ljapunov approach can be applied, if a fundamental matrix is defined transforming the time-variant system into a time-invariant system.

The principle idea of the Floquet theory is described for T-periodic systems as:

$$\dot{x} = A(t)x \quad ; \quad A(t + T) = A(t) \tag{6.3.17}$$

and that a fundamental matrix  $\Phi$  can be written for multiples of the period T such that

$$\Phi(t + mT, t_0) = \Phi(t, t_0)B^m \tag{6.3.18}$$

with B being a constant non-singular (nxn) matrix. For values of  $t=t_0$  one develops:

$$\Phi(t_0, t_0) = E \tag{6.3.19}$$

and

$$B^m = \Phi(t_0 + mT, t_0) \tag{6.3.20}$$

Applying  $t_0=0$  and  $m=1$ , B has the form:

$$B = \Phi(T, 0) \tag{6.3.21}$$

A matrix R exists for each constant matrix B [115], so that the following equation is satisfied:

$$\mathbf{B} = e^{RT} \quad 6.3.22$$

Applying this, a T-periodic matrix can be derived transforming the time-variant system into a time-invariant system, so that the previously described stability criteria can be applied.

$$\Phi(t, t_0) = Z(t, t_0)e^{R(t-t_0)} \quad 6.3.23$$

The time-variant system is transformed by utilising the equation:

$$x = Z(t, t_0)y \quad ; \quad Z(t_0, t_0) = E \quad 6.3.24$$

into the time-invariant system:

$$\dot{y} = R y \quad 6.3.25$$

This is a linear, time-invariant description of the system. The transformation matrix is valid for all times and the stability criteria can be deployed from the eigenvalues  $\lambda_i$  of the constant system matrix R according the rules described by Ljupanov [116].

A principle investigation was performed by Weyh [117] analysing the stability of a multi-cylinder engine with respect to the design parameters: amplitude of oscillation  $p$ , crankshaft stiffness  $k$  and system damping  $\delta$ . The dimensionless properties  $k$  and  $\delta$  are defined as  $k = c/(4\Omega^2 J)$  and  $\delta = d/(2\Omega J)$  respectively. The applied method is based on Ljupanov's stability criteria. The accepted amplitudes of oscillation  $p$  are altered from 0 to 1.0, whereas values of  $p > 0.4$  are not important for practical application. The obtained results are shown in Figure 6.3.4 for damping properties varying from  $\delta = 0.0-0.05$  and in Figure 6.3.5 for damping properties of  $\delta = 0.075-0.2$ .

Studying the stability charts in more detail, one can obtain some significant findings:

- all margins of stability are within the undamped case bounded between the value 0.8 and 1.0 at the axis of oscillation amplitude  $p$
- all areas of instability are reduced with increasing system damping and the regions between the  $k$ -axis and the margins of instability are increasing
- areas of different instability regions, such as harmonic and sub-harmonic instability, are overlapping
- many margins of instability are congruent between different areas of instability
- an influencing effect between different areas of instability can be obtained.

From this investigation it is obvious that a significant sensitivity of the areas of instability can be detected with increasing system damping. The sub-harmonic area of instability vanishes at a damping value of  $\delta=0.1$ . The harmonic area of instability fades out at damping values of approximately  $\delta=0.26$ .

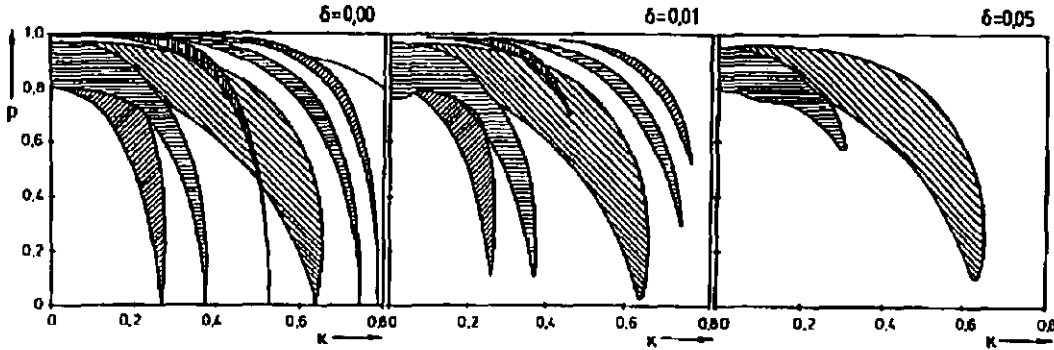


Figure 6.3.4 Stability Chart of Multi-Cylinder Engine (Part I) [Weyh]

The values of the engine studied in this investigation for  $k$  are in between 0.3-0.7 depending on the engine speed. The corresponding damping properties are calculated with  $\delta=0.1-0.3$ . Analysing the stability charts for these values of  $\delta$  and  $k$ , it must be assumed that instability will most probably not occur. The final stability assessment will be performed applying Ljapunov's criteria in Chapter 8.

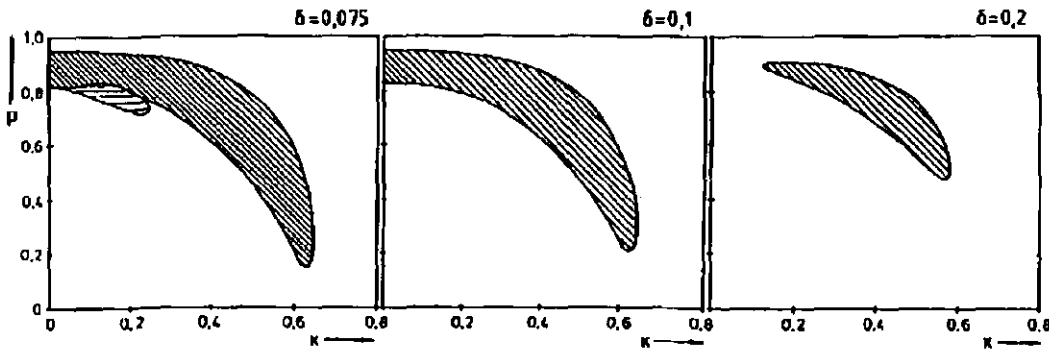


Figure 6.3.5 Stability Chart of Multi-Cylinder Engine (Part II) [Weyh]

### 6.4 Forced Response Analysis

If the general system eqns. 6.1.2 and 6.1.3 are recovered from section 6.1 and both are rewritten in the form of a periodically forced, non-linear, general dynamic system, the following equation can be obtained:

$$M(t)\ddot{u}(t) + [\Omega G(t) + D(t)]\dot{u}(t) + K(t)u(t) = f(t) \tag{6.4.1}$$

Although all matrices and vectors are assumed to be periodic, due to the periodicity of the described system, it should be clear that some of the solutions of this problem are not necessarily of a periodic nature. As the non-periodic solutions of this problem cannot be solved by applying a frequency dependent solution algorithm, it is necessary to understand that the solution covering all cases, periodic and non-periodic, can only be derived from the time domain approach. Utilising some background information of solution algorithm for time dependent solutions, it is clear that solution strategies for the time domain require at least one convergence criterion to determine the level of accuracy achieved within the time step integral. Applying this to the above problem and bearing in mind that the solution is not necessarily periodic, a convergence criteria cannot be defined by comparing the system response vector  $u(t)$  with the results of two revolutions. An energy convergence criteria cannot be applied either, as the total system is of dissipative character and therefore no constant energy level can be defined. A literature survey of research work concerned with crankshaft time integral solutions shows that no algorithm is used within several independent projects ([118],[119],[120]), applying the theory of non-periodic systems.

It has therefore been decided to concentrate on the periodic solution to develop a method for describing the motion of the crankshaft-crankcase assembly by utilising the frequency dependent solution algorithm. With that limitation, the components of eqn. 6.4.1 can be expanded using Fourier series.

The forcing function  $f(t)$  is written as:

$$f(t) = \frac{f_{oc}}{2} + \sum_{k=\frac{1}{2},1,\frac{3}{2},2,\dots}^{+\infty} f_{kc} \cos(k\Omega T) + f_{ks} \sin(k\Omega T) \quad 6.4.2$$

The Fourier series of the response vector has already been derived in eqns. 6.1.8 through to 6.1.10 and those of the stiffness matrix in eqns. 6.1.5 through to 6.1.6 .

If we assume the system to be gyroscopically conservative, as already described in section 6.1, the gyroscopic matrix  $G$  needs no expansion by Fourier series. This means that the inertia effects are presumed to be dynamically symmetric about the axis of rotation, which will result in a constant matrix  $G$  and a gyroscopically conservative system. Finally, again utilising the assembled vibration harmonic order matrices  $\tilde{\Lambda}$ , which has already been defined in eqn. 6.1.20, the general non-linear matrix differential equation of motion, which is given in eqn. 6.4.1 in time domain, can be transformed as:

$$[-\Omega^2 \tilde{M} \tilde{\Lambda}^2 + \Omega(\tilde{D} - \tilde{G})\tilde{\Lambda} + \tilde{K}]\tilde{u} = \tilde{f} \quad 6.4.3$$

This formulation is now given in the frequency domain. Further, eqn. 6.4.3 can be rewritten as:

$$\tilde{\mathbf{B}}(\Omega)\tilde{\mathbf{u}} = \tilde{\mathbf{f}} \quad 6.4.4$$

with

$$\tilde{\mathbf{B}}(\Omega) = -\Omega^2\tilde{\mathbf{M}}\tilde{\Lambda}^2 + \Omega(\tilde{\mathbf{D}} - \tilde{\mathbf{G}})\tilde{\Lambda} + \tilde{\mathbf{K}} \quad 6.4.5$$

= spin vibration, dynamic stiffness matrix

The spin vibration, dynamic stiffness matrices are generally non-symmetric. Nevertheless, they are of banded form if the matrix coefficient Fourier expansions are applied using truncated series. This is probably the case, because unlimited series cannot be applied within this kind of mathematical formulation. In addition, unlimited series are not applied in engineering practice, as the accuracy of the results would not increase from this increased number of coefficients. Under these circumstances, various algorithms can be applied to evaluate the forced frequency response solution.

One consideration to emerge from the study of coupled vibrations, is that one should understand that the solution of this equation is not limited to that frequency being the exciting one. In other words, any given frequency component in the forcing function can result in many frequency components in the response. This is quite a major difference to standard frequency response analysis, where the solution frequency is identical to the forcing frequency set and only the amplitude and phase responses differ.

Summarising the theoretical approach to solve the crankshaft crankcase coupled vibration in the frequency domain as described above, the application of common frequency response methodologies to solve the mathematical problem is a straightforward matter. This approach must then be altered to cover the non-linear effects as well as the time-dependent or position-dependent properties of the cranking system as described and discussed earlier.

When examining eqns. 6.4.3 and 6.4.4, the periodic solution of this equation can be obtained by applying the forced vibration algorithm offered from finite element packages. The solution of the crankshaft engine-block assembly will therefore be solved by applying a standard FEM package. Studying the available commercial codes, the study is restricted to two packages being available within Ford. Hence, HKS/Abaqus and MSC/Nastran are those being compared to be used within this study. MSC/Nastran was chosen to solve this problem. This package offers a wide range of capabilities to modify the matrix assembly strategy and to add additional matrices, such as the gyroscopic one, to the differential equation and is therefore predestinated for this application. Further advantages of MSC/Nastran over HKS/Abaqus are computational efficiency and numerical stability. The above described theory is covered through a brief description of the applied tools within the following section.

## 6.5 Solution Method / FEM-Application

As described in section 6.1, the gyroscopic matrix  $G$  needs no expansion by Fourier series. This means that the inertia effects are presumed to be dynamically symmetric about the axis of rotation. This results in a constant matrix  $G$  and a gyroscopically conservative system. The important matter is the constancy of the gyroscopic matrix. Applying this property of the matrix  $G$  it is permissible to reduce the computational effort significantly by establishing the constant matrix  $G$  only once. Therefore it is practical to calculate the gyroscopic matrix for each pre-defined engine speed within an individual analysis run and store this matrix within a database for later application in either complex modal or forced response analysis. The constant components of the differential stiffness matrix as described in section 6.3.1 can be calculated in the same approach. The constant terms of the differential stiffness matrix are determined for each pre-defined engine speed within an individual analysis run and stored afterwards within the same database as the gyroscopic matrix for later application in either complex modal or forced response analysis.

Hence, a single analysis run can be defined for each engine speed. This run will add both, the gyroscopic matrix to the damping matrix, and the differential stiffness matrix to the initial stiffness matrix. The MSC/Nastran approach of this problem is to apply an altered linear static solution run. The linear static solution (SOL 101) allows us to calculate the constant inertia effects of rotating structures and the constant deflection through an external load. The Nastran alter will then add the gyroscopic and differential stiffness terms to the superelement stiffness and damping matrices. The introduction of the structured solution sequences allows for the introduction of different gyroscopic and differential stiffness effects to individual components represented by separate superelements. The modified matrices are stored in the database incorporating the gyroscopic effect and the differential stiffness effect. After this initial static run the model can be restarted in any solution sequence and the differential stiffness and gyroscopic effect will be included. The restart sequences applied in this work are namely complex modal and a modified forced response analysis. The complex modal analysis sequence is used to investigate the effect of the rotating structures with respect to the gyroscopic effect as discussed in Chapter 3 and to evaluate the system stability as described in section 3.4. The modified forced response analysis is applied to calculate the dynamic response of the rotating structures in the frequency domain as described in Chapter 6.

While the above listed items cover the work concerned with MSC/Nastran, additional work has to be performed to allow for the appropriate analysis of the derived results. This work will be described in Chapter 7.

## **Chapter 7**

### **Noise Analysis Methodologies**

This chapter presents a compacted resume of the known techniques to determine engine radiated noise. The focus of the summary is not to explain all the methods in detail, but to compare experimental and analytical techniques. In depth discussion and verification is presented for the modified and developed noise radiation tools.

As discussed in detail in Chapter 1 the engine is one of the major contributors to structural vibration. The transfer paths are the so called 'Structure Borne Noise' and 'Air Borne Noise' paths. In this chapter, the focus is on the latter.

Studying the source and the transmission of vibrations in an engine in more detail, two different paths can be drawn, as shown in Figure 7.1. The vibration originated from the combustion process is transmitted through the cylinder head to the outer surfaces of the engine upper half. This path is called the 'Outer Structure Borne Noise Path'. The second path is characterised by transmitting the combustion vibration through the piston, piston-pin, connecting rod, crankshaft and main bearings to the outer surfaces of the engine lower half. Consequently, this path is called the 'Inner Structure Borne Noise Path'.

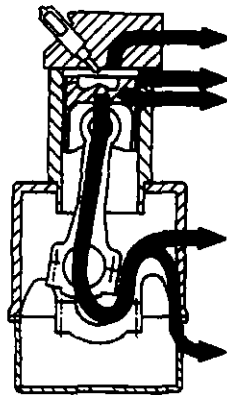


Figure 7.1 Structure Borne Noise Path

Additionally, the vibration of the engine bottom half is influenced by the cranktrain assembly. The vibration of the cranktrain component is overlaid to the combustion originated vibration via the transmission through the inner noise path. Further contributors to the engine surface vibration are the engine block resonances and collisional impacts originated from moving components.

Vibrating surfaces are enforcing their movement to the surrounding medium (air), which is the basic phenomenon of noise radiation. Bending vibrations of panels, especially,



are the route source for radiated noise, as the direction of the panel vibration is perpendicular to the oscillating surface. It is, therefore, essential to investigate the behaviour of the surface vibration of an engine as it is one of the major sources of radiated noise.

### 7.1 General Overview and Analysis Methods

The structure and air borne noise can be studied either analytically or through measurements (Figure 7.1.1). Due to the limited development time for modern engines, it is necessary to estimate the detailed noise radiation characteristic of a new engine at the concept or Phase-I design stage. At this time major modifications and design changes are feasible to optimise the engine for structural vibration and noise behaviour. But as there is no hardware available at this stage, analytical tools and models must be resorted to calculate the noise and vibration characteristic prior to any hardware tests.

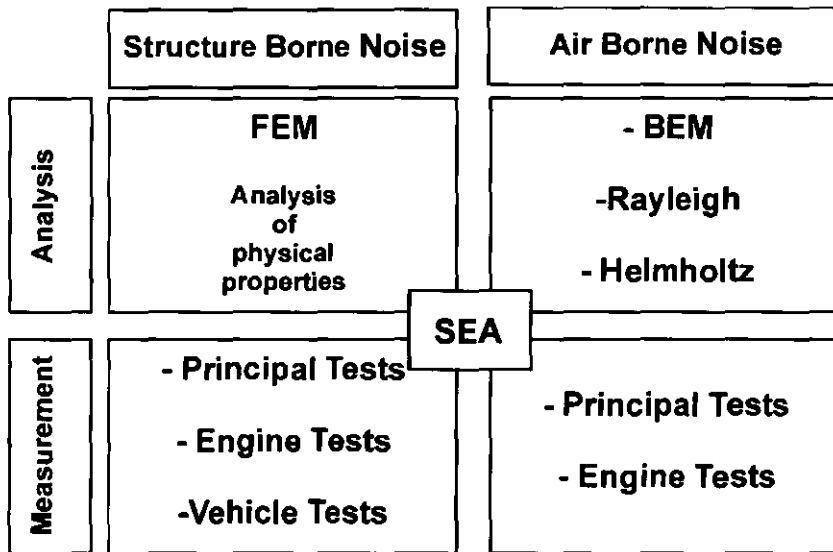


Figure 7.1.1 Analysis Methods for Structure and Air Borne Noise [121]

Therefore, analytical exciting vibration data must be developed to be applied in dynamic Finite-Element studies for the analysis of the resulting dynamic behaviour of an engine design. The theoretical background of the exciting data calculation of a running engine and its dynamic description have been developed and described in the previous chapters. Assuming that the derived theoretical approaches for the system description of a running/rotating engine are solved and finally incorporated in the Finite-Element package, it is a straightforward task to compute the physical degrees displacement, velocity and acceleration at any place of the model. The radiated noise data thus

calculated must be post-processed in a way to be directly comparable with test results. Looking briefly at the available measurement technologies, the findings are summarised in Table 11.

Physical Property	No. of Locations	Comment
Displacement (relative)	< 10	very small values are difficult to measure; instrumentation is difficult and expensive; only few points can be studied
Displacement (absolute)	< 10	interpretation is difficult as results are the combination of rigid body movements and elastic deformation; small values of elastic deformation are negligible compared to rigid body movements; instrumentation is difficult and expensive
Velocity (direct instrumentation on surface)	< 60	instrumentation is convenient; but with reduced number of locations.
Velocity (Laser interferometry)	total surface	no direct instrumentation required; surface is scanned by laser; analysis of total engine surface; only few measurement devices available; relative expensive
Acceleration	< 60	instrumentation is convenient; but with reduced number of locations; commonly applied method for analysing specific locations of the engine structure

Table 11 Available Measurement Techniques

Summarising the above measuring techniques, only the acceleration measurements are applied on a daily basis at a considerable amount of work and cost. But, the number of locations, which can be measured at the same time, is limited. With a maximum of 64 channels, three directional accelerations, triggering, speed, and timing signal, a maximum number of 20 locations are achievable for measurement at the same time. But a 64 channel test cell is not a standard configuration and is very expensive to install. Using this measurement technology, potential areas of interest are the oil-sump,

crankcase-rail, water-jacket, combustion chamber, and engine mounts and brackets to identify the local dynamic characteristic rather than the global behaviour. Hence, a maximum number of 20 locations is insufficient for covering the whole engine dynamic behaviour. Analytically obtained results of a global nature cannot clearly be compared. Therefore, a measurement method must be applied accounting for the global dynamic behaviour of the engine as well as for local dynamic effects. This method should easily be applicable in practice.

If this is considered from the engineering point of view, only a few specific locations (e.g. engine mounts, bearing caps) are studied regarding the local acceleration data. As the major issue for modern engine development work is concerned with the reduction of engine noise, we do not have to measure the engine dynamic characteristics at all locations, but to retrieve the global and local radiated noise perception.

Hence, today's engine measurement procedures are mostly defined by measuring the local acceleration data at the above mentioned locations and the global dynamic characteristic by retrieving the radiated noise data. These noise measurements are performed on a regular basis to obtain the overall engine dynamic structural behaviour. The main argument is that vibrating surfaces do radiate noise and this noise can easily be measured. In practice two different measurement techniques are commonly applied, namely the 'Near Field Intensity Measurement' and the 'Far Field' or 'Sound Pressure/Power Measurements'.

The 'Near Field Intensity Measurement' is the more detailed approach being capable of locating local sources of high noise radiation as the measurements are performed in an averaged distance of 10 to 15 cm. Typical results from a running engine are shown in Figure 7.1.2. Applying this measurement technique, a detailed analysis of the individual areas and components of the engine is possible, as the engine surface is divided into small areas of the same size. At each of these areas a microphone is positioned to measure the radiated noise of this partial surface at that specific location. Hence, the number of required microphones is linked to the required details. To reduce the number of microphones, another technique can be applied in which only one microphone is used. This microphone is moved by a robot arm to the centre of the defined individual small areas and the radiated noise is then measured one after another. Storing the measured data for each individual surface in a single database, a complete picture of the radiated near field noise characteristic can be drawn afterwards applying computerized post-processing software. Utilising the near field intensity plots, it is a straightforward task to identify local areas of high noise radiation and surface vibration. From this, design optimisation of local effects can easily be achieved.

Inlet Side; No Load (dBA)						Inlet Side; Full Load (dBA)						A-0,2916m <sup>2</sup>
75,1	80,4	82,0	82,9	79,8	77,0	86,5	88,6	89,1	89,7	88,0	85,7	Valve Cover
76,7	82,8	84,7	82,9	83,6	80,8	89,3	88,0	91,8	89,9	90,5	87,7	Cylinder Head
83,7	86,3	86,6	85,0	84,7	82,2	90,3	90,8	92,2	91,3	91,9	88,1	Engine Block
82,3	80,2	81,3	84,2	83,7	82,2	92,1	88,9	88,9	91,2	90,9	86,9	
81,6	84,8	84,7	84,6	83,5	82,9	88,3	88,9	89,7	92,2	90,5	87,2	
87,0	89,5	91,0	87,3	82,4	80,5	87,7	87,5	87,9	89,5	85,6	85,7	Oil Pan
Front			Back			Front			Back			

Figure 7.1.2 Near Field Intensity Measurement (Zetec-SE)[7]

But as these facilities are very expensive and the measurements are time consuming, a downgraded configuration for the assessment of radiated noise has been developed.

The 'Far Field Sound Power/Pressure Measurement' is the more general approach as the measurements are obtained in 1 m distance. This set-up utilises a reduced number of measurement locations at the far field of the engine. With up to six microphones, positioned at the front, rear, top, bottom, left and right side of the engine, only the sound power or sound pressure values of the total radiating surfaces are measured and analysed. The used configuration is schematically shown in Figure 7.1.3.

This 'Far Field Sound Power/Pressure Measurement' is the commonly used procedure. In this set-up one single value is obtained for each microphone position. Using this set of reduced data, a fast and easy methodology is applicable to detect specific booms or peaks throughout the frequency range. But the major disadvantage of this method is the data reduction. There is no information of specific areas or components being a source of the radiated noise, booms or peaks. Hence, it is difficult to locate the main contributing sources and, therefrom, derive the appropriate optimisation strategies. A schematic description of this method is shown in Figure 7.1.4. It is not possible to deduce which of the surfaces 1-4 is the most contributing one to the noise.

Methods must be developed to calculate the radiated noise characteristic of an engine from the analytically derived surface velocity values. The analysis procedure should provide results compatible with either near field intensity or sound pressure measurements acquired over the engine speed range considering load variations.

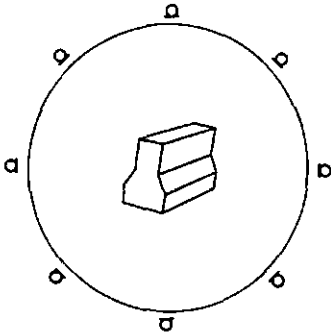


Figure 7.1.3 Sound Power Measurement

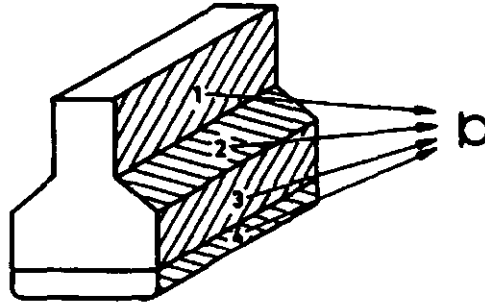


Figure 7.1.4 Summation of Sound Participation

The current analysis process and the incorporation of test results is shown in Figure 7.1.5. The link between analytical and measurement results is visualised with dotted lines. The measurement tools applied to evaluate noise radiation quantities are either waterfall diagrams, third octave band plots or near field intensity diagrams. Modal results are used in addition to running engine measurements. Necessarily, the required software tools must calculate waterfall diagrams, contour plots, third octave band plots and narrow band plots of the engine radiated noise behaviour. Contour plots are coloured noise intensity plots displayed on the engine surface. These plots are directly comparable to noise intensity plots being derived from measurements. They are applied to identify areas with significant contribution to the overall noise level. A detailed description of the analysis procedure is given in section 7.2.2.

Discussing near field intensity measurements in more detail, one must consider that the total engine surface is usually divided into 20-40 areas of equal size. The results displayed in Figure 7.1.2 show a 6x6 measurement configuration. The engine block lower half including the oilpan is represented by 18 measurement locations only. The major disadvantage is that specific local dynamic effects are barely detected, as the density of the measurement locations may be insufficient. But a considerable increase of measurement locations is not practical, because of the manual approach positioning the microphone. It is planned for the future to install a robot-arm positioning the microphone. This will allow for an increased density of the measurement positions and an increased repeated positioning accuracy.

The advantage of analytical tools, such as the Finite-Element method, is that the number of analysis locations can be considerably increased.

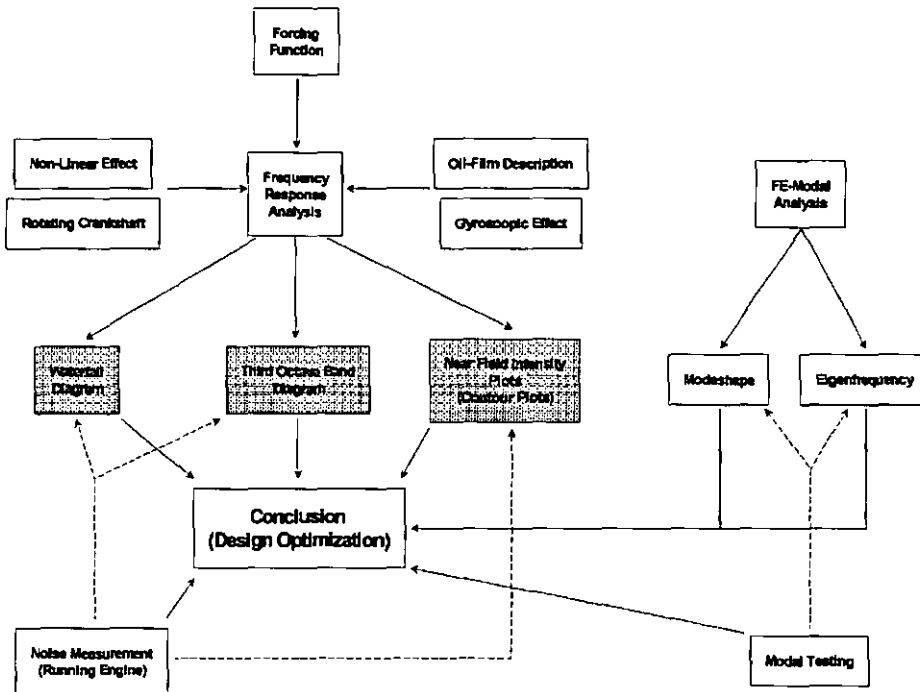


Figure 7.1.5 Analysis Process

The final goal of this study is to investigate the radiated noise behaviour over the entire engine speed range for various load conditions. From this data it is possible to detect individual speeds at which a significant increase of noise radiation is perceived. Results which are obtained in this way are directly comparable with either small band or third octave band measurements. A representative graph of the results is shown in Figure 7.1.6.

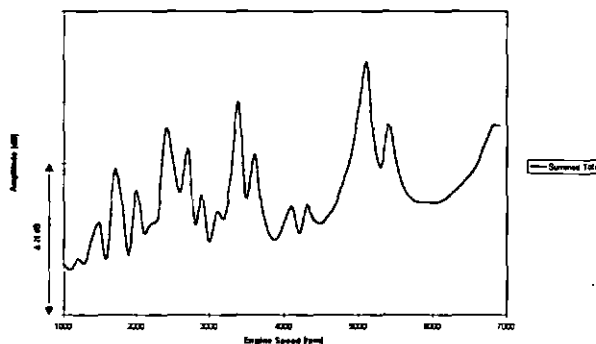


Figure 7.1.6 Summed Surface Velocity [dB rel  $v_0$ ]

The original plan was to incorporate all nodes laying on the engine surface in the analysis throughout an engine speed sweep. After a considerable number of experimental and pilot frequency response analyses, the conclusion must be drawn that even today's

fastest and most powerful supercomputers are not able to perform these kinds of engine speed sweeps with the planned number of analysis locations. Throughout a significant number of bench mark studies a maximum number of 60 engine speeds (1000rpm-6900) and 2000 analysis locations have been shown to be the optimum in terms of achievable accuracy and computational effort. While rotational degrees do not contribute to noise radiation, only translational degrees are exploited and used for data output from the finite element software. Further bench mark studies have shown that individual speed steps of more than 100 rpm over the engine speed range are not acceptable. Individual noise intensity peaks cannot be detected with certainty and may be covered by neighbouring levels. The studies have shown that speed steps of 20 rpm are the most suitable compromise between accuracy and computational effort. With the limitation of approximately 2000 analysis points, the corresponding locations on the model surface must be selected. While this problem occurs also in other analysis work (e.g. transient studies), a so called 'Mesh-Coarsener' software is under development. Applying this tool, unique surfaces of structures will be combined to one individual surface for post-processing purposes. The analysis will then be performed with the detailed model and the results are only perceived for the nodes belonging to both, the analysis model and the coarse post-processing model. The required disk capacity and computational effort for post-processing is reduced dramatically, whereas the analytically achievable accuracy is not reduced by using the detailed model. While this software was not available at that time, a manual selection process was performed to establish the 2000 locations on the engine surface.

As we have already indicated, the required computational effort of running a complete radiated noise study of approximately 60 engine speeds with a frequency range of up to 3500 Hz is not acceptable. So, a reduced set of nodes belonging to the engine surface are considered to derive the summed noise intensity data. At this point, whether it is appropriate to apply a reduced set of surface nodes for an initial noise intensity calculation, is something which has to be verified. Measurements were obtained by Anderton [122] showing engine surface vibration data at various surface locations. Vibration variations are perceived with minimum 10 dB at lower frequencies and up to 20-25 dB at higher frequencies as shown in Figure 7.1.7. Consequently, adequate averaged values can only be achieved by using a large number of measurement locations. Anderton postulates a minimum of 10 points per surface. Locating these points with some engineering experience, it should be possible to account for individual design weakness and other effects. Applying 2000 points for the noise estimation as done in this study, a sufficient accuracy should be achieved by using much more data than Anderton suggested.

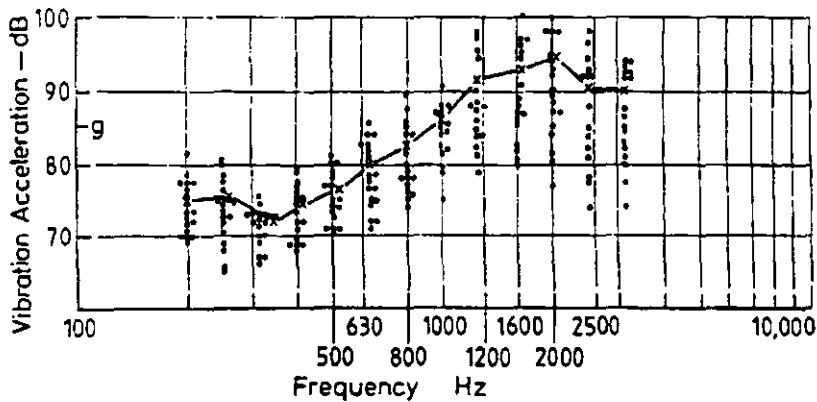


Figure 7.1.7 Variation of Vibration over Engine Block Surface [by Anderton]

In addition an investigation was performed comparing the noise intensity results of 12 points on the engine surface (Figure 7.1.8) with data obtained from a study utilising all surface points. The two graphs representing the entire and reduced set of surface nodes are shown in Figure 7.1.9.

Utilising Anderton's investigation an excellent correlation for trend information and detection of peak levels is achieved for the reduced and entire set of surface nodes. It is obvious that the peak level at specific engine speeds are different for two analysis sets considering different numbers of surface points. But, the results are acceptable for detecting peak levels at critical engine speeds. The results indicate that peaks are detected by the reduced and the entire set of surface nodes. Hence, every study incorporating more than twelve points must be of improved accuracy. Consequently, 2000 nodes would seem to be sufficient in terms of accuracy. A study comparing 2000 points with the entire set of surface nodes was not performed. The required cpu-time was estimated at approximately one week. As the differences between both sets are relatively small, one can expect that the results of the 2000 node set are very similar to the results of the entire set.

Once single or multiple engine speeds are detected as critical running conditions in terms of calculated noise intensity levels, a more sophisticated analysis procedure is required to study the reason and source for this enlarged rank. Third octave band, narrow band plots and modal information can be applied to relate the corresponding peak values to individual frequencies or frequency bands. But the detailed investigation to ascertain the source area of this peak intensity is impractical using these methods. There is no information available linking the intensity results to originating surfaces. An additional forced vibration analysis is then performed at those operating condition exhibiting the



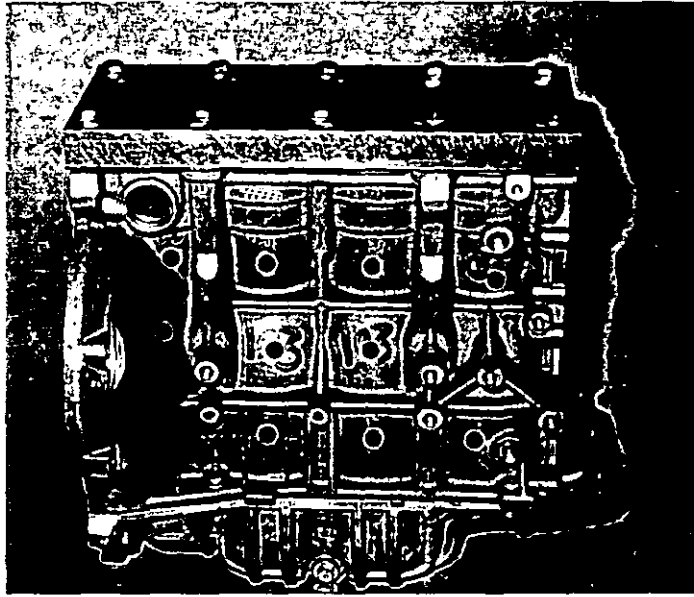


Figure 7.1.8 Analysis Points on Engine Surface

peak values. All surface nodes are included in the analysis and the required information is stored to relate the radiated noise to the vibrating surfaces. A contour plot is used to display the surface mobility data and locate the areas of high amplitudes.

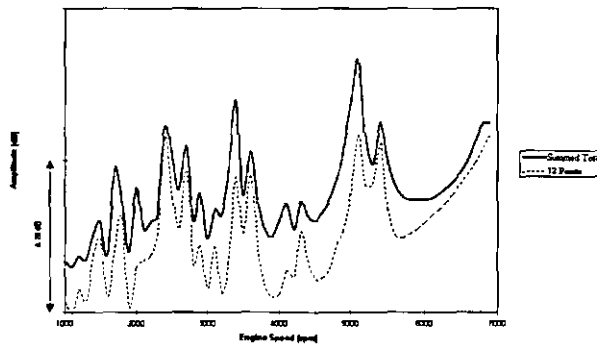


Figure 7.1.9 Summed Surface Velocity of Engine Block [dB rel  $v_0$ ]

After locating the critical areas, detailed knowledge of the participating factors is required before appropriate counter-measures can be applied. Third band and narrow band investigations are applied in addition to modal analyses. Radiated noise levels are then calculated for particular frequency bands at the most critical engine speeds. Comparing this with obtained modal eigenvalue results, it is easy to establish the characteristic participating modes. Modal participation studies are a means to manifest the actual contribution of an individual mode to the excited response. These modes are then identified as the source of the boom or peak in the third octave band. Effective counter-measures can be introduced to shift or eliminate the most critical eigenfrequencies.

The structure is then modified and used in a second loop of the analysis/design procedure.

This procedure will be described in more detail in section 7.2.2, concerning the individual investigation in a flowchart of an overall analysis. Having established the order of various design proposals based on the noise evaluation methods, it is essential that the radiated noise in space is considered as well. This method calculates the radiated sound pressure values at a certain point in space. The data thus obtained can then be applied in comparative investigations or further post-processing to make the noise audible. This will be explained in detail in section 7.3.

## 7.2 Noise Evaluation Methods

### 7.2.1 General Overview and Existing Methods

There are many publications, books and reports available dedicated to the numerical acoustic analysis of engineering problems. So it is not possible to completely cover this wide field in this work. Effort will be concentrated on an overview of available methods and techniques to solve acoustical problems in the engine engineering field.

The mathematical description of sound fields in a fluid (air) is given with a scalar sound pressure and a vector called sound velocity. Both values are dependent upon the point and time of investigation. Two equations can be applied to couple both values [123]:

$$\rho \frac{\partial v}{\partial t} = -\text{grad}p \quad 7.2.1$$

$$\text{div}v = -\frac{1}{\rho c^2} \frac{\partial p}{\partial t} \quad 7.2.2$$

The sound pressure equation can be rewritten by eliminating the sound velocity through the combination of eqns. 7.2.1 and 7.2.2:

$$\text{div grad}p = \Delta p = \frac{1}{c^2} \frac{\partial^2 p}{\partial t^2} \quad 7.2.3$$

The lossy Helmholtz equation can, therefrom, be derived such that:

$$\Delta p + k_{He}^2 p = 0 \quad 7.2.4$$

with:

$$k_{He} = \frac{\omega}{c}$$

Essentially two numerical approaches are currently available to solve acoustical problems of the Helmholtz equation, namely the Finite Element Method (FEM) and the Boundary Element Method (BEM). Both methods can be used in the specific formulation of acoustic problems and do deliver appropriate results. If the question arises as to the best tool for analysing acoustic problems of running engines, the answer is not a straightforward one. External or unbounded acoustic problems, such as engine radiated noise or drive-by noise, can be solved by using the Boundary Element Method. The Finite Element Method approach is theoretically developed, but this technique is currently not implemented in commercial software packages. Only closed cavities or bounded systems can be studied. A typical representative is the vehicle interior noise analysis. An unbounded formulation is under development at the University of Darmstadt. Initial analyses have been carried out which show a good correlation with measurements and an improved accuracy compared to the Boundary Element Methodology [124].

As the definition of the noise radiation problem is of exterior or unbounded character, the BEM seems to be the appropriate method for calculating the radiated noise of the excited engine structures. A comprehensive study [125] was performed to investigate the application of the BEM-code 'SYSNOISE' for the engine noise radiation problem. The results obtained are promising and correlate with measurements. The most significant drawback shows up in the enormous computer resources required to solve the boundary formulation. In a typical SYSNOISE study the analysis frequency range was defined between 400 Hz and 2400 Hz applying 8 Hz increments. The required Cray-C90 cpu-time was with approximately 33000 seconds for one subcase. This timing was achieved using an interpolation algorithm for a frequency range of 200 Hz within the frequency boundaries. A solution could not be obtained without this interpolation algorithm due to excessive cpu requirements. Applying the previously discussed number of required 60 engine speeds (loadcases), a simple pre-calculation shows that the cpu requirements sum up to 550 h or 22.5 days. These requirements are not realistic. Hence, new iterative solution algorithms are under development to reduce the cpu-requirements of the BEM codes significantly.

The final goal of this project is the development of a method for studying the engine dynamic behaviour over a wide range of different speeds. The amount of derived data will multiply with the number of analysed engine speeds. Additionally, the number of Fourier coefficients required to allow for investigations in that frequency range will factorize the amount of results by the number of applied coefficients. The investigated engine speed range is defined between 1000 rpm and 6000 rpm with speed increments

of 100 rpm . The upper frequency limit is defined with at least 2500 Hz. The used model contains about 35000 nodes from which we calculate the quantity of expected results in the order of 40 gigabytes. Reducing the speed increment to 25 rpm the amount of result data would exceed 160 gigabytes. This quantity of result data cannot be handled without major problems on today's super-computers.

Summarising the theoretical limitations and the practical restraints one has to consider, the BEM-code 'SYSNOISE' can be judged as the appropriate tool for engine noise radiation investigation applying a single subcase only. But with respect to the required numbers of engine speeds, this approach does not suit this kind of study with respect to the required computational effort. Because of the absence of improved solution algorithms, another theoretical and practical approach is essential to conduct for the analysis of the noise radiation in this research project. A more detailed description of the applied solution strategy is given later.

## 7.2.2 Development of Noise Estimation Model

Repeating the already explained phenomena of noise radiation, vibrating surfaces impose the velocity at the surface structure on the surrounding medium (Figure 7.2.1) from which these surfaces are identified as the source of radiated noise. The sound power is proportional to the surface integral of the radiating surface of the squared averaged velocity  $v$ . The proportionality factors are the radiation efficiency  $\sigma_{rad}$  of the structure, the density of the medium  $\rho_0$ , and the sonic speed  $c_0$ . The radiated sound power  $P$  is defined as:

$$P = \sigma_{rad} \rho_0 c_0 \int v_{RMS}^2 dA \quad 7.2.5$$

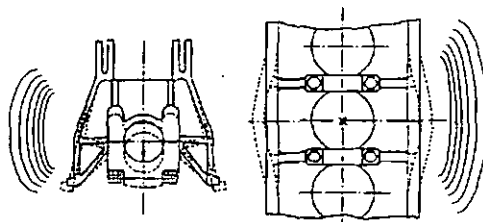


Figure 7.2.1 Noise Radiation Phenomena

The unknown property within this equation is the radiation efficiency  $\sigma_{rad}$ . The radiation efficiencies can be mathematically derived for simple geometries such as plates and boxes. For more general geometries, such as curved surfaces or engine structures, it is difficult to predict the value of  $\sigma_{rad}$  and the required computational effort increases

dramatically. A schematic picture of the radiation efficiency of a simple plate is shown in Figure 7.2.2. Studying the radiation efficiency characteristics in more detail, three different areas can be seen. They are separated by border frequencies  $f_u$  and  $f_o$ . The lower bound frequency is defined as  $f_u$  given in eqn. 7.2.6, while the upper bound frequency is defined as  $f_g$  given in eqn. 7.2.8 .

$$f_u = \frac{f_o^2}{f_g} \tag{7.2.6}$$

with

$$f_o = \frac{c}{\sqrt{2\pi A}} \tag{7.2.7}$$

$$f_g = \frac{c^2}{2\pi h_{pl}} \sqrt{\frac{12\rho_{pl}(1-\mu_{pl}^2)}{E}} \tag{7.2.8}$$

The noise radiation efficiency exhibits a +20dB per decade slope below  $f_u$ . The slope is declining to approximately +5dB/dec above  $f_u$  and below  $f_g$ . Frequencies above  $f_g$  exhibit a constant radiation efficiency of  $\pm 0$ dB/dec.

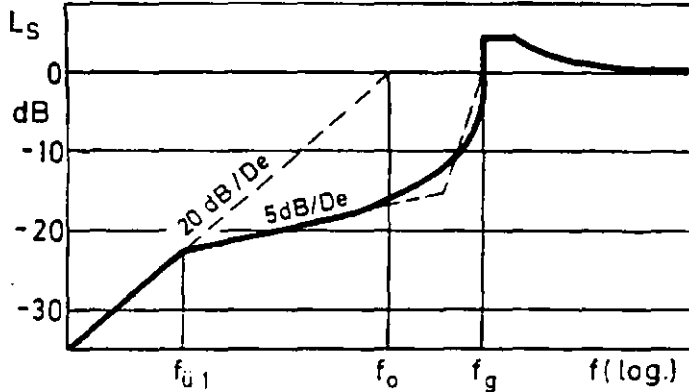


Figure 7.2.2 Radiation Efficiency of a Plate

Analysing eqns. 7.2.6 and 7.2.8 , it is apparent that the radiation efficiency is dependent on the material property E, surface A and thickness h of the vibrating wall. The most important dependency is shown implicitly, i.e. the structure itself, because the exhibited equations are valid for plates only. Hence, the design of a vibrating structure is of higher relevance than the basic material attributes.

Anderton *et al* [122] performed detailed investigations to calculate the radiation efficiency of various geometries. The obtained theoretical data were verified with measurements. For typical theoretical and practical applications some exemplary

radiation efficiencies are shown in Figure 7.2.3. It is evident that the radiation efficiency can be treated as a constant property above frequencies of 500 Hz. Below this border frequency a slope of 10-20dB/dec is noticed depending on the actual geometry of the investigated part. Radiation efficiencies are shown for engine type application in sub-figure d). The theoretical band width of radiation efficiency is calculated with nearly  $\Delta 10$  dB. The slope below 500 Hz is derived with 10dB/dec. Efficiencies above 500 Hz show constant values. Experimental results are shown for four- and six-cylinder applications for a limited frequency range only. The gained efficiencies are constant and are located within the theoretically derived band width.

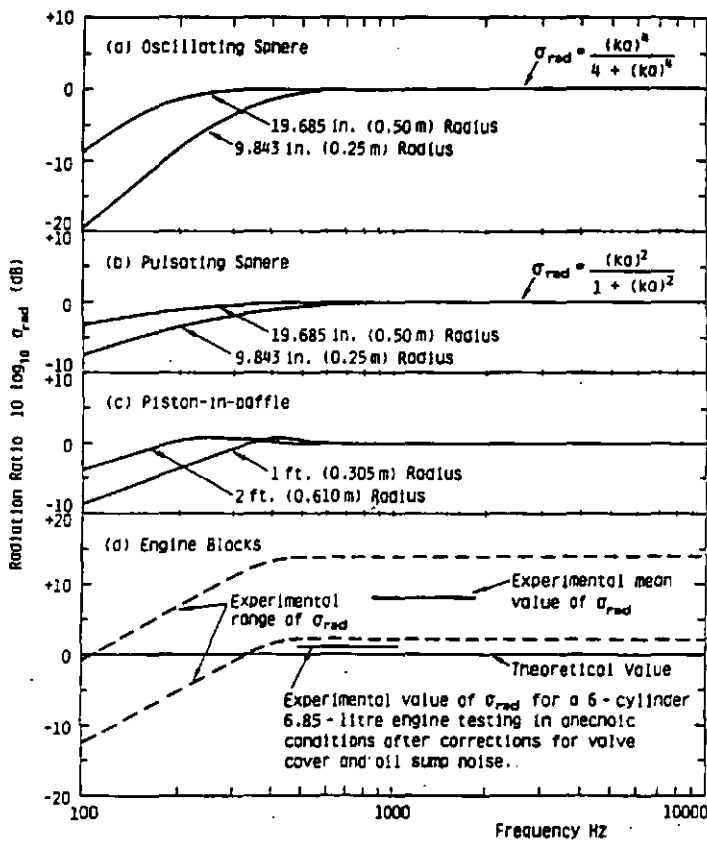


Figure 7.2.3 Measured and Calculated Radiation Efficiency [Anderton]

Radiation efficiencies of real cast iron panels are measured considering dimensional variations. Obtained results are shown in Figure 7.2.4. Displayed data for real engine size geometries exhibit values within the theoretical bandwidth. Nevertheless, the results are not as uniform as the theoretically derived data. A similar slope is distinguishable below approximately 500 Hz, while all investigated geometries exhibit an increase at 1500 Hz. For frequencies above 1500 Hz the radiation efficiency decreases to around  $\pm 0$ dB. The plate results representing the geometrical dimensions of a four-cylinder

engine block reveal the most straight-lined behaviour of all tested species. The applied dimensions fit those of the engine block considered in this work. The slope below 500 Hz is given with 10dB/dec. The local maximum in radiation efficiency exhibits the lowest increase of all with about +3dB at 1500 Hz.

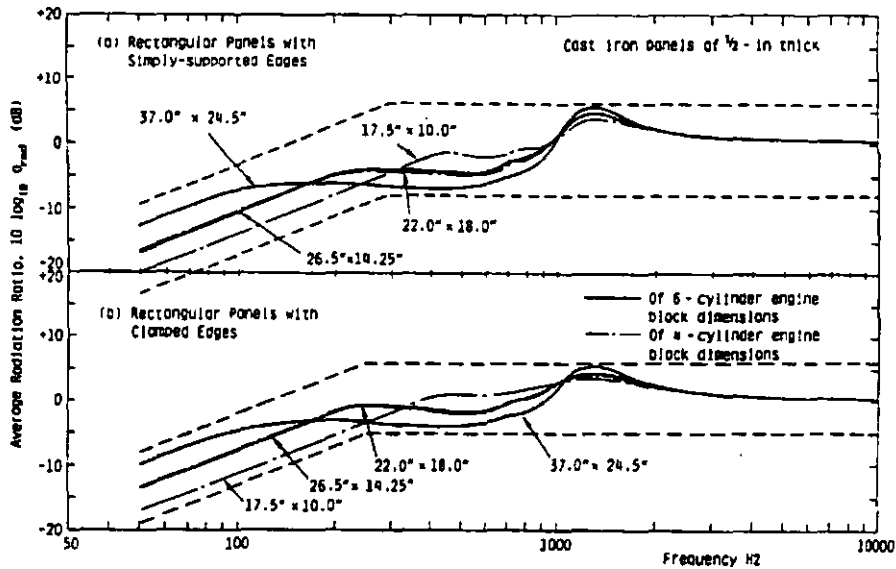


Figure 7.2.4 Measured Radiation Efficiency [Anderton]

At this point it must be considered again that the main purpose of this project is to establish methods for comparative investigations of various crankshaft and engine block design alternatives. The changes made to the crankshaft and to the engine block internal structures will not affect the size of the external surface nor the handling of the design stiffness for noise radiation. Even external changes made to the engine block will not change the radiation efficiency, as these changes are commonly ribbing actions and local design modifications. Complying with the restriction and assumption that only competitive analyses will be performed, it is permissible to eliminate the variable radiation efficiency from the equation [126]. A proportionality is introduced instead. In this first approach the radiation efficiency will, therefore, be treated as a unity constant,  $\sigma_{rad}=1.0$ . The drawback of the proportional instead of absolute measures can be accepted for this first approach, as two or more design alternatives will be investigated and the radiation efficiency can be treated as a constant parameter across various design proposals. Therefore, we derive from eqn. 7.2.5:

$$P \propto \int v_{RMS}^2 dA \tag{7.2.9}$$

This result is called integrated surface velocity and is proportional to the radiated sound power level.

The final research intention is to investigate engine bottom-end noise radiation characteristics with respect to various design alternatives. As discussed in section 7.1 the entire engine speed range must be analysed considering sufficient increments within the operation speed range. The applied analysis procedure and developed software tools will be described later.

Detailed bench-mark studies [see section 7.1] showed that the required computational effort indicates the necessity of performing the noise estimation analysis on a super-computer, in this case Ford's Cray C90. The advantage of this approach is that the dynamic analysis and the subsequent noise-estimation can be done on the same computer without transferring result data between computers. While the main dynamic analysis is performed applying the Finite-Element software MSC/Nastran, the accessed result file is based on that software. Binary result files are available, but the interface is more difficult to develop and dependent on the software release level. Hence, a decision was made to develop the required post-processing tools applying the standardised Punch-file format. The investigated operation conditions are defined between 1000 and 6900 rpm with speed increments of 100 rpm. This results in 60 load- or subcases, which must be solved independently. The result file will contain the surface velocity information of all nodes belonging to the engine surface for all directions, all frequencies and all loadcases. The amount of data from that investigation is in the order of about 3.6 GB. While the rotational degrees of freedom do not contribute to noise radiation, all data referring to those degrees of freedom may be eliminated directly after the analysis. A software tool was developed to modify the MSC/Nastran punch output file in such a way as to assure that no rotational velocities be included to reduce the amount of required disk space. Applying this software, the averaged file size is halved to about 1.8 GB. Actually this amount of data can not directly be used for further post-processing as it is very difficult and time consuming to look for specific data within this huge file. Hence, further procedures were developed to simplify the post-processing of these large files. Some information is deleted due to duplication, and other information is used for the analysis of the described noise radiation properties. The resulting file size is approximately 15% of the original file size or equivalent 0.5 GB . The results thereby obtained can be used and post-processed on an engineering work-station according to the analysis plan shown in Figure 7.2.5. For compatibility reasons, analysis procedures are



adopted to match the analytical method of noise estimation with those procedures being applied within measurements as shown in Figure 7.1.5 . This allows a direct comparison between measured and predicted results.

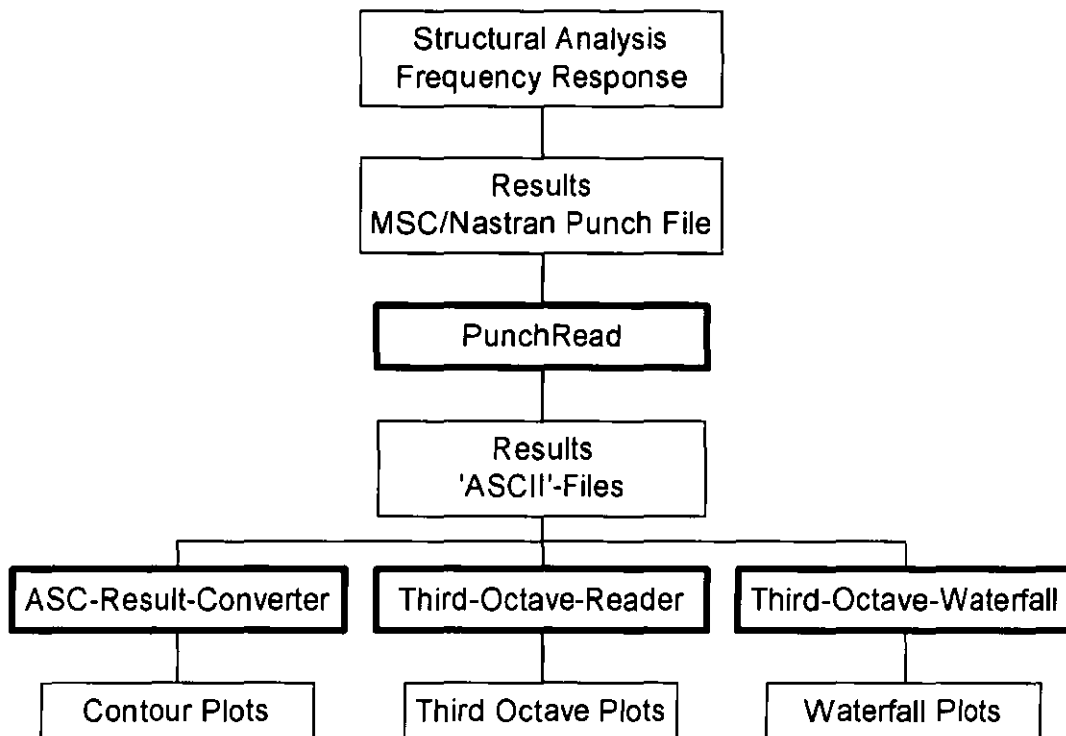


Figure 7.2.5 Analysis Process

A short description of all developed post-processing tools is given subsequently explaining the purpose of the individual programs. An overview is shown in Table 12 relating the tool and the corresponding information considered for output.

Following the process plan description from Figure 7.2.5 MSC/Nastran velocity results are considered as the primary input for post-processing. As mentioned previously this file contains all required information, but can hardly be used for further post-processing. After deleting all duplicated information and reducing the file-size to an absolute minimum by applying compressed formats, a tool called 'PUNCHREAD' is applied for the initial post-processing. This tool is the main post-processing software developed for noise investigation. The output is calculated for each individual node and engine speed for all translational degrees of freedom. The output is formatted using ASCII format and the frequency information content is removed. The intensity levels are calculated for each frequency according to:

Program	Output-Files	Frequency	Nodal-Information	Engine Speed
Punchread	X-db.asc	yes	yes	yes
	Y-db.asc	yes	yes	yes
	Z-db.asc	yes	yes	yes
	XYZ-db.asc	yes	yes	yes
	X-Third-Octave-Level.plt	yes	no	yes
	Y-Third-Octave-Level.plt	yes	no	yes
	Z-Third-Octave-Level.plt	yes	no	yes
	Total-Third-Octave-Level.plt	yes	no	yes
	Summed-db.plt	no	no	yes
ASC-RESULT-Converter	XYZ-db.dis	no	yes	no
	RES-db.dis	no	yes	no
Third-Octave-READER	free	yes <sup>2</sup>	no	no
Third-Octave-Waterfall	free	yes <sup>3</sup>	no	no

Table 12 Tools and Related Output

$$L_{Order} = 10 \log \left( \frac{v}{v_0} \right)^2 \quad 7.2.10$$

with

$$v_0 = 5 \cdot 10^{-8} \frac{m}{s}$$

The frequency dependent levels are summed to calculate the total level:

2: Frequency Information in Third Octave Information only  
3: Frequency Information in Third Octave Information only

$$L_{tot} = 10 \log \left( \sum_{i=1}^n \left( 10^{\left( \frac{L_i}{10} \right)} \right) \right) \quad 7.2.11$$

The output files are then used for all subsequent post-processing actions. Result data are provided for three principal directions. The major radiation directions are defined by the structure. In case of engine structures, these directions are commonly defined as being co-linear with the principal coordinate directions X, Y and Z. A further step in post-processing is the application of so called 'Summed Averaged' values describing the summed intensity information over all three directions. This information can not directly be used for identifying frequencies or locations of high noise radiation, but for comparing and illustrating different design alternatives. Total intensity levels are derived from narrow band information by utilising the third-octave band format for all major analysis directions and the 'summed averaged' results. The amount of data is reduced dramatically by applying third octave rather than narrow band information. Third octave data are commonly applied in theoretical and practical noise investigations and the data reduction does not impede the interpretation of the results too much [127]. The results showing the highest data compression ratio are stored in the output file 'SUM-dB.plt'. Frequency and nodal point information are deleted. The calculated results exhibit the noise intensity information for all three coordinate directions and the 'summed averaged' data with respect to the investigated speed range. There is only one value stored for each direction and speed. The summed averaged value is comparable to measured sound power data averaged over four or five microphone positions. These results can then be used as a starting point to detect individual engine speeds with characteristic peak levels. A typical plot is shown in Figure 7.2.6 for all engine speeds. All principal directions are displayed including the 'summed averaged' result. Once critical engine speeds are identified it is necessary to examine the main cause of the noise radiation. Hence, critical frequencies and locations must be located at the end where those peaks occur.

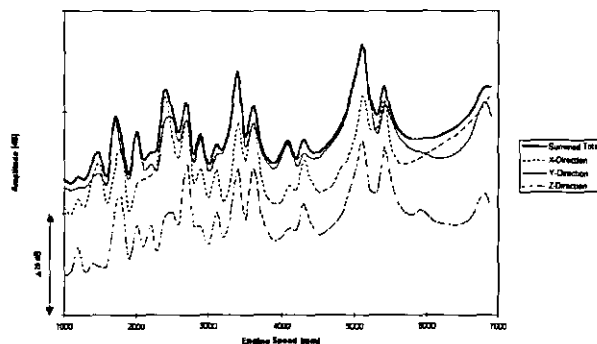


Figure 7.2.6 Integrated Surface Velocity vs. Engine Speed [dB rel  $v_0$ ]

Near field intensity measurements, as shown in section 7.1, are applied to identify the distribution of noise levels on the engine surface for a single point of operation. Similar information can be gained from this investigation, if the corresponding engine speed is selected. A tool called 'ASC-RESULT-CONVERTER' was developed to generate contour information for the engine surface using the calculated intensity values from 'PUNCHREAD'. As output, a neutral 'MSC/Patran' format was chosen, which can easily be used for graphical post-processing. Utilising this data, individual areas of high intensity values can be detected and the required counter-measures are more easily established. The information thus derived is compatible with near field intensity measurements. Two examples are shown for a selected engine speed. The summed averaged surface velocity is displayed in Figure 7.2.7. This information is compatible with measured 'summed averaged' noise radiation figures. The corresponding information for all principal directions is shown in Figure 7.2.8 displaying the directional components of the surface velocities. In both applications the calculated data are displayed as contoured information.

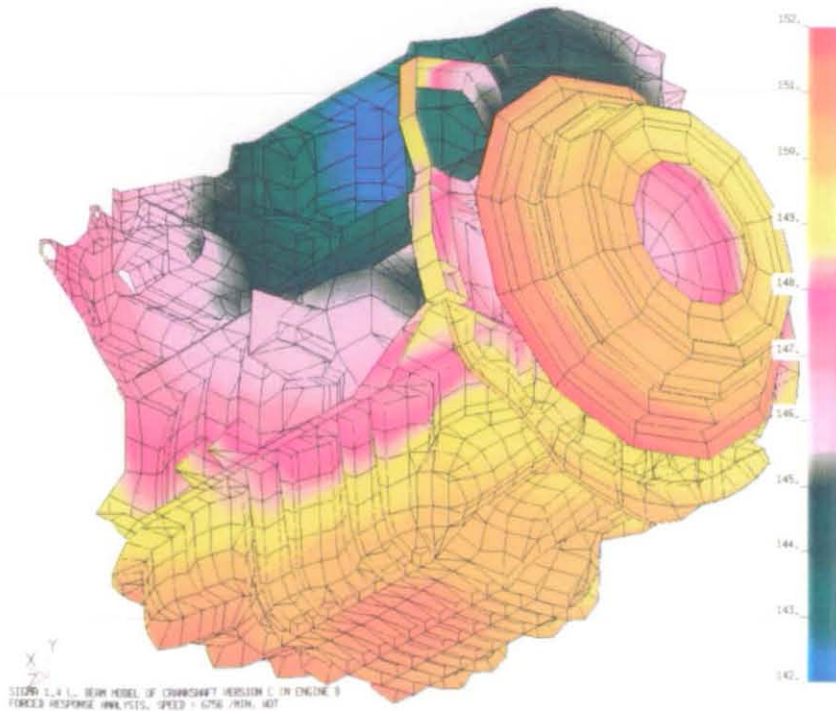


Figure 7.2.7 Overall Surface Velocity

For post-processing the obtained results further requirements are satisfied by extracting and plotting third-octave data. Within the response spectrum critical frequencies are directly visible applying this information. A tool, 'Third-Octave-Reader', was developed

to prepare the raw information in a way that a single point of operation is extracted, all principal directions or the 'summed averaged' results are shown and a linear or A-weighted treatment is done. Typical results are shown in Figure 7.2.9.

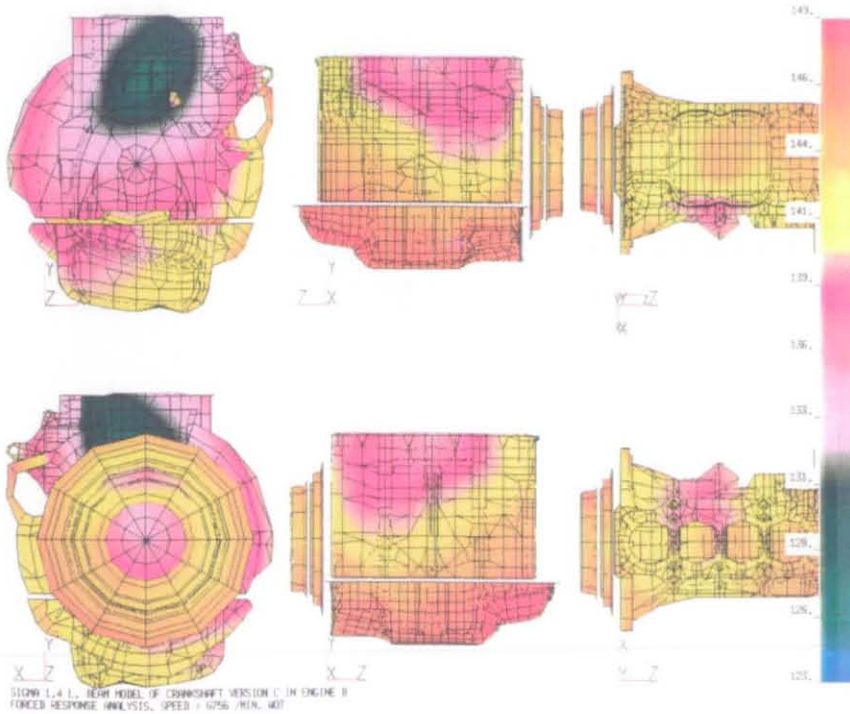


Figure 7.2.8 Component Surface Velocity

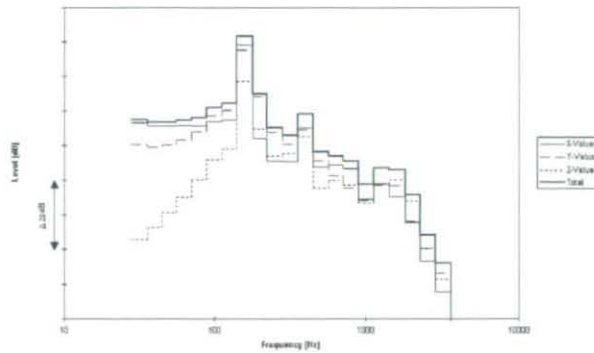


Figure 7.2.9 Third Octave Band Integrated Surface Velocity [dB rel  $v_0$ ]

Employing third-octave data for an individual point of operation critical frequencies are easy to perceive, but it is difficult to judge whether these resonances are introduced by system eigenfrequencies or excitations. A convenient solution is to plot the third-octave information, not only for an individual point of operation, but for all studied engine speeds. A tool similar to 'Third-Octave-Reader' has been developed to extract and prepare the available data. The generated set of information is used to plot a waterfall diagram as

shown in Figure 7.2.10. With this plot critical engine speeds or frequency bands are easily detected and interpreted. Critical areas on the engine surface are found by examining either contoured integrated surface velocity levels or modal analysis results, or both.

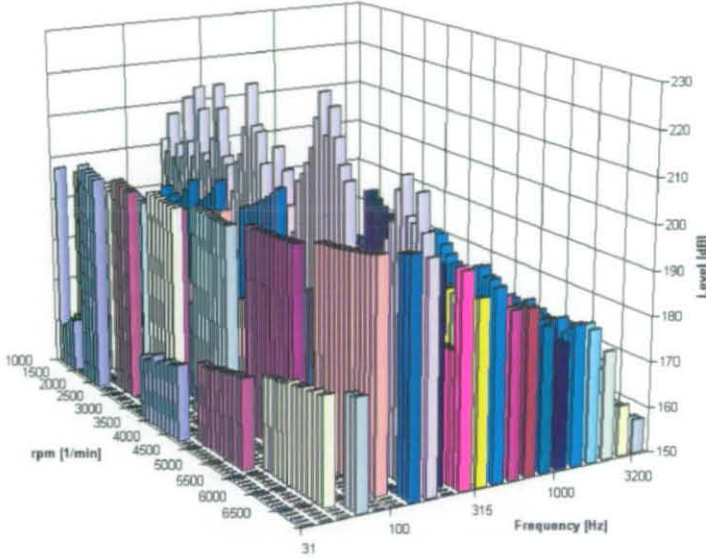


Figure 7.2.10 Third Octave Band Integrated Surface Velocity Waterfall Diagram [dB rel  $v_0$ ]

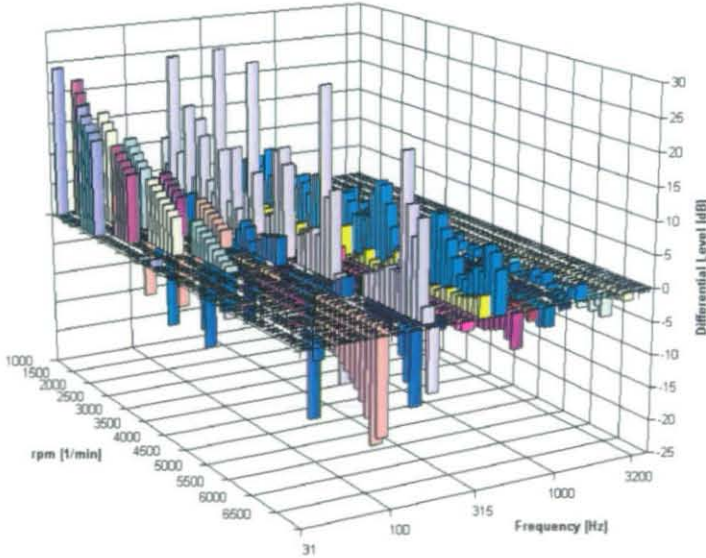


Figure 7.2.11 Differential Third Octave Band Integrated Surface Velocity Waterfall Diagram [dB rel  $v_0$ ]

Because comparable studies of design proposals is one of the ultimate objectives of this project, a further post-processing capability was developed to directly compare results between alternatives. The difference in integrated surface velocity results is calculated for every data point and shown as a differential waterfall diagram. The advantage or disadvantage of a proposal is directly assessed by interpreting the differences. Comparing the effect of two flywheel alternatives on the integrated surface velocities a typical differential waterfall diagram is shown in Figure 7.2.11. Regarding the radiated noise behaviour, results above zero indicate that the investigated flexible flywheel is better compared to a conventional solid flywheel. Levels below zero indicate that the conventional solid flywheel is better.

### 7.3 Rayleigh-Method

The approach described herein is used to predict the radiated sound pressures at arbitrary points in space. The method is discussed in detail. Advantages and disadvantages are shown and verified with measurements and the BEM software 'Sysnoise'.

#### 7.3.1 Theory

It is assumed that a vibrating body is emitting sound power to the surrounding medium. It is further assumed that the surrounding medium air is significantly lighter compared to the structure. A repercussion can therefore be neglected and the theory can be derived applying an uncoupled solution. The sound pressure is derived from the wave equation [128]:

$$\nabla^2 p - \frac{1}{c^2} \cdot \frac{\partial^2 p}{\partial t^2} = 0 \quad 7.3.1$$

Imposing a harmonic motion this can be rewritten in complex formulation such that:

$$p(x, t) \Rightarrow \text{Re} \{ p(x) \exp(i\omega t) \}$$

from which the Helmholtz equation is derived:

$$\nabla^2 p + k_{He}^2 p = 0 \quad 7.3.2$$

with  $k_{He} = \frac{\omega}{c}$

Applying the impulse conservation theorem, the sound velocity is defined through

$$\nabla p = -\rho_o \frac{\partial \vec{v}}{\partial t} \quad 7.3.3$$

Defining  $\vec{e}_r$  as a unity vector which determines the direction of radiation, one writes for the far-field solution:

$$p \cdot \vec{e}_r = \rho_0 c \vec{v} \quad 7.3.4$$

Using complex formulation the intensity  $I = p\vec{v}$  writes as  $I = 0.5Re\{p\vec{v}^*\}$ . The entire sound power  $P$  is calculated by integrating the intensity over a closed surface:

$$P = \oint_S p \vec{v}^* \cdot d\vec{F} \equiv \frac{1}{\rho_0 c} \oint_S p^2 \vec{e}_r \cdot d\vec{F} \quad 7.3.5$$

Multiplying the Helmholtz equation with a currently unknown function  $G_r$ , introduced by Green and integrating the result throughout the closed surface we get:

$$\int (\nabla^2 + k_{He}^2) p \cdot G_r dV = 0 \quad 7.3.6$$

Applying Green's formula we write:

$$\int (\nabla^2 + k_{He}^2) p \cdot G_r dV = \int (\nabla^2 + k_{He}^2) G_r \cdot p dV - \oint p \frac{\partial G_r}{\partial n} dF + \oint G_r \frac{\partial p}{\partial n} dF = 0 \quad 7.3.7$$

The function  $G_r$  is selected such that the following equation is true:

$$(\nabla^2 + k_{He}^2) G_r(\vec{x} - \vec{x}_0) = \delta(\vec{x} - \vec{x}_0) \quad 7.3.8$$

Considering the last condition one derives the sound pressure within a known volume through the solution of the subsequent surface integral:

$$p(\vec{x}_0) = \oint p \frac{\partial G_r}{\partial n} dF - \oint G_r \frac{\partial p}{\partial n} dF \quad 7.3.9$$

The previously discussed equations and formulations are valid for all kind of methods predicting noise radiation phenomena. The shown equation are now applied to formulate the Rayleigh integral. Eqn. 7.3.7 is applied to establish the sound pressure  $p$  for an arbitrary location in space. The radiator is defined as a planar oscillating body imbedded into an infinite and reflecting surface. The following formulation supposes an orientation within the  $x/y$ -plane. The solution for other planes is derived by replacing the corresponding indices. Eqn. 7.3.9 is rewritten as:

$$p(\vec{x}) = \frac{1}{4\pi} \iint [p \vec{\nabla}_s G_r - G_r \vec{\nabla}_s p]_{z_s=0} \cdot \vec{e}_z dx_s dy_s \quad 7.3.10$$

Green's function has the form for planar application as:



$$G_r(x_0, x_s) = \frac{1}{4\pi R_1} \exp(-ik_{He}R_1) + \frac{1}{4\pi R_2} \exp(-ik_{He}R_2) \quad 7.3.11$$

with 
$$R_{1,2} = \sqrt{(x_s - x_0)^2 + (y_s - y_0)^2 - (z_s \pm z_0)^2}$$

This formulation is valid, because the assumption is true for a point-source and as the inverse for the corresponding source is defined through reflection. Then,  $d/dz_s(G)=0$  for  $z_s=0$  and with eqn. 7.3.3 the Rayleigh integral becomes:

$$p(\vec{x}) = -2i\omega\rho_0 \iint v_z(x_s, y_s) \frac{1}{4\pi R_1} e^{-ik_{He}R_1} dx_s dy_s \quad 7.3.12$$

The Rayleigh integral is applied within a numerical discretisation and is solved by utilising surface velocities from a finite element analysis. The computational effort for solving this equation is significantly reduced compared to a solution applying the Boundary-Element approach.

The Rayleigh integral is an accurate solution for those problems satisfying the above described planar problem. All other problems violate the above prerequisites more or less. The perceived accuracy is dependent on the actual geometry, phase angles of the structural vibrations and frequency domain.

It is assumed that complex structures are split into a definite number of surfaces, which independently emit noise. The sources radiate noise to all directions without consideration of a preferred direction. Reflections and diffractions are not considered. Since energy dissipates due to reflections and diffractions, the Rayleigh integral will overpredict sound pressure values. However, since only those surfaces are considered for radiation which are oriented towards the measurement location, the measured results will underpredict the sound pressure value. The measure for the participation of an individual surface is defined through the angle between the surface normal and the orientation towards the measurement location. The angular value at which a surface does not participate in the noise radiation prediction is a user defined value and relies on the user experience. This approach is considered in the software 'NOISE' [129]. The solution for individual locations is more sensitive to the above described effects than the overall sound power prediction. The overall sound power prediction compensates for this by averaging the effect. From a user point of view, it is difficult to estimate whether the predicted results are a reduced or increased level. It is, therefore, suggested that the Rayleigh method is verified for the planned application. A detailed discussion of the verification analyses is given in section 7.3.2. It is further assumed that every radiating element is neighbouring to an infinite and reflecting surface. This assumption correlates

well for structures having a significant curvature radius compared to the considered wave length. The sound pressure is thus assumed to be predicted with an increased level [130]. Again, this phenomenon will be verified in the following chapter.

### **7.3.2 Application and Verification using Component Models**

The verification of the Rayleigh method will be shown by using component models. The chosen components are a catalytic converter, structural aluminium oilpan and a cast-iron engine block. The catalytic converter was chosen because of the simple geometry. Local effects due to cancellation, reflection and diffraction are more easily disclosed and correlated to the surface vibration. The oilpan has been selected for the material and geometric plainness. Finally, a comprehensive investigation on engine blocks is performed to verify the previous findings for complex structures. Complete verification studies have been performed for all three components employing the Boundary-Element code 'SYSNOISE' and the Ford owned Rayleigh software 'NOISE'. The analytical results are compared with measurements for the oilpan and engine block studies.

The comparison of the Boundary-Element method and the Rayleigh approach was the main driver for studying the catalytic converter. The obtained absolute sound pressure results are of negligible interest. Hence, any arbitrary forces can be applied to excite the model in both approaches, but the analytical differences between both methods will be studied in detail. That is why a relative simple geometry is applied in this study and no significant emphasise is made on the derivation of the absolute correct forcing function. This investigation is based on a modal comparison using a unity excitation function. The derived absolute radiation level are, therefore, much too high. But this will not affect the competitive characteristic. This investigation was performed in a joined research effort between IABG, Dr. von Estorff supporting the 'SYSNOISE' studies, and Ford-Werke AG, T.Grünert supporting the Rayleigh tool 'NOISE'. The major research work was done by M.Klemenz in his Master's project. The results shown and discussed are related to the verification of the Rayleigh method only. The interested reader may refer to the project of M.Klemenz [131] for further details and a detailed description of the applied model, modal superposition and SYSNOISE analyses.

The catalytic converter's design and structural mesh is shown in Figure 7.3.1. The sound pressure levels at defined positions and the total sound pressure are the measures for comparing the analytical results. The sound pressure measurement locations are shown in Figures 7.3.2 and 7.3.3 and defined in Table 13.

Location 'A'	$430 > x > -50$	$y = 300$	$Z = 125$
Location 'B'	$720 > x > 0$	$y = 800$	$Z = 320$

Table 13 Location of Measurement ([mm] about coordinate origin{rel. model centre})

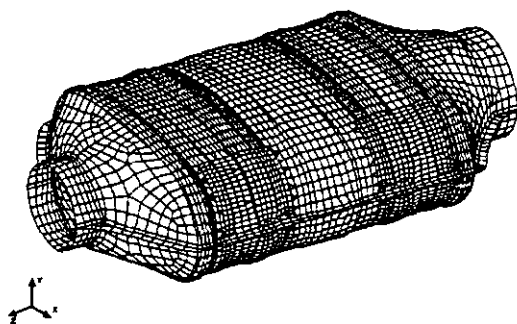


Figure 7.3.1 Model of Catalytic Converter (Courtesy of EBERSPÄCHER)

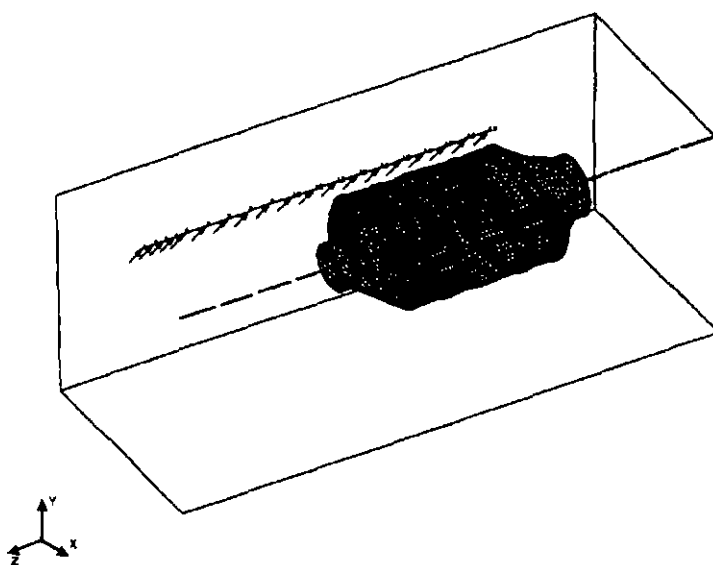


Figure 7.3.2 Position of Measurement Locations 'A'

The total radiated sound power is derived for the far field using the method of envelope surfaces. The approach considered in 'NOISE' is an average of the sound pressure values over multiple locations. This formulates a closed surface around the structure. The surface is split into multiple surfaces with analysis coordinates in the centre of each sub-surface. The sound power is calculated by applying eqns. 7.3.4 and 7.3.5. The effect of an increased distance between the source and measurement location is considered by using two envelope surfaces divided into 96 sub-surfaces as shown in Figures 7.3.4 and 7.3.5. The dimensions are detailed in Table 14.

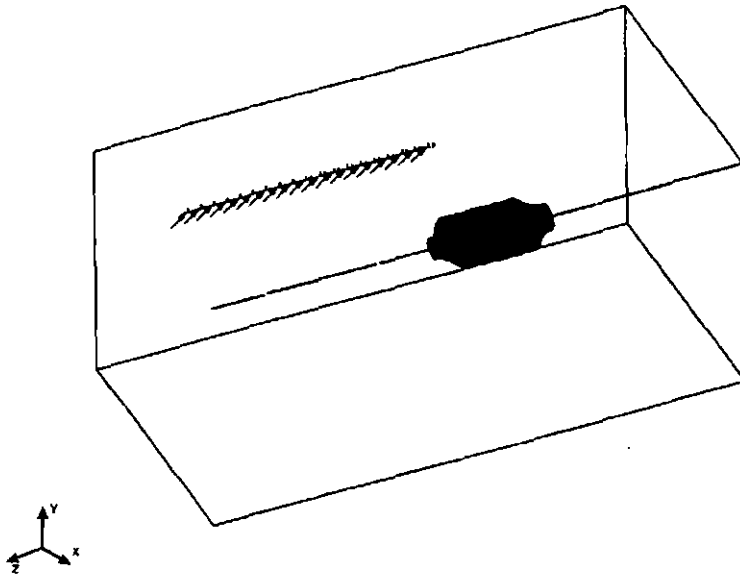


Figure 7.3.3 Position of Measurement Locations 'B'

Envelope Surface 1	$-600 < x < 1000$	$-1000 < y < 1000$	$-1000 < z < 1000$
Envelope Surface 2	$-400 < x < 600$	$-400 < y < 400$	$-400 < z < 400$

Table 14 Envelope Surfaces ([mm] about coordinate origin{rel. model centre})

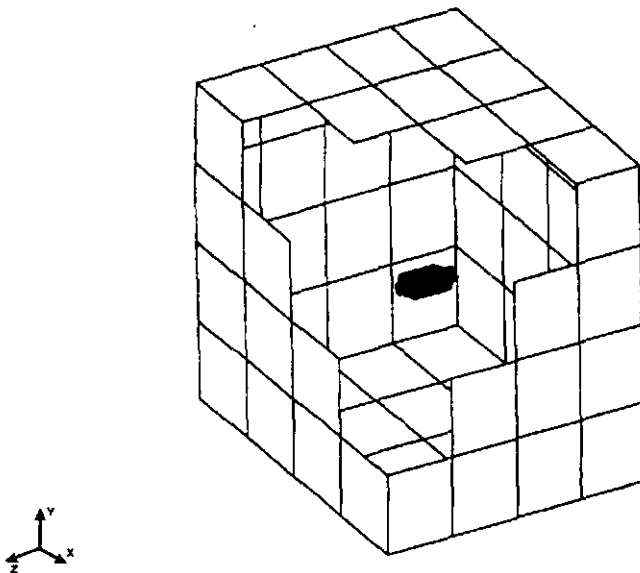


Figure 7.3.4 Envelope Surface 1

The application of a cube as the envelope surface is strictly speaking not correct. A spherical envelope surface is necessary in order to comply with the theory of radial propagation of sound waves. But the total sound power level may be multiplied with a

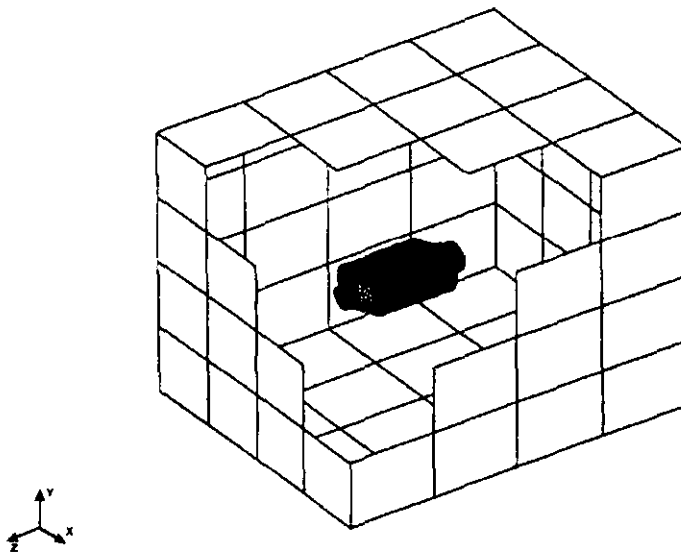


Figure 7.3.5 Envelope Surface 2

constant factor of 0.8. This matches the surface of the sphere with that of a cube. The calculated total sound power values are listed in Table 15 and Table 16 for both methods and envelope surfaces. The results of each mode are shown separately.

Mode	1	2	3	4	7	8
$P_{Ray}$	0.44	1.09	0.42	3.81	1.59	4.00
$P_{Sys}$	0.36	1.16	0.45	1.55	2.51	1.33
$10lg(P_{Ray}/P_{Sys})$	+0.87	-0.26	-0.30	+3.91	-1.98	+4.78

Table 15 Total Sound Power (Envelope Surface 1)

Mode	1	2	3	4	7	8
$P_{Ray}$	0.43	0.86	0.38	2.66	1.17	2.15
$P_{Sys}$	0.36	1.16	0.45	1.55	2.51	1.33
$10lg(P_{Ray}/P_{Sys})$	+0.77	-1.30	-0.73	+2.35	-3.31	+2.09

Table 16 Total Sound Power (Envelope Surface 2)

Typical spatial sound pressure results are shown for mode 1 and location 'A' in Figure 7.3.6 and for mode 2 in Figure 7.3.7. The corresponding results for all other modes are shown in the appendix in Figures Appendix 4.11 to Appendix 4.16.

The results vary between the Boundary-Element and the Rayleigh methods. The local sound pressure results have similar trends, but different absolute values. Constant positive offsets are observed with values between +3dB and +12dB for modes 1, 2, 7 and 8. Significant positive offsets are detected for modes 4, 7 and 8 between +13dB and +32dB combined with negative offsets for locations showing a significant extinguishing (mode 2; -10dB). Localised deflections of extinguished locations are observed in modes 2 and 4. The results for modes 3 and 4 differ significantly.

The total sound power levels vary between positive and negative deviation. The difference is significantly lower for mode 1 through 3 compared to mode 4, 7 and 8. The maximum difference is about +4.78dB.

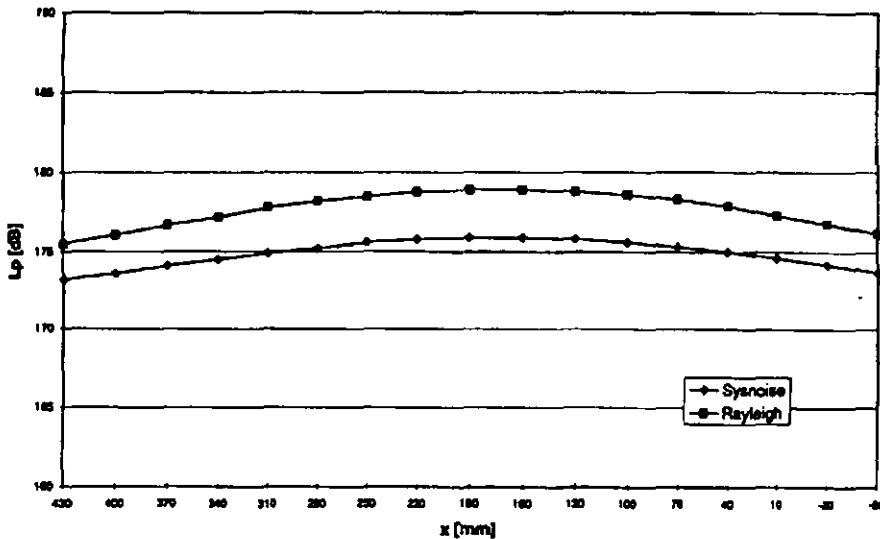


Figure 7.3.6 Spatial Sound Pressure (Mode 1; Location 'A')

The competitive study between the Boundary-Element and the Rayleigh method for the catalytic converter shows that the differences in total sound power are less compared with those for the spatial locations. The most significant differences are calculated at locations showing extensive cancellation effects. This comes from sound waves of different phase angles but similar amplitudes. This confirms the already discussed drawback of the Rayleigh approach that cancellation effects are not predicted to a high level of accuracy. Phenomena such as reflections and diffractions are not considered. The analysis establishes that lacking this feature may be compensated by an averaging approach in the total sound power calculation as shown in the previous two tables. The total sound power prediction shows that the level increases with increasing distance as shown in Table 15 compared to Table 16. Studies on other components showed a decreasing sound power level with increasing distance. The effect can not be genera-

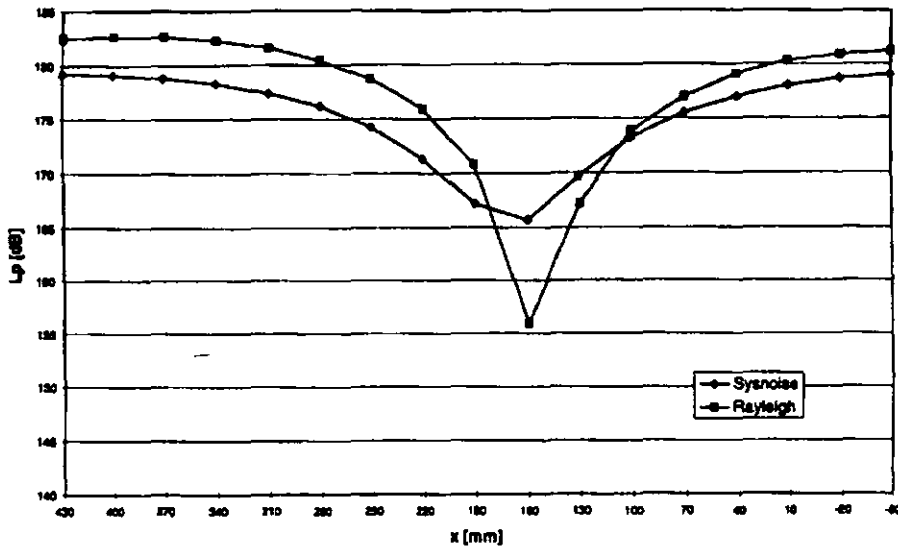


Figure 7.3.7 Spatial Sound Pressure (Mode 2; Location 'A')

lised and quantified. It is most likely to be dependent on the structural design of the studied component. A reasonable explanation may be given for the oscillations detected at mode 4. The local sound pressure distribution moved to the y-direction resulting in significant changes for the x-direction. While the position of the studied locations are fixed in space, little vertical variations will alter the horizontal results significantly. This must be considered, if the results from mode 4 are discussed regarding achieved accuracy. Nevertheless, a significant dependency on the measurement location must be considered for the Rayleigh method. This is especially true for modeshapes and vibrations with major cancellation effects. The previously discussed assumption that sound pressure levels are increasing with decreasing frequency can not be correlated.

A general rejection or acceptance of the Rayleigh method in comparison to the Boundary-Element method is not possible for the purposes of this comparison. The total sound power results deliver appropriate accuracy. Local sound pressure results may vary significantly and rely critically on the mode-shapes, spatial location and finally on the geometry of the component. A general prediction about practically achievable accuracy can not be given in advance. Case studies are required to establish a profound information about the specific application. This first assessment judges the Rayleigh method for initial and competitive rather than absolute investigations. Two further comparisons were made on real components to establish a more profound assessment.

An in-house study[132] on a structural aluminium oilpan (Figure 7.3.8) compared test with SYSNOISE and NOISE results. The applied finite element model was correlated against prototype hardware by utilising modal results and transfer functions. The correlation was between at best  $\pm 2\%$  and at worse  $\pm 8\%$  in modal results based on the variance in material thickness. The analytical and test transfer functions are used to establish modal damping values within the frequency domain. Acoustic investigations were performed by exciting the structure with a pneumatic hammer and measuring the sound pressure and intensity in an anechoic chamber. The boundary conditions are defined as free-free supporting the oilpan with rubber bands.

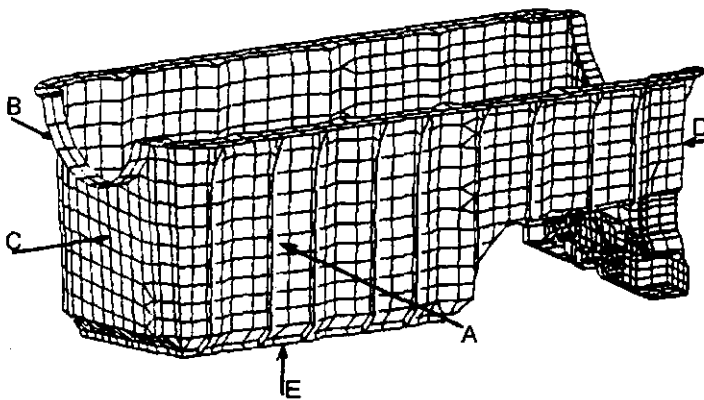


Figure 7.3.8 Structural Aluminium Oilpan

Three analysis locations are studied in more detail. These points are located at the oilpan sides 'B' and 'C'. The distance to the surface is 100 mm. One additional investigation is performed for side 'C' for a distance of 500 mm. The sound pressure results are shown for location 'B' in Figure 7.3.9. Results obtained for this side may be applied to side 'A' also due to symmetry. The comparison for side 'C' is shown in Figure 7.3.10 for 100 mm distance and in Figure 7.3.11 for 500 mm correspondingly. The graphs show the third octave summation as comparison between measured and analytical results derived from SYSNOISE and NOISE. A significant difference is seen for all locations at frequency values below 600 Hz.



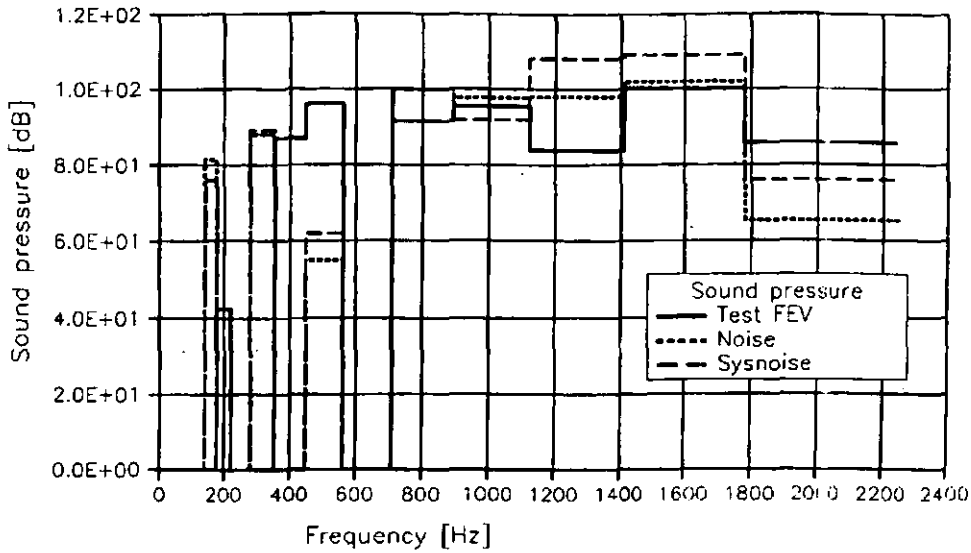


Figure 7.3.9 Oilpan Sound Pressure Comparison (Location 'B')[132]

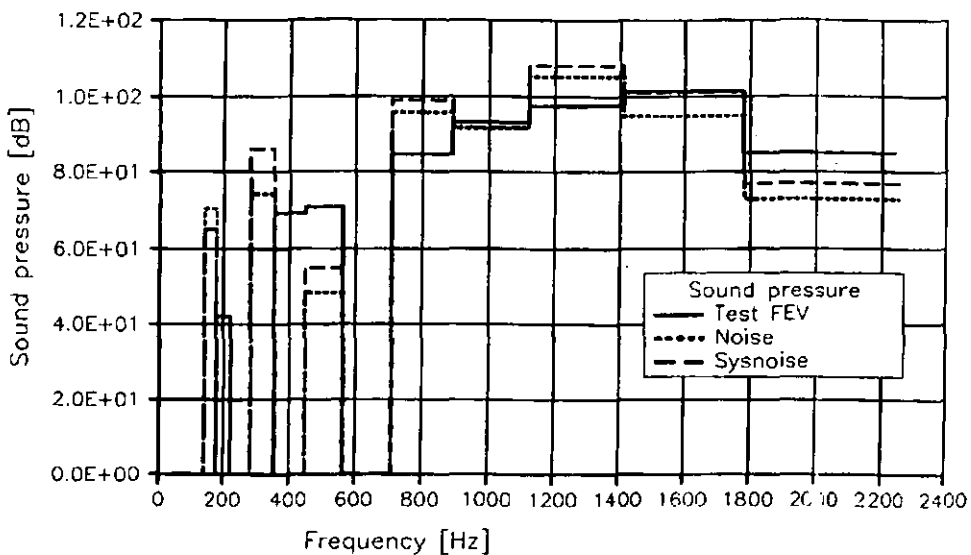


Figure 7.3.10 Oilpan Sound Pressure Comparison (Location 'C'; 100 mm)[132]

One outcome is that small shifts in eigenfrequency may result in a different classification within the octave bands. This effect masters the third octaves at 200 Hz and 500 Hz. But even if one shifts the pressure values from the test or the analysis to the appropriate band, the difference between tested and calculated pressure values is still accentuated in the lower frequency range. Studying the rationale for the perceived deviation in more detail, it is evident that the investigated aluminium structure shows very low damping values at those frequencies[132]. This affects the analytical transfer function from which the surface velocities and finally the radiated sound pressure are calculated.

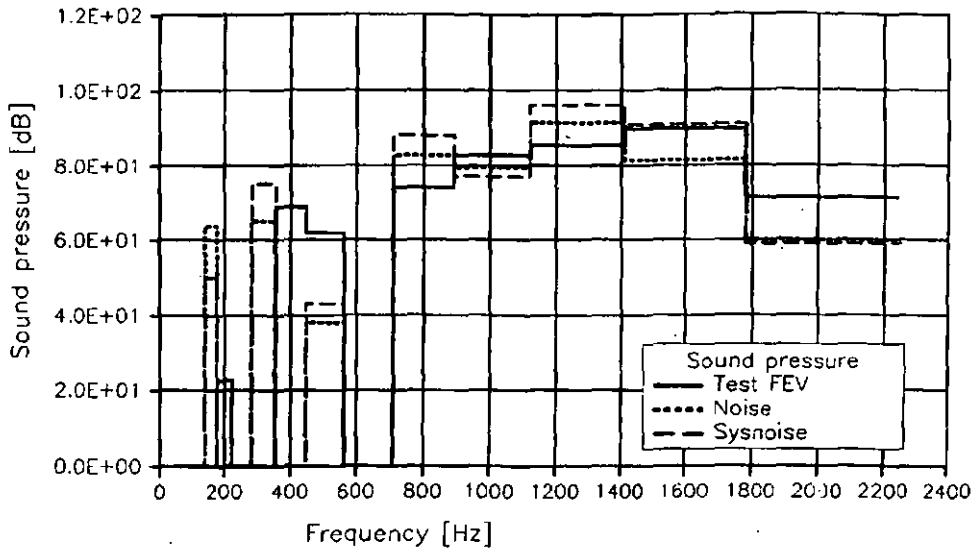


Figure 7.3.11 Oilpan Sound Pressure Comparison (Location 'C'; 500 mm)[132]

The comparison for higher frequencies show a significantly improved correlation. The results from NOISE show significant improved accuracy compared to Sysnoise especially for frequencies between 900 Hz and 1800 Hz. This inverts for frequencies above 1800 Hz and 100 mm distance, while the analysis results at 500 mm distance are identical.

From the comparison of these three solution points no preference can be derived for one of the two programs. The differences between test and analysis are comparable for NOISE and SYSNOISE. Dependent on the requested accuracy, both analytical tools are not capable to predict the absolute radiated sound power with  $\pm 5$  dB. Applying the tools for design decisions, one may apply one or the other tool for competitive design investigations only. At least this assessment is valid for the investigated structure.

So far only components have been applied to verify the Rayleigh method against the Boundary-Element approach. This correlation study considers the engine main structures (Figure 7.3.12). The assembly consists of engine block, ladderframe girdle, oilpan and a solid plate. This plate represents the stiffness of the cylinder head. The structure was excited with a pneumatic hammer at the main bearing 4 with a force of 1 N throughout the frequency range from 0 Hz to 3000 Hz.

The correlation was done by comparing the measured results with those obtained from SYSNOISE and NOISE. The approaches exercised with SYSNOISE are the traditional method ('method 1') and a so called 'Modal Expansion Method' ('method 2'). The traditional method utilises the FEM forced response analysis results as input for the

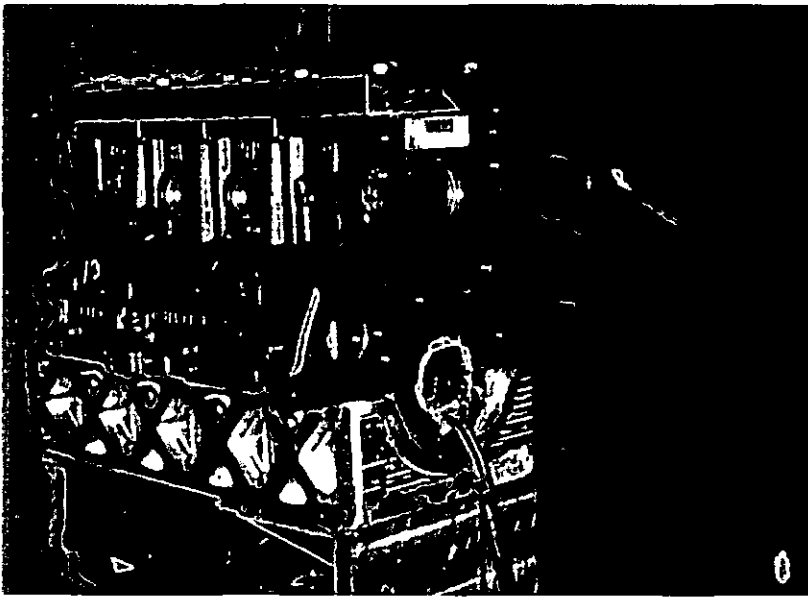


Figure 7.3.12 Physical Model of Engine Assembly

SYSNOISE acoustic radiation prediction. The physical properties used are normal velocities at the structure surface. The Modal Expansion Method was developed by NIT as a consequence of this project and will be implemented into SYSNOISE. The method uses the analytical modal basis of the structure, the BEM model and a limited number of acceleration measurements. Using the measured data, for every frequency SYSNOISE calculates participation factors for the structural modes by applying a singular value decomposition algorithm. This leads to a structural response that matches the experimental data at the measurement points. The assumptions made are the correctness of the experimental data and analytical mode shapes. It is further assumed that the number of measurement points is sufficient to represent the global behaviour of the entire structure. As the Modal Expansion method requires measurement data as input, it can not be applied for design development work at an early stage, where hardware is not available. The advantage of this method is, however, that it does not request a correlated forced response model.

The results are obtained for microphone positions defined with 0.1 m (Figure 7.3.13), 0.3 m (Figure 7.3.14) and 1.0 m (Figure 7.3.15) distance from the engine surface. All results are an average over the six microphone positions for each instance. The comparisons show that the compliance for all methods decreases with increasing distance from the engine. The coincidence of the NOISE results is good for near and middle field (0.1 m and 0.3 m) distances. The accuracy is comparable with SYSNOISE 'method 1' results as diffraction effects, influenced from the sides of the engine, are negligible. At 1.0 m distance NOISE accuracy is decreasing as diffraction effects play an increasing

role, hence the calculated sound pressure values are too low. A comparison with SYSNOISE 'method 2' results shows very good correlation above 1000 Hz. The correlation below 1000 Hz is less good as the oilpan is dominating the acoustic behaviour, which cannot be adequately described by modal information utilising only two measurement points. This shows that method 2 delivers acceptable results if the measured modal information is dense enough.

A further important argument for the analysis tool selection in this project is the required CPU time for solving the problem. A detailed comparison of the required CPU resources is shown in Table 17. SYSNOISE studies performed at work-station require about 193 times longer than with NOISE. While NOISE requires a medium range work-station only, SYSNOISE requires a high end work-station. Utilising a supercomputer for improved analysis turn-around times the performance relation can be dropped to about 40.

	NOISE	SYSNOISE 'Method 1'	SYSNOISE 'Method 2'
Work-station	900 sec.	174050 sec.	$\approx 160000$ sec.
CRAY-YMP	-	37400 sec.	34800 sec.

Table 17 Comparison of CPU-Requirements

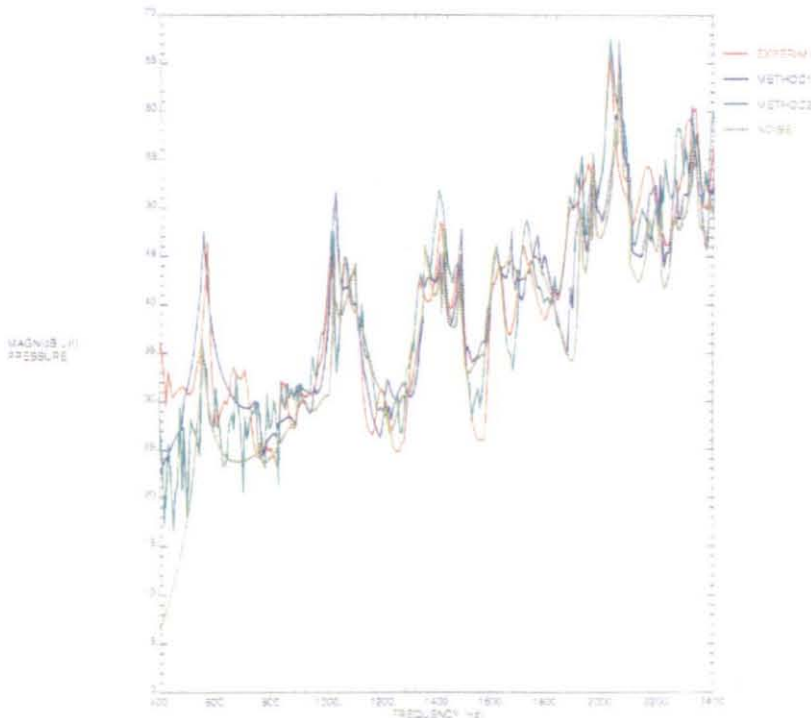


Figure 7.3.13 Comparison of Acoustic Results at 0.1 m

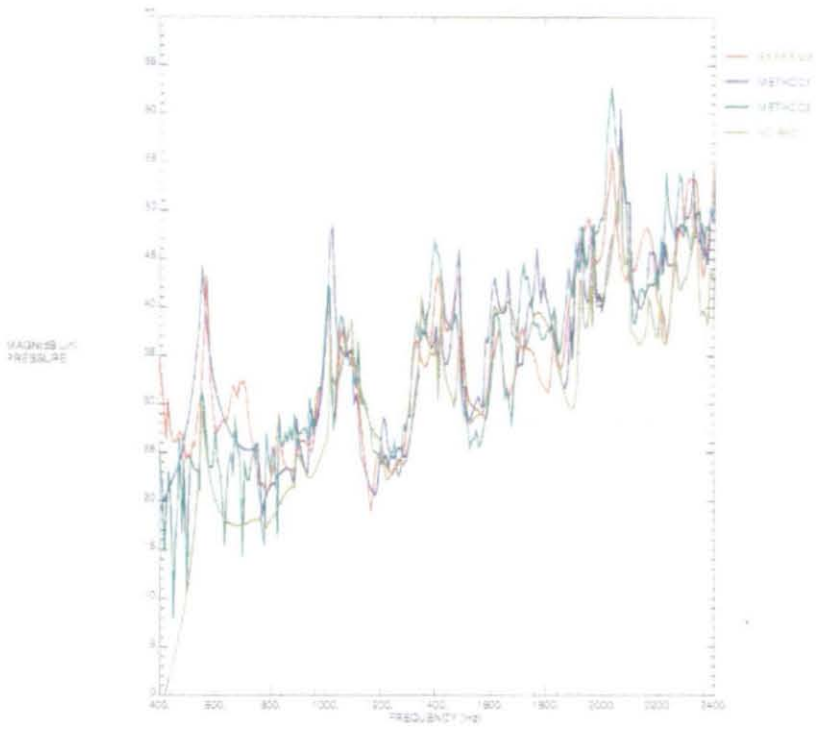


Figure 7.3.14 Comparison of Acoustic Results at 0.3 m

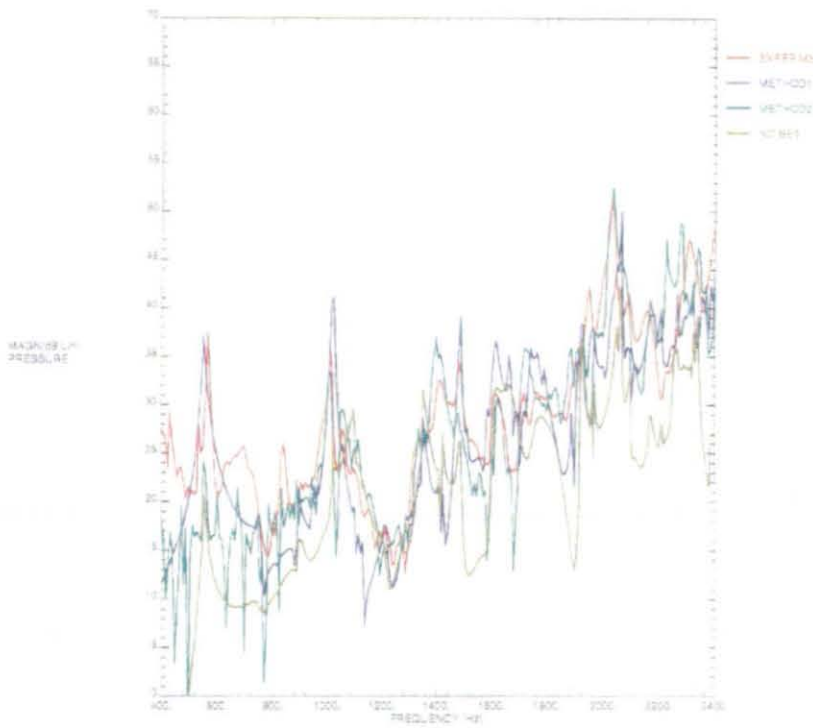


Figure 7.3.15 Comparison of Acoustic Results at 1 m

All projects showed that the correlation of the structural FEM model with measurements is still the most difficult area. Significant effort and expertise must be invested to get reasonably good structural correlation. Once structural responses are correct, both tools can be applied for predictive noise radiation analyses. The NOISE sound pressure predictions at near field (0.1 m; 0.3 m) correlates well with measured data for frequencies above 1000 Hz. Results below that frequency suffer from the defined constant radiation efficiency value applied within NOISE. Therefore, NOISE can be used to investigate initial designs, design modifications and to perform strategic acoustic optimisation studies for main engine structures. Acoustic prediction towards absolute values can only be performed with a BEM approach such as SYSNOISE.

Considering the intention of this project to compare individual design alternatives of the coupled crankshaft-crankcase system, NOISE is the selected tool to predict the radiated noise.

### **7.3.3 Enhancements**

The original software NOISE based on the Rayleigh approach is limited to a maximum analysis frequency of 2400 Hz. This limitation is not acceptable within this project, as many measurements are done accounting frequencies of up to 6000 Hz. Therefore, modifications are made to the source code in a way that the upper frequency limit matches the maximum values obtained in measurements of 6000 Hz. Case studies were performed to evaluate the theoretical solution of defined cases with those derived from the modified software NOISE.

Additional enhancements have been introduced by adding features for A-weighted, octave and third-octave band analysis to compare analytical and measured results. Principle case studies were performed to verify the modified software with theoretical results and the obtained results match the theoretical solution.

## **Chapter 8**

### **Design Analysis and Verification**

A study is made with an assembled powertrain applying the previously described theoretical approaches. Potential design alternatives are introduced and compared to the base design in terms of vibration and noise radiation perception. It is shown that the predicted results correlate with measurement results and that the derived analysis procedure can be applied for trend prediction and competitive investigation.

## 8.1 Design Studies

The selection process of the powertrain considered in this thesis was based upon two arguments. The first is that the engine fitted should be one of the best developed by Ford with respect to noise and vibration. From this two further development paths may be considered. One is to improve the engine noise and vibration performance by introducing additional technical features such as added ribbing, damped flywheel clutch, flexible flywheel and others. The alternate path is driven by cost reduction efforts. As economic pressure is increasing costs must be cut at every point, where possible from the point of view of overall performance. In terms of noise and vibration perception technical features may be deleted or replaced by more cost effective solutions. Here we find potential savings such as deleting ribbing pattern, replacing bearing beams with individual bearing caps, deleting torsional dampers and others. Both directions are contradictory and the coherent engineering question is to predict and judge on the resulting noise and vibration perception gained from the one or the other directional change.

The second is based on financial restrictions in funding test cells. The test work necessary to correlate the analytical approach with measurement results leads to several weeks of testing. It was therefore necessary to link the analytical work with an engine programme being developed to fund the required test work.

As an outcome of this, the new Ford ZETEC-SE Powertrain for Fiesta and Focus type application was selected as the benchmark in this thesis. The engine is known for good noise and vibration performance compared to internal and external competitor powertrains.

Based on the sound NVH performance of this engine, further development actions may be carried out to improve the noise and vibration characteristics. Potential technical upgrade features could be a damped flywheel clutch or a flexible flywheel replacing the standard cast iron flywheel. Further ribbing actions at the engine main structure or oil-sump are not promising, as these features have been already considered and optimised within the base design. Additional investigations on that field are therefore not given in this project. On the other hand, this engine is known for its relatively high



cost entailed by introduced technical features. Hence, potential cost saving efforts may focus on feature deletion not significantly diminishing the NVH performance of the engine. Realisable actions are the substitution of the one-piece bearing beam by paired or individual bearing caps or the replacement of the structural oil-sump by a sheet metal sump. Other proposals consider the deletion of major parts of the ribbing pattern of the engine main structure and the structural oil-sump. The reduction in piece cost is funded through the mass saved multiplied by the material cost. The abolition of the ribbing pattern and saving a few grams of material has no significant cost saving potential and is not further considered.

The list of conceivable design proposals is endless and a discussion of every alternative would not suit this project. Considering the previously discussed development paths and technical solutions one must be conscious of implementing properly designed alternatives achieving the stretched objectives of NVH improvement or savings. From bench-marking results and publications it is known that competitor engines are sometimes equipped with a flexible flywheel to upgrade the NVH performance of an existing engine configuration. On the other hand production engines are commonly equipped with individual bearing caps rather than a single bearing beam for cost and weight reasons. This is especially true for deep skirt engine block configurations. Detailed descriptions of further bottom-end design alternatives and the advantages and disadvantages are given in Chapter 2.

Hence, the design alternatives considered within this thesis are:

- ZETEC-SE powertrain with base configuration (current production)
- ZETEC-SE powertrain with flexible flywheel
- ZETEC-SE powertrain with individual bearing-caps

All three design alternatives are described in detail in section 8.1.1.

The flexible flywheel is expected to improve the NVH performance at increased cost while the individual bearings caps are expected to deteriorate the NVH perception at reduced cost and weight. The developed methodology should predict the correct order of all three options and the level of expected deterioration and improvement.

### **8.1.1 Engine Description and Modelling Approach**

The engine was recently introduced into production and the use of aluminium for the main engine structure represents a new trend for European Ford engines. A cut-away of the entire engine is shown in Figure 8.1.1.

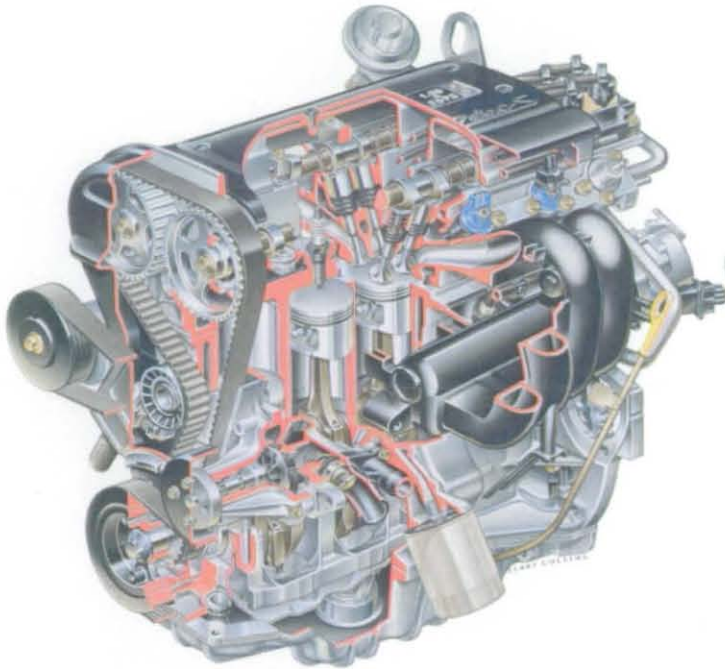


Figure 8.1.1 ZETEC-SE Engine Cut Away

The main engine structure is a ribbed and contoured aluminium casting with a single piece cast aluminium bearing beam (Figure 8.1.2). A structural aluminium oil-sump is used to achieve a high powertrain bending stiffness and to support the lower end of the engine block structure. In comparison with other light duty gasoline engines, the powertrain is quieter than average at 100% load over most of the speed range. At idle and maximum speed this engine is best in class in terms of radiated noise compared with other engines from the Ricardo database (Figure 8.1.3). The powertrain noise shows a linear progressive increase with speed. No one component had a dominant contribution of more than 10% to the overall sound power levels. Even the aluminium oil-sump, which is frequently a significant contributor, contributes less than 8.5% of the total sound power. In case of the engine block a minimal participation of less than 4% can be found (Figure 8.1.4). In general the entire engine is designed to minimise NVH.

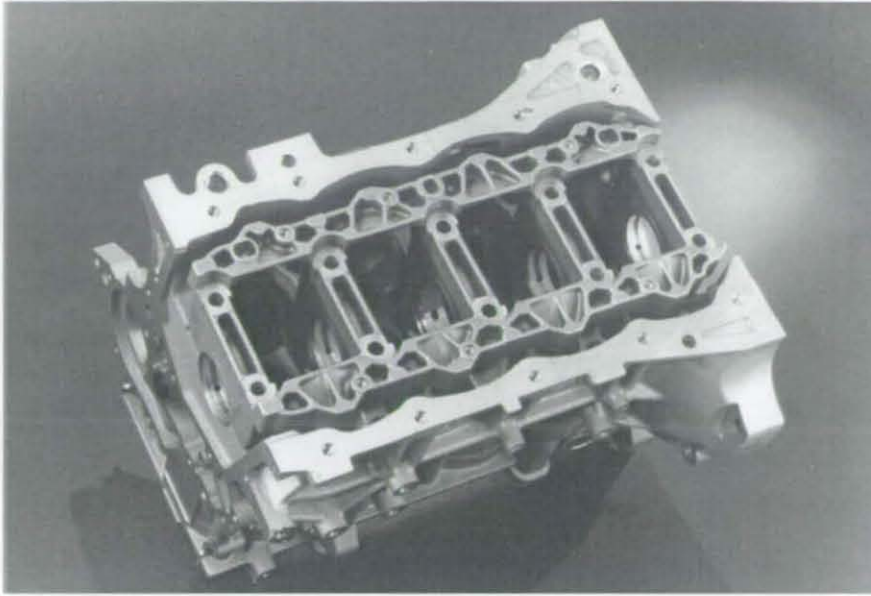


Figure 8.1.2 Aluminium Engine Block and Bearing Beam

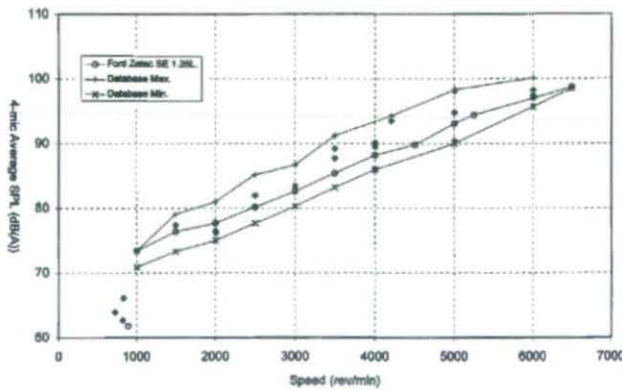


Figure 8.1.3 Sound Power Level Spreadband of ZETEC-SE Class Engines (Competitor Data by Ricardo)[134]

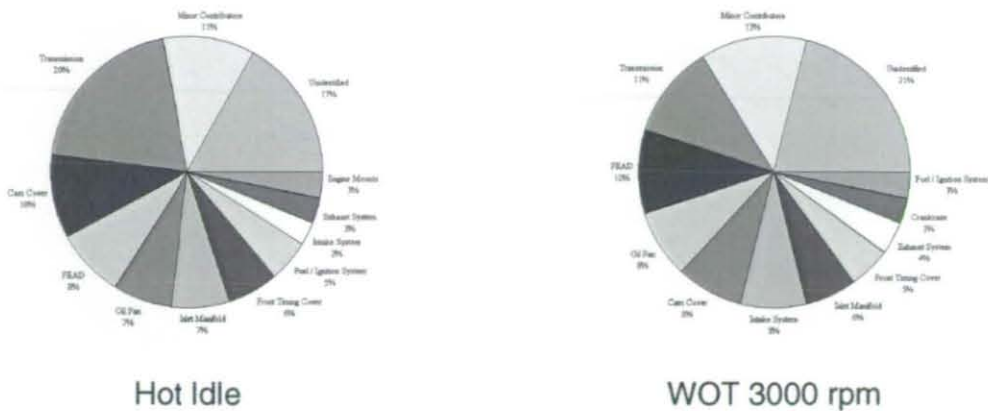


Figure 8.1.4 Sound Intensity Participation (Entire Engine)[134]

The main engine structural components and the important technical NVH features are described hereafter. An overview of the basic dimensions is given in Table 18 including significant cranktrain data.

Engine Configuration	4 Cylinder, 4 Stroke In-Line
Valves per Cylinder	4
Swept Volume	1242 cm <sup>3</sup>
Bore/Stroke	71.9 mm / 76.5 mm
Compression Ratio	10.0:1
Firing Order	1 - 3 - 4 - 2
Governed Speed	6500 rev/min
Max. Power	53.8kW at 5000 rpm
Max. Torque	107.6 Nm at 4000 rpm
Mass <sub>Crankshaft</sub>	12 kg
Main Bearing Diameter	48 mm
Pin Diameter	40 mm
Mass <sub>Connecting Rod</sub>	378 g
Length <sub>Connecting Rod</sub>	136.3
Mass <sub>conv. Flywheel</sub>	8.4 kg
Inertia <sub>conv. Flywheel</sub>	87.1E <sup>-3</sup> kgm <sup>2</sup>
Mass <sub>flexible Flywheel</sub> (optional)	10.1 kg
Inertia <sub>flexible Flywheel</sub> (optional)	100.2E <sup>-3</sup> kgm <sup>2</sup>
Individual Bearing Caps (optional)	1.5 kg weight reduction vs. bearing beam
Transmission	Ford IB5 5-speed Manual

Table 18 Basic Engine Data

### Cylinder Block Assembly

- deep skirt heavily contoured cast aluminium design with cast-in liners, 4-6mm wall thickness - strategically located (thinner in the centre of panels), 19.9kg mass including bearing beam (Figure 8.1.5)
- aluminium bearing beam without iron inserts (Figure 8.1.6)
- 8mm minimum oil pan rail thickness increasing to 12mm, 15 to 25mm wide
- rear face of block (bell housing attachment) is well flared and braced by ribs on both sides with seven attachment points to the transmission (Figure 8.1.7)
- all bolt bosses for externally attached components are well braced
- axial thrust bearing is located at the third main bearing

- bearing 1 and 5 are slightly more flexible in axial direction

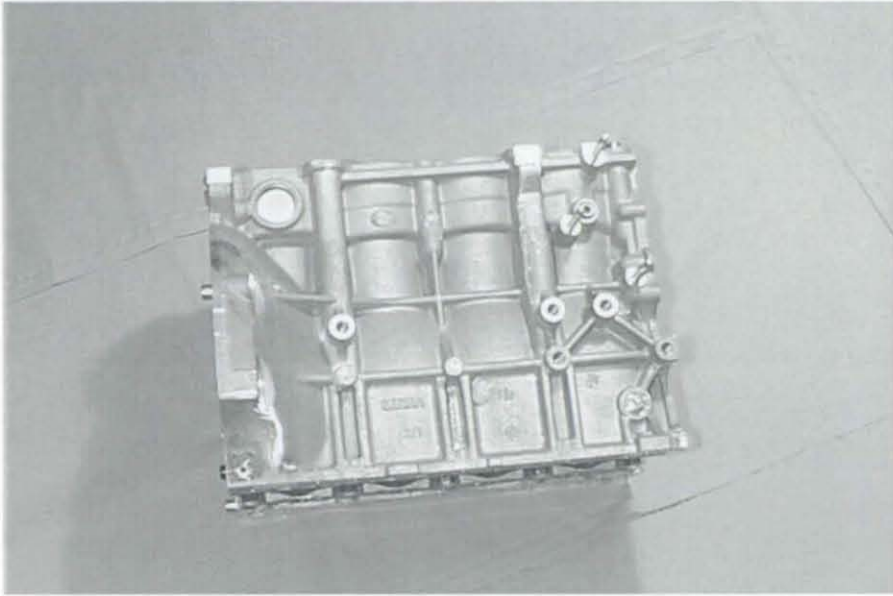


Figure 8.1.5 Cylinder Block (RHS)

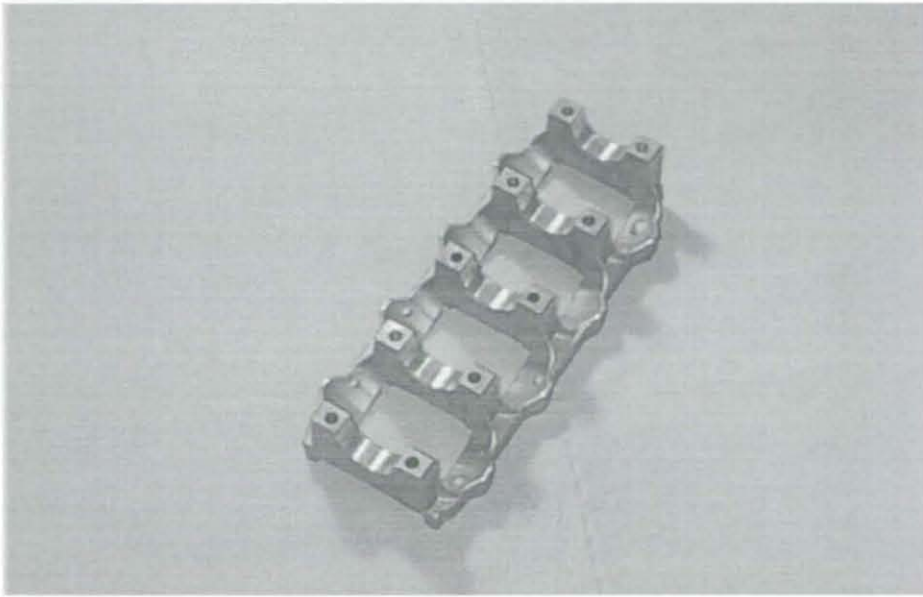


Figure 8.1.6 Bearing Beam (Single Piece; Cast Aluminium)

#### Oil-sump

- cast aluminium with a powertrain stiffening functionality (Figure 8.1.8)
- four attachment points to transmission bell housing
- panels broken up by contoured sections and external ribbing
- steel gasket for metal to metal contact between sump and block

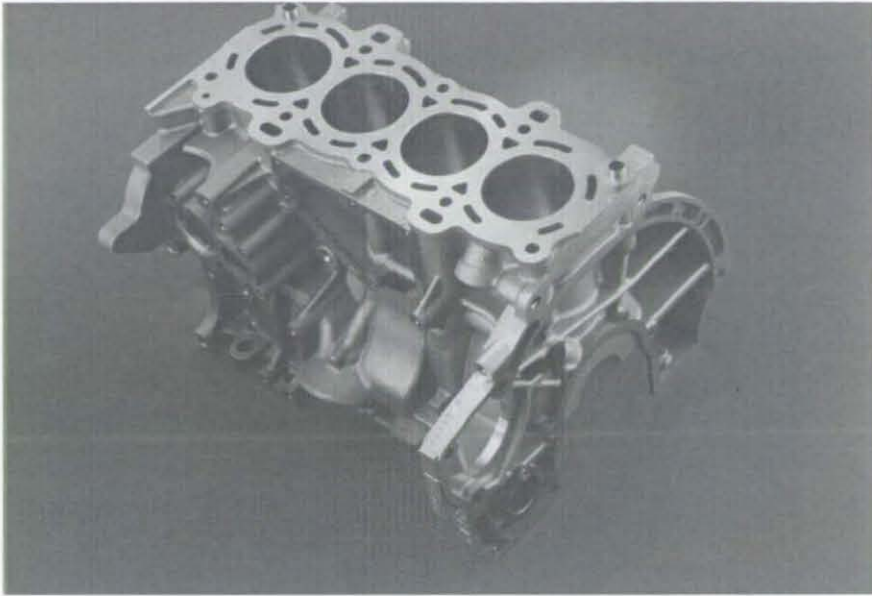


Figure 8.1.7 Cylinder Block (LHS;Rear)

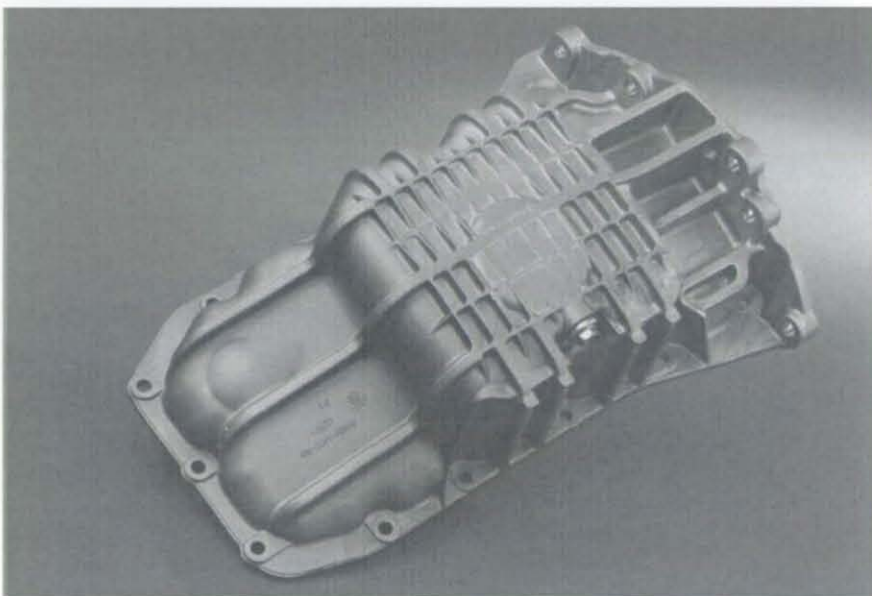


Figure 8.1.8 Oil Pan (Cast Aluminium)

#### Cranktrain Assembly

- cast iron crankshaft, fully counter-weighted (Figure 8.1.9)
- conventional clutch plate without pre-damper
- crankshaft front pulley incorporates crankshaft torsional damper
- piston with low mass
- cast iron flywheel, high inertia for low torsional vibration (Figure 8.1.10)
- connecting rod; low mass design, sinter forged cracked big end caps, no weight grading (Figure 8.1.11)

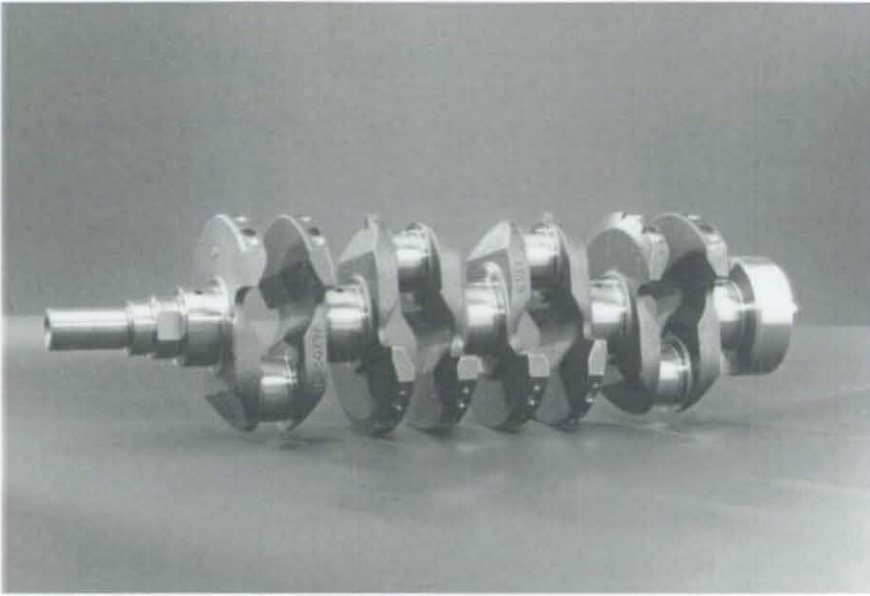


Figure 8.1.9 Crankshaft (Cast Iron)



Figure 8.1.10 Flywheel (Cast Iron)

As explained previously and in Chapter 2, several new engines are equipped with a flexible flywheel. NISSAN especially applies this design features in both large and small engines (i.e. Nissan Micra 1.3l, Nissan Maxima 3.0l). According to their publications a flexible flywheel is used on these engines to improve the NVH performance. With this design the critical flywheel whirling and tilting vibration in the 200-300 Hz region should be eliminated. The flexible flywheel (Figure 8.1.12) was supplied by UNISIA, who is the manufacturer and patent holder of this design. The design consists mainly of a sheet metal membrane disk and a cast iron inertia ring. The inertia ring accommodates the



Figure 8.1.11 Cranktrain Assembly

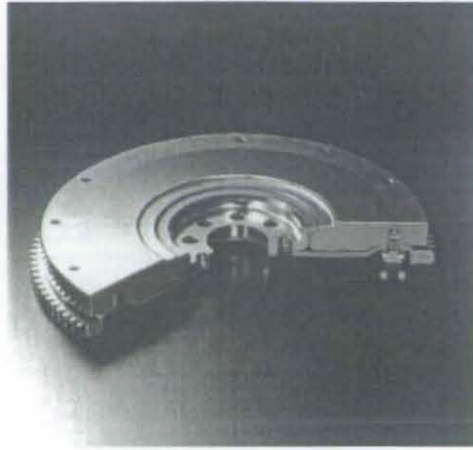
starter ring and is designed to replace most of the standard flywheel inertia. The disk thickness is 3mm bolted to the crankshaft and the inertia ring. This design transfers the torsional moment and decouples axial and bending vibration. There is no design guide-line available to calculate the membrane thickness and hence tune the overall system response. It is the author's experience that UNISIA uses the 3mm sheet metal for all variants of flexible flywheel application. Even the previously mentioned engines from Nissan, which are significantly different in displacement, inertia and configuration, utilises the same sheet metal membrane properties. As a consequence it is doubtful, whether the flexible flywheel will show the NVH upgrade potential as claimed by the supplier. The author's opinion is that the flexible membrane properties must be adjusted for the specific type of engine application. This will tune the resonance frequencies and hence the NVH upgrade performance of the device. UNISIA states that no work was or is being done in that respect.

As discussed previously and in Chapter 2, several engines are equipped with individual bearing caps especially in combination with a deep skirt engine block design. This approach saves a significant amount of weight (approx. 1.5 kg) compared to a bearing beam design. On the other hand individual bearing caps are commonly manufactured from cast iron or do have cast iron inserts to increase the rigidity of the single cap and to reduce the thermal expansion and minimise the housing swell. It is therefore important to investigate the NVH perception of individual bearing caps vs. a bearing beam design keeping all other design parameters constant. The individual bearing caps (Figure 8.1.13) are machined from the single piece cast aluminium bearing beam. Some





Test Configuration



Cut Away View

Figure 8.1.12 Flexible Flywheel

additional material of the original beam design may be deleted in a final version as shown in Figure 8.1.14. The additional material at main bearing cap no. 2 and no. 4 is required to attach the oil-sump baffle preventing oil dilution.

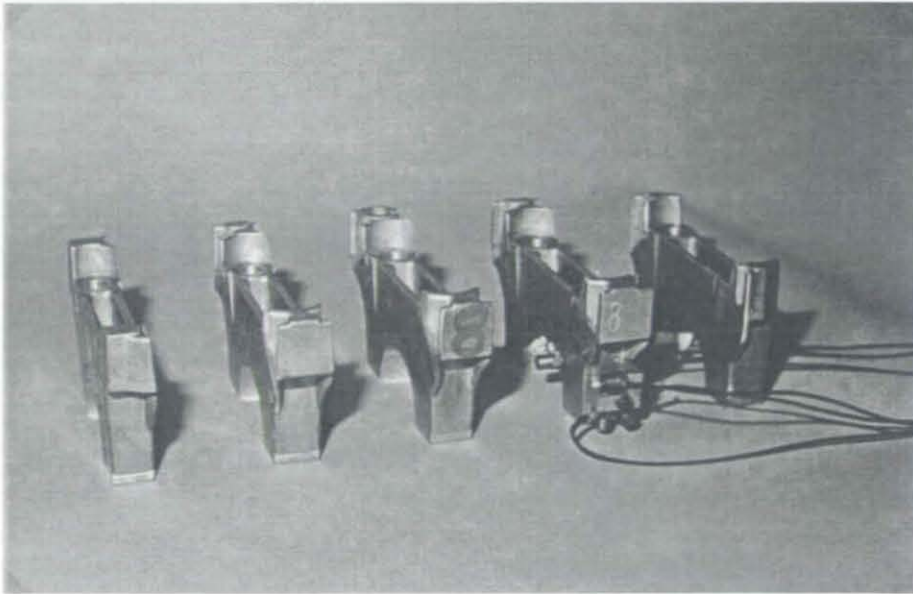


Figure 8.1.13 Individual Bearing Caps

The FEM models representing the above hardware are pictured below. The model description is given briefly only as accurate modelling techniques are well known and published many time in the past. The component models are correlated individually with measurement results from modal analyses. As this verification is commonplace, processes and results are not described here.

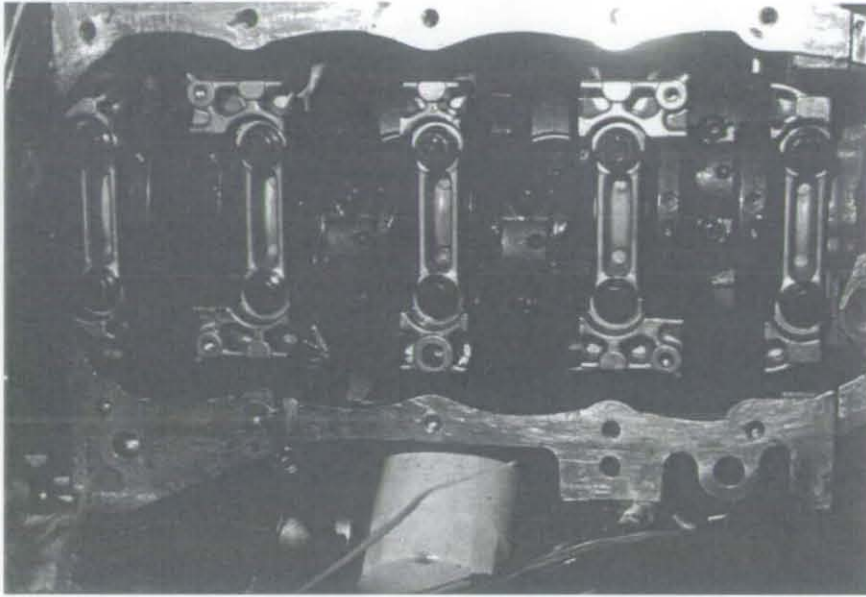


Figure 8.1.14 Individual Bearing Cap (Assembly)

The assembled powertrain representation is depicted in Figure 8.1.15. The engine block and oil-sump consist of mainly second order shell elements representing the thinner section of the components. The flanges and the interior bottom end are modelled with solid elements. The transmission is meshed with a higher mesh density applying linear elements only. The cylinder head is modelled by a plate model adjusted to represent the bending and torsional stiffness of the cylinder head assembly. The model summary is given below.

Nodes	66000
Bar/Beam Elements	1800
Shell Elements	18000
Solid Elements	31000

The powertrain assembly is modelled utilising rigid links (RBE). The characteristic properties of seals and rubbers between individual structural components are not included [133]. Corresponding damping properties are adjusted through the material properties of the structural components.

The powertrain support reflects the Fiesta type application. Three rubber mounts are modelled representing the bushes at the right-hand-side (RHS), left-hand-side (LHS) engine mount and the rear-roll-restrictor (RRR). The mounting components are represented by rigid elements while the rubber components are adjusted to fit measured mount properties.

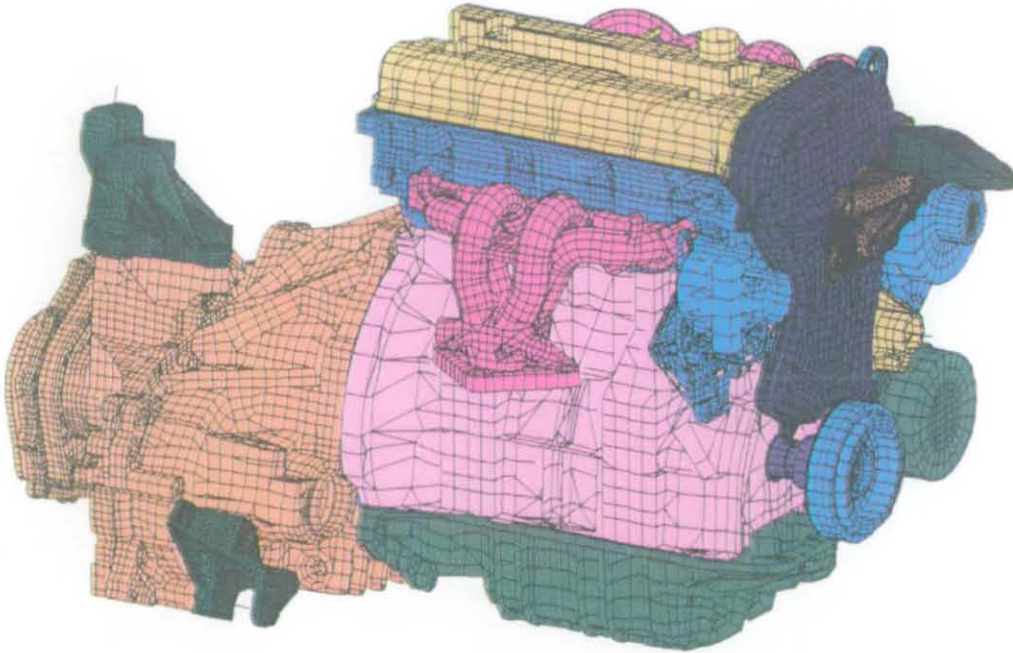


Figure 8.1.15 Powertrain FEM Model

The crankshaft assembly is depicted in Figure 8.1.16 and modelled utilising solid elements only. Experience and competitive investigations showed that a modelling approach with beam elements do not adequately present the crankshaft stiffness properties. The model summary is given below. The membrane of the flexible flywheel is represented applying shell elements. Competitive investigations showed that a modelling approach with solid elements do not accurately reflect the bending properties of the flexible plate. Shell elements are used instead keeping the number of applied degrees of freedom in a practical range.

Nodes	22500
Solid Elements	18000

The cranktrain forces are applied for every cylinder via rigid elements. The combustion pressure is distributed to the cylinder head while the piston side forces are assigned to the liner area. Forces acting on the crankpin are split into radial and tangential forces and are applied to the crankshaft at the centre of the crank-pins and are distributed over the pin dimension utilising rigid elements.

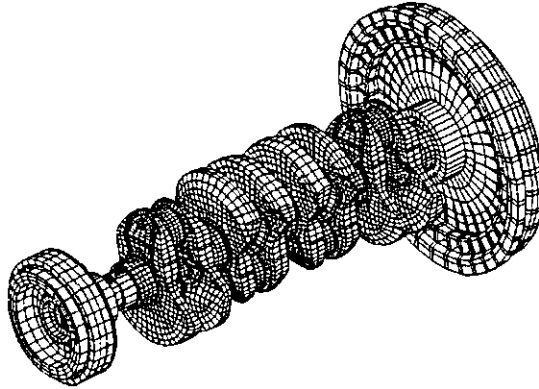


Figure 8.1.16 Crankshaft Assembly

### 8.1.2 Powertrain Modal Analysis

A powertrain modal analysis was performed to verify the accuracy of the assembled system. Free-free normal modes analysis was chosen to compare the eigenfrequencies and eigenvectors within a frequency range of up to 600 Hz. From literature and former sections this range is known as the most important for crankshaft and flywheel whirling. Correlation and adjustment of the assembled base design powertrain are the main purpose of this study.

The tested configuration differs from the later applied fully assembled powertrain. It is known from previous powertrain investigations that some of the accessory modes are in the range of the first flywheel and crankshaft modes. Hence, all of the accessory components are not attached to avoid mode duplication and difficulties in interpretation of the measured results. This must be considered if one compares the results with the later described from the running mode investigation.

The applied coupling properties between the crankshaft and the crankcase are linearised and adjusted to an average value occurring during operation. The test configuration utilises an especially developed method applying Teflon as the coupling material. Extensive analytical and measurement studies were made in the pre-phase of this project to verify this approach with known results from running mode investigations. This test set-up is also used by other car manufacturers and has been verified independently.

The acquired analytical and measured results are summarised in Table 19. Corresponding mode eigenvectors are shown in the appendix. The first analytically derived vertical and lateral flywheel bending frequencies occur at 273 Hz and 282 Hz respectively. The shown eigenvector clearly identifies that the vibration is not limited to

Eigenvector	Analytical Eigenvalue [Hz]	Measured Eigenvalue [Hz]	Difference [%]
1 <sup>st</sup> Flywheel vertical	273	286	4.8
1 <sup>st</sup> Flywheel lateral	282	289	2.5
1 <sup>st</sup> Powertrain lateral	322	359	11.5
1 <sup>st</sup> Powertrain vertical	360/390	435	16.0
2 <sup>nd</sup> Powertrain lateral	433	476	9.9

Table 19 Powertrain Modal Analysis

the flywheel only. The crankshaft and the last main bearing are significantly participating in that mode. The first vertical and lateral powertrain bending eigenfrequencies are obtained at 322 Hz and 360 Hz showing a less emphasized importance of an individual component. The first crankshaft torsional mode can be found at 459 Hz. The measured surface accelerations are displayed in the appendix in Figure Appendix 4.22 . A comparison of the measured and calculated results exhibit an excellent correlation of less than 5% difference for the first vertical and lateral modes. The eigenvectors are also nearly identical. A comparison of the first lateral powertrain mode exhibit a difference of 11.5% . The first measured vertical powertrain mode at 435 Hz correlates with two analytical modes at 360 Hz and 390 Hz. A clear interpretation is not possible as the results of the measured mode-identification function does not show a single clear mode. The most probable interpretation is that the obtained mode-identification is a combination of both modes derived analytically. The first measured torsional eigenfrequency occurs at 459 Hz showing a 9.9% difference to the calculated value of 378 Hz. This discrepancy is explained through the application of the Teflon material as the coupling property. This material represents the radial stiffness of the oilfilm. But additional shear stiffnesses are introduced into the test set-up coupling the crankshaft torsional degree of freedom with the crankcase. This problem is known and one has to consider this when interpreting the measured torsional eigenvalues. Taking this into consideration, a 9% difference of the torsional eigenfrequency is an adequate correlation. Finally, one summarises that the first crankshaft or flywheel bending eigenvalues correlate very well and that the assembled model can be applied for further studies.

## 8.2 Crankshaft and Flywheel Whirling

The analysis of the whirling phenomenon is executed for the powertrain assembly. Results subsequently discussed are primarily based on the original powertrain design,

utilising a single piece bearing beam and a conventional flywheel. The results obtained are compared with measurements and a judgement of correlation is given.

Further analyses are performed applying the flexible flywheel as shown in section 8.1. The results obtained are compared with those of the conventional flywheel and a first judgement is given for this design alternative.

### **8.2.1 Analytical Approach**

The analysis and interpretation of the powertrain model is done by applying the theory discussed in section 3.5. The investigation covers both the whirling analysis of the entire powertrain and of the crankshaft assembly only. The powertrain is supported at the mount as described in section 8.1. The stand alone assembled crankshaft model is supported at the main bearing pins utilising a simplified approach of linearised springs as established in section 3.2. This additional investigation allows us to compare the results from the anisotropic analysis with those from a isotropic modelling approach. A conclusion may be drawn from this as to whether a detailed investigation with a significant increase in labour and computational effort may be dispensed with overcome by a first estimate utilising a simplified approach.

Recapitulating the theory from sections 3.6 and 3.7, one has to consider changes in eigenfrequency and eigenvalue with respect to the crankangle. These changes are periodic. The maximum changes are predominantly perceived under those conditions showing an extreme stiffness relation between the block and the rotating crankshaft. In case of the crankshaft we find the most significant change in stiffness property in the direction of the crank throw and normal to that. The plane established through the crank throws will be called 'Crank-Plane' or 'CP'. The vector pointing to either the right or left hand side of that plane when looking from the crankshaft front to the rear will be called 'Normal-Plane' or 'NP'.

In case of the engine block assembly we find the most significant change in stiffness property in the vertical or lateral direction, when looking along the installed engine axis. The direction along the cylinder liner will be called 'Block-Cylinder-Plane' or 'BCP', while the normally oriented plane will be called 'Block-Normal-Plane' or 'BNP'.

The analysis of the whirling modes is done for the first six modes. Accounting for the duplicated modes as described in section 3.6, twelve eigenvalues are considered and described by six eigenvectors, namely flywheel-whirling in crank and normal plane (FW-CP; FW-NP), pulley-whirling in crank and normal plane (P-CP; P-NP), 1<sup>st</sup> torsional and 2<sup>nd</sup> longitudinal.

The first axial mode of the crankshaft assembly, described as a uniform vibration of the crankshaft against the axial bearing, is not considered in this discussion. The scaled eigenvector showed substantially reduced displacements compared to that of the spring supported crankshaft and the eigenvalues are also reduced. As the first axial vibration of the crankshaft is mainly influenced by the support stiffness of the engine block, a direct comparison of the spring and block supported models is not correct. The spring supported model utilises a judged axial spring stiffness only based on some publications and experience representing the axial bearing properties. The block stiffnesses are not accounted for in the spring supported model at all. The analysis revealed that the first judgment on this stiffness property is inadequate and needs some refinement for the purpose of future analysis.

The eigenvalues of the whirling crankshaft are not significantly altered by changing crank angles. Studying the animations in detail the general whirling effect is as effective as applying the simplified spring supported model. Significant changes in eigenvectors are not considered between both modelling approaches.

Investigating the supporting crankcase deformations in detail one can ignore the crankcase torsional deformation. The forces resulting from the torsional deformation are negligible compared to those resulting from bending vibration. Here we have to differentiate between the vertical and lateral directions. The vertical direction does not show a significant deformation, due to the high moment of resistance originated from the high cylinder block and the assembled cylinder head. The deformation in the lateral direction is significant and can be observed even at low engine speeds (1000 rpm). The most significant structural weakness is detected at the area between the third and fourth cylinders, where the engine bell housing supports the transmission clutch housing. The relatively low resistance against lateral bending is a main drawback of scanty engine block designs.

The changes in eigenvalues are significantly larger for the powertrain model compared to the spring supported crankshaft model. The differences are mainly influenced by relative small alterations of the corresponding eigenvector over crankangle. Studying the eigenvectors only, these changes are marginal and are not observed under normal conditions. Another effect is that the radial support of the crankshaft within the powertrain model is slightly modified to accomplish the mesh density of the engine block at the main bearings. The number of supporting elements representing the oilfilm properties must be adjusted to two elements over the main bearing width. The spring supported model utilises three supporting elements over the bearing width accomplishing the same absolute supportive stiffness and damping properties.

The results observed from the powertrain assembly are shown in Figure 8.2.1 . The system responses of the anisotropic model are compared with results obtained from the isotropic model.

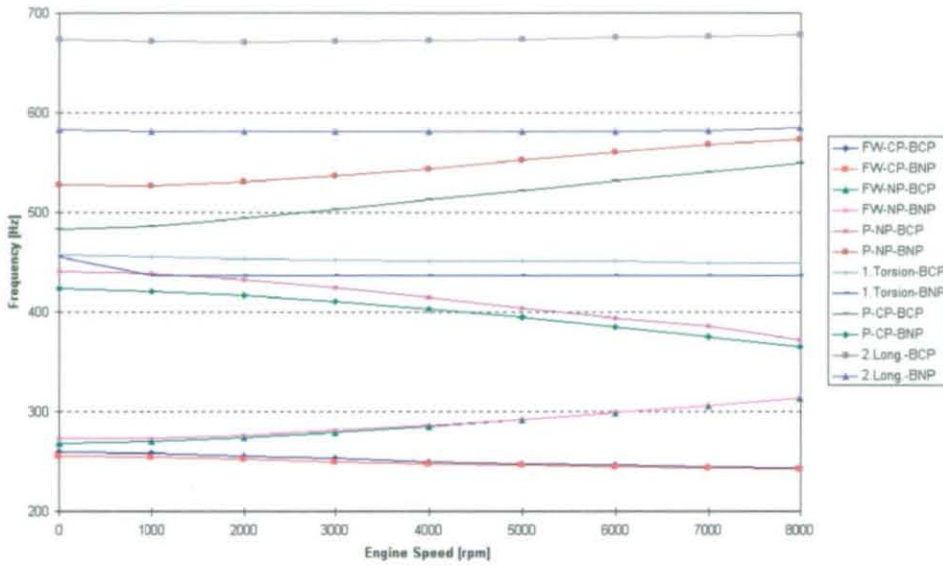


Figure 8.2.1 Powertrain Whirling Frequencies vs. Engine Speed

The change in the 2<sup>nd</sup> longitudinal vibration mode is shown in Figure 8.2.2 for both models with respect to engine speed. The most significant result displayed in this figure is that the 2<sup>nd</sup> crankshaft longitudinal vibration mode is independent of the engine speed. Disregarding the block stiffness properties, especially the structural axial stiffness of the third bearing results in a difference of approximately 100 Hz.

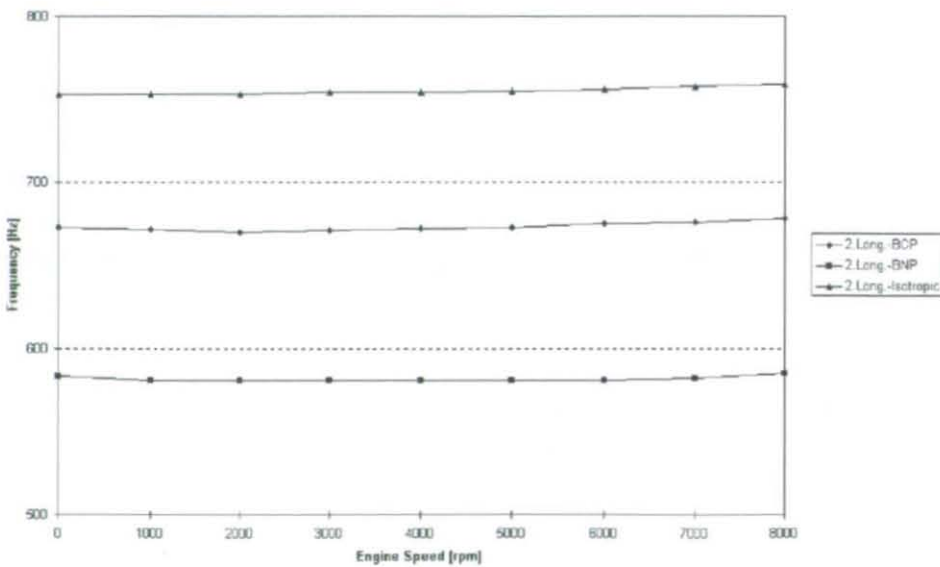


Figure 8.2.2 2<sup>nd</sup> Longitudinal Vibration



Analysing the graph in more detail one must consider that the results shown for the powertrain model exhibit two extreme eigenfrequency values. The upper value is derived for the vertical crankshaft position ('BCP') while the lower value represents the lowest obtained frequency value for the horizontal or normal direction ('BNP'). Only the upper and lower extreme results are shown. The values derived for other crank angles vary between those two extremes throughout the crankshaft rotation.

A similar result is gained from the torsional frequencies shown in Figure 8.2.3. The eigenvalues are independent of the engine speed. Some modulation is observed at those engine speeds where the torsional eigenfrequencies are derived at similar values as the 1<sup>st</sup> pulley whirling mode at approx. 1000 rpm and 3900 rpm. A major difference compared to the 2<sup>nd</sup> longitudinal vibration mode is not observed between both models. This phenomenon is mainly driven by a reduced importance of bending effects occurring in crankshaft torsional vibration. Again, one must consider the appearing range of torsional eigenfrequencies with changing crank angles. The maximum eigenvalues occur at the BNP position whereas the BCP delivers the lowest values. It is remarkable because the most significant bending effects happen in the CNP and the effective supporting stiffness would be the 90° rotated block stiffness property. Hence one should expect swapped values of the lower and upper border frequencies.

Considering the little bandwidth during rotation the most probable explanation is that the effect of the pulley whirling is of more importance than the alterations in block stiffness with respect to the changing crankangle.

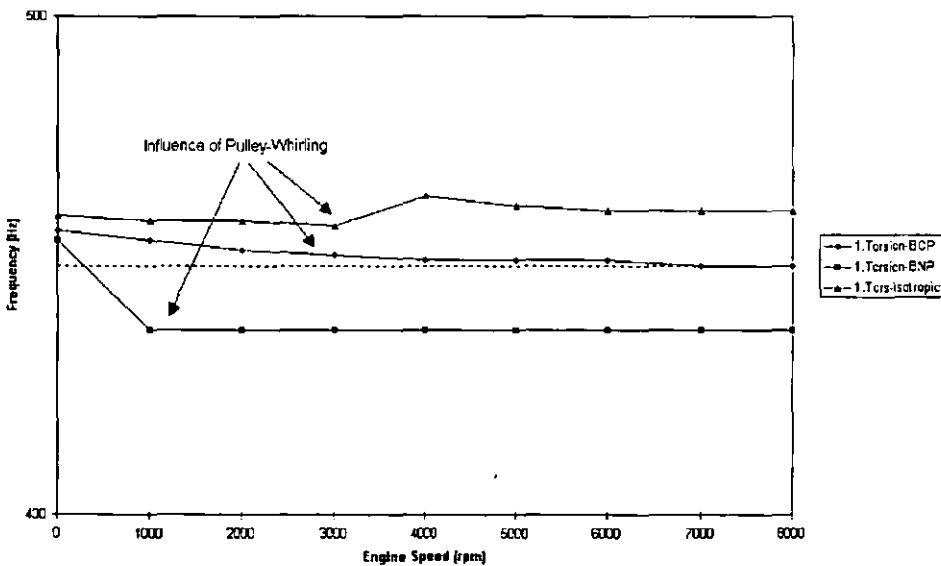


Figure 8.2.3 1<sup>st</sup> Torsional Vibration

The flywheel whirling frequencies are shown in Figure 8.2.4 for the crank-plane ('CP') and normal-plane ('NP') oriented vibration. The powertrain results shown reflect the maximum and minimum values depending on the crankshaft position. The powertrain resonance frequencies show a dissimilar behaviour for both crank planes (CP and NP) in the vertical (BCP) and horizontal (BNP) principal directions of the engine block. The eigenfrequencies of the CP direction are increased, while the NP direction eigenfrequencies are reduced compared to the isotropic supported model. The most significant difference occurs under those conditions showing the direction of the weakest block stiffness supporting the corresponding whirling deflection of the crankshaft in either CP or NP direction. The attention is also attracted from the disappearing difference in frequencies between the CP and NP direction for both principal block directions. The system introduced difference in support stiffness becomes less important and the related change in whirling frequencies vanishes. At higher RPM eigenvalues and eigenvectors are mainly driven by the stabilising gyroscopic effect.

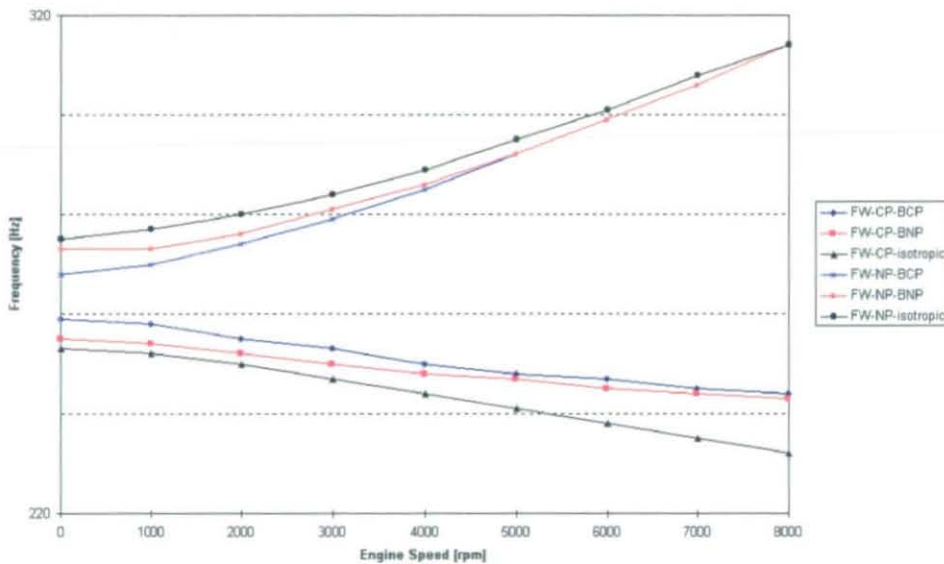


Figure 8.2.4 1<sup>st</sup> Flywheel Whirling ('CP' and 'NP' Oriented)

The obtained results of the pulley whirling are shown in Figure 8.2.5 for the crank-plane ('CP') and normal-plane ('NP') oriented vibration. Again powertrain results reflect the maximum and minimum values depending on the crankshaft position. The change in pulley whirling frequency display equal perceptions for the flywheel whirling frequencies. For those conditions impacted by the weaker block stiffness in lateral direction, values obtained show a significant reduced frequency compared to the 90° rotated direction. These results are mostly identical to those of the isotropically supported model. Unlike the flywheel whirling resonances, common plane pulley frequencies do not show a

tendency to strive for a single resonance at higher engine speeds. The phenomenon is explained by the smaller pulley inertia. The stabilising gyroscopic effect is hence much smaller than at the flywheel and the influencing block stiffness properties are more effective. Further exceptional results are discovered for those directions occurring in the block-cylinder-plane ('BCP'). The frequencies obtained for the crank-plane ('CP') increase while the values in the normal-plane ('NP') are lowered. The most logical explanation of this behaviour is the directional stiffnesses of the engine block supporting the crankshaft front-end.

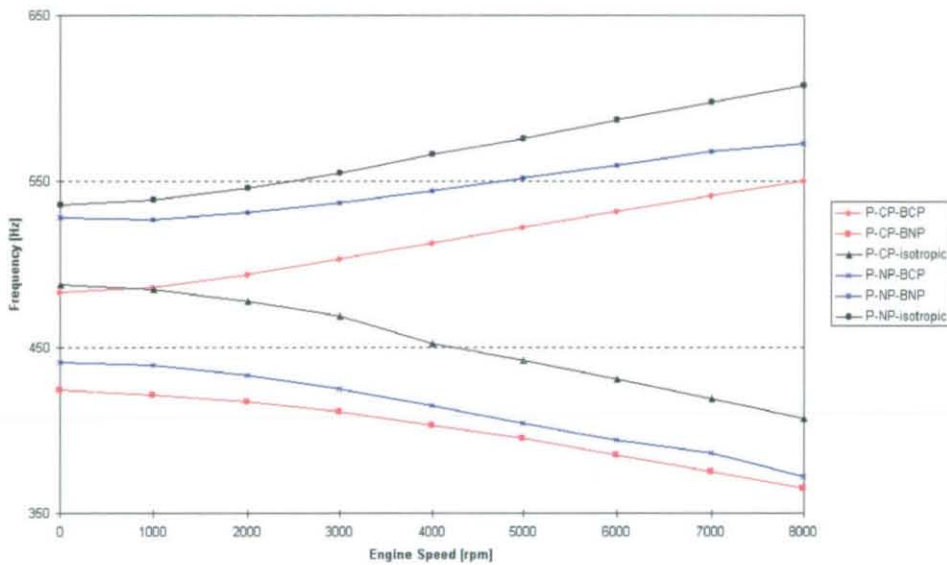


Figure 8.2.5 1<sup>st</sup> Pulley Whirling ('CP' and 'NP' Oriented)

The results and the percentage differences are summarised in Table 20 for 7000 rpm engine speed under no load condition. A comparison is given for the powertrain and the isotropically spring supported model. Examining these results, a significant influence of the block supporting properties is tracked down. The isotropically spring supported crankshaft model delivers quite good results for both the flywheel and pulley whirling frequencies, but lacks the duplicated results of the an-isotropic system as derived in section 3.5, which may be significantly different.

Comparing the findings so far, isotropically supported models may be used for quick and first analyses, keeping in mind that all of the duplicated results are missing. The percentage error is acceptable and the gained experience of the whirling frequencies may be used as a first information for a detailed resonance investigation. Discussing the results one must also consider the engineering and computer resources required to solve both problems. While the spring supported model can be solved in approx. 240 seconds CPU-time on a CRAY-YMP for a single engine speed, the solution of the

entire powertrain requires about 7000 seconds CPU-time for one speed only. The manual effort for preparing the powertrain model assembly is about 10 times that for the spring supported model.

So far, the results are not surprising and are in-line with the theory derived *a priori*. The fully an-isotropic investigation delivers a significant insight in the resonance characteristic of the rotating crankshaft assembly.

Whirling Mode	Powertrain Model BCP (an-isotropic)	Powertrain Model BNP (an-isotropic)	Spring Supported Model (isotropic)
Flywheel CP	-6%	-5%	-12%
Flywheel NP	+14%	+12%	+16%
Pulley CP	+12%	-12%	-17%
Pulley NP	-13%	+8%	+14%

Table 20 Percentage Difference in Whirling Frequencies (7000 rpm)

While the influence of the engine speed on the whirling frequencies of the system has been discussed *a priori*, the deflection characteristic shapes of the whirling crankshaft assembly has also to be considered. The main effects may be classified by separating the torsional and longitudinal vibration from the whirling modes.

The mode shapes of the torsional and longitudinal vibrations are marginally altered. As cranked structures cannot show pure translational or torsional vibrations, all deflection shapes comprise some bending vibration. Hence, engine speed dependent effects are introduced by those coupled bending vibrations.

An in-line four cylinder crankshaft reveals a coupled CP-bending oscillation for every longitudinal vibration. This deflection is then subjected to the gyroscopic effect. Consequently, bending displacements occur in the crankshaft normal plane ('NP') and increase with increasing engine speed. This also introduces a minor torsional deformation due to the cranked geometry of the shaft.

A similar effect is observed for the torsional vibration. The introduced bending deflection is much smaller compared to that of the longitudinal resonance frequency, but the effect is still noticeable. The explanation of the physical phenomenon is given in the reverse order to that given for the longitudinal vibration. Nevertheless, four schemes of vibration

are observed at crankshaft torsional vibrations, especially at higher engine speeds. These schemes are predominantly torsional paired with minor effects of CP- and NP-bending and longitudinal deflections.

The changes in deflection are significant for all bending vibrations. The oscillation of the free crankshaft end transforms from a pure vertical or horizontal vibration viewed from the crankshaft at zero engine speed to elliptical vibration with increasing speeds. The change in deflection is significant even at low engine speeds and increases with increasing speed. The speed range considered in this study is 1000 rpm to 8000 rpm. The distortion observed for individual modes is at least 50% of the original vibration amplitude under a condition of rest. The percentage distortion as later shown in the graphs is calculated from the displacements at the centre of the crankshaft. The transformation approach is straightforward and data are converted from the real-imaginary to the amplitude-phase format where necessary. Vectors are defined at the crankshaft front and rear ends. These vectors are oriented so that the vectors are in-line with the crankshaft axial direction. The displacement amplitudes at the vector tips of the crankshaft front and rear ends are then applied to calculate the vertical and horizontal deflections. The displacements are oriented so that the values are obtained in a crankshaft synchro-rotating coordinate system. The displacement values of the mainstream direction are scaled to unity and the distortion is shown in relation to this value. The shown percentage diversion describes the ratio of the axis length of the elliptical crankshaft vector tip orbits.

The data from this methodology are inaccurate with respect to the applied bearing clearance of the crankshaft main bearings. This value is included in the displacement information and cannot be back calculated. This is because the displacement information in the bearings of the operating engine include elastic deformations. These are significantly larger than the pure clearances of the plain bearings.

Accounting for that problem one can use this deformation data as a whirling indicator, but not as a measure for absolute amplitudes of whirling displacements.

The derived distortion data are displayed for the conventional flywheel in Figure 8.2.6. The results can be briefly summarised so that the amount of whirl at zero engine speed equals zero. Pure vertical and horizontal bending occurs without any whirling influence. The whirling amplitudes show a degressive amplification with increasing engine speed. A couple of side effects are recognized showing system resonances exerting influence on whirling modes of the crankshaft. The maximum distortion is calculated with less than 100% for whirling modes not exploited to influencing resonances. Without external resonance influences all whirling amplitudes in the crank-plane are obtained with smaller

amplitudes than whirling amplitudes at the normal plane. This effect is mainly driven by the stiffness properties of the crankshaft for the different directions. A further interpretation of the obtained results will be given in the next section comparing the analytical and the measured results and in the subsequent discussion matching the conventional and flexible flywheel results.

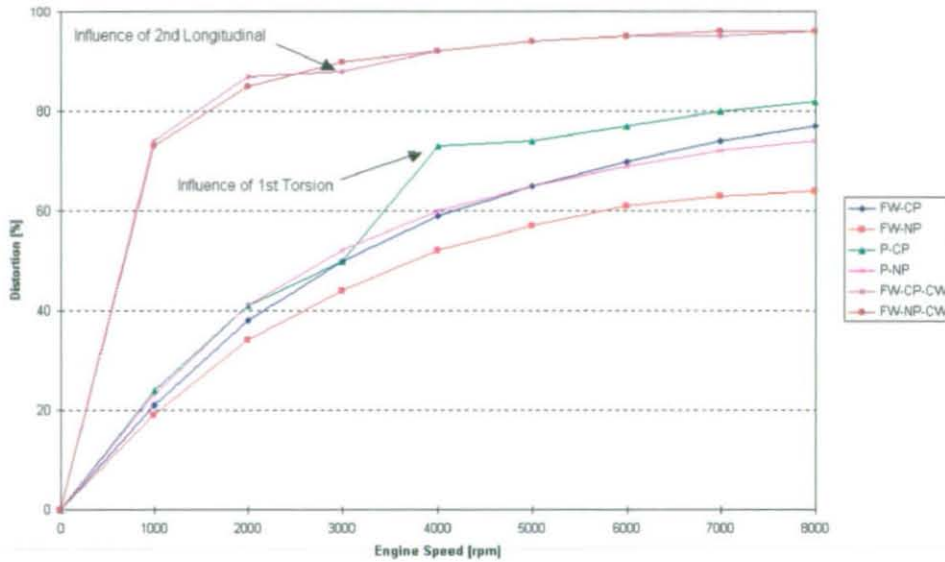


Figure 8.2.6 Flywheel Whirl (Conventional Flywheel)

Comparing the resonance behaviour of the conventional and flexible flywheel, an overview of the calculated whirling frequencies is displayed for the conventional flywheel assembly in Figure 8.2.7 and for the flexible flywheel in Figure 8.2.8. The basic results are comparable to the findings already discussed and are not assessed again. But an important phenomenon must be highlighted at this point. The mutating whirling frequencies are passing through resonances of other modes. Typical examples are shown in the next figure. Some anomalies are obtained under those conditions for both resonances. One has to consider that the results are derived within engine speed increments of 1000 rpm. Hence, crossing frequencies are never accurately determined in this study and no definite data are available, whether the frequency graphs show folds or not.

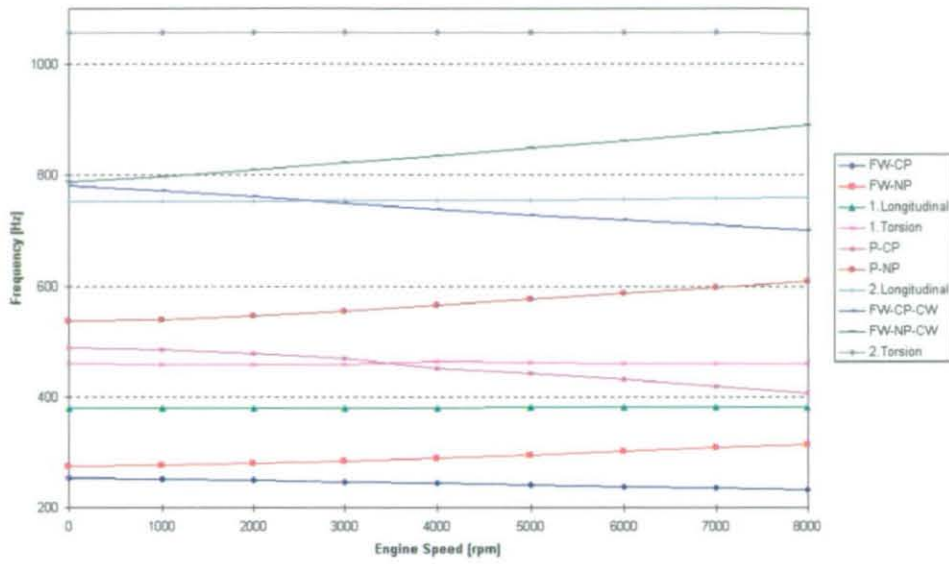


Figure 8.2.7 Whirling Frequencies of Conventional Flywheel System

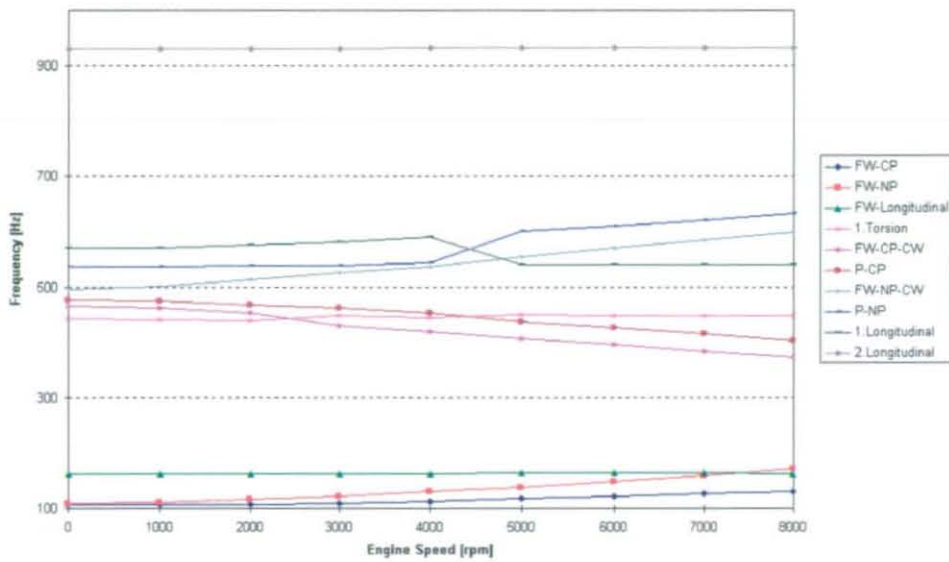


Figure 8.2.8 Whirling Frequencies of Flexible Flywheel System

The crankshaft longitudinal and torsional vibrations are shown for the conventional and flexible flywheel assembly in Figure 8.2.9 .

The longitudinal vibrations do not mutate with engine speed. Some exceptions must be made for conditions where whirling modes do affect or graphically cross the pure longitudinal resonances as highlighted in the graph. An identical behaviour must be stated for the torsional vibrations. The frequency values mutate only at those engine speeds where whirling modes occur at the same values as shown in the graph.

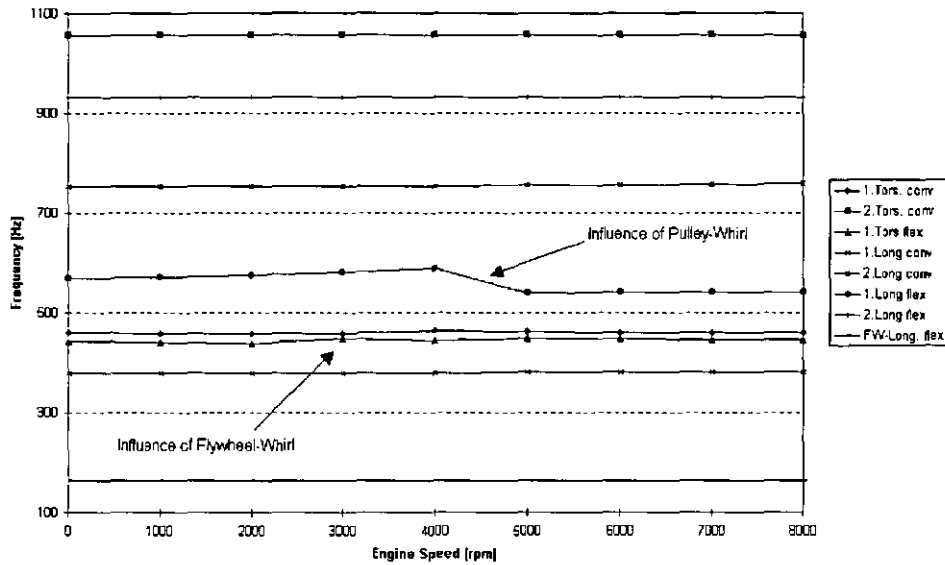


Figure 8.2.9 Longitudinal and Torsional Vibration of Conventional vs. Flexible Flywheel

Significant frequency changes are seen for the whirling modes as described theoretically in section 3.6. With increasing engine speed the resonance frequencies decrease for the crank-plane and increase for the normal-plane whirling modes as shown in Figure 8.2.4 and Figure 8.2.5. On the basis of the explained theory whirling frequencies increase with rotational speed for those systems with polar mass moments of inertia larger than the axial mass moment of inertia. The relation of the axial and polar mass moment of inertia is not only distinguished by the system geometry and mass distribution, system stiffness distribution and hence whirling displacements are also influencing parameters. A typical example is given with a flywheel whirling resonance. Assuming a significantly stiff support from the main bearing structure, one locates the centre of whirling displacement next to the last bearing. The same geometry will have its centre of whirling oriented towards the crankshaft front, if the supporting stiffness is not high enough. The geometry and the inertias are the same for both cases, but the relation between polar and contributing axial mass moment of inertia are changed due to the altered centre of whirling.

Analysing the whirling shapes of the conventional flywheel system with respect to the previously stated theory, the crank-plane whirling modes centre is located nearly at the last crank cheek. Whereas the normal-plane whirling modes centre can be found at the fifth main bearing due to the higher stiffness values of the crankshaft in the normal-plane.



The different axial mass moments of inertia result from the heterogeneous distance from the centre of whirling rather than from the different geometry and stiffness distribution of the crankshaft in the crank- and normal-plane.

A comparison of the syncro-rotating 1<sup>st</sup> whirling modes are shown in Figure 8.2.10 for the conventional and the flexible flywheels. The basic principle of modulated frequencies can be identified in this graph with the exception of the flexible flywheel crank-plane whirling. The main reason for the increasing frequency is that the flexible flywheel whirls about the sheet metal membrane rather than the last crankshaft cheek. This significantly reduces the axial mass moment of inertia influencing a resonance frequency increase.

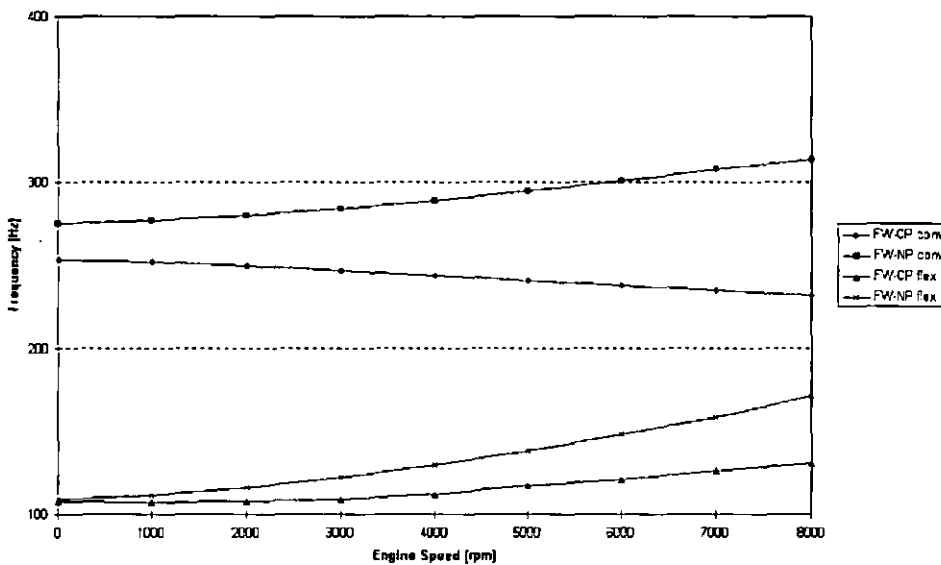


Figure 8.2.10 1<sup>st</sup> Flywheel Whirling of Conventional vs. Flexible Flywheel (Syncro-Rotating)

The percentage differences in whirling frequencies are summarised in Table 21 for 7000 rpm engine speed under no load condition. A comparison is given for the conventional and flexible flywheel systems. Figure 8.2.11 displays a comparison of the contra-rotating flywheel whirl resonances, whereas the pulley whirling is posted in Figure 8.2.12. Only marginal differences are obtained when comparing the pulley results of the conventional and flexible systems. This shows that the flywheel design is effective at the rear end and the contributing effect on the front end is negligible. A potential performance increase with respect to NVH can only be expected at the engine rear end utilising a flexible flywheel. Comparing the absolute values of the whirling frequencies between both systems an increase of the 1<sup>st</sup> whirling resonance can be achieved

applying a flexible flywheel rather than a deteriorated 1<sup>st</sup> whirling mode. But both whirling modes of the flexible flywheel are conversely in the range of the first engine order and hence significantly excited.

Whirling Mode	Conventional Flywheel	Flexible Flywheel
Flywheel CP <small>(syncro-rot.)</small>	-7%	+17%
Flywheel NP <small>(syncro-rot.)</small>	+12%	+45%
Pulley CP	-14%	-13%
Pulley NP	+12%	+15
Flywheel CP <small>(contra-rot.)</small>	-9%	-18%
Flywheel NP <small>(contra-rot.)</small>	+11%	+18%

Table 21 Percentage Difference in Whirling Frequencies (7000 rpm)

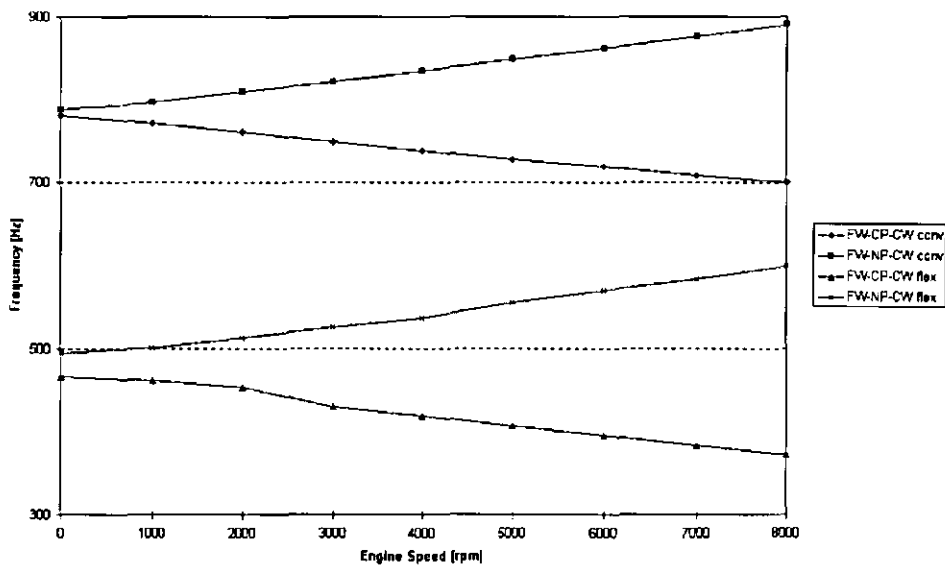


Figure 8.2.11 1<sup>st</sup> Flywheel Whirling of Conventional vs. Flexible Flywheel (Contra-Rotating)

Comparing the distortions in whirl amplitudes of the syncro-rotating mode significant lower values are obtained for the conventional flywheel (Figure 8.2.13) . The main rationale for this is due to the lower conventional flywheel inertia. Another discrepancy is derived for the contra-rotating whirl exhibiting a considerable higher slope at lower engine speeds for the conventional flywheel compared to the flexible flywheel (Figure 8.2.14) . The pulley whirling results show minor differences only. But side effects are introduced from other resonances influencing the whirl amplitudes within

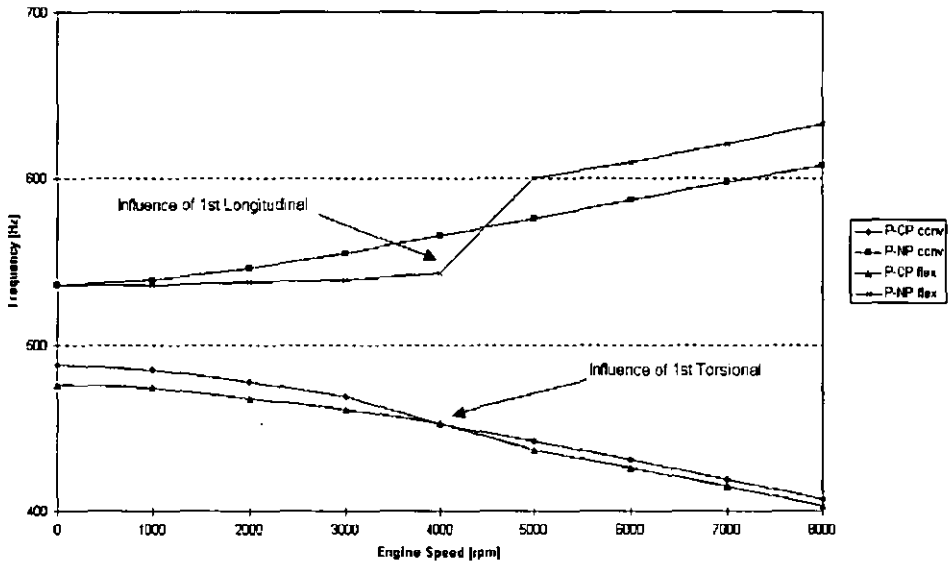


Figure 8.2.12 Pulley Whirling of Conventional vs. Flexible Flywheel

narrow engine speed bands (Figure 8.2.15). This supports the *a priori* mentioned interpretation that the crankshaft rear-end configuration does not affect the overall crankshaft response but is mainly limited to the rear-end response.

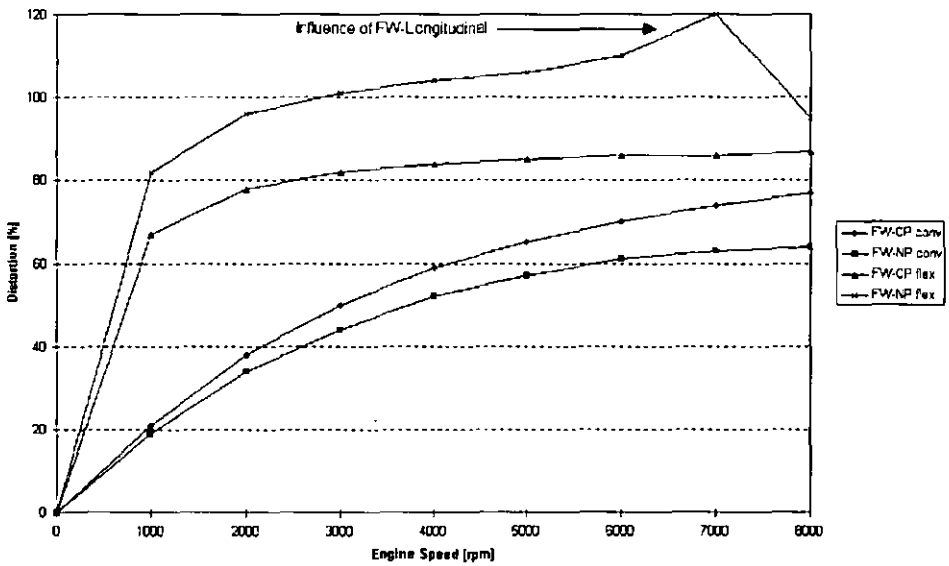


Figure 8.2.13 Flywheel Whirl of Conventional vs. Flexible Flywheel (Syncro-Rotating)

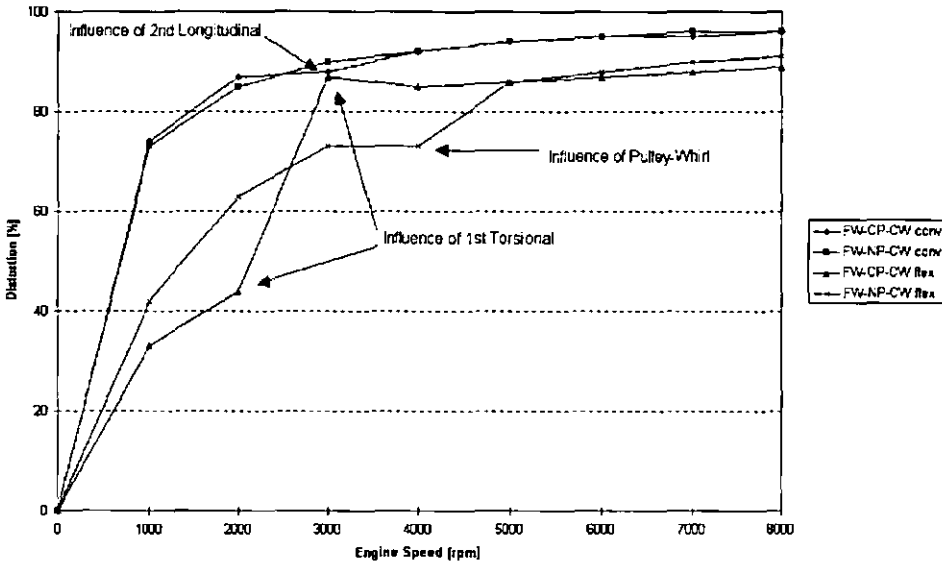


Figure 8.2.14 Flywheel Whirl of Conventional vs. Flexible Flywheel (Contra-Rotating)

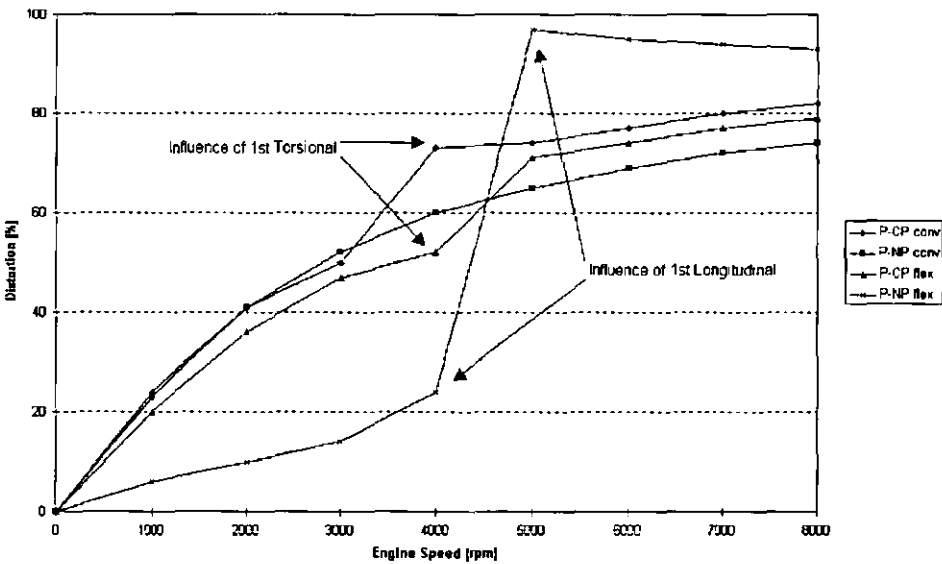


Figure 8.2.15 Pulley Whirl of Conventional vs. Flexible Flywheel

The interpretation of the frequency and whirling distortion results exhibit a basic phenomenon when comparing the conventional and flexible flywheels. The flexible flywheel decouples the main inertia from the crankshaft. The resisting bending moments introduced by the crankshaft to tilt the flywheel are hence significantly reduced. This in parallel reduces the bending stress within the crankshaft and here especially within the last crank throw. The rigidly linked conventional flywheel couples the deformed crank-

shaft with a large inertia. This inertia introduces a resistance against tilting through the coupled self-stabilising rotating inertia. The stresses within the last throw of the crankshaft are increased, but the stabilising effect reduces the crankshaft deformation and therefore the main bearing loads at the rear end and hence the main bearing excitation.

The advantage of the flexible flywheel is therefore given within a stress reduction rather than an excitation reduction at the crankshaft main bearings. This interpretation is opposing published reports and will be verified in section 8.3 within this thesis by noise analysis and correlation measurements.

Having discussed the first set of results received from the mathematical formulation of the coupled crankshaft-crankcase system, we also have to consider the previously discussed stability criterion. As already briefly described in section 3.4, system differential equation of motion describe the system response with respect to a perturbation on the right hand side of the equation. The differential equation therefore also describes the stability of a system with respect to this perturbation. The system stability criterion are recorded here from section 6.3.3:

- asymptotic stable       $\text{Re} (\lambda_i (A_0)) < 0 , i=1, \dots, n$
- marginal stable       $\text{Re} (\lambda_i (A_0)) \leq 0 , i=1, \dots, n$   
and  
at least one  $\text{Re} (\lambda_i (A_0)) = 0$
- unstable       $\text{Re} (\lambda_i (A_0)) > 0$

A similar approach is applied for periodical systems utilising the theory of Floquet. The properties of periodic time-variant systems are similar to those of time-invariant systems, so that the Ljapunov approach can be applied, if a fundamental matrix is defined transforming the time-variant system into a time-invariant system. The transformation matrix is valid for all times and the stability criteria can be employed from the eigenvalues  $\lambda_i$  of the constant system matrix R according to the rules described by Ljupanov [section 6.3.3].

All obtained solutions considering all geometrical alternatives show negative real values for all roots of  $\lambda_i$ . Applying Ljapunov's criterion to the engine model generated for this application all of the solutions are in the asymptotic stable domain, so the entire system must be at least asymptotic stable. Having established this, no further investigation is conducted to calculate the margin of stability. Doing this would require a significant amount of work with no important added value to the results of this investigation.

## 8.2.2 Measurements and Verification

A correlation study [134] was carried out to investigate the motion of the flywheel in four degrees of freedom. The considered degrees are the rotational about the crankshaft axis, angular about the horizontal and vertical axes and crankshaft axial direction.

Two test conditions are considered:

- Full load speed sweep, 1000-6500 rpm, 45 seconds duration
- No load speed sweep, 1000-6500 rpm, 45 seconds duration

The details of the calibration work, data acquisition and analysis procedure are outlined in the appendix.

The results are obtained for both conditions. During the analysis a significant influence of the gas forces on the flywheel displacements are observed. The results which appear contain less clear order signals to identify the whirl modes of the flywheel-crankshaft assembly under full-load. The signals measured under no-load condition are more precise and are hence applied to identify the whirling modes. The measured colour-map results are shown for the full-load condition in the appendix.

Examining the colour-maps of the flywheel whirl results, one has to consider that no absolute measures are shown but relative amplitudes only. Red indicates larger displacements than black. The flywheel axial displacements (Figure 8.2.16) shows that the motion is dominated by first and second orders with a significant but well damped resonance at approximately 165 Hz. The rotational degree of freedom is dominated by second and half engine order displacements (Figure 8.2.17).

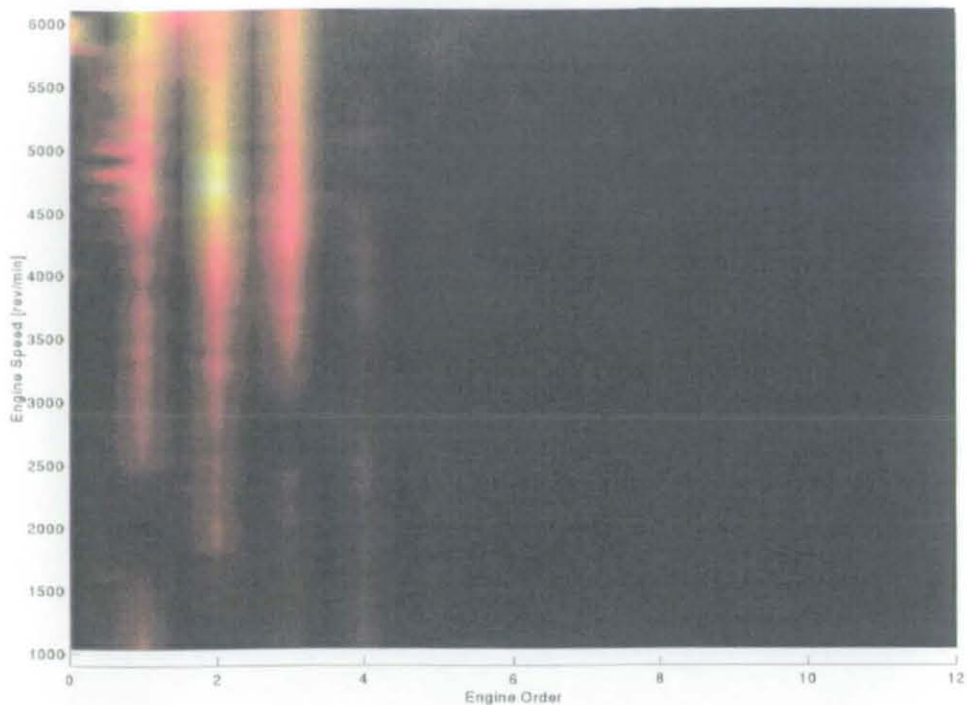


Figure 8.2.16 Flywheel Axial Displacement [No load]

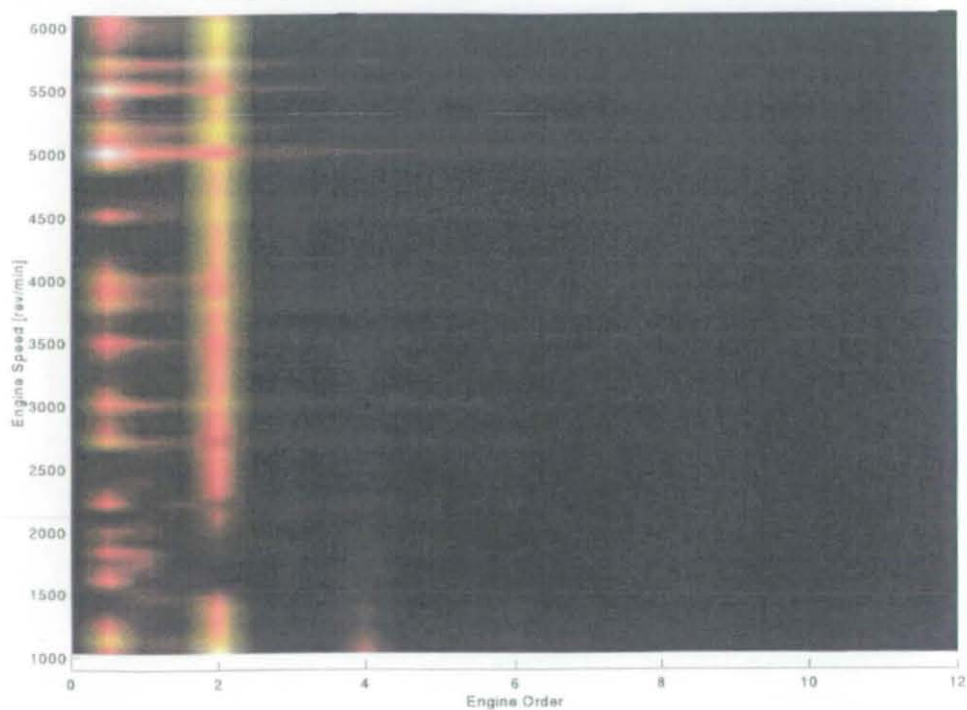


Figure 8.2.17 Flywheel Rotational Displacement [No load]

Examination of the corresponding colour-maps of the vertical (Figure 8.2.18) and horizontal (Figure 8.2.19) angular displacements shows a clear resonance, again at approximately 165 Hz.

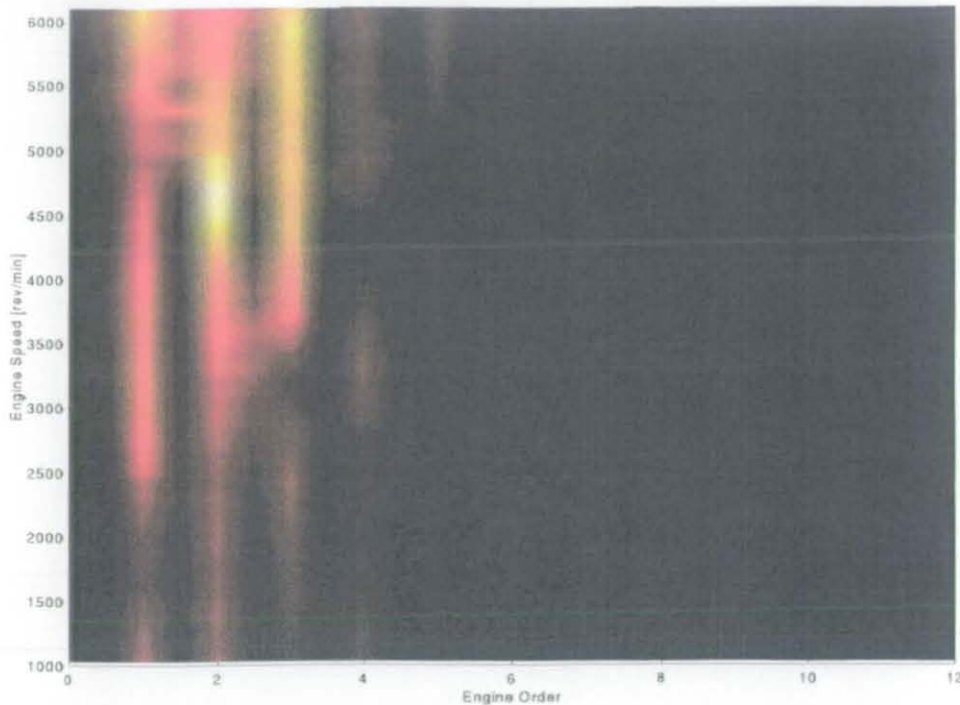


Figure 8.2.18 Flywheel Vertical Displacement [No load]

Analysing the vertical and horizontal displacement of the tip of a vector normal to the surface of the flywheel throughout the speed range, it can be seen that the direction of the whirl at the given order can change direction during the speed sweep. As the engine approaches these transitions, the whirl motion becomes more elliptical with the displacement generally predominant about an axis inclined at approximately  $10^\circ$  to the vertical. This is due to the fact that the whirl motion at any order consists of a forward and a reverse whirl component. For example, whirl occurring at 3E with respect to ground consists of +2E and -4E components with respect to the crankshaft since the crankshaft is rotating at first order. These components intersect to produce the elliptical motion and, when of similar magnitude, produce the pitching motion. The axis of this pitching motion is defined by the phasing of the two whirl components. These components cannot be separated from the test data using a Fourier transformation approach as they occur at the same frequency.



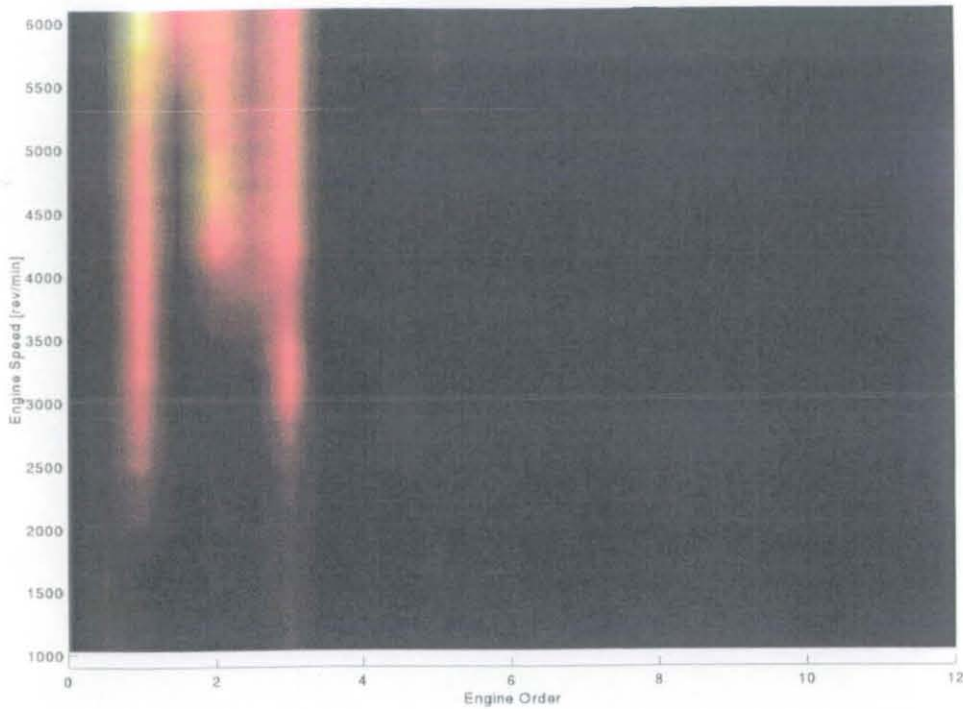


Figure 8.2.19 Flywheel Horizontal Displacement [No load]

Estimates of the magnitudes of the forward and reverse components were derived using the method and assumptions discussed in the appendix. These estimates at full and no-load condition are derived with arbitrary units which allow a comparison of the relative magnitudes of the components. The static whirl with respect to the crankshaft is most probably influenced by a misalignment of the flywheel to the engine block and would therefore be expected to remain constant with increasing engine speed. But the measurements show that the unity estimate of the static whirl level increases with engine speed. Since this estimate assumes the whirl for any single component would result in a circular motion of the normal vector tip, it is obvious that the reverse second order whirl must be of elliptical shape and this affects the result of the estimation process. The results of this poor circular motion assumption are also evident for the higher whirl modes, where an increase in the estimated level of one whirl component generally leads to an inaccurate increase in the other estimate. If the whirl motions due to each individual component are not circular, the resulting estimates from the measurements will not be independent.

The elliptical whirl motion resulting from any single whirl vector is likely to be due to different crankshaft stiffnesses in crank-plane and normal-plane as discussed previously. Additionally, this is due to different bearing stiffnesses or clearances in different directions of the crankcase.

Two resonances occur at 5000 rpm and 3500 rpm respectively. These are forward first, and forward second order whirl and they appear at 80 Hz and 115 Hz on the crankshaft. When the effect of these orders is considered with respect to ground, they correlate both to a single resonance at 165 Hz. This is the resonance seen in the colour-maps. It is not a resonance of a probe as this can be seen for all probes of the flywheel and it is most unlikely to be a measurement error caused by a component mode, as the resonance is not seen at all probe positions. Furthermore, this effect occurs at both the no-load and the full-load condition and is hence independent of the driving combustion process. It is not absolutely clear where this resonance originates, however a rigid-body vertical bounce mode of the powertrain on the engine bed occurs in the range of 156-180 Hz and could increase the angular deflection of the crankshaft at this frequency. It is therefore more difficult to extract the whirl related amplitudes from the colour-maps and some variability of the results must be accepted.

Extracting the appropriate flywheel whirl modes from the colour-maps for the vertical and horizontal direction, the analytically derived results are shown in comparison to measurement results. As the measured results are not very specific for engine speeds below 2000 rpm, correlation is shown for the engine speed range between 2000-6000 rpm. The measurement results are plotted including a band width as established from the measurements. These band widths are not considering a firm range, as the measured results can be interpreted and the shown levels on these colour-maps are not exhibiting a definite frequency value. The measurement results are shown in Figure 8.2.20 as dotted black points. Linear trend-lines are plotted for the horizontal and vertical pairs and 5%-error bars are shown for the analytical results.

Comparing the measured and the analytical results of the flywheel whirling frequency, an excellent correlation is given for all engine speeds. The discrepancy is almost lower than 5% for engine speeds below 4000 rpm, while the results above 4000 rpm exhibit an error of about 8%. Considering that the results were achieved without any model refinement this is an excellent correlation of the measured results and the modelling approach to predict the whirling frequencies of a rotating cranktrain system.

Correlating the measured whirl amplitudes of the flywheel with the analytically obtained results (Figure 8.2.21), one has to consider the formerly expressed concerns about the static flywheel whirl. A static whirl resonance should be independent of the engine speed, but the obtained results indicate a clear dependency on engine speed. The obtained whirling shape is of circular form and will further overlay the higher order resonances and increase the corresponding whirl amplitudes. This can be seen at the measured first engine order whirl. This shows a significant influence of the static whirl at engine

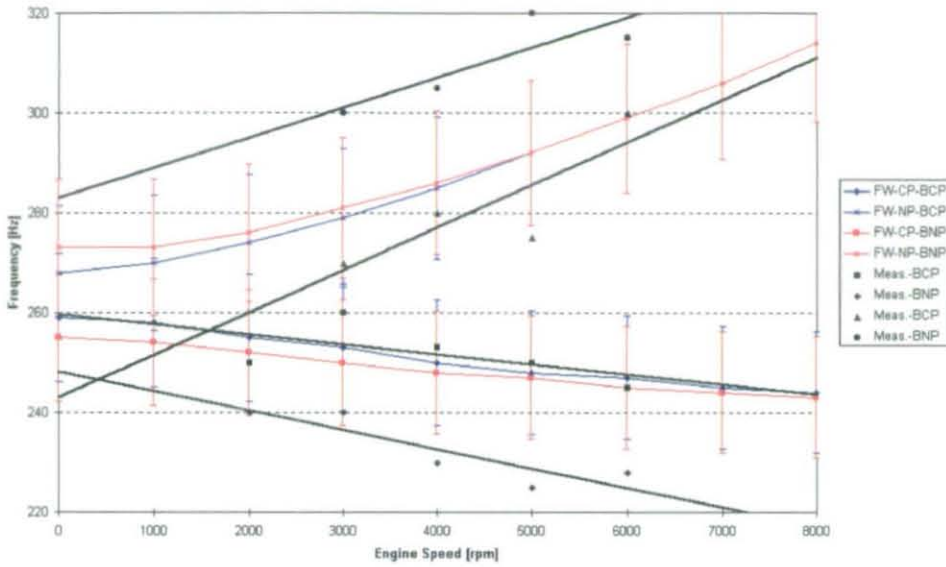


Figure 8.2.20 Flywheel Whirl Frequency Correlation

speeds above 5000 rpm. In view of this phenomenon, an excellent correlation is given for whirl amplitudes at engine speeds below 5000 rpm with the single exception of that at 2000 rpm. This engine speed reveals a significant drop in whirl amplitude, but given the other results, one should consider this as a measured local resonance.

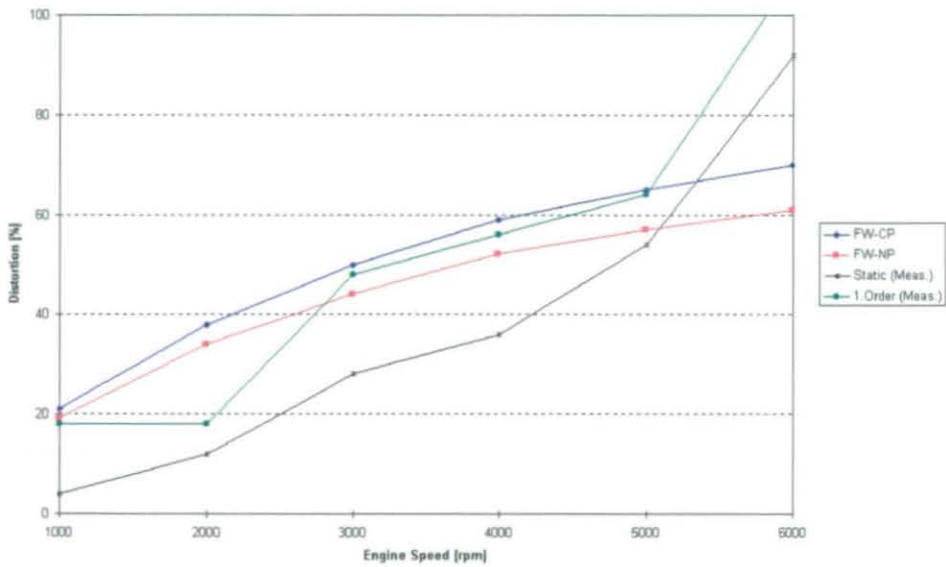


Figure 8.2.21 Flywheel Whirl Amplitude Correlation

An assessment of the measured and analytical results exhibits an excellent correlation. Analytically derived whirl modes compare to the measured values within an error band of 5%. Whirl amplitudes show up with a very good overall correlation leaving out of

consideration the static crankshaft whirl effect at 6000 rpm.

To sum up: the flywheel whirl correlates very well and the modelling approach can be applied for such kinds of analysis.

### **8.3 Noise Radiation**

The analysis of the radiated noise perception is done in three steps. Firstly, the noise estimation model from section 7.2.2 is applied to identify those engine speeds showing a significant contribution of the engine block. Waterfall diagrams and third octave plots are generated for these speeds. This technique is then also applied to the design alternative and a first interpretation of the obtained differences is given. Measurements of the surface velocities are made to correlate the analyses. Secondly, two particular engine speeds are selected and a detailed noise radiation investigation is performed applying the methods described in section 7.3. The thereby obtained results and the ranking of the various design alternatives are then correlated with measurements. Thirdly, an auralisation is performed on the analytical results. The obtained noise samples are compared with measured engine noise.

Finally a judgement is made of the applied techniques and their respective advantages, disadvantages and limitations.

#### **8.3.1 Surface Velocity Investigation**

Figure 8.3.1 displays the integrated surface velocity results obtained for the conventional and flexible flywheel throughout the engine speed range. The general trend exhibits an increase in integrated surface velocities with increasing engine speed illustrating a growth in noise radiation. But three peaks attract the attention at 2400, 3500 and 5100 rpm. While the solid flywheel always exhibits two peaks at these engine speeds, the flexible flywheel shows a single peak at shifted engine speeds. The shift in engine speed between both design alternatives indicates that resonance frequencies with minor differences occur.

To prove this assumption third octave band waterfall diagrams are calculated applying the approach from section 7.2.2. The obtained results are displayed for the conventional flywheel in Figure 8.3.2 and for the flexible flywheel in Figure 8.3.3. The engine orders and especially the first half and full order are clearly displayed in both versions. The amplitude of the flexible flywheel exhibits significant larger amplitudes in integrated surface velocities at the first engine order than the solid flywheel. Comparing both graphs a significant frequency range of 100-600 Hz can be obtained, presenting reasonable resonances for both flywheel versions.

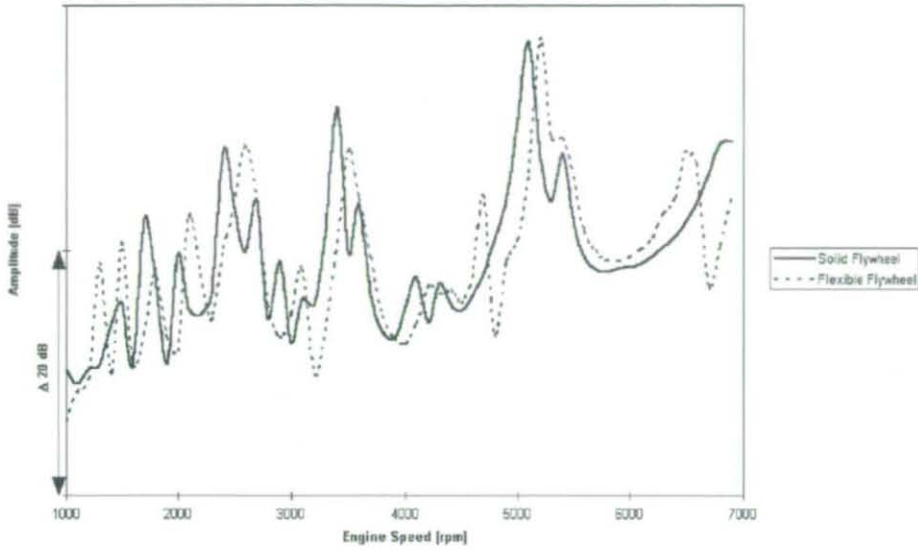


Figure 8.3.1 Summed Surface Velocity [dB rel  $v_0$ ]

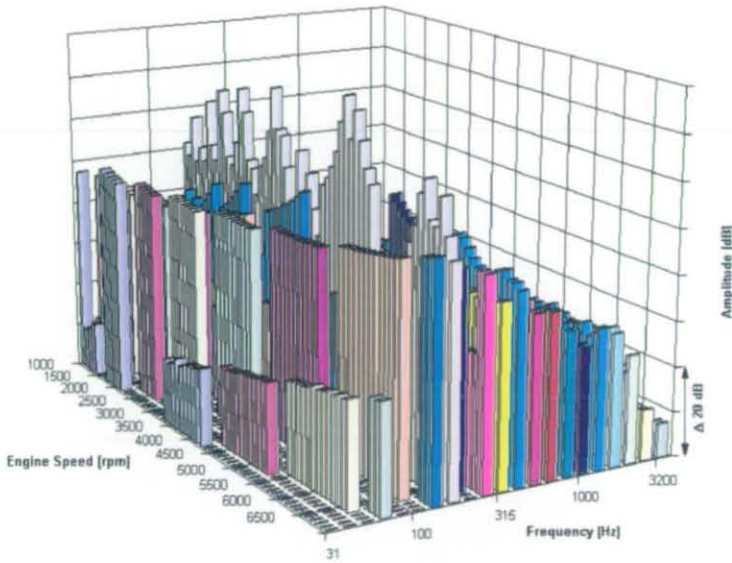


Figure 8.3.2 Integrated Surface Velocity - Solid Flywheel [dB rel  $v_0$ ]

The interpretation is simplified by plotting the result difference of both flywheel designs. The result data of the flexible flywheel are subtracted from the solid flywheel results and are shown in Figure 8.3.4. Positive values indicate that the conventional flywheel shows higher integrated surface velocities, while negative values exhibit larger values for the flexible flywheel. The data obtained can be interpreted in a way that for positive values the conventional flywheel radiate more noise than the flexible flywheel and the other way round. Again the most significant frequency range is obtained from 100-600 Hz displaying a substantial difference in surface velocity. The solid flywheel discloses high

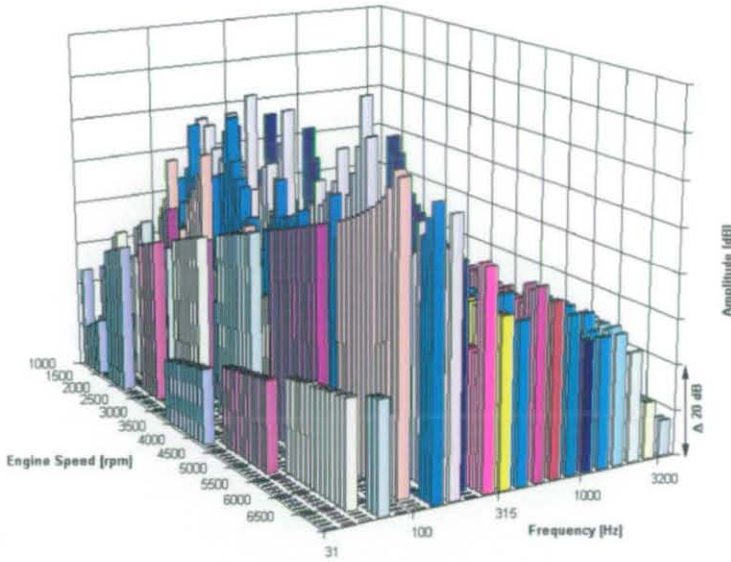


Figure 8.3.3 Integrated Surface Velocity - Flexible Flywheel [dB rel  $v_0$ ]

surface velocity levels at low engine speeds. Here we find significant increased levels at the 0.5th and 1st engine order degrading with an exponential slope. Furthermore, a resonance frequency is seen at approx. 240 Hz, showing the first flywheel whirl resonance. The flexible flywheel displays a similar resonance at a lower frequency and an amplitude increasing with second order two octave bands below the solid flywheel resonance. The significant shift of peak surface velocity values implies the emergence of shifted resonance frequencies between the flexible and standard flywheel. It is therefore necessary to investigate the summed surface velocities at various constant engine speeds. The waterfall diagrams are post-processed as described in section 7.2.2. Third octave plots of the summed surface velocity are derived for the following engine speeds: 2400, 2700, 3400, 3500, 3600, 4700 and 5100 rpm.

For 2400 rpm engine speed the third octave plot is shown in Figure 8.3.5 displaying differences within the 112-141 Hz and 141-178 Hz third octave band. Both are mainly driven from the crankshaft modes being excited at the 3<sup>rd</sup>, 3.5<sup>th</sup> and 4<sup>th</sup> engine order. While the solid flywheel resonance is mainly influenced by vertical crankshaft vibrations, the flexible flywheel shows primarily two axial vibrations. The engine block surfaces therefore are mostly excited by the vertical vibration of the solid version rather than from the axial of the flexible flywheel.

Similar results are derived at 2700 rpm engine speed as shown in Figure 8.3.6. The 112-141 Hz third octave band is driving the differences between both flywheel versions. But the flexible flywheel axial vibration contributes more to the block horizontal vibration and hence influences the surface velocity results significantly within that band.

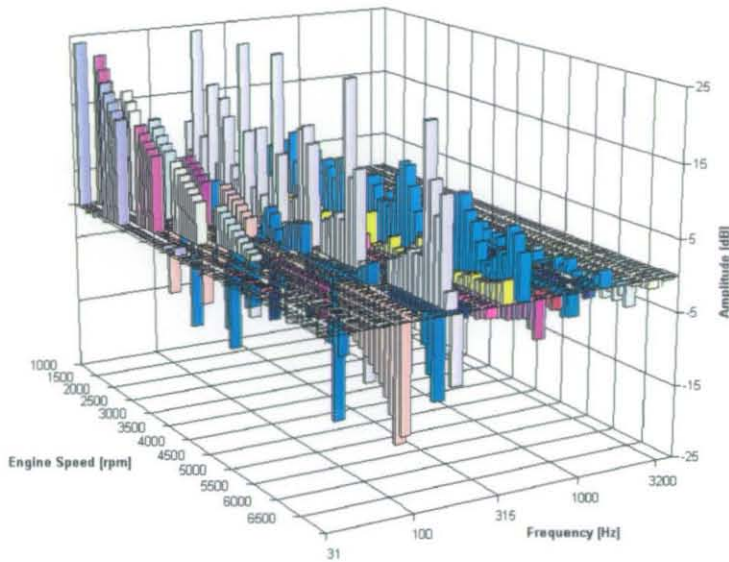


Figure 8.3.4 Integrated Surface Velocity - Solid vs. Flexible Flywheel [dB rel  $v_0$ ]

The results for 3400 rpm and 3500 rpm engine speeds must be analysed together. At 3400 rpm the solid flywheel exhibits a significant resonance within the 141-178 Hz third octave band showing a dramatically worse level than the flexible flywheel (Figure 8.3.7). The resonance is derived with 169 Hz and is mainly excited with the 3<sup>rd</sup> engine order at 3380 rpm. The corresponding 3<sup>rd</sup> engine order resonance occurs for the flexible flywheel at 3500 rpm or 173 Hz within the same band (Figure 8.3.8).

Data accessed in Figure 8.3.9 at 3600 rpm engine speed show unique results between both flywheels with the exception of the 112-141 Hz third octave band. The flexible version shows a reduced level within that band as explained previously.

Another significant engine speed is detected at 4700 rpm showing a significant increase for the flexible flywheel within the 141-178 Hz band (Figure 8.3.10). This peak is primarily driven by a resonance of the flexible flywheel combining a vertical and axial vibrations. Within the 112-141 Hz band the solid flywheel shows an increase as already explained before. But this level does not effect the maximum overall level.

The summed surface velocity levels show significant peaks at 5100 rpm for the solid and at 5200 rpm for the flexible flywheel. The calculated third octave plots are shown in Figure 8.3.11 for 5100 rpm and in Figure 8.3.12 for 5200 rpm. Again both alternatives show exaggerated levels at the 141-178 Hz third octave band excited at the 2<sup>nd</sup> engine order. The engine speed is calculated with 5070 rpm for the solid and with 5220 rpm for the flexible flywheel. The corresponding resonances are again calculated with 169 Hz and 174 Hz respectively.

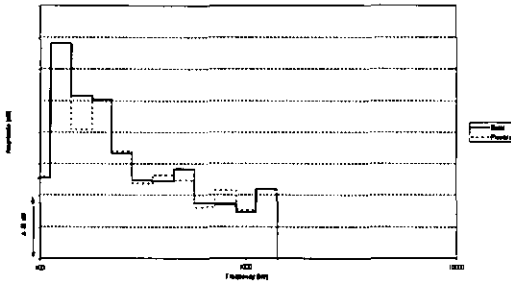


Figure 8.3.5 2400 rpm

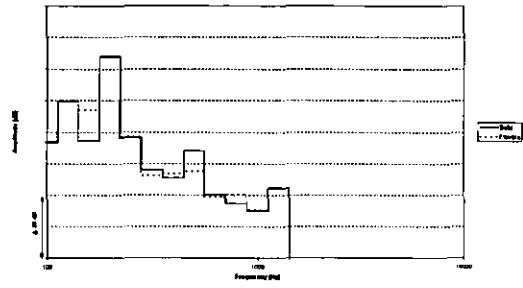


Figure 8.3.6 2700 rpm

Integrated Surface Velocity - Solid vs. Flexible Flywheel [dB rel  $v_0$ ]

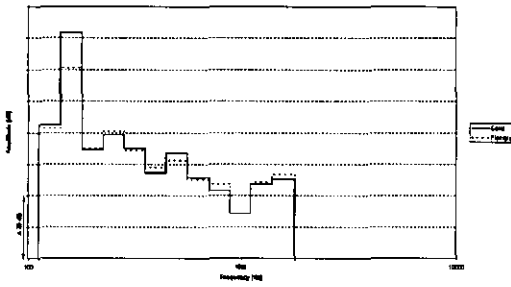


Figure 8.3.7 3400 rpm

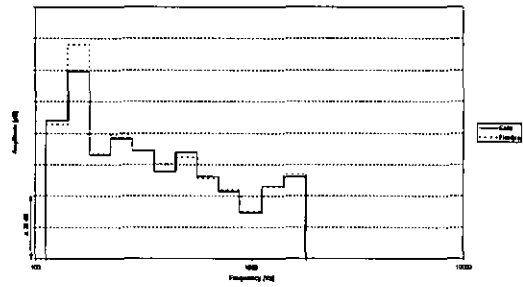


Figure 8.3.8 3500 rpm

Integrated Surface Velocity - Solid vs. Flexible Flywheel [dB rel  $v_0$ ]

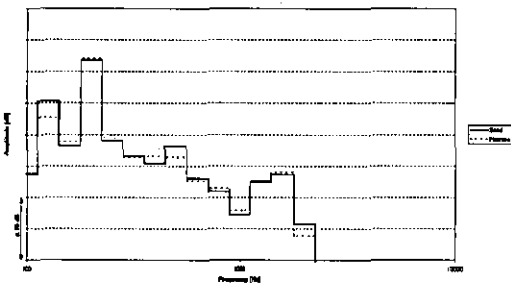


Figure 8.3.9 3600 rpm

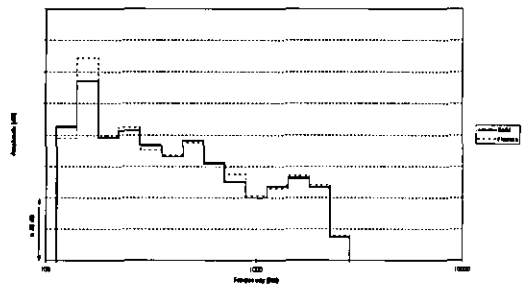


Figure 8.3.10 4700 rpm

Integrated Surface Velocity - Solid vs. Flexible Flywheel [dB rel  $v_0$ ]

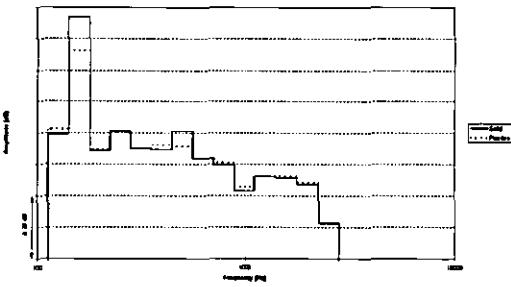


Figure 8.3.11 5100 rpm

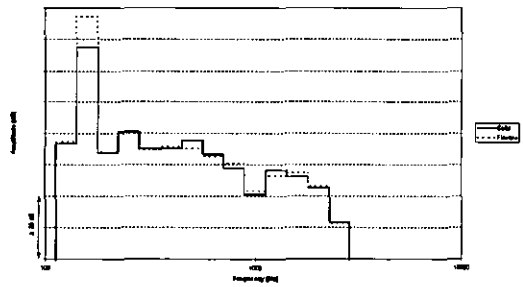


Figure 8.3.12 5200 rpm

Integrated Surface Velocity - Solid vs. Flexible Flywheel [dB rel  $v_0$ ]



Studying the integrated surface velocities with respect to the estimated radiated noise perception and frequency content is one means of post-processing the derived data. As explained in detail in section 7.2.2 we may also utilise the integrated surface velocities to locate regions of large vibrational amplitude. Applying this information and the frequency domain results identifying structural weaknesses and participating eigenvalues is straightforward. From this effective countermeasures can be developed.

Measurements were obtained to establish the integrated surface vibration at specific engine speeds. The tested configuration is shown exemplarily for the left and right hand sides of the engine structure in Figure 8.3.13 and 8.3.14. The bottom side is displayed in Figure 8.3.15. The fired engine test was done independently from the analysis. Hence, some differences in analytical and measured engine speeds may occur. For some instances such inconsistencies are marginal and can therefore be disregarded. Some operating conditions do not match and show a discrepancy of 250-300 rpm. The obtained results can hence be used as an indicator only a fact to be taken into consideration when comparing the data.

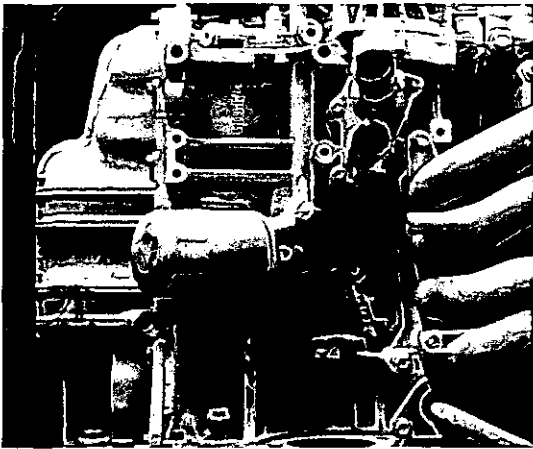


Figure 8.3.13 Surface Velocity Measurement - Left Engine Side

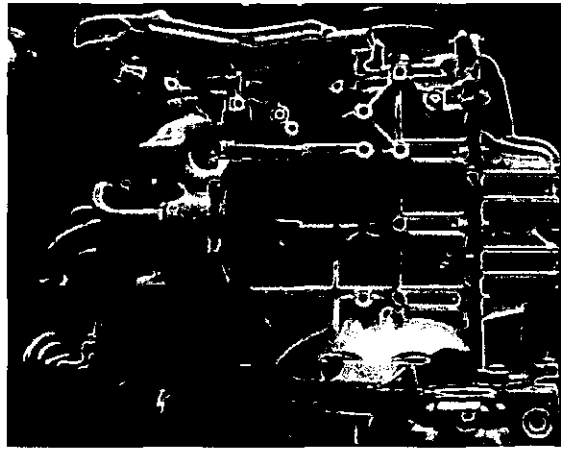


Figure 8.3.14 Surface Velocity Measurement - Right Engine Side

A typical set of measured results is shown in Figure 8.3.16 for the left hand engine side. The corresponding analytical outcome is posted in Figure 8.3.17 for 5000 rpm engine speed. The bottom side results are given in Figures 8.3.18 and 8.3.19. Similar measured and analytical results are shown for other engine speeds and directions in the appendix. In cases of significant differences in measured and analytical engine speeds two adjacent measurement results are shown covering lower and higher speed values.

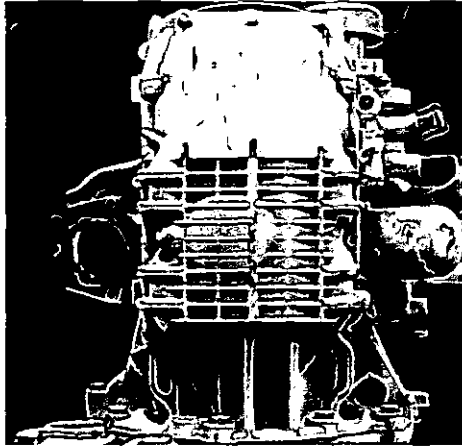


Figure 8.3.15 Surface Velocity Measurement - Oilpan

Comparing the measured results for the left hand engine side at 4918 rpm with analytically derived data at 5000 rpm a good correlation is seen at the centre and front of the oilpan and at the flange areas. Both sources are indicating similar regions of high amplitudes and hence noise radiation. Drawing a comparison between the results perceived for the bottom side of the engine a similar picture is seen. The areas of high activity are shown at the centre and front of the oilpan for both sources. Additionally the non-symmetric surface velocities at the engine rear side are also clearly shown in both methods.

A comparison for other engine speeds exhibits similar results. The identified areas of high activity are comparable for both the measured and analytical results. The only operation condition showing a divergence is found at 3000 rpm and the oilpan direction. The most probable explanation is that the measured and analysis engine speeds do not match exactly enough, so that some differences may occur influenced by shifted excitation frequencies and resonances. The distinction between the measured and calculated engine speed is 67 rpm after analysing the data in more detail another definite reason could not be established for that phenomenon.

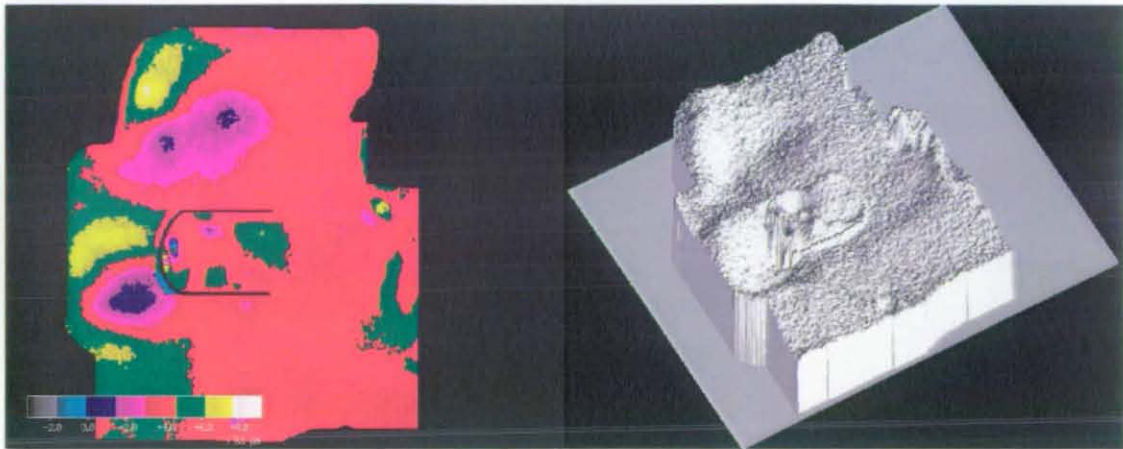


Figure 8.3.16 Left Engine Side Surface Velocity (Test @ 4918 rpm)[mm/s]

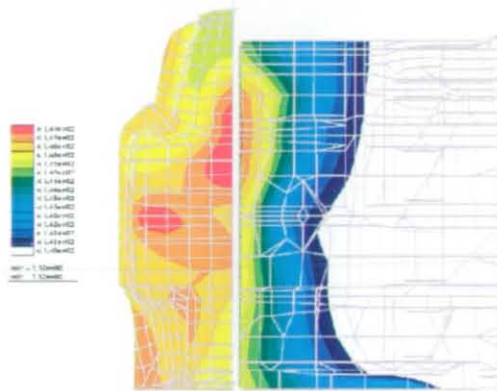


Figure 8.3.17 Left Engine Side Surface Velocity (Analysis @ 5000 rpm)[mm/s]

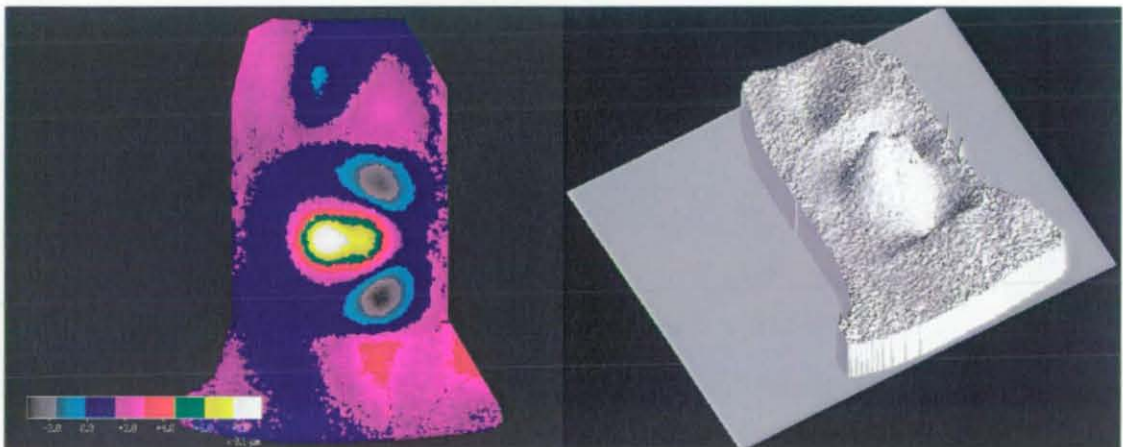


Figure 8.3.18 Oilpan Surface Velocity (Test @ 5101 rpm)[mm/s]

In summary the shown results indicate that the calculated and measured data correlate. The derived theoretical approach for predicting areas of high surface velocities can be applied to establish a first indication of the engine noise radiation characteristic

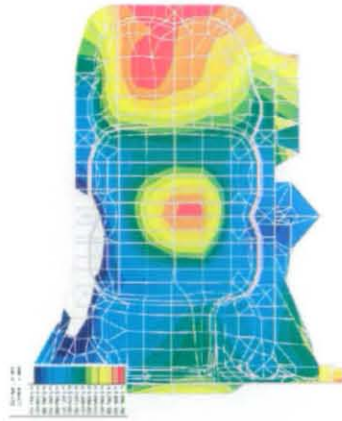


Figure 8.3.19 Oilpan Surface Velocity (Analysis @ 5000 rpm)[mm/s]

throughout the speed range. It is worth mentioning that the response of the engine surface from both measured and predicted results change significantly with increasing engine speed and even with small changes. Approaches as published in literature ([5],[6],[13]) and discussed previously which do not consider an analysis throughout the engine speed range, may mislead in interpreting the results. The perception of various design alternatives at a single engine speed are most probably different compared to studies considering the entire speed range. This has been proven by this correlation study.

### 8.3.2 Noise Measurements

In the measurement project [135] described below the influence of the flexible flywheel was measured on the noise and vibration behaviour. Also, the influence of the bearing beam design was investigated in comparison to individual bearing caps. The noise and vibration measurements for all design modifications on the ZETEC-SE 1.4l series A2 were conducted in a semi-anechoic test cell at FEV Motorentchnik. To account for a reasonable level of vehicle installation and to reproduce the installed perception, the complete powertrain, i.e. engine with transmission and original mounts, was used. The power was delivered to both drive-shafts. This ensured that the radiated powertrain noise and the low frequency powertrain vibration are considered. The transmission was engaged in the 5<sup>th</sup> gear. In order to eliminate any disturbing noise source, the engine was not equipped with a Front-End-Accessory-Drive (FEAD). Also the alternator was deleted. Additionally the plastic intake manifold was encapsulated for the noise measurements. The transmission was also encapsulated. Pictures of the powertrain installed in the semi-anechoic test cell are documented in Figures 8.3.20 and 8.3.21. The attained measured radiated noise results are supplied in electronic form, so that the analysis results can be directly compared.

Further measurements are obtained to establish the vibration excitation input into the vehicle by the powertrain. The excitation was evaluated by means of three-dimensional acceleration measurements on all three engine mounts. All acceleration data are available, but are not utilised in this study. The main focus is given to the noise radiation and the subjective human perception between the design alternatives.

The measurement results are discussed and compared with analytically derived findings in section 8.3.3.

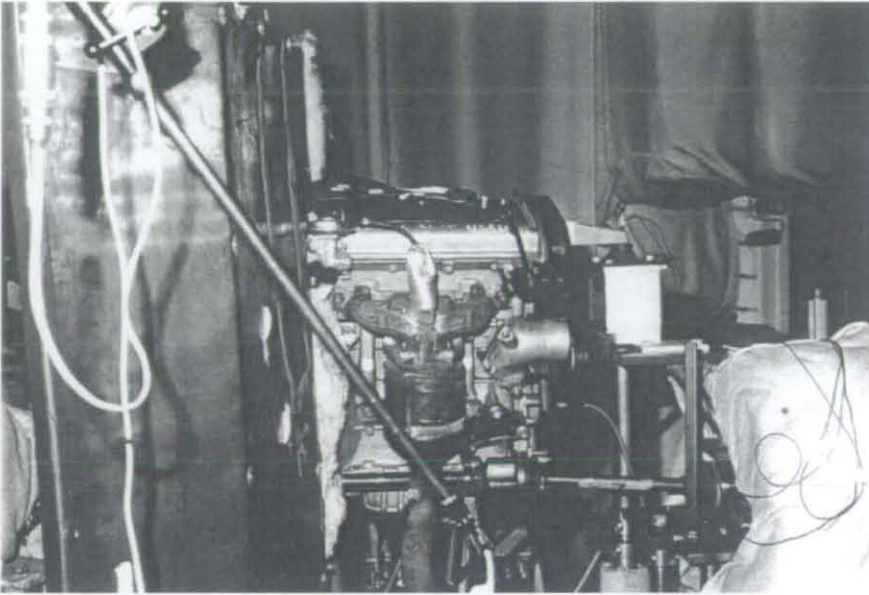


Figure 8.3.20 Powertrain in Anechoic Cell - Exhaust Side

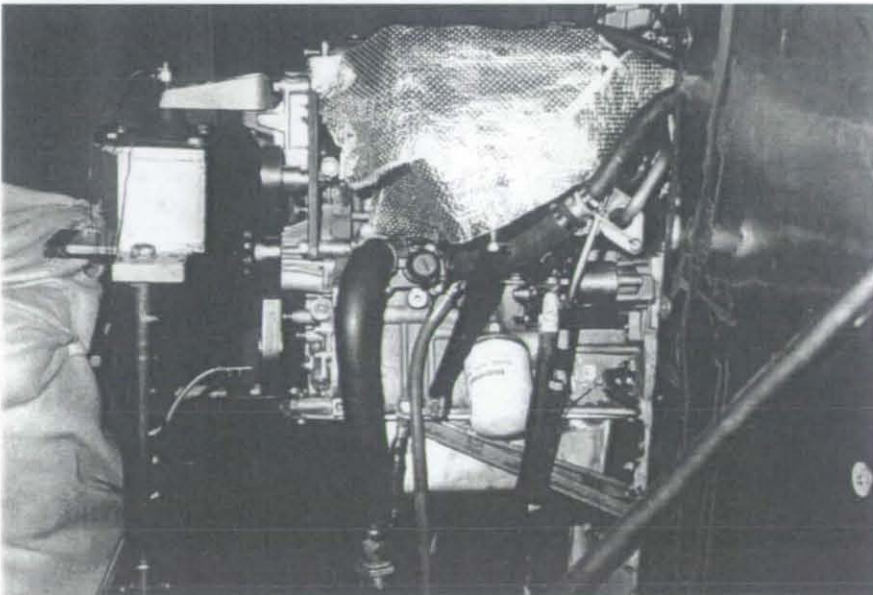


Figure 8.3.21 Powertrain in Anechoic Cell - Intake Side

### 8.3.3 Noise Analysis and Verification

The quality of an analysis is subjected to various aspects of interpretation. For the type of investigation developed in this project measured and calculated data may be compared as narrow band, third octave, octave and summed sound pressure results. The depth of information is reduced with an increasing level of reduction. A comparison between alternatives on the basis of an overall sound pressure value is easy to achieve. But this may be misleading. If only the peak value is imprecisely predicted, the absolute pressure maximum and hence the comparison between alternatives is not anticipated correctly. It is therefore necessary to study the obtained results in more depth. Starting from an overall view and comparing the total sound pressure results further analyses must also consider octave, third octave and narrow band information. The evaluation of the noise evaluation approach developed in this work follows this argumentation and correlates the analytical results with measured data from a top to bottom approach.

The narrow band information, third octave and octave band data and summed sound pressure values are available for 24 different cases. The altered parameters are :

- three geometrical alternatives
  - a) Base design with bearing-beam and conventional flywheel
  - b) as a), but bearing-beam replaced by individual bearing-caps
  - c) as a), but conventional flywheel replaced by flexible flywheel
- two engine speeds
  - a) 3000 rpm
  - b) 6000 rpm
- two observation locations
  - a) left hand engine side at 1 m distance
  - b) bottom side at 0.15 m distance
- analysis and measurement results

The analysis and all further post-processing activities consider the left hand and bottom side of the engine only. As shown in Figure 8.3.20 the right hand engine side is mainly covered by the closed coupled catalyst and the attached heat shield not shown here. The obtained measurement results indicate that the catalyst is a major source of noise radiation at this side and that the noise coming from the engine block surface are of minor importance. It has therefore been decided to skip the analysis and correlation on that side as the catalyst and the corresponding excitations are not considered within the applied modelling approach, so the remaining sides to be studied and correlated are the left hand and bottom side of the engine.

Going over the results of the summed surface velocities and the corresponding third octave data we can see that mainly two speed ranges show substantially different results comparing the conventional and flexible flywheel. While the conventional design exaggerates significant peaks at approximately 3000 rpm, peaks are obtained for the flexible alternative at about 6000 rpm. These two engine speeds are therefore considered for a detailed investigation and comparison in terms of noise radiation and subjective perception. If not explicitly mentioned all subsequently shown data are A-weighted to account for the human perception profile.

The derived total sound pressure values are shown for measurement and analysis results within Table 22 for 3000 rpm and Table 23 for 6000 rpm.

	Left Engine Side		Bottom	
	Measurement	Analysis	Measurement	Analysis
Base Design	81.1	77.5	87.8	98.0
Bearing Caps	83.4	78.9	87.0	94.3
Flexible Flywheel	88.3	79.0	83.3	93.0

Table 22 Total Sound Pressure Level (3000 rpm; [dB(A)])

	Left Engine Side		Bottom	
	Measurement	Analysis	Measurement	Analysis
Base Design	96.2	80.2	105.1	106.0
Bearing Caps	97.4	90.6	102.8	101.3
Flexible Flywheel	104.4	102.6	97.5	104.9

Table 23 Total Sound Pressure Level (6000 rpm; [dB(A)])

The analytically derived results are in the same magnitude as the test data. The absolute maximum difference is derived with 16dB<sub>A</sub> at 6000 rpm at the left engine side. This compares to a percentile difference of 16.7%. Generally, a satisfactory correlation can be found for all other results. As already established in section 8.3.1, the summed sound pressure results increase with engine speed as expected.

The main emphasis of this approach is to establish an analytical method which allows us to compare various design alternatives on a relative basis. Comparing designs and establishing the correct hierarchy in terms of noise radiation is the essential reason for this method.

Applying this approach to the studied alternatives and comparing the analysis results with measurement data, an excellent correlation is established. The trend prediction between two alternatives is always established in the correct order for all versions and all speeds. Hence, a design decision based on analysis results would be 100% correct in terms of noise radiation comparing the base design with the two alternatives.

Establishing a trend prediction between all three alternatives, three out of four hierarchies show the same order as obtained by the measurements. The only difference is accessed for the oilpan side at 6000 rpm. The prediction correctly shows the base design as the loudest version whilst the flexible flywheel is observed as the quietest one. The measurements also observed the base design as the loudest version, but the individual bearing cap design is measured as the quietest one.

In total 12 cases are available to compare analysis and measurement results. A comparison of the analysis results shows that 11 of 12 cases are correctly predicted compared to measurements. A simple statistical study is applied to verify the percentage accuracy of the analysis results. Assuming that the analysis may predict better versus worse comparing two alternatives, a 50% probability is established by guessing the result. The total probability of the study to guess 11 of 12 comparisons with a correct hierarchy is derived applying a binomial distribution:

$$\begin{aligned}
 P_T &= \binom{n_T}{n_R} p_T^{n_R} (1 - p_T)^{n_T - n_R} \\
 &= \frac{n_T!}{n_R!(n_T - n_R)!} p_T^{n_R} (1 - p_T)^{n_T - n_R} \\
 &= 0.15\%
 \end{aligned}
 \tag{8.3.1}$$

with

$n_T = 12$	:	number of tips
$n_R = 11$	:	number of correct tips
$p_T = 0.5$	:	probability of individual correct tip

The probability for a correct guess of 11 out of 12 trends is calculated with 0.15%. From a statistical point of view it is obvious that this cannot realistically be achieved with a



poor model. The statistical analysis shows that the correlated accuracy of the modelling approach is derived with about 90% reliability. This is an excellent result showing the potential of this tool for competitive investigations.

Comparing the base and individual bearing cap design a correct prediction is reached in all cases (100%). Measurements and analyses indicate that only one operation condition exhibits an advantage of the individual bearing caps over the bearing beam design. The condition is 6000 rpm engine speed and the location is given at the left hand engine side showing the absolute highest sound pressure values. Comparing both alternatives one has to decide between a reduced peak level or an decreased overall level throughout a wide frequency range as established with the bearing beam design.

A comparison between the flexible and conventional flywheel designs favours the former at the engine bottom side. But, the results from the engine side indicate a general advantage of the conventional flywheel design.

A comparison is shown for the measured and calculated sound pressure differences in Table 24 for 3000 rpm and in Table 25 for 6000 rpm respectively. It is conspicuous that, although the general trend and hierarchy are predicted in accordance with the measured results, absolute differences are not predicted correctly. The results vary significantly between measured and analysis results. A general trend or constant error offset cannot be derived. Both higher and lower sound pressure differences are predicted compared with measurements.

Variants	Left Engine Side		Bottom	
	Measurement	Analysis	Measurement	Analysis
Base - Caps	2.3	1.4	0.8	3.7
Base - Flex. FW	7.2	1.5	4.5	5.0
Caps - Flex. FW	4.9	0.1	3.7	1.3

Table 24 Differential Sound Pressure Level (3000 rpm; [dB(A)])

Summarising the results obtained one can state that the derived approach can be applied for qualitative summed sound pressure analyses comparing design alternatives and establishing a design hierarchy in term of overall noise radiation. The accuracy probability is at least 90% compared with measurement correlation.

Variants	Left Engine Side		Bottom	
	Measurement	Analysis	Measurement	Analysis
Base - Caps	1.2	10.4	3.7	4.7
Base - Flex. FW	8.2	22.4	7.6	1.1
Caps - Flex. FW	7.0	12.0	(5.3) <sup>4</sup>	(3.6)

Table 25 Differential Sound Pressure Level (6000 rpm; [dB(A)])

Comparing the results for the octave and third-octave band data, the individual bands do not match to the same extent as the summed sound pressure results. The peak level determining values are not obtained at the same frequencies for various design alternatives. This outcome is to be expected, as the design resonances and peak levels must occur at different frequencies for the individual design proposals. A one by one comparison of octave and third-octave bands must necessarily deliver a reduced number of matching bands. An averaged comparison of correlating octave bands is shown in Table 26 exhibiting an overall trend of suiting octave bands of 43.1%. An analysis of the octave band results with respect to engine speed, direction and design proposals is summarised in Table 27.

Octave [Hz]	125	250	500	1000	2000	4000
Averaged Correlation	66.7	41.7	66.7	41.7	41.7	33.3

Table 26 Averaged Octave Band Correlation [%]

	Base - Flex. FW		Base - Ind. Caps		Ind.Caps - Flex.FW	
	Bottom	Side	Bottom	Side	Bottom	Side
3000 rpm	33.3	50.0	16.7	50.0	33.3	50.0
6000 rpm	33.3	100.0	33.3	50.0	16.7	50.0

Table 27 Octave Band Correlation [%]

The basis of this correlation are those six octave band results obtained for the individual design proposal for two sides and two engine speeds. The available number of data do not allow for a general assessment. The outcome is that the octave band correlation is

4: Not Correlated

far higher for the engine side than for the engine oilpan direction. Doing a similar analysis for the third-octave band results, a similar reverberation can be obtained as shown in Table 28.

	Base - Flex. FW		Base - Ind. Caps		Ind.Caps - Flex.FW	
	Bottom	Side	Bottom	Side	Bottom	Side
3000 rpm	47.1	47.1	35.3	47.1	47.1	64.7
6000 rpm	29.4	88.2	5.9	41.2	40.0	82.4

Table 28 Third Octave Band Correlation [%]

A comparison for the two observation locations exhibits an increased correlation for the engine side compared to the bottom side. Recalling the assumption made in the discussion of the Rayleigh approach,  $r_i/a_i \gg 1$  must be satisfied for all radiating surfaces. While the microphone at the engine bottom side is located at a distance of 0.15 m from the radiating surface, the ratio  $r_i/a_i$  is 12.3. This may be the main reason for incorrectly predicted sound pressure values throughout the frequency range. Due to the spatial limitation of the test cell a correlation with an increased distance could not be obtained. Another contributor to this phenomenon may be found in the modelling approach of the oilpan and the contained oil. The oil is not modelled within this approach but the system damping properties are to some extent accounting for the oil properties. Recent measurements [136] indicate that the oil properties do affect the damping properties of the oilpan significantly, but do not alter the resonances of the system. The oil mass is of minor effect. This effect explains the peak values occurring at the bottom side to some extent. Introducing a significant higher damping property at the oilpan would significantly reduce the peak values of the bottom side sound pressure values.

A comparison of the achieved averaged correlation for the third-octave band results is given in Table 29. The correlation data are in a similar range to those of the octave band correlation.

The analysis of the third-octave and octave band results shows that the general trend of individual bands correspond with the obtained summed sound pressure level. Comparing the measured trend prediction between the considered design alternatives almost 93% of the third-octave bands and 88% of the octave bands coincide with the order derived from the summed sound pressure level results. The analytically derived third-octave and octave band results coincide to an average of 70% and 65% respectively. It is surprising that the octave band coincidence level is smaller compared

Third Octave [Hz]	125	160	200	250	315	400
Averaged Correlation	50	59	55	50	42	67
	500	630	800	1000	1250	1600
	75	67	50	67	50	42
	2000	2500	3200	4000	5000	
	42	34	34	59	42	

Table 29 Averaged Third-Octave Band Correlation [%]

to the third-octave band level. Studying the corresponding data in more detail one has to consider that the narrow band frequency results of the analytical model do show a significantly more uneven or 'peak-value' oriented perception compared to the measured data sets. Recalling the calculation procedure for third-octave and octave bands only a single peak value next to a border frequency may drive the one or the next band result to a higher or lower level. From this, analytical results must be carefully investigated prior to any design assumption based on third- and octave band results. Exemplarily measured and analysis results are compared for the left hand and bottom engine sides at 3000 rpm shown in Figures 8.3.22 and 8.3.23 respectively.

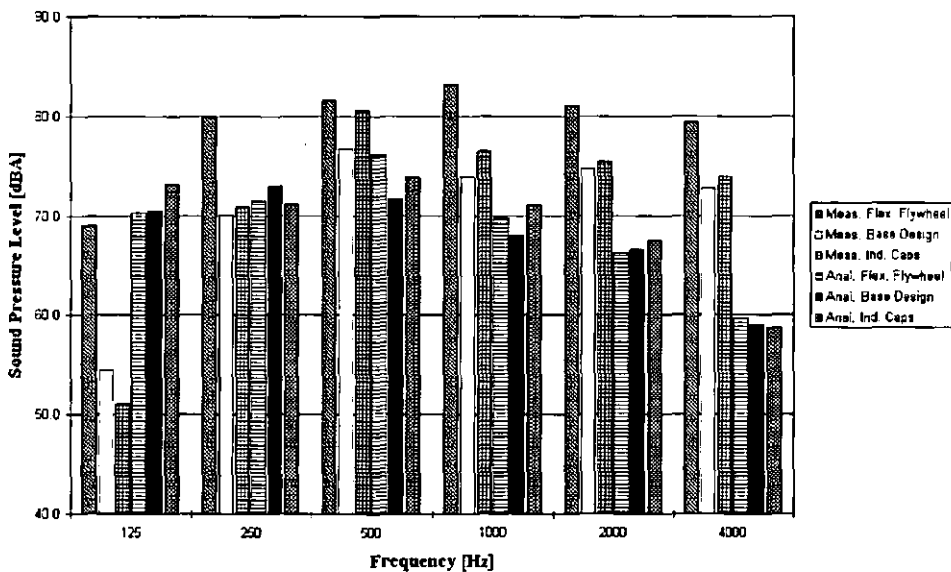


Figure 8.3.22 Measured vs. Analytical Octave Band [3000 rpm; Left Side]

The maximum levels are obtained for the left hand engine side from the analytical approach in the 500 Hz and 1000 Hz octave band while the measured results post the peak value in the 1000 Hz octave band dominating the total sound pressure result. The

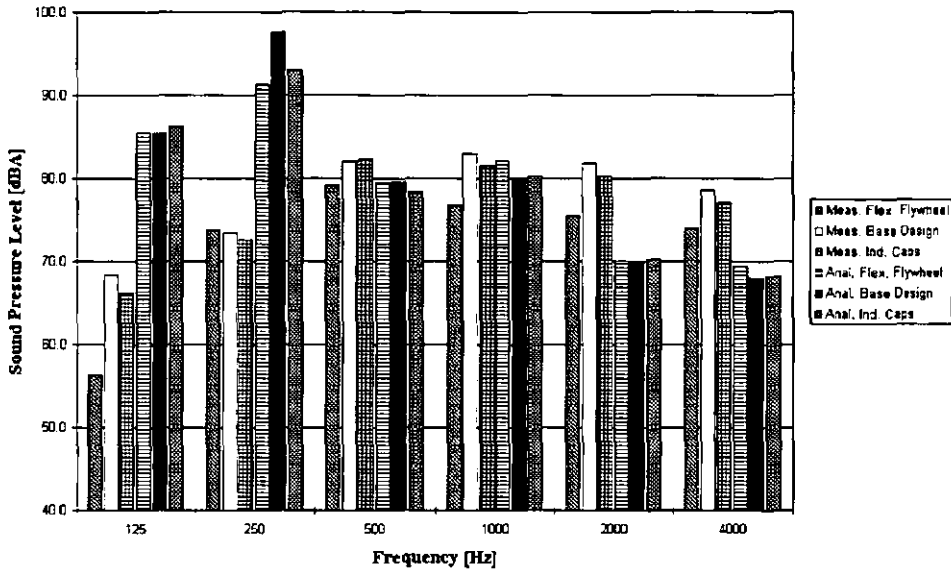


Figure 8.3.23 Measured vs. Analytical Octave Band [3000 rpm; Bottom Side]

bottom side results are mainly driven from the 250 Hz octave band in the analytical solution while the measurements exhibit peak values in the 500 Hz and 1000 Hz band. The total sound pressure values of the measured and analytical approach are hence dominated by different octave bands at the left and bottom engine side.

The reduced analytical octave band results at higher frequency values are mainly influenced by: (i) the Rayleigh approach calculating higher values at lower frequencies. The precondition that the acoustic wavelength is much shorter than the geometric dimensions of the engine block may probably be violated. This especially influences the bottom side results showing an increase at the 125 Hz and 250 Hz octave band; (ii) the assumption of velocity dependent material damping properties may not be accurate enough throughout a wide frequency range. Further effects such as contact surfaces, seals and others are not considered in this approach. Detailed investigations should be performed to establish more accurate damping property models and correlate these with measurements; (iii) further excitation phenomena must be considered especially at higher frequencies. High frequency impacts, such as piston-slap, combustion irregularities and others are not considered. Experimental investigations showed that these phenomena are commonly not periodic with either one or two crankshaft revolutions. It therefore constitutes a system limitation that these high frequency irregularities cannot be introduced within the derived analysis approach. The major prerequisite is violated if non-periodic effects are introduced.

Hence a comparison of the derived octave band levels is required to correlate the perceived findings. The total sound pressure levels are re-calculated neglecting the higher frequency content. The maximum considered octave band is the 500 Hz band. A comparison is given in Table 30 for both sides and all geometric and speed variants. A judgement of correlation is established by comparing the measured and analysis results. If both coincide, a positive correlation is defined and *vice versa*.

	Design	Location	Derived Higher Level at		Correlation
			Measurement	Analysis	
3000 rpm	Ind. Caps	Bottom	Base	Base	+
	- Base	Side	Caps	Caps	+
	Flex.FW	Bottom	Flex	Base	-
	- Base	Side	Flex	Flex	+
	Flex.FW	Bottom	Flex	Caps	-
	- Ind. Caps	Side	Flex	Flex	+
6000 rpm	Ind. Caps	Bottom	Caps	Base	-
	- Base	Side	Caps	Caps	+
	Flex.FW	Bottom	Base	Base	+
	- Base	Side	Flex	Flex	+
	Flex.FW	Bottom	Caps	Flex	-
	- Ind. Caps	Side	Flex	Flex	+

Table 30 Octave Band Correlation [-500 Hz]

Eight out of twelve combinations show a positive correlation between measurements and analyses. The four divergent cases are always from bottom side analyses.

Summarising the findings so far we are led to conclude that the bottom side noise radiation results should not be considered in an assessment of design variants. This is due to the limitations of the Rayleigh approach already described, in predicting correct sound pressure values at distances close to the radiating surface. Additionally, some modelling inaccuracies as described previously may amplify this effect. But this phenomenon is open to discussion. The modelling approach of the oil and oil-sump and the appropriate noise radiation approach for near field investigations should be investigated and clarified outside of this research project.

Referring to the previous table it becomes obvious that the applied noise radiation approach of Rayleigh provides accurate results for those points with larger distances from the radiating surface. The trends are predicted correctly for all conditions at 1 m distance. Looking into the results in more detail even the compared pairs of design alternatives are always correctly predicted. The developed analysis approach may thus not only be applied to compare two design alternatives with each other but can also be used to establish a sequence between the design proposals with respect to the radiated sound pressure level. The results are shown for the left engine side in Figure 8.3.24.

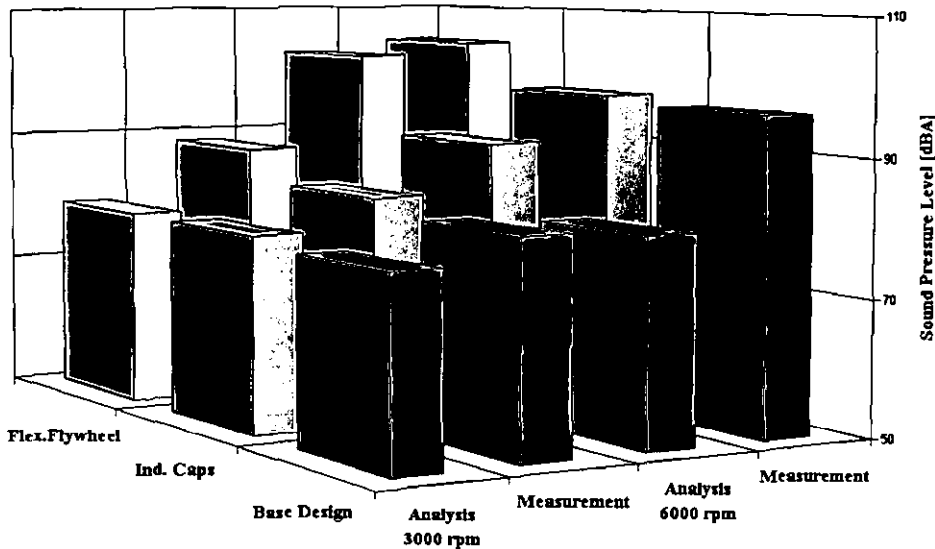


Figure 8.3.24 Total Sound Pressure Level Comparison [Left Side]

The presented results and sequence correlate with measurements at 3000 rpm and 6000 rpm. But the difference between design proposals may be used in a design assessment. The predicted differences in sound pressure magnitude obtained at 3000 rpm coincide with the results from measurements and are much lower than those presented at 6000 rpm. Again, this correlates with measured data. Nevertheless, one should not utilise the analytically obtained differences between design proposals as absolute values. The difference in sound pressure level indicates a directional change only. So to speak a version 'A' is 'much' or 'marginally' better than a version 'B', according to whether the respective predicted difference is of large or minor significance.

It is important to remember that the primary emphasis of this work is to establish an analytical method to compare various design alternatives on a relative basis. Applying this approach to the studied alternatives and comparing the analysis results with measurement data, an excellent correlation is established for all types of results at the left hand engine side. The trend prediction between the alternatives is established in

the correct order for all versions and all speeds. Hence, a design decision based on analysis results would be 100% correct in terms of noise radiation comparing the base design with the given two alternatives. Methodical shortfalls are established for those conditions predicting radiated noise values next to the structure's surface (bottom side). This disadvantage is principally impacted by the Rayleigh approach rather than the excitation or surface velocity prediction technique.

### **8.3.4 Auralisation**

A relative difference between the studied design alternatives was established with respect to objective measurables. Whirling modes, surface velocities and sound pressure levels are utilised to establish a sequence between all proposals. While all of these measurables are correct and valuable to use one may not disregard the human perception of engine noises. This customer oriented subjective assessment is commonly known as 'Sound Quality', whilst the definition of sound quality is somewhat difficult and dependent upon individual perception, so design alternatives must be compared by many individuals in order to accomplish a useful assessment of the noise factor. Today, this approach can only be considered after different design proposals are available in hardware and have been tested. The measured noise is then used within clinics establishing a common customer rating. This process is a lengthy, time consuming and very expensive approach. A significant process improvement could be achieved if analysis tools are available establishing the artificial radiated noise of design proposals from the customer's viewpoint.

The methodology described previously generates a narrow band sound pressure data set at 1 m distance from the radiating engine surface. This is an analytical description of the engine noise at a specific customer's location. This artificial noise must be made audible to allow for a subjective assessment of the considered design proposals.

The data sets used in this study are the left hand engine side results, as the perceived accuracy is much better compared to the bottom side investigations. Narrow band frequency domain data are transferred to the BAS system utilised within Ford to post-process measured noise data. The post-processing of the analytical data sets was done by C.Vorwerk.

The frequency domain results are transferred to the time domain considering an in-phase correction of the full engine orders. The resulting time domain solution is displayed in the upper half within Figure 8.3.25 . The lower half describes the time signal with respect to the frequency content and sound pressure levels in a three-dimensional graph.



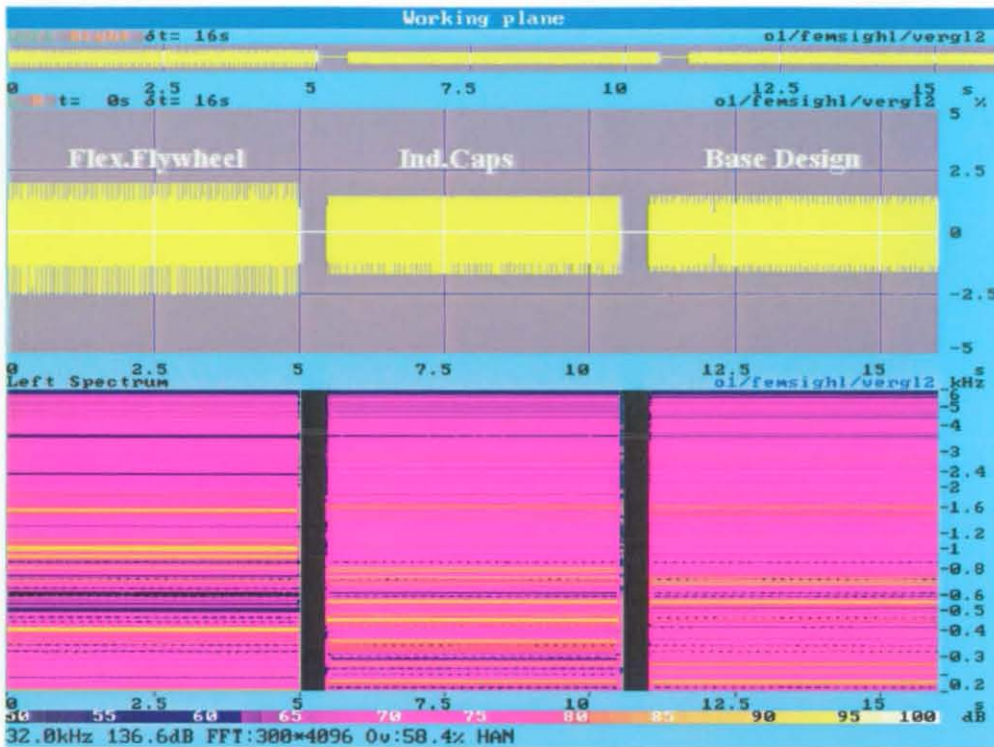


Figure 8.3.25 Noise Auralisation Comparison [3000 rpm; Left Side]

Particular disadvantages of the flexible flywheel are observed in the frequency range between 400 Hz and 1.2 kHz, which is critical for rumble noise. The design delivers a sharper kind of noise than the base design applying a conventional flywheel. Replacing the bearing beam with individual bearing caps deteriorates the overall noise especially within the above mentioned critical frequency range for rumble noise.

A floppy disk is presented with this thesis containing the results of the previous study. Files describing the audible noise are included for the individual design alternative and for the comparison of all considered proposals. These files can be reproduced using a commonplace WAV- or media player as distributed within Windows-95<sup>®</sup>. The delivered files are shown in Table 31.

File Name	Description
Base.wav	Base Design (Bearing Beam; Conventional Flywheel)
IBC.wav	Individual Bearing Caps (Conventional Flywheel)
Flex.wav	Flexible Flywheel (Bearing Beam)
Comparison.wav	Comparison of all design alternatives

Table 31 Audible Sound Files

---

The author's opinion is that the base design demonstrates the best sound quality, followed by the individual bearing cap design. The flexible flywheel reveals the poorest sound quality out of all versions considered.

It is for the reader to make a subjective assessment of the proposed design variants and make up his mind on the sound quality delivered from the various alternatives.

Having gone through this exercise, we can clearly see that analytically derived noises can be converted to audible noises. These are then applicable to subjective assessments to classify various design proposals with respect to the subjective sound quality measurable based on customer clinics.

## **Chapter 9**

### **Discussions and Conclusions**

The main goal of this work was the development of a set of tools to analyse the coupled crankshaft-crankcase response and the contributing effects in bottom-end engine noise radiation. To achieve this, various modelling techniques, applied previously for various studies, have been reviewed. The drawbacks and advantages of the individual approaches were discussed, leading to the conclusion that the available models were not capable of fulfilling the requirements of the coupled vibration analysis throughout the engine speed range. Hence, a new analytical model had to be developed to investigate the coupled crankshaft-crankcase dynamic response. Further work had to be accomplished to analyse the dynamic response data with respect to engine noise radiation. The developed methods are detailed and accurate enough to describe trend-wise analyses correctly, and to establish the correct hierarchy of various design alternatives.

This results in the development of a modal description combining both modal and discrete approaches. Most properties of the system are linear, but time variant. Therefore a solution method is applied which solves the response efficiently in the frequency domain, and allows for a large number of operation conditions to be investigated due to the numerical efficiency of the approach. As most of the system properties are linear, time variant and periodic with respect to two engine revolutions, the base period is the same as for the major excitation forces. It is therefore possible to describe all these properties as Fourier series with the base period of two crankshaft revolutions. Further work was done to incorporate the gyroscopic effect into the base properties of the rotating part of the model. This was achieved by introducing a complex damping matrix consisting of the material or viscous damping and the gyroscopic part.

This reduces the problem to a linear one with constant coefficients for an individual crankshaft position. The response is calculated for each position, order and harmonic separately followed by a superposition leading to the combined response of the assembled system.

Introducing non-linear coefficients between the crankshaft and crankcase this approach has to be altered. Each component is described by Fourier series independently. These are then linked through a frequency domain description of the coupling properties of the main bearing oilfilm. Each solution cannot be solved independently, but the complete response is solved in one step. This approach is less efficient than that of the linear one with constant coupling properties, but it is still more efficient than a solution in the time domain. Using this process, entire engine speed sweeps can thus be studied with available supercomputers, while a time base solution cannot be obtained with today's

equipment. On the other hand, further advantages are gained from the modal description of the base properties, so that for example material properties can be described more precisely in the frequency rather than time domain.

To establish the important main bearing oilfilm properties, an independent investigation was accomplished. The non-linear damping and stiffness characteristics are described with frequency domain properties. These properties are then stored in data tables, and are applied as reference tables within the frequency domain solution of the coupled system. The advantage of this approach is that the main bearing properties need to be determined only once and that the coupled solution refers to already established data. The drawbacks are that the reference tables have to account for all theoretically possible operation conditions and that the computational effort to establish these tables is significant.

The direct output of this work is:

- 1) An approach has been developed to efficiently solve non-linear coupled linear systems with periodically time variants with a high number of degrees of freedom. This tool has been successfully applied to the coupled crankshaft-crankcase system. Direct as well as indirect measures (noise radiation) correlate with measurements. Further work has been accomplished to establish subjective assessments of predicted noises and to make these artificial noises audible.
- 2) The use of the tool enables the analysis of the crankshaft-crankcase system throughout a wide range of engine speeds with an acceptable amount of required computer resources.
- 3) Throughout this study, a set of programs have been developed or enhanced, which allow the prediction of non-linear bearing properties with respect to the frequency domain, post-process the derived physical measures, and establish the radiated noise level at a defined point in space.

Also, two deficiencies are discovered, where further research work is required, leading to even more details in the findings.

The first drawback of the modelling approach is the application of harmonic excitation forces, especially for the piston side forces and the combustion pressure. The other modelling drawback is found in the limited accuracy of the modelling strategy for a filled oilpan. Establishing a more detailed modelling technique for a filled oilpan is the future challenge. The deficiencies in modelling the forcing functions must be discussed with regard to two aspects. Firstly, one has to remember that the derived approach is limited to harmonic functions only, either on the system or forcing side of the equation. Intro-

ducing non-harmonic forcing functions requires that the solution to this problem be transferred to the time domain, with all the disadvantages which that is known to entail. Secondly, higher frequency domain excitations should be considered more precisely to improve the accuracy within that frequency range. As it is known from experiments, piston side impacts may significantly influence the noise radiation characteristic of an engine. How this kind of non-harmonic high frequency excitation can be modelled in the frequency domain or whether the time domain solution must be applied for this kind of problem, is therefore an obvious subject for further research.

The second field open for further improvements is that of the near field noise prediction. The research work presented here shows that the applied Rayleigh approach correlates with measurements at the far field. Near field sound pressure results do not correlate to the same level of accuracy. This methodology driven drawback can be overcome by also measuring the bottom side noise levels at the far field. Whether the Rayleigh approach may be modified and improved for near field application, or whether another tool should be deployed to solve the noise radiation problem is likewise an obvious subject for further research.

The discussion of the above drawbacks shows that one must not accept all the results from this approach. The applied modelling and analysis techniques do not replace well founded engineering experience. On the other hand, this tool can be applied to help in the faster development and competitive assessment of various cranktrain design alternatives.

Based on the analyses done so far the following engineering conclusions can be drawn from the results:

- 1) The crankshaft behaves as an asymmetrical shaft with an attached rotor supported by asymmetrical casing properties. The rotating shaft will show whirl modes in the forward and reverse direction. This effect occurs at the front and rear end of the crankshaft, with the major influence detected at the rear.
- 2) The first occurring whirl mode is a reverse whirl with respect to ground. This is the first excited mode, and the excitation frequencies are low order multiples of the crankshaft rotational frequency. There is no way of avoiding these modes within design limitations given in modern engine structures.
- 3) The whirling path may alter with respect to mainly engine speed and design characteristics. Nevertheless, the whirling path is described as an elliptical orbit, which may at the extreme become a circular path.

- 4) There are profound indications showing that the bearing pin journals next to the crankshaft's ends also describe a more or less elliptical path. But the ellipses are commonly altered by gas-pressure driven bearing forces.
- 5) If the first whirling frequencies are the main subject of investigation, then a probable simplification may be introduced to the model by replacing the crankcase stiffness and the oil-film properties with linearised elastic springs at the crankshaft main bearings. This allows for tilting and axial displacements within the bearing support. The thrust bearing is then constrained. Applying this simplified approach, correlation can be shown for the first whirling modes within 10% compared to the detailed description.
- 6) The theoretical and measured mode shapes of the whirling modes are consistent at the rear of the crankshaft. Significant amount of bending occurs in the web nearest to the flywheel for the lowest pair of whirling modes. The web stiffness significantly influences the whirling modes, and the design should account for that by introducing a more stiff web design at the rear end of the crankshaft.
- 7) The position of the thrust bearing seems to have only a minor influence on the lower whirling modes. Higher whirling modes may be influenced more by moving the axial bearing to the crankshaft end. But this will drastically increase the axial loads due to the axial vibration at the crankshaft rear end.
- 8) The application of linearised bearing properties is sufficient to establish the crankshaft stresses. The linearised description of the bearing properties are developed within this project. However, if the purpose of the study is to predict the coupled crankshaft-crankcase dynamic response non-linear main bearing properties should be considered. A linearised approach will drastically change the perceived responses, especially at the mid frequency range.
- 9) With respect to the flywheel whirl modes, significant increased displacements are obtained under these resonance conditions linked with high stress levels. The subjected areas are the fillet radii at the last web at either the main or crank pin.
- 10) The low frequency whirl mode may be influenced by design actions. Introducing a light flywheel, a thick web at the crankshaft rear, a wide and stiff main bearing casing structure and a small bearing clearance helps to increase the first whirl modes.

- 11) The introduction of a flexible coupled inertia (flexible flywheel) changes the whirl characteristic of the crankshaft. From the results obtained in this research work, however, the flexible flywheel as used in some Japanese engines should not be introduced to minimise rear end whirling, but should be applied if the crankshaft fails due to excessive stress levels. Due to the flexible coupled inertia, reduced bending moments are introduced into the last web, reducing the stress at the fillet radii. But on the other hand, no stabilising effect is perceived from the rotating inertia. The results showed that the main bearing excitations are increased with the flexible flywheel application. Increased acceleration is obtained, especially at the two rear end bearings, because the gyroscopic stabilising effect of a rigidly attached inertia is lacking.

To sum up, a conventional flywheel reduces the excitation and combustion process driven forces at the rear bearings and hence the radiated noise, while increasing the stress level at the last web. The flexible flywheel reduces the stress level but increases the excitation and forces at the rear main bearings with a subsequent negative effect on noise radiation.

Which solution is preferred depends on the pertaining engineering situation.

The previous discussion and the listed design contributions mainly summarises the overall picture and the conclusions reached from this study. The analytical approach developed in this research work is shown to be valuable for the prediction of crankshaft-crankcase dynamic responses and their contributing effect on noise radiation. The analysis results correlate with measurements and the method can be applied for related studies. However, some important issues are recommended for future investigation.



### References

- [1] Lürenbaum, K., "Vibrations of crankshaft propeller systems", SAE Trans. 38-9 469., 1936
- [2] Kimmel, A., "Die erregenden Biegekräfte bei Flugmotoren mit unmittelbarer Pleuelanlenkung", Luftf.-Forschung S.403, 1941
- [3] Benz, W., "Biegeschwingungen von Kurbelwellen, insbesondere bei schweren Schwungrädern", ATZ S.405, 1935
- [4] Hodgetts, D., "Vibrations of a Crankshaft", IMechE C99/71, 1971
- [5] Ishihara, S., Hiraishi, M. and Yamanouchi, K., "Reduction of Powerplant Vibration Level in the Acceleration Noise Region Based on Analysis of Crankshaft System Behaviour", SAE 922087, 1992
- [6] Usaba, Y., Nagayama, I., Araki, Y. and Kakuta, K., "The Role of Static and Dynamic Finite Element Analysis in Designing Low-Noise Cylinder Blocks", SAE 830251, 1983
- [7] Joerres, M.(Ford), Schneider, M.(FEV) and Wolschendorf, J.(FEV), "Noise and Vibration Investigations of ZETEC-SE 1.4l, Series B", Internal Document of Ford Motor Co., 1994
- [8] Pfingsthorn, B., Favardin, S. and Grünert, T., "Crankshaft Layout for Optimised NVH", Internal Document of Ford Motor Co., 1998
- [9] Grünert, Thomas, "Development of a Finite-Element-Model for the Analysis of Cranktrain Dynamics", MSc Thesis Loughborough University, 1993
- [10] Ohgami, E. and Ohsawa, N., "Nissan's New V8 and L4 Aluminium Cylinder Block- Design and Production", SAE-910431, 1991
- [11] Asatsuma, K., Ishihara, A. and Nashif, A., "Noise Reduction of Engines by Structural Modifications", SAE 840483, 1984
- [12] Usaba, Y., Nagayama, I., Araki, Y. and Kakuta, K., "The Role of Static and Dynamic Finite Element Analysis in Designing Low-Noise Cylinder Blocks", SAE 830251, 1983
- [13] Vorwerk, C., "Simulation der Betriebsanregung in den Hauptlagern von Ottomotoren zur akustischen Strukturbeurteilung", Diss. RWTH Aachen, 1994
- [14] Naumann, F., Voigt, D. and Deutsch, H., "Der neue VR6-Motor von Volkswagen", MTZ 52, 1991

- 
- [15] Willenbockel, O. Indra, F., "Der neue Opel 3.0l 24 Ventil-Motor", 2. Aachener Koll. Fahrzeug- und Motorentechnik, 1989
  - [16] Basshuysen, R. Stock, D. and Bauder, R., "Entwicklung eines DI-Turbo-Diesel-Motors", 2. Achener Koll. Fahrzeug- und Motorentechnik, 1989
  - [17] Riding, D. and Weeks, R., "The Application of Noise Simulation Techniques to Conceptual Automotive Powertrain Design", SAE 911077, 1991
  - [18] Crocker, M., "Engine Noise: Practicalities and Prediction; Part 1: Hardware Evaluation", SAE 870977, 1987
  - [19] Busch, G., Maurell, R., Meyer, J. and Vorwerk, C., "Investigations on Influence of Engine Block Design Features on Noise and Vibration", SAE 911071, 1991
  - [20] Meyer, J., Kaiser, H.-J. and Maurell, R., "Bottom End Design Selection", Internal Document of Ford Motor Co., 1990
  - [21] Pischinger F., "Verbrennungsmotoren", RWTH Aachen, 1986
  - [22] Atsumi, T. and Nakakubo, T., "Engine Downsizing and Noise", JSAE p19ff, 1981
  - [23] Gruenert, T., "ZETEC-SE 1.4l Crankshaft Design Investigation", Internal Document of Ford Motor Co., 1994
  - [24] Pfingsthorn, B., Favardin, S. and Gruenert, T., "Strategy to Layout Crankshafts for Good NVH", Internal Document of Ford Motor Co., 1997
  - [25] LUK (Kohlhage, E., et al), "Torsional Vibrations in the Drive Train", 4th International Symposium Baden-Baden, 1990
  - [26] Ziegler, G., "Noise Reduction on a Passenger Car- SI- Engine", BMFT, 1983
  - [27] Pott, J. and Gruenert, T., "FE-Auslegung eines asymmetrischen Schwungrades unter Berücksichtigung des Schwingverhaltens eines Vier-Zylinder-Reihenmotors", Thesis FH Hamburg, 1993
  - [28] Kohno, S., "Improvement of Engine Sound Quality with Flexible Flywheel", UNISIA Internal Report
  - [29] Yamanouchi, K., Hiraishi, M. and Ishihara, S., "Reduction of Powerplant Vibration Level in the Acceleration Noise Region Based on Analysis of Crankshaft System Behaviour", SAE 922087, 1992

- 
- [30] Yamanouchi, K., Yamashita, K., Mamiya, N., Yamazaki, T. and Yamazaki, I., "Application of Predictive Noise and Vibration Analysis to the Development of a New-Generation Lightweight 3-Liter V6 Nissan Engine", SAE 940993, 1993
- [31] Dimentberg, F., "Flexural vibrations of rotating shafts", Butterworth, 1961
- [32] Tondl, A., "Some problems of rotor dynamics", Chapman & Hall, 1965
- [33] Stodola, A., "Dampf- und Gasturbinen", Springer, 1924
- [34] Föppl, A., "Das Problem der Laval'schen Turbinenwelle", Civilingenieur 41, 1895
- [35] Gasch, R. and Pfützner, H., "Rotordynamik", Springer, 1975
- [36] Traupel, W., "Thermische Turbomaschinen (Band 2)", Springer, 1960
- [37] Föppl, A., "Kritische Drehzahlen rasch umlaufender Wellen", VDI 63, 1919
- [38] Kimball, A.L. and Lovell, D.E., "Internal Friction in Solids", Physical Review, 1927
- [39] Kellenberger, W., "Die Stabilität rotierender Wellen infolge innerer und äußerer Dämpfung", Ingenieur Archiv 32, 1963
- [40] Tondl, A., "Der Einfluß der inneren trockenen Reibung und der äußeren nichtlinearen Dämpfung auf die Bewegung und Stabilität des Rotors", Acta Technica 4, 1960
- [41] Dorf, Richard C., "Modern Control Systems", Addison Wesley, 1989
- [42] McDonald, A.C. and Lowe, H., "Feedback and Control Systems", Reston Publ., 1981
- [43] Beards, C.F., "Vibrations and Control Systems", Ellis Horwood, 1988
- [44] Newland, D.E., "Mechanical vibration analysis and computation", Longman Scientific & Technical, 1989
- [45] Houben, H., "Erzwungene und freie Drehschwingungen sowie ihre Instabilitäten erster und zweiter Art in Maschinensätzen mit antreibendem Asynchronmotor", VDI-Verlag; Fortschrittberichte, Reihe 9, Nr.8, 1970
- [46] Krumm, H., "Die Stabilität einfach gekoppelter parametererregter Drehschwingungssysteme mit typischen Ausführungsbeispielen", Westdeutscher Verlag, 1975

- [47] Meyer, F., "Stability Analysis of Large Parametrically Excited Linear Vibration Systems", Diss. ETH Zürich, 1984
- [48] Tondl, A., "Some problems of rotor dynamics", Chapman & Hall, 1965
- [49] Glienicke, J., "Feder- und Dämpfungskonstanten von Gleitlagern für Turbomaschinen und deren Einfluß auf das Schwingungsverhalten eines einfachen Rotors", Diss. TH Karlsruhe, 1966
- [50] Someya, T., "Schwingungs- und Stabilitätsverhalten einer in zylindrischen Gleitlagern laufenden Welle mit Unwucht", VDI-Forschungsheft 510, 1965
- [51] Hahn, H.W., "Das zylindrische Gleitlager endlicher Breite unter zeitlich veränderlicher Belastung", Diss TH Karlsruhe, 1957
- [52] Sassenfeld, H. and Walther, A., "Gleitlagerberechnungen", VDI-Forschungsheft 441, 1954
- [53] Hagg, A.C. and Sankey, G.O., "Oilfilm properties for unbalance vibration calculations", Trans. ASME.J.Appl.Mech.25 p.141ff, 1958
- [54] Narkis and Cohen, "Numerical method for Determination of the Stability of linear Systems with Periodic Coefficients", Journal of Sound and Vibration, p.571ff, 1976  
and  
Föllinger, O., "Regelungstechnik", AEG-Telefunken Sonderausgabe, 1980
- [55] Stodola, A., "Neue kritische Drehzahlen als Folge der Kreiselwirkung der Laufräder", Zeitschrift f.d.ges. Turbinenwesen 15, 1918
- [56] Grammel, R., "Kritische Drehzahl und Kreiselwirkung", VDI 64, 1920
- [57] Benz, W., "Biegeschwingungen von mit einer Masse besetzten Wellen", MTZ 11, 1950
- [58] Kowalewski, P., "Untersuchungen über den Gegenlauf bei biegekritischen Drehzahlen", Diss. TU Berlin, 1971
- [59] Kellenberger, W., "Biegeschwingungen einer unrunder, rotierenden Welle in horizontaler Lage", Ingenieur Archiv 26, 1958
- [60] Maske, H., "Rotierende Welle in anisotrop elastischen Lagern bei asymmetrischer Wellensteifigkeit und asymmetrischer Rotordrehmasse", Diss. TU Berlin, 1972

- 
- [61] Jäger, B., "Die Eigenschwingungszahlen eines gelagerten oder freien Rotors mit runder zylindrisch-ovaler oder verwunden-ovaler Welle", Diss. TH Karlsruhe, 1960
- [62] Michatz, J., "Das Biegeverhalten einer einfach besetzten unrunder rotierenden Welle unter Berücksichtigung äußerer und innerer Dämpfungseinflüsse", Diss. TU Berlin, 1970
- [63] Pflingstorn, B., "Crankshaft Fluctuation", Internal Document of Ford Motor Co., 1995
- [64] Bishop, R.E. and Parkinson, A.G., "Second order vibration of flexible shafts", Phil. Trans(A) 259, 1966
- [65] Someya, T., "Stabilität einer in zylindrischen Gleitlagern laufenden, unwucht-freien Welle -Beitrag zur Theorie des instationär belasteten Gleitlagers", Dissertation Univ. Karlsruhe Verlag, 1962
- [66] Someya, T., "Das dynamisch belastete Radial-Gleitlager beliebigen Querschnitts -Grundlegende Untersuchungen über die Ausbildung eines tragfähigen Schmierfilms zwischen reibungsbehafteten gleitenden Flächen bei statischer und dynamischer Belastung-", Forschungsbericht 2-211/9 Book 43, FVV, 1964
- [67] Glienicke, J., "Feder- und Dämpfungskonstanten von Gleitlagern für Turbomaschinen und deren Einfluß auf das Schwingungsverhalten eines einfachen Rotors", Forschungsbericht 2-211/12 Book 67, FVV, 1967
- [68] Schaffrath, G., "Eine Methode zur Berechnung der vier Feder- und vier Dämpfungskoeffizienten von Radialgleitlagern", Forschungsbericht 2-211/18 Book 97, FVV, 1969 and Dissertation Univ. Karlsruhe, 1967
- [69] Klumpp, R., "Computer-Program zur Berechnung der Feder- und Dämpfungskonstanten und der statischen Gleichgewichtslinien von Gleitlagern mit beliebiger Schmierspaltform", Book 144, FVV, 1973
- [70] Lang, O.R. and Steinhilper, W., "Gleitlager", Springer-Verlag, 1978
- [71] Fränkel, A., "Berechnung von zylindrischen Gleitlagern", Dissertation ETH Zürich, 1944
- [72] Ott, H.H., "Zylindrische Gleitlager bei instationärer Belastung", Dissertation ETH Zürich, 1948
- [73] Booker, J.F., "Dynamically Loaded Journal Bearing. Mobility Method of Solution.", Journal of Basic Engineering, Trans. ASME, Series D/p537, 1965

- 
- [74] Hahn, H.W., "Das zylindrische Gleitlager endlicher Breite unter zeitlich veränderlicher Belastung", Dissertation Univ. Karlsruhe, 1957
- [75] Holland, J., "Beitrag zur Erfassung der Schmierverhältnisse in Verbrennungskraftmaschinen", VDI-Forschungsheft 475, 1959
- [76] Bronstein, I.N. and Semendjajew, K.A., "Taschenbuch der Mathematik", Verlag Harri Deutsch, 1965
- [77] Gruenert, T. and Meyer, J., "Shift of First Powertrain Eigenfrequency Above 300 Hz", Internal Document of Ford Motor Co., 1994
- [78] Hahn, H.W., "Das zylindrische Gleitlager endlicher Breite unter zeitlich veränderlicher Belastung", Dissertation Univ. Karlsruhe, 1957
- [79] Ott, H.H., "Zylindrische Gleitlager bei instationärer Belastung", Dissertation ETH Zürich, 1948
- [80] Vogelpohl, G., "Zur Integration der Reynolds'schen Gleichung für das Zapfenlager endlicher Breite", Ingenieur Archiv Bd.14, 1943
- [81] Someya, T., "Das dynamisch belastete Radial-Gleitlager beliebigen Querschnitts", Ingenieur Archiv Bd.34, 1965
- [82] Gnanadoss, A.A. and Osborne, M.R., "The Numerical Solution of Reynolds' Equation for a Journal Bearing", Mech.&Appl.Math, Vol.XVII, Pt.2, 1964
- [83] Frössel, W., "Berechnung der Reibung und Tragkraft eines endlich breiten Gleitschuhes auf ebener Gleitbahn", ZAMM, Bd.21, 1941
- [84] Warner, C.P., "Static and Dynamic Properties of Partial Journal Bearings", Transactions of the ASME, 1963
- [85] Schaffrath, G., "Das Gleitlager mit beliebiger Schmierspaltform -Verlagerung des Wellenzapfens bei zeitlich veränderlicher Belastung-", Dissertation Univ. Karlsruhe, 1967
- [86] Harbodt, J. and Klumpp, R., "Computer-Programm zur Berechnung der Verlagerungsbahn, der örtlichen Drücke und des tatsächlichen Schmierspalt in Gleitlagern mit beliebiger Geometrie unter statischer und dynamischer Last", Forschungsvereinigung Verbrennungskraftmaschinen (FVV), 1972
- [87] Radermacher, K., "Das instationär belastete zylindrische Gleitlager -Experimentelle Untersuchung-", Dissertation Univ. Karlsruhe, 1962

- 
- [88] Grünert, T., "GRKUR 4.0; Program Description", Internal Document of Ford Motor Co., 1992
- [89] Affenzeller, J., Priebisch, H. and Kuipers, G., "Structure Borne Noise Prediction Techniques", SAE-900019, 1990
- [90] Affenzeller, J. and Thien, G., "Evaluating Engine Design for Low Noise Using Dynamic Structural Modelling", SAE-820435, 1982
- [91] Jubel, C. and Grünert, T., "Berechnung von frequenzabhängigen Kopplungsgrößen zwischen Kurbelwelle und Motorblock", Thesis Humboldt University Berlin, 1995
- [92] Phillip, U., "Structure Borne Noise Excitation by Main Bearing Excitation", FVV-Research-Report 342, 1988
- [93] Zhang, J., "PACLOAD- An Automated Procedure for Analysis of Engine Crankshaft Dynamic Loads", Internal Document of Ford Motor Co., 1992
- [94] Ishihara, S., Hiraishi, M. and Yamanouchi, K., "Reduction of Powerplant Vibration Level in the Acceleration Noise Region Based on Analysis of Crankshaft System Behaviour", SAE 922087, 1992
- [95] Yamanouchi, K., Yamashita, K., Mamiya, N., Yamazaki, T. and Yamazaki, I., "Application of Predictive Noise and Vibration Analysis to the Development of a New-Generation Lightweight 3-Liter V6 Nissan Engine", SAE 940993, 1994
- [96] Heath, A. and McNamara, P., "Crankshaft Stress Analysis- The Combination of Finite Element and Classical Analysis Techniques", ICE-Vol. 9, Book No. 100295, 1989
- [97] Cronin, D., "Flexible Powertrain Analysis", Internal Document of Ford Motor Co., 1987
- [98] Spessart, B., "Untersuchung des akustischen Verhaltens von Kurbelgehäusen und Zylinderblöcken unter besonderer Berücksichtigung des inneren Körperschalleitweges", Dissertation Aachen, LAT, 1987
- [99] Hodgetts, D., "The Vibrations of Crankshafts", PhD Thesis University of London, 1974
- [100] Newland, D., "Mechanical Vibration Analysis and Computation", Longman Scientific & Technical, 1989
- [101] Mathieu, E., "Memoire sur le Mouvement Vibratoire d'une Membrane d Forme Elliptique", J.deMath.Pures et Appliques, Vol.13,No.137, 1868

- 
- [102] Tucker, J.R., "Overview of Complex Modal Analysis and Forced Frequency Response", Internal Document of Ford Motor Co., 1989
- [103] Yamamoto, T., "On the Unstable Vibrations of a Shaft With Unsymmetrical Stiffness Carrying an Unsymmetrical Rotor", Journal of Applied Mechanics, Vol.31, p.515f, 1964
- [104] Zienkiewicz, O.C., "Methode der finiten Elemente", Hanser Verlag, 1984
- [105] Fox, L., "An Introduction to Numerical Linear Algebra", Oxford University Press, 1965
- [106] Rall, L.B., "Computational Solution of Non-Linear Operator Equations", J.Wiley & Son, 1969
- [107] Oden, J.T., "Numerical Formulation of Non-Linear Elasticity Problems", Proc.Am.Soc.Civ.Eng.,93,ST3,235-55, 1967
- [108] Zürbes, A and Nordmann, R., "Calculation of Coupled Crankshaft Bending and Torsional Vibration", VDI-Conference, 1992
- [109] Gasch, R. and Knothe, K., "Strukturodynamik - Band 2", Springer Verlag, 1989
- [110] Müller, P.C. and Schiehlen, W.O., "Lineare Schwingungen", Akademische Verlagsgesellschaft Wiesbaden, 1976
- [111] Hahn, W., "Stability of Motion", Springer, 1967
- [112] Müller, P.C., "Stabilität und Matrizen", Springer, 1977
- [113] Willems, J.L., "Stability Theory of Dynamical Systems", Nelson, 1970
- [114] Cesari, L., "Asymptotic Behaviour and Stability Problems in Ordinary Differential Equations", Springer, 1963
- [115] Leipholz, H., "Stabilitätstheorie - Eine Einführung in die Theorie der Stabilität dynamischer Systeme und fester Körper", Teubner, 1968
- [116] Malkin, I.G., "Theorie der Stabilität einer Bewegung", Oldenburg, 1959
- [117] Weyh, B., "Parametererregte Schwingungen in Maschinen und Mechanismen", Haus der Technik, 1996
- [118] Knoll, G. and Müller, J., "Structural Dynamics of Crankshafts", RWTH Aachen, 1993
- [119] AVL-LIST Gmbh, "Brite/Euram Research Project on Crankshaft Dynamics", Graz, 1992-95



- 
- [120] Ricardo Consulting, "Crankshaft Dynamics", Internal Document of Ford Motor Co., 1993
- [121] Vorwerk, C., "Simulation der Betriebsanregung in den Hauptlagern von Ottomotoren zur akustischen Strukturbeurteilung", Diss. RWTH Aachen, 1994
- [122] Anderton, D., "Surface Vibration and Radiated Noise in I.C. Engines", Institute of Sound and Vibration
- [123] Wynendaele, H. and Guisset, P., "FEM und BEM zur Lösung akustischer Probleme in der Praxis", Seminar Notes NIT, April 1992
- [124] Kollmann, F.G. and Landfester, A., "Vergleichende Untersuchung rechnergestützter Simulationsverfahren für die Vorausberechnung der Schallabstrahlung einer Struktur ins Freifeld", FVV Interim-Report "Kurbelgehäuseakustik", 1997
- [125] Becker, P. and Waller, H., "Vergleich der Methoden der Finite-Elemente und der Boundary-Elemente bei der numerischen Berechnung von Schallfeldern"
- [126] Schmillen, K., "Geräuschanalyse und Rechentechniken im Motorenbau", Lecture Notes RWTH Aachen, 1993/94
- [127] Kinsler, L.E., Frey, A.R., Coppens, A.B. and Sanders, J.V., "Fundamentals of Acoustics", John Wiley & Sons, 1982
- [128] Pierce, A.D., "Acoustics - An Introduction to its physical principles and applications", Acoustical Society of America, New York, 1989
- [129] Viersbach, U. and Maurell, R., "SYSNOISE - Noise Radiation for the ZETA Engine", Internal Document of Ford Motor Co., 1994
- [130] Schulze-Schwering, W., "EAO's Method for Computing Noise Radiation", Internal Document of Ford Motor Co., 1986
- [131] Klemenz, M., "Akustische Analyse eines Katalysators mit der Boundary-Element-Methode", TU Berlin, 1994
- [132] Giazitzis, G., "Evaluation of SYSNOISE and NOISE", Internal Document of Ford Motor Co., 1991
- [133] Affenzeller, J., "Anwendung der Computer-Simulation zur Geräuschminderung an Motoren", Symposium 'Motor und Umwelt', 1990

- 
- [134] SONAR Powertrain NVH Benchmarking Consortium (Croker, M.D. et al), "Ford Zetec-SE Flywheel Motion Investigation", Internal Document of Ford Motor Co., DP97/0802, 1997
  - [135] FEV / Ford (Joerres, M. et al), "Acoustical Investigations on Sigma 1.4l with Flexible Flywheel", Internal Document of Ford Motor Co., 1995
  - [136] Masenger, U., "Oilpan Investigation: Comparison between different oil-pans", Internal Document of Ford Motor Co., 1996

### Appendices

#### Appendix 1 Frequency Dependent Forcing Function

The Fourier series expansion is given below for a reduced number of speeds. These data are used to automatically generate the MSC/Nastran CASE control and BULK-DATA deck entries.

ORDER	SPEED = 1000.00 1/min			
	TANGENTIAL FORCE		RADIAL FORCE	
	AMPLITUDE IN N	PHASE IN DEG	AMPLITUDE IN N	PHASE IN DEG
0.5	1293.27	-27.20	1875.94	3.55
1.0	1061.88	-52.94	1941.54	-11.79
1.5	1020.83	-82.23	1959.63	-28.02
2.0	725.65	-91.14	1539.27	-36.87
2.5	699.87	-100.90	1417.42	-42.26
3.0	569.14	-107.93	1230.37	-50.16
3.5	490.57	-118.89	1063.99	-59.35
4.0	387.22	-122.63	891.83	-64.37
4.5	330.13	-129.19	783.33	-70.77
5.0	279.41	-135.59	692.33	-76.69
5.5	223.09	-143.67	597.93	-83.78
6.0	190.15	-147.24	528.15	-88.04
6.5	159.22	-155.58	466.67	-93.61
7.0	135.52	-160.82	418.22	-97.61
7.5	114.38	-167.55	372.87	-102.39
8.0	100.74	-173.62	333.59	-105.96
8.5	84.71	-179.80	297.66	-109.16
9.0	76.39	175.04	269.65	-111.76
9.5	66.12	168.55	242.70	-114.70
10.0	58.39	162.90	217.11	-116.61
10.5	51.60	158.54	196.22	-118.15
11.0	46.30	151.81	176.39	-119.10
11.5	40.86	147.50	160.39	-120.11
12.0	36.64	141.54	143.71	-120.14
12.5	33.08	136.71	130.51	-120.04
13.0	29.02	131.30	118.36	-118.42
13.5	26.90	126.90	108.85	-117.83
14.0	23.38	121.05	99.32	-115.25
14.5	21.34	116.71	92.06	-113.20
15.0	18.66	112.27	86.65	-109.64
15.5	16.97	105.95	81.99	-107.16
16.0	14.50	102.40	78.95	-103.55
16.5	13.15	95.35	76.26	-100.52
17.0	11.19	91.18	75.64	-97.19
17.5	9.83	83.82	75.07	-94.91
18.0	8.56	79.36	75.05	-92.58
18.5	7.17	69.95	75.56	-90.70
19.0	6.16	65.94	76.55	-89.21
19.5	5.05	55.45	77.62	-88.55
20.0	4.24	47.12	78.45	-87.78
20.5	3.19	35.22	79.52	-87.74
21.0	2.78	20.20	80.60	-87.47
21.5	2.03	-1.51	81.52	-88.24
22.0	2.02	-23.63	82.14	-88.53
22.5	1.90	-49.15	82.54	-89.48
23.0	2.32	-69.11	83.25	-90.11
23.5	2.37	-84.87	83.24	-91.49
24.0	2.95	-95.81	83.39	-92.45
24.5	3.07	-106.79	82.93	-93.80
25.0	3.55	-115.65	82.86	-94.95
25.5	3.70	-122.20	82.18	-96.46
26.0	4.13	-130.94	81.49	-97.84
26.5	4.24	-135.43	80.42	-99.22
27.0	4.59	-142.91	79.51	-100.57
27.5	4.72	-147.20	78.32	-102.10
28.0	4.86	-153.75	76.87	-103.46
28.5	5.04	-157.39	75.41	-104.87
29.0	5.05	-163.86	73.82	-106.07
29.5	5.18	-167.79	72.27	-107.53
30.0	5.13	-173.36	70.40	-108.64

In the following the Nastran CASE-Control data are shown for six engine speeds:

```

$ PLEASE COPY THIS FILE INTO YOUR CASE CONTROL DECK
$
VELOCITY = ALL
$
$ SOL 111
$
SUBCASE = 1
DLOAD = 10000
FREQUENCY = 100
$
SUBCASE = 2
DLOAD = 10001
FREQUENCY = 101
$
SUBCASE = 3
DLOAD = 10002
FREQUENCY = 102
$
SUBCASE = 4
DLOAD = 10003
FREQUENCY = 103
$
SUBCASE = 5
DLOAD = 10004
FREQUENCY = 104
$
SUBCASE = 6
DLOAD = 10005
FREQUENCY = 105
$
    
```

The corresponding BULK-DATA deck is given subsequently. The data are reduced to one subcase only to avoid the upbringing of uninteresting data.

```

$
$ PLEASE APPEND THIS FILE TO YOUR BULK-DATA-FILE.
$
$
$ DAREA-CARDS OF CRANKPINS AND COMBUSTION CHAMBERS OF CYL. 1T4
$
DAREA      100      1      2      -1.      5      2      1.
DAREA      101      2      2      -1.      6      2      1.
DAREA      102      3      2      -1.      7      2      1.
DAREA      103      4      2      -1.      8      2      1.
$
$ DPHASE-CARDS OF CRANKPINS AND COMBUSTION CHAMBERS OF CYL. 1T4
$
DPHASE     100      1      2      0.0      5      2      0.0
DPHASE     101      2      2      180.0     6      2      0.0
DPHASE     102      3      2      180.0     7      2      0.0
DPHASE     103      4      2      0.0      8      2      0.0
$
$ REAL PARTS OF AMPLITUDES, SPEED = 1000.00 /min, RADIAL FORCES
$
TABLED1    100
+Z 101      8.33 1872.33 16.67 1900.61 25.00 1729.85 33.33 1231.36+Z 101
+Z 102      41.67 1049.09 50.00 788.26 58.33 542.43 66.67 385.75+Z 102
+Z 103      75.00 257.95 83.33 159.38 91.67 64.83 100.00 18.08+Z 103
+Z 104      108.33 -29.41 116.67 -55.38 125.00 -80.02 133.33 -91.75+Z 104
+Z 105      141.67 -97.67 150.00 -99.98 158.33 -101.41 166.67 -97.24+Z 105
+Z 106      ENDT
$
$ IMAGINARY PARTS OF AMPLITUDES, SPEED = 1000.00 /min, RADIAL FORCES
$
TABLED1    101
+Z 201      8.33 116.32 16.67 -396.56 25.00 -920.73 33.33 -923.64+Z 201
+Z 202      41.67 -953.15 50.00 -944.70 58.33 -915.34 66.67 -804.09+Z 202
+Z 203      75.00 -739.63 83.33 -673.73 91.67 -594.40 100.00 -527.84+Z 203
+Z 204      108.33 -465.74 116.67 -414.54 125.00 -364.19 133.33 -320.73+Z 204
+Z 205      141.67 -281.18 150.00 -250.43 158.33 -220.50 166.67 -194.12+Z 205
+Z 206      ENDT
$
$ DELAY CARDS FOR CRANKPINS 1T4, RADIAL FORCES , SPEED = 1000.00 /min
$
DELAY      100      1      2      0.0000      5      2      0.0000
DELAY      101      2      2      0.0900      6      2      0.0900
DELAY      102      3      2      0.0300      7      2      0.0300
DELAY      103      4      2      0.0600      8      2      0.0600
$
    
```

\$ LOAD CARDS FOR CRANKPINS 1T4, RADIAL FORCES  
\$ SPEED = 1000.00 /min

RLOAD1	100	100	100	100	100	101
RLOAD1	101	101	101	101	100	101
RLOAD1	102	102	102	102	100	101
RLOAD1	103	103	103	103	100	101

\$ DAREA-CARDS OF CRANKPINS AND CYLINDER SIDES OF CYL. 1T4

DAREA	200	1	1	-1.	9	1	1.
DAREA	201	2	1	-1.	10	1	1.
DAREA	202	3	1	-1.	11	1	1.
DAREA	203	4	1	-1.	12	1	1.

\$ DPHASE-CARDS OF CRANKPINS AND CYLINDER SIDES OF CYL. 1T4

DPHASE	200	1	1	0.0	9	1	0.0
DPHASE	201	2	1	180.0	10	1	0.0
DPHASE	202	3	1	180.0	11	1	0.0
DPHASE	203	4	1	0.0	12	1	0.0

\$ REAL PARTS OF AMPLITUDES, SPEED = 1000.00 /min, TANGENTIAL FORCES

TABLED1	200									+Z	1401
+Z	1401	8.33	1150.27	16.67	639.89	25.00	138.07	33.33	-14.42	+Z	1402
+Z	1402	41.67	-132.38	50.00	-175.26	58.33	-237.00	66.67	-208.81	+Z	1403
+Z	1403	75.00	-208.63	83.33	-199.58	91.67	-179.73	100.00	-159.90	+Z	1404
+Z	1404	108.33	-144.97	116.67	-128.00	125.00	-111.69	133.33	-100.12	+Z	1405
+Z	1405	141.67	-84.71	150.00	-76.10	158.33	-64.80	166.67	-55.81	+Z	1406
+Z	1406	ENDT									

\$ IMAGINARY PARTS OF AMPLITUDES, SPEED = 1000.00 /min, TANGENTIAL FORCES

TABLED1	201									+Z	1501
+Z	1501	8.33	-591.12	16.67	-847.43	25.00	-1011.45	33.33	-725.51	+Z	1502
+Z	1502	41.67	-687.24	50.00	-541.49	58.33	-429.52	66.67	-326.10	+Z	1503
+Z	1503	75.00	-255.85	83.33	-195.54	91.67	-132.17	100.00	-102.90	+Z	1504
+Z	1504	108.33	-65.83	116.67	-44.52	125.00	-24.66	133.33	-11.19	+Z	1505
+Z	1505	141.67	-0.30	150.00	6.61	158.33	13.13	166.67	17.17	+Z	1506
+Z	1506	ENDT									

\$ DELAY CARDS FOR CRANKPINS 1T4, TANGENTIAL FORCES, SPEED = 1000.00 /min

DELAY	200	1	1	0.0000	9	1	0.0000
DELAY	201	2	1	0.0900	10	1	0.0900
DELAY	202	3	1	0.0300	11	1	0.0300
DELAY	203	4	1	0.0600	12	1	0.0600

\$ LOAD CARDS FOR CRANKPINS 1T4, TANGENTIAL FORCES

\$ SPEED = 1000.00 /min

RLOAD1	200	200	200	200	200	201
RLOAD1	201	201	201	201	200	201
RLOAD1	202	202	202	202	200	201
RLOAD1	203	203	203	203	200	201

\$ FREQ-CARD FOR SPEED = 1000.00 /min

FREQ1	100	8.33	8.33	19
-------	-----	------	------	----

\$ FREQ-CARD FOR SPEED = 2000.00 /min

FREQ1	101	16.67	16.67	19
-------	-----	-------	-------	----

\$ FREQ-CARD FOR SPEED = 3000.00 /min

FREQ1	102	25.00	25.00	19
-------	-----	-------	-------	----

\$ FREQ-CARD FOR SPEED = 4000.00 /min

FREQ1	103	33.33	33.33	19
-------	-----	-------	-------	----

\$ FREQ-CARD FOR SPEED = 5000.00 /min

FREQ1	104	41.67	41.67	19
-------	-----	-------	-------	----

\$ FREQ-CARD FOR SPEED = 6000.00 /min

FREQ1	105	50.00	50.00	19
-------	-----	-------	-------	----

\$ DLOAD-CARDS FOR SPEED =1000.00 /min,

DLOAD	10000	1.0	1.0	100	1.0	101	1.0	102+ZXX	0	
+ZXX	0	1.0	103	1.0	200	1.0	201	1.0	202+ZXX	1
+ZXX	1	1.0	203							

### Appendix 2 Frequency Coupled System Matrices

Using the frequency domain Fourier coefficient vectors  $a_0, a_{\frac{1}{2}}, b_{\frac{1}{2}}, a_1, b_1, a_{\frac{1}{2}}, \dots$ , the corre-

sponding coupled mode shape vector for whole-order solutions is given by

$$\tilde{\mathbf{u}} = [\mathbf{a}_0^T, \mathbf{a}_1^T, \mathbf{b}_1^T, \mathbf{a}_2^T, \dots]$$

and the corresponding vector for half-order solutions is

$$\tilde{\mathbf{u}} = \left[ \mathbf{a}_{\frac{1}{2}}^T, \mathbf{b}_{\frac{1}{2}}^T, \mathbf{a}_{\frac{1}{2}}^T, \mathbf{b}_{\frac{1}{2}}^T, \dots \right]$$

The stiffness matrix  $\tilde{\mathbf{K}}$  for the whole-order solution can be written in the form

$$\tilde{\mathbf{K}} = \begin{bmatrix} \frac{\mathbf{K}_{0c}}{2} & \mathbf{K}_{1c} & \mathbf{K}_{1s} & \mathbf{K}_{2c} & \mathbf{K}_{2s} & 0 & 0 & 0 & 0 & \dots \\ \mathbf{K}_{1c} & \mathbf{K}_{0c} + \mathbf{K}_{2c} & \mathbf{K}_{2s} & \mathbf{K}_{1c} & \mathbf{K}_{1s} & \mathbf{K}_{2c} & \mathbf{K}_{2s} & 0 & 0 & \dots \\ \mathbf{K}_{1s} & \mathbf{K}_{2s} & \mathbf{K}_{0c} - \mathbf{K}_{2c} & -\mathbf{K}_{1s} & \mathbf{K}_{1c} & -\mathbf{K}_{2s} & \mathbf{K}_{2c} & 0 & 0 & \dots \\ \mathbf{K}_{2c} & \mathbf{K}_{1c} & -\mathbf{K}_{1s} & \mathbf{K}_{0c} & 0 & \mathbf{K}_{1c} & \mathbf{K}_{1s} & \mathbf{K}_{2c} & \mathbf{K}_{2s} & \dots \\ \mathbf{K}_{2s} & \mathbf{K}_{1s} & \mathbf{K}_{1c} & 0 & \mathbf{K}_{0c} & -\mathbf{K}_{1s} & \mathbf{K}_{1c} & -\mathbf{K}_{2s} & \mathbf{K}_{2c} & \dots \\ 0 & \mathbf{K}_{2c} & -\mathbf{K}_{2s} & \mathbf{K}_{1c} & -\mathbf{K}_{1s} & \mathbf{K}_{0c} & 0 & \mathbf{K}_{1c} & \mathbf{K}_{1s} & \dots \\ 0 & \mathbf{K}_{2s} & \mathbf{K}_{2c} & \mathbf{K}_{1s} & \mathbf{K}_{1c} & 0 & \mathbf{K}_{0c} & -\mathbf{K}_{1s} & \mathbf{K}_{1c} & \dots \\ 0 & 0 & 0 & \mathbf{K}_{2c} & -\mathbf{K}_{2s} & \mathbf{K}_{1c} & -\mathbf{K}_{1s} & \mathbf{K}_{0c} & 0 & \dots \\ 0 & 0 & 0 & \mathbf{K}_{2s} & \mathbf{K}_{2c} & \mathbf{K}_{1s} & \mathbf{K}_{1c} & 0 & \mathbf{K}_{0c} & \dots \\ \dots & \dots & \dots & \dots & \dots & \dots & \dots & \dots & \dots & \dots \end{bmatrix}$$

and for the half-order solution as

$$\tilde{\mathbf{K}} = \begin{bmatrix} \mathbf{K}_{0c} + \mathbf{K}_{1c} & \mathbf{K}_{1s} & \mathbf{K}_{1c} + \mathbf{K}_{2c} & \mathbf{K}_{1s} + \mathbf{K}_{2s} & \mathbf{K}_{2c} & \mathbf{K}_{2s} & 0 & 0 & \dots \\ \mathbf{K}_{1s} & \mathbf{K}_{0c} - \mathbf{K}_{1c} & -\mathbf{K}_{1s} + \mathbf{K}_{2s} & \mathbf{K}_{1c} - \mathbf{K}_{2c} & -\mathbf{K}_{2s} & \mathbf{K}_{2c} & 0 & 0 & \dots \\ \mathbf{K}_{1c} + \mathbf{K}_{2c} & -\mathbf{K}_{1s} + \mathbf{K}_{2s} & \mathbf{K}_{0c} & 0 & \mathbf{K}_{1c} & \mathbf{K}_{1s} & \mathbf{K}_{2c} & \mathbf{K}_{2s} & \dots \\ \mathbf{K}_{1s} + \mathbf{K}_{2s} & \mathbf{K}_{1c} - \mathbf{K}_{2c} & 0 & \mathbf{K}_{0c} & -\mathbf{K}_{1s} & \mathbf{K}_{1c} & -\mathbf{K}_{2s} & \mathbf{K}_{2c} & \dots \\ \mathbf{K}_{2c} & -\mathbf{K}_{2s} & \mathbf{K}_{1c} & -\mathbf{K}_{1s} & \mathbf{K}_{0c} & 0 & \mathbf{K}_{1c} & \mathbf{K}_{1s} & \dots \\ \mathbf{K}_{2s} & \mathbf{K}_{2c} & \mathbf{K}_{1s} & \mathbf{K}_{1c} & 0 & \mathbf{K}_{0c} & -\mathbf{K}_{1s} & \mathbf{K}_{1c} & \dots \\ 0 & 0 & \mathbf{K}_{2c} & -\mathbf{K}_{2s} & \mathbf{K}_{1c} & -\mathbf{K}_{1s} & \mathbf{K}_{0c} & 0 & \dots \\ 0 & 0 & \mathbf{K}_{2s} & \mathbf{K}_{2c} & \mathbf{K}_{1s} & \mathbf{K}_{1c} & 0 & \mathbf{K}_{0c} & \dots \\ \dots & \dots & \dots & \dots & \dots & \dots & \dots & \dots & \dots \end{bmatrix}$$

The coupled gyroscopic matrices are given with

$$\tilde{\mathbf{G}}_{\text{whole-order}} = \begin{bmatrix} 0 & 0 & 0 & 0 & 0 & 0 & \dots \\ 0 & 0 & -\mathbf{G}_{0c} & 0 & 0 & 0 & \dots \\ 0 & \mathbf{G}_{0c} & 0 & 0 & 0 & 0 & \dots \\ 0 & 0 & 0 & 0 & -\mathbf{G}_{0c} & 0 & \dots \\ 0 & 0 & 0 & \mathbf{G}_{0c} & 0 & 0 & \dots \\ \dots & \dots & \dots & \dots & \dots & \dots & \dots \end{bmatrix}$$

$$\tilde{\mathbf{G}}_{half-order} = \begin{bmatrix} 0 & -\mathbf{G}_{0c} & 0 & 0 & \dots \\ \mathbf{G}_{0c} & 0 & 0 & 0 & \dots \\ 0 & 0 & 0 & -\mathbf{G}_{0c} & \dots \\ 0 & 0 & \mathbf{G}_{0c} & 0 & \dots \\ \dots & \dots & \dots & \dots & \dots \end{bmatrix}$$

The corresponding mass matrices are developed, so that:

$$\tilde{\mathbf{M}}_{whole-order} = \begin{bmatrix} 0 & 0 & 0 & 0 & \dots \\ 0 & \mathbf{M}_{0c} & 0 & 0 & \dots \\ 0 & 0 & \mathbf{M}_{0c} & 0 & \dots \\ 0 & 0 & 0 & \mathbf{M}_{0c} & \dots \\ \dots & \dots & \dots & \dots & \dots \end{bmatrix}$$

$$\tilde{\mathbf{M}}_{half-order} = \begin{bmatrix} \mathbf{M}_{0c} & 0 & 0 & 0 & \dots \\ 0 & \mathbf{M}_{0c} & 0 & 0 & \dots \\ 0 & 0 & \mathbf{M}_{0c} & 0 & \dots \\ 0 & 0 & 0 & \mathbf{M}_{0c} & \dots \\ \dots & \dots & \dots & \dots & \dots \end{bmatrix}$$

Finally, the vibration harmonic order matrices are written such as:

$$\tilde{\Lambda}_{whole-order} = \begin{bmatrix} 0 & 0 & 0 & 0 & \dots \\ 0 & \mathbf{I} & 0 & 0 & \dots \\ 0 & 0 & \mathbf{I} & 0 & \dots \\ 0 & 0 & 0 & 2\mathbf{I} & \dots \\ \dots & \dots & \dots & \dots & \dots \end{bmatrix}$$

$$\tilde{\Lambda}_{half-order} = \begin{bmatrix} \frac{1}{2}\mathbf{I} & 0 & 0 & 0 & \dots \\ 0 & \frac{1}{2}\mathbf{I} & 0 & 0 & \dots \\ 0 & 0 & \frac{3}{2}\mathbf{I} & 0 & \dots \\ 0 & 0 & 0 & \frac{3}{2}\mathbf{I} & \dots \\ \dots & \dots & \dots & \dots & \dots \end{bmatrix}$$

### **Appendix 3 Flywheel Whirl Test and Analysis Procedure**

The test and analysis procedures refer to RICARDO's approach measuring and analysing flywheel whirl.

#### **TEST PROCEDURE**

The following instrumentation is required for the measurement of the flywheel motion in 4 DOFs:

- Inductive probe targeted at the flywheel teeth.
- 3 proximity probes targeted at the face of the flywheel at known positions relative to the centre of the flywheel.
- Once per rev. pulse.
- Once per cycle pulse from camshaft or HT lead.

The proximity transducers used were Micro-Epsilon UI probes with a measurement range of 1 mm and recommended offset of 0.2 mm, which require a flat target area of diameter 12 mm. The probes were wound in and out of the mounting in order to vary the distance between the probe and the flywheel. Zero, gain and linearity settings were adjusted to give a linear calibration as follows:

- The probe position was set to be at a minimum distance to the target i.e. 0.2 mm, and the zero control adjusted to give 0 V output.
- The probe position was set to be approximately at the mid point of the measurement range i.e. 0.6 mm, and the gain control adjusted to give the required voltage i.e. 0.8 V.
- The probe position was set to be at the maximum distance from the target i.e. 1.2 mm, and the linearity control adjusted to give the required voltage i.e. 2 V.
- This was repeated as necessary, checking voltages and adjusting as required.

The probes were then adjusted to give 0.7 mm clearance from the flywheel at the static position.

The run-out of the flywheel was measured prior to the assembly of the transmission using a clock gauge. If this is significant compared to the measured displacement at any probe, it should be accounted for during analysis.



## ACQUISITION AND ANALYSIS PROCEDURE

### Acquisition of motion data:

All motion data were digitally acquired as throughput files using LMS CADA-X Fourier Monitor. No further processing is carried out in CADA-X as the data is loaded into Matlab (a mathematical matrix manipulation environment) using the Ricardo 'TFD' function. Processing was carried out using a custom Matlab routine which perform the following:

### Step 1: Calculation of the Normal Vector, Angular and Axial Motion

If  $p_1, p_2, p_3$  are the positions where the proximity probes were targeted, then the vectors  $p_1p_2$  and  $p_1p_3$  must both lie in the plane of the flywheel. If the flywheel is rigid, the cross product of these two vectors will always be normal to the surface. i.e.:

$$n = p_1p_2 \times p_1p_3$$

It is a simple matter to obtain the angular motion of the flywheel from this normal vector. Furthermore, for any other point on the flywheel surface,  $p_n$ , the dot product of the normal vector and  $p_1p_n$  will be zero. i.e.:

$$p_1p_n \cdot n = 0$$

Given the x and y coordinates of the point  $p_n$ , this could be solved for  $p_1p_n$  and ultimately for the z coordinate of  $p_n$ .

In reality, these vectors were time histories, with the x and y components constant (since it was assumed that there was no horizontal or vertical translational motion) with the z component known or solved.

### Step 2: Demodulate the tooth passing signals

Ricardo uses the Hilbert Transform demodulation techniques to obtain ramps from gear tooth passing signals. The Hilbert transformation is used to synthesize the imaginary part of the full analytical signal from the original data. The instantaneous argument of this analytical signal increases by  $2\pi$  for each tooth that passes and is not affected by amplitude variations. Phase-unwrapping and scaling the argument gives the displacement ramp of the gear. This approach is considered to be superior to traditional zero crossing detection techniques because it provides information once per sample point rather than once per tooth and can resolve at frequencies higher than tooth passing with the correct tooth passing filter. This technique was used to obtain the rotational motion of the flywheel.

### Step 3: Resampling into Engine Cycle Domain

Ricardo use digital resampling techniques within Matlab utilising interpolation filters to obtain sample points at constant flywheel displacement intervals. Data in this format is referred to as being in the engine cycle domain.

### Step 4: Filtering and Order Cutting

Flywheel motion was animated in Matlab for both overall motion and for given orders. The overall or real time motion of the flywheel simply requires low pass filtering to remove contamination at tooth passing frequencies (particularly the rotational degree of freedom). Since the Fourier transform of engine cycle domain data gives data in the order domain, the phase and magnitude of the relevant order contained in one spectral line in the transformed data can be used to reconstruct the angle domain signal due to that order for each DOF. This process was carried out for all 4 DOF's and the results are used to perform the animation of the flywheel in Matlab.

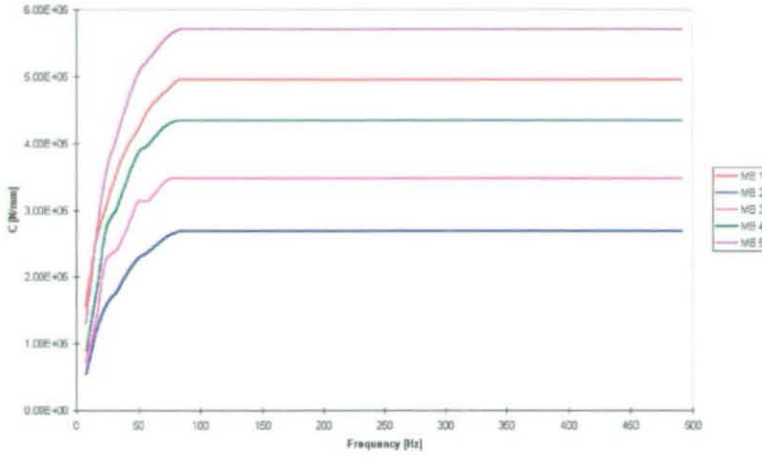
### Step 5: Examination of the Forward and Reverse Whirl Components

A simple approach to examining the whirling motion of the flywheel in detail is to consider the motion, in a plane normal to the crank axis, of the tip of a vector normal to the surface of the flywheel. This would, for example, describe a circle for a constant whirl angle and a line for a rocking motion of the flywheel about a fixed axis. Since the angular displacements are small the motion of the vector tip can be assumed to be proportional to the angular displacements.

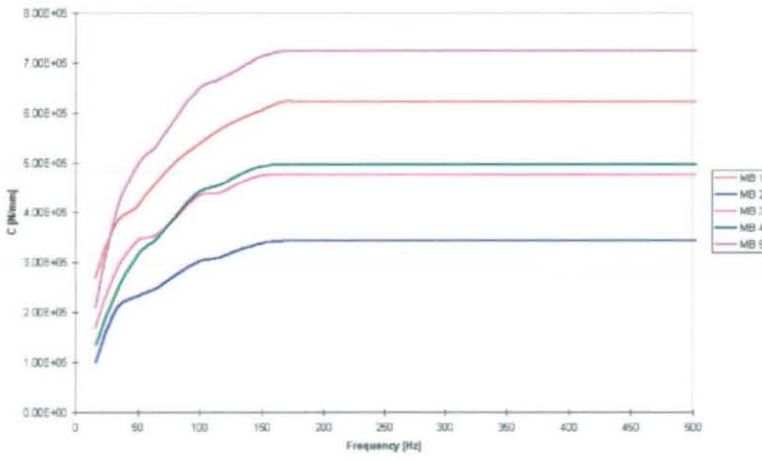
Order cuts of this data can be performed using step 4. This gives the whirl occurring at a given order with respect to ground. However, whirl motion at a given order consists of a forward and reverse component i.e. 3E whirl with respect to ground consists of +2E and -4E whirl with respect to the crankshaft. These components cannot be separated by a Fourier transform approach as they occur at the same frequency to a stationary transducer, but with opposing directions. If it is assumed, however, that a single whirl component will result in a circular motion of the normal vector (i.e. it is assumed that crank and bearing stiffnesses are constant despite the direction) it is possible to estimate the magnitude of each component given the shape of the ellipse described by the normal vector and the direction of its rotation. The major axis of the ellipse is related to the sum of the magnitudes of the whirl components while the minor axis is related to the difference of the magnitudes of the components.

## **Appendix 4 Figures**

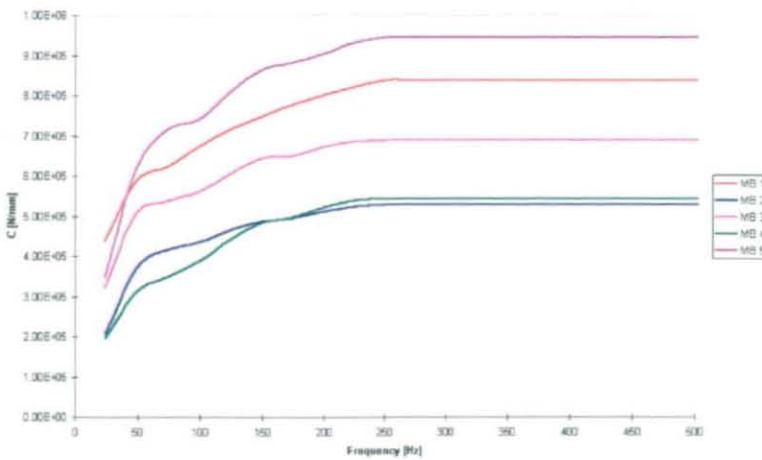
### Stiffness- and Damping-Properties of Plain Bearings



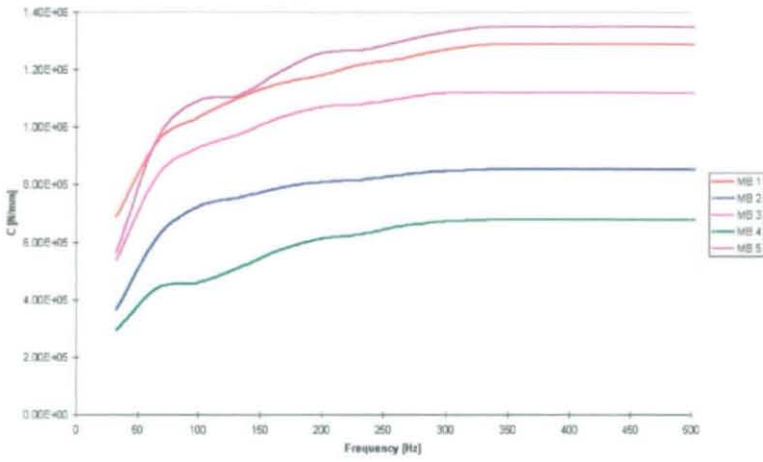
a) 1000 rpm



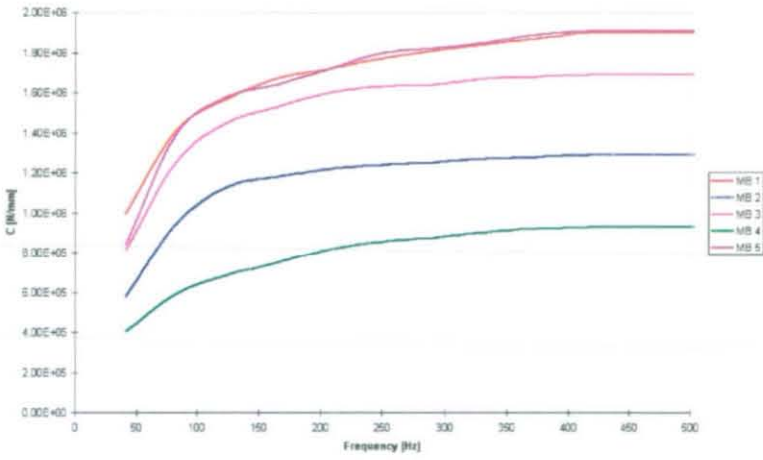
b) 2000 rpm



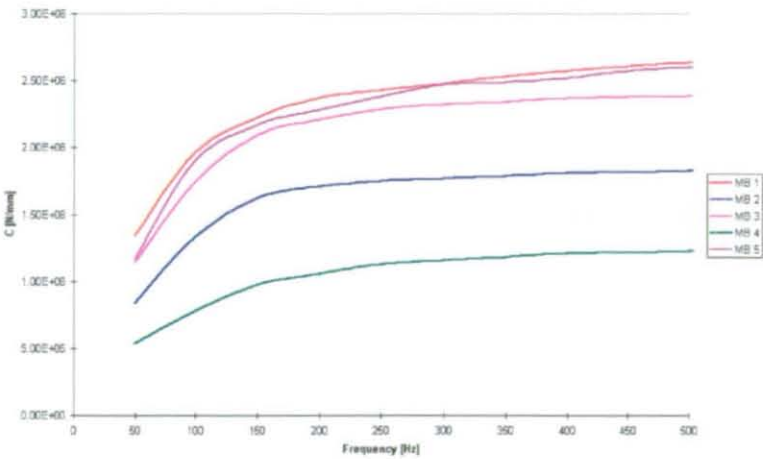
c) 3000 rpm



d) 4000 rpm

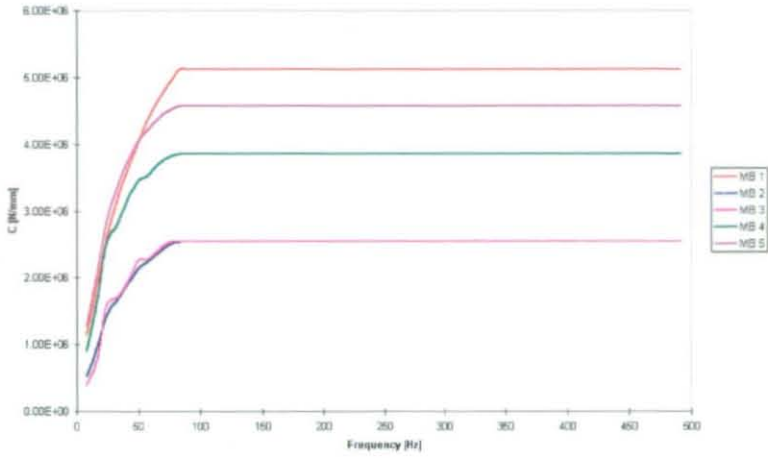


e) 5000 rpm

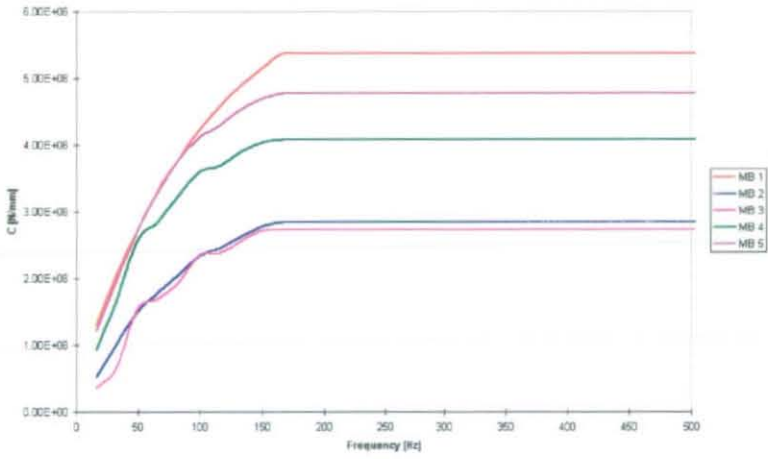


f) 6000 rpm

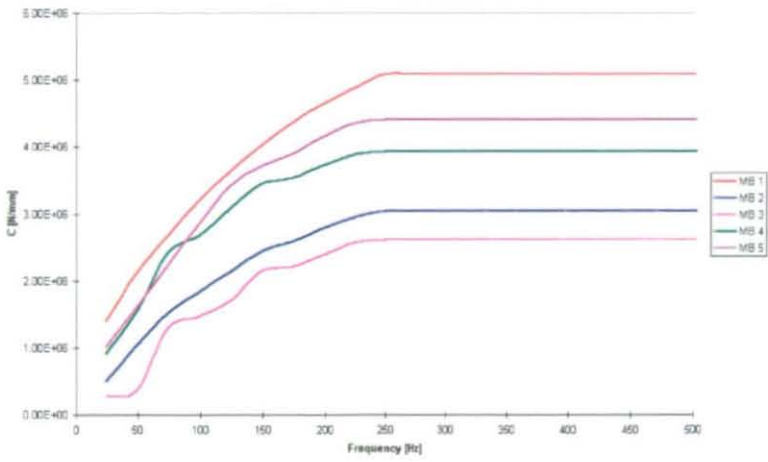
Figure App.4.1 (a-f) Stiffness Properties [1st Principal Direction; Full Load]



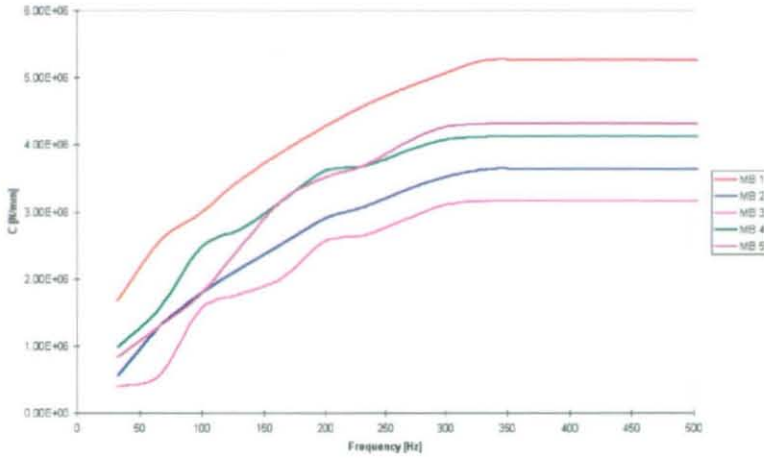
a) 1000 rpm



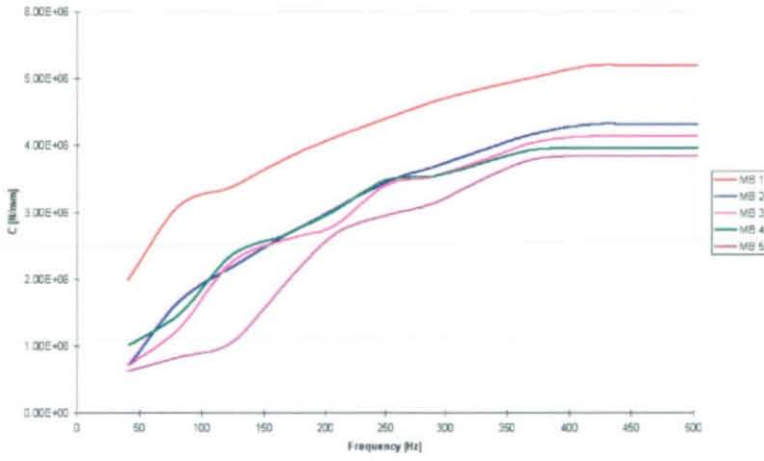
b) 2000 rpm



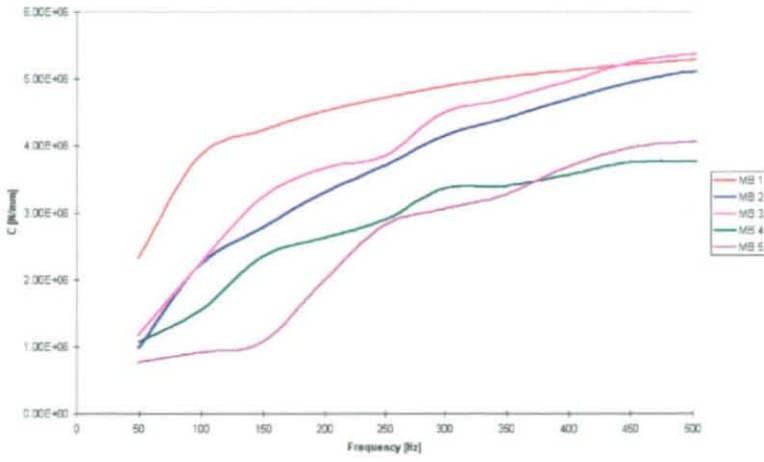
c) 3000 rpm



d) 4000 rpm

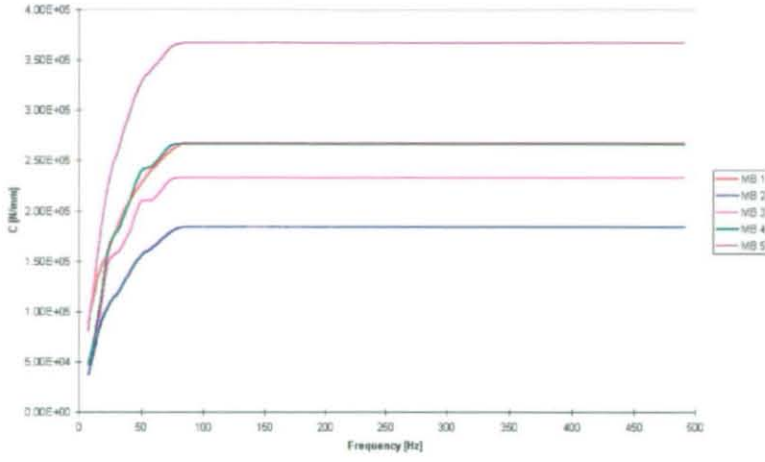


e) 5000 rpm

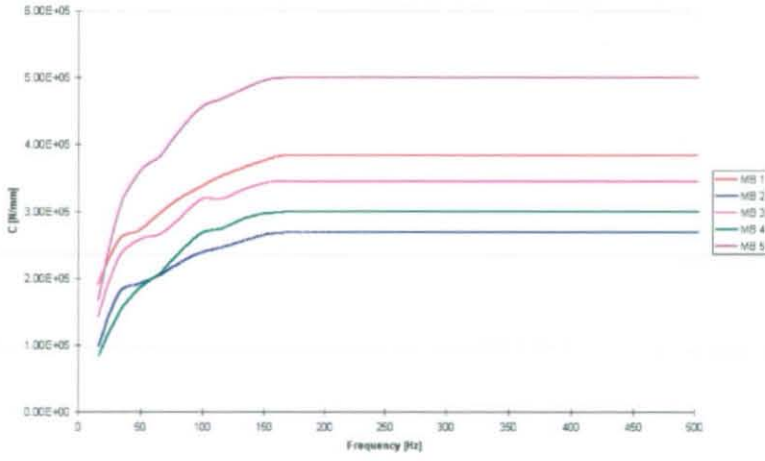


f) 6000 rpm

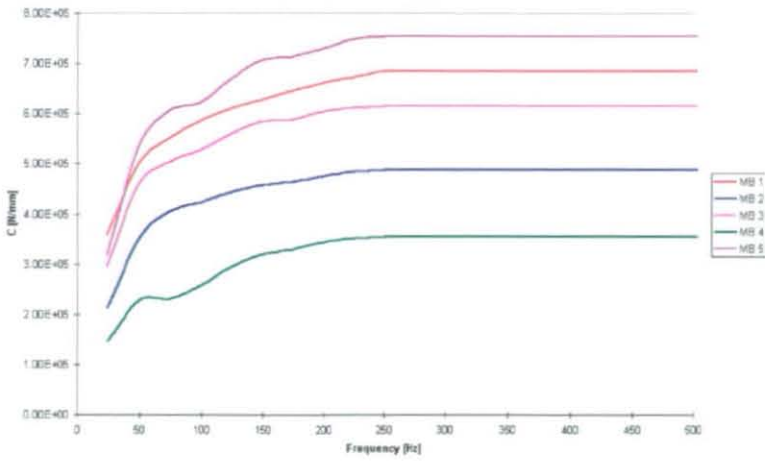
Figure App.4.2 (a-f) Stiffness Properties [2nd Principal Direction; Full Load]



a) 1000 rpm

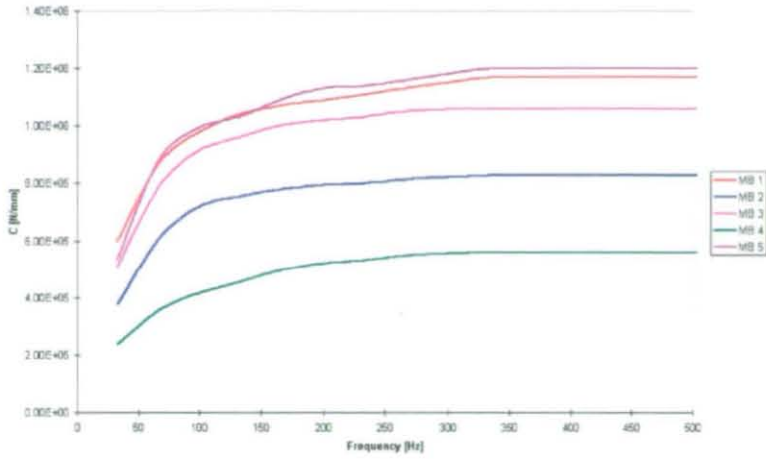


b) 2000 rpm

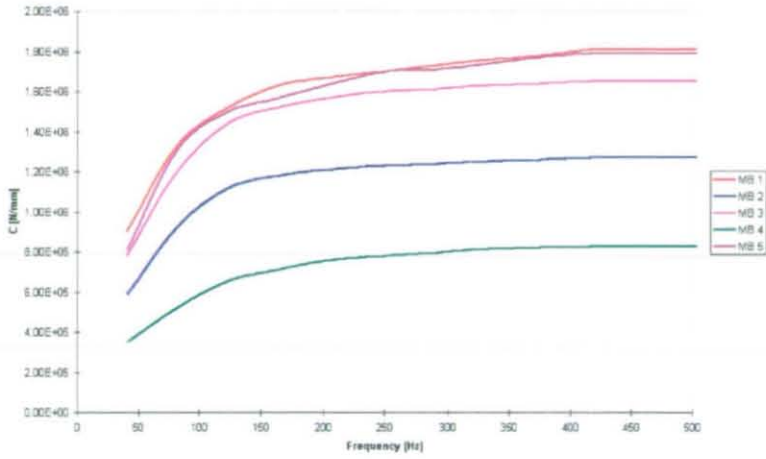


c) 3000 rpm

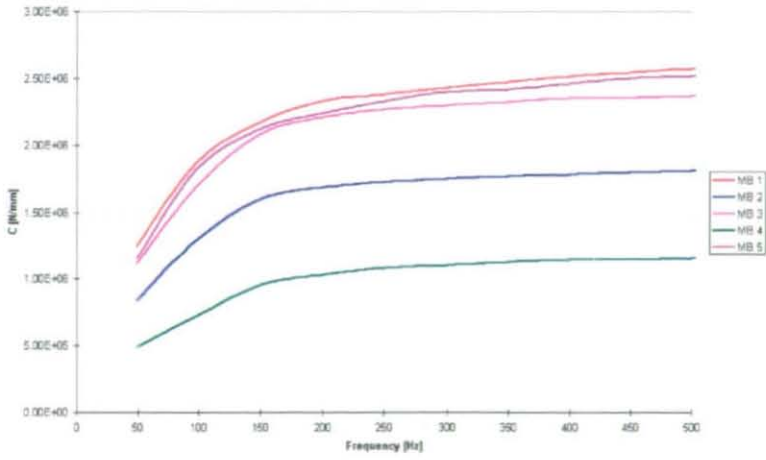




d) 4000 rpm

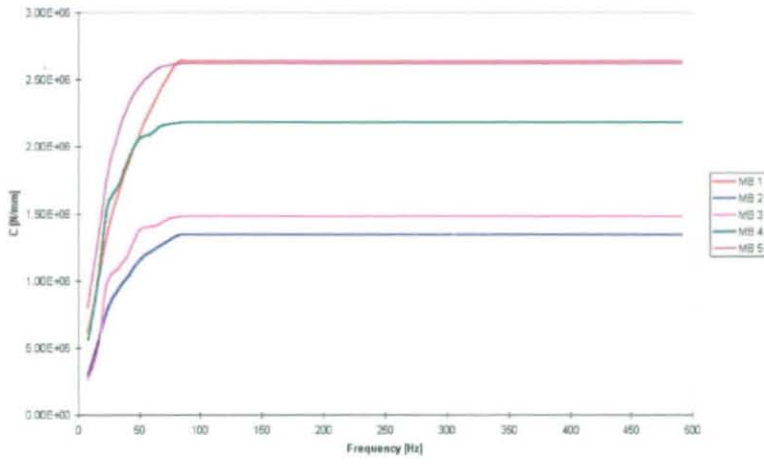


e) 5000 rpm

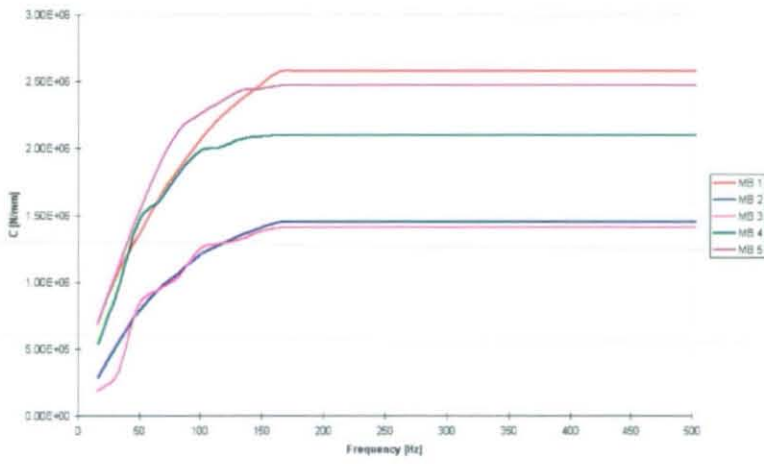


f) 6000 rpm

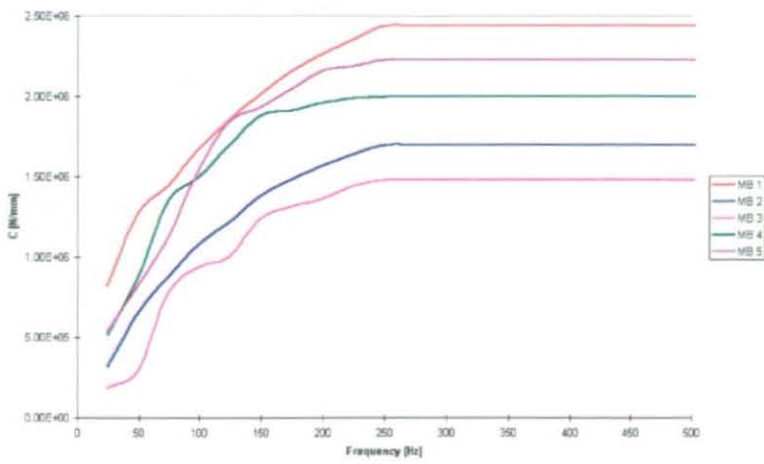
Figure App.4.3 (a-f) Stiffness Properties [1st Principal Direction; 1/3 Load]



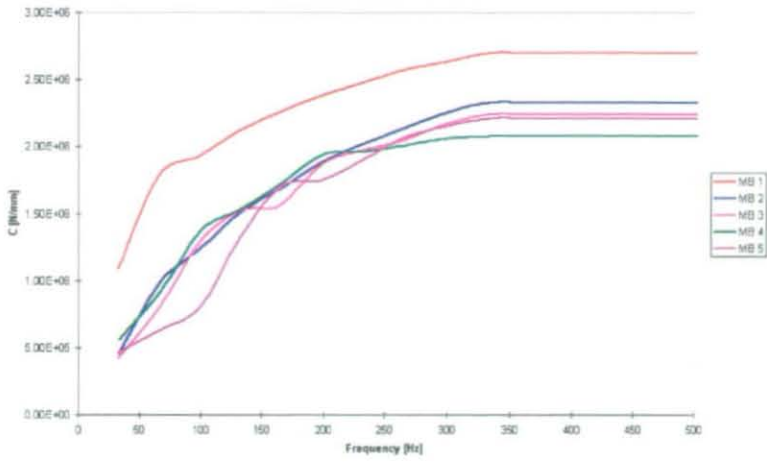
a) 1000 rpm



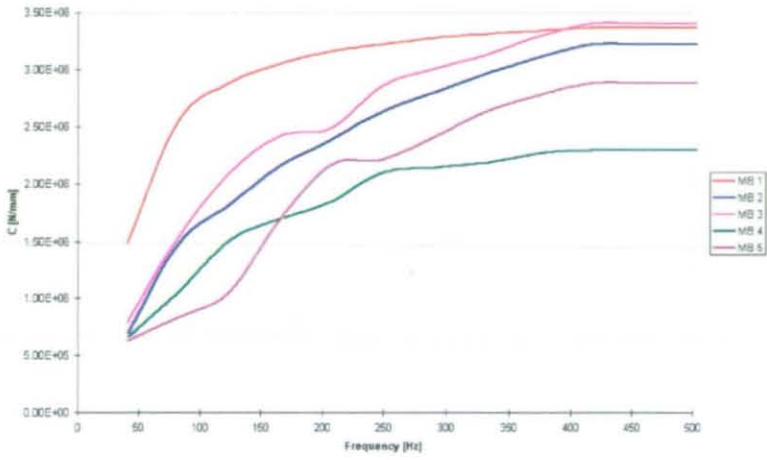
b) 2000 rpm



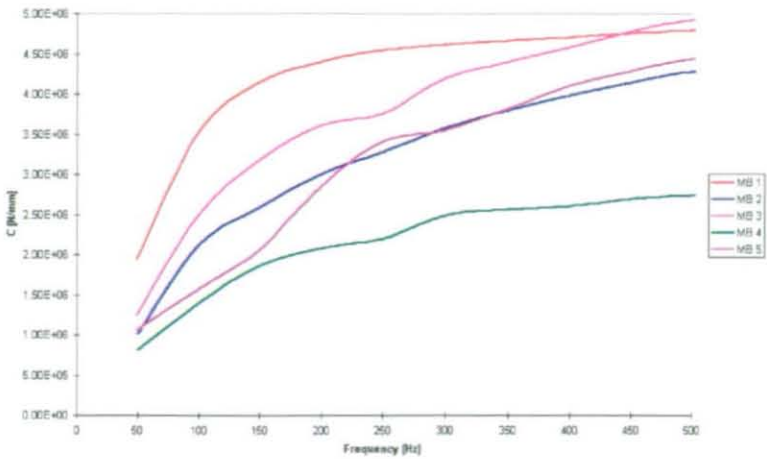
c) 3000 rpm



d) 4000 rpm

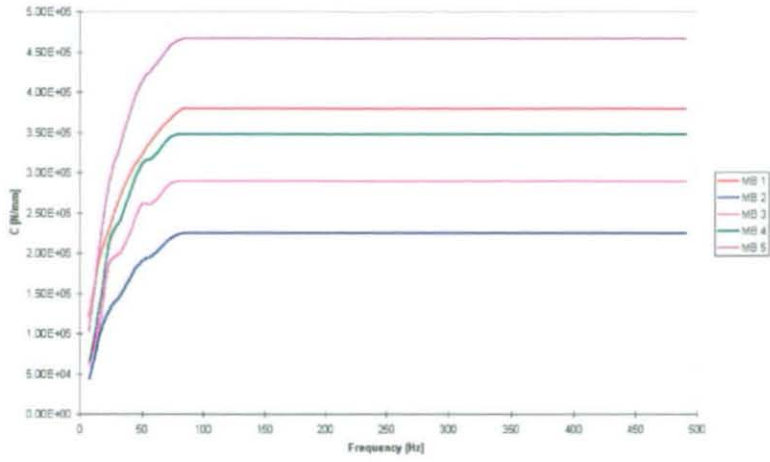


e) 5000 rpm

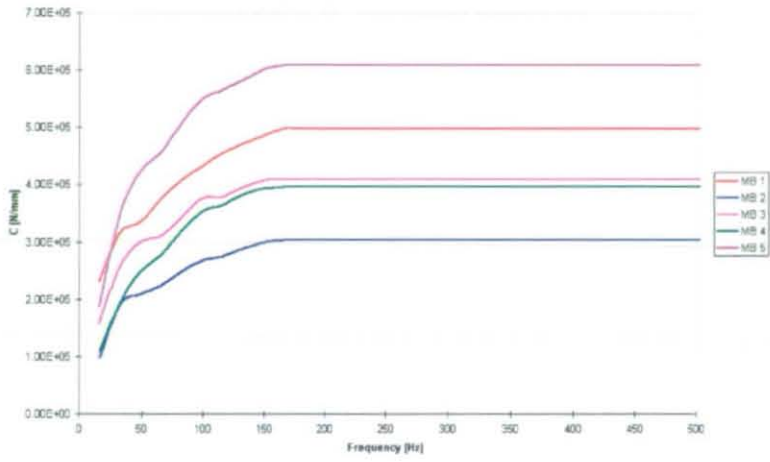


f) 6000 rpm

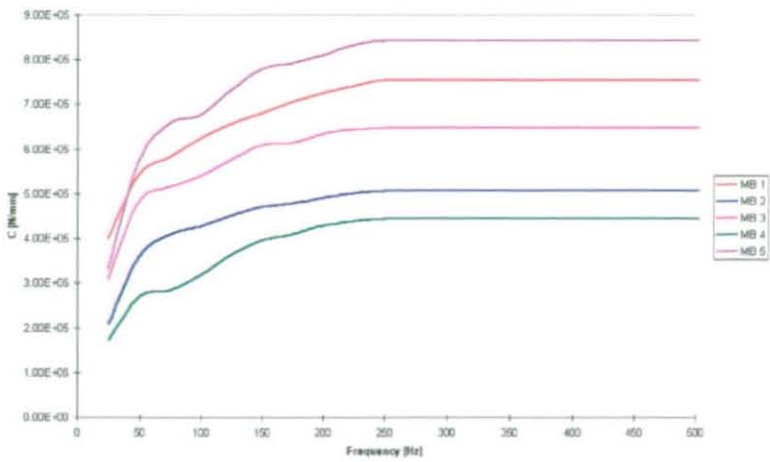
Figure App.4.4 (a-f) Stiffness Properties [2nd Principal Direction; 1/3 Load]



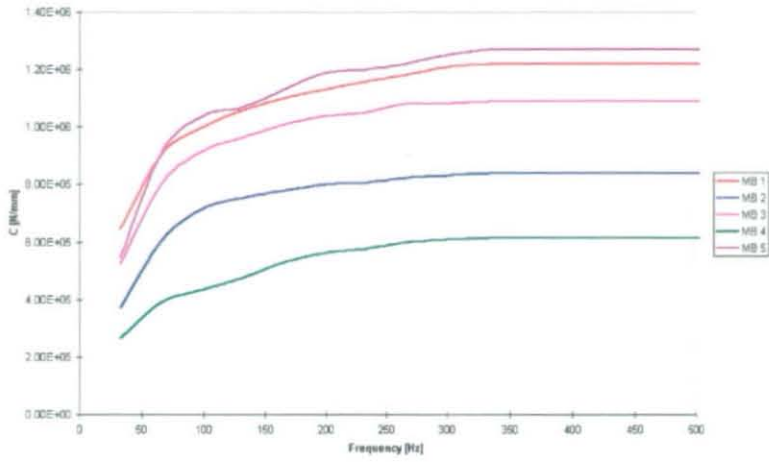
a) 1000 rpm



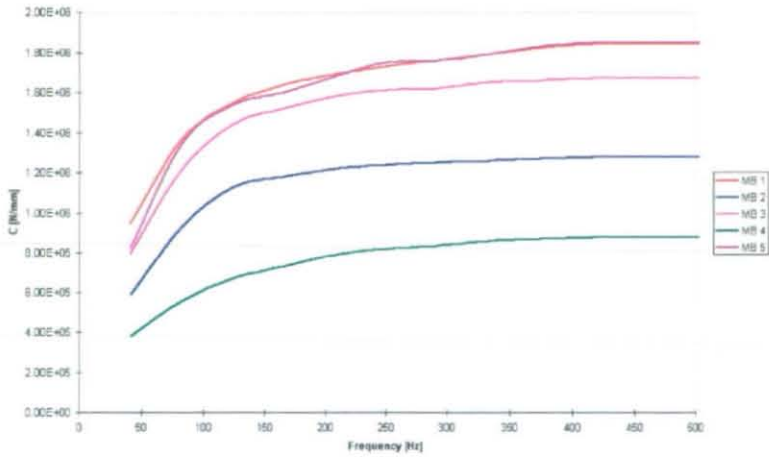
b) 2000 rpm



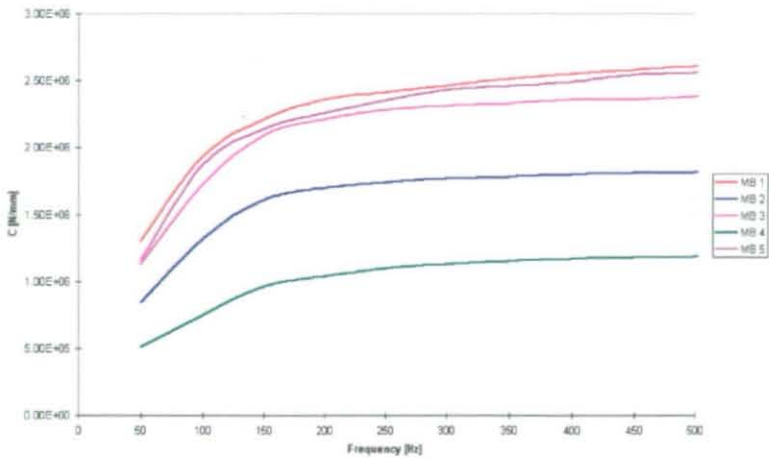
c) 3000 rpm



d) 4000 rpm

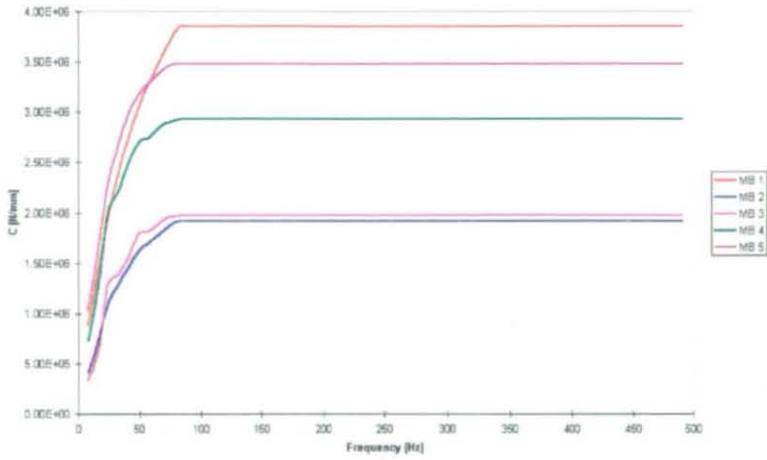


e) 5000 rpm

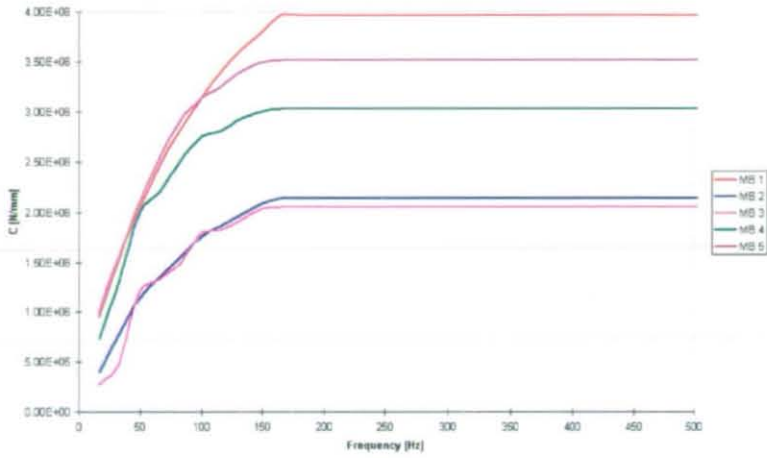


f) 6000 rpm

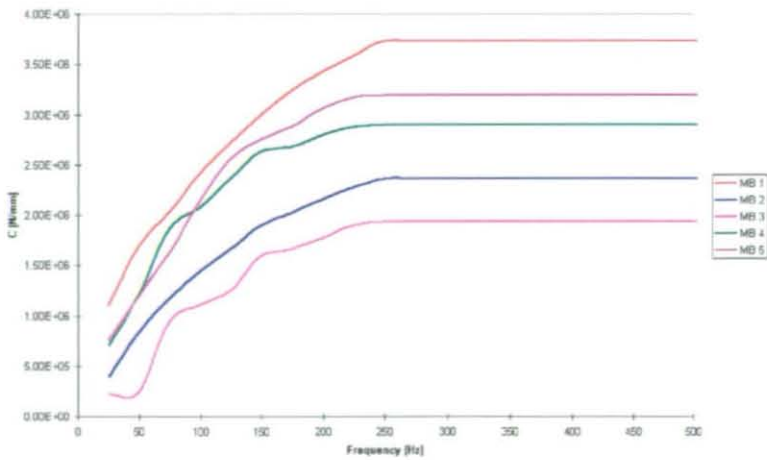
Figure App.4.5 (a-f) Stiffness Properties [1st Principal Direction; 2/3 Load]



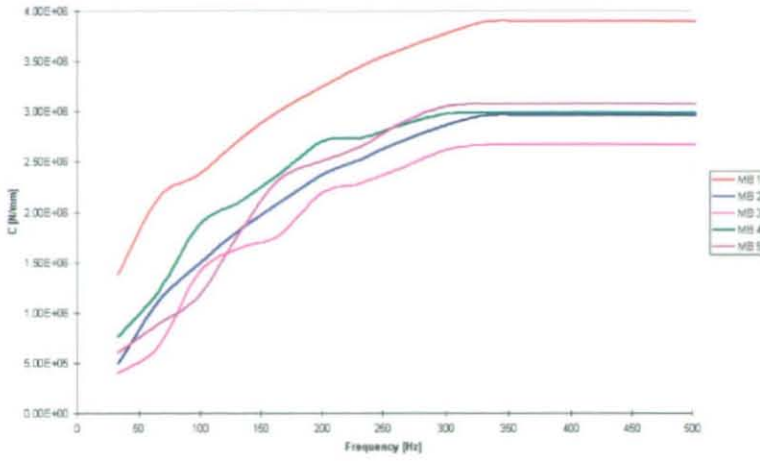
a) 1000 rpm



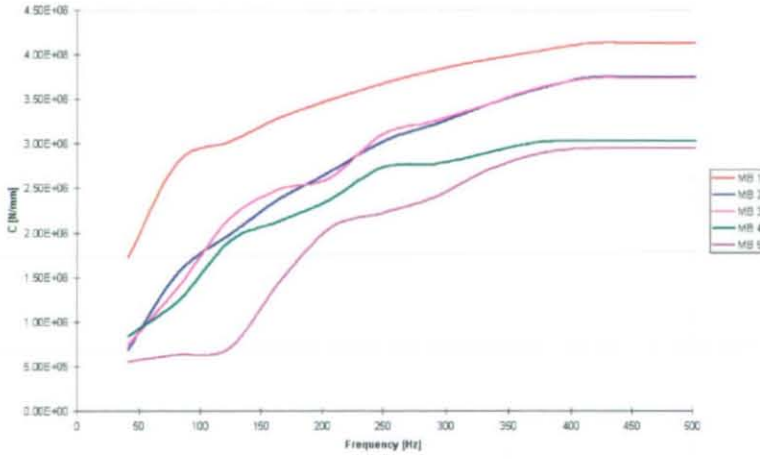
b) 2000 rpm



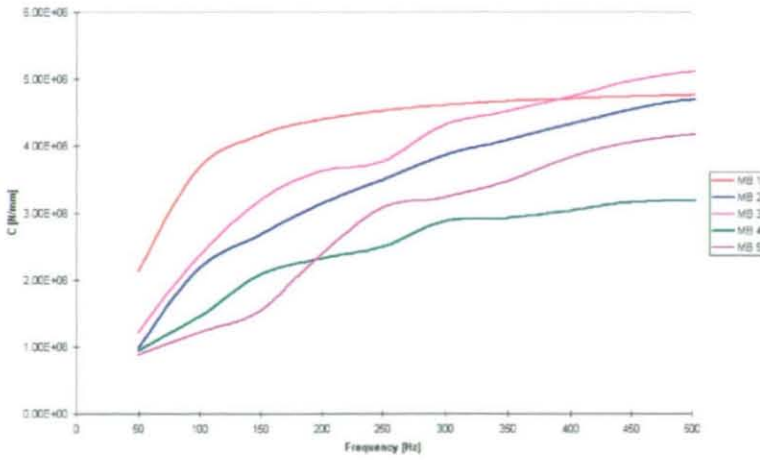
c) 3000 rpm



d) 4000 rpm

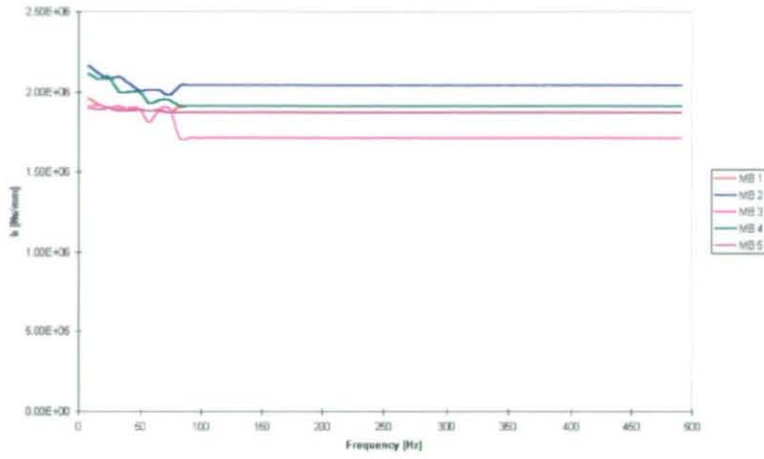


e) 5000 rpm

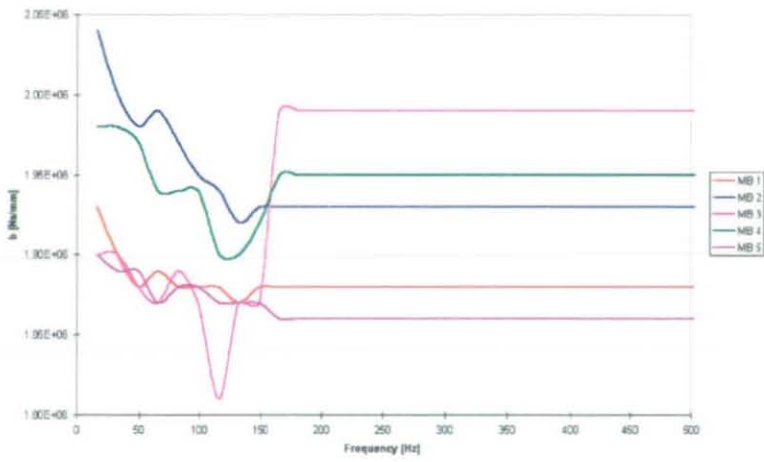


f) 6000 rpm

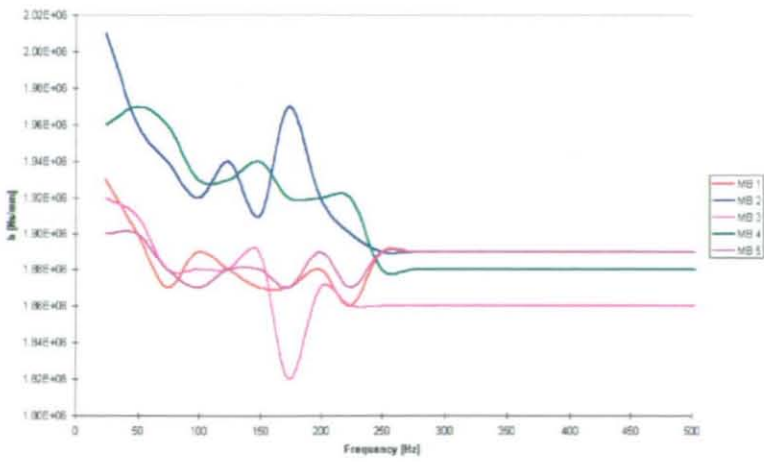
Figure App.4.6 (a-f) Stiffness Properties [2nd Principal Direction; 2/3 Load]



a) 1000 rpm

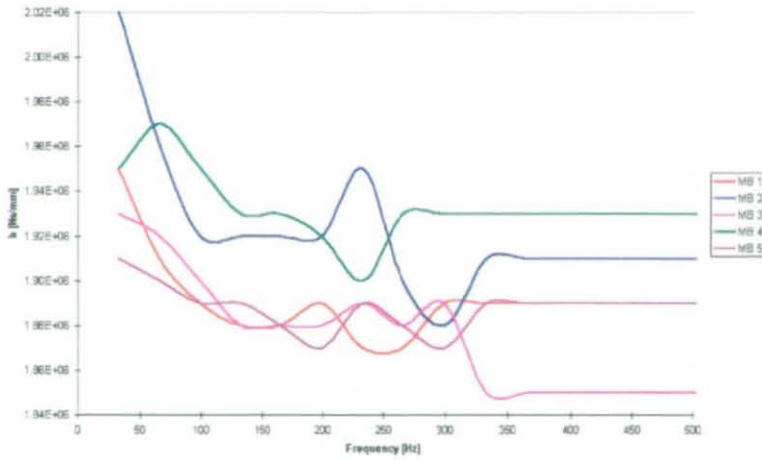


b) 2000 rpm

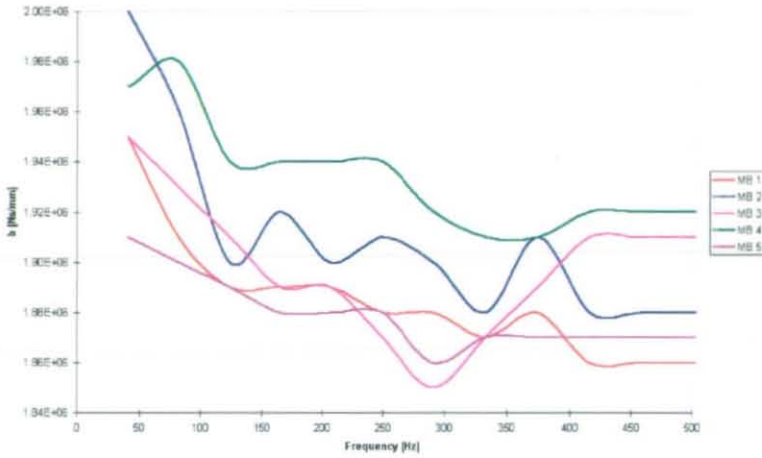


c) 3000 rpm

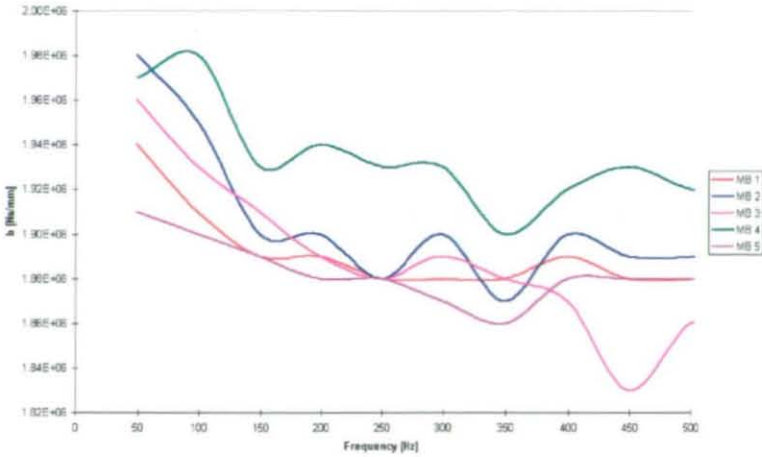




d) 4000 rpm

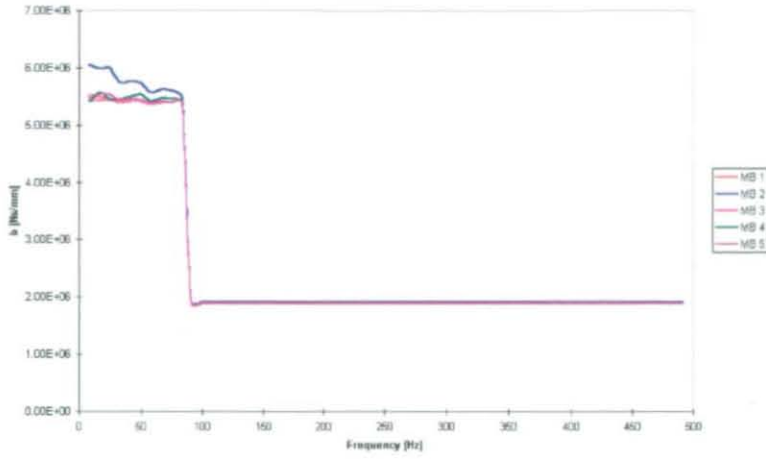


e) 5000 rpm

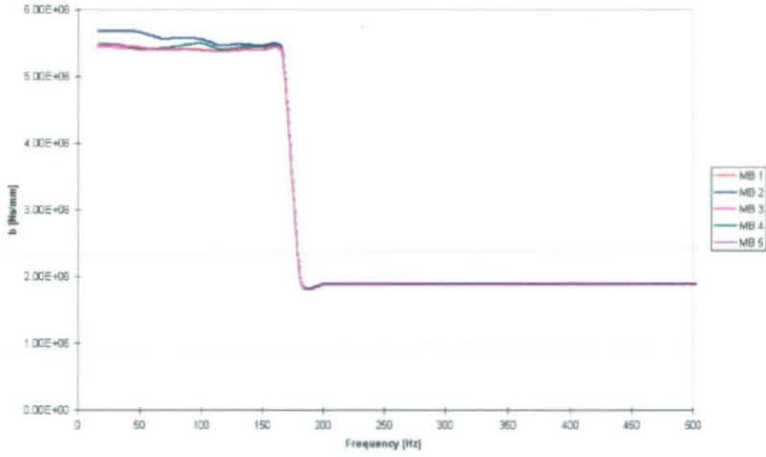


f) 6000 rpm

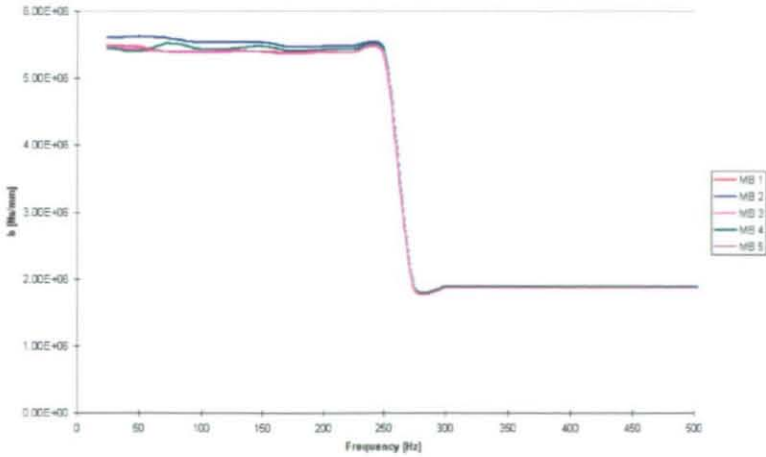
Figure App.4.7 (a-f) Damping Properties [1st Principal Direction; Full Load]



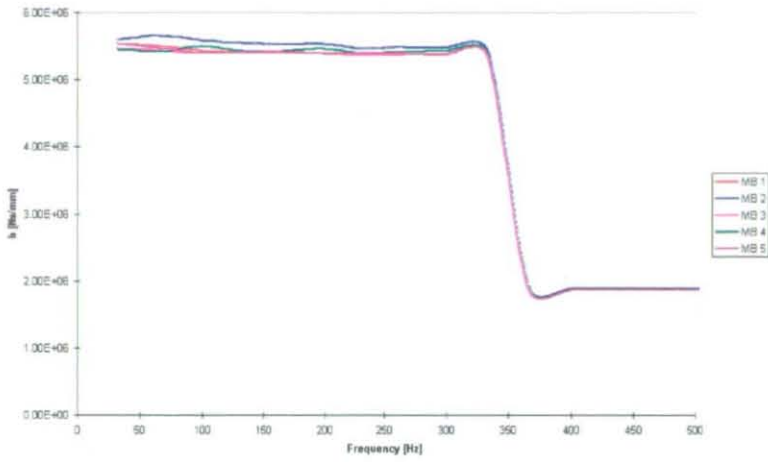
a) 1000 rpm



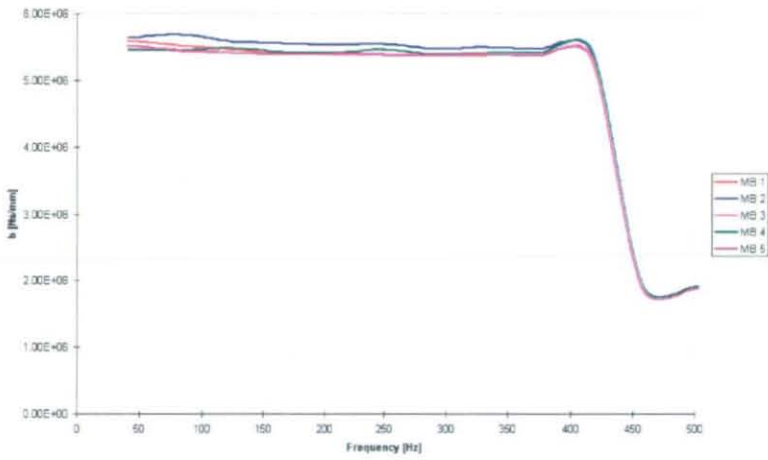
b) 2000 rpm



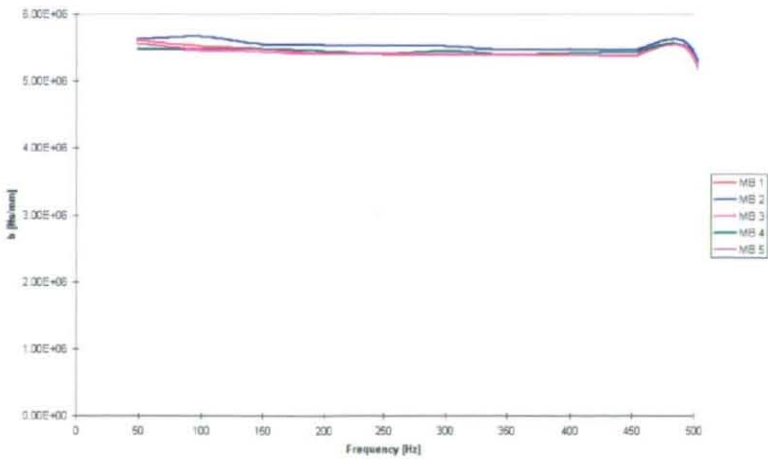
c) 3000 rpm



d) 4000 rpm

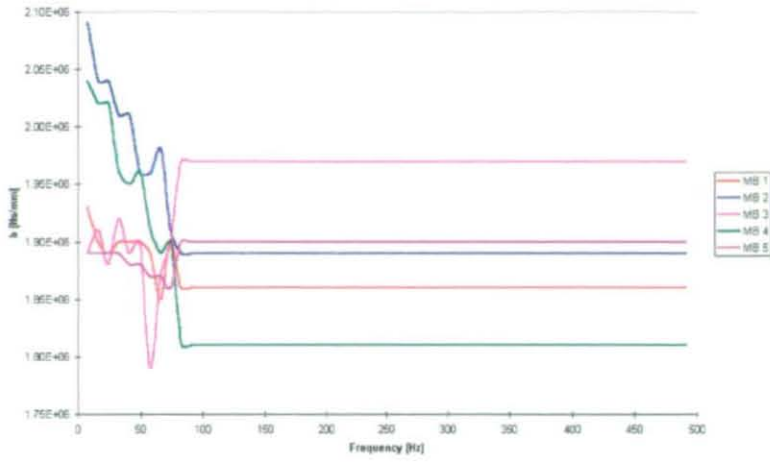


e) 5000 rpm

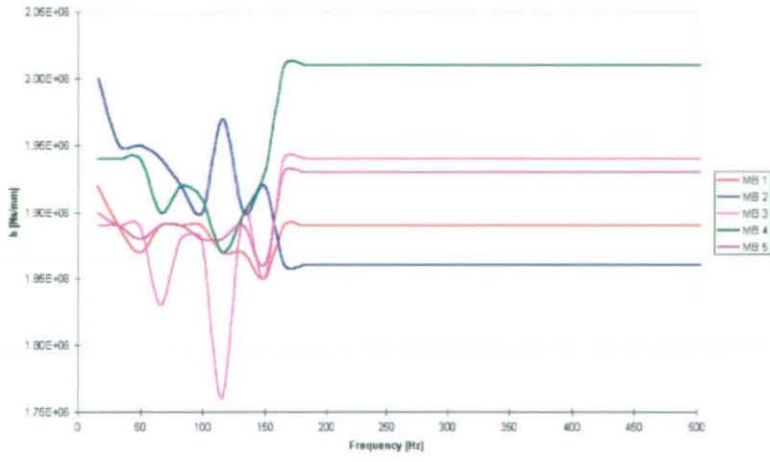


f) 6000 rpm

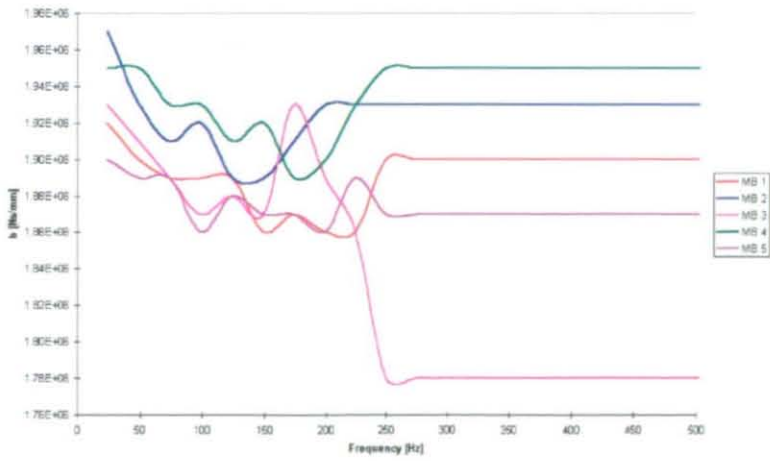
Figure App.4.8 (a-f) Damping Properties [2nd Principal Direction; Full Load]



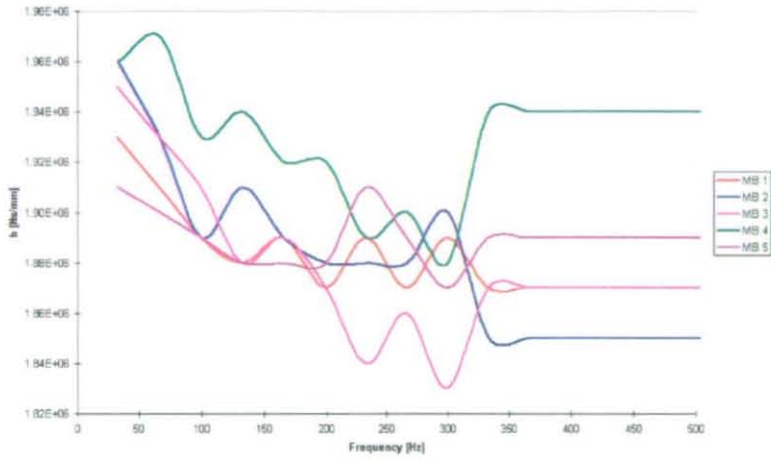
a) 1000 rpm



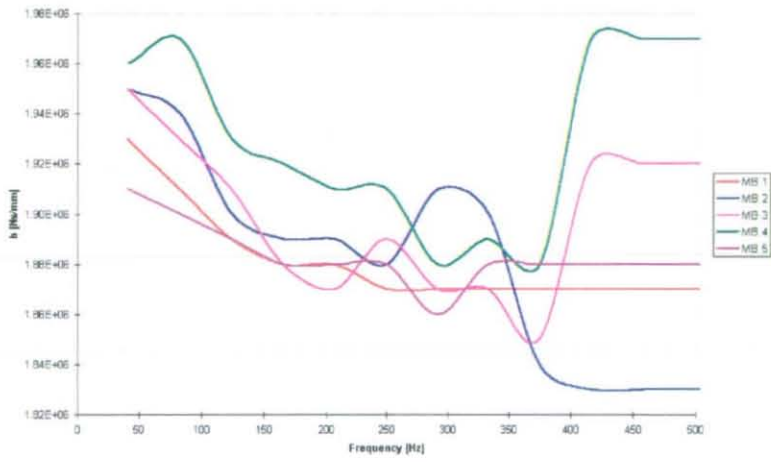
b) 2000 rpm



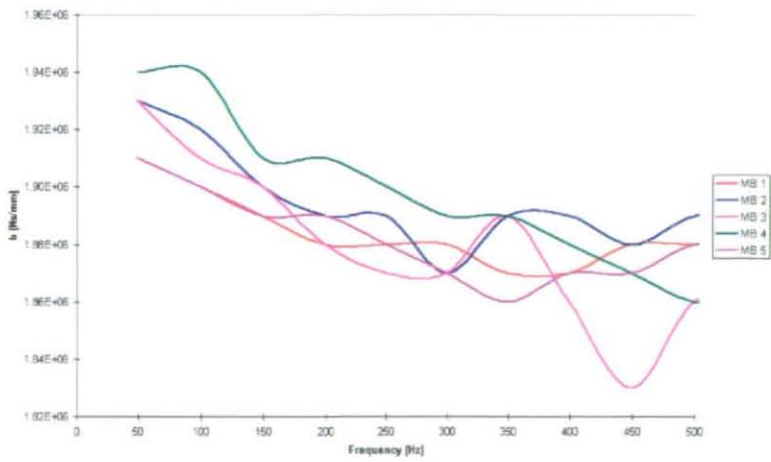
c) 3000 rpm



d) 4000 rpm

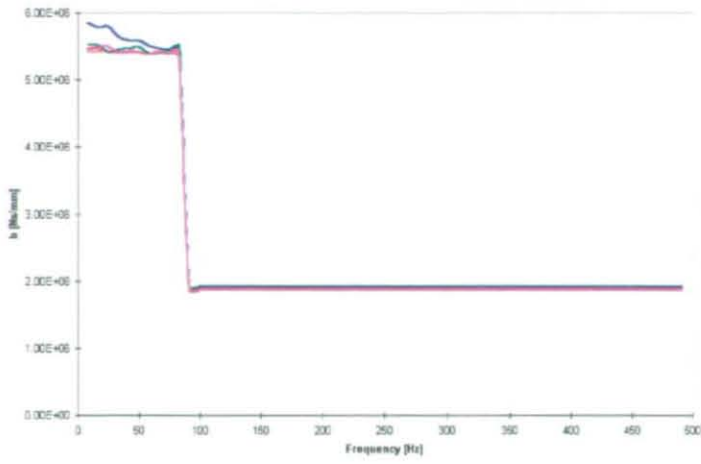


e) 5000 rpm

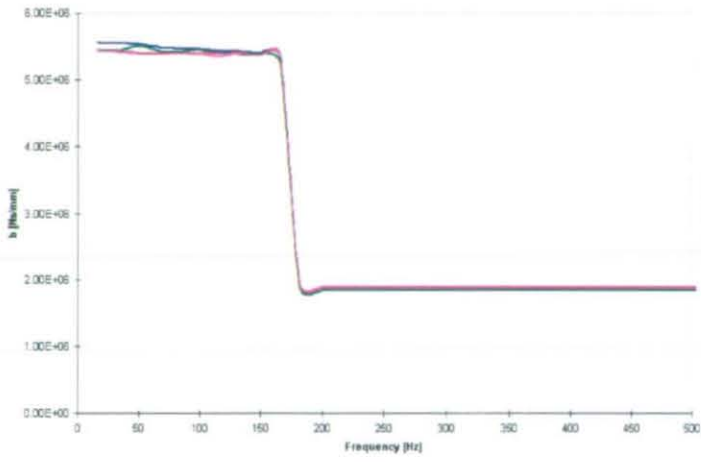


f) 6000 rpm

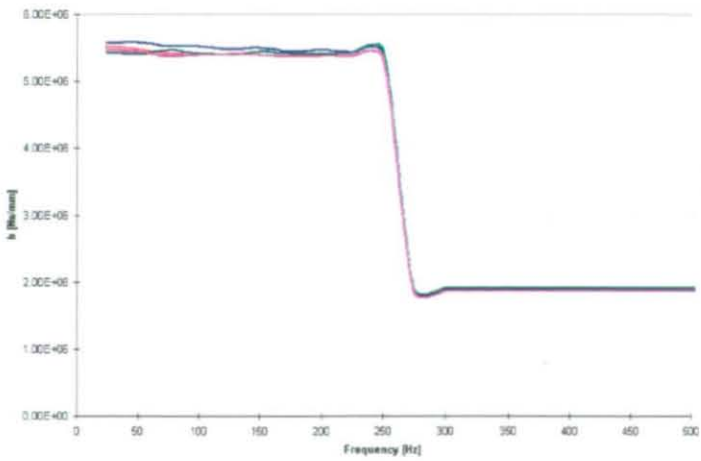
Figure App.4.9 (a-f) Damping Properties [1st Principal Direction; 1/3 Load]



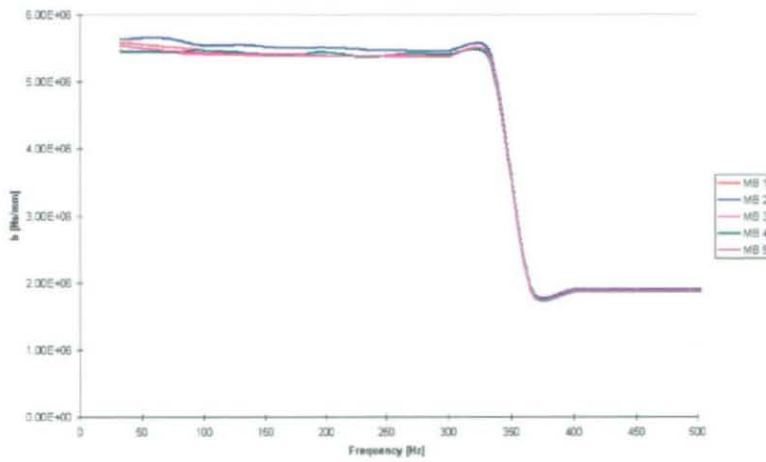
a) 1000 rpm



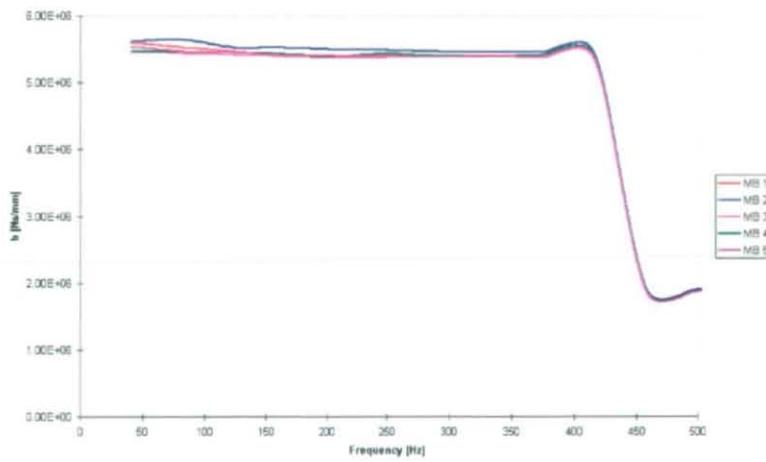
b) 2000 rpm



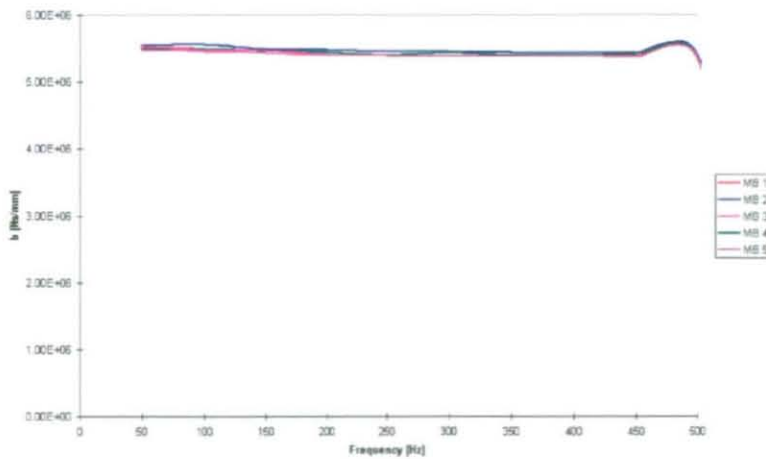
c) 3000 rpm



d) 4000 rpm



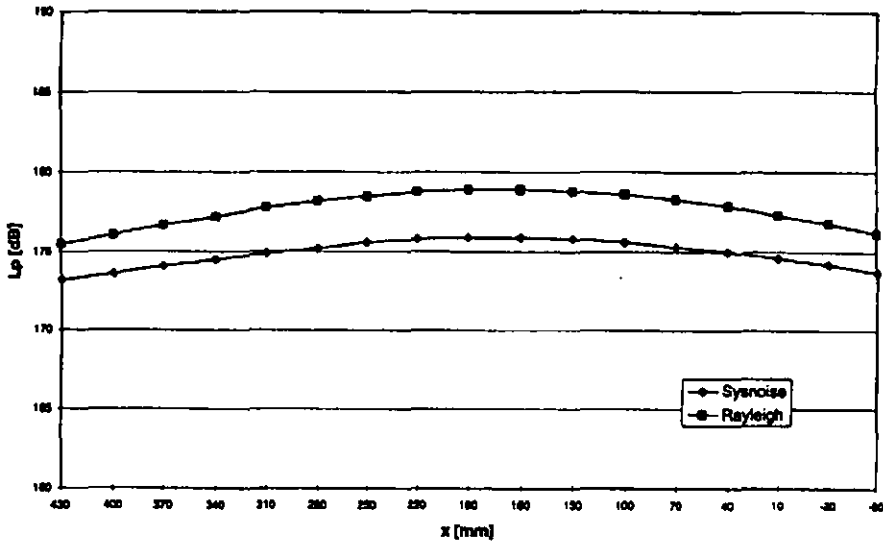
e) 5000 rpm



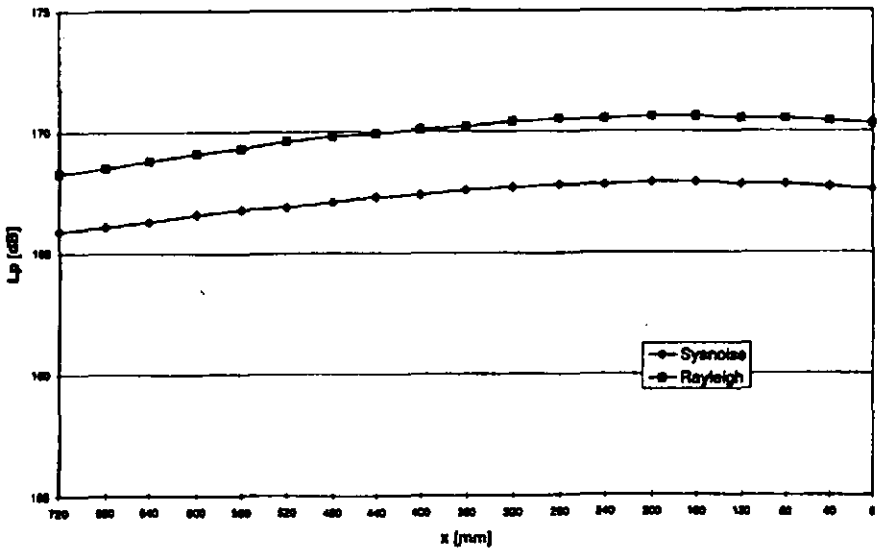
f) 6000 rpm

Figure App.4.10 (a-f) Damping Properties [2nd Principal Direction; 1/3 Load]

### Spatial Sound Pressure Distribution of Catalytic Converter



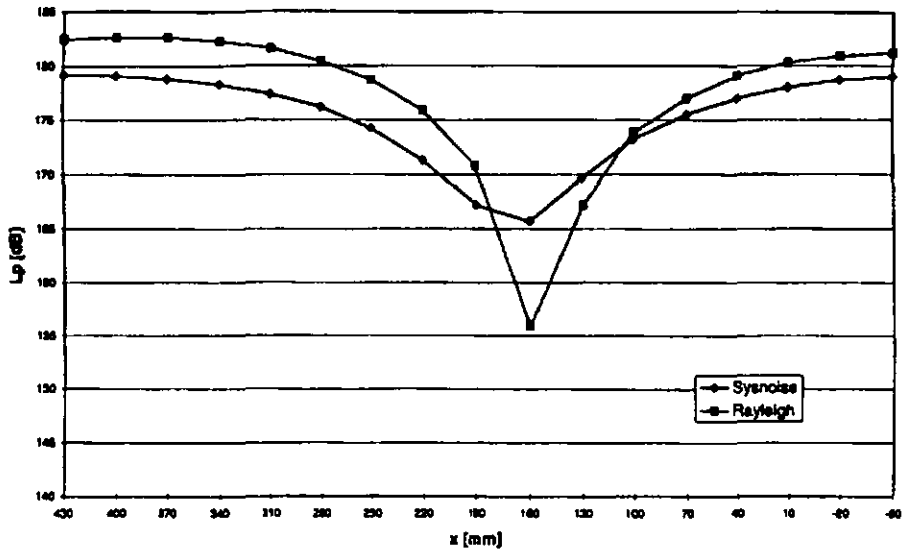
a) Location 'A'



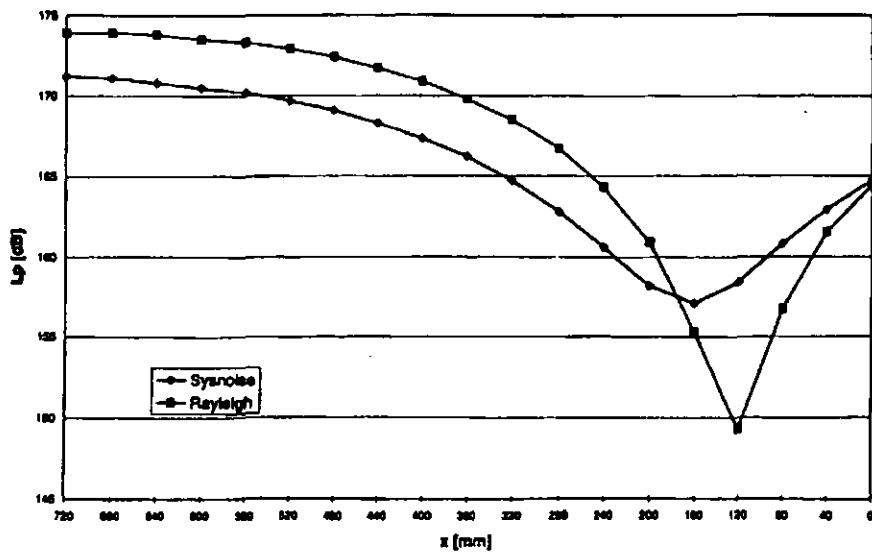
b) Location 'B'

Figure App.4.11 (a-b) Spatial Sound Pressure (Mode 1; Location 'A'+ 'B')



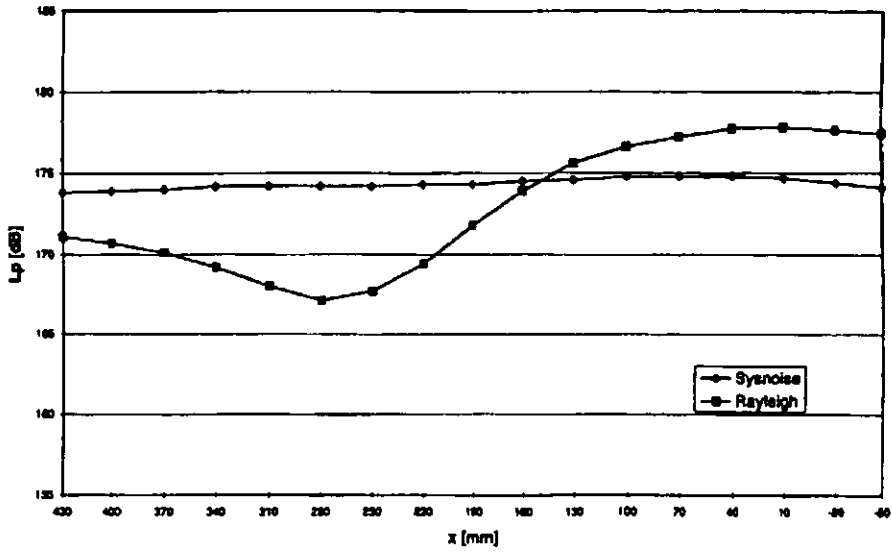


a) Location 'A'

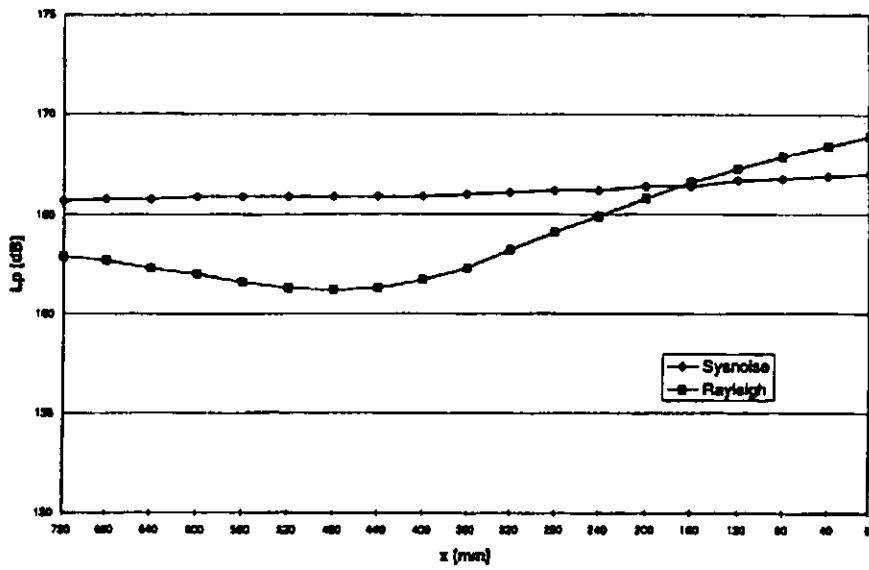


b) Location 'B'

Figure App.4.12 (a-b) Spatial Sound Pressure (Mode 2; Location 'A'+ 'B')

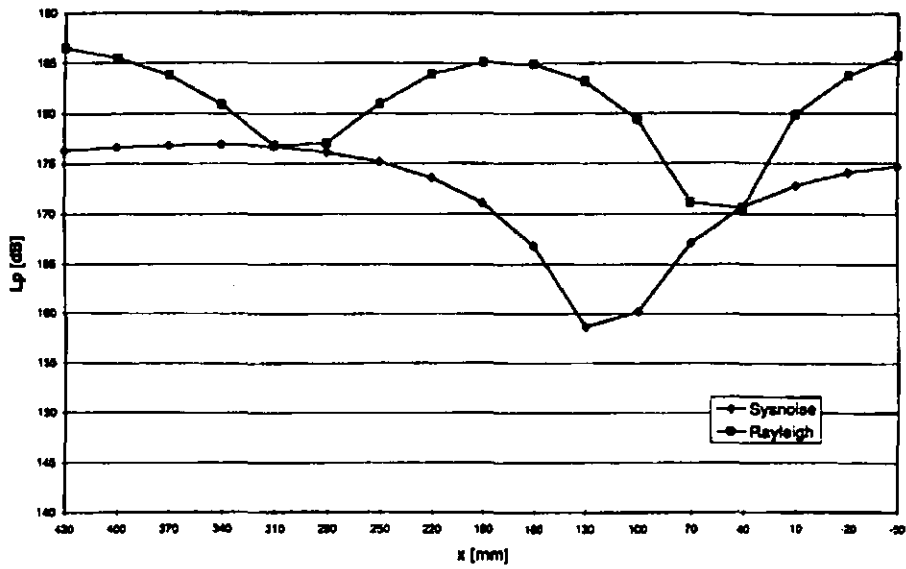


a) Location 'A'

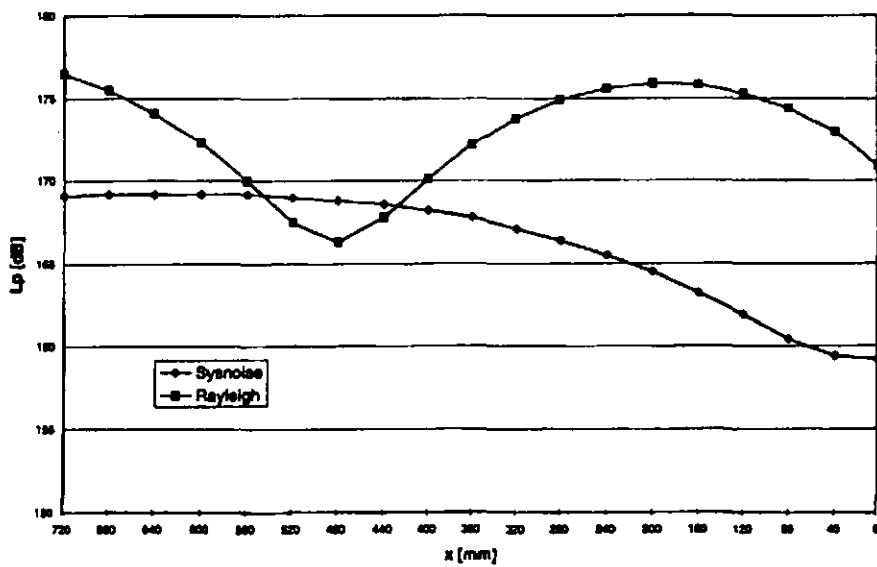


b) Location 'B'

Figure App.4.13 (a-b) Spatial Sound Pressure (Mode 3; Location 'A'+ 'B')

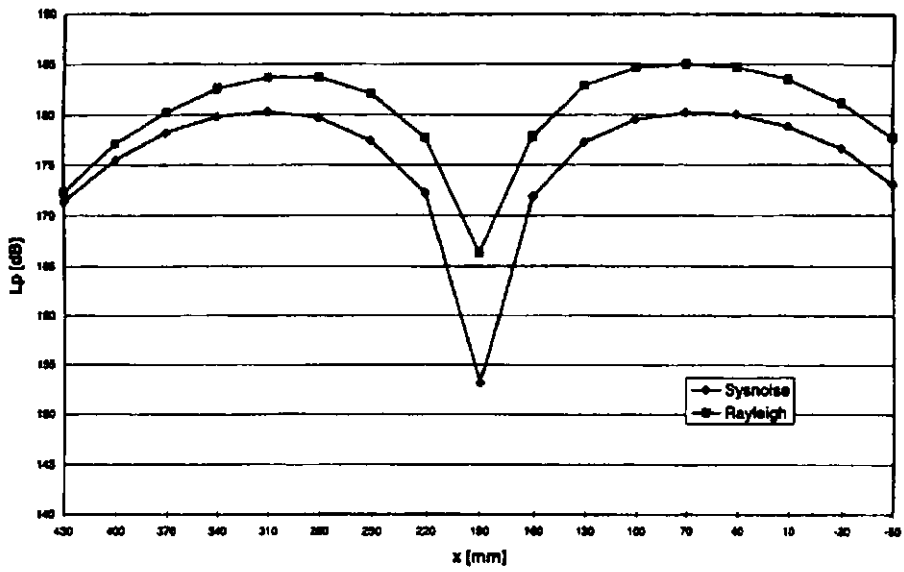


a) Location 'A'

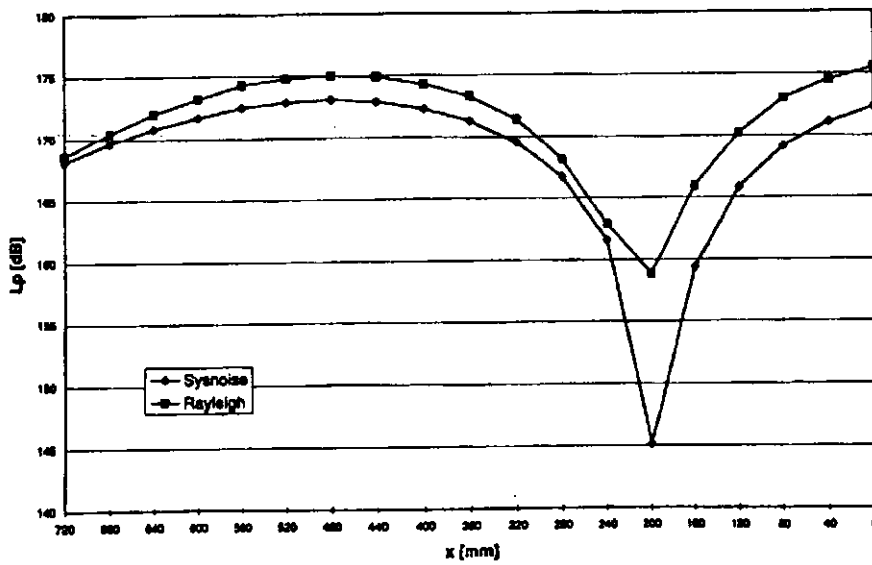


b) Location 'B'

Figure App.4.14 (a-b) Spatial Sound Pressure (Mode 4; Location 'A'+'B')

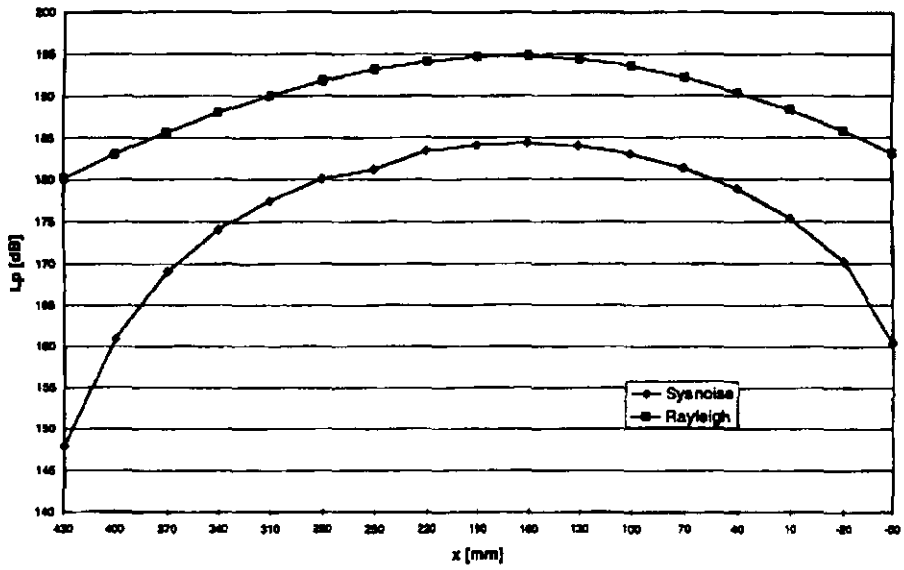


a) Location 'A'

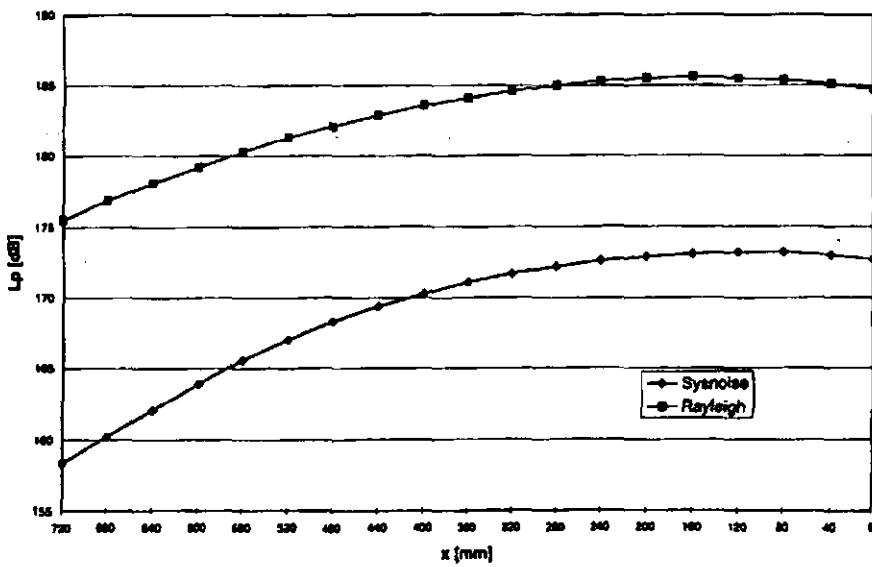


b) Location 'B'

Figure App.4.15 (a-b) Spatial Sound Pressure (Mode 7; Location 'A'+ 'B')



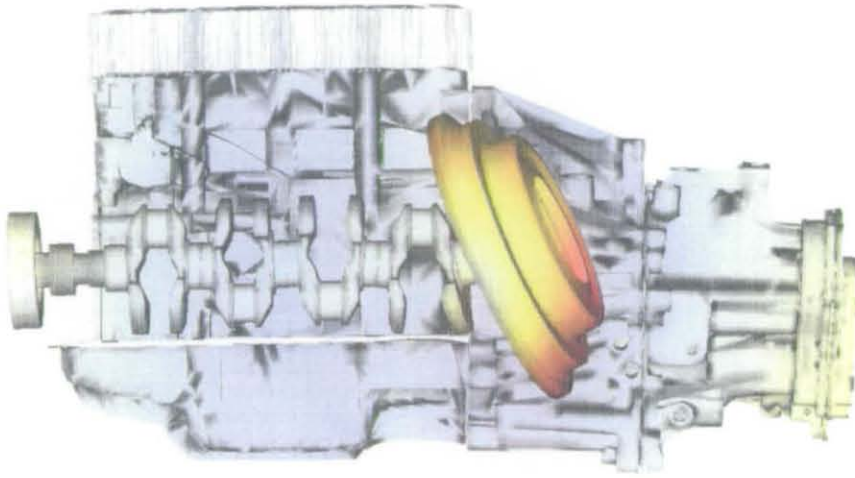
a) Location 'A'



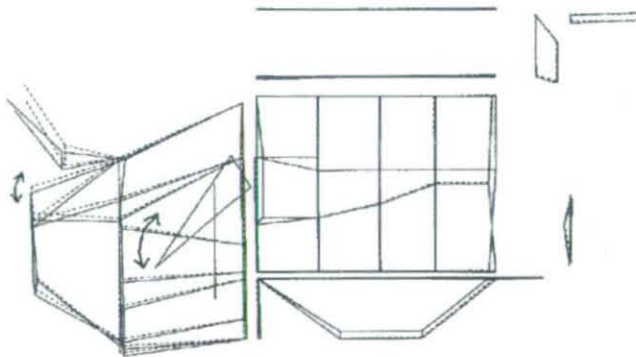
b) Location 'B'

Figure App.4.16 (a-b) Spatial Sound Pressure (Mode 8; Location 'A'+ 'B')

### Powertrain Modal Analysis

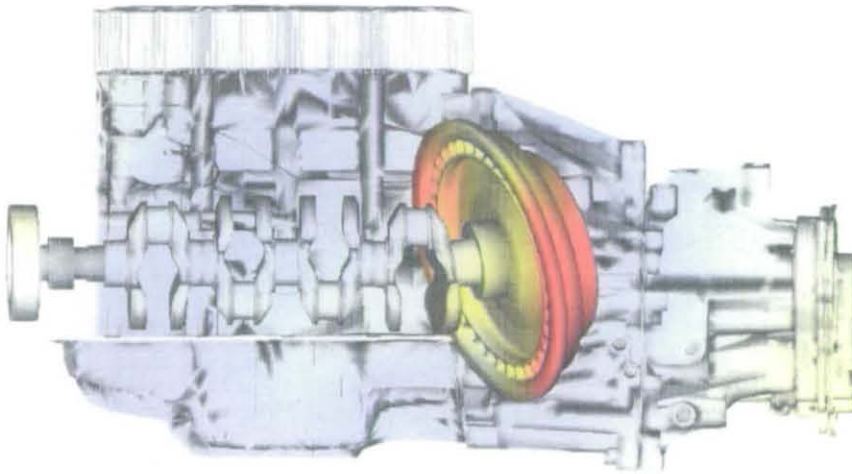


a) Analysis

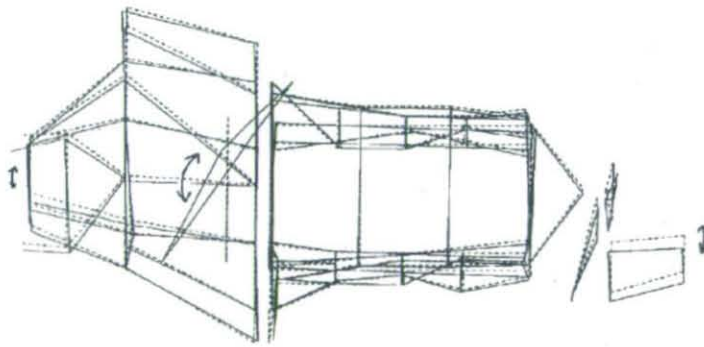


b) Measurement

Figure App.4.17 (a-b) Powertrain Modal Analysis (1<sup>st</sup> Flywheel vertical)

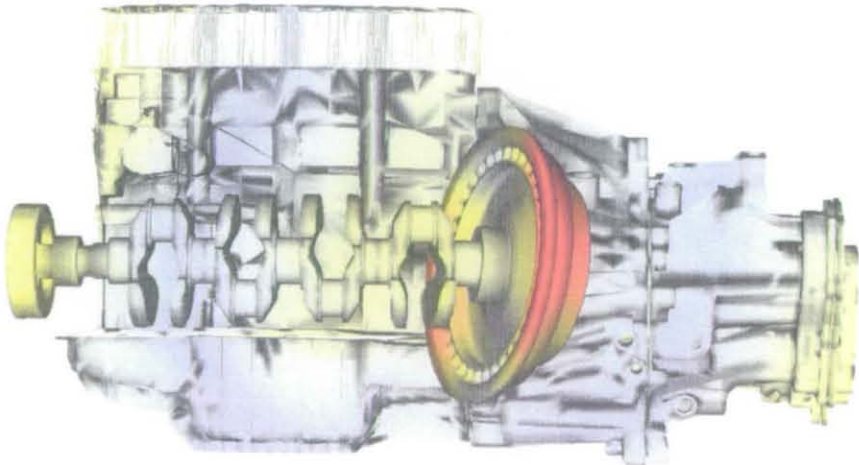


a) Analysis

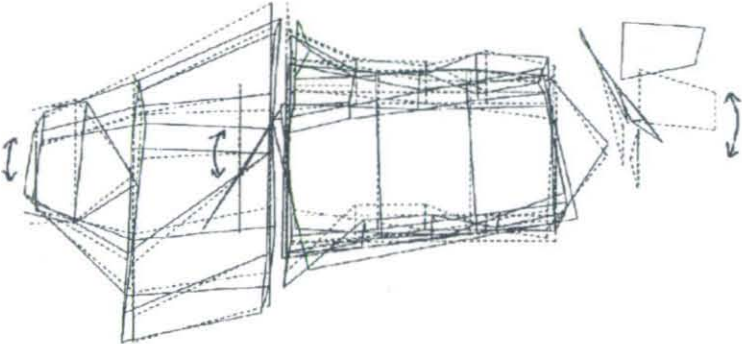


b) Measurement

Figure App.4.18 (a-b) Powertrain Modal Analysis (1<sup>st</sup> Flywheel lateral)



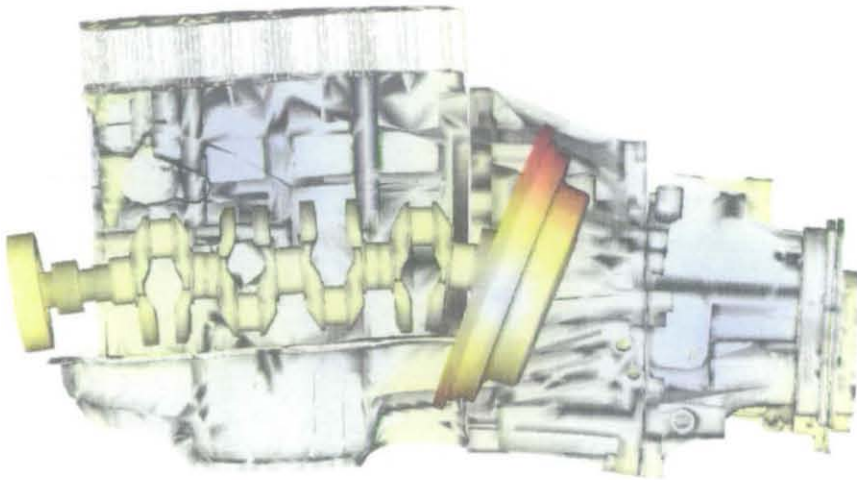
a) Analysis



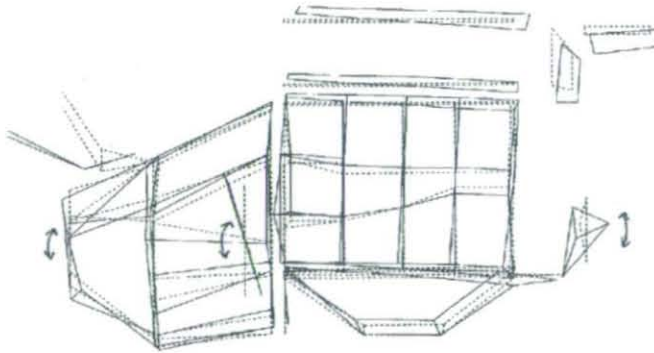
b) Measurement

Figure App.4.19 (a-b) Powertrain Modal Analysis (1<sup>st</sup> Powertrain lateral)



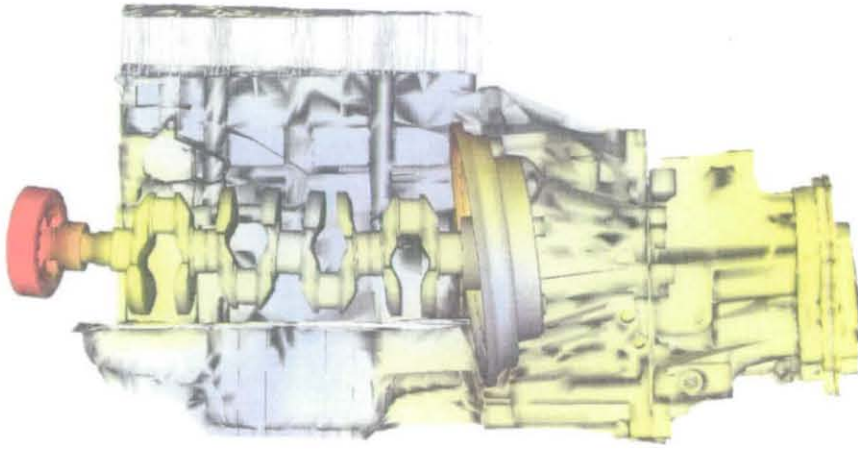


a) Analysis

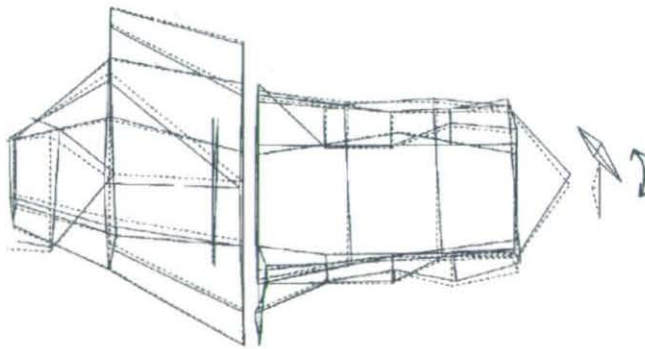


b) Measurement

Figure App.4.20 (a-b) Powertrain Modal Analysis (1<sup>st</sup> Powertrain vertical)



a) Analysis



b) Measurement

Figure App.4.21 (a-b) Powertrain Modal Analysis (2<sup>nd</sup> Powertrain lateral)

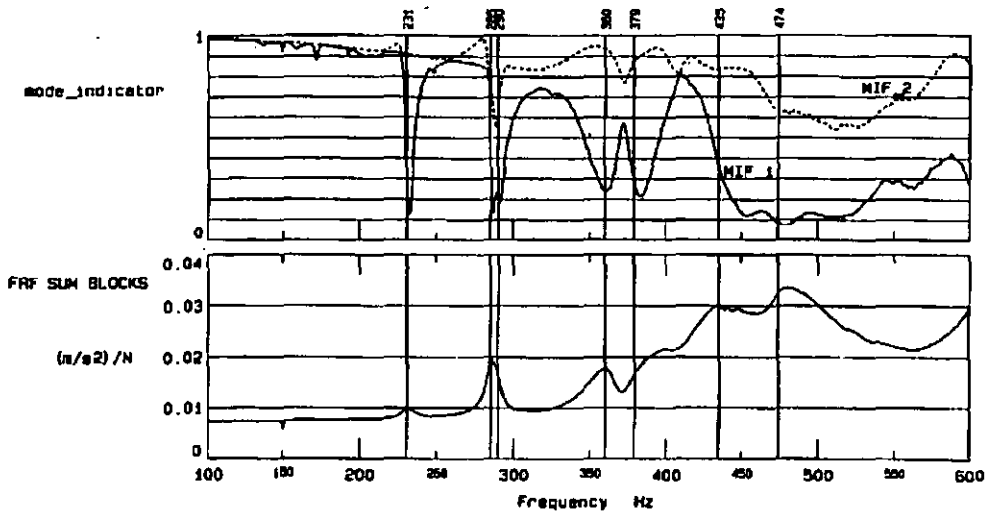


Figure App.4.22 Powertrain Modal Analysis (Mode Indicator Function)

### Flywheel Whirl Colour-Maps

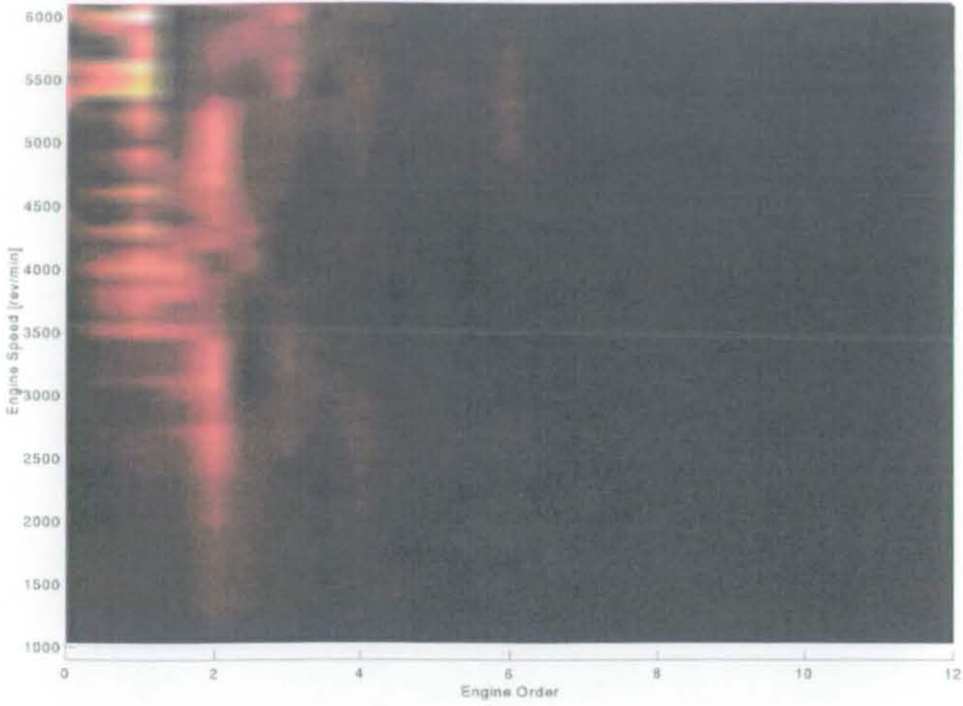


Figure App.4.23 Flywheel Axial Displacement [Full load]

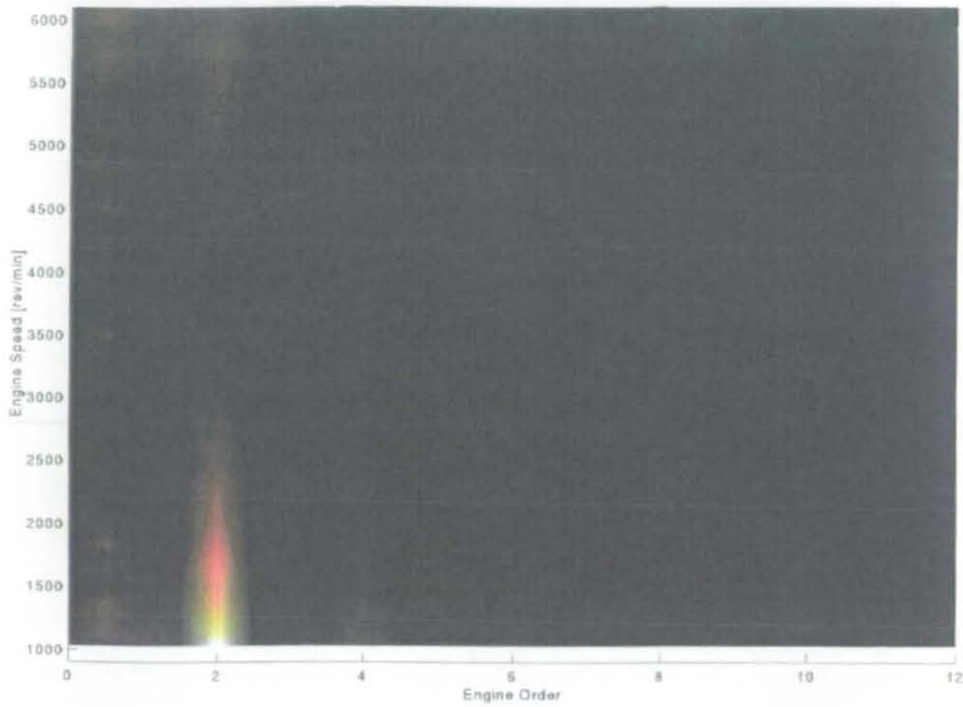


Figure App.4.24 Flywheel Rotational Displacement [Full load]

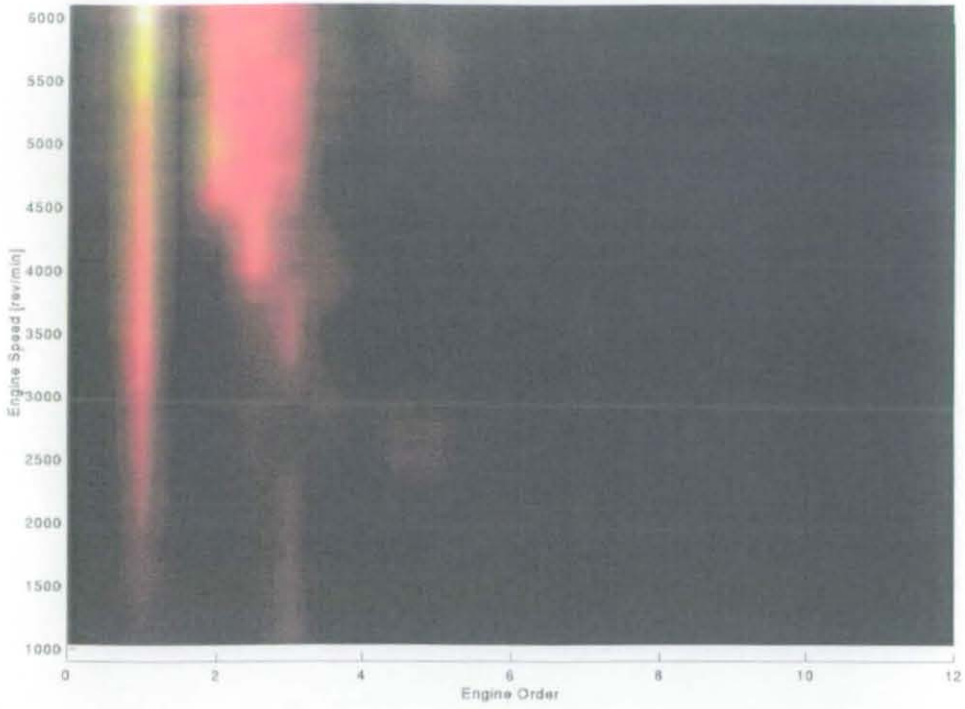


Figure App.4.25 Flywheel Horizontal Displacement [Full load]

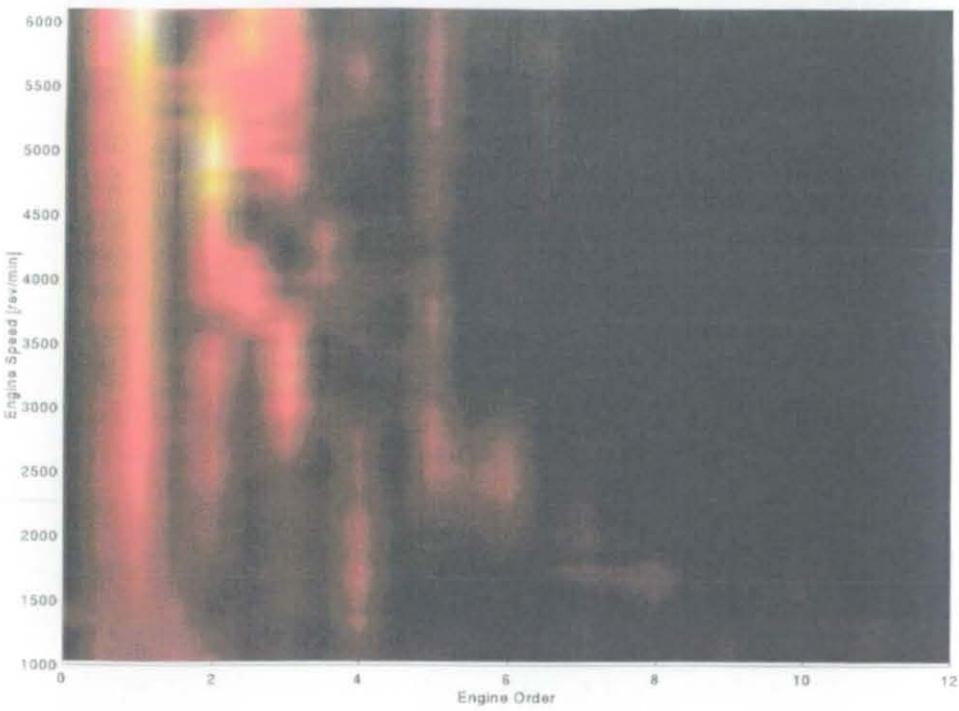


Figure App.4.26 Flywheel Vertical Displacement [Full load]

### Engine Block and Oilpan Surface Velocities

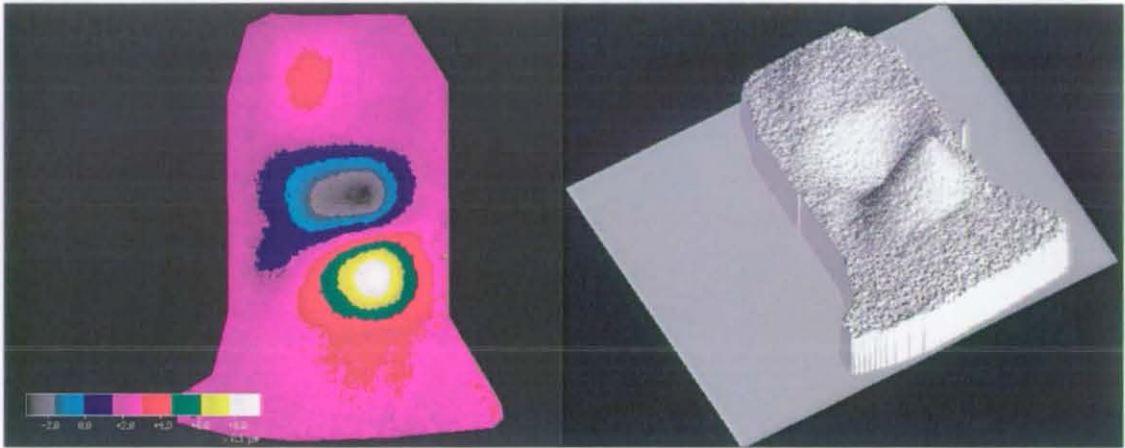


Figure App.4.27 Oilpan Surface Velocity (Test @ 3067 rpm)[mm/s]

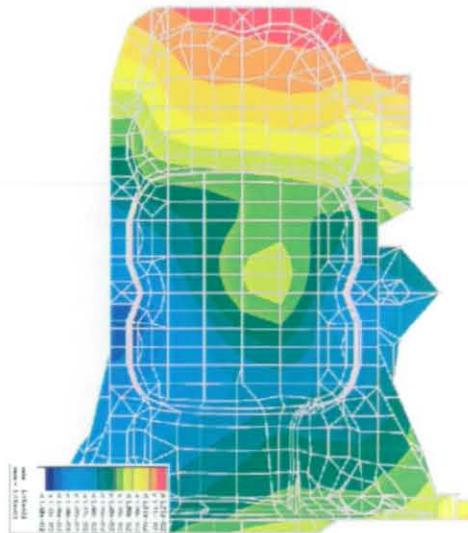


Figure App.4.28 Oilpan Surface Velocity (Analysis @ 3000 rpm)[mm/s]

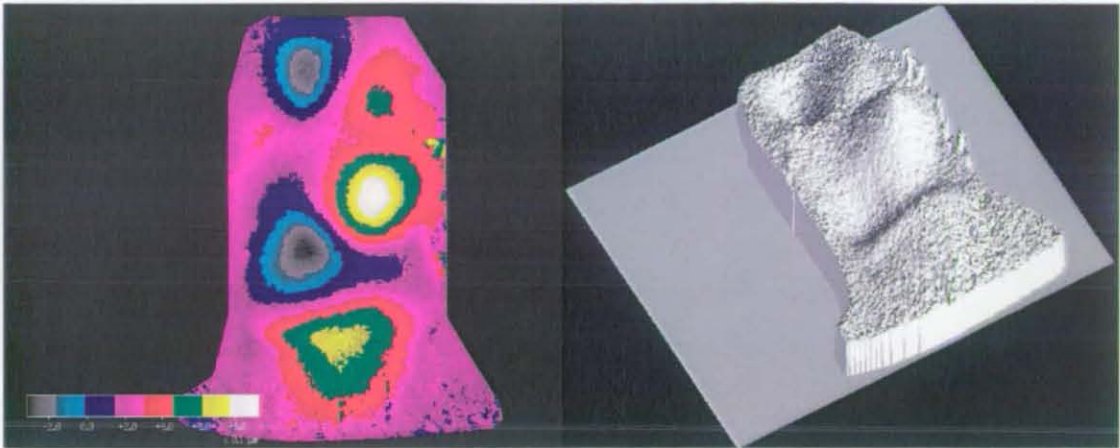


Figure App.4.29 Oilpan Surface Velocity (Test @ 3723 rpm)[mm/s]

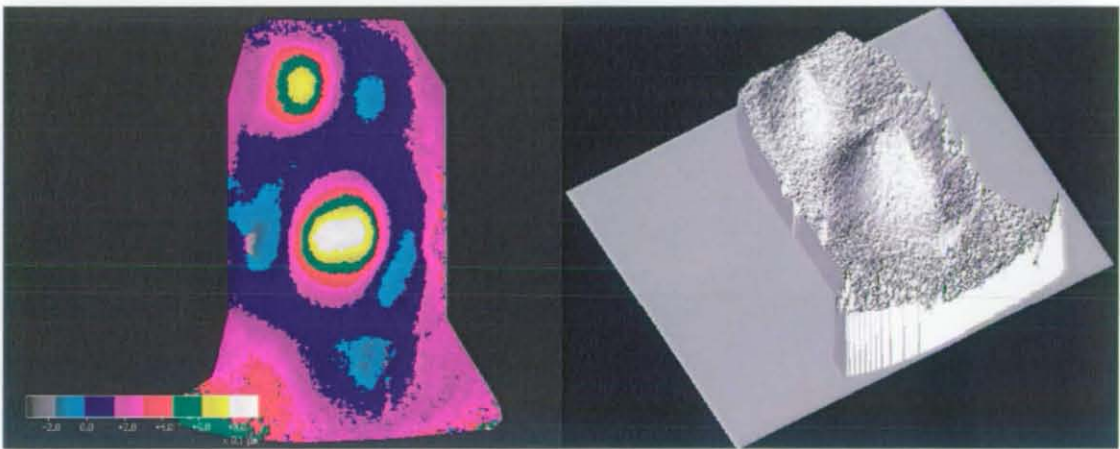


Figure App.4.30 Oilpan Surface Velocity (Test @ 4235 rpm)[mm/s]

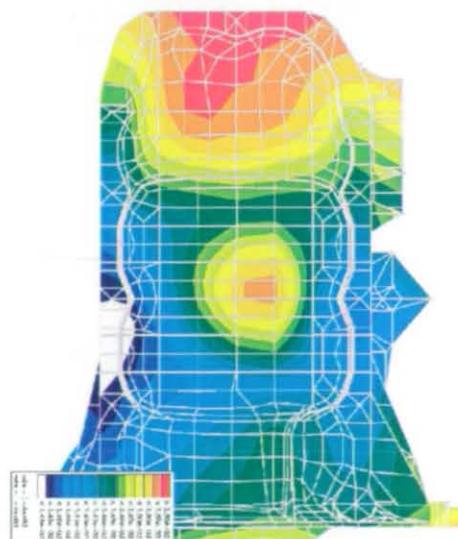


Figure App.4.31 Oilpan Surface Velocity (Analysis @ 4000 rpm)[mm/s]

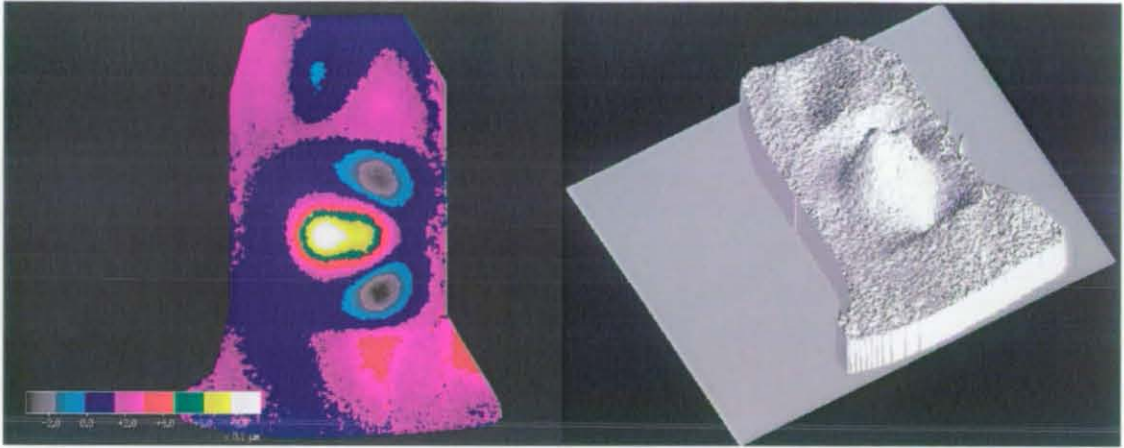


Figure App.4.32 Oilpan Surface Velocity (Test @ 5101 rpm)[mm/s]

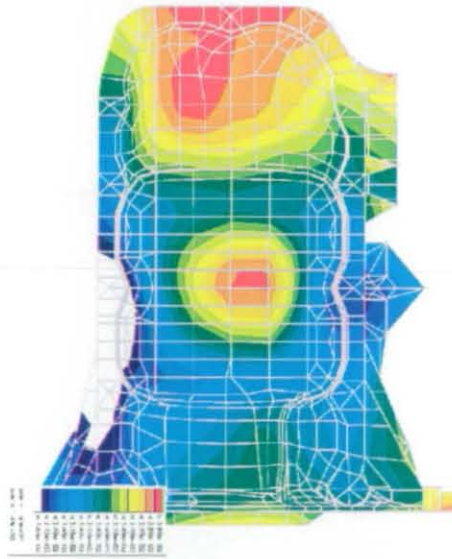


Figure App.4.33 Oilpan Surface Velocity (Analysis @ 5000 rpm)[mm/s]

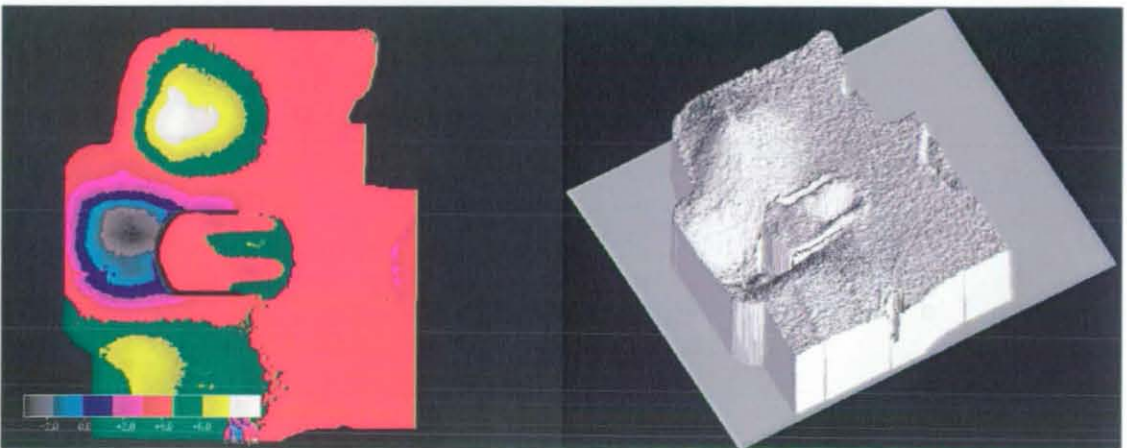


Figure App.4.34 Left Engine Side Surface Velocity (Test @ 2985 rpm)[mm/s]



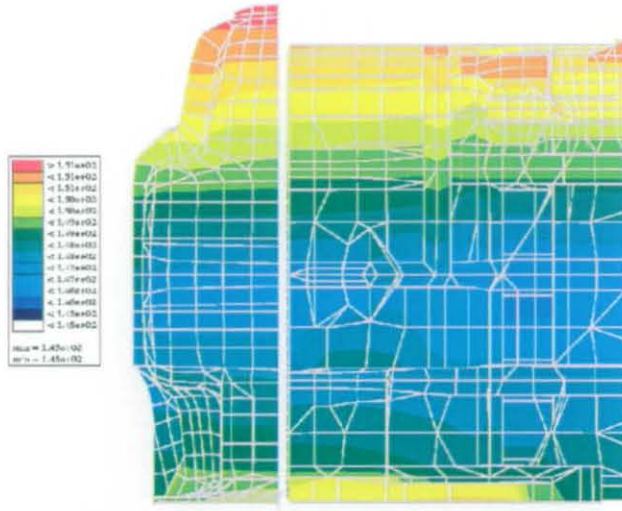


Figure App.4.35 Left Engine Side Surface Velocity (Analysis @ 3000 rpm)[mm/s]



Figure App.4.36 Left Engine Side Surface Velocity (Test @ 3945 rpm)[mm/s]

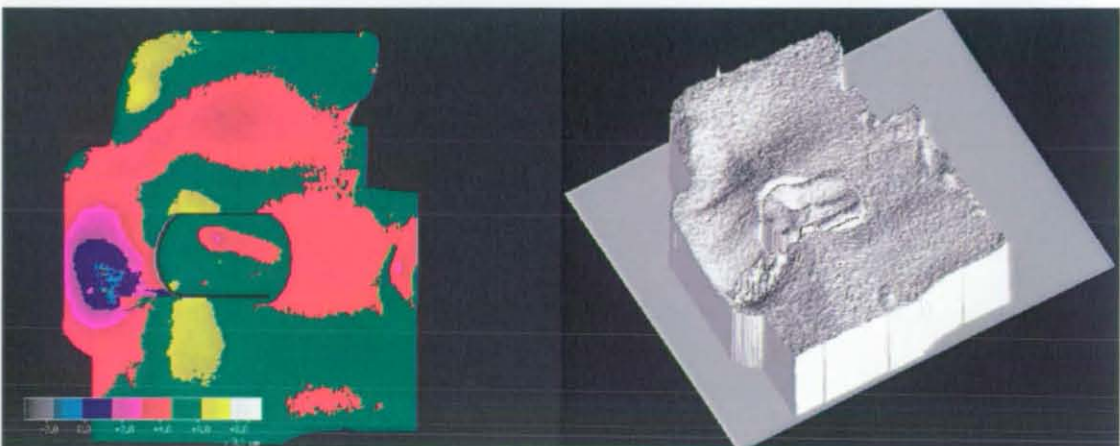


Figure App.4.37 Left Engine Side Surface Velocity (Test @ 4030 rpm)[mm/s]

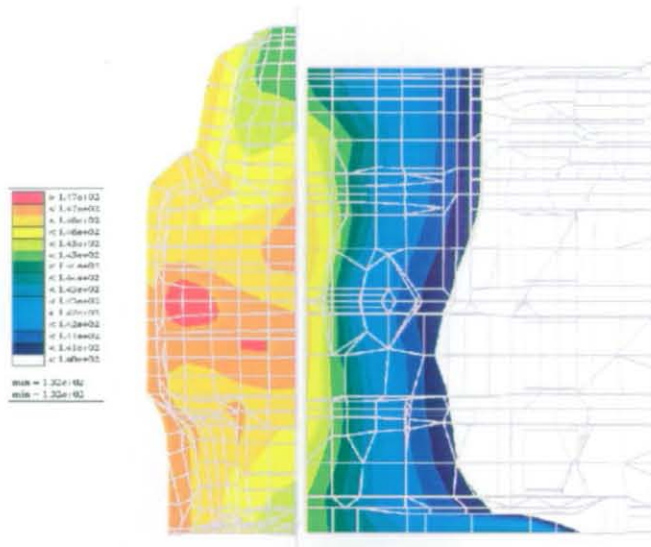


Figure App.4.38 Left Engine Side Surface Velocity (Analysis @ 4000 rpm)[mm/s]

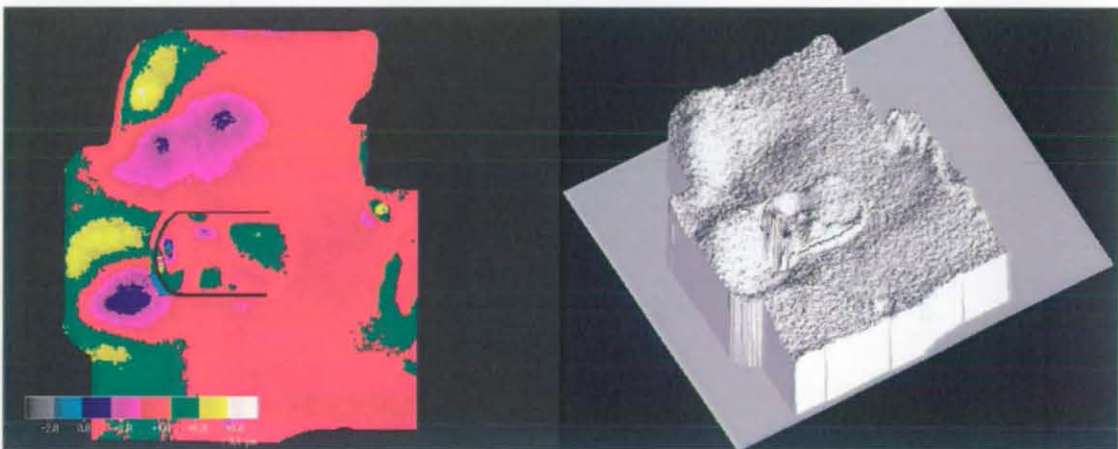


Figure App.4.39 Left Engine Side Surface Velocity (Test @ 4918 rpm)[mm/s]

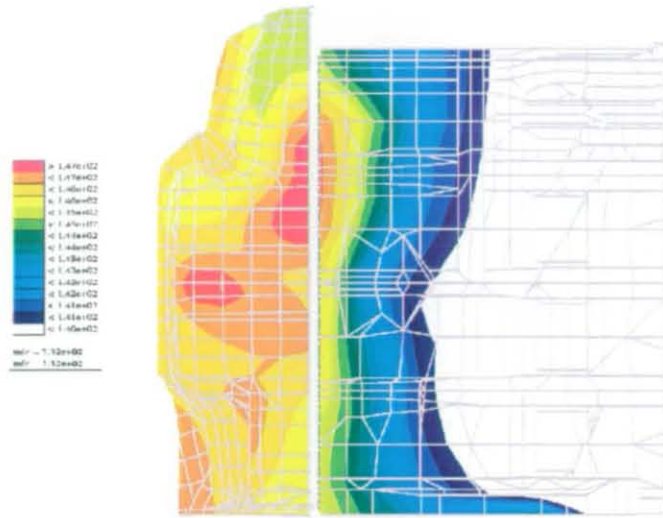


Figure App.4.40 Left Engine Side Surface Velocity (Analysis @ 5000 rpm)[mm/s]

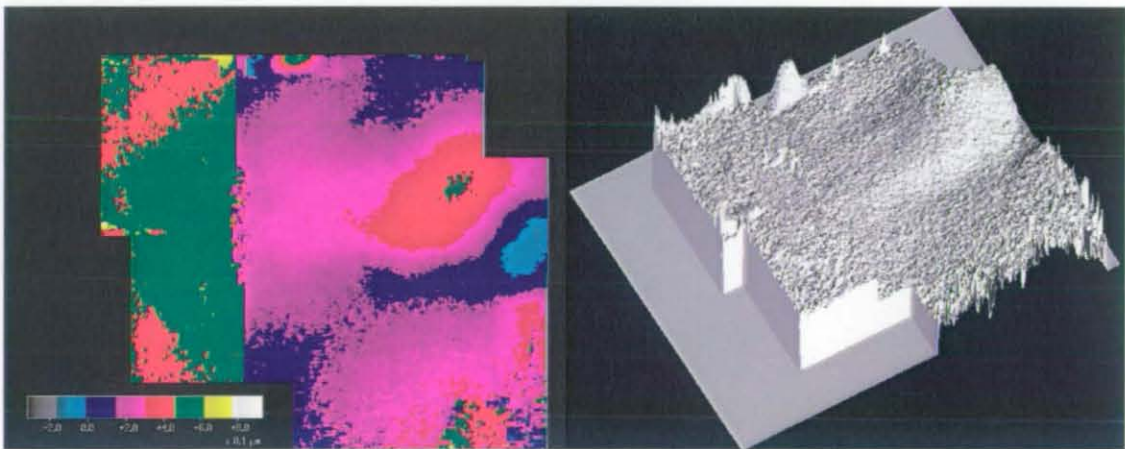


Figure App.4.41 Right Engine Side Surface Velocity (Test @ 3160 rpm)[mm/s]

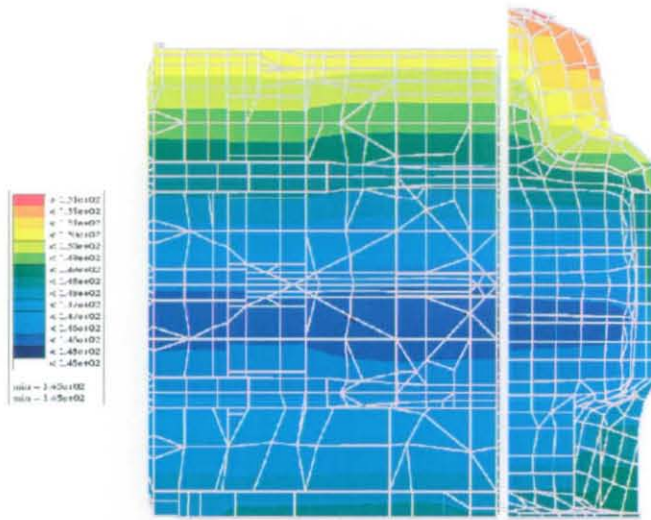


Figure App.4.42 Right Engine Side Surface Velocity (Analysis @ 3000 rpm)[mm/s]

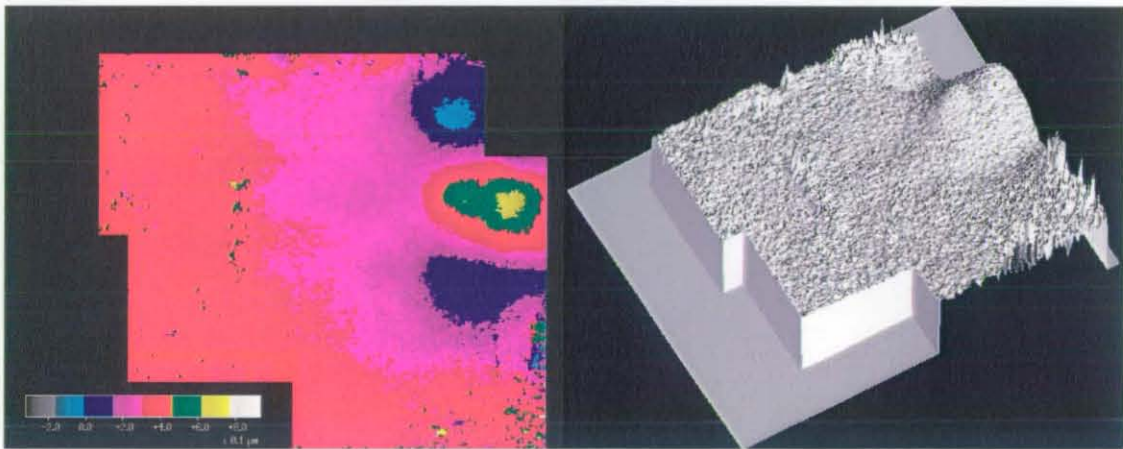


Figure App.4.43 Right Engine Side Surface Velocity (Test @ 3940 rpm)[mm/s]

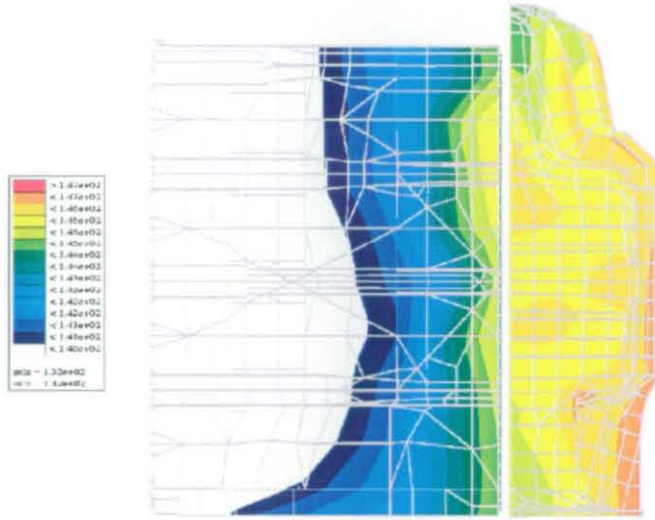


Figure App.4.44 Right Engine Side Surface Velocity (Analysis @ 4000 rpm)[mm/s]

### Noise Radiation Results

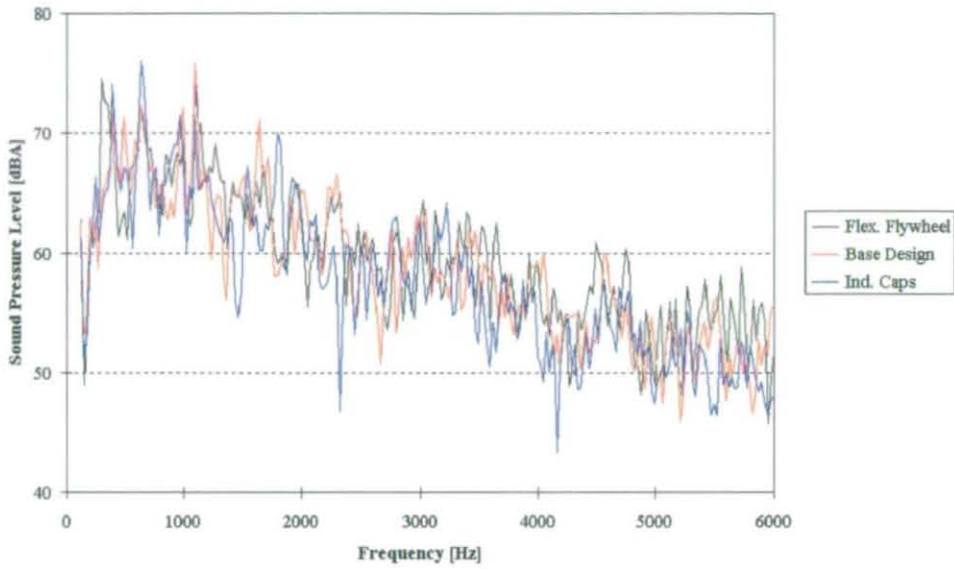


Figure App.4.45 Measured Narrow Band Results [3000 rpm; Bottom Side]

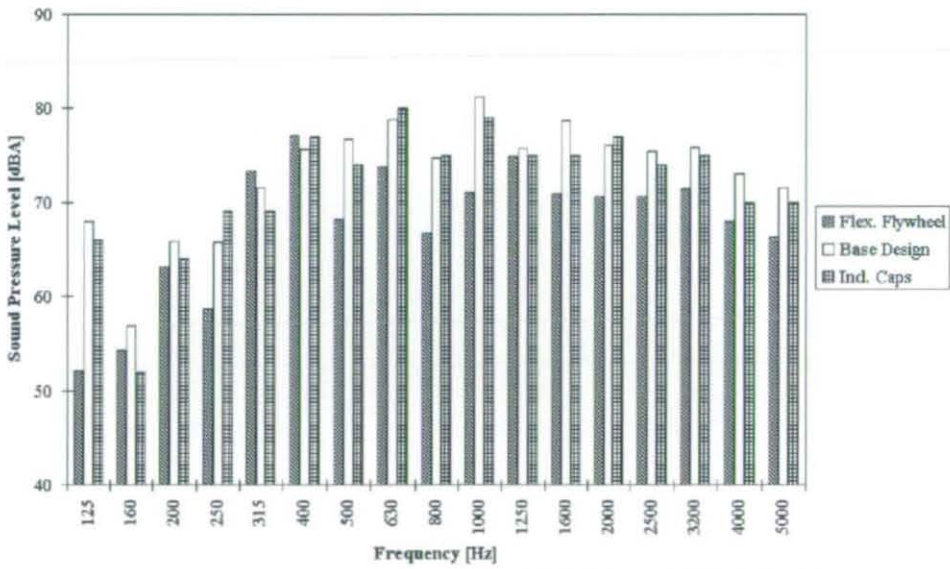


Figure App.4.46 Measured Third-Octave Band Results [3000 rpm; Bottom Side]

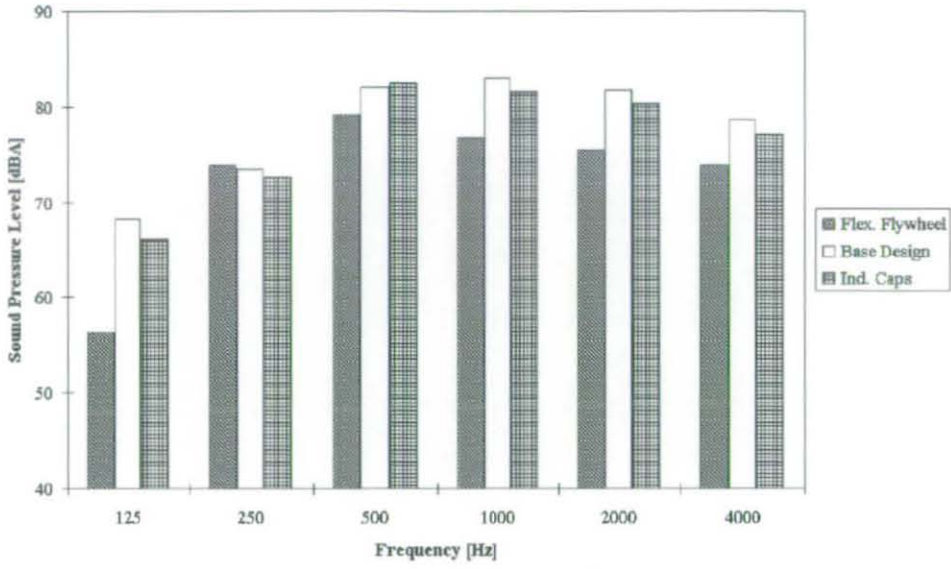


Figure App.4.47 Measured Octave Band Results [3000 rpm; Bottom Side]

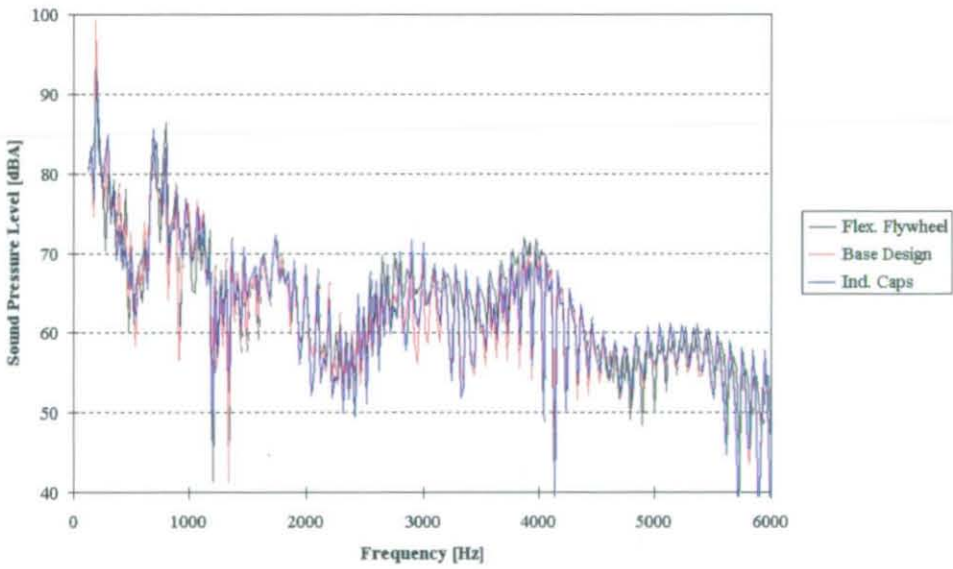


Figure App.4.48 Analysis Narrow Band Results [3000 rpm; Bottom Side]

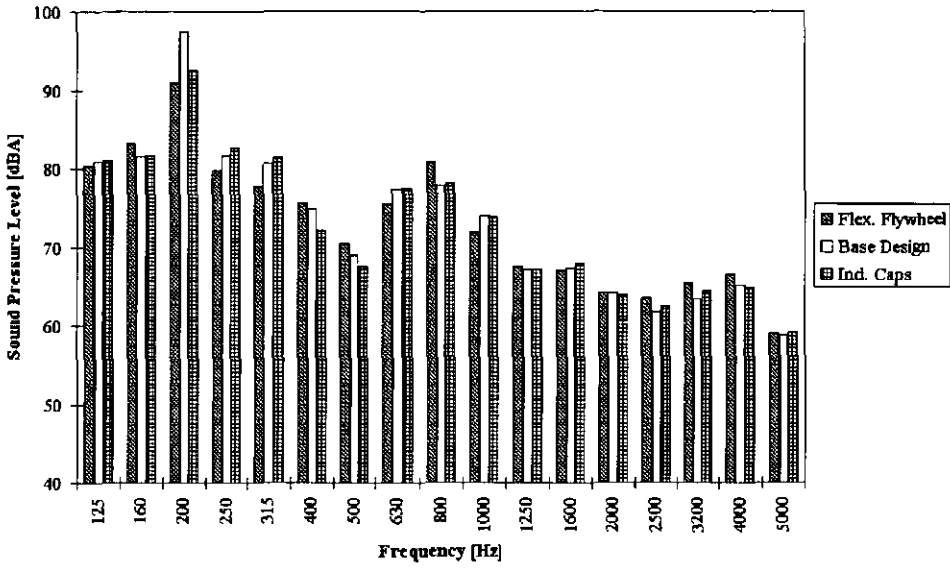


Figure App.4.49 Analysis Third-Octave Band Results [3000 rpm; Bottom Side]

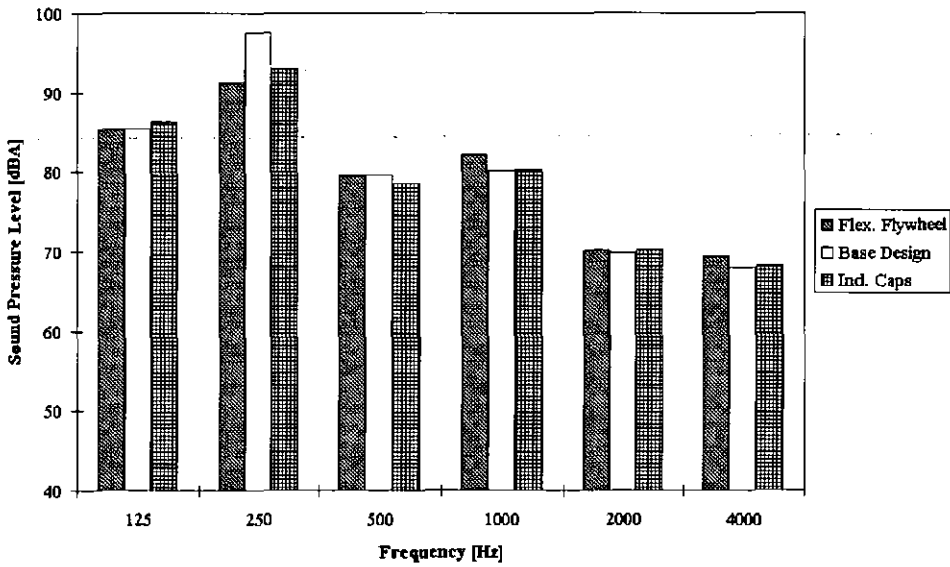


Figure App.4.50 Analysis Octave Band Results [3000 rpm; Bottom Side]



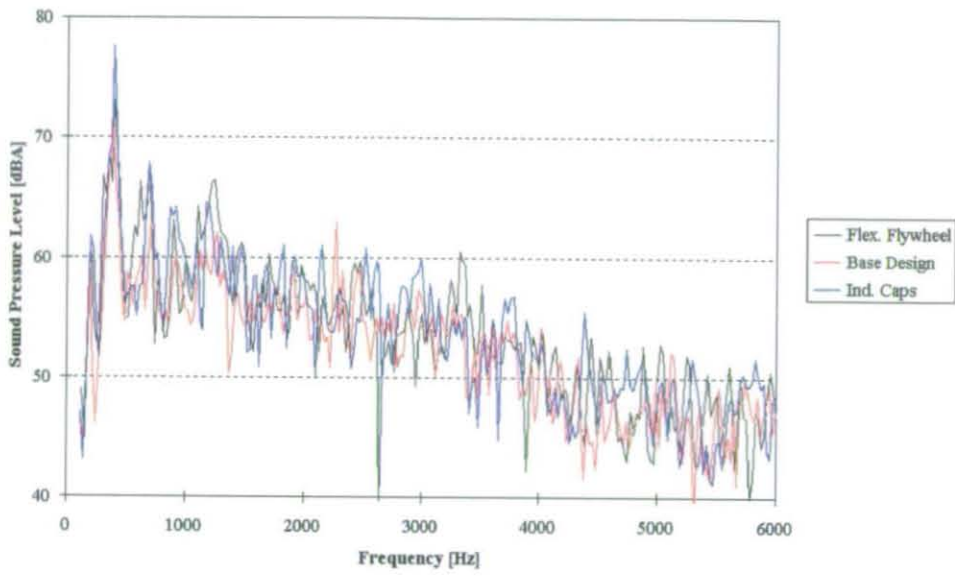


Figure App.4.51 Measured Narrow Band Results [3000 rpm; Left Side]

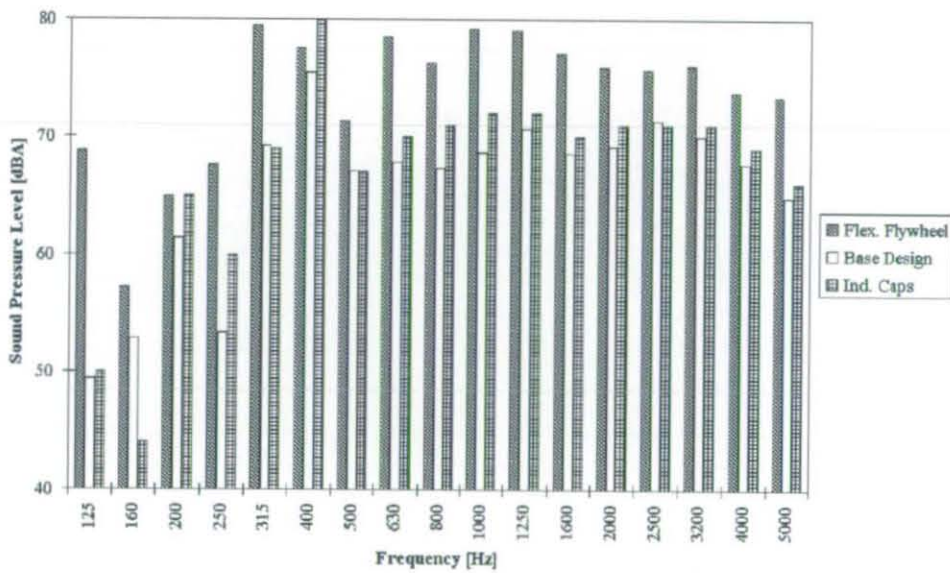


Figure App.4.52 Measured Third-Octave Band Results [3000 rpm; Left Side]

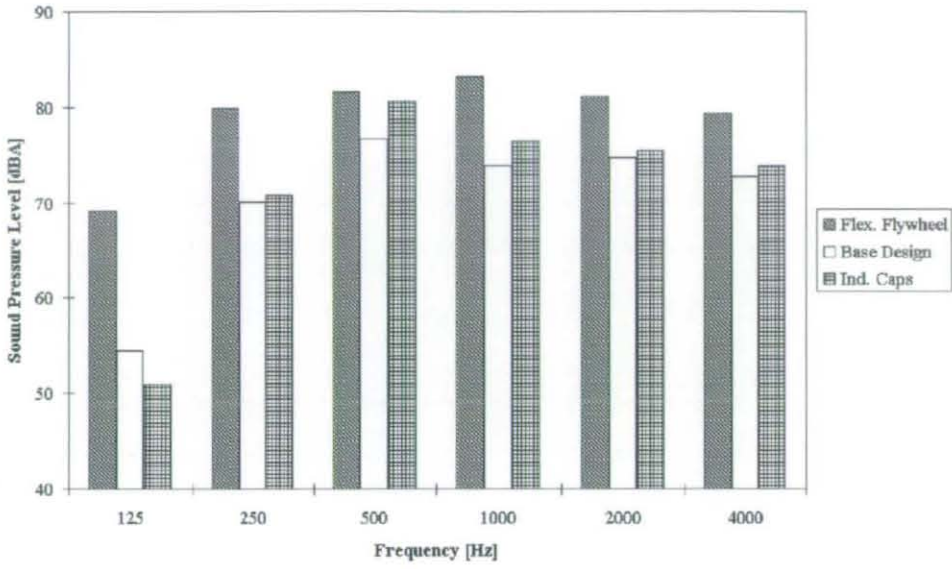


Figure App.4.53 Measured Octave Band Results [3000 rpm; Left Side]

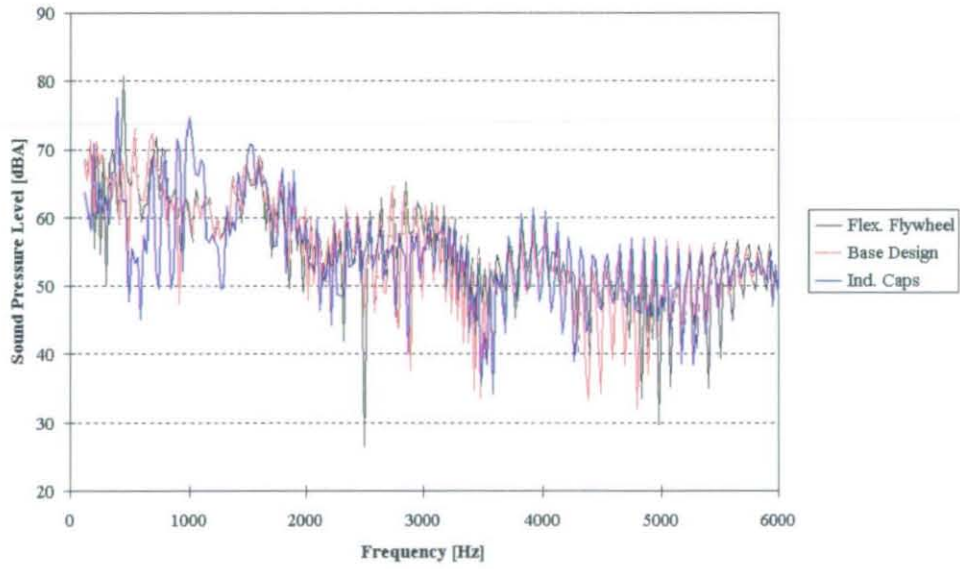


Figure App.4.54 Analysis Narrow Band Results [3000 rpm; Left Side]

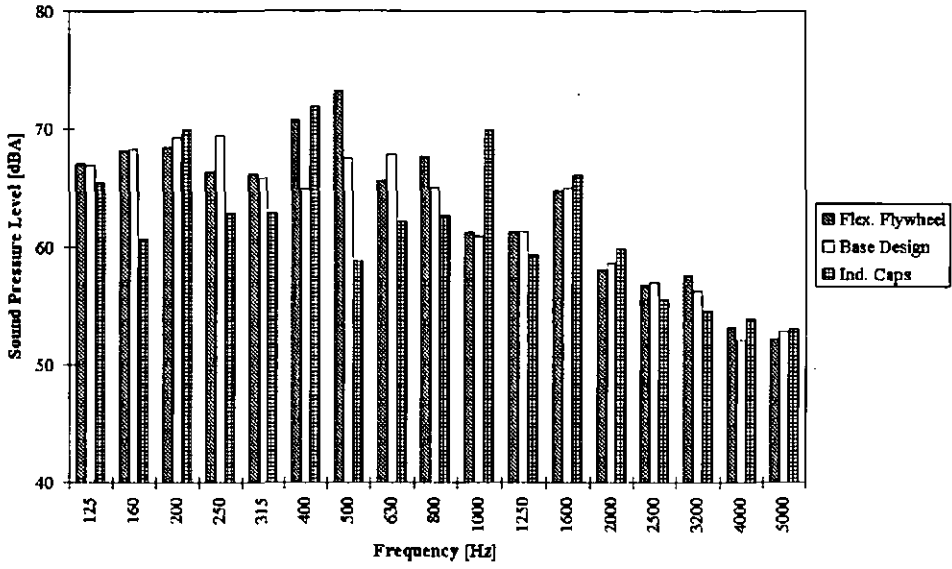


Figure App.4.55 Analysis Third-Octave Band Results [3000 rpm; Left Side]

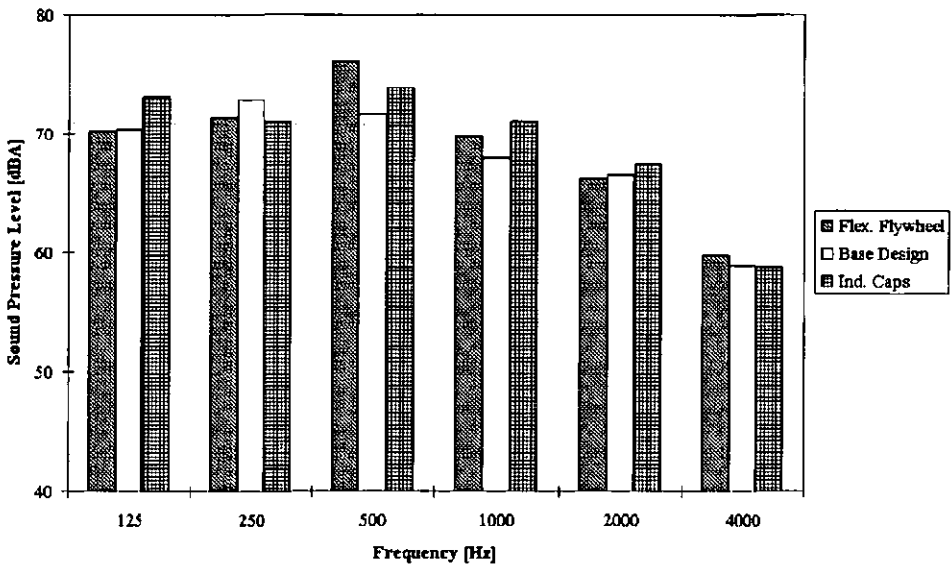


Figure App.4.56 Analysis Octave Band Results [3000 rpm; Left Side]

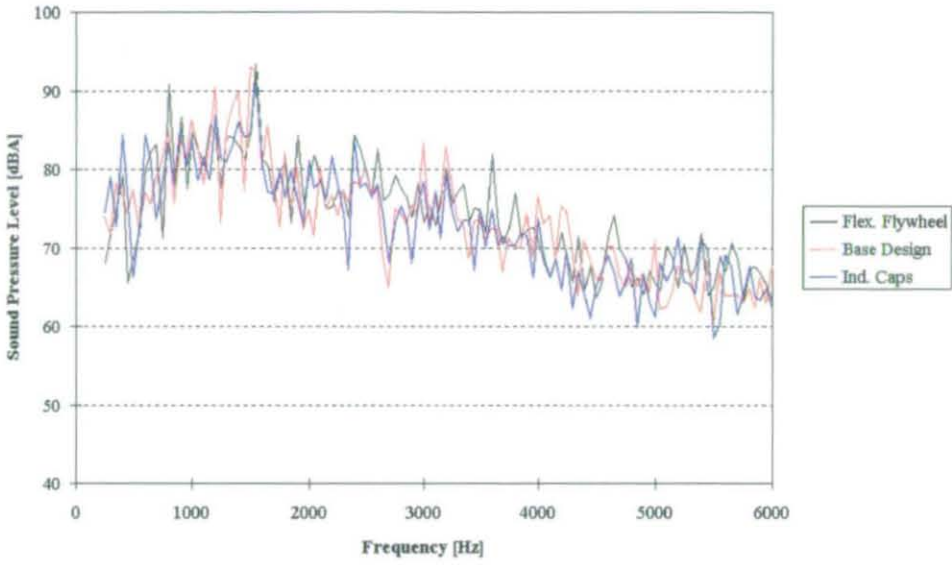


Figure App.4.57 Measured Narrow Band Results [6000 rpm; Bottom Side]

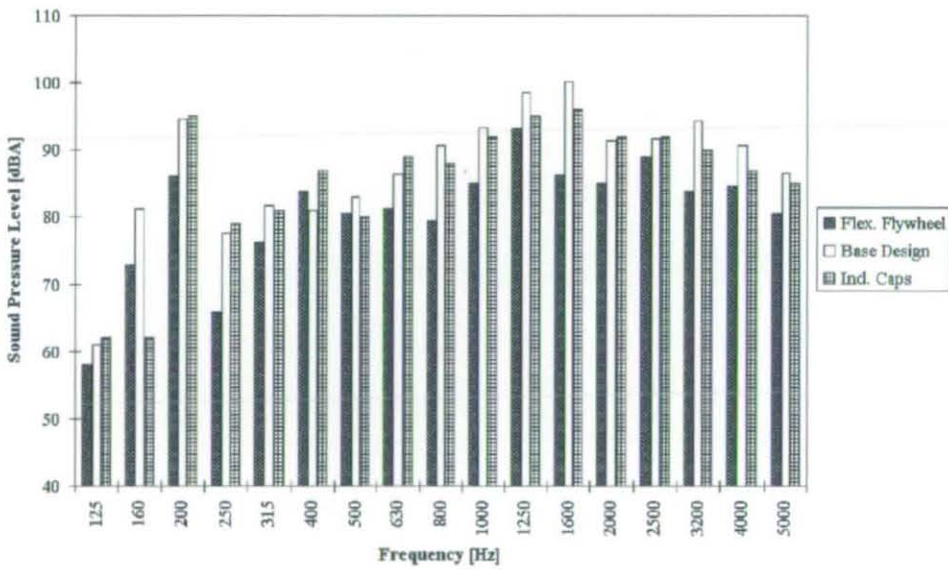


Figure App.4.58 Measured Third-Octave Band Results [6000 rpm; Bottom Side]

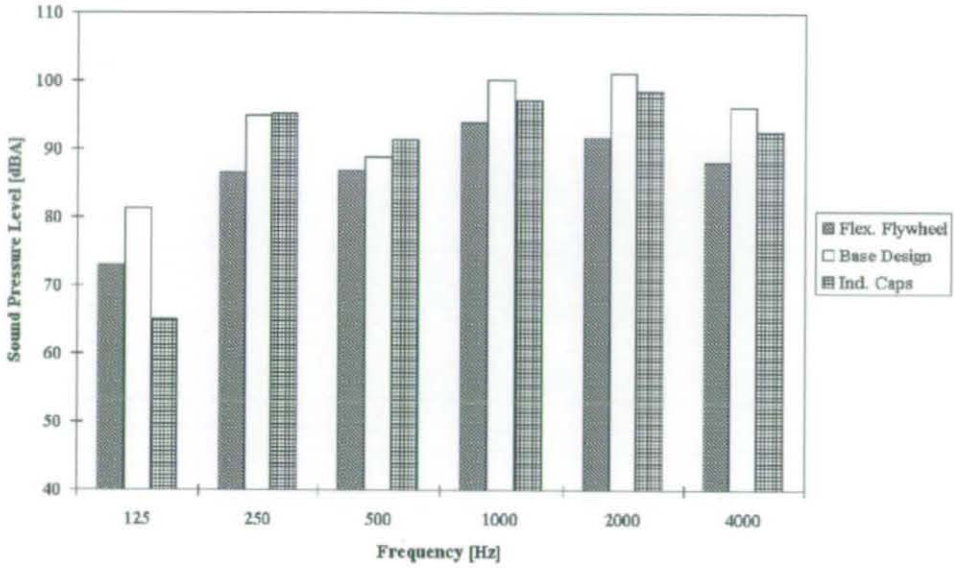


Figure App.4.59 Measured Octave Band Results [6000 rpm; Bottom Side]

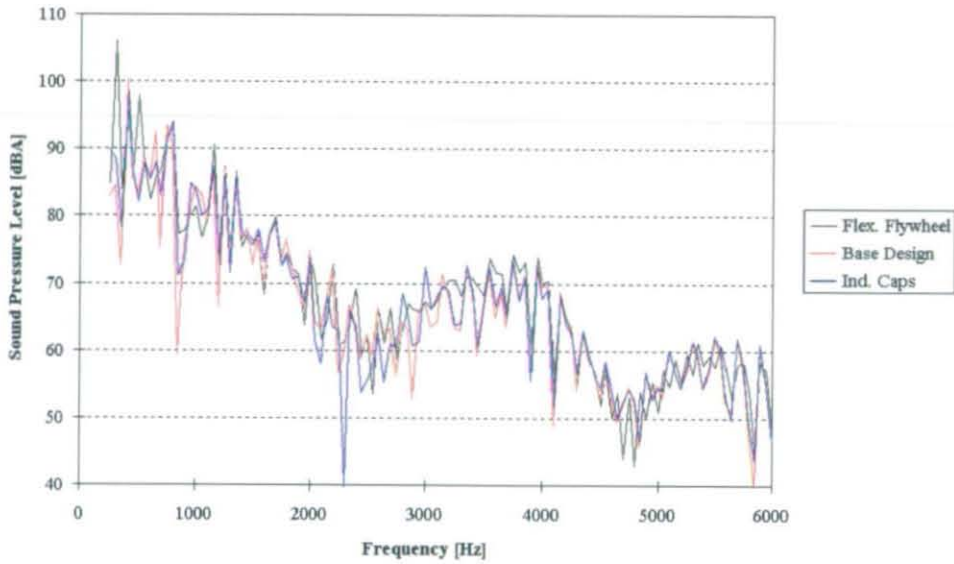


Figure App.4.60 Analysis Narrow Band Results [6000 rpm; Bottom Side]

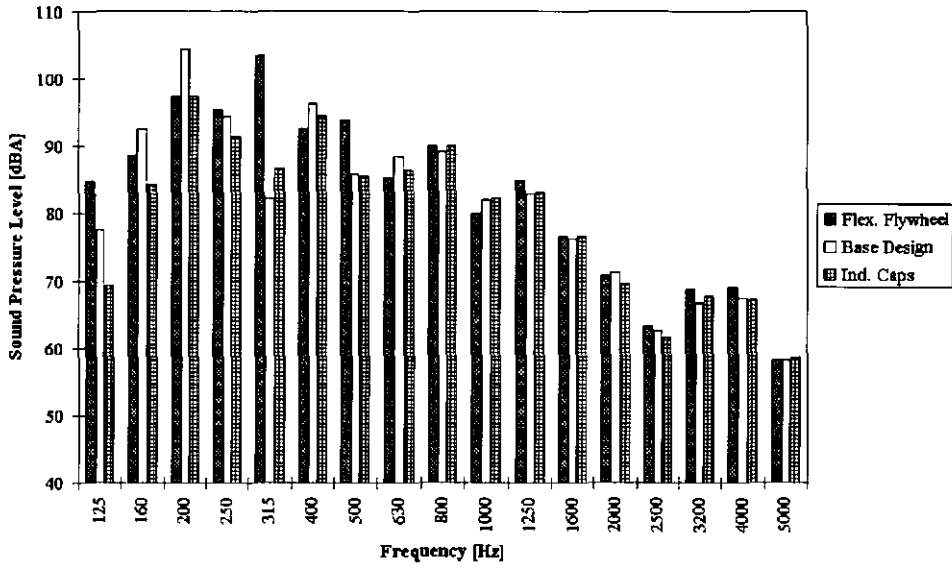


Figure App.4.61 Analysis Third-Octave Band Results [6000 rpm; Bottom Side]

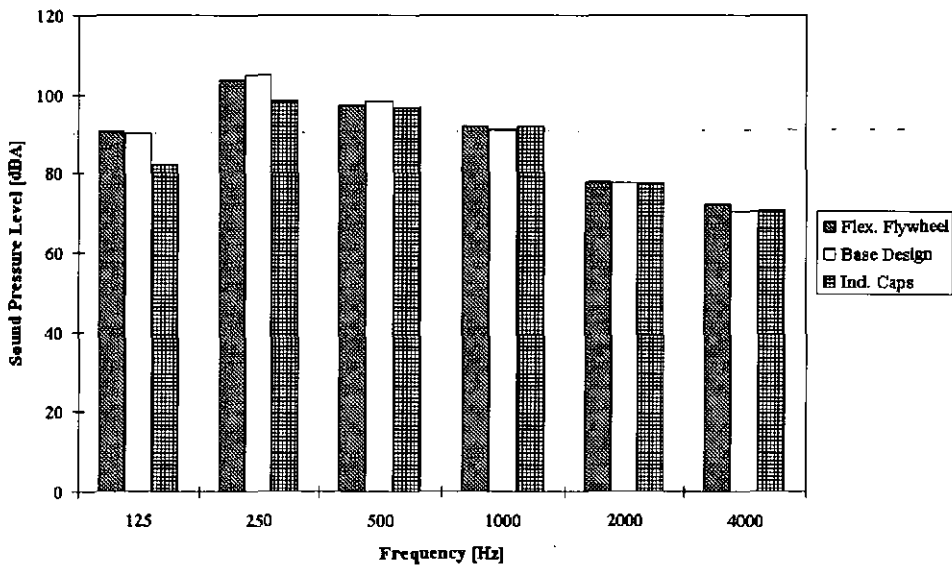


Figure App.4.62 Analysis Octave Band Results [6000 rpm; Bottom Side]

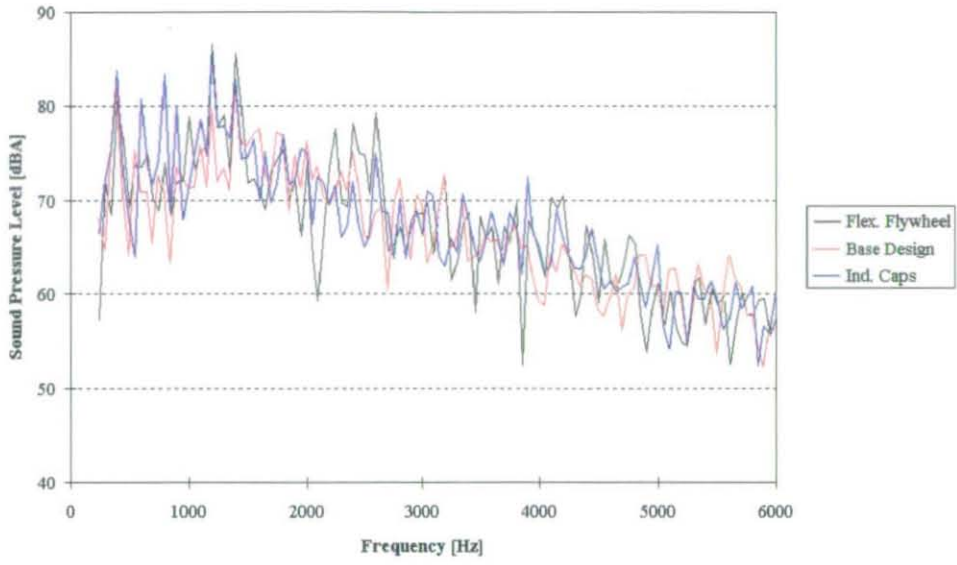


Figure App.4.63 Measured Narrow Band Results [6000 rpm; Left Side]

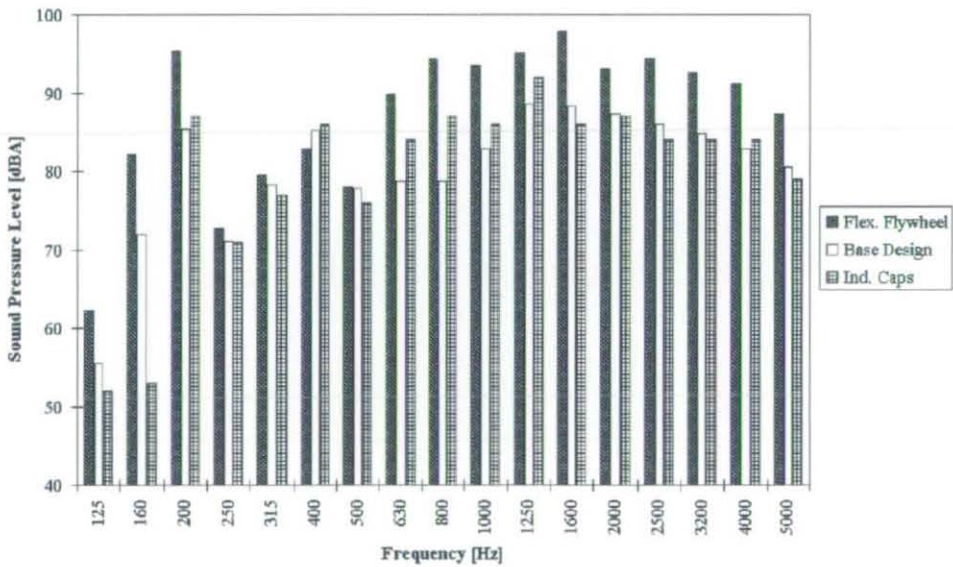


Figure App.4.64 Measured Third-Octave Band Results [6000 rpm; Left Side]

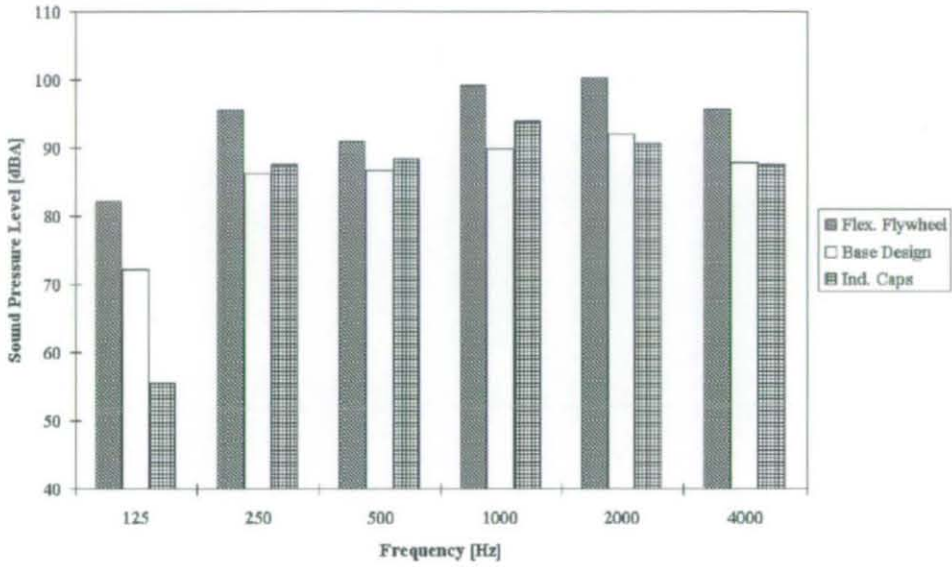


Figure App.4.65 Measured Octave Band Results [6000 rpm; Left Side]

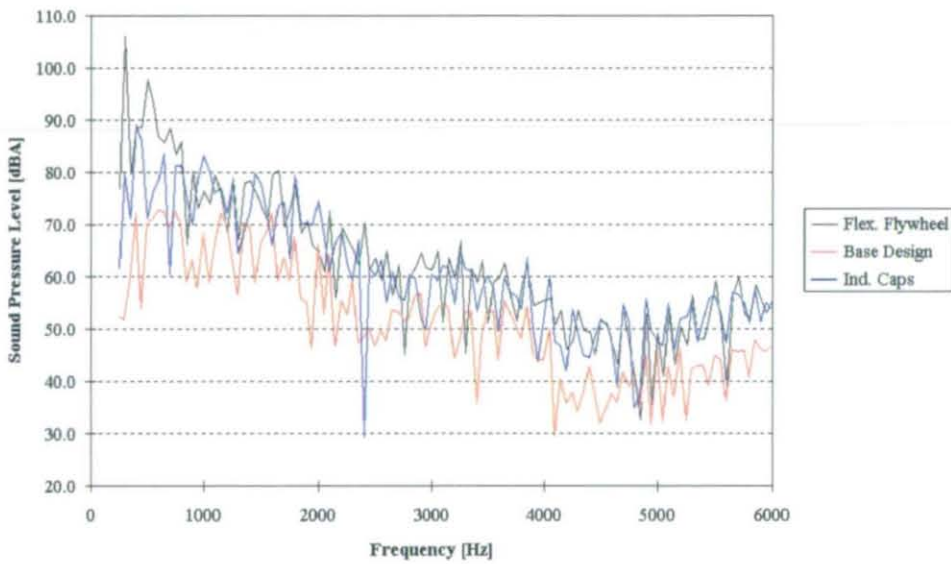


Figure App.4.66 Analysis Narrow Band Results [6000 rpm; Left Side]



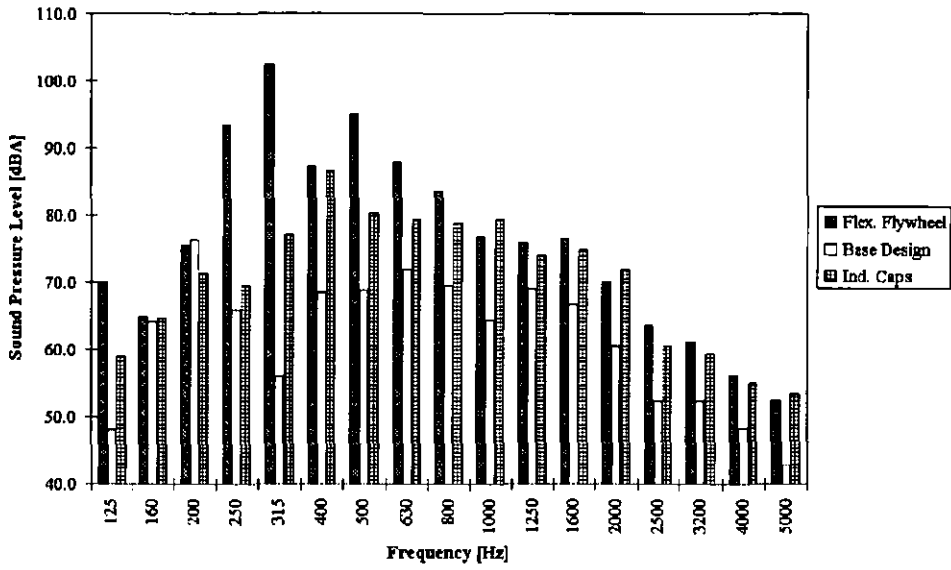


Figure App.4.67 Analysis Third-Octave Band Results [6000 rpm; Left Side]

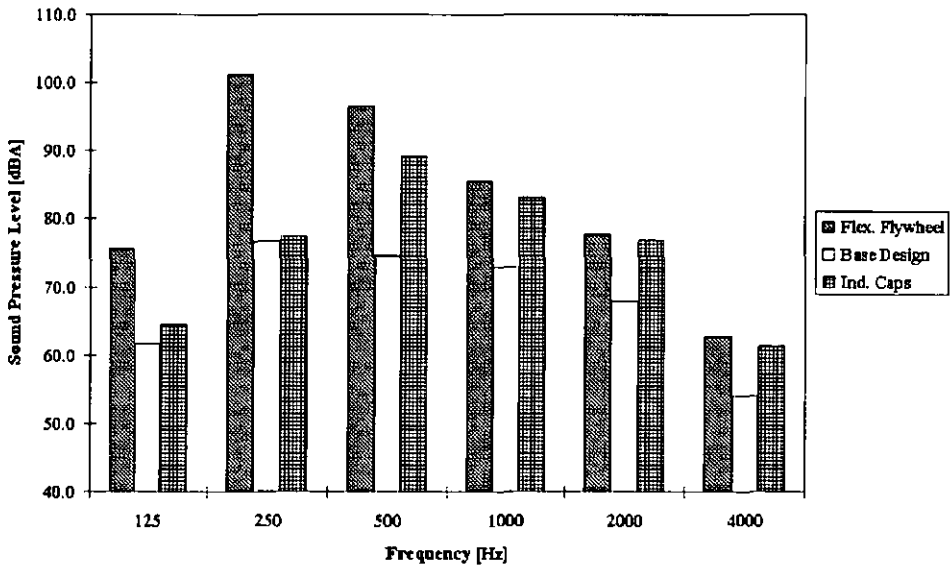


Figure App.4.68 Analysis Octave Band Results [6000 rpm; Left Side]

## Appendix 5 Tables

### Frequency Dependent Stiffness and Damping Properties

```

$ SPECIAL INPUT FOR DMAP ALTER $ FREQUENCY-DEPENDENT STIFFNESS
$DMI  KFZ  0  2  2  0  MAXF#  MAXFZ#
DMI,  KFZ,  0,  2,  1,  0,  6,  2
=,    =,    1,  1,  4000., 5000., 5100.
, 4900., 4700., , 4000.
DMI,  KFZ,  2,  1,  40000., 50000., 51000., 49000., 47000.,
, 40000.
$DMI  KFZ  MT#  1,  K(F1)  K(F2)  ...

$ FREQUENCY-DEPENDENT DAMPING
$DMI  BFZ  0  2  2  0  MAXF#  MAXMT#
DMI,  BFZ,  0,  2,  1,  0,  6,  2
DMI,  BFZ,  1,  1,  400., 500., 510., 490., 470.,
, 400.
DMI,  BFZ,  2,  1,  400., 500., 510., 490., 470.,
, 400.

$ LIST OF FREQUENCIES WHERE IMPEDANCES ARE TABULATED
$DMI  OMEGAZ  0  2  2  0  MAXF#  1
DMI,  OMEGAZ,  0,  2,  1,  0,  6,  1
DMI,  OMEGAZ,  1,  1,  .5,  2,  3,  6,  9.
, 14.
$DMI  OMEGAZ  1  1,  F1  F2  ...
$ FREQUENCIES MUST BE IN CYCLES PER UNIT TIME.

$ THE MOUNT INCIDENCE MATRIX, UGX
$DMIG  UGX  0  9  1  0  ,  ,  MAXX#
DMIG,  UGX,  0,  9,  1,  0,  ,  ,  4
DMIG,  UGX,  1,  ,  ,  13,  1,  1.0 ,
, 14,  1,  -1.0
DMIG,  UGX,  2,  ,  ,  13,  3,  1.0 ,
, 14,  3,  -1.0
DMIG,  UGX,  3,  ,  ,  53,  1,  1.0 ,
, 54,  1,  -1.0
DMIG,  UGX,  4,  ,  ,  53,  3,  1.0 ,
, 54,  3,  -1.0
    
```

Table 32 Example Input Format

```

$ THIS IS THE INPUT-FILE OF THE PROGRAM
FREQ_DEP_STIFF.F
$
...1...><...2...><...3...><...4...><...5...><...6
...><...7...><...8...>
$CELAS2  EID      K      G1      C1      G2
C2      TABLE#
CELAS2  130012  49522. 100060  1
125012  1  1
CELAS2  130011  26849. 100060  2
125011  2  6
CELAS2  130014  49522. 100061  1
125014  1  1
CELAS2  130013  26849. 100061  2
125013  2  6
CELAS2  130016  49522. 100062  1
125016  1  1
CELAS2  130015  26849. 100062  2
125015  2  6
CELAS2  130022  34730. 100072  1
125022  1  2
CELAS2  130021  43361. 100072  2
125021  2  7
CELAS2  130024  34730. 100073  1
125024  1  2
CELAS2  130023  43361. 100073  2
125023  2  7
CELAS2  130026  34730. 100073  1
125026  1  2
CELAS2  130025  43361. 100074  2
125025  2  7
CELAS2  130028  57022. 100084  1
125032  1  3
CELAS2  130027  511647. 100084  2
125031  2  8
CELAS2  130030  57022. 100085  1
125034  1  3
CELAS2  130029  511647. 100085  2
125033  2  8
CELAS2  130032  57022. 100086  1
125036  1  3
CELAS2  130031  511647. 100086  2
125035  2  8
CELAS2  130034  254468. 100096  1
125042  1  4
CELAS2  130033  254172. 100096  2
125041  2  9
CELAS2  130036  254468. 100097  1
125044  1  4
CELAS2  130035  254172. 100097  2
125043  2  9
CELAS2  130038  254468. 100098  1
125046  1  4
CELAS2  130037  254172. 100098  2
125045  2  9
CELAS2  130040  385107. 100108  1
125052  1  5
CELAS2  130039  477384. 100108  2
125051  2  10
CELAS2  130042  385107. 100109  1
125054  1  5
CELAS2  130041  477384. 100109  2
125053  2  10
CELAS2  130044  385107. 100110  1
125056  1  5
CELAS2  130043  477384. 100110  2
125055  2  10
$
    
```

STABLE , NO.  
TABLE 1

\$

\$FREQ	STIFF	DAMP
8.3	.156E+06	.196E+07
16.7	.255E+06	.192E+07
25.0	.303E+06	.190E+07
33.3	.354E+06	.191E+07
41.7	.394E+06	.189E+07
50.0	.420E+06	.189E+07
58.3	.447E+06	.188E+07
66.7	.466E+06	.189E+07
75.0	.481E+06	.187E+07
83.3	.495E+06	.191E+07
91.7	.495E+06	.191E+07
100.0	.495E+06	.191E+07
108.3	.495E+06	.191E+07
116.7	.495E+06	.191E+07
125.0	.495E+06	.191E+07
133.3	.495E+06	.191E+07
141.7	.495E+06	.191E+07
150.0	.495E+06	.191E+07
158.3	.495E+06	.191E+07
166.7	.495E+06	.191E+07
175.0	.495E+06	.191E+07
183.3	.495E+06	.191E+07
191.7	.495E+06	.191E+07
200.0	.495E+06	.191E+07
208.3	.495E+06	.191E+07
216.7	.495E+06	.191E+07
225.0	.495E+06	.191E+07
233.3	.495E+06	.191E+07
241.7	.495E+06	.191E+07
250.0	.495E+06	.191E+07
258.3	.495E+06	.191E+07
266.7	.495E+06	.191E+07
275.0	.495E+06	.191E+07
283.3	.495E+06	.191E+07
291.7	.495E+06	.191E+07
300.0	.495E+06	.191E+07
308.3	.495E+06	.191E+07
316.7	.495E+06	.191E+07
325.0	.495E+06	.191E+07
333.3	.495E+06	.191E+07
341.7	.495E+06	.191E+07
350.0	.495E+06	.191E+07
358.3	.495E+06	.191E+07
366.7	.495E+06	.191E+07
375.0	.495E+06	.191E+07
383.3	.495E+06	.191E+07
391.7	.495E+06	.191E+07
400.0	.495E+06	.191E+07
408.3	.495E+06	.191E+07
416.7	.495E+06	.191E+07
425.0	.495E+06	.191E+07
433.3	.495E+06	.191E+07
441.7	.495E+06	.191E+07
450.0	.495E+06	.191E+07
458.3	.495E+06	.191E+07
466.7	.495E+06	.191E+07
475.0	.495E+06	.191E+07
483.3	.495E+06	.191E+07
491.7	.495E+06	.191E+07

endt  
\$

TABLE 2

\$

\$FREQ	STIFF	DAMP
8.3	.531E+05	.216E+07
16.7	.121E+06	.211E+07
25.0	.159E+06	.208E+07
33.3	.179E+06	.209E+07
41.7	.207E+06	.205E+07
50.0	.228E+06	.201E+07
58.3	.237E+06	.201E+07
66.7	.251E+06	.201E+07
75.0	.263E+06	.198E+07
83.3	.268E+06	.204E+07
91.7	.268E+06	.204E+07
100.0	.268E+06	.204E+07
108.3	.268E+06	.204E+07
116.7	.268E+06	.204E+07
125.0	.268E+06	.204E+07
133.3	.268E+06	.204E+07

141.7	.268E+06	.204E+07
150.0	.268E+06	.204E+07
158.3	.268E+06	.204E+07
166.7	.268E+06	.204E+07
175.0	.268E+06	.204E+07
183.3	.268E+06	.204E+07
191.7	.268E+06	.204E+07
200.0	.268E+06	.204E+07
208.3	.268E+06	.204E+07
216.7	.268E+06	.204E+07
225.0	.268E+06	.204E+07
233.3	.268E+06	.204E+07
241.7	.268E+06	.204E+07
250.0	.268E+06	.204E+07
258.3	.268E+06	.204E+07
266.7	.268E+06	.204E+07
275.0	.268E+06	.204E+07
283.3	.268E+06	.204E+07
291.7	.268E+06	.204E+07
300.0	.268E+06	.204E+07
308.3	.268E+06	.204E+07
316.7	.268E+06	.204E+07
325.0	.268E+06	.204E+07
333.3	.268E+06	.204E+07
341.7	.268E+06	.204E+07
350.0	.268E+06	.204E+07
358.3	.268E+06	.204E+07
366.7	.268E+06	.204E+07
375.0	.268E+06	.204E+07
383.3	.268E+06	.204E+07
391.7	.268E+06	.204E+07
400.0	.268E+06	.204E+07
408.3	.268E+06	.204E+07
416.7	.268E+06	.204E+07
425.0	.268E+06	.204E+07
433.3	.268E+06	.204E+07
441.7	.268E+06	.204E+07
450.0	.268E+06	.204E+07
458.3	.268E+06	.204E+07
466.7	.268E+06	.204E+07
475.0	.268E+06	.204E+07
483.3	.268E+06	.204E+07
491.7	.268E+06	.204E+07

endt  
\$

TABLE 3

\$

\$FREQ	STIFF	DAMP
8.3	.720E+05	.191E+07
16.7	.136E+06	.192E+07
25.0	.224E+06	.190E+07
33.3	.240E+06	.189E+07
41.7	.272E+06	.190E+07
50.0	.311E+06	.189E+07
58.3	.313E+06	.181E+07
66.7	.331E+06	.189E+07
75.0	.346E+06	.189E+07
83.3	.347E+06	.171E+07
91.7	.347E+06	.171E+07
100.0	.347E+06	.171E+07
108.3	.347E+06	.171E+07
116.7	.347E+06	.171E+07
125.0	.347E+06	.171E+07
133.3	.347E+06	.171E+07
141.7	.347E+06	.171E+07
150.0	.347E+06	.171E+07
158.3	.347E+06	.171E+07
166.7	.347E+06	.171E+07
175.0	.347E+06	.171E+07
183.3	.347E+06	.171E+07
191.7	.347E+06	.171E+07
200.0	.347E+06	.171E+07
208.3	.347E+06	.171E+07
216.7	.347E+06	.171E+07
225.0	.347E+06	.171E+07
233.3	.347E+06	.171E+07
241.7	.347E+06	.171E+07
250.0	.347E+06	.171E+07
258.3	.347E+06	.171E+07
266.7	.347E+06	.171E+07
275.0	.347E+06	.171E+07
283.3	.347E+06	.171E+07
291.7	.347E+06	.171E+07
300.0	.347E+06	.171E+07

308.3	.347E+06.171E+07	475.0	.434E+06.191E+07
316.7	.347E+06.171E+07	483.3	.434E+06.191E+07
325.0	.347E+06.171E+07	491.7	.434E+06.191E+07
333.3	.347E+06.171E+07	endt	
341.7	.347E+06.171E+07	\$	
350.0	.347E+06.171E+07	TABLE	5
358.3	.347E+06.171E+07	\$	
366.7	.347E+06.171E+07	\$FREQ	STIFF DAMP
375.0	.347E+06.171E+07	8.3	.129E+06.190E+07
383.3	.347E+06.171E+07	16.7	.260E+06.189E+07
391.7	.347E+06.171E+07	25.0	.356E+06.190E+07
400.0	.347E+06.171E+07	33.3	.408E+06.188E+07
408.3	.347E+06.171E+07	41.7	.460E+06.188E+07
416.7	.347E+06.171E+07	50.0	.503E+06.189E+07
425.0	.347E+06.171E+07	58.3	.524E+06.188E+07
433.3	.347E+06.171E+07	66.7	.543E+06.188E+07
441.7	.347E+06.171E+07	75.0	.561E+06.187E+07
450.0	.347E+06.171E+07	83.3	.570E+06.187E+07
458.3	.347E+06.171E+07	91.7	.570E+06.187E+07
466.7	.347E+06.171E+07	100.0	.570E+06.187E+07
475.0	.347E+06.171E+07	108.3	.570E+06.187E+07
483.3	.347E+06.171E+07	116.7	.570E+06.187E+07
491.7	.347E+06.171E+07	125.0	.570E+06.187E+07
endt		133.3	.570E+06.187E+07
\$		141.7	.570E+06.187E+07
TABLE	4	150.0	.570E+06.187E+07
\$		158.3	.570E+06.187E+07
\$FREQ	STIFF DAMP	166.7	.570E+06.187E+07
8.3	.879E+05.211E+07	175.0	.570E+06.187E+07
16.7	.181E+06.208E+07	183.3	.570E+06.187E+07
25.0	.273E+06.209E+07	191.7	.570E+06.187E+07
33.3	.304E+06.200E+07	200.0	.570E+06.187E+07
41.7	.348E+06.200E+07	208.3	.570E+06.187E+07
50.0	.386E+06.200E+07	216.7	.570E+06.187E+07
58.3	.397E+06.193E+07	225.0	.570E+06.187E+07
66.7	.416E+06.195E+07	233.3	.570E+06.187E+07
75.0	.430E+06.195E+07	241.7	.570E+06.187E+07
83.3	.434E+06.191E+07	250.0	.570E+06.187E+07
91.7	.434E+06.191E+07	258.3	.570E+06.187E+07
100.0	.434E+06.191E+07	266.7	.570E+06.187E+07
108.3	.434E+06.191E+07	275.0	.570E+06.187E+07
116.7	.434E+06.191E+07	283.3	.570E+06.187E+07
125.0	.434E+06.191E+07	291.7	.570E+06.187E+07
133.3	.434E+06.191E+07	300.0	.570E+06.187E+07
141.7	.434E+06.191E+07	308.3	.570E+06.187E+07
150.0	.434E+06.191E+07	316.7	.570E+06.187E+07
158.3	.434E+06.191E+07	325.0	.570E+06.187E+07
166.7	.434E+06.191E+07	333.3	.570E+06.187E+07
175.0	.434E+06.191E+07	341.7	.570E+06.187E+07
183.3	.434E+06.191E+07	350.0	.570E+06.187E+07
191.7	.434E+06.191E+07	358.3	.570E+06.187E+07
200.0	.434E+06.191E+07	366.7	.570E+06.187E+07
208.3	.434E+06.191E+07	375.0	.570E+06.187E+07
216.7	.434E+06.191E+07	383.3	.570E+06.187E+07
225.0	.434E+06.191E+07	391.7	.570E+06.187E+07
233.3	.434E+06.191E+07	400.0	.570E+06.187E+07
241.7	.434E+06.191E+07	408.3	.570E+06.187E+07
250.0	.434E+06.191E+07	416.7	.570E+06.187E+07
258.3	.434E+06.191E+07	425.0	.570E+06.187E+07
266.7	.434E+06.191E+07	433.3	.570E+06.187E+07
275.0	.434E+06.191E+07	441.7	.570E+06.187E+07
283.3	.434E+06.191E+07	450.0	.570E+06.187E+07
291.7	.434E+06.191E+07	458.3	.570E+06.187E+07
300.0	.434E+06.191E+07	466.7	.570E+06.187E+07
308.3	.434E+06.191E+07	475.0	.570E+06.187E+07
316.7	.434E+06.191E+07	483.3	.570E+06.187E+07
325.0	.434E+06.191E+07	491.7	.570E+06.187E+07
333.3	.434E+06.191E+07	endt	
341.7	.434E+06.191E+07	\$	
350.0	.434E+06.191E+07	TABLE	6
358.3	.434E+06.191E+07	\$	
366.7	.434E+06.191E+07	\$FREQ	STIFF DAMP
375.0	.434E+06.191E+07	8.3	.115E+07.548E+07
383.3	.434E+06.191E+07	16.7	.190E+07.550E+07
391.7	.434E+06.191E+07	25.0	.258E+07.544E+07
400.0	.434E+06.191E+07	33.3	.315E+07.542E+07
408.3	.434E+06.191E+07	41.7	.362E+07.543E+07
416.7	.434E+06.191E+07	50.0	.402E+07.542E+07
425.0	.434E+06.191E+07	58.3	.437E+07.539E+07
433.3	.434E+06.191E+07	66.7	.465E+07.541E+07
441.7	.434E+06.191E+07	75.0	.490E+07.540E+07
450.0	.434E+06.191E+07	83.3	.512E+07.538E+07
458.3	.434E+06.191E+07	91.7	.512E+07.188E+07
466.7	.434E+06.191E+07	100.0	.512E+07.188E+07

```

108.3 .512E+07.188E+07
116.7 .512E+07.188E+07
125.0 .512E+07.188E+07
133.3 .512E+07.188E+07
141.7 .512E+07.188E+07
150.0 .512E+07.188E+07
158.3 .512E+07.188E+07
166.7 .512E+07.188E+07
175.0 .512E+07.188E+07
183.3 .512E+07.188E+07
191.7 .512E+07.188E+07
200.0 .512E+07.188E+07
208.3 .512E+07.188E+07
216.7 .512E+07.188E+07
225.0 .512E+07.188E+07
233.3 .512E+07.188E+07
241.7 .512E+07.188E+07
250.0 .512E+07.188E+07
258.3 .512E+07.188E+07
266.7 .512E+07.188E+07
275.0 .512E+07.188E+07
283.3 .512E+07.188E+07
291.7 .512E+07.188E+07
300.0 .512E+07.188E+07
308.3 .512E+07.188E+07
316.7 .512E+07.188E+07
325.0 .512E+07.188E+07
333.3 .512E+07.188E+07
341.7 .512E+07.188E+07
350.0 .512E+07.188E+07
358.3 .512E+07.188E+07
366.7 .512E+07.188E+07
375.0 .512E+07.188E+07
383.3 .512E+07.188E+07
391.7 .512E+07.188E+07
400.0 .512E+07.188E+07
408.3 .512E+07.188E+07
416.7 .512E+07.188E+07
425.0 .512E+07.188E+07
433.3 .512E+07.188E+07
441.7 .512E+07.188E+07
450.0 .512E+07.188E+07
458.3 .512E+07.188E+07
466.7 .512E+07.188E+07
475.0 .512E+07.188E+07
483.3 .512E+07.188E+07
491.7 .512E+07.188E+07
endt
$
TABLE 7
$
$FREQ STIFF DAMP
8.3 .527E+06.606E+07
16.7 .970E+06.598E+07
25.0 .144E+07.600E+07
33.3 .167E+07.575E+07
41.7 .191E+07.576E+07
50.0 .213E+07.574E+07
58.3 .224E+07.557E+07
66.7 .237E+07.562E+07
75.0 .249E+07.559E+07
83.3 .254E+07.547E+07
91.7 .254E+07.191E+07
100.0 .254E+07.191E+07
108.3 .254E+07.191E+07
116.7 .254E+07.191E+07
125.0 .254E+07.191E+07
133.3 .254E+07.191E+07
141.7 .254E+07.191E+07
150.0 .254E+07.191E+07
158.3 .254E+07.191E+07
166.7 .254E+07.191E+07
175.0 .254E+07.191E+07
183.3 .254E+07.191E+07
191.7 .254E+07.191E+07
200.0 .254E+07.191E+07
208.3 .254E+07.191E+07
216.7 .254E+07.191E+07
225.0 .254E+07.191E+07
233.3 .254E+07.191E+07
241.7 .254E+07.191E+07
250.0 .254E+07.191E+07
258.3 .254E+07.191E+07
266.7 .254E+07.191E+07

```

```

275.0 .254E+07.191E+07
283.3 .254E+07.191E+07
291.7 .254E+07.191E+07
300.0 .254E+07.191E+07
308.3 .254E+07.191E+07
316.7 .254E+07.191E+07
325.0 .254E+07.191E+07
333.3 .254E+07.191E+07
341.7 .254E+07.191E+07
350.0 .254E+07.191E+07
358.3 .254E+07.191E+07
366.7 .254E+07.191E+07
375.0 .254E+07.191E+07
383.3 .254E+07.191E+07
391.7 .254E+07.191E+07
400.0 .254E+07.191E+07
408.3 .254E+07.191E+07
416.7 .254E+07.191E+07
425.0 .254E+07.191E+07
433.3 .254E+07.191E+07
441.7 .254E+07.191E+07
450.0 .254E+07.191E+07
458.3 .254E+07.191E+07
466.7 .254E+07.191E+07
475.0 .254E+07.191E+07
483.3 .254E+07.191E+07
491.7 .254E+07.191E+07
endt
$
TABLE 8
$
$FREQ STIFF DAMP
8.3 .395E+06.544E+07
16.7 .775E+06.543E+07
25.0 .160E+07.545E+07
33.3 .170E+07.539E+07
41.7 .193E+07.541E+07
50.0 .226E+07.542E+07
58.3 .228E+07.536E+07
66.7 .241E+07.539E+07
75.0 .253E+07.539E+07
83.3 .254E+07.540E+07
91.7 .254E+07.189E+07
100.0 .254E+07.189E+07
108.3 .254E+07.189E+07
116.7 .254E+07.189E+07
125.0 .254E+07.189E+07
133.3 .254E+07.189E+07
141.7 .254E+07.189E+07
150.0 .254E+07.189E+07
158.3 .254E+07.189E+07
166.7 .254E+07.189E+07
175.0 .254E+07.189E+07
183.3 .254E+07.189E+07
191.7 .254E+07.189E+07
200.0 .254E+07.189E+07
208.3 .254E+07.189E+07
216.7 .254E+07.189E+07
225.0 .254E+07.189E+07
233.3 .254E+07.189E+07
241.7 .254E+07.189E+07
250.0 .254E+07.189E+07
258.3 .254E+07.189E+07
266.7 .254E+07.189E+07
275.0 .254E+07.189E+07
283.3 .254E+07.189E+07
291.7 .254E+07.189E+07
300.0 .254E+07.189E+07
308.3 .254E+07.189E+07
316.7 .254E+07.189E+07
325.0 .254E+07.189E+07
333.3 .254E+07.189E+07
341.7 .254E+07.189E+07
350.0 .254E+07.189E+07
358.3 .254E+07.189E+07
366.7 .254E+07.189E+07
375.0 .254E+07.189E+07
383.3 .254E+07.189E+07
391.7 .254E+07.189E+07
400.0 .254E+07.189E+07
408.3 .254E+07.189E+07
416.7 .254E+07.189E+07
425.0 .254E+07.189E+07
433.3 .254E+07.189E+07

```

```

441.7 .254E+07.189E+07
450.0 .254E+07.189E+07
458.3 .254E+07.189E+07
466.7 .254E+07.189E+07
475.0 .254E+07.189E+07
483.3 .254E+07.189E+07
491.7 .254E+07.189E+07
endtc
$
TABLE 9
$
SFREQ STIFF DAMP
 8.3 .908E+06.542E+07
 16.7 .167E+07.556E+07
 25.0 .253E+07.545E+07
 33.3 .279E+07.546E+07
 41.7 .317E+07.550E+07
 50.0 .345E+07.554E+07
 58.3 .353E+07.541E+07
 66.7 .370E+07.547E+07
 75.0 .381E+07.546E+07
 83.3 .385E+07.540E+07
 91.7 .385E+07.188E+07
100.0 .385E+07.188E+07
108.3 .385E+07.188E+07
116.7 .385E+07.188E+07
125.0 .385E+07.188E+07
133.3 .385E+07.188E+07
141.7 .385E+07.188E+07
150.0 .385E+07.188E+07
158.3 .385E+07.188E+07
166.7 .385E+07.188E+07
175.0 .385E+07.188E+07
183.3 .385E+07.188E+07
191.7 .385E+07.188E+07
200.0 .385E+07.188E+07
208.3 .385E+07.188E+07
216.7 .385E+07.188E+07
225.0 .385E+07.188E+07
233.3 .385E+07.188E+07
241.7 .385E+07.188E+07
250.0 .385E+07.188E+07
258.3 .385E+07.188E+07
266.7 .385E+07.188E+07
275.0 .385E+07.188E+07
283.3 .385E+07.188E+07
291.7 .385E+07.188E+07
300.0 .385E+07.188E+07
308.3 .385E+07.188E+07
316.7 .385E+07.188E+07
325.0 .385E+07.188E+07
333.3 .385E+07.188E+07
341.7 .385E+07.188E+07
350.0 .385E+07.188E+07
358.3 .385E+07.188E+07
366.7 .385E+07.188E+07
375.0 .385E+07.188E+07
383.3 .385E+07.188E+07
391.7 .385E+07.188E+07
400.0 .385E+07.188E+07
408.3 .385E+07.188E+07
416.7 .385E+07.188E+07
425.0 .385E+07.188E+07
433.3 .385E+07.188E+07
441.7 .385E+07.188E+07
450.0 .385E+07.188E+07
458.3 .385E+07.188E+07
466.7 .385E+07.188E+07
475.0 .385E+07.188E+07
483.3 .385E+07.188E+07

```

```

491.7 .385E+07.188E+07
endtc
$
TABLE 10
$
SFREQ STIFF DAMP
 8.3 .128E+07.553E+07
 16.7 .206E+07.554E+07
 25.0 .284E+07.554E+07
 33.3 .334E+07.544E+07
 41.7 .375E+07.545E+07
 50.0 .404E+07.544E+07
 58.3 .421E+07.539E+07
 66.7 .438E+07.541E+07
 75.0 .450E+07.540E+07
 83.3 .457E+07.538E+07
 91.7 .457E+07.188E+07
100.0 .457E+07.188E+07
108.3 .457E+07.188E+07
116.7 .457E+07.188E+07
125.0 .457E+07.188E+07
133.3 .457E+07.188E+07
141.7 .457E+07.188E+07
150.0 .457E+07.188E+07
158.3 .457E+07.188E+07
166.7 .457E+07.188E+07
175.0 .457E+07.188E+07
183.3 .457E+07.188E+07
191.7 .457E+07.188E+07
200.0 .457E+07.188E+07
208.3 .457E+07.188E+07
216.7 .457E+07.188E+07
225.0 .457E+07.188E+07
233.3 .457E+07.188E+07
241.7 .457E+07.188E+07
250.0 .457E+07.188E+07
258.3 .457E+07.188E+07
266.7 .457E+07.188E+07
275.0 .457E+07.188E+07
283.3 .457E+07.188E+07
291.7 .457E+07.188E+07
300.0 .457E+07.188E+07
308.3 .457E+07.188E+07
316.7 .457E+07.188E+07
325.0 .457E+07.188E+07
333.3 .457E+07.188E+07
341.7 .457E+07.188E+07
350.0 .457E+07.188E+07
358.3 .457E+07.188E+07
366.7 .457E+07.188E+07
375.0 .457E+07.188E+07
383.3 .457E+07.188E+07
391.7 .457E+07.188E+07
400.0 .457E+07.188E+07
408.3 .457E+07.188E+07
416.7 .457E+07.188E+07
425.0 .457E+07.188E+07
433.3 .457E+07.188E+07
441.7 .457E+07.188E+07
450.0 .457E+07.188E+07
458.3 .457E+07.188E+07
466.7 .457E+07.188E+07
475.0 .457E+07.188E+07
483.3 .457E+07.188E+07
491.7 .457E+07.188E+07
endtc
$
$RPM 1000. 6000. 1000.
$
$ ----- end of input file -----

```

Table 33 Input of Program FREQ\_DEP\_STIFF.F

```

$$$$$$$$$$$$$$$$$$$$$$$$$$$$$$$$$$$$$$$$$$$$$$$$$$$$$$$$$$$$$$$$$$$$$$$$$$$$$$$$$$$$$$$$$$$$$$$$$$$$$$$$$$$$
$
$   OUTPUT FROM PROGRAM "FREQ_DEPNDNT_STIFF.X"
$
$...1.>>...2.>>...3.>>...4.>>...5.>>...6.>>...7.>>...8.>>...9.>>...10.>>
DMI   OMEGAZ      0       2       1       0       59       1
DMI   OMEGAZ      1       1       8.3     16.7    25.0    33.3    41.7
           50.0    58.3    66.7    75.0    83.3    91.7   100.0   108.3
           116.7   125.0   133.3   141.7   150.0   158.3   166.7   175.0
           183.3   191.7   200.0   208.3   216.7   225.0   233.3   241.7
           250.0   258.3   266.7   275.0   283.3   291.7   300.0   308.3
           316.7   325.0   333.3   341.7   350.0   358.3   366.7   375.0
           383.3   391.7   400.0   408.3   416.7   425.0   433.3   441.7
           450.0   458.3   466.7   475.0   483.3   491.7
$...1.>>...2.>>...3.>>...4.>>...5.>>...6.>>...7.>>...8.>>...9.>>...10.>>
$DMI  KFZ        0       2       1       0   MAXF#   MAXZ#
DMI   KFZ        0       2       1       0          59        10
DMI   KFZ        1       1.156E+06.255E+06.303E+06.354E+06.394E+06
         .420E+06.447E+06.466E+06.481E+06.495E+06.495E+06.495E+06.495E+06
         .495E+06.495E+06.495E+06.495E+06.495E+06.495E+06.495E+06.495E+06
         .495E+06.495E+06.495E+06.495E+06.495E+06.495E+06.495E+06.495E+06
         .495E+06.495E+06.495E+06.495E+06.495E+06.495E+06.495E+06.495E+06
         .495E+06.495E+06.495E+06.495E+06.495E+06.495E+06.495E+06.495E+06
         .495E+06.495E+06.495E+06.495E+06.495E+06.495E+06.495E+06
DMI   KFZ        2       1.531E+05.121E+06.159E+06.179E+06.207E+06
         .228E+06.237E+06.251E+06.263E+06.268E+06.268E+06.268E+06.268E+06
         .268E+06.268E+06.268E+06.268E+06.268E+06.268E+06.268E+06.268E+06
         .268E+06.268E+06.268E+06.268E+06.268E+06.268E+06.268E+06.268E+06
         .268E+06.268E+06.268E+06.268E+06.268E+06.268E+06.268E+06.268E+06
         .268E+06.268E+06.268E+06.268E+06.268E+06.268E+06.268E+06
DMI   KFZ        3       1.720E+05.136E+06.224E+06.240E+06.272E+06
         .311E+06.313E+06.331E+06.346E+06.347E+06.347E+06.347E+06.347E+06
         .347E+06.347E+06.347E+06.347E+06.347E+06.347E+06.347E+06.347E+06
         .347E+06.347E+06.347E+06.347E+06.347E+06.347E+06.347E+06.347E+06
         .347E+06.347E+06.347E+06.347E+06.347E+06.347E+06.347E+06.347E+06
         .347E+06.347E+06.347E+06.347E+06.347E+06.347E+06.347E+06
DMI   KFZ        4       1.879E+05.181E+06.273E+06.304E+06.348E+06
         .386E+06.397E+06.416E+06.430E+06.434E+06.434E+06.434E+06.434E+06
         .434E+06.434E+06.434E+06.434E+06.434E+06.434E+06.434E+06.434E+06
         .434E+06.434E+06.434E+06.434E+06.434E+06.434E+06.434E+06.434E+06
         .434E+06.434E+06.434E+06.434E+06.434E+06.434E+06.434E+06.434E+06
         .434E+06.434E+06.434E+06.434E+06.434E+06.434E+06.434E+06
DMI   KFZ        5       1.129E+06.260E+06.356E+06.408E+06.460E+06
         .503E+06.524E+06.543E+06.561E+06.570E+06.570E+06.570E+06.570E+06
         .570E+06.570E+06.570E+06.570E+06.570E+06.570E+06.570E+06.570E+06
         .570E+06.570E+06.570E+06.570E+06.570E+06.570E+06.570E+06.570E+06
         .570E+06.570E+06.570E+06.570E+06.570E+06.570E+06.570E+06.570E+06
         .570E+06.570E+06.570E+06.570E+06.570E+06.570E+06.570E+06
DMI   KFZ        6       1.115E+07.190E+07.258E+07.315E+07.362E+07
         .402E+07.437E+07.465E+07.490E+07.512E+07.512E+07.512E+07.512E+07
         .512E+07.512E+07.512E+07.512E+07.512E+07.512E+07.512E+07.512E+07
         .512E+07.512E+07.512E+07.512E+07.512E+07.512E+07.512E+07.512E+07
         .512E+07.512E+07.512E+07.512E+07.512E+07.512E+07.512E+07.512E+07
         .512E+07.512E+07.512E+07.512E+07.512E+07.512E+07
DMI   KFZ        7       1.527E+06.970E+06.144E+07.167E+07.191E+07
         .213E+07.224E+07.237E+07.249E+07.254E+07.254E+07.254E+07.254E+07
         .254E+07.254E+07.254E+07.254E+07.254E+07.254E+07.254E+07.254E+07
         .254E+07.254E+07.254E+07.254E+07.254E+07.254E+07.254E+07.254E+07
         .254E+07.254E+07.254E+07.254E+07.254E+07.254E+07.254E+07.254E+07
         .254E+07.254E+07.254E+07.254E+07.254E+07.254E+07.254E+07
DMI   KFZ        8       1.395E+06.775E+06.160E+07.170E+07.193E+07
         .226E+07.228E+07.241E+07.253E+07.254E+07.254E+07.254E+07.254E+07
         .254E+07.254E+07.254E+07.254E+07.254E+07.254E+07.254E+07.254E+07
         .254E+07.254E+07.254E+07.254E+07.254E+07.254E+07.254E+07.254E+07
         .254E+07.254E+07.254E+07.254E+07.254E+07.254E+07.254E+07.254E+07
         .254E+07.254E+07.254E+07.254E+07.254E+07.254E+07.254E+07
DMI   KFZ        9       1.908E+06.167E+07.253E+07.279E+07.317E+07
         .345E+07.353E+07.370E+07.381E+07.385E+07.385E+07.385E+07.385E+07
         .385E+07.385E+07.385E+07.385E+07.385E+07.385E+07.385E+07.385E+07

```





```

.188E+07.188E+07.188E+07.188E+07.188E+07.188E+07.188E+07.188E+07
.188E+07.188E+07.188E+07.188E+07.188E+07.188E+07.188E+07.188E+07
.188E+07.188E+07.188E+07.188E+07.188E+07.188E+07.188E+07.188E+07
.188E+07.188E+07.188E+07.188E+07.188E+07.188E+07.188E+07
DMI BFZ 10 1.553E+07.554E+07.554E+07.544E+07.545E+07
.544E+07.539E+07.541E+07.540E+07.538E+07.188E+07.188E+07.188E+07
.188E+07.188E+07.188E+07.188E+07.188E+07.188E+07.188E+07.188E+07
.188E+07.188E+07.188E+07.188E+07.188E+07.188E+07.188E+07.188E+07
.188E+07.188E+07.188E+07.188E+07.188E+07.188E+07.188E+07.188E+07
.188E+07.188E+07.188E+07.188E+07.188E+07.188E+07.188E+07.188E+07
.188E+07.188E+07.188E+07.188E+07.188E+07.188E+07.188E+07.188E+07
.188E+07.188E+07.188E+07.188E+07.188E+07.188E+07.188E+07.188E+07
$...1.><...2.><...3.><...4.><...5.><...6.><...7.><...8.><...9.><...10.>
$DMIG UGX 0 9 1 0 #mt_dofs
DMIG UGX 0 9 1 0 30
DMIG UGX 1 100060 1 1.00
125012 1 -1.00
DMIG UGX 2 100060 2 1.00
125011 2 -1.00
DMIG UGX 3 100061 1 1.00
125014 1 -1.00
DMIG UGX 4 100061 2 1.00
125013 2 -1.00
DMIG UGX 5 100062 1 1.00
125016 1 -1.00
DMIG UGX 6 100062 2 1.00
125015 2 -1.00
DMIG UGX 7 100072 1 1.00
125022 1 -1.00
DMIG UGX 8 100072 2 1.00
125021 2 -1.00
DMIG UGX 9 100073 1 1.00
125024 1 -1.00
DMIG UGX 10 100073 2 1.00
125023 2 -1.00
DMIG UGX 11 100073 1 1.00
125026 1 -1.00
DMIG UGX 12 100074 2 1.00
125025 2 -1.00
DMIG UGX 13 100084 1 1.00
125032 1 -1.00
DMIG UGX 14 100084 2 1.00
125031 2 -1.00
DMIG UGX 15 100085 1 1.00
125034 1 -1.00
DMIG UGX 16 100085 2 1.00
125033 2 -1.00
DMIG UGX 17 100086 1 1.00
125036 1 -1.00
DMIG UGX 18 100086 2 1.00
125035 2 -1.00
DMIG UGX 19 100096 1 1.00
125042 1 -1.00
DMIG UGX 20 100096 2 1.00
125041 2 -1.00
DMIG UGX 21 100097 1 1.00
125044 1 -1.00
DMIG UGX 22 100097 2 1.00
125043 2 -1.00
DMIG UGX 23 100098 1 1.00
125046 1 -1.00
DMIG UGX 24 100098 2 1.00
125045 2 -1.00
DMIG UGX 25 100108 1 1.00
125052 1 -1.00
DMIG UGX 26 100108 2 1.00
125051 2 -1.00
DMIG UGX 27 100109 1 1.00
125054 1 -1.00
DMIG UGX 28 100109 2 1.00
125053 2 -1.00
DMIG UGX 29 100110 1 1.00
125056 1 -1.00
DMIG UGX 30 100110 2 1.00
125055 2 -1.00
$...1.><...2.><...3.><...4.><...5.><...6.><...7.><...8.><...9.><...10.>
$DMI UXZ 0 2 1 0 #total #unique
DMI UXZ 0 2 1 0 30 10
DMI UXZ 1 1 1.00 .00 1.00 .00 1.00
.00 .00 .00 .00 .00 .00 .00 .00
.00 .00 .00 .00 .00 .00 .00 .00
.00 .00 .00 .00 .00 .00 .00 .00
DMI UXZ 2 1 .00 .00 .00 .00 .00 .00
    
```



## Appendix 6 Description of Ford Zetec-SE Engine

With model year 1996 Ford introduced a new engine family of four cylinder engines coded ZETEC-SE. This engine family is produced in the Ford Valencia engine plant in Spain with a displacement of 1.25 and 1.4 litres. The 1.6 litres version is produced in the Bridgend engine plant in United Kingdom. A cut-away view of the entire engine assembly is shown in Figure App.6.1. An overview of the technical data is given in Table 32. The corresponding side and front view are shown in Figure App.6.2 and App.6.3.

Engine Configuration	4 Cylinder, 4 Stroke In-Line
Valves per Cylinder	4
Swept Volume	1242 cm <sup>3</sup>
Governed Speed	6500 rev/min
Max. Power	55 kW at 5200 rpm
Max. Torque	110 Nm at 4000 rpm
Torque at 1500 rpm	92 Nm
Firing Order	1 - 3 - 4 - 2
Bore/Stroke	71.9 mm / 76.5 mm
Stroke-Bore-Ratio	1.064
Compression Ratio	10.0:1
Fuel Type	Super 95 ROZ
Cyl.-Cyl. Distance	87 mm
Connecting Rod Length	136.3
Deck Height	203 mm
Block Length	508 mm
Main Bearing Diameter	48 mm
Pin Diameter	40 mm
Transmission	Ford IB5 5-speed Manual

Table 35 Zetec-SE 1.25l Technical Data

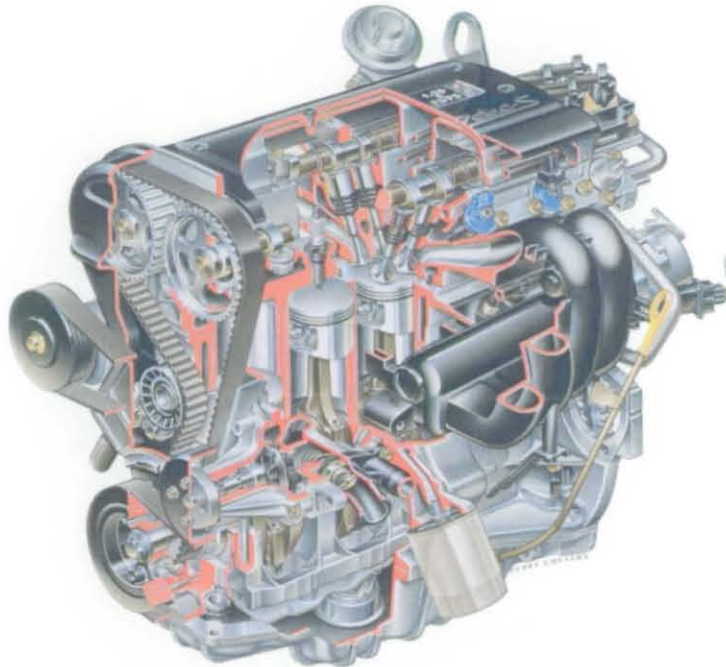


Figure App.6.1 ZETEC-SE Engine Assembly Cut-away

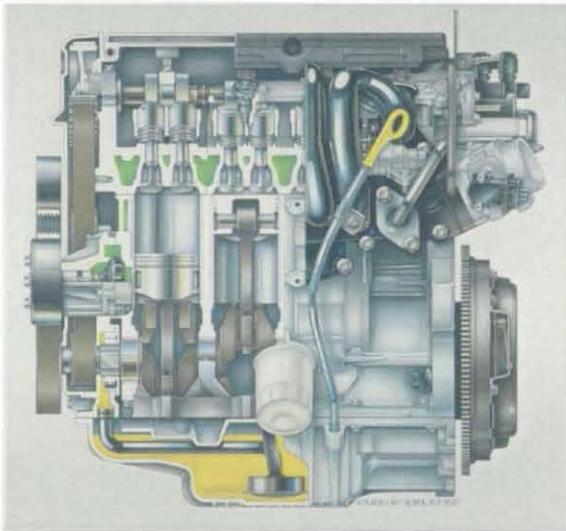


Figure App.6.2 Zetec-SE Side View

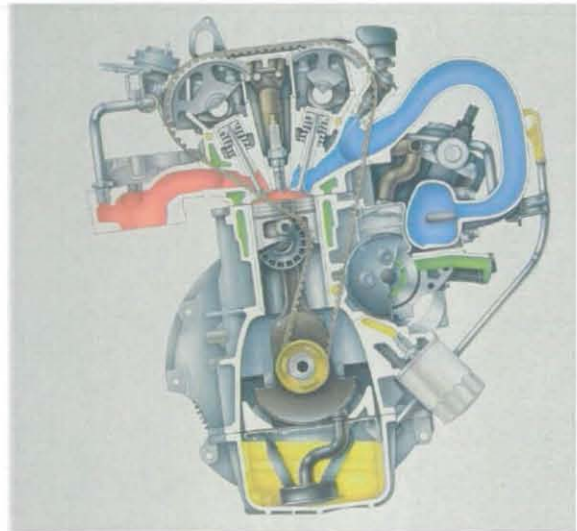


Figure App.6.3 Zetec-SE Front View

The main development targets were excellent fuel economy, low emissions, quiet running, reduced vibrations and minimum service. The engine uses light alloy for its main structural components. The engine block is a deep skirt design with a main bearing beam. Further engine features are structural oilpan, a plastic intake manifold and a magnesium cam cover. All base engine components are discussed and displayed in section 8.1.1.

To provide good engine breathing and low exhaust emissions the engine features a double overhead camshaft 16-valve configuration (Figure App.6.4). Friction reduction was another important design objective and a number of engine systems have been optimized accordingly, for example the valve train and crank train. Both the overall engine and the valve train friction are best-in-class.

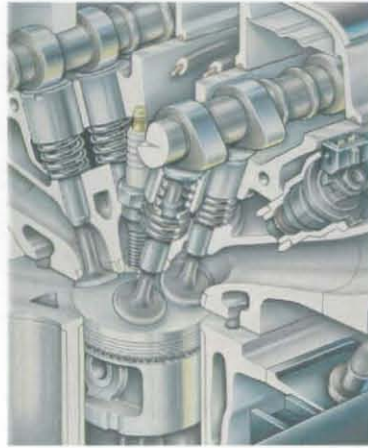


Figure App.6.4 Zetec-SE 16-Valves Cylinder Head Assembly

The intake manifold was optimized to achieve exceptional low-end torque while maintaining excellent 4-valve top end performance (Figure App.6.5). Low emission levels were realized by a closed coupled catalyst and an optimized injection system with 4 hole injection nozzles. The EGR system provides good fuel economy at part load and low  $\text{NO}_x$  emissions in the view of future legislation. The latest engine management system EEC V is used, featuring sequential electronic fuel injection, electronic distributorless ignition, and EGR control. The calibration system represents state-of-the-art technology for improved cold start, idle quality, and transient fuel control.

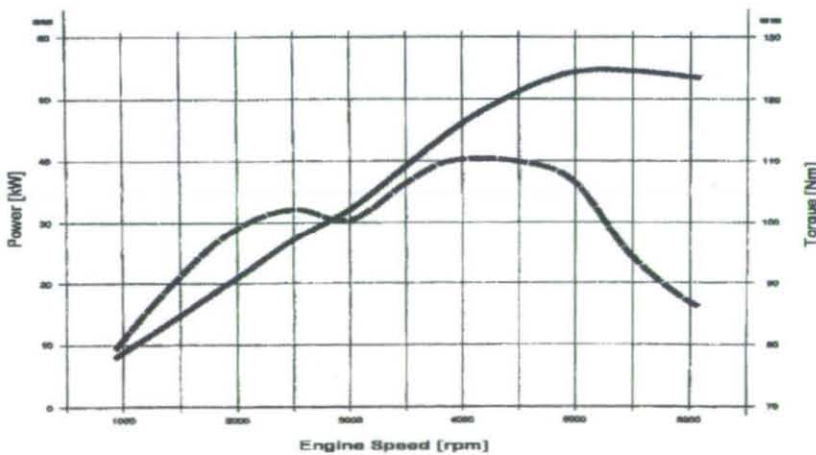


Figure App.6.5 Zetec-SE 1.25l Torque and Power Output

Further actions were taken to minimize the structure borne noise of the installed powertrain. A new Torque-Roll-Axis (TRA; Figure App.6.6) powertrain mounting system was applied to minimize the effect of powertrain movements and vibration on the body structure. The vertical or mass forces are supported by the Right-Hand-Side [RHS]- and Left-Hand-Side [LHS]-engine mounts. Both mounts are located on the roll or main inertia axis. The LHS mount is a rubber mount, while the RHS mount is a hydro mount tuned to minimize idle vibration. Powertrain rolling is supported by the Rear-Roll-Restrictor mount. A speciality is the larger, vertical rubber mount at the sub-frame improving the ground clearance and the absorption of powertrain vibration.

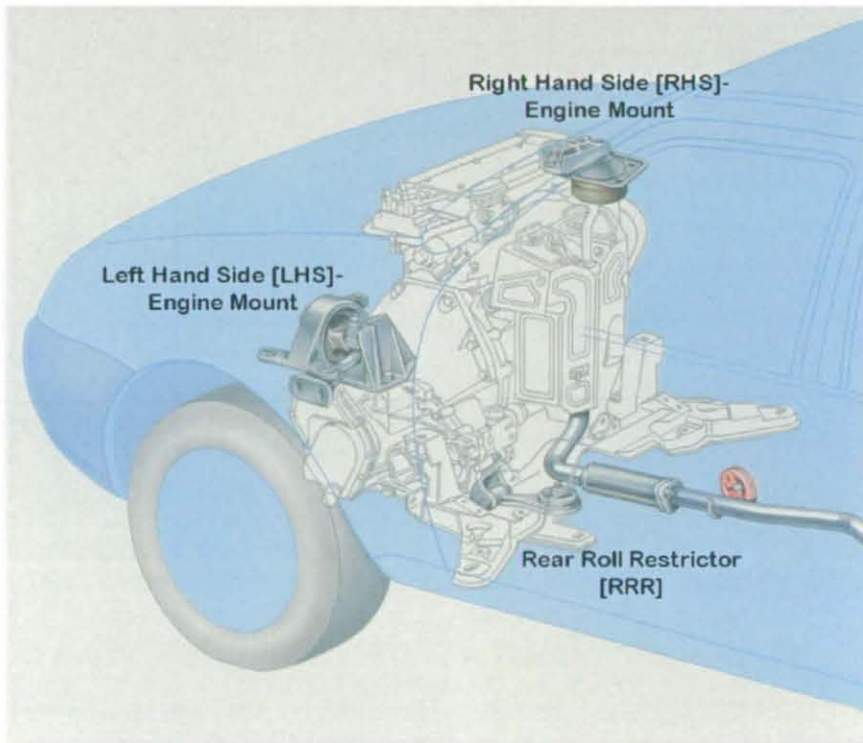


Figure App.6.6 Zetec-SE Powertrain Installation

**Publications**

---

# **Analysis of Engine Main Bearing Excitation by Application of Cranktrain Modelling and Optimization Methods**

**T. Grünert, B. Pfingsthorn, and J. Meyer**  
Ford Motor Co.

**R. Ali**  
Loughborough University of Technology



# Analysis of Engine Main Bearing Excitation by Application of Cranktrain Modelling and Optimization Methods

T. Grünert, B. Pflingsthor, and J. Meyer  
Ford Motor Co.

R. Ali  
Loughborough University of Technology

## ABSTRACT

The study presented in this paper is concerned with the application of a finite element based technique to deal with crankshaft-crankcase interaction. A finite element model of the crankshaft and the crankcase was developed and appropriately reduced. This model was used for a crankshaft optimization, strategy to analyse related effects on the NVH performance with focus on main bearing acceleration.

The crankshaft and the cylinder block were modelled using beam and shell elements with structural and dynamic properties correlated up to 1600 Hz. The interaction between crankshaft and the cylinder block was represented by using non-linear properties. Applying this model, the dynamic crankshaft and engine block behaviour and repercussion on NVH performance was analysed by investigating main bearing acceleration.

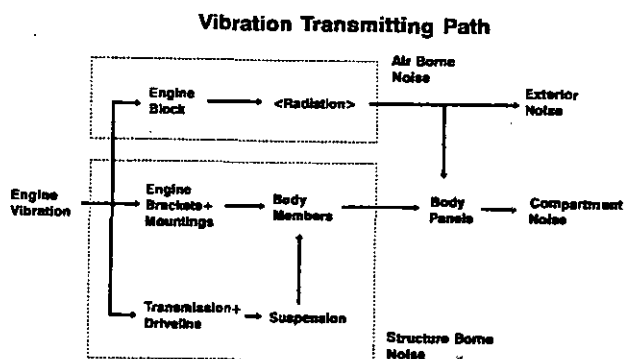
## 1. INTRODUCTION

During the past few years quality requirements of vehicles have changed due to a variety of reasons. Legislation has become increasingly restrictive in terms of absolute measurable noise and emissions. To this is added increased consciousness of the customer towards greater degree of comfort demanding lower overall sound level and vibrations, durability, economy and performance. These demands can be accomplished by optimizing the total vehicle and its subsystems. A great deal of effort is being spent to reduce the absolute noise and vibration level for the optimization of the sound quality.

Since majority of design requirements are conflicting, the development has to aim for the best compromise. This can be achieved more easily and in a cost effective way if changes are affected during the concept phase. This strategy for engine sub-system design requires CAE predictive tools for the analysis of different engine concepts with respect to their NVH behaviour.

This paper deals with the NVH study of a four stroke petrol engine. Vibration and noise phenomenon of the engine originated by the lower crankcase assembly have been studied and factors contributing to overall NVH performance such as excitation mechanism, structural vibration, and noise radiation have been addressed. Coupled behaviour of the engine block/cranktrain has been examined closely for the assessment of the influence of structural changes on the dynamic characteristics of the power train subsystem.

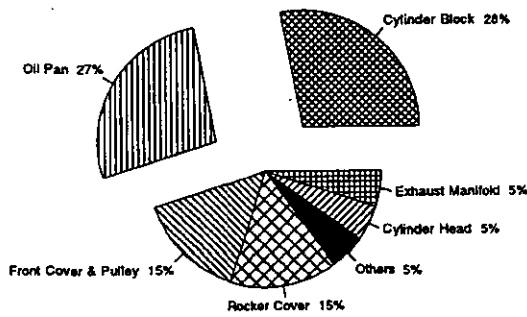
For the generation and transmission of powertrain noise, different noise transmission paths have to be clearly identified. These paths are schematically shown in figure 1.



Vibration Transmission Path

Figure 1

For a typical four cylinder spark ignition engine, running at 4000 rpm with wide open throttle (WOT), the sound energy that the individual components contribute to the total is shown in figure 2.



## Radiated Engine Noise

Figure 2

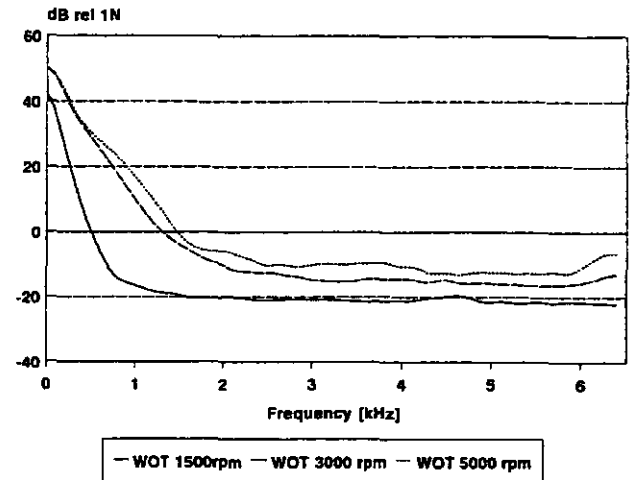
A markedly high contribution is made by the lower part of the crankcase, where the oil pan and the cylinder block approximately have an equal share and together emit more than 50% of the total sound energy. The reason for this is the excitation cylinder block and the oilpan receive from the bearing forces and gas pressure variations. This area is therefore the most effective for optimization of radiated and structure borne noise.

The main direct sources for external excitation of the powertrain are mainly the accessories. These are mounted to the crankcase and radiate noise which excites the engine block surface. The indirect vibration sources can be subdivided into mechanical and combustion oriented excitations. Both paths can be split into groups of cyclic and collisional effects. Collisional excitation is caused by contact changes and impacts of mechanical components following a transition point with no applied resulting force. The cyclic variation in load condition is invoked by the change in combustion pressure and the dynamic forces resulting from the crank slider mechanism. The investigation described here will be confined to the analysis and modelling aspects for the cyclic and collisional excitation forces originated from the crankshaft/crankcase interaction with coupling via the hydrodynamic main bearings.

## 2. DEVELOPMENT OF THE MAIN BEARING FORCING SPECTRUM

For the development of a reliable dynamic finite element model it is necessary to consider the frequency range up to which an accurate system

representation should be guaranteed. It is well known that forcing spectrum of the combustion pressure is of negative slope. A significant excitation amplitude can only be obtained in frequency range of 1500-1600 Hz. To prove this phenomenon, measurements were performed to obtain this data for the engine configuration used within this investigation. The forcing function was developed by measuring the time variant combustion pressure at the spark plug position and performing the necessary Fourier-transformation yielding the exciting forcing spectrum. To allow for different engine speeds, these values were measured for wide open throttle at engine speeds of 1500, 3000 and 5000 rpm. The acquired spectra are shown in figure 3.

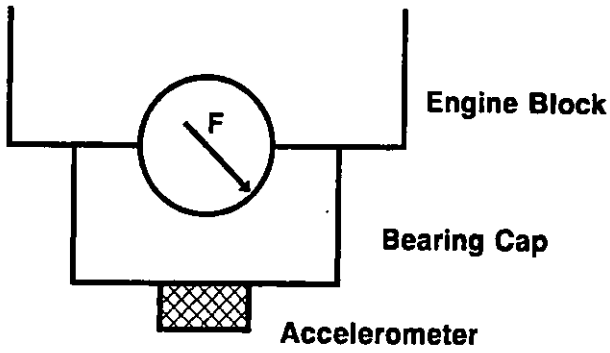


## Combustion Excitation Spectra; Full Load

Figure 3

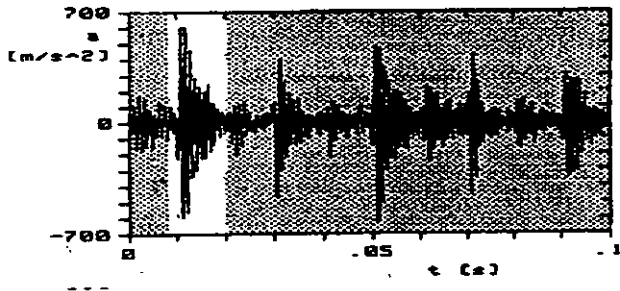
This figure proves the foregoing assumptions. The desirable frequency range of required accuracy for cranktrain components can thus be established with good degree of confidence and can be set to 1800 Hz including a 10% safety margin. The bottom end of the cranktrain/crankcase assembly has to be analysed similarly.

The excitation forcing spectrum at the main bearing is a function of the combustion pressure spectrum. Because of the elasticity of the participating components and the main bearing clearance, the forcing function cannot be developed linearly from the combustion pressure. The actual main bearing forcing function has therefore been measured by obtaining the time dependent accelerations for all principal directions at the main bearing cap number three as shown in figure 4.



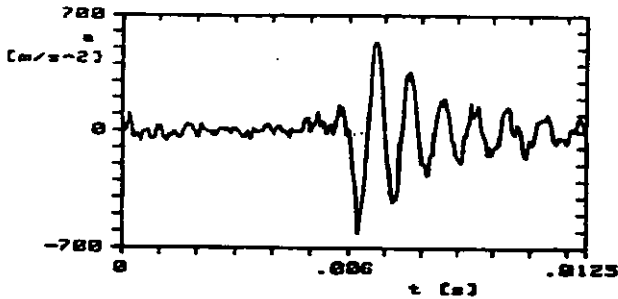
Measurement of Main Bearing Acceleration

Figure 4



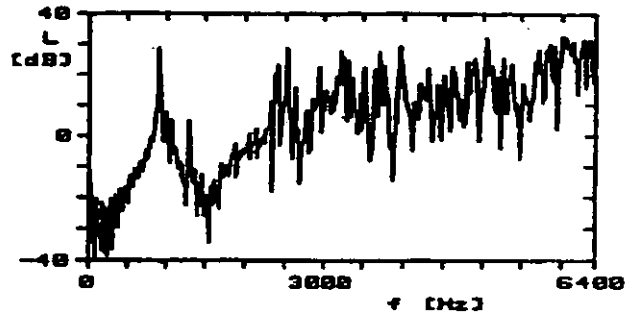
Time Domain Axial Main Bearing Acceleration

Figure 5



Time Domain Axial Main Bearing Acceleration of Single Cycle

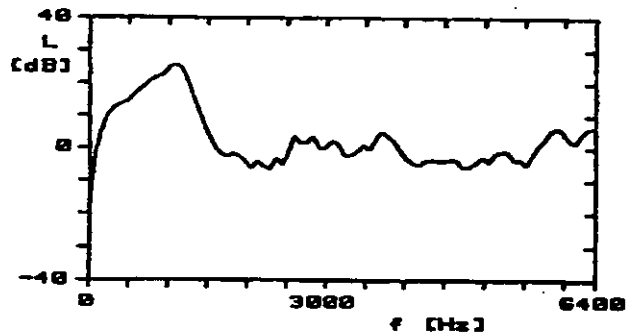
Figure 6



Transfer Function of Acceleration/Force

Figure 7

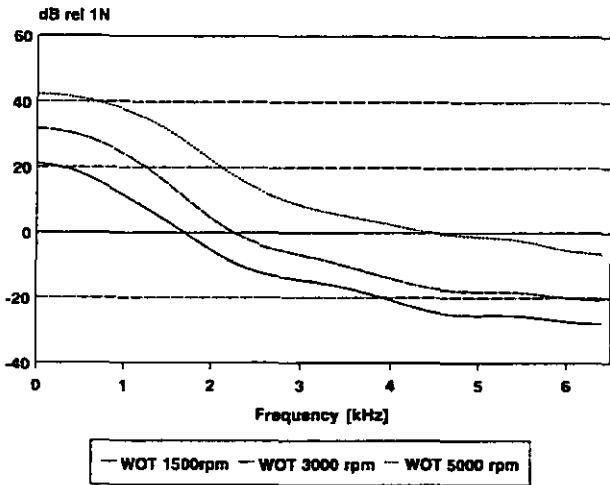
The main bearing accelerations sampled under running conditions are shown in figure 5 and for a single cyclic period in figure 6. The signal shown in figures 6 and 7 is not the main bearing forcing function but the measured response function at the bearing cap surface. The transfer function between the location of measurement and the actual location of forcing within the main bearing must therefore be considered. This transfer function was obtained by applying an impulsive broad-band signal at the main bearing and measuring the response using an accelerometer. The corresponding transfer function between the main bearing surface and the mounted accelerometer is displayed in figure 7. The estimated main bearing forcing spectrum can be obtained by subtracting this function from the developed Fourier-transformed main bearing acceleration function shown in figure 8.



FTDC-Spectrum Acceleration

Figure 8

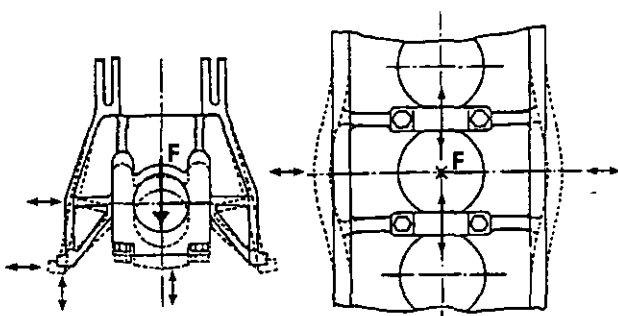
The forcing spectrum for the main bearings shown in figure 9 was obtained by incorporating the three main co-ordinate directions signals into a single acceleration spectrum by utilizing weighted averages.



**Averaged Main Bearing Excitation Spectra**  
**Figure 9**

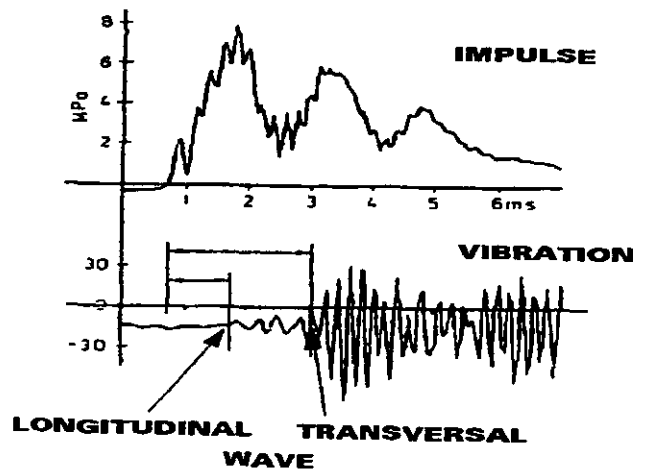
It should be noted that the acquired data has been developed for main bearing number three only and the structural or load distributions may alter the spectrum in amplitude and/or frequency for different bearings. From the measured time domain data for the main bearing acceleration as shown in figures 5 and 6, two sections with unequal vibration behaviour can be identified. Initially a band with high amplitude and steep negative slope occurs followed by an interval of relative low amplitude and less negative slope but with much shorter wave length. It can be assumed that both oscillations result from different effects.

Considering the basic principal response of an engine block loaded at the main bearings, the deformation pattern shown in figure 10 may be assumed.



**Principle Deformation of Cylinder Blocks**  
**Figure 10**

The displayed deformations are representative of static and dynamic loads oscillating with relatively low frequency. If elastic structural response is accounted for, the initial deformations due to the dynamic main bearing loads are followed by harmonic vibrations of the engine block structure oscillating at their corresponding eigen-frequencies. The amplitude and duration as well as the frequency content of the main bearing forcing function will modify the resulting frequency and shape of the structural vibration. For a given excitation spectrum all eigenvalues will not necessarily participate in the vibration, even if the corresponding eigen frequency is within the bandwidth of excitation. If the time dependent acceleration data shown in figure 6 is analysed, it is seen that the high amplitude oscillations occur at a frequency of approximately 1000 Hz and the high frequency oscillation at about 2500-3000 Hz. The relatively high acceleration levels at 1000 Hz can be explained by the natural eigenfrequency of the main bearing caps being close to this value. Measurements and the analytical modal analysis shows that the main bearing caps contribute five different axial modes within this frequency range. The high frequency occurring at about 2500-3000 Hz can be related to a longitudinal wave propagation through the cylinder block which excites the main bearings in a longitudinal direction. Theoretical investigations were carried out to determine the influencing parameters and their weighting factors which affect the structural response of the cylinder block to dynamic excitations. These showed a distinctive sensitivity to longitudinal and transverse bending vibrations at the crankcase walls. In these investigations a vertical force was applied to two adjacent main bearings via a solid shaft. The resulting time variant acceleration signals are shown in figure 11.



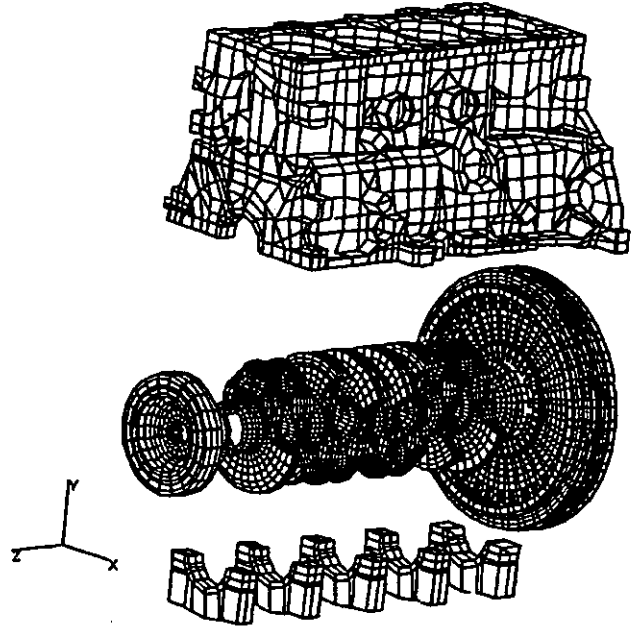
**Surface Vibration of Engine Block under Piston Load**  
**Figure 11**

It is evident that the natural frequencies are in the order of 3000 Hz for longitudinal and 5000 Hz for the transverse oscillations of the crankcase walls. Due to the positioning of the accelerometer at the bearing cap, the transverse vibration in the crankcase walls could not be measured in our test procedure. In view of these results a high acceleration amplitude at frequencies around 1000 Hz and 3000 Hz can be expected. Hence the main bearing acceleration spectra show significant peaks at these frequencies which are not evident at the combustion pressure spectra. This investigation was restricted to the study of the lower part of the crankcase/crankshaft assembly only and the upper limit of the frequency for the dynamic analysis was taken as 1600 Hz.

The crankshaft is another important component for investigations. The rotating crank shaft is subjected to bending and torsional vibrations by forces from combustion and moving masses. Relative to the crankcase, four stroke engines show full and half order excitation. Besides the force vector of orders 0 rotating with the crankshaft, only the vectors of first and third order have significant amplitudes. As a result the upper frequency limit for dynamic investigations of the crankshaft rotating at 6600-7000 rpm can be estimated to be approximately 750-800 Hz.

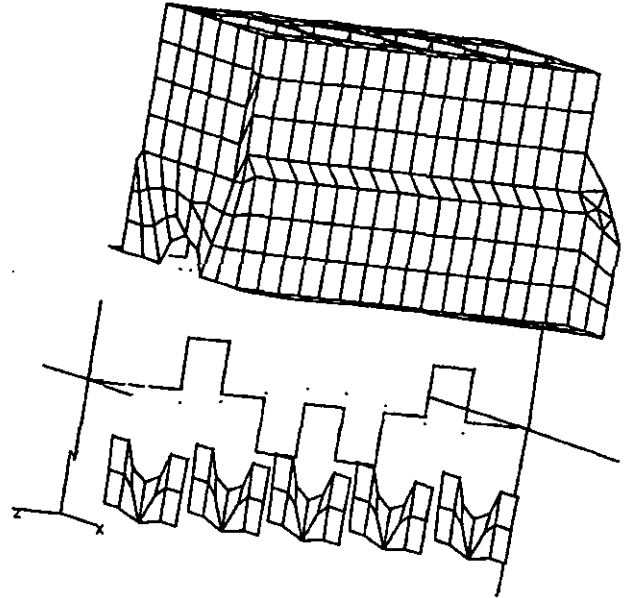
### 3. FINITE ELEMENT MODELLING

A finite element model of the crankshaft and the cylinder block was prepared for the theoretical analysis and was reduced appropriately for dynamic predictions. Since non-linear analyses are cpu-time intensive, attempts were made to reduce the computational effort for solving a single incremental step to the absolute minimum. The energy theorem was applied to reduce the stiffness matrices of the engine block and the crankshaft separately. The mass and inertia matrices were calculated with a standard program and then reduced to the relevant node points. Since this method is not exact, the individual mass matrices were used to adjust the dynamic properties of the components until the results matched those of the reference model and measured results. It is felt that the static reduction (energy method) is appropriate for the above stated frequency range of up to 1600 Hz. The reference and the reduced finite element models are shown in figures 12 and 13 respectively.



Assembled Reference Model

Figure 12



Assembled Reduced Model

Figure 13

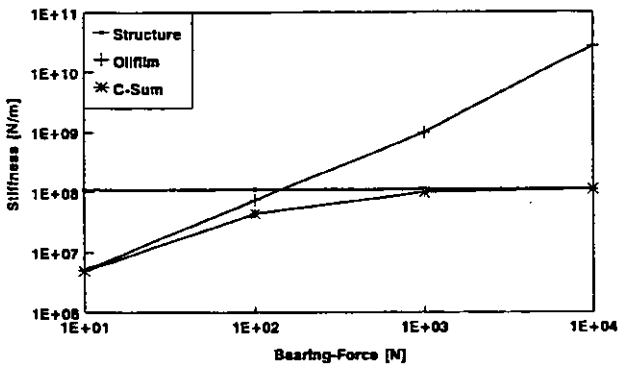
A comparison of the natural frequencies of the engine crankcase obtained from the reference and reduced finite element models is given in the following table.

**COMPARISON OF NATURAL FREQUENCIES OF THE CRANKCASE  
(NATURAL FREQUENCIES - HZ)**

	Reference F.E. Model	Reduced F.E. Model	Measured
1st Torsion Mode	568	621	575
1st Bending Mode	933	919	939
2nd Bending Mode	1039	1370	1295

For the representation of the dynamic behaviour of the crankshaft block system it is necessary to determine the characteristics of the slide bearing. An analysis was carried out for the determination of the hydro-dynamic oil film characteristics of the bearing in the time domain taking into account effects such as eccentricity, bearing force, angular velocity etc. The oil film model was implemented by applying externally derived properties at specific running and load conditions to a simplified model. The hydrodynamic effects were represented as a parallel combination of a non-linear spring and damper. For the calculation of the actual main bearing eccentricities as a function of different applied bearing forces, a table relating the applied load to the eccentricity was developed and from this equivalent spring stiffnesses for a specific load condition were obtained. The equivalent damping coefficient was derived similarly. The oil film stiffness in the main bearing according to the theory of Holland-Lang results in the distribution shown in figure 14.

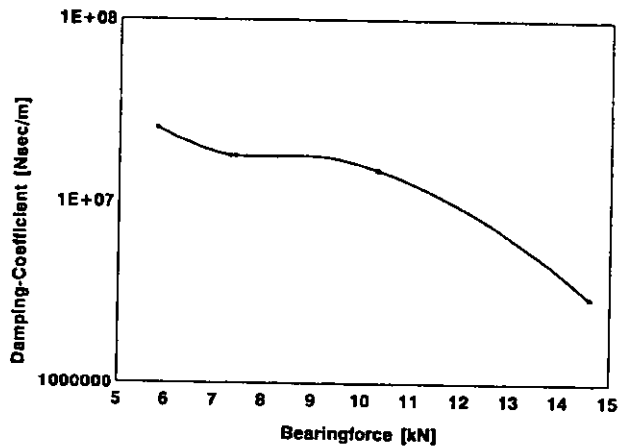
**Comparison of Stiffnesses  
Mainbearing vs Oilfilm**



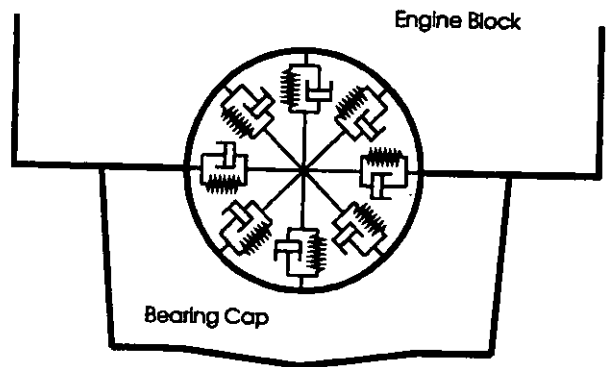
Comparison of Structure and Oilfilm Stiffnesses

Figure 14

The structural stiffnesses shown in figure 14 are developed from a non-linear finite element calculation using the derived models. The oil film properties were calculated under the assumption of infinite stiff bearings. It can be seen that the oil film stiffness is larger than those of the bearings, even in the case of small bearing loads. Since the two stiffnesses are coupled, a simulation by series connection of the two spring rates will not be precise. Considering the acting forces in the main bearings, the bearing stiffness can be approximated by non-linear springs. The relevant spring-rate curve was developed using the models of Holland-Lang. Non-linear effects on the non-pressure side of the bearing in the range of up to 1 kN bearing force were simulated in the theoretical model. The damping is related to the acting force. From measurements and theoretical calculations, the damping coefficients were derived and are plotted in figure 15. It can be seen that the damping of the slide bearing decreases with increasing load. The modelling technique used in the assembled finite-element representation is schematically shown in figure 16.



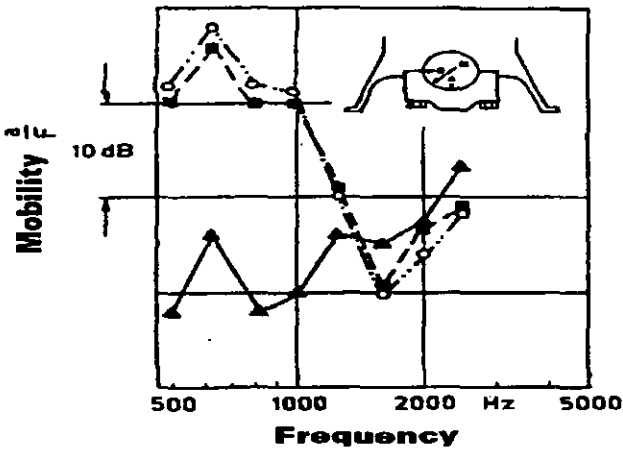
Damping Coefficient under Full Load at 2400rpm  
Figure 15



Oil Film Representation  
Figure 16

#### 4. CRANKCASE-CRANKSHAFT SUB-SYSTEM DESIGN OPTIMIZATION

The idea of this optimization approach is to minimize the main bearing forces by variation of the counterweights. Ignoring modifications of the combustion process as one possible design parameter for main bearing excitation improvements, the design parameters crankshaft and crankcase stiffness and crankshaft balancing are possible variables for an optimization procedure. However modifications to the crankcase or crankshaft stiffness cannot be easily achieved. Crankshaft balancing optimization seems to be the easiest strategy to achieve an optimum crankcase - crankshaft design in term of main bearing excitation. Recovering the transfer functions of the engine under different loading directions at the main bearings crankcase mobility graphs as shown in figure 17 can be obtained.

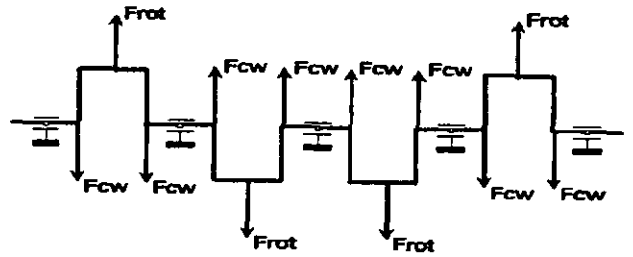


Transfer Behaviour of the Engine Block

Figure 17

From the mobility transfer functions it can be assessed that there are areas at different angular positions within the main bearing showing a significant sensitivity to bearing loads. The pertinent design question is now the unbalance which needs to be applied at the counterweights to achieve the goal of minimizing the main bearing loads at those crank angles which are most sensitive. It is clear that an optimization strategy has to account for the crankcase and crankshaft stiffness as well as the combustion and inertia dependent loads to achieve an optimum design. Optimizing the static balancing of the crankshaft only may lead to misinterpretations as the dynamic behaviour may be worse at specific crankangles. Hence crankshaft and crankcase stiffness properties derived from FEM models were incorporated in the optimization routine to account for stiffness variation. This effect is not negligible as the main bearing loads

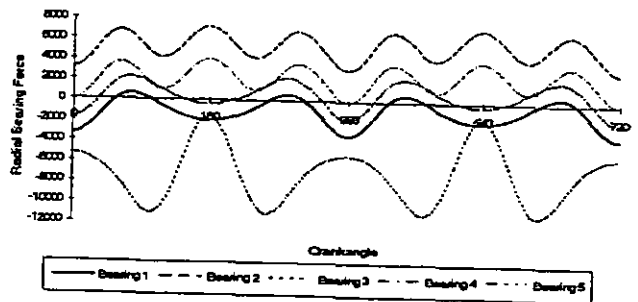
are varying due to unsymmetrical stiffness and mass properties. An idealized system is shown in figure 18.



Crankshaft System Approximation

Figure 18

Using this set up a set of equations describing the crankshaft as a beam subjected to various forms of loading were established. Using standard theory, distortions caused by each loading at all main bearings were calculated and the counterweights were determined to minimize the main bearing loads for the user defined crankangle. The radial bearing forces prior to optimization are shown in figure 19 for the centrifugal loads and in figure 20 for the fired engine loads. Comparing the results obtained by the centrifugal load calculation prior to and after optimization, a clear advantage of the optimized design proposal can be seen.

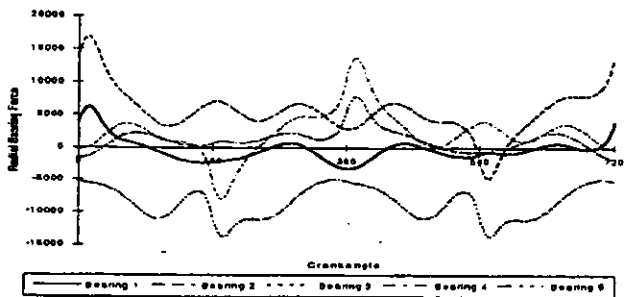


Radial Bearing Force (prior Optimization)  
[Centrifugal Loads]

Figure 19

## 5. CONCLUSIONS

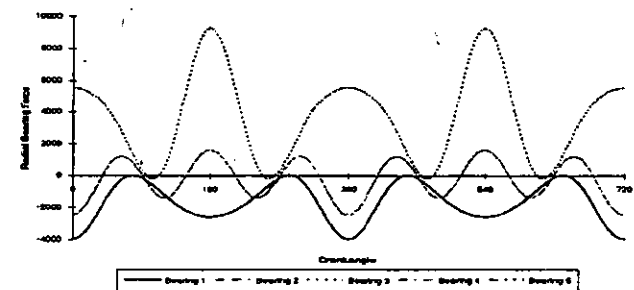
The adequate treatment of a crankshaft balancing procedure is very important in the development of optimized and harmonised crankshaft-crankcase subsystems. The approach of dynamic balancing discussed here shows a dramatic influence on the main bearing loads under most running conditions. The coupling of this strategy with the mass-elastic model description, developed for dynamic, noise and sensitivity analyses for the definition of the most critical bearing positions, exhibits a major advantage over the application of individual approaches to achieve the best design proposal for the cranktrain system.



Radial Bearing Force (prior Optimization)  
[Engine Firing & Centrifugal Loads]

Figure 20

The total bearing loads are shown in figure 21 under engine running condition. The radial forces are optimized to match the most sensitive angular position of the crankcase for all main bearings. The averaged load could be reduced further, but this supplemental reduction was rejected for matching the lowest bearing force to the sensitive crank angle of main bearing 3. It should be noted that this optimization approach can be applied for one specific running condition only being linked to a fixed engine speed and load condition.



Radial Bearing Force (after Optimization)  
[Centrifugal Loads]

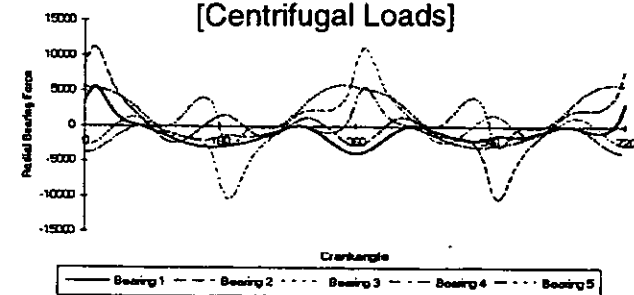


Figure 21

Radial Bearing Force (after Optimization)  
[Engine Firing & Centrifugal Loads]



# **The Whirl Modes of Vibration of Crankshafts in Powertrain Assemblies**

**Thomas Grünert, FORD-Werke AG  
and  
Dr. Rafat Ali, Loughborough University  
United Kingdom**

97VR013

## **Abstract**

The study presented in this paper is concerned with the development and application of a finite element based technique to deal with complex modes of powertrain assemblies. A finite element model of the crankshaft and the crankcase was developed and coupled through a reduced description of the hydrodynamic bearing properties. This model was used to establish the response of the rotating crankshaft assembly. Applying these an analysis of the vibrations of the complete powertrain assembly predicts the natural frequencies of the forward and reverse whirals and the complex deflection shapes at the whirling speeds. It is shown that different flywheel and crankshaft designs have a significant influence on the frequencies, system response and amplitudes of the whirling modes. The performed analyses indicate that a deletion of the properties of rotating structures, namely the gyroscopic and differential stiffness effects, will alter the results significantly up to 40% compared to corresponding modes of rested systems.

## **Introduction**

In the past, quality requirements of vehicles have changed due to a variety of reasons. While legislation has become increasingly restrictive in terms of absolute measurable noise and emissions, increased consciousness of the customer is added towards greater degree of comfort demanding lower overall sound level and vibrations. These demands can be accomplished by optimising all the sub-systems of a vehicle and primarily the powertrain assembly. The design of powertrain components is commonly restricted by numerous other design requirements, such as performance and durability et al. Therefore usually vibration sources are not addressed directly, but the vibration transmissibility of the participating sub-systems is of major interest and applied to many experimental and theoretical studies under optimisation purposes /8;9/. For the generation and transmission of powertrain noise, different noise transmission paths have to be clearly identified and can be described as the 'Air-Borne' and 'Structure-Borne' noise paths. These paths and the contributing components of vibration transmission are schematically shown in figure 1. The excitation created by the combustion process is transferred through the cranktrain assembly and engine block to the surfaces and the powertrain mounts. Within the dynamic response of the cranktrain the crankshaft contributes significantly to the powertrain structural and air borne noise. This component is therefore of interest in many experimental and theoretical optimisation processes.

The resonance of the whirling modes of a crankshaft assembly is often suspected as one cause for bearing fatigue failures and excessive 'bearing noise'. Several names are given to this phenomenon, including 'roughness', 'bearing trash', and 'rumble'/7/. A more complete knowledge of the crankshaft vibration and the contributing parameters is a useful step towards an understanding of the sub-system response.

Another effect contributing to the noise phenomena is the occurrence of two or more modes at the

same frequency accompanied by resonance peaks at the powertrain mounts and surfaces. With varying eigenfrequencies of the crankshaft assembly due to changes of engine speeds, mode separation is of increasing interest to avoid local booms and increased acceleration levels /1/.

This paper deals with the vibration study of a four stroke, four cylinder petrol engine. The vibration phenomena of the engine and powertrain have been studied accounting for excitation originated by the lower half of the engine. This considers a three-dimensional crankshaft structure, which may vibrate simultaneously with several other components. Contributing factors to the vibration receptance are presented such as design alternatives, the necessity of representing the total powertrain assembly, and modelling guidelines.

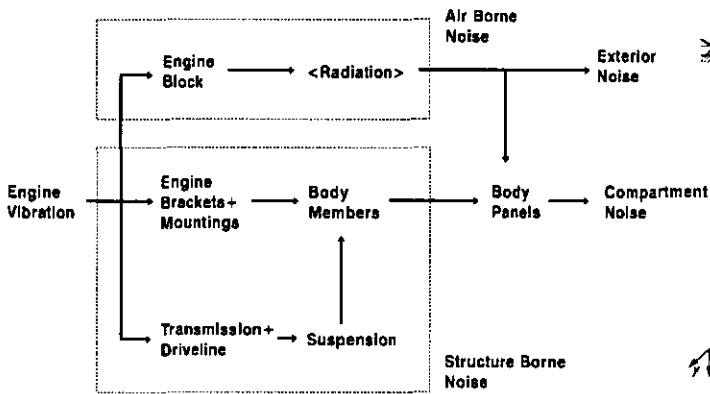


Figure 1: Noise Transmission Path

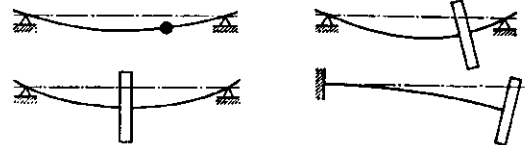


Figure 2a: Rotor Principles

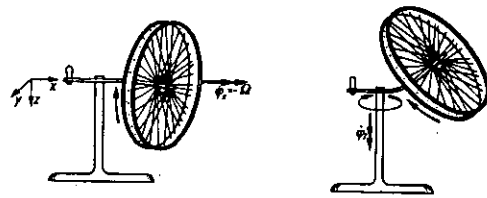


Figure 2b: Gyroscopic Principle

### Theoretical Work on the Vibration of Rotating Structures

A complete theoretical discussion of the analysis of rotating structures carrying a flywheel is far beyond the scope of this work /2/. However, it is essential for the understanding to refer to selected topics in order to follow the development of the analyses and the interpretation of the results given in this paper. The physical properties of a rotating crankshaft within an elastic structure are similar to those of a 'Laval-Rotor' and are straightforward. These will not be described herein, but a brief introduction to the differences is given. The major difference can be illustrated as shown in figure 2a and is defined with an angular displacement of the rotating disk. The gyroscopic effect occurs, if the rotating disk is deflected to a direction perpendicular to the rotation axis (figure 2b). This effect is based on the principle of the conservation of the moment of momentum and increases with increasing angular velocity and angular moment of inertia. The components of the moment of momentum can be written for axis-symmetric systems as shown in equation (1). While the equilibrium of internal and external forces and moments must be applied, we write the assembled matrix equation as given in (2). Using the assembly of the rotating disk and the carrying structure we derive the complete set of equations in matrix formulation (3). Converting the translations and rotations to complex numbers and applying some geometrical relationship, equation (4) is received. The homogeneous solution of this problem can be obtained by solving the non-trivial solution of equation (4). This is given, if the determinant equals to zero as shown in equation (5). This leads within this example to a fourth order problem with corresponding four different eigenfrequencies  $\omega_v$  being dependent on the following characteristic system properties:  $[m, \Theta_a, \Theta_p, c_{ik}]$ . A typical solution for this problem is shown in figure 3a.

The so far described axis-symmetric systems are constrained either by rigid bearings or by isotropic bearings with stiffness properties being included in the shaft stiffness properties  $c_{ik}$ . Shafts supported by anisotropic bearings, like engine blocks, show a different system behaviour in the major

co-ordinate directions. The assembly of the matrix equation applying complex formulation as used in (4) is no longer allowed and the perceived set of equations can be written in matrix form as shown in (6). Again, this problem is solved, if the non-trivial solution [Det |A| = 0] can be obtained. A typical solution for this problem is shown in figure 3b.

$$\begin{aligned} L_x &= \Theta_p \dot{\phi}_{Sx} \\ L_y &= \Theta_a \dot{\phi}_{Sy} \\ L_z &= \Theta_a \dot{\phi}_{Sz} \end{aligned} \quad (1)$$

$$\begin{bmatrix} F_z \\ M_y \\ F_y \\ M_z \end{bmatrix} = \begin{bmatrix} m & 0 \\ 0 & \Theta_a \\ & m & 0 \\ & 0 & \Theta_a \end{bmatrix} \begin{bmatrix} \ddot{z}_s \\ \ddot{\phi}_{sy} \\ \ddot{y}_s \\ \ddot{\phi}_{sz} \end{bmatrix} + \begin{bmatrix} 0 & 0 \\ 0 & -\Omega\Theta_p \\ 0 & 0 \\ 0 & +\Omega\Theta_p \end{bmatrix} \begin{bmatrix} \dot{z}_s \\ \dot{\phi}_y \\ \dot{y}_s \\ \dot{\phi}_z \end{bmatrix} \quad (2)$$

$$\begin{bmatrix} m & 0 \\ 0 & \Theta_a \\ & m & 0 \\ & 0 & \Theta_a \end{bmatrix} \begin{bmatrix} \ddot{z}_s \\ \ddot{\phi}_{sy} \\ \ddot{y}_s \\ \ddot{\phi}_{sz} \end{bmatrix} + \begin{bmatrix} 0 & 0 \\ 0 & -\Omega\Theta_p \\ 0 & 0 \\ 0 & +\Omega\Theta_p \end{bmatrix} \begin{bmatrix} \dot{z}_s \\ \dot{\phi}_y \\ \dot{y}_s \\ \dot{\phi}_z \end{bmatrix} + \begin{bmatrix} c_{11} & c_{12} \\ c_{12} & c_{22} \\ & c_{11} & -c_{12} \\ & -c_{12} & c_{22} \end{bmatrix} \begin{bmatrix} z_w \\ \phi_{wy} \\ y_w \\ \phi_{wz} \end{bmatrix} = 0. \quad (3)$$

$$\begin{bmatrix} m & 0 \\ 0 & \Theta_a \end{bmatrix} \begin{bmatrix} \ddot{r}_w \\ \ddot{\phi}_w \end{bmatrix} + \begin{bmatrix} 0 & 0 \\ 0 & -j\Theta_p\Omega \end{bmatrix} \begin{bmatrix} \dot{r}_w \\ \dot{\phi}_w \end{bmatrix} + \begin{bmatrix} c_{11} & -jc_{12} \\ jc_{12} & c_{22} \end{bmatrix} \begin{bmatrix} r_w \\ \phi_w \end{bmatrix} = \Omega^2 \begin{bmatrix} m & \varepsilon & e^{j\beta} \\ (\Theta_a - \Theta_p)\alpha & e^{j\gamma} & \end{bmatrix} e^{j\Omega t} \quad (4)$$

$$\begin{vmatrix} -m\omega_v^2 + c_{11} & -jc_{12} \\ jc_{12} & -\Theta_a\omega_v^2 + \Theta_p\Omega\omega_v + c_{22} \end{vmatrix} = 0 \quad (5)$$

$$\begin{bmatrix} m & 0 \\ 0 & \Theta_a \\ & m & 0 \\ & 0 & \Theta_a \end{bmatrix} \begin{bmatrix} \ddot{z}_w \\ \ddot{\phi}_{wy} \\ \ddot{y}_w \\ \ddot{\phi}_{wz} \end{bmatrix} + \begin{bmatrix} 0 & 0 \\ 0 & -\Omega\Theta_p \\ 0 & 0 \\ 0 & +\Omega\Theta_p \end{bmatrix} \begin{bmatrix} \dot{z}_w \\ \dot{\phi}_{wy} \\ \dot{y}_w \\ \dot{\phi}_{wz} \end{bmatrix} + \begin{bmatrix} c^z_{11} & c^z_{12} \\ c^z_{12} & c^z_{22} \\ & c^y_{11} & c^y_{12} \\ & c^y_{12} & c^y_{22} \end{bmatrix} \begin{bmatrix} z_w \\ \phi_{wy} \\ y_w \\ \phi_{wz} \end{bmatrix} = \Omega^2 \begin{bmatrix} m\varepsilon \cos(\Omega t + \beta) \\ (\Theta_a - \Theta_p)\alpha \sin(\Omega t + \gamma) \\ m\varepsilon \sin(\Omega t + \beta) \\ (\Theta_a + \Theta_p)\alpha \cos(\Omega t + \gamma) \end{bmatrix} \quad (6)$$

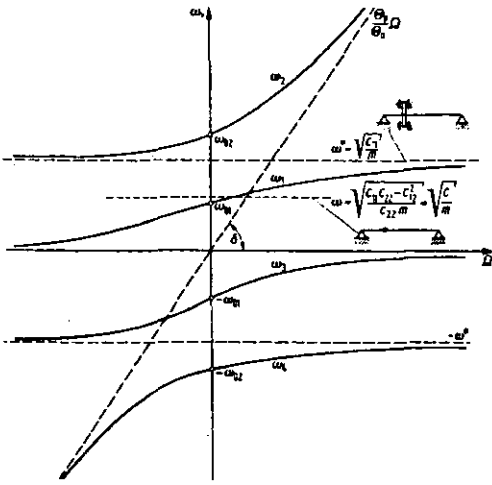


Figure 3a: Eigenfrequencies of Isotropic System

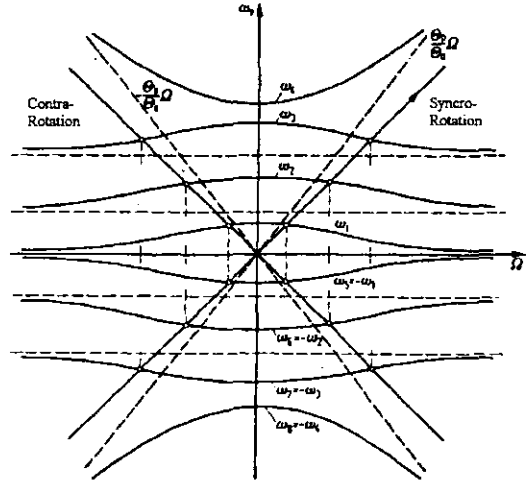


Figure 3b: Eigenfrequencies of Anisotropic System

The theory described so far covers circular components only. But a crankshaft is a non-circular system and even the flywheel can be of non-circular shape (i.e. 'asymmetrical flywheel' /3/). Assuming that this systems can be described by using two different stiffness properties for the principle directions, we perceive a second order self-excitation due to the oscillating change of stiffness causing resonance. Describing the problem in a stationary reference system, the differential equations are still linear but the stiffness properties are oscillating. This formulates so called 'Mathieu Differential Equations'. Applying this to the crankshaft assembly, the system differential equation is shown in (7) applying  $\hat{c}_{\eta}^k$  as the oscillating stiffness property for the rotating shaft. The solution of this set of equations results in four eigenvalues being either a real or imaginary number. Those solutions having a positive real component of the eigenvalue are in the unstable response domain. This instability can be expressed as a function of the relationship  $\mu$  between the stiffness properties  $c_{\eta}$  and  $c_{\xi}$  as described in (8) defining the eigenfrequency  $\omega$  as a mean value between the corresponding upper and lower eigenfrequencies  $\omega_{\eta}$  and  $\omega_{\xi}$  of the asymmetric system. A principle 'stability chart' is shown in figure 4a as a function of  $\mu$  ( $0 < \mu < 1$ ) and in figure 4b for a constant relation  $\mu$  for varying shaft speeds  $\Omega$ .

$$\begin{bmatrix} m & 0 \\ 0 & \Theta_a \end{bmatrix} \begin{bmatrix} \ddot{z}_w \\ \ddot{\varphi}_{wy} \end{bmatrix} + \begin{bmatrix} 0 & 0 \\ 0 & -\Omega \Theta_p \end{bmatrix} \begin{bmatrix} \dot{z}_w \\ \dot{\varphi}_{wy} \end{bmatrix} + \begin{bmatrix} m & 0 \\ 0 & \Theta_a \end{bmatrix} \begin{bmatrix} \ddot{y}_w \\ \ddot{\varphi}_{wz} \end{bmatrix} + \begin{bmatrix} 0 & 0 \\ 0 & +\Omega \Theta_p \end{bmatrix} \begin{bmatrix} \dot{y}_w \\ \dot{\varphi}_{wz} \end{bmatrix} \quad (7)$$

$$\begin{bmatrix} c^z_{11} + \hat{c}^z_{\xi} & c^z_{12} + \hat{c}^z_{\xi} \\ c^z_{21} + \hat{c}^z_{\xi} & c^z_{22} + \hat{c}^z_{\xi} \\ c^y_{11} + \hat{c}^y_{\eta} & c^y_{12} + \hat{c}^y_{\eta} \\ c^y_{21} + \hat{c}^y_{\eta} & c^y_{22} + \hat{c}^y_{\eta} \end{bmatrix} \begin{bmatrix} z_w \\ \varphi_{wy} \\ y_w \\ \varphi_{wz} \end{bmatrix} = \Omega^2 \begin{bmatrix} m \varepsilon \cos(\Omega t + \beta) \\ (\Theta_a - \Theta_p) \alpha \sin(\Omega t + \gamma) \\ m \varepsilon \sin(\Omega t + \beta) \\ (\Theta_a + \Theta_p) \alpha \cos(\Omega t + \gamma) \end{bmatrix}$$

$$\mu = \frac{c_{\eta} - c_{\xi}}{c_{\xi} + c_{\eta}} = \frac{\omega_{\eta}^2 - \omega_{\xi}^2}{2\omega^2} \quad (8)$$

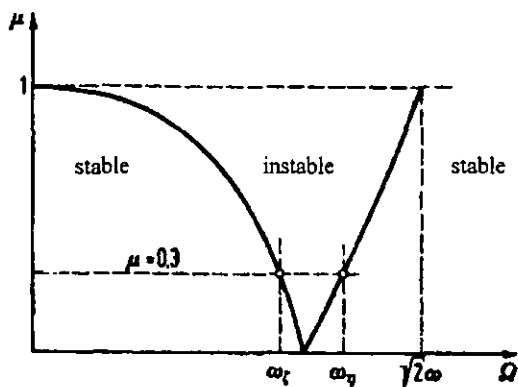


Figure 4a: Stability Chart

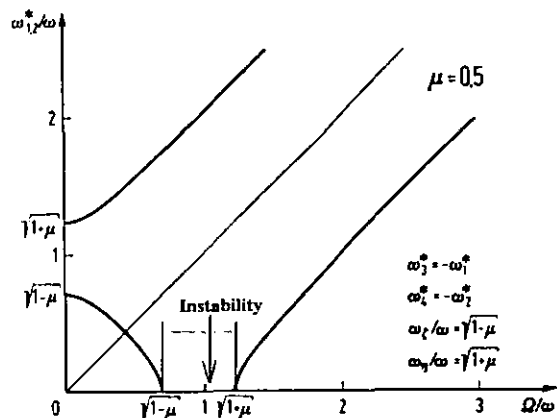


Figure 4b: Stability Chart

### Analytical Method

Two finite element assemblies were prepared for the analysis embodying the described theory. The crankshaft system is shown in figure 5a for the design alternative using a conventional flywheel. Within many publications crankshaft modelling techniques were described to be fully acceptable applying a beam representation with concentrated masses only, since it can describe most phenomena /4/. Studies of the authors showed, that this modelling technique can not be applied here, as the perceived differences between a beam and a full three-dimensional description are in the order of approximately more than 15% for the eigenvalues (figure 11; /6/) and modeshapes. The greatest differences could be obtained for those flywheel and pulley whirling modes being dominated by the bending properties of the last and first web. Other major influencing effects are the crankshaft-crankcase coupling through the journal bearings and the representation of the stiffness properties of the bearing housing within the engine block.

The assembled powertrain system is shown in figure 5b consisting of 370000 elements and 280000 nodes (950000 DOF). Since the whirling modes of the crankshaft assembly are expected to be in the frequency range of other attached components, a complete representation of almost all powertrain components is required within this analysis to study the association between crankshaft whirling and component modes. From experience it is known, that crankshaft whirling modes as a function of engine speed may influence or overlay other component modes, i.e. powertrain mount or accessory modes, quite significantly. As powertrain mount resonances are one criterion for increased structure borne noise (see figure 1), decoupling and mode separation of crankshaft whirling and component modes are the most effective countermeasures.

For the representation of the dynamic behaviour of the crankshaft block system it is necessary to determine the characteristics of the slide bearing. An analysis was carried out for the determination of the hydro-dynamic oil film characteristics of the bearing in the time domain taking into account effects such as eccentricity, bearing force, angular velocity etc.. The oil film model was implemented to describe the stiffness and damping properties by applying the externally derived attributes at specific running and load condition using an individual 'look-up' table for each radial and axial bearing.

Within a comparative study it was observed that the structural damping properties, not considered in other investigations or publications, have some influence on the eigenfrequencies of the system. But, as in most mechanical systems, the effect of damping on the eigenfrequencies is not great and the effect tends to be of lower significance compared to the "damping influence" of the gyroscopic effect. Beside this, damping was introduced to be prepared for later analyses applying excitation forces to the system. The property validation of the modelled components with test results is not described nor discussed here, as this is a standard technology /5/.

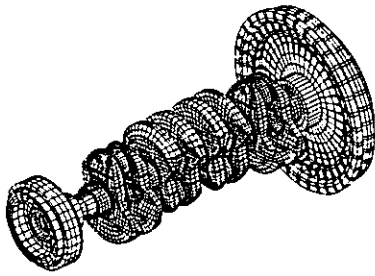


Figure 5a: Crankshaft Assembly

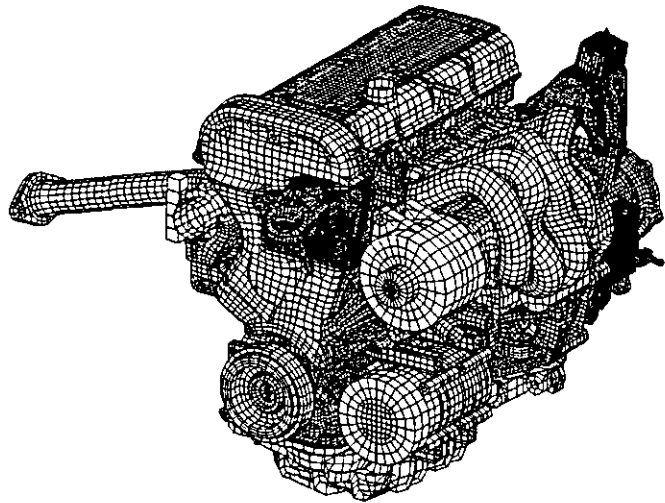


Figure 5b: Powertrain Assembly

### Analysis Results

The first series of studies were carried out on a stand-alone crankshaft assembly (figure 5a) with corresponding bearing and isotropic crankcase stiffness properties being derived from external analyses. This enables to perform fast and easy methodology validation and first principle studies on the system responses.

One of the first studies was a simple sensitivity investigation of the dependence of the first whirling mode on the crankcase stiffness properties. A clear insignificance can be obtained for the modal response, as the frequency variation is negligible for possible errors in modelling accuracy of the crankcase stiffness. This indicates, that principle studies can be performed with that kind of simple system representation, if the boundary conditions are set with care and respect to externally derived properties. The error to be accepted by simplified bearing and engine block representation is below almost 3-5%.

The results from this first study are described in figure 6a for a conventional flywheel design showing the expected complex conjugate solutions. The real component of the solution describing the amount of damping at specific frequencies is almost negligible. An additional effect, not mentioned yet, is the 'static' pre-load induced by the inertia forces of the rotating system which can be compared with a pre-stressed system. This effect is represented by an updated stiffness matrix accounting for the additional required load to deform the pre-stressed system. In matrix terminology, this stiffness increase is called 'Differential Stiffness' and is numerically added to the standard stiffness matrix. Accounting for this effect, differences in eigenvalues are obtained being in the order of averaged 2%. The maximum change could be acquired with 7% at the lowest whirling eigenfrequencies at high engine speeds. Especially on the first two flywheel whirling modes the differential stiffness effect has an increasing positive offset implication on the frequency changes with respect to engine speed as shown in figure 6a. Due to the changing frequencies of the whirl modes it is possible that these modes cross the frequency range of modes of constant frequency. This induces a slight deterioration of both modes within this speed range. Crankshaft longitudinal and torsional modes are not varying with engine speed and the corresponding changes in eigenvalues are negligible. The analysis of the eigenvalues of the crankshaft assembly with flexible flywheel exaggerates a similar effect but at lower frequencies due to the reduced axial and bending stiffness of the flex-plate (figure 6b).

One significant difference is received from the lowest flywheel whirling mode showing an increase in eigenfrequency throughout the engine speed range compared with a frequency decrease of the standard flywheel assembly. From equation 5 it is obvious that the relation of  $\Theta_a$  and  $\Theta_p$  is driving

the characteristic solution of the system. Hence,  $\Theta_a$  and  $\Theta_p$  are dependent on the geometrical design of the crankshaft, but also dependent on the whirling centre of the inertia. With the flexible flywheel this centre is located next to the centre of gravity of the flywheel, while the conventional assembly is whirling about the centre of the last web. The axial moment of inertia  $\Theta_a$  is consequently smaller for the oscillating component of the flywheel inertia and hence result in an increase in eigenfrequency with increasing engine speed compared to the standard flywheel assembly. However, we find the lowest eigenfrequency of the flexible flywheel assembly next to the first order engine speed frequency ensuing possible resonance during the engine speed up.

The relation of the vertical and normal displacement at the pulley and flywheel are shown for the whirling modes only in figure 7a for the conventional and in figure 7b for the flexible flywheel. The diversion describes the shape of the whirling modes. A value of zero indicates that the vibration is a simple in-plane oscillation. With increasing values a more and more elliptical orbit can be perceived, which finally becomes a circular orbit at 100% diversion representing that the displacements in and normal to a co-ordinate system rotating with the crankshaft are of the same magnitude. Under specific circumstances one can discover a diversion of more than 100% representing whirling modes becoming elliptical again, being perpendicular to the original oscillation. This is influenced by modes being coupled with these whirling modes. The torsional and axial modes of the crankshaft assembly are not represented here, as these modal shapes are influenced marginally only. Studying the whirling modes of the standard and flexible flywheel in detail, one can obtain a clear difference between the two designs. The whirling modes of the conventional flywheel are coupled with the crankshaft vibration. This induces that the transformation from simple oscillating to whirling modes can be noticed throughout the entire engine speed range. Whereas the flexible flywheel is decoupled from the crankshaft vibration and starts to whirl on a nearly perfect circular orbit at relatively low engine speeds. While whirling refers to the bent shape of the crankshaft as it rotates with the coupled conventional flywheel, this introduces high bending stresses at the last web and leads to possible crankshaft failures.

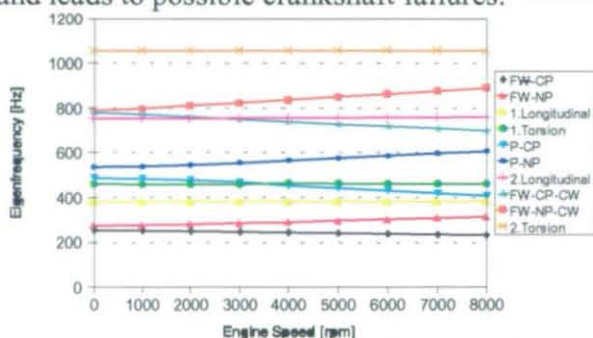


Figure 6a: Conventional Flywheel Eigenfrequency

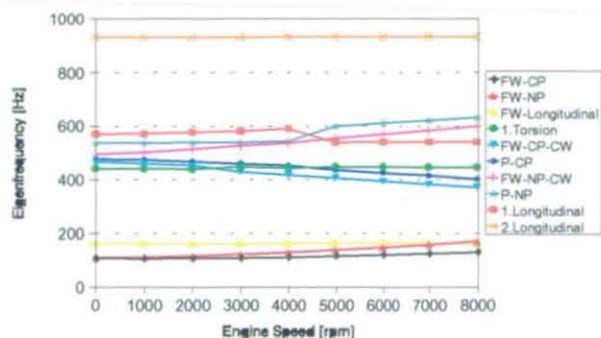


Figure 6b: Flexible Flywheel Eigenfrequency

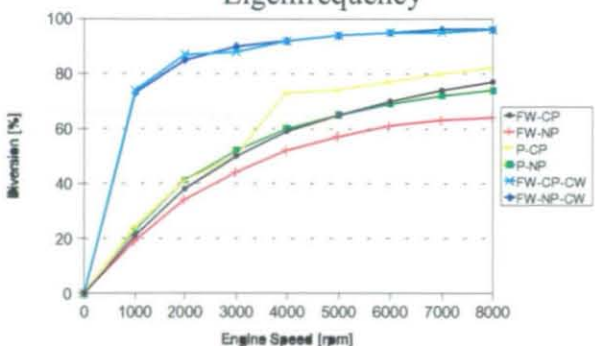


Figure 7a: Conventional Flywheel Diversion

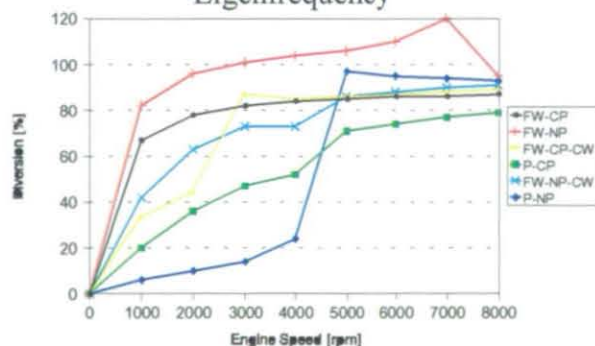


Figure 7b: Flexible Flywheel Diversion

Applying a decoupled flexible flywheel, these bending stresses are reduced significantly combined with a reduction of the stabilising effect from the coupled inertia. This increases the sensitivity of the crankshaft to vibrate and deform under operating loads and therefrom to excite the main bearings of the engine block. An interesting point about the design of the flexible flywheel is that the

axial flexibility appears to be relatively unimportant for the modal shapes and engine block excitation.

Applying the theory of asymmetrical rotors with anisotropic bearings, a fully assembled powertrain can be studied for whirling modes of the rotating crankshaft and coupled vibrations of the crankshaft and other accessories. The acquired whirling modes of the crankshaft assembly are detailed in figure 8a. As derived in (7) and shown in figure 3b, the expected eight eigenvalues of the anisotropic supported crankshaft are obtained. This leads to doubled solutions at identical eigenfrequencies. Hence, only four different flywheel and pulley modes are displayed in figure 8a. Within this configuration, no region of instability could be perceived. The longitudinal oscillation of the crankshaft is not shown, as these are influenced by the axial stiffness of the carrying structure. The shown torsional vibration are affected by the position of the crankshaft as even torsional vibration of cranked structures induce slight bending vibration. Additionally, a minor influence of the pulley vibration could be detected at the lower engine speed range. The derived eigenvalues vary between an upper and lower limit being defined by the anisotropic casing stiffness properties as shown in figure 8b. The derived differences in eigenvalues between the vertical and lateral angular position for the in-plane direction of the crankshaft tend to fade away with increasing engine speed approaching a common asymptote with the results gained from an isotropic bearing description. The results within the perpendicular crankshaft plane show a significant difference compared to the isotropic bearing definition at even high engine speeds. But again, differences are fading away for the vertical and lateral direction, because the gyroscopic effect is increasing with engine speed and becomes finally much greater than the influence of the varying engine block stiffness.

Studying the animation results of the coupled crankshaft-crankcase-assembly no major significant change in modal shapes could be gained compared with the isotropic bearings analysis supporting the philosophy that the main bearing structure is following the crankshaft deformation. The overall engine block vibration is negligible in vertical direction, while a significant vibration can be gained in the lateral direction due to the reduced system immanent stiffness.

Apart from flywheel design parameters the most important variable for influencing the whirling modes is the control of the local deflection at either the first or last crankshaft web. Analyses indicate that local deflections of the crankcase and bearing caps account for a significant part of the whirling amplitudes. The two most practical solutions are: stiffening of the support of the first and last bearing within the crankcase and thickening the first and last crankshaft web.

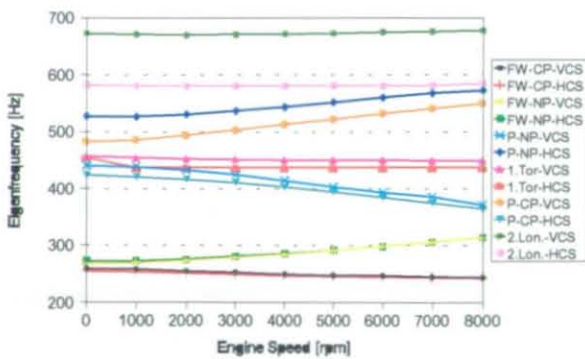


Figure 8a: Crankshaft Whirling Modes in Powertrain Assembly

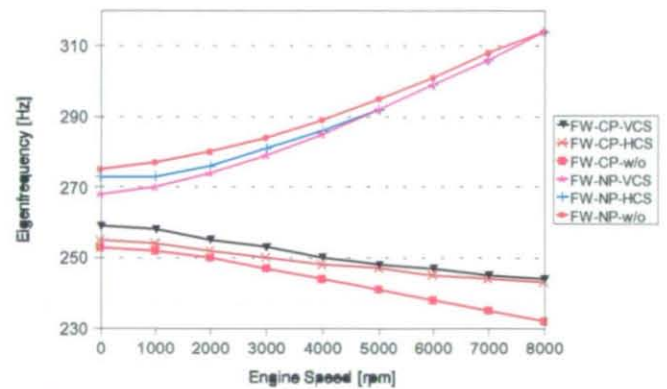


Figure 8b: Isotropic vs. Anisotropic Supported 1<sup>st</sup> Whirling Modes

Recovering that crankshaft whirling modes, changing with engine speed, may influence or overlay multiple other component modes, one typical example is given in figure 9a and b showing a combined crankshaft and accessory mode. Some of the occurring modes being influenced by the first crankshaft whirling mode are given in table 1. While the lowest whirling resonance influences the global powertrain eigenfrequency only, it is obtained that the accessories and especially the powertrain mounts are influenced at higher frequencies or engine speeds respectively. This will result in increased powertrain mount vibration and hence increased structure borne noise. A typical example



of the powertrain mount response spectra is given in figure 10 with whirling modes of this pre-optimised design exhibiting a significant contribution to the overall response level. This testifies the necessity to apply the derived method and study the whirling modes of the powertrain assembly to reduce the vibration and noise level of a powertrain.

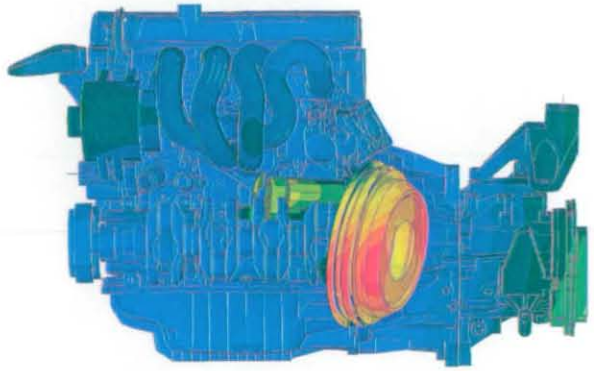
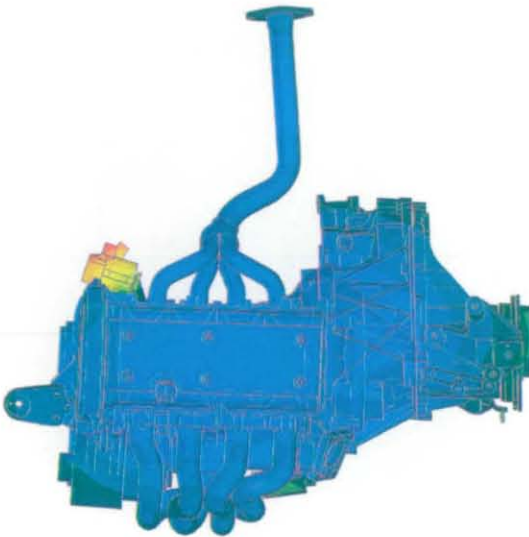


Figure 9a: Combined Powertrain Mode

Figure 9b: Combined Powertrain Mode

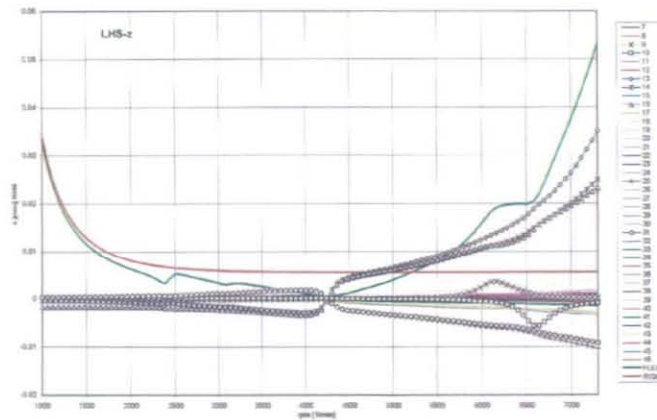


Figure 10: Mount Resonance Spectrum

## Conclusion

Applying the herein described methodology it is possible that the rotating crankshaft can be modelled adequately within the elastic powertrain structure to provide the eigenvalues and mode-shapes

of the coupled vibrations. The crankshaft behaves as an asymmetrical shaft being excited to whirl in the forward and reverse direction. The whirling path is altered by the engine speed from simple in-plane to complex shapes depending on the design configuration. Simplified and detailed modelling techniques were applied to represent the crankshaft assembly and it was found that a 3-D representation is required to correctly represent the stiffness and mass properties. Obtained results affirm that a qualitative representation of the engine structure and main bearing stiffness properties applying a pinned bearing model is acceptable for principle studies. A quantitative description applying a full powertrain and a simplified main bearing representation lead to a more accurate system representation, because at almost all eigenvalues deflections and restraints at the main bearings are so great that the bearing house will distort within the engine block following the crankshaft deformation.

Comparing standard and flexible flywheel designs a clear advantage is received from the standard flywheel in terms of crankshaft and powertrain vibration and therefrom impelled radiated noise, while the flexible flywheel reduce the stress amplitudes at the last web due to the decoupling of the crankshaft vibration from the flywheel oscillation.

Overall, the adequate treatment of the crankshaft dynamic properties in the powertrain assembly is very important in the development of optimised and harmonised systems. The approach of modelling running modes shows a dramatic influence on the all in all powertrain resonance under most running conditions. It would seem to be relatively easy to sketch the crankshaft assembly for a new engine design so that resonance will not occur or will be minimised within the running range of the engine. While the emphasis has been on crankshaft and powertrain eigenvalues and to some extent on main bearing acceleration it is certain that the more important consequence of crankshaft dynamics will be perceived on the structural and air-borne (radiated) noise of the powertrain.

### Acknowledgements

Dr.- Rafat Ali died in the final stages of this work. Thomas Grünert wishes to express his gratitude for all the help Dr. Ali gave him in his Ph.D. work, from which the substance of this paper was taken.

### Appendices

Mode	Description
9	Flywheel whirl and vertical transmission bending
10	Flywheel whirl, powertrain lateral bending, power-steering-pump
11	Flywheel whirl and power-steering-pump
13	Flywheel whirl, power-steering-pump, intake manifold, starter-motor, alternator, spark-plug-cover and left-hand-side-engine-mount
14	Flywheel whirl, spark-plug-cover, timing-belt-cover and left-hand-side-engine-mount
24	Pulley whirl, intake-manifold, timing-belt-cover and left-hand-side-engine-mount
31	Pulley whirl, intake-manifold, spark-plug-cover, alternator and left-hand-side-engine-mount

Table 1: Combined Whirling And Accessory Modes

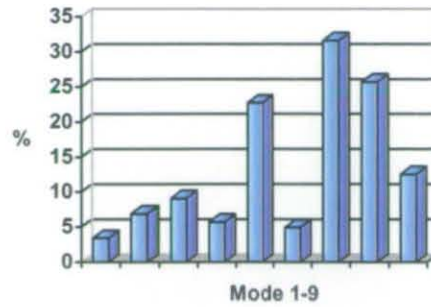


Figure 11: Percentage Difference of Beam- and Solid-Crankshaft Represented Whirling Modes

## References

- /1/ **Structure Borne Noise Prediction Techniques**  
SAE 900019; H.Priebsch, J.Affenzeller, G.Kuipers
- /2/ **Rotordynamik**  
Springer-Verlag; R.Gasch, H.Pfützner
- /3/ **Improvement of Engine Sound Quality Through a New Flywheel System Flexibly Mounted to the Crankshaft**  
SAE 900391; S.Ide, T.Uchida, K.Ozawa, K.Izawa
- /4/ **Vibrations of a Crankshaft**  
IMechE C99/71; D.Hodgetts
- /5/ **A Non-Linear Approach on Crank-Train Modelling**  
FORD CAE Technical Exchange; T.Grünert, J.Meyer
- /6/ **Development of a Finite-Element-Model for the Analysis of Cranktrain Dynamics**  
MSc-Thesis Loughborough University; T.Grünert
- /7/ **The Identification and Characterisation of Rumble and Thud**  
SAE Trans. 1960 68; E.Starkman, W.Sytz
- /8/ **Analysis of Engine Main-Bearing Excitation by Application of Cranktrain Modelling and Optimisation Methods**  
SAE 960985; T.Grünert, B.Pfingsthorn, J.Meyer, R.Ali
- /9/ **Structural Optimisation of Reciprocating Engines for Minimum Noise Radiation**  
PhD-Thesis Loughborough University; T.Zhang

